Geofluids

Coupled Geoflow Processes in Subsurface: CO_2-Sequestration and Geoenergy Focus

Lead Guest Editor: Meng Lu
Guest Editors: Tianfu Xu and Weon-Shik Han

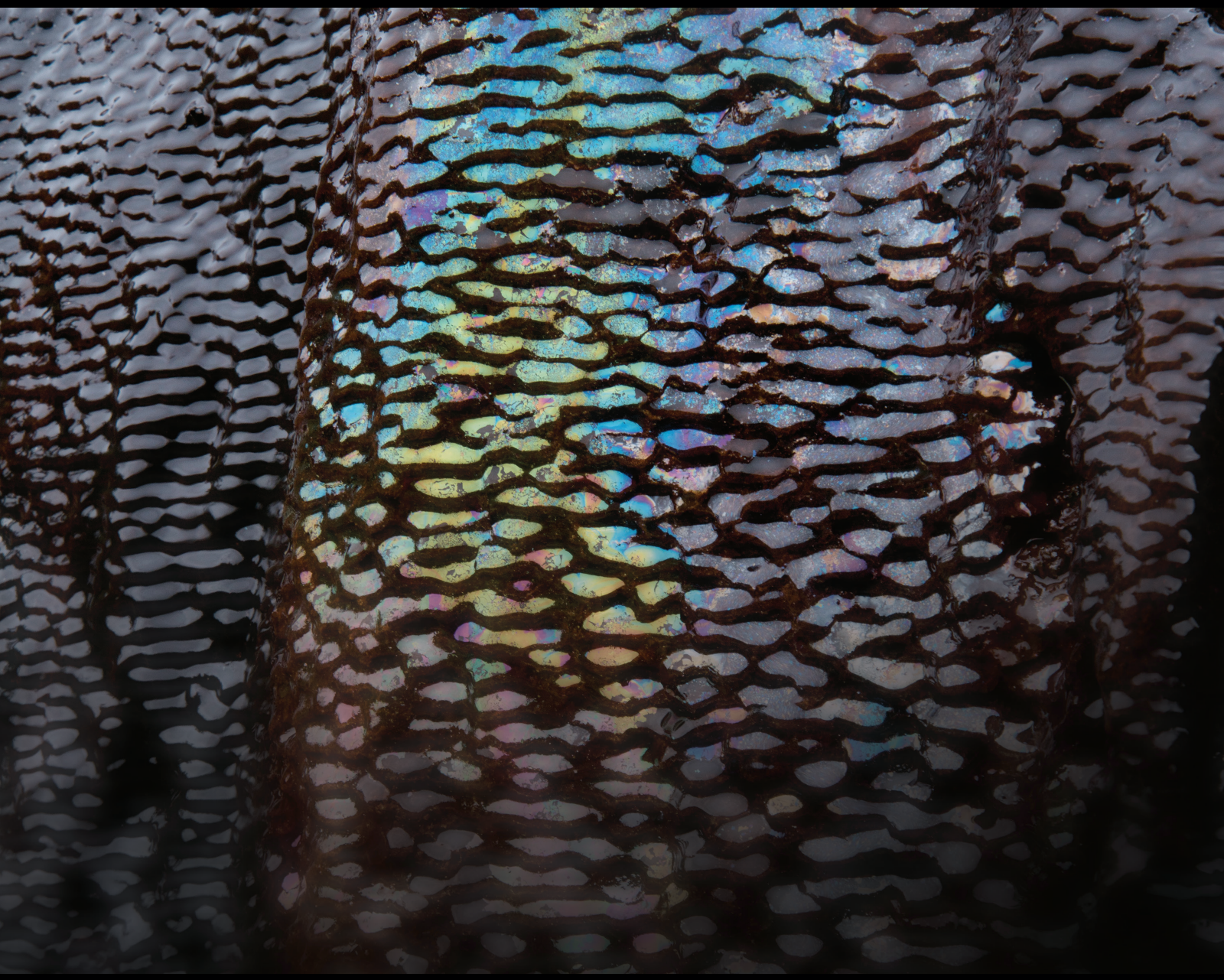

Coupled Geoflow Processes in Subsurface: CO_2-Sequestration and Geoenergy Focus

Geofluids

Coupled Geoflow Processes in Subsurface: CO_2-Sequestration and Geoenergy Focus

Lead Guest Editor: Meng Lu
Guest Editors: Tianfu Xu and Weon Shik Han

Editorial Board

Contents

Mesoscale Assessment of CO_2 Storage Potential and Geological Suitability for Target Area Selection in the Sichuan Basin
Yujie Diao, Guowei Zhu, Hong Cao, Chao Zhang, Xufeng Li, and Xiaolin Jin
Volume 2017, Article ID 9587872, 17 pages

On the Role of Thermal Stresses during Hydraulic Stimulation of Geothermal Reservoirs
Gunnar Jansen and Stephen A. Miller
Volume 2017, Article ID 4653278, 15 pages

Hindawi
Geofluids
Volume 2017, Article ID 5687586, 2 pages
https://doi.org/10.1155/2017/5687586

Editorial

Coupled Geoflow Processes in Subsurface: CO_2-Sequestration and Geoenergy Focus

Meng Lu,[1] Tianfu Xu,[2] and Weon Shik Han[3]

[1]*CSIRO, Canberra, ACT, Australia*
[2]*Key Laboratory of Groundwater Resources and Environment, Ministry of Education, Jilin University, Jilin, China*
[3]*Department of Earth System Sciences, Yonsei University, Seoul, Republic of Korea*

Correspondence should be addressed to Meng Lu; meng.lu@csiro.au

Received 27 September 2017; Accepted 28 September 2017; Published 20 November 2017

Global efforts to control greenhouse gas emissions into the atmosphere are currently made in two parallel aspects. One focuses on developing non-fossil energy technologies which generate no carbon. These include extensive use of solar, wind, and nuclear energies, acceleration of the pace of replacing fuel-powered vehicles by electric ones, and development of new techniques to boost the performance of energy storage devices. The other aspect is dedicated to using geology-based technologies to process carbon generated by the combustion of fossil fuels, namely, using carbon capture and storage (CCS) and geothermal energy techniques to mitigate greenhouse gas emission.

Although progress in pursuing those non-fossil energy technologies has been rapid, they still "satisfy only a small portion in the global energy demand" [1]. Even from the most optimistic point of view, the transition would need at least several decades for the fossil energy system on which modern civilisation is built to be replaced by these clean renewables or zero-carbons. On the other hand, the global emission of carbon is estimated currently at over 35,000 million tonnes per annum [2], and that emission rate may persist or even continue to increase until 2030 or later [3]. According to the IEA analysis, the world needs to capture and store around 4,000 million tonnes per annum (Mtpa) of CO_2 in 2040 till the end of this century. Otherwise, the ultimate goal of the Paris Agreement (limiting the temperature increase to "well below" 2°C) would not be reached [4]. In short, in terms of today's knowledge, geology-based technologies are considered to be the most realistic and a less costly major way to achieve reduction in global carbon emission. Development in this aspect is encouraging. For example, the "Global Status of CCS: 2016 Summary Report" listed 38 large-scale CCS projects launched or to be launched shortly around the world. These major projects, plus some others, were/are operated in North America (USA, Canada), South America, Europe, the Asia-Pacific region (China, Australia, Japan, Korea, etc.), and the Middle East. These projects will provide further insights into the safety, reliability, adaptability, and cost-efficiency involved.

This special issue provides some of the latest research outcomes in this aspect, and we want to share them with relevant communities of interest. The 11 articles published here are selected from 24 submissions. Many of the unselected ones contained valuable insights but regrettably did not meet the reviewers' strict standards. Of the 11 papers, 6 are related to CO_2-sequestration and the other 5 deal with geothermal energy utilisation. These articles, except for one review paper, demonstrate the relevant theoretical, numerical, laboratory, and field efforts at various organisational levels. A brief summary of the selected topics is given below.

For CO_2-sequestration, we have the following:

(i) The paper by A. R. Adebayo et al. presents an experimental study. The authors used Berea sandstone and Indiana limestone core samples to investigate the directional effect of water/gas flow that is associated with the CO_2-flow behaviour in pertinent sedimentary rocks.

(ii) The papers by both G. Yang et al. and L. Shi et al. are concerned with the Shenhua CCS demonstration

project in China, respectively. The former paper considers the relevant geochemistry in the formation, using numerical simulation to investigate the CO_2-injectivity there. The latter paper, based on analytical analyses, discusses the potential reservoir/wellbore failure risks during CO_2-sequestration in the formation where multilayered geological structures are present.

(iii) B. Bai et al. present a CO_2-EOR case study in the Shengli oilfield in China, while Y. Diao et al. propose a new method for assessing the suitability of a geological formation for CO_2-sequestration or CO_2-EOR/EGR/EWR and apply the method to analyse the suitability of the targeted Sichuan Basin (China) for these CO_2-related operations.

(iv) H. J. Liu et al. present a state-of-the-art review to the status of carbon capture, utilisation, and storage (CCUS) in the world, particularly summarising the latest progress of CCUS in China.

For geothermal energy utilisation, we have the following:

(i) K. J. Bakhsh et al. discuss the transport mechanisms within a thin thermally shocked region of an enhanced geothermal system (EGS) reservoir.

(ii) G. Jansen and S. A. Miller discuss the effect of thermal stresses during hydraulic stimulation of geothermal reservoirs.

(iii) F. Pan et al. conduct a field-scale geochemical simulation to investigate the CO_2-fluid-rock interaction in EGS reservoirs.

(iv) T. Xu et al., on the basis of the geological conditions of the Qingshankou Formation, Songliao Basin (China), investigate the CO_2 flow behaviour in a CO_2-plum geothermal system (CPG).

(v) B. Wu et al. work out an approximate solution for predicting heat extraction and preventing heat loss from a closed-loop geothermal reservoir.

We trust these works can further improve our understanding of the complex coupled geoflow processes in the subsurface in relation to CCS and the utilisation of geothermal energy. We expect these new observations, along with the previous knowledge and experience already disclosed elsewhere, may help further minimise the relevant risks and maximise operational efficiency. We look forward to seeing the implementation of more CCS and geothermal projects in the near future. The current scale of projects is far from sufficient to reach the Paris Agreement's goal. We wish that the formidable climate scenario which has been projected by various scientific analyses can ultimately be avoided through more active and effective human action.

Meng Lu
Tianfu Xu
Weon Shik Han

References

[1] Global status of CCS: 2016 summary report, Global CCS Institute, https://www.globalccsinstitute.com/publications/global-status-ccs-2016-summary-report.

[2] "Trends in Global CO_2 Emissions: 2016 Report," PBL Netherland Environmental Assessment Agency, http://edgar.jrc.ec.europa.eu/news_docs/jrc-2016-trends-in-global-co2-emissions-2016-report-103425.pdf.

[3] IEA, "Energy and Climate Change: World Energy Outlook Special Briefing for COP21," 2015, https://www.iea.org/media/news/WEO_INDC_Paper_Final_WEB.PDF.

[4] IPCC, "Climate Change 2014 Synthesis Report Summary for Policymakers," https://www.ipcc.ch/pdf/assessment-report/ar5/syr/AR5_SYR_FINAL_SPM.pdf.

Hindawi
Geofluids
Volume 2017, Article ID 5675370, 11 pages
https://doi.org/10.1155/2017/5675370

Research Article

Evaluation of CO_2-Fluid-Rock Interaction in Enhanced Geothermal Systems: Field-Scale Geochemical Simulations

Feng Pan,[1,2] Brian J. McPherson,[1,2] and John Kaszuba[3,4]

[1] *Energy & Geoscience Institute, The University of Utah, Salt Lake City, UT 84108, USA*
[2] *Department of Civil and Environmental Engineering, The University of Utah, Salt Lake City, UT 84112, USA*
[3] *Department of Geology & Geophysics, The University of Wyoming, Laramie, WY 82071, USA*
[4] *School of Energy Resources, The University of Wyoming, Laramie, WY 82071, USA*

Correspondence should be addressed to Feng Pan; fpan@utah.gov

Received 31 March 2017; Revised 3 August 2017; Accepted 5 September 2017; Published 18 October 2017

Academic Editor: Tianfu Xu

Recent studies suggest that using supercritical CO_2 ($scCO_2$) instead of water as a heat transmission fluid in Enhanced Geothermal Systems (EGS) may improve energy extraction. While CO_2-fluid-rock interactions at "typical" temperatures and pressures of subsurface reservoirs are fairly well known, such understanding for the elevated conditions of EGS is relatively unresolved. Geochemical impacts of CO_2 as a working fluid ("CO_2-EGS") compared to those for water as a working fluid (H_2O-EGS) are needed. The primary objectives of this study are (1) constraining geochemical processes associated with CO_2-fluid-rock interactions under the high pressures and temperatures of a typical CO_2-EGS site and (2) comparing geochemical impacts of CO_2-EGS to geochemical impacts of H_2O-EGS. The St. John's Dome CO_2-EGS research site in Arizona was adopted as a case study. A 3D model of the site was developed. Net heat extraction and mass flow production rates for CO_2-EGS were larger compared to H_2O-EGS, suggesting that using $scCO_2$ as a working fluid may enhance EGS heat extraction. More aqueous CO_2 accumulates within upper- and lower-lying layers than in the injection/production layers, reducing pH values and leading to increased dissolution and precipitation of minerals in those upper and lower layers. Dissolution of oligoclase for water as a working fluid shows smaller magnitude in rates and different distributions in profile than those for $scCO_2$ as a working fluid. It indicates that geochemical processes of $scCO_2$-rock interaction have significant effects on mineral dissolution and precipitation in magnitudes and distributions.

1. Introduction

Recent studies suggest that supercritical CO_2 ($scCO_2$) as a heat transmission fluid in Enhanced Geothermal Systems (EGS) can improve energy extraction compared to conventional water-based EGS [1–3]. We refer to such systems as CO_2-EGS and to EGS with water as a working fluid as H_2O-EGS. Advantages of using CO_2 as a heat transmission fluid include larger expansivity (compressibility) and lower viscosity compared to water; CO_2 is also a poor mineral solvent compared to water [1]. Disadvantages of CO_2 as a working fluid include a lower mass heat capacity than water, reducing its net energy content per unit volume, as well as the propensity for aqueous CO_2 to promote chemical reactions leading to changes in reservoir rock porosity and permeability [4]. However, CO_2-EGS data, as well as comparisons of CO_2-EGS to H_2O-EGS, are limited. A primary goal of this study is to constrain geochemical reactions induced by CO_2-fluid-rock interactions in EGS reservoirs. An additional goal is to compare geochemical impacts of CO_2-EGS to the geochemical impacts of H_2O-EGS.

Several recent experimental and numerical efforts quantify geochemical reactions associated with CO_2 injection in EGS reservoirs [2, 3, 5–10]. Pruess [2, 3] compared CO_2 and water with respect to heat extraction rate and mass flow rate in EGS reservoirs. Heat extraction and flow rate largely increase with CO_2 as the working fluid, suggesting that CO_2 offers potential benefits as a working fluid in EGS reservoirs. Rosenbauer et al. [8] experimentally tested CO_2-brine-rock interactions at 120°C and 20–30 MPa. Results suggested that dissolved CO_2 may enhance water-rock interaction and CO_2

sequestration in carbonate minerals. Lo Ré et al. [6] conducted five hydrothermal experiments to evaluate geochemical and mineralogical response of fractured granitic rocks to CO_2 injection at geothermal conditions of at 250°C and 25–45 MPa. Experimental results suggest that precipitation of clay (smectite and illite) may affect reservoir porosity and permeability, and carbonate formation may require extended periods of time. Jung et al. [5] performed reactive transport modeling to study fluid-rock interactions in a typical geothermal system and calibrated the geochemical model by adjusting the reactive surface area to fit the experimental data of mineral dissolution. Na et al. [7] performed laboratory experiments to study CO_2-fluid-rock chemical reactions at high temperatures and pressures in geothermal systems and conducted batch simulations to analyze the experimental data. Wan et al. [9] and Xu et al. [10] simulated geochemical processes of fluid-rock interactions within CO_2-EGS under high pressures and temperatures, and results suggest that significant CO_2 may be stored in EGS reservoirs by mineral trapping by precipitation of carbonate minerals. Xu et al. [11] also performed batch geochemical simulations for three different aquifer lithologies to evaluate long-term CO_2 disposal in deep aquifers. Results suggest that CO_2 sequestration by mineral trapping varies largely with rock type and mineral composition, and porosity decreases due to precipitation of carbonates. André et al. (2007) conducted numerical modeling of fluid-rock chemical interactions of two CO_2 injection scenarios, CO_2-saturated water and supercritical CO_2, in a deep carbonate aquifer. Their results suggest that geochemical reactivity with supercritical CO_2 injection was much lower than reactivity with CO_2-saturated water.

Although these experimental and numerical studies address many aspects of geochemical reactions induced by CO_2-fluid-rock interactions in geothermal systems, three-dimensional (3D) geochemical simulations of CO_2-fluid-rock interaction at high temperature and pressure in EGS reservoirs are relatively rare. Therefore, a primary objective of this study is to simulate and evaluate geochemical processes induced by CO_2-fluid-rock interactions at the elevated temperatures and pressures of a CO_2-EGS. A secondary objective is to compare geochemical impacts within a CO_2-EGS to those within an H_2O-EGS. The TOUGHREACT model [12] with the ECO2H module [13] was used to conduct simulations of CO_2-fluid-rock interactions in a CO_2-EGS reservoir. The St. John's Dome CO_2-EGS research site in Arizona was used as a case study example.

2. Material and Methods

2.1. St. John's Dome CO_2-EGS Research Site. St. John's Dome is located along the boundary between Arizona and New Mexico, about half way between the Four Corners area and the Mexican Border. St. John's Dome is part of the Colorado Plateau and covers an area of approximately 1,800 km^2 ([14]; Rauzi, personal communication, 2013). The dome consists of a broad, asymmetric anticline that trends northwest with an axis that plunges to the northwest and the southeast. The dome is notable for hosting a gas field consisting of nearly pure CO_2; the Fort Apache, Big A Butte, and Amos Wash members of the Supai Formation (Permian) are the primary CO_2 reservoirs. The caprock above each CO_2-rich zone consists of anhydrite and mudstones [15]; basement consists of Precambrian granite.

Exploration and research of the geothermal potential of St. John's Dome extends back at least into the 1970s. More than 40 wells have been drilled to determine the gas reserves. Bottom-hole temperature measurements have been taken in seven of these wells. Temperature gradients appear to be highest in the south-central portion of the dome; the temperature at a depth of 3 km in this part of the dome is 150°C or greater. Based on identified geothermal resources and large volumes of CO_2, the St. John's Dome is uniquely suitable for developing CO_2-EGS because it greatly reduces the risk and cost of testing and developing the technology.

2.2. 3D Model Setup. We elected to adopt a 5-spot well pattern because of its wide application in oil fields and geothermal reservoirs [3, 9, 17–22]. The resulting 3D model domain with its 5-spot well pattern is illustrated in Figure 1. Due to the symmetry of the 5-spot well pattern, we employed a 1/8 symmetry domain (of the 5-spot pattern) for all simulations (Figure 1). The domain is 500 m in the vertical direction with a layered geological setting, including 100 m thick fractured rock at the middle and 200 m thick granite above and below the fractured rock zone, respectively (Figure 1). The grid cell size is uniform at 70.7 m horizontally (X and Y directions) and 50 m vertically (Z direction). We also implemented a dual-continuum approach at the 100 m thick center of the model domain to represent a typical fractured EGS reservoir.

We collected all publicly-available hydrologic data for wells near St. John's Dome, primarily from files of Arizona Geological Survey. The mean value of measured permeability (0.25 mD) was assigned to all fractured aspects of the model. The MINC (multiple interacting continua) of TOUGH2 code [23] is used to represent matrix-fracture heat transfer with a fracture spacing of 50 m and fracture volume fraction of 2%. Injection and production wells are placed at the bottom of the fractured rock layer with a depth of 275 m from the top of domain and 2000 m from the surface (Figure 1). Assigned initial conditions include hydrostatic pressure and conductive heat flow (temperature gradient 40°C/km), with 20 MPa and 200°C at 275 m depth from the top of the domain. A Dirichlet boundary condition (constant pressure) is assigned to boundaries of injection and production, with a pressure drop of 2.5 MPa between the injection and production wells. For wells, constant pressure is assigned as initial plus 1.25 MPa at the injection well and initial minus 1.25 MPa at the production well. A Neumann condition (no flow) is assigned on all other sides. Details of parameter settings are summarized in Table 1.

2.3. Mineralogical Assemblages in St. John's Dome Field Site. Two core samples of the Precambrian granite from one of the Arizona wells (22-1X State) at Springerville-St. John's CO_2 research site [24] were analyzed using X-ray diffraction

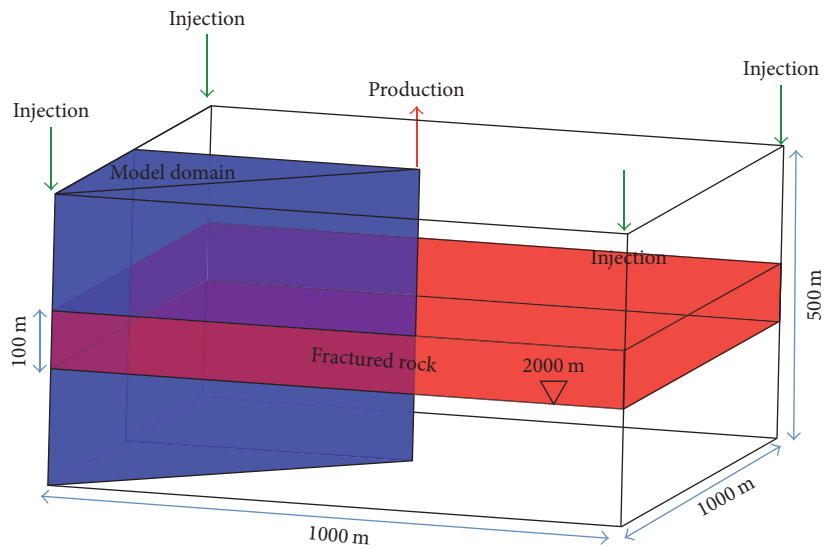

Figure 1: Schematic of the 3D numerical model domain with a 5-spot well pattern (1/8 system domain used for all simulations).

Table 1: Hydrologic parameters, initial, and injection/production boundary conditions used for 3D simulations of a 5-spot well pattern.

Properties	
Fractured rock permeability	$2.47 * 10^{-16}$ m^2 (0.25 mD)
High granite permeability	$9.87 * 10^{-18}$ m^2 (0.01 mD)
Fracture spacing	50 m
Fracture volume fraction	2%
Fracture porosity	0.50
Granite porosity	0.08
Fracture tortuosity	1.0
Thermal conductivity	2.51 W/m°C
Rock specific heat	1000 J/kg°C
Rock grain density	2650 kg/m^3
Initial condition	
Reservoir fluid	All water
Initial temperature	200°C at the layer of production well with 40°C/km geothermal gradient
Initial pressure	Hydrostatic pressure with 20 Mpa at the layer of production well
Production/injection condition	
Injection/production Well distance	707 m
Injection pressure	Initial +1.25 MPa
Injection temperature	50°C
Production pressure	Initial −1.25 MPa

(XRD) at the Energy & Geoscience Institute, University of Utah. The Arizona well 22-1X State is located near the northern boundary of the St. John's CO_2 field at an elevation of 1949 m at the ground level; the well penetrates the Permian Supai Formation at a depth from 195 m to 628 m below the surface and Precambrian granite below that [14]. The two core samples for Precambrian granite were collected at depths of 640.8 m and 647.4 m. The two samples consist mainly of quartz (45–50%), plagioclase (26–30%), and K-feldspar (19–21%). An average percentage of the mineralogical assemblages of the two samples (Table 2) were used in the simulations. Potential secondary minerals were identified using equilibrium batch modeling, as follows. Firstly, CO_2 was added to the initial formation brine in contact with the primary mineral assemblage, and the saturation indices of all minerals present in the database were calculated and analyzed. Minerals that became supersaturated and have the potential to form under the given conditions were included as secondary minerals. Then, batch models were reexecuted with the new (resulting) mineral assemblage until an equilibrium aqueous solution was reached. The primary mineral assemblage and possible secondary minerals are listed in Table 3; kinetic properties for these minerals are listed in Table 4. The kinetic properties (rate constant, activation

Table 2: Mineral assemblages of core samples from Precambrian granite in Arizona well 22-1X State in the St. John's CO_2 field.

Minerals	Minerals composition (Sample 1 at 640.8 m)	Minerals composition (Sample 2 at 647.4 m)
Quartz	50%	45%
Plagioclase	26%	30%
K-feldspar	21%	19%
Biotite	1%	2%
Muscovite	2%	3%
Total	100%	99%

Table 3: Chemical composition and initial volume fractions of primary and secondary minerals for geochemical simulations of the St. John's CO_2 field site.

Mineral	Chemical composition	Initial volume fraction of minerals
	Primary	
Quartz	SiO_2	0.475
Oligoclase	$Na_{0.77}Ca_{0.23}Al_{1.23}Si_{2.77}O_8$	0.280
K-Feldspar	$KAlSi_3O_8$	0.200
Annite[a]	$KFe_3AlSi_3O_{10}(OH)_2$	0.0075
Phlogopite[a]	$KAlMg_3Si_3O_{10}(OH)_2$	0.0075
Muscovite	$KAl_3Si_3O_{10}(OH)_2$	0.025
	Secondary	
Calcite	$CaCO_3$	0.0
Magnesite	$MgCO_3$	0.0
Illite	$(K,H_3O)(Al,Mg,Fe)_2(Si,Al)_4O_{10}[(OH)_2,(H_2O)]$	0.0
Smectite	$K_{0.04}Ca_{0.5}(Al_{2.8}Fe_{0.53}Mg_{0.7})(Si_{7.65}Al_{0.35})O_{20}(OH)_4$	0.0
Kaolinite	$Al_2Si_2O_5(OH)_4$	0.0
Chlorite	$Mg_{2.5}Fe_{2.5}Al_2Si_3O_{10}(OH)_8$	0.0
Albite	$NaAlSi_3O_8$	0.0
Hematite	Fe_2O_3	0.0
Dolomite	$CaMg(CO_3)_2$	0.0
Ankerite	$CaMg_{0.3}Fe_{0.7}(CO_3)_2$	0.0
Dawsonite	$NaAlCO_3(OH)_2$	0.0
Siderite	$FeCO_3$	0.0

[a]Biotite is assumed as 50% of Annite and 50% of Phlogopite.

Table 4: Kinetic rate parameters of primary and secondary minerals and reactive surface area for the geochemical simulations of the St. John's CO_2 research site.

Mineral	Neutral mechanism		Acid mechanism			Base mechanism			Reactive surface area
	$\log k$[a]	E_a[b]	$\log k$[a]	E_a[b]	n[c]	$\log k$[a]	E_a[b]	n[c]	(cm^2/g)
					Primary				
Quartz	−13.99	87.7	—	—	—	—	—	—	9.8
Oligoclase	−11.84	69.8	−9.67	65.0	0.457	—	—	—	9.8
K-feldspar	−12.41	38.0	−10.06	51.7	0.500	−21.2	94.1	−0.823	9.8
Annite[d]	−12.55	22.0	−9.84	22.0	0.525	—	—	—	9.8
Phlogopite	−12.40	29.0	—	—	—	—	—	—	9.8
Muscovite	−13.55	22.0	−11.85	22.0	0.370	−14.55	22.0	−0.220	151.6
					Secondary				
Calcite	−5.81	23.5	−0.30	14.4	1.000	—	—	—	9.8
Magnesite	−9.34	23.5	−6.38	14.4	1.000	—	—	—	9.8
Illite[e]	−13.55	22.0	−11.85	22.0	0.370	−14.55	22.0	−0.220	151.6
Smectite	−12.78	35.0	−10.98	23.6	0.340	−16.52	58.9	−0.400	151.6
Kaolinite	−13.16	22.2	−11.31	65.9	0.777	−17.05	17.9	−0.472	151.6
Chlorite	−12.52	88.0	−11.11	88.0	0.500	—	—	—	9.8
Albite	−12.56	69.8	−10.16	65.0	0.457	−15.6	71.0	−0.572	9.8
Hematite	−14.60	66.2	−9.39	66.2	1.000	—	—	—	9.8
Dolomite	−7.53	52.2	−3.19	36.1	0.500	−5.11	34.8	0.500	9.8
Ankerite[f]	−7.53	52.2	−3.19	36.1	0.500	−5.11	34.8	0.500	9.8
Dawsonite	−7.00	62.8	—	—	—	—	—	—	9.8
Siderite	−8.90	62.8	−3.19	36.1	0.500	—	—	—	9.8

Note. Kinetic rate parameters from Palandri and Kharaka [16]; [a]$\log k$: kinetic rate constant k at 25°C ($mol/m^2/s$); [b]E_a: activation energy (KJ/mol); [c]n: power term with respect to H^+; [d]set to Biotite; [e]set to Muscovite; [f]set to Dolomite.

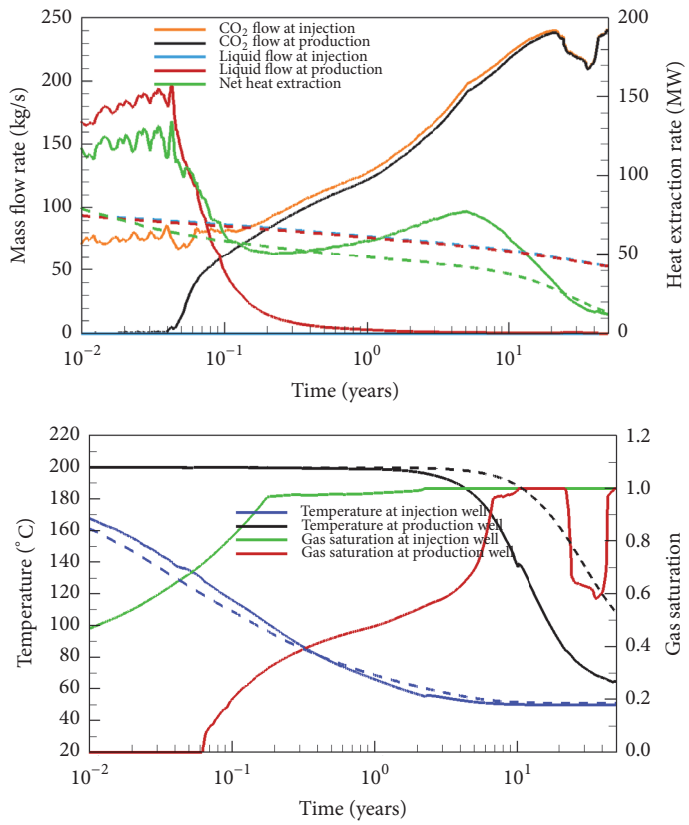

Figure 2: Simulated heat extraction rate, mass flow rate, temperature, and gas saturation next to production well for $scCO_2$ (solid line) and water (dash line) as working fluids, respectively.

energy, and power term) of multiple mechanisms (neutral, acid, and base) for primary and possible secondary minerals are taken from Palandri and Kharaka [16]. The reactive surface areas of some minerals (e.g., quartz, oligoclase, albite, K-feldspar, calcite, magnesite, kaolinite, siderite, illite, and smectitie) are taken from Xu et al. [11]. Values for other minerals are assumed as 9.8 cm^2/g. All geochemical simulations utilize the EQ3/6 thermodynamic database v7.2b (data0.dat; [25]), and all flow aspects are simulated (for 50-year simulation time) using the TOUGHREACT/ECO2H model [12, 26]. A set of batch simulations were conducted first, to obtain initial aqueous solutions that would be in equilibrium with the primary minerals.

2.4. Numerical Models. The TOUGHREACT model [12] with its ECO2H module [13] was used to conduct all geochemical simulations. The TOUGHREACT code was developed to simulate nonisothermal multicomponent reactive fluid flow and geochemical transport by addressing reactive geochemistry with multiphase flow and heat flow [12, 26]. TOUGHREACT has been applied to subsurface thermophysical-chemical processes in various environmental problems and geologic systems. The ECO2H module of TOUGHREACT code is designed for applications to geological sequestration of CO_2 in saline aquifers at high temperature and pressure [13]. The resident equation of state provides an accurate and comprehensive description of thermodynamics and thermophysical properties of water-brine-CO_2 mixtures to 243°C and 67.6 MPa [19].

3. Results

3.1. Results of Flow and Heat Simulation at St. John's Dome Site. Figure 2 plots net heat extraction rate, mass flow rate, temperature and gas saturation at the gridblock next to the injection, and production wells for the model with $scCO_2$ as the working fluid. Results for water as a working fluid are also plotted in Figure 2. For the case of $scCO_2$ as a working fluid, flow containing water only is produced at a rate of ~180 kg/s during the initial stages of simulation. After 0.05 years, the produced water flow rate sharply decreases as the flow rate of produced CO_2 increases, demonstrating the mixture of water and CO_2 produced when $scCO_2$ has reached the production well. With continuous CO_2 injection and increases in gas saturation at the production well, the produced CO_2 flow rate significantly increases with no water production. The oscillation in mass flow and heat extraction rate at the early stages of simulation (Figure 2) is a simulation artifact. Specifically, this minor oscillation is a numerical response to maintain constant pressure at the wellbore; an absolute constant pressure in a wellbore cannot exist in nature, and to force such in a simulation translates to some oscillatory

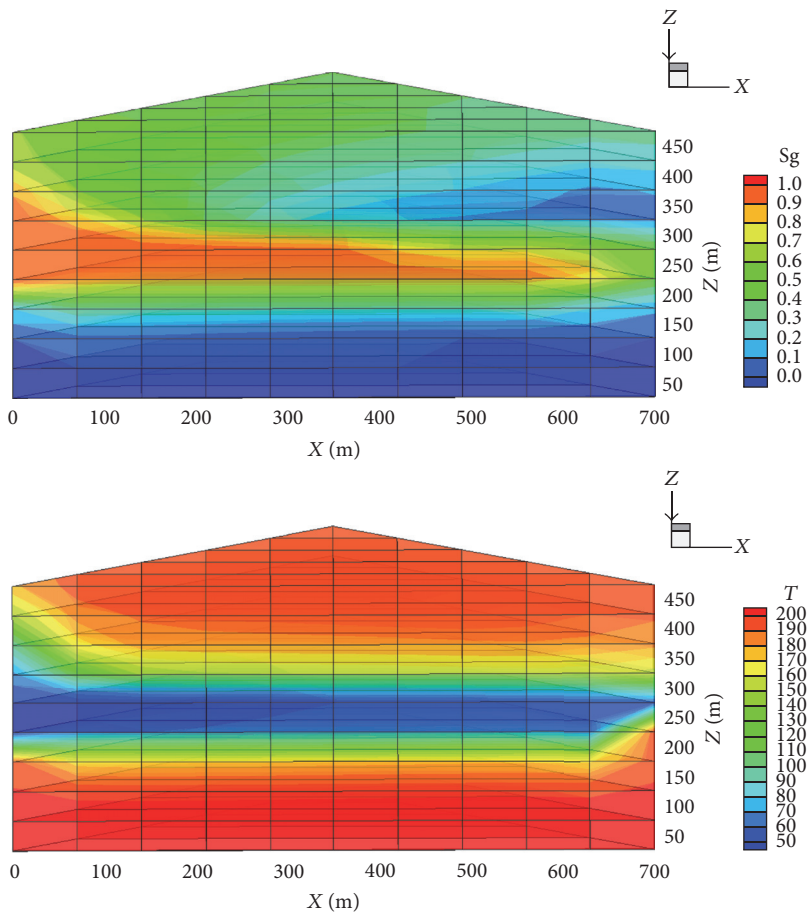

Figure 3: Simulated 3D profiles of gas saturation and temperature after 30-year injection of $scCO_2$ as a working fluid.

variability in flows. We adopted fixed wellbore pressure at depth, despite the minor oscillation artifact, because it is a common approach of analysis. The net heat extraction rate is around 120 MW in the initial stage of simulation and decreases to 60 MW after 0.1 years, a trend similar to the produced water flow rate. With increases of produced CO_2 flow rate, the net heat extraction increases to its maximum of 80 MW after 5 years of CO_2 injection. With continuous increase of CO_2 gas saturation at the production well, the net heat extraction decreases to 12 MW after 50 years of CO_2 injection. This is due to more rapid thermal depletion of CO_2 compared to water, associated with the rapid decrease of simulated temperature (Figure 2). The CO_2 saturation next to the injection well becomes 100% after 0.2 years of CO_2 injection. The CO_2 flow breaks through to the production well after 0.06 years of injection and gas saturation continues increasing to 1.0 after 10 years of CO_2 injection. However, the gas saturation decreases from 1.0 to 0.6 at the production well after 20 years of CO_2 injection, demonstrating possible CO_2 leakage to upper-lying layers (Figure 3). The temperature next to the injection well decreases from the initial temperature of 200°C to the injection temperature of 50°C. The temperature next to the production well remains constant at the initial temperature of 200°C until around 2 years of CO_2 injection and then drops to 65°C after 50 years of CO_2 injection.

Figure 3 plots simulated 3D profiles of gas saturation and temperature after 30 years of $scCO_2$ injection (as a working fluid). The gas saturation at the layer of injection/production well decreases from 1.0 to 0.5 toward the production well after 30 years. The gas saturation varies from 0.2 to 0.5 in the area of upper-lying layers after 30 years, demonstrating that simulated CO_2 leakage occurs and CO_2 breakthrough in caprock may constitute a leakage risk. The gas saturation is around 0.5 in the layer just below the injection/production well (Figure 3). The 3D temperature profile exhibits a similar trend as the gas saturation profile, which increases from 50°C at the injection well to 80°C at the production well (Figure 3), similar to the results in Figure 2. The temperature drop also occurs in the layers just above and below the injection/production layer, associated with large gas saturation in that area.

For water as a working fluid, the mass flow rate next to the production well decreases from 100 kg/s at the initial stage of simulation to 53 kg/s after 50 years of water injection (Figure 2), which is less than the 180 kg/s initial rate and less than the 150 to 250 kg/s of the produced CO_2 flow rate at the late stage of simulations with $scCO_2$ as a working fluid. A possible explanation for this phenomenon is the lower viscosity of $scCO_2$ compared to water. The net heat extraction for water as a working fluid has similar trends

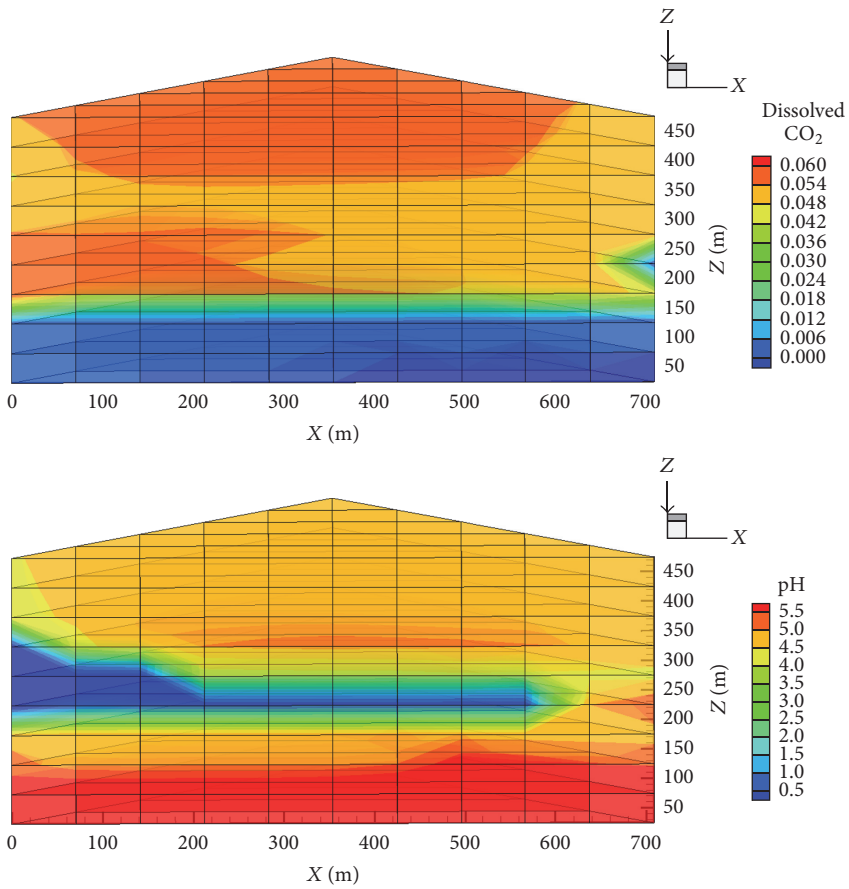

Figure 4: Simulated 3D profiles of dissolved CO_2 mass fraction in aqueous phase and pH values after 30-year injection of $scCO_2$ as a working fluid.

for the produced water flow rate, which also decreases from 80 MW at the initial stage to 10 MW after 50 years (Figure 2). The net heat extraction rate for $scCO_2$ as a working fluid varies from 12 to 180 MW during the simulation period and is much larger than the rate for water as a working fluid, indicating that $scCO_2$ as a working fluid could enhance heat extraction compared to water, at least for a generic 5-spot well pattern.

3.2. Results of Geochemical Simulation at St. John's Dome Site. Figure 4 plots simulated 3D profiles of aqueous CO_2 mass fraction and pH values after 30 years. Figures 5 and 6 illustrate simulated 3D profiles of changes of mineral abundances (in volume fraction) for selected primary minerals (oligoclase and quartz) and secondary minerals (calcite and illite). From the beginning of $scCO_2$ injection, $scCO_2$ dissolution in water increased the dissolved CO_2 concentration and lowered pH values (compared to the initial pH value of 5.4) (Figure 4). The pH values are artificially set to 0 if the saturation in gas phase is 1.0. The dissolved CO_2 and lowered pH values induced dissolution of primary minerals and precipitation of secondary minerals. Aqueous CO_2 is observed at the upper- and lower-lying layers (Figure 4), which exhibits larger dissolved CO_2 mass fractions than values at the injection/production layer after 30 years. A reverse trend is associated with the gas saturation distribution (Figure 3), indicating that more CO_2 dissolves in the aqueous phase with lower gas saturation in upper- and lower-lying layers. The pH values in the injection/production layer are smaller than the initial pH value of 5.4 and increase toward the production well (Figure 4), which is similar to the pattern of gas saturation (Figure 3). The higher the gas saturation, the lower pH values, in general.

The primary mineral oligoclase dissolves from the beginning of CO_2 injection. As indicated by Figure 5, a general trend of more dissolution in the upper-lying layers and the layer just below the injection/production layer is observed after 30 years of CO_2 injection. We infer this to be because water is produced gradually from the production well while supercritical CO_2 (gas phase) spreads from the injection well toward the production well, and no chemical reactions occur between $scCO_2$ (nonaqueous CO_2) and minerals. The primary mineral quartz may precipitate or dissolve after 30 years (Figure 5). The quartz slightly dissolves in water-dominated areas and precipitates in CO_2-laden areas (Figure 5). We infer this to be because the lower pH values in areas reached by CO_2 result in precipitation of quartz; pH values approaching 5.4 in the water-dominated area lead to dissolution of quartz. The distribution of quartz precipitation has similar patterns and characteristics to the mineral oligoclase. The more

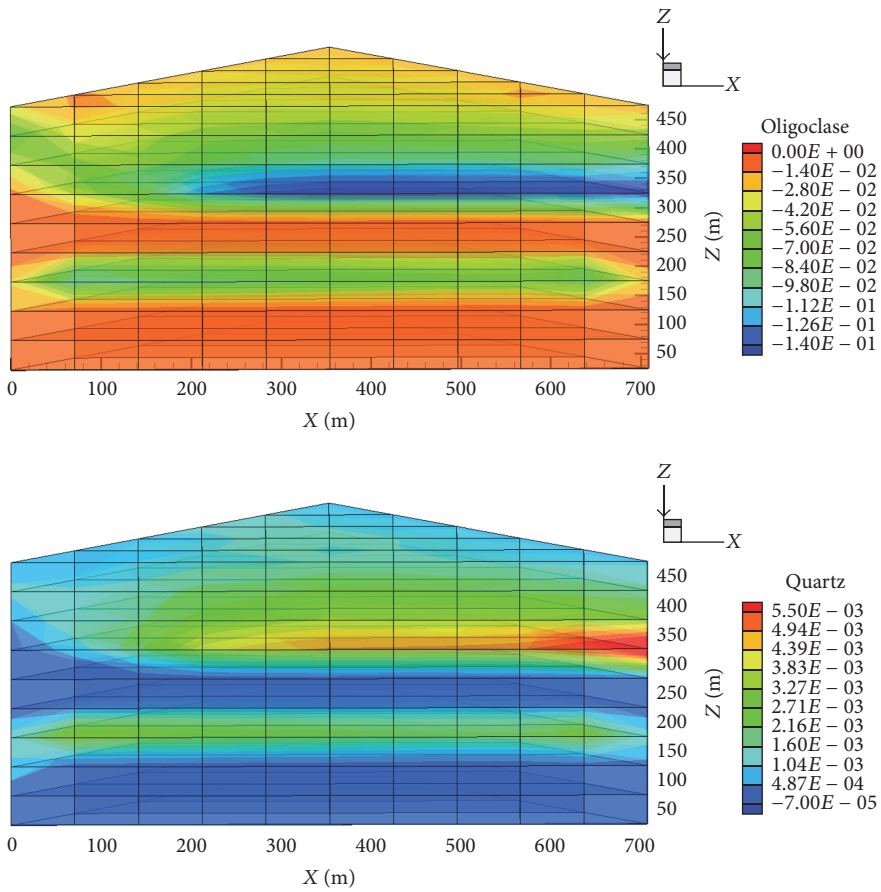

Figure 5: Simulated 3D profiles of changes of mineral abundance (in volume fraction) for primary minerals (oligoclase and quartz) after 30-year injection of $scCO_2$ as a working fluid.

precipitation of quartz occurs within the upper-lying layers and the layer just below injection/production layer (Figure 5).

Calcite precipitates after 1 year of CO_2 injection (figure not shown). The calcite precipitation distribution also shows similar patterns to the oligoclase dissolution profile. More calcite is precipitated in the upper-lying layers and the layer just below injection/production layer after 30 years (Figure 6) than the injection/production layer, tracking the distribution of dissolved CO_2 in the aqueous phase (Figure 4) and CO_2 in gaseous phase (Figure 3). Relatively large amounts of illite precipitation also occur in the same areas with large amounts of calcite precipitation, also tracking aqueous phase CO_2. The characteristics and distributions of dissolution or precipitation for other minerals (e.g., albite, K-feldspar, and siderite) are similar to trends for oligoclase, calcite, and illite (figures not shown).

Figure 7 describes the cumulative CO_2 sequestered by carbonate mineral precipitation for $scCO_2$ as a working fluid after 30 years. The total CO_2 sequestered by carbonate precipitation is around 1.5–3.0 kg/m^3 in the upper-lying layers, which is much larger than the value of 0.2 kg/m^3 at the injection/production layer. The 3D distribution of total CO_2 sequestered is identical to the amount consumed by calcite precipitation (Figure 6) and to the dissolved aqueous CO_2 amount (Figure 6) after 30 years of CO_2 injection. This relationship is consistent with $scCO_2$ in the gas phase mainly occupying the layer of injection/production wells (Figure 4) and the two phases of water-gas mixtures exist in the area of the upper-lying layers after 30 years, resulting in more dissolved CO_2 in these areas (Figure 3). Therefore, more dissolution and precipitation occur in the upper-lying layers.

To compare the effects of $scCO_2$ as a working fluid (to water) on chemical interactions, we also simulated the 3D geochemical processes at St. John's Dome Site for water as a working fluid for 50 years. Figure 8 plots simulated pH values and changes of mineral abundances (in volume fraction) for primary mineral (oligoclase) after 30 years for water as a working fluid. The simulated pH values for water as a working fluid increase from the initial value of 5.4 (Figure 8), which decrease for $scCO_2$ as a working fluid (Figure 4). The dissolution of mineral oligoclase for water as a working fluid (Figure 8) shows smaller magnitude in rates and different distributions in profile than the ones for $scCO_2$ as a working fluid (Figure 5). The more dissolution of oligoclase occurs in the area above the injection well, and the area close to the production well for water as a working fluid but more dissolution of oligoclase is simulated in the area above the injection/production layer for $scCO_2$ as a working fluid. Other primary and secondary minerals also exhibit significantly different dissolution or precipitation rates and

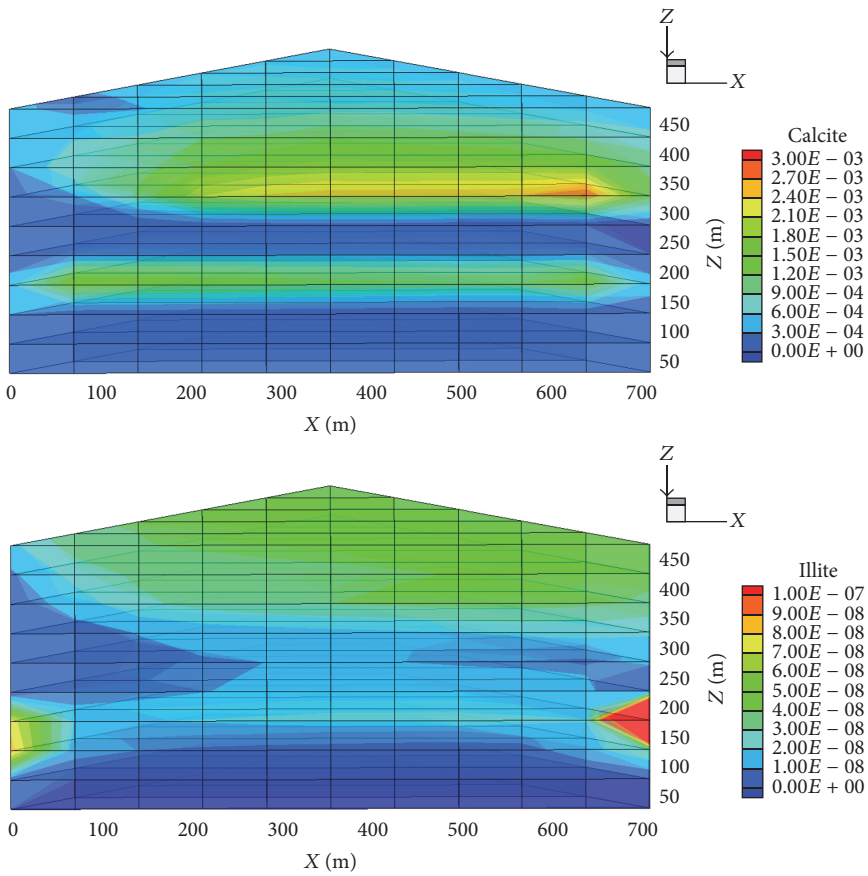

Figure 6: Simulated 3D profiles of changes of mineral abundance (in volume fraction) for secondary minerals (calcite and illite) after 30-year injection of $scCO_2$ as a working fluid.

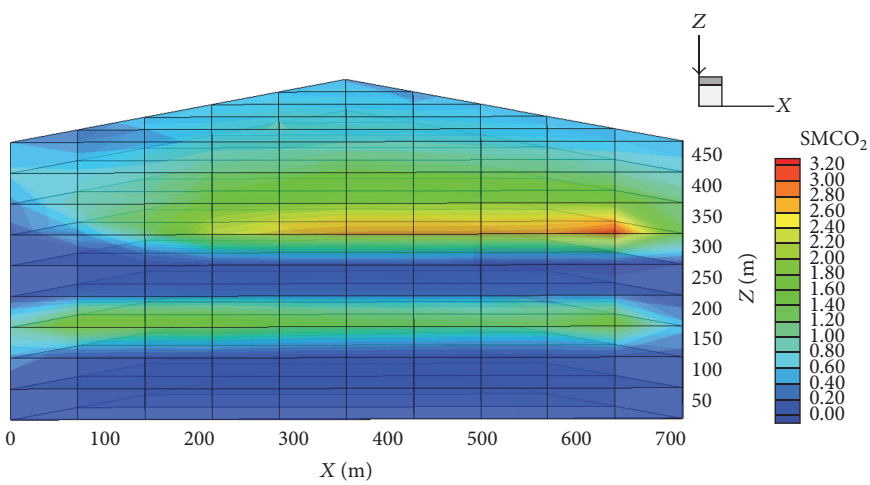

Figure 7: Simulated 3D profile of cumulative CO_2 sequestered (kg/m^3) by carbonate mineral precipitation after 30-year injection of $scCO_2$ as a working fluid.

patterns for water as a working fluid (figures not shown) from the ones for $scCO_2$ as a working fluid. It indicates that the geochemical processes of $scCO_2$-rock interaction have significant effects on mineral dissolution and precipitation in magnitudes and distributions.

4. Conclusions

A 3D model of the St. John's Dome CO_2-EGS site was employed to simulate flow, heat extraction, and geochemical processes induced by CO_2-fluid-rock interactions. Net heat

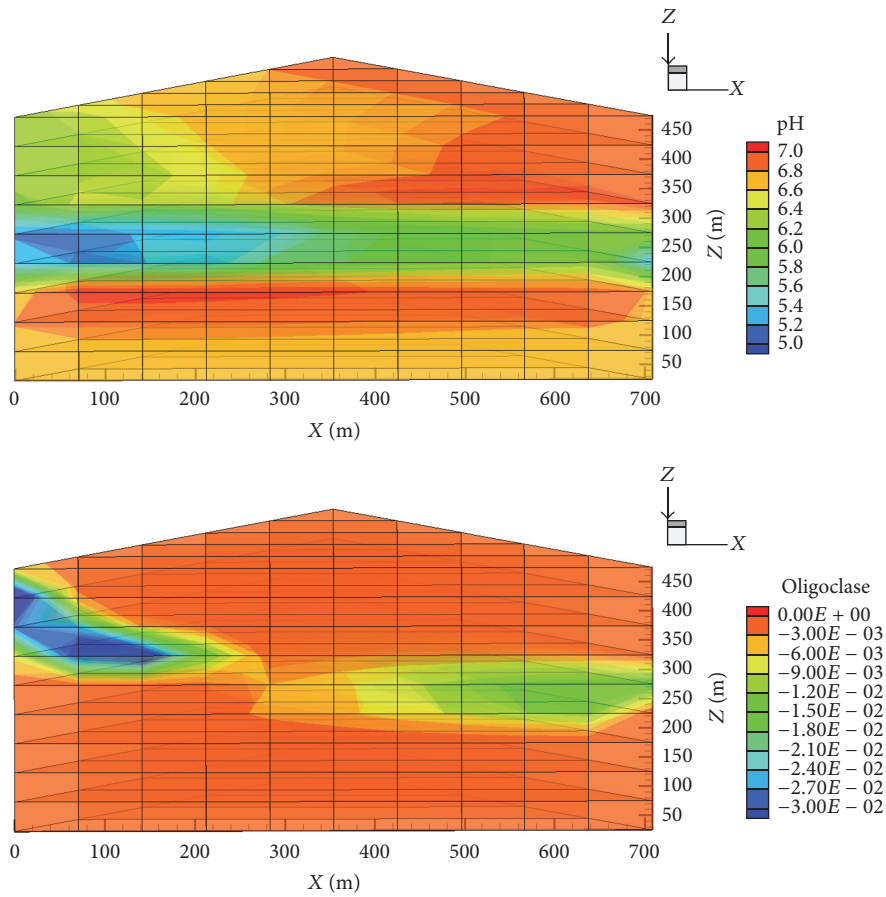

Figure 8: Simulated 3D profiles of pH values and changes of mineral abundance (in volume fraction) for primary mineral oligoclase after 30-year injection of water as a working fluid.

extraction and mass flow production rates for $scCO_2$ as a working fluid were larger (X to Y) compared to water (A to B) as a working fluid, indicating $scCO_2$ as a working fluid may enhance EGS heat extraction (consistent with Pruess [2, 3]). Simulated CO_2 saturation suggests that CO_2 breakthrough in caprock may constitute a leakage risk, at least for the specific case of the St. John's Dome CO_2-EGS research site. Simulations also suggest that more aqueous CO_2 accumulates within the upper- and lower-lying layers than within the injection/production layer, decreasing pH values and promoting dissolution and precipitation of minerals in the upper- and lower-lying layers of the system. Precipitation of carbonate minerals in the upper-lying layers suggests favorable CO_2 storage (with respect to mineral trapping) in EGS reservoirs. Dissolution of oligoclase for water as a working fluid shows smaller magnitude in rates and different distributions in profile than those for $scCO_2$ as a working fluid. It indicates that geochemical processes of $scCO_2$-rock interaction have significant effects on mineral dissolution and precipitation in magnitudes and distributions. Results of this study improve understanding of geochemical processes within CO_2-EGS reservoirs and provide implications for enhanced energy extraction and geological CO_2 sequestration.

Conflicts of Interest

The authors declare that they have no conflicts of interest.

Acknowledgments

This study was supported by the Geothermal Technologies Program of the US Department of Energy under Contract no. DE – EE0002766. The research of the first author is partly supported by the Utah Science Technology and Research Initiative (USTAR). The authors would like to thank Drs. Tianfu Xu and Hailong Tian at Jilin University for their help on TOUGHREACT model; Drs. Peter Lichtner and Satish Karra at Los Alamos National Laboratory for their help on the reactive transport simulations; Dr. Joe Moore at the University of Utah for the XRD analysis on two rock samples in St. John's Dome; Mr. John Muir and Mr. Alan Eastman for their help on the information of St. John's Dome CO_2-EGS site.

References

[1] D. Brown, "A hot dry rock geothermal energy concept utilizing supercritical CO_2 instead of water," in *Proceedings of Twenty-Fifth Workshop on Geothermal Reservoir Engineering*, Stanford University, Stanford, California, 2000.

[2] K. Pruess, "Enhanced geothermal systems (EGS): Comparing water and CO_2 as heat transmission fluids," in *Proceedings of New Zealand Geothermal Workshop*, Auckland, New Zealand, 2007.

[3] K. Pruess, "On production behavior of enhanced geothermal systems with CO_2 as working fluid," *Energy Conversion and Management*, vol. 49, no. 6, pp. 1446–1454, 2008.

[4] T. Xu, G. Feng, Z. Hou, H. Tian, Y. Shi, and H. Lei, "Wellbore–reservoir coupled simulation to study thermal and fluid processes in a CO_2-based geothermal system: identifying favorable and unfavorable conditions in comparison with water," *Environmental Earth Sciences*, vol. 73, no. 11, article 6, pp. 6797–6813, 2015.

[5] Y. Jung, T. Xu, P. F. Dobson, N. Chang, and M. Petro, "Experiment-based modelling of geothermal interactions in CO2-based geothermal systems," in *Proceedings of Thirty-Eighth Workshop on Geothermal Reservoir Engineering*, Stanford University, Stanford, California, 2013.

[6] C. Lo Ré, J. P. Kaszuba, J. N. Moore, and B. J. McPherson, "Fluid-rock interactions in CO_2-saturated, granite-hosted geothermal systems: Implications for natural and engineered systems from geochemical experiments and models," *Geochimica et Cosmochimica Acta*, vol. 141, pp. 160–178, 2014.

[7] J. Na, T. Xu, Y. Yuan, B. Feng, H. Tian, and X. Bao, "An integrated study of fluid-rock interaction in a CO_2-based enhanced geothermal system: A case study of Songliao Basin, China," *Applied Geochemistry*, vol. 59, pp. 166–177, 2015.

[8] R. J. Rosenbauer, T. Koksalan, and J. L. Palandri, "Experimental investigation of CO_2-brine-rock interactions at elevated temperature and pressure: Implications for CO_2 sequestration in deep-saline aquifers," *Fuel Processing Technology*, vol. 86, no. 14-15, pp. 1581–1597, 2005.

[9] Y. Wan, T. Xu, and K. Pruess, "mpact of fluid-rock interactions on enhanced geothermal systems with CO_2 as heat transmission fluid," in *Proceedings of Thirty-Sixth Workshop on Geothermal Reservoir Engineering*, Stanford University, Stanford, California, 2011.

[10] T. Xu, K. Pruess, and J. Apps, "Numerical studies of fluid-rock interactions in enhanced geothermal systems (EGS) with CO2 as working fluid," in *Proceedings of Thirty-third Workshop on Geothermal Reservoir Engineering*, Stanford University, Stanford, California, 2008.

[11] T. Xu, J. A. Apps, and K. Pruess, "Numerical simulation of CO_2 disposal by mineral trapping in deep aquifers," *Applied Geochemistry*, vol. 19, pp. 917–936, 2004.

[12] T. Xu, E. Sonnenthal, N. Spycher, and K. Pruess, "TOUGHREACT—A simulation program for non-isothermal multiphase reactive geochemical transport in variably saturated geologic media: Applications to geothermal injectivity and CO_2 geological sequestration," *Computers & Geosciences*, vol. 32, pp. 145–165, 2006.

[13] N. Spycher and K. Pruess, "A model for thermophysical properties of CO_2-brine mixtures at elevated temperatures and pressures," in *Proceedings of Thirty-six Workshop on Geothermal Reservoir Engineering*, Stanford University, Stanford, Calif, USA, 2011.

[14] S. L. Rauzi, "Carbon dioxide in the St. John's – Springerville area, Apache County, Arizona," Arizona Geological Survey Open-file Report 99-2, Tucson, Arizona, 1999.

[15] D. Coblentz, "Quarterly progress report, activities description: national risk assessment partnership," *AARRA Quarterly Report*, 2011.

[16] J. L. Palandri and Y. K. Kharaka, "A compilation of rate parameters of water-mineral interaction kinetics for application to geochemical modelling," in *U.S. Geological Survey Open File Report*, Menlo Park, California, 2004.

[17] K. Pruess, "Enhanced geothermal systems (EGS) using CO_2 as working fluid—a novel approach for generating renewable energy with simultaneous sequestration of carbon," *Geothermics*, vol. 35, no. 4, pp. 351–367, 2006.

[18] N. Spycher and K. Pruess, "A Phase-partitioning model for CO_2-brine mixtures at elevated temperatures and pressures: application to CO_2-enhanced geothermal systems," *Transport in Porous Media*, vol. 82, no. 1, pp. 173–196, 2010.

[19] A. Borgia, K. Pruess, T. J. Kneafsey, C. M. Oldenburg, and L. Pan, "Simulation of CO_2-EGS in a fractured reservoir with salt precipitation," in *Proceedings of the 11th International Conference on Greenhouse Gas Control Technologies, GHGT 2012*, pp. 6617–6624, jpn, November 2012.

[20] J. B. Randolph and M. O. Saar, "Combining geothermal energy capture with geologic carbon dioxide sequestration," *Geophysical Research Letters*, vol. 38, 2011.

[21] F. Pan, B. J. McPherson, Z. Dai et al., "Uncertainty analysis of carbon sequestration in an active CO2-EOR field," *International Journal of Greenhouse Gas Control*, vol. 51, pp. 18–28, 2016a.

[22] F. Pan, B. J. McPherson, R. Esser et al., "Forecasting evolution of formation water chemistry and long-term mineral alteration for GCS in a typical clastic reservoir of the Southwestern United States," *International Journal of Greenhouse Gas Control*, vol. 54, pp. 524–537, 2016b.

[23] K. Pruess, C. Oldenburg, and G. Moridis, "TOUGH2 User's Guide Version 2," Tech. Rep. LBNL-43134, Lawrence Berkeley National Laboratory, Berkeley, Calif, USA, 1999.

[24] J. Moore, M. Adams, R. Allis, S. Lutz, and S. Rauzi, "Mineralogical and geochemical consequences of the long-term presence of CO_2 in natural reservoirs: an example from the Springerville-St. Johns Field, Arizona, and New Mexico, U.S.A," *Chemical Geology*, vol. 217, no. 3-4, pp. 365–385, 2005.

[25] T. J. Wolery, "Software package for geochemical modeling of aqueous system: Package overview and installation guide (version 8.0)," Lawrence Livermore National Laboratory Report UCRL-MA-110662 PT I, Livermore, California, USA, 1992.

[26] T. Xu, N. Spycher, E. Sonnenthal, G. Zhang, L. Zheng, and K. Pruess, "TOUGHREACT version 2.0: a simulator for subsurface reactive transport under non-isothermal multiphase flow conditions," *Computers & Geosciences*, vol. 37, no. 6, pp. 763–774, 2011.

Hindawi
Geofluids
Volume 2017, Article ID 6059142, 14 pages
https://doi.org/10.1155/2017/6059142

Research Article

Evaluating Reservoir Risks and Their Influencing Factors during CO_2 Injection into Multilayered Reservoirs

Lu Shi, Bing Bai, Haiqing Wu, and Xiaochun Li

State Key Laboratory of Geomechanics and Geotechnical Engineering, Institute of Rock and Soil Mechanics, Chinese Academy of Sciences, Wuhan 430071, China

Correspondence should be addressed to Lu Shi; shilu.whrsm@qq.com

Received 13 March 2017; Revised 18 July 2017; Accepted 14 August 2017; Published 1 October 2017

Academic Editor: Tianfu Xu

Wellbore and site safety must be ensured during CO_2 injection into multiple reservoirs during carbon capture and storage projects. This study focuses on multireservoir injection and investigates the characteristics of the flow-rate distribution and reservoir-risk evaluation as well as their unique influences on multireservoir injection. The results show that more CO_2 enters the upper layers than the lower layers. With the increase in injection pressure, the risks of the upper reservoirs increase more dramatically than those of the low reservoirs, which can cause the critical reservoir (CR) to shift. The CO_2 injection temperature has a similar effect on the injection flow rate but no effect on the CR's location. Despite having no effect on the flow-rate distribution, the formation-fracturing pressures in the reservoirs determine which layer becomes the CR. As the thickness or permeability of a layer increases, the inflows exhibit upward and downward trends in this layer and the lower layers, respectively, whereas the inflows of the upper layers remain unchanged; meanwhile, the risks of the lower layer and those of the others decrease and remain constant, respectively. Compared to other parameters, the reservoir porosities have a negligible effect on the reservoir risks and flow-rate distributions.

1. Introduction

Carbon capture and storage (CCS) is widely recognized as an effective approach for greatly reducing CO_2 levels in the atmosphere [1–5]. Many CCS projects have been conducted worldwide, including the Sleipner project [6, 7] in Norway, the Weyburn project in Canada [8], the Otway Pilot project in Australia [9], the In Salah project in Algeria [6], and the Shenhua CCS demonstration project in China [10]. Wellbore and site safety must be ensured in all fluid injection projects [11, 12]. In many CCS projects, particularly those with large-scale CO_2 injection, multiple reservoirs are employed for simultaneous injection to achieve a preset injection target amount of CO_2 (see [13–16]). Layers of caprocks and reservoirs are sequentially spaced to form multiple suits of cap rock-reservoir combinations, which significantly increase the complexity of fluid migrations [14]. A mature design methodology for safe and effective CO_2 injection through deep wellbores requires an in-depth understanding of the reservoir performance and safety and their influencing factors in terms of CO_2 injection.

The injection of CO_2 with multiple layers differs considerably from single-layer injection in several respects. First, safe injection requires that the pressure in each reservoir does not exceed the maximum allowable value. Second, the flow rate of each reservoir is unknown in advance of the initial injection. Third, the most dangerous reservoir, based on which wellbore working parameters should be used, is also not known in advance. Therefore, the analysis and evaluation of the risks involved with multiple reservoir injection are difficult.

Bai et al. [14] derived an analytical solution for two-phase flows based on the work of Nordbotten et al. [17], and a solution was derived to designate the wellhead injection pressure. These authors characterized the risks of a reservoir using the ratio of the actual pressure of the fluid to the maximum allowable pressure. A higher ratio indicates that the corresponding reservoir is more dangerous. The reservoir that has the largest ratio is the weakest reservoir, which is also defined as the critical reservoir (CR). As the shortest slab in terms of the Cask principle, the CR actually constrains the maximum allowable wellhead injection pressure. Although the actual injection pressures are typically less than the maximum

allowable value, the injection flow rates can vary, which may lead to variation of CR's location. On such occasions, one cannot determine which layer is the CR because the downhole pressures and flow rates of all the reservoirs are initially unknown. Therefore, investigations of the effects of the injection parameters on the allocations of the total flow rates among multiple layers are extremely valuable.

This paper investigates the determination of CRs and their influencing factors during multireservoir CO_2 injection. For this purpose, the allocation percentage of the total flow rates among the multiple reservoir layers and the risk evaluation of the reservoirs must be simultaneously investigated. Such an investigation is expected to enrich the analysis and design methodologies for CO_2 injection operations. First, we outline the basic theory of the wellbore pressure and temperature. Then, a base case for determining the CR is presented. Next, we analyze the influences of the injection parameters and reservoir properties on the allocation percentage of the total flow rate, the reservoir risk, and the position of the CR. Finally, we summarize our main findings and conclude the study.

2. Fundamental Theory

To achieve the goal of this study, the coupling calculations for the flow and heat transfer of the wellbore and formation must be performed. Although various methods, including three-dimensional numerical simulations, could be employed, a semianalytical method developed by Bai et al. [14] and based on a fast, explicit numerical method and an analytical solution is used to calculate the wellbore flow and heat exchange between the wellbore and formations in this paper. The method is fast and can be applied successfully. In this method, the wellbore is discretized into a series of one-dimensional elements, and the model should include the following assumptions:

(1) One-dimensional flow with homogenous fluid is assumed in the vertical wellbore, and all the state variables and properties are assumed to be uniform at the same section.

(2) Only radial heat transfer is considered, and the temperature at each point is updated using Ramy's solution [18].

(3) The influence of the phase change on the fluid properties is not considered.

(4) All of the fluid properties should be constant within an element.

(5) The portion of the wellbore in the reservoir is simplified as an element node; that is, the variation in the state variables of the wellbore fluid is held constant in a reservoir.

The CO_2 pressure can be determined when the injection pressure at the wellhead is known; then, the fluid pressure P_{j+1} at the end point of the j-th well segment can be acquired from the following equation when P_j is already known:

$$P_{j+1} = P_j \left[1 + \frac{\Delta x_j \left(P_j^2 Mg/RT_j Z_j - \left(\gamma \overline{C}_j^2 RT_j/4r_0 \right) \left(Z_j/M \right) \right)}{\left(P_j^2 - \left(\overline{C}_j^2 RT_j/M \right) Z_j \right)} \right], \quad (1)$$

where $\overline{C}$ is the mass flow velocity of the wellbore cross section ($kg \cdot m^{-2} \cdot s^{-1}$), Δx is the discretized segment (m), g is the acceleration of gravity (m/s^2), r_0 is the inner radius of the tubing (m), M is the gas molar mass (kg/mol), R is the universal gas constant, γ is the coefficient of friction, Z is the compression factor obtained by solving the Peng-Robinson equation [19], and T is the thermodynamic temperature (K). The subscript j is used to number the discretized segments of the wellbore in the finite difference method.

As noted above, Ramy's analytical solution is used to obtain the CO_2 temperature of the wellbore. The details of the derivations are provided in the studies of Liu et al. [15] and Wu et al. [16], and the heat transfer between the wellbore and the surrounding earth is detailed in the study by Streit and Hillis [13].

The steady two-phase flow for the CO_2 flooding in the reservoir can be characterized by an equation proposed by Nordbotten et al. [17], with the assumption that a reservoir can be divided into CO_2-saturated and brine-saturated zones with a sharp interface. Obtaining an analytic solution from Nordbotten's equation is almost impossible. According to the derivation, by introducing two-phase mobility into the Darcy formula of a single-phase flow and assuming that the CO_2 plume is radially symmetric, as suggested by Wu et al. [20, 21] and Bai et al. [12], the mass flow rate C_i^r, which enters the i-th reservoir from the wellbore, can be expressed as follows:

$$C_i^r = 2\pi k_i B_i \rho_i \cdot \frac{P_{ki} - P_{0i}}{(1/\lambda_{ci}) \ln (R_{ci}/r_0) + (1/\lambda_{wi} - 1/\lambda_{ci}) + (1/\lambda_{wi}) \ln (R_{0i}/R_{\max i})}, \quad (2)$$

where P_0 is the initial formation pressure of the reservoir (Pa); P_k is the injection pressure on the wellface of the reservoir (Pa); R_0 is the maximum influence radius of the flow in the reservoir (m); R_c and $R_{\max}$ are the radii of the CO_2 plume at the bottom and top of the reservoir, respectively (m); k is the absolute permeability of the reservoir (m^2); B is the thickness of the reservoir (m); ρ is the density of the CO_2 (kg/m^3); and λ_c and λ_w are the mobility of CO_2 and the mobility of brine ($m \cdot s/kg$), which are defined as the ratios of their relative permeability to their fluid viscosity, that is, $\lambda_c = k_{rc}/\mu_c$ and $\lambda_w = k_{rw}/\mu_w$. Since the saturations of brine in the CO_2 and brine domains of a reservoir are zero and one, respectively, the relative permeabilities of k_{rc} and k_{rw} are both equal to one.

Moreover, three of the parameters in (2), R_0, and R_c, and $R_{\max}$, are used to describe the distributions of CO_2 and brine

in a reservoir. These parameters are time-dependent and can be calculated as follows:

$$R_0 = \sqrt{\frac{2.24kt}{\mu_w \varphi \left(\alpha_p + \beta_w\right)}} + R_{\max}, \tag{3a}$$

$$R_c = \sqrt{\frac{\lambda_w V^r(t)}{\lambda_c \varphi \pi B}}, \tag{3b}$$

$$R_{\max} = \sqrt{\frac{\lambda_c V^r(t)}{\lambda_w \varphi \pi B}}, \tag{3c}$$

where t is the injection time (s); $V^r(t)$ is the total flow into a reservoir during 0–t (m^3); φ is the reservoir porosity; α_p is the pore compressibility (m^2/N); β_w is the compressibility of brine (m^2/N); and μ_w is the viscosity of brine (kg/m/s).

According to the flow equilibrium conditions, the inflow of the section of the wellbore in the i-th reservoir is equal to the summation of the outflow into the next well segment and the corresponding reservoir [12]. Therefore, the following equation is obtained:

$$\overline{C}_i = \frac{2k_i B_i \rho_i}{r_0^2} \cdot \frac{P_{ki} - P_{0i}}{(1/\lambda_{ci}) \ln(R_{ci}/r_0) + (1/\lambda_{wi} - 1/\lambda_{ci}) + (1/\lambda_{wi}) \ln(R_{0i}/R_{\max i})} + \frac{\rho_i}{\rho_{i+1}} \overline{C}_{i+1}. \tag{4}$$

When (4) is used for the bottom reservoir, the second term on the right-hand side disappears.

Typically, the site stability and the flow-rate target must also be satisfied and form the constraints during CO_2 injections. The wellbore constraints include the pressure and flow-rate constraints. The lower limit of the latter can be determined during the project-feasibility stage, whereas the upper limit requires each branch flow to meet the corresponding constraint conditions. Therefore, the complete wellbore constraints can be expressed as

$$\begin{gathered} P_{0i} + P_{bi} < P_{ki} \le [P_{ki}], \\ C_i^r \le [C_i^r], \end{gathered} \tag{5}$$

where P_b represents the capillary pressure (Pa); $[P_{ki}]$ is the maximum allowable pressure of the i-th reservoir (Pa), which is the formation-fracturing pressure multiplied by a synthetic design coefficient η; and $[C^r]$ is the available reservoir capacity (kg/s).

3. Example of the Shenhua CCS Demonstration Project

The Shenhua CCS demonstration project is the first fully implemented CCS project in China; the storage target of this project was set to 100,000 tons/year. A single injection well, which is referred to as ZSZ1, was drilled to a depth of 2,450 m, penetrating 21 reservoir-cap rock pairs, which were then combined and reduced to eight reservoir-cap rock units for analysis by Bai et al. [14]. From top to bottom, the geological formations include the Zhifang group, Heshanggou group, Liujiagou group, Shiqianfeng group, Shihezi group, Shanxi group, Taiyuan group, Benxi group, and Majiagou group. Table 1 lists the computational parameters of the reservoir-cap rock units from top to bottom. The other parameters, that is, the inner radius of the tubing r_0, pore compressibility α_p, brine compressibility β_w, CO_2 viscosity μ_c, and brine viscosity μ_w, were set to 31 mm, 4.5×10^{-10} m^2/N, 4.5×10^{-10} m^2/N, 88 kg/m/s, and 552 kg/m/s, respectively.

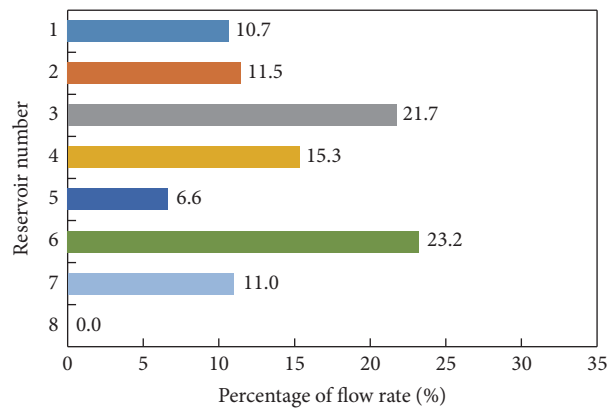

Figure 1: Flow-rate distribution among the reservoirs for the base case of the Shenhua CCS project.

As noted above, a forward analysis is employed in this study. Therefore, the parameters of the wellhead, such as the wellhead injection pressure and injection flow rate, must be prepared before the aforementioned method can be used to obtain the pressure and CO_2 injection flow rates of the reservoirs. Based on these values, the ratio $P_{ki}/[P_{ki}]$ can be obtained for the i-th reservoir. The synthetic design coefficient for obtained $[P_{ki}]$ is 0.8. The boundary conditions, that is, the injection pressure and injection rate at the wellhead, are 5 MPa and 4.63 kg/s, respectively, in the base case, which is consistent with the actual operational values at a certain injection stage. In addition, the calculated injection time is 3 years.

According to the distribution of the flow rates in the eight reservoirs plotted in Figure 1, the CO_2 flows are greater in the upper reservoirs under the given injection parameters. The flow rates of the upper four reservoirs account for 59.2% of the CO_2 flow, although the sixth reservoir has the largest flow rate, accounting for 23.2% of the total. Reservoirs 5, 7, and 8 comprise considerably lower percentages of the total flow rate.

The risk factors of all eight reservoirs, which are defined as the ratios of the actual pressures of the fluid P_{ki} to the maximum allowable pressures $[P_{ki}]$ at the entrances of the reservoirs, are shown in Figure 2. Reservoir 8 has the highest risk factor and is thus the CR. Bai et al. [14] found that a different reservoir was the CR when using different injection parameters. Hence, the CR is closely related to the injection

Table 1: Parameters of the reservoir-caprock units of the Shenhua CCS project.

Reservoir number	Thickness of reservoir (m)	Thickness of caprock (m)	Logging permeability ($\times 10^{-3}$ μm^2)	Logging porosity (%)	Fracturing pressure (MPa)	Formation pressure (MPa)
1	9	1699	2.81	10.6	35.29	17.45
2	5	57	5.47	12.4	37.53	17.89
3	40	191	1.431	9.7	38.95	20.15
4	8	43	6.58	12.9	42.60	21.43
5	4	119	5.99	12.6	47.00	22.94
6	26	114	2.738	12.5	43.47	23.1
7	8	52	5.1	11.9	46.03	23.84
8	12	178	0.039	5.2	45.68	22.75

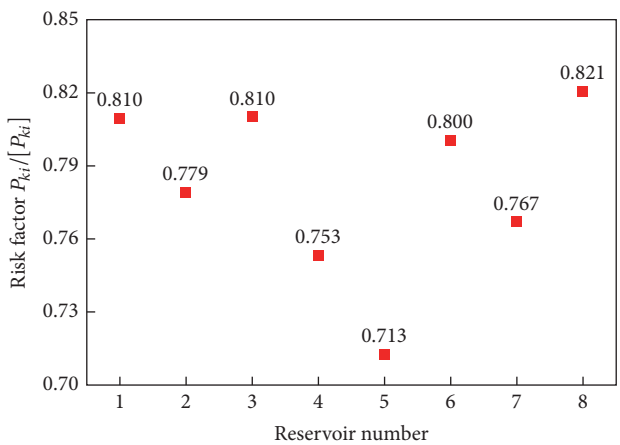

Figure 2: Risk factors of each reservoir for the base case of the Shenhua CCS project.

parameters. Because all the risk factors are less than 1.0, the given combination of injection parameters will not induce reservoir failure; the CR has a safety reserve of nearly 18%. In addition, Reservoir 8, which exhibits the minimum proportions of CO_2 entry, is the most dangerous reservoir, which indicates that the pressure might build up sharply at the wellface because of the poor injectivity under the given injection conditions.

4. Analysis of the Influencing Factors

Because the injection parameters are typically not constant during the actual injection operations, it is valuable to know how the risks and proportions of the flow rates in each reservoir depend on the injection conditions. Knowing whether the CR will shift because of the variations in the injection parameters is more important. In addition to these injection parameters, the characteristic parameters of the reservoirs are believed to be important influencing factors. The typical characteristic parameters of reservoirs include the reservoir thickness, porosity, permeability, initial formation pressure, and formation-fracturing pressure [2]. The two classes of factors, that is, the injection and characteristic factors, will be investigated in a subsequent study. The injection fluid is assumed to be pure CO_2, so the effects of impurities are not considered. Although the saturation of the fluid can significantly affect the distribution of the wellbore pressure and the wellhead pressure in particular, this factor will not change the CR [12]. Therefore, the effects of the characteristic physical parameters of the fluids will not be further investigated in this study.

4.1. Injection Parameters. In this subsection, we utilize the wellbore model and analysis method presented in the previous section. The main injection parameters of interest in this section are the injection pressure, injection flow rate and injection temperature. Ten injection cases are described in Table 2 based on combinations of these three parameters. The settings of the parameter values, which are chosen by considering the base case in the previous section and the actual injection history, are likely to be used in actual injection practices. Therefore, the results should provide valuable guidance for any subsequent injection operations during the Shenhua CCS project. The cases shown in Table 2 were designed with four targets, that is, determining the effect of variations in the injection pressures (Cases 1A to 1D), injection rates (Cases 1D to 1F), injection temperatures (Cases 1G to 1J), and combinations of the first two factors (Cases 1C, 1E, and 1G) on the percentages of the CO_2 inflows and the risks of each reservoir. All the designed parameter values ensure the safety of each reservoir because the target of this study is not the failure properties of the formations but the sensitivities of the CR to the parameters. The responses of the percentages of the CO_2 flow rates and the risk factors for each reservoir are illustrated in Figures 3 and 4, respectively.

Figure 3(a) shows that the proportion of CO_2 that flows into each reservoir varies with changes in the injection pressure under the given flow rates and temperatures at the wellhead. With greater injection pressures, the inflows into Reservoirs 1–5 increase monotonically, the inflows into Reservoir 6 initially increase and then decrease, and the inflows into Reservoirs 7-8 gradually decrease. These variation trends indicate that a greater injection pressure causes more CO_2 to enter the upper reservoirs because of the increase in the fluid pressure at the wellbores in the reservoirs and the constant total flux at the wellheads. Figure 4(a) indicates that the reservoir risk also increases due to the increased injection pressure. More importantly, the risk-increasing trends of the upper

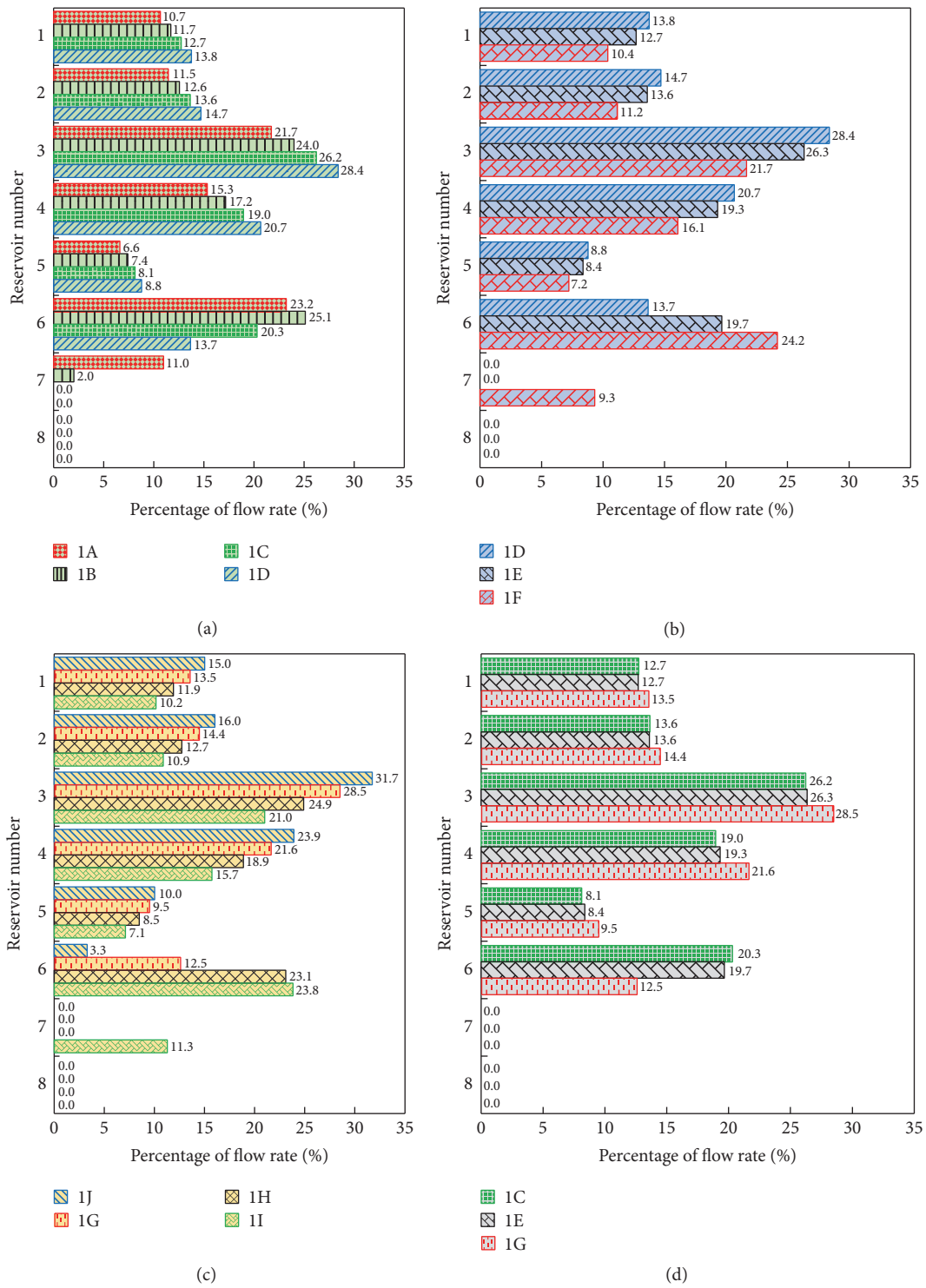

Figure 3: Distributions of the flow rates that correspond to the different injection parameters at the wellhead of the Shenhua CCS project. (a), (b), and (c) are the results for different injection pressures, flow rates, and temperatures, respectively. (d) shows the investigation of the influences of simultaneous changes of the injection pressures and flow rate.

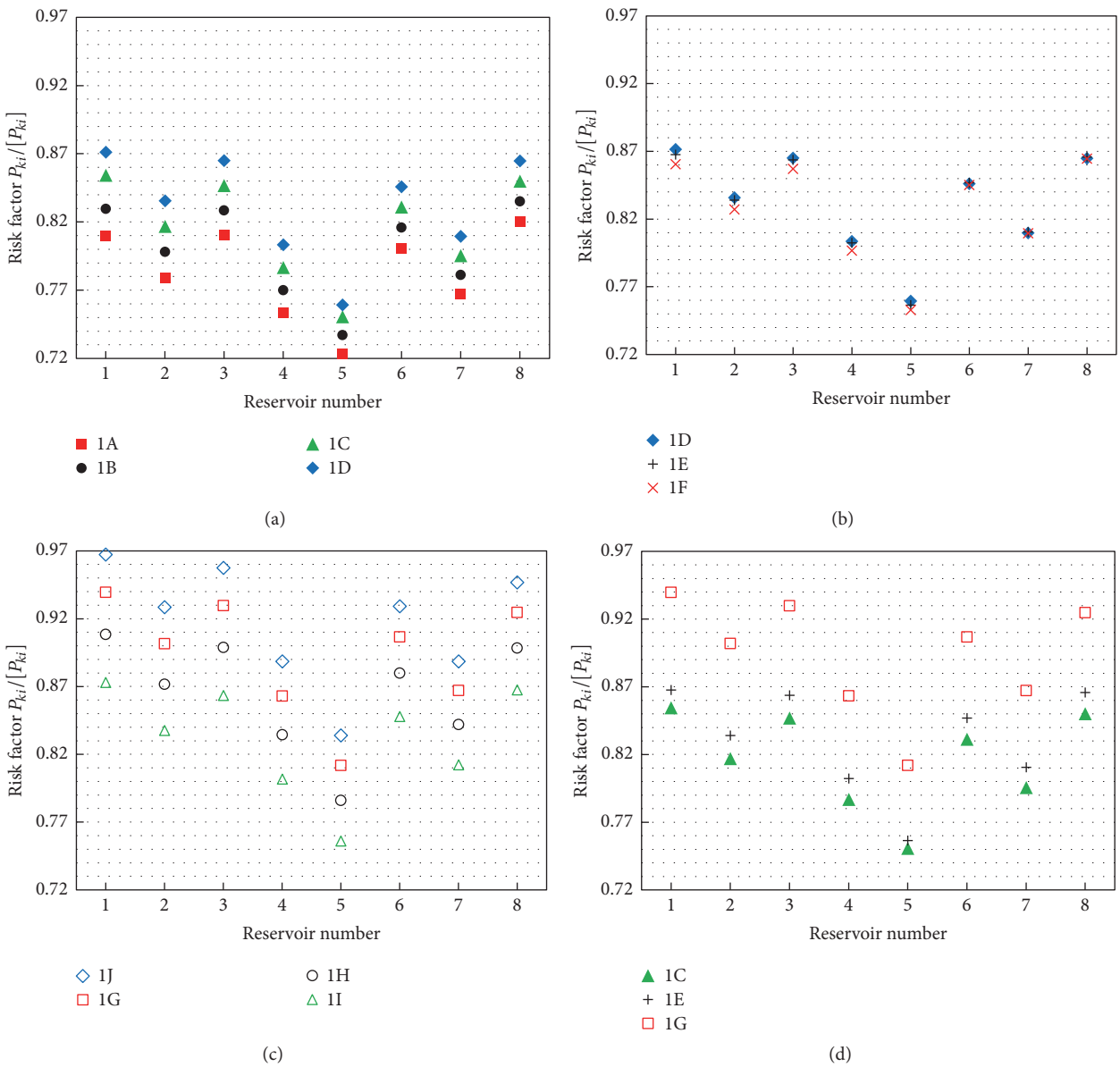

Figure 4: Risk factors of each reservoir which correspond to the different injection parameters at the wellhead of the Shenhua CCS project. (a), (b), and (c) are the results for the different injection pressures, flow rates, and temperatures, respectively. (d) Investigation of the influences of simultaneous changes of the injection pressures and flow rates.

Table 2: Injection parameters for the described cases of the Shenhua CCS project.

Case	Injection pressure (MPa)	Injection flow rate (kg/s)	Injection temperature of CO_2 (°C)
1A	5	4.63	−5
1B	6	4.63	−5
1C	7	4.63	−5
1D	8	4.63	−5
1E	8	5	−5
1F	8	6	−5
1G	10	6	−5
1H	10	6	5
1I	10	6	15
1J	10	6	−15

Table 3: Characteristic parameters of the reservoirs in the conceptual engineering model.

Reservoir number	Thickness of reservoir (m)	Thickness of caprock (m)	Logging permeability ($\times 10^{-3}$ μm^2)	Logging porosity (%)	Fracturing pressure (MPa)	Formation pressure (MPa)
1	10	1390	6	12	35	15
2	10	190	5	11	38	17
3	10	190	4	10	41	19
4	10	190	3	9	44	21

reservoirs are more dramatic than those of the lower reservoirs. When the injection pressure reaches 7.0 MPa, the CR transfers from Reservoir 8 to Reservoir 1, indicating that the injection pressure can control the overall risks of the reservoirs and that concentrating CO_2 in the upper reservoirs causes the CR to shift to the top reservoir because of the increased injection pressure.

Figure 3(b) shows the variations of the distributions of the CO_2 flow rates among the reservoirs with increases in the injection flow rates when the injection pressure and injection temperature are known. In contrast to Figure 3(a), a higher total injection flow rate increases the proportion of CO_2 that flows into the lower reservoirs. This is mainly because the pressure attenuation increases with the injection flow rate such that the flows into the upper reservoirs are reduced. Moreover, as shown in Figure 4(b), the risks of all the reservoirs gradually decrease from Case 1D to Case 1F, and the CR shifts back to Reservoir 8, which differs from the results presented in Figure 4(a). However, the risk reductions of these reservoirs are relatively small, particularly for the lower reservoirs, even when their flow rates are increased. Thus, the injection flow rate has a smaller impact on the risk of a reservoir than the injection pressure does, and both parameters have larger impacts on the risks of the upper reservoirs than on the risks of the lower reservoirs.

As the injection temperature of CO_2 increases, the variation trends of the flow rates in each layer become opposite to those induced by the increases in the injection pressure, despite agreeing well with those shown in Figure 3(b) for the gradually increasing concentrations of CO_2 in the upper reservoirs, as shown in Figure 3(c). Similarly, Figure 4(c) indicates that the changes in the reservoir risks are approximately opposite to those in Figure 4(a). This decrease in the reservoir risk is likely induced by a drop in the viscosity, which can accelerate the transport of fluids and lead to a partial dissipation of pressure because of the increasing injection temperature. Furthermore, Reservoir 1 remains the CR, even though the reservoir risk decreases with the increasing injection temperature.

Given the synchronous variations in injection pressures and flow rates, the injection proportion of each reservoir remains almost invariant, except for that of Reservoir 6, which exhibits a 7.5% decrease in Case 1G, as shown in Figure 3(d). However, the risks of all the reservoirs in Figure 4(d) increase significantly, but Reservoir 1 remains the CR. In combination with the results shown in Figures 4(a) and 4(b), the injection pressure is shown to predominantly control the overall risks of the reservoirs, and the injection flow rate is shown to be able to affect the position of the CR to a certain extent.

4.2. Characteristic Parameters of the Reservoirs

4.2.1. Parameter Settings. The injectivity of the reservoir and the downhole limitations of the injection pressure depend on the reservoir's characteristic parameters; variations in these parameters can affect the intake percentages and risks of each reservoir. For a CCS project, these parameters are typically considered to be constant. The objective of this section is to determine the effects of these parameters; therefore, the assumed parameters rather than the experimental parameters of the Shenhua CCS project are employed to conduct a parameter sensitivity analysis. A conceptual engineering model that contains four reservoir-cap rock units with a single injection well that penetrates 2,000 m underground is established. The formations in the conceptual model, from top to bottom, are as follows: Cap rock 1, Reservoir 1, Cap rock 2, Reservoir 2, Cap rock 3, Reservoir 3, Cap rock 4, and Reservoir 4. The depths of the bottoms of these formations are 1390 m, 1400 m, 1590 m, 1600 m, 1790 m, 1800 m, 1990 m, and 2000 m, respectively. The basic characteristic parameters of the reservoirs are listed in Table 3, and the parameters of the wellbores are the same as those for the Shenhua CCS project. For the base case, the wellhead injection pressure, injection flow rate, and injection temperature of CO_2 are set to 10 MPa, 4 kg/s, and -5°C, respectively. Five cases with the same initial states as the base case (Table 3) are designed to study the influence of each reservoir's parameters. The injection time is set to ten years.

4.2.2. Influence of the Formation-Fracturing Pressure. As presented above, the concept of the CR depends on the $P_{ki}/[P_{ki}]$ ratio. $[P_{ki}]$ is typically obtained from the formation-fracturing pressure multiplied by the synthetic design factor, which is smaller than 1.0. In this conceptual model, the synthetic design factor is set to 0.6. Therefore, $[P_{ki}]$ represents the intrinsic ability of a formation to resist damage and is a decisive factor in determining the risk of a reservoir and the position of the CR, which will be investigated first. Five groups of fracturing pressures are designed and listed in Table 4. In Cases 2B and 2C, the formation-fracturing pressures of Reservoirs 2 and 3, respectively, are obtained by slightly decreasing the corresponding values in Case 2A.

Table 4: Cases with different formation-fracturing pressures (MPa).

Reservoir number	2A (base case)	2B	2C	2D	2E
1	35	35	35	35.5	36
2	38	37	38	38.5	39
3	41	41	40	41.5	42
4	44	44	44	44.5	45

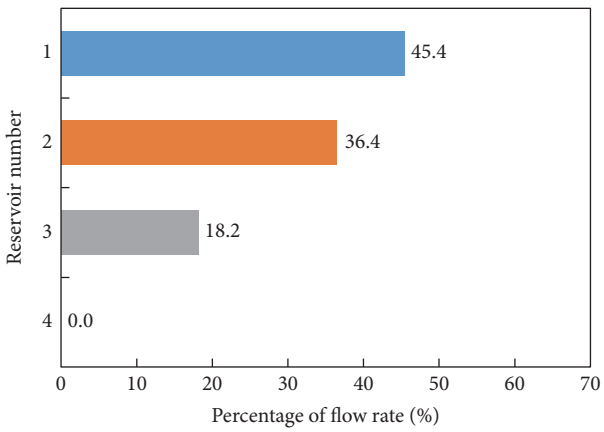

Figure 5: Flow-rate distribution of a conceptual model with the corresponding parameters of the formations in Table 3; the injection pressure, flow, and temperature are 10 MPa, 4 kg/s, and −5°C, respectively.

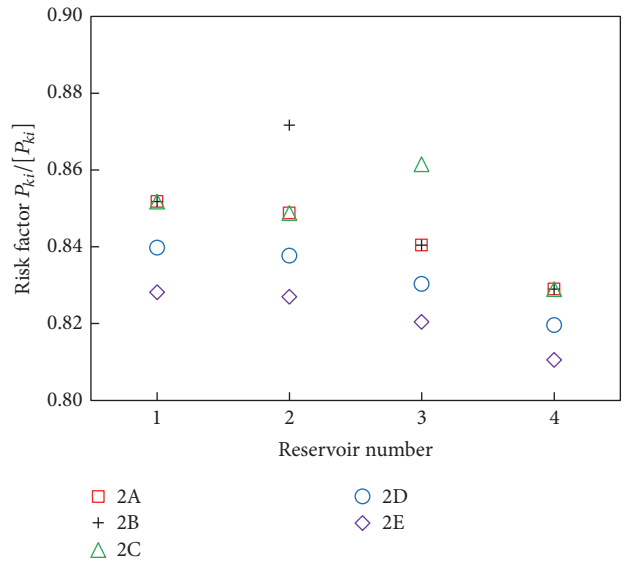

Figure 6: Variations in the risk factors of the reservoirs at different formation-fracturing pressures for the conceptual engineering model.

Therefore, the effect of the decrease in the formation-fracturing pressure of a single reservoir on the intake percentage and the risk of each reservoir can be investigated by comparing the results from Cases 2A to those of 2C. In Cases 2D and 2E, the fracturing pressures of all the reservoirs increased by 0.5 and 1.0 MPa, respectively. Using these results, the effects of a synchronous increase in the formation-fracturing pressures can be studied. The percentages of the inflows and the risks of each reservoir in these five cases are illustrated in Figures 5 and 6, respectively.

The formation-fracturing pressure does not influence the CO_2 pressure or injectivity. Therefore, modifying the formation-fracturing pressures does not alter the proportion of CO_2 that flows into each reservoir. As shown in Figure 5, the majority of CO_2 enters the upper two reservoirs. In contrast, variations of the formation-fracturing pressure considerably affect the risks of the reservoirs (Figure 6) and can cause the CR to shift. A comparison of the results of Cases 2A, 2B, and 2C indicates that when the fracturing pressure of only one reservoir formation is reduced, the risk of this reservoir immediately increases, such that this reservoir will become the CR when the formation-fracturing pressure decreases to a certain value. Furthermore, an identical increment in the formation-fracturing pressures of all the reservoirs should improve the safety of the reservoirs, and the reservoir with the smallest fracturing pressure will exhibit the largest decrease in risk. Similarly, increasing all the reservoirs' formation-fracturing pressures should decrease the risks of the reservoirs without altering the position of the CR.

4.2.3. Influence of the Initial Formation Pressure. In engineering practices, the initial formation pressure is used to determine the lower limit of the injection pressure of the reservoir. Because the injection pressure is typically considerably higher than the initial formation pressure, variations in the initial formation pressure will not affect the reservoir risk directly but will affect the intake percentage of each reservoir. As discussed above, the uppermost reservoir is the CR for the original set of parameters used in this study. Because the pressure at this reservoir can be calculated directly from the wellhead conditions and is not related to the proportion of the CO_2 inflow, the uppermost reservoir will remain the CR with the use of the original set of parameters. To further investigate these characteristics, another base case in which the CR is not the uppermost reservoir must be constructed, and the initial case can then be used as a reference to investigate the effects of varying the initial formation pressure.

Because the formation-fracturing pressure can affect the position of the CR considerably, directly changing its value allows the construction of a reference case. Therefore, two scenarios (i.e., S-1 and S-2) with two sets of formation-fracturing pressures are presented, and the settings of the formation-fracturing pressures of S-1 and S-2 are the same as those of Cases 3A and 3C, respectively, as shown in Table 4. Five different initial formation pressures for each scenario are provided in Table 5.

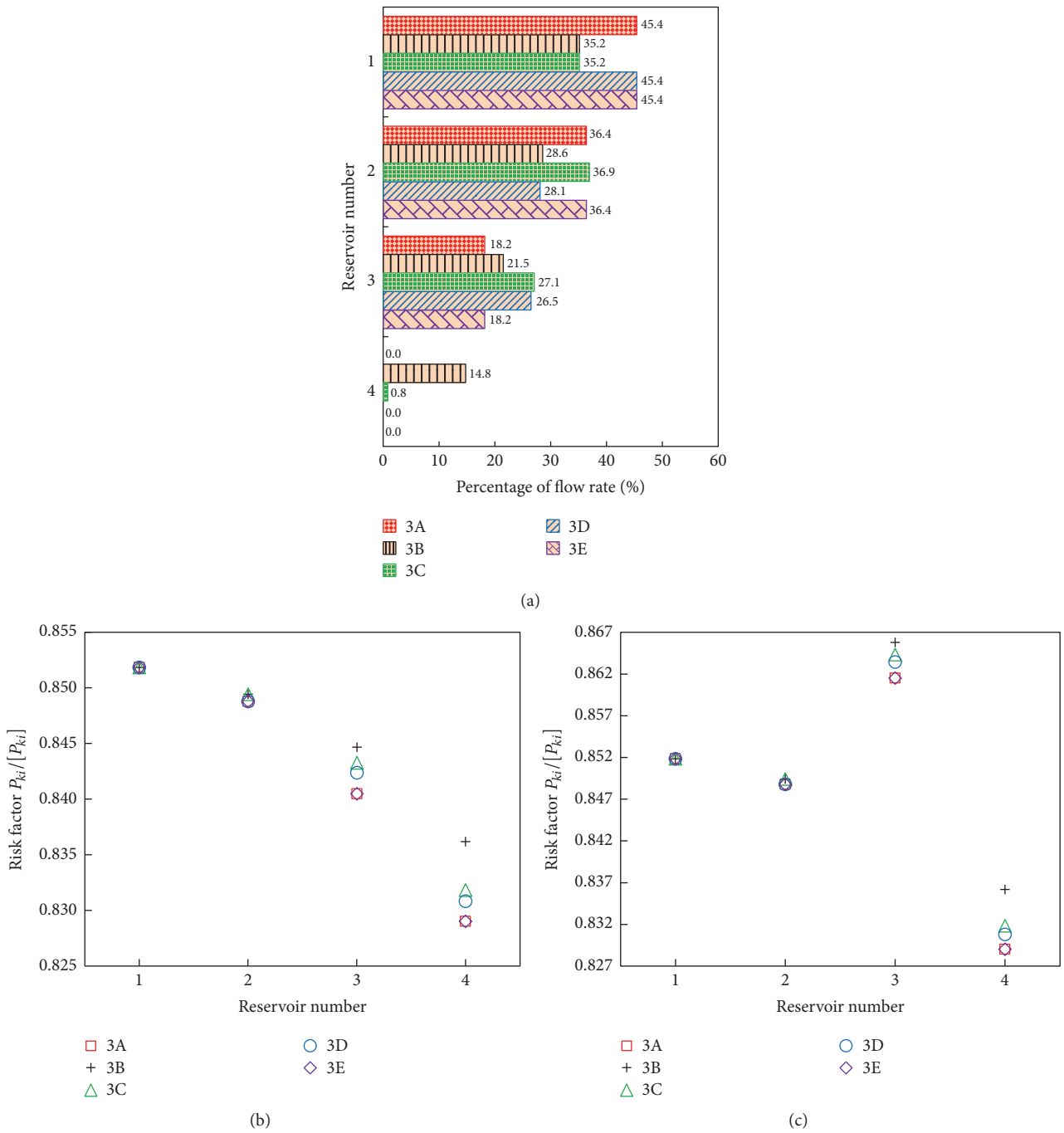

Figure 7: Proportions of the inflows (a) and risk factors of each reservoir under different initial formation pressures for the two scenarios of the conceptual engineering model. (b) and (c) are the risk-factor results for Scenarios S-1 and S-2, respectively.

As noted above, the proportion of CO_2 that flows into each reservoir is not related to the formation-fracturing pressure. The distributions of the flow rates among the reservoirs in S-1 and S-2 shown in Figure 7(a) are identical. Overall, when the initial formation pressure of a layer increases, the injection proportion of this layer decreases, whereas the flow rate that enters the layer beneath also increases. The inflow proportion for the uppermost reservoir changes only when its initial formation pressure changes. However, the initial formation pressures of the first and second reservoirs affect the inflow proportion of the second reservoir. The remaining inflow proportions can be deduced via an analogy; that is, the percentage of CO_2 that enters a reservoir is related to the variation of the initial formation pressure of the reservoir itself and its upper reservoirs.

As the initial formation pressure increases, the risks of the reservoirs below the uppermost reservoir also increase, whereas the risk of the uppermost reservoir remains constant.

Table 5: Five cases with different initial formation pressures (MPa).

Reservoir number	3A (base case)	3B	3C	3D	3E
1	15	17	17	15	15
2	17	19	17	19	17
3	19	21	19	19	21
4	21	23	21	21	21

Table 6: Five cases with different reservoir thicknesses (m).

Reservoir number	4A (base case)	4B	4C	4D	4E
1	10	20	20	10	10
2	10	20	10	20	10
3	10	20	10	10	20
4	10	20	10	10	10

Table 7: Five cases with different reservoir logging permeabilities ($\times 10^{-3}$ μm^2).

Reservoir number	5A (base case)	5B	5C	5D	5E
1	6	12	12	6	6
2	5	10	5	10	5
3	4	8	4	4	8
4	3	6	3	3	3

Table 8: Five cases with different reservoir logging porosities (%).

Reservoir number	6A (base case)	6B	6C	6D	6E
1	12	24	24	12	12
2	11	22	11	22	11
3	10	20	10	10	20
4	9	18	9	9	9

Moreover, the initial formation pressure has a greater effect on the lower reservoirs than on the upper reservoirs, as shown in Figures 7(b) and 7(c). A comparison between the five cases of the two scenarios indicates that changes in the initial formation pressures have greater effects on the risks of the upper reservoirs than on the risks of the lower reservoirs. Reservoirs 1 and 3 are the CRs in S-1 and S-2, respectively. Thus, changes in the initial formation pressures also influence the position of the CR. In S-1, when the initial formation pressure of Reservoir 1 continues to increase, the risks of the lower reservoirs increase, and both Reservoirs 2 and 3 have the potential to become the CR. In S-2, when the initial formation pressure of Reservoir 1 or Reservoir 2 decreases to a certain value, then the risk of Reservoir 3 decreases and Reservoir 1 becomes the CR. Thus, when the first layer is not the CR, the risk of the CR can be reduced by decreasing the initial formation pressure of the upper reservoirs, which can help improve the safety and injectivity of the target site.

4.2.4. Influences of the Thickness, Permeability, and Porosity of the Reservoir. The thickness, permeability, and porosity of the reservoirs affect the capacity and injectivity of the reservoirs, which then affect the inflow and CO_2 pressure in the wellbore, which is similar to the role of the initial formation pressure. Therefore, in this section, the aforementioned scenarios, S-1 and S-2, are used as the working models. The cases in Tables 6–8 were designed to investigate the effects of these three parameters, respectively. Changing the parameters of the last reservoir alone does not affect any of the results for the entire wellbore; hence, only the parameter sensitivities of the first three reservoirs are investigated.

Figure 8(a) shows the proportion of CO_2 injected into each reservoir, considering the different reservoir thicknesses. The results in Figures 7(a) and 8(a) illustrate that as the thickness of a reservoir increases, the CO_2 inflows into its upper reservoirs remain unchanged, whereas those of the reservoir itself and its lower reservoirs increase and decrease, respectively. As shown in Figures 8(b) and 8(c), an increase in the thickness of a single reservoir can effectively reduce the risks of its lower reservoirs without affecting those of its upper reservoirs, which is similar to the decreasing effect of the initial formation pressure. Therefore, the risk of the first reservoir is always fixed, regardless of whether the thickness of the reservoir varies. Moreover, increasing the thicknesses of the upper reservoirs to reduce the reservoir risk is significantly more effective than increasing the thicknesses of the lower reservoirs. In Cases 4B and 4C of S-2, the CR shifts from Reservoir 3 to Reservoir 1, which can effectively improve the safety of the wellbore and verify the conclusion that the CR might shift with changes in the formation-fracturing pressure. Additionally, the results for Cases 4B and 4C are the same in each of the three subpanels of Figure 8, which does not mean that doubling the thickness of Reservoir 1 produces the same effect as scaling up the thicknesses of all the reservoirs at the same time. This phenomenon occurs because the flow rate into Reservoir 1 accounts for 94% of the total flow after scaling up its thickness by one under the given injection conditions, and the remaining flow rate does not satisfy the capacity of the lower reservoir. In other words, when the total injection flow rate is adequate, the differences between the results of Cases 4B and 4C will clearly manifest themselves.

The scheme for generating the cases used to examine the reservoir permeability is the same as that used for the reservoir thicknesses. As shown in Figure 9, the influence of the permeability of the reservoir on the distribution of the flow rates and the risks of the reservoirs is nearly the same as that of the thickness of the reservoir, as shown in Figure 8, because the inflow of a reservoir, as expressed by (2), is proportional to the thickness and permeability of the reservoir. Therefore, we do not describe Figure 9 in further detail. However, subtle differences do exist in the flow-rate distributions and risks of the results shown in Figures 8 and 9 for the two scenarios. In short, the permeability has less significant effects than the thickness of the reservoirs.

Figure 10 shows the results when considering different reservoir porosities. The distributions of the flow rates and

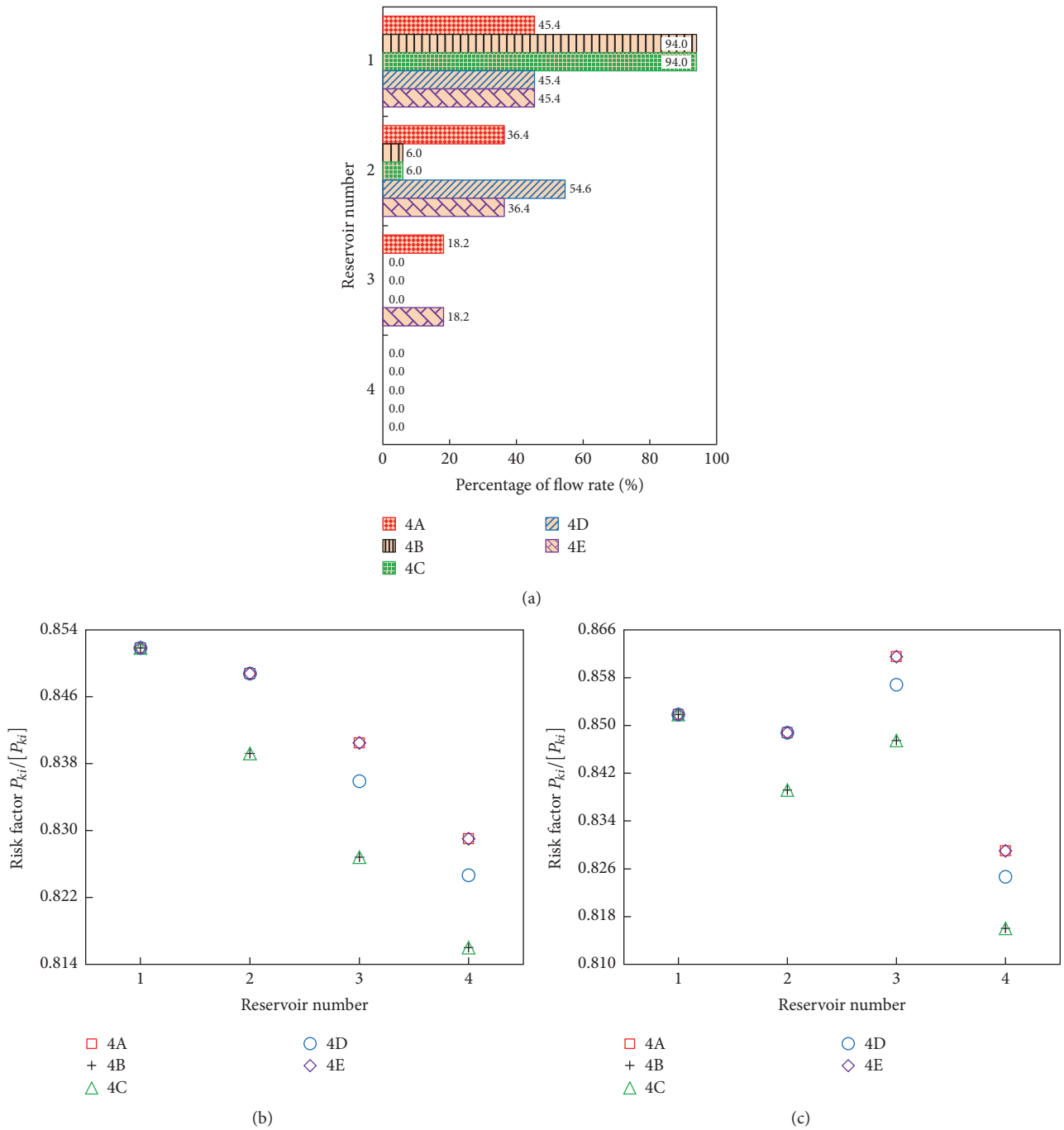

Figure 8: Proportions of the inflows (a) and risk factors of each reservoir for different reservoir thicknesses for the two scenarios of the conceptual engineering model. (b) and (c) are the risk-factor results for Scenarios S-1 and S-2, respectively.

risks of the reservoirs for each case agree well with each other. Thus, the effect of the variations in porosity can be neglected.

5. Conclusions

This paper presented a systematic study on the key issues that arise from multiple CO_2 injections during CCS projects, namely, the distributions of the flow rates among the reservoirs, the CRs, and their influencing factors. Understanding these issues is essential for both pressure design and field operations at wellheads. The calculation methods and programs were based on those in our previous work. Some specific conclusions of the study are given as follows.

(1) Assuming that all the reservoirs had identical properties, including thickness, porosity, and permeability, the

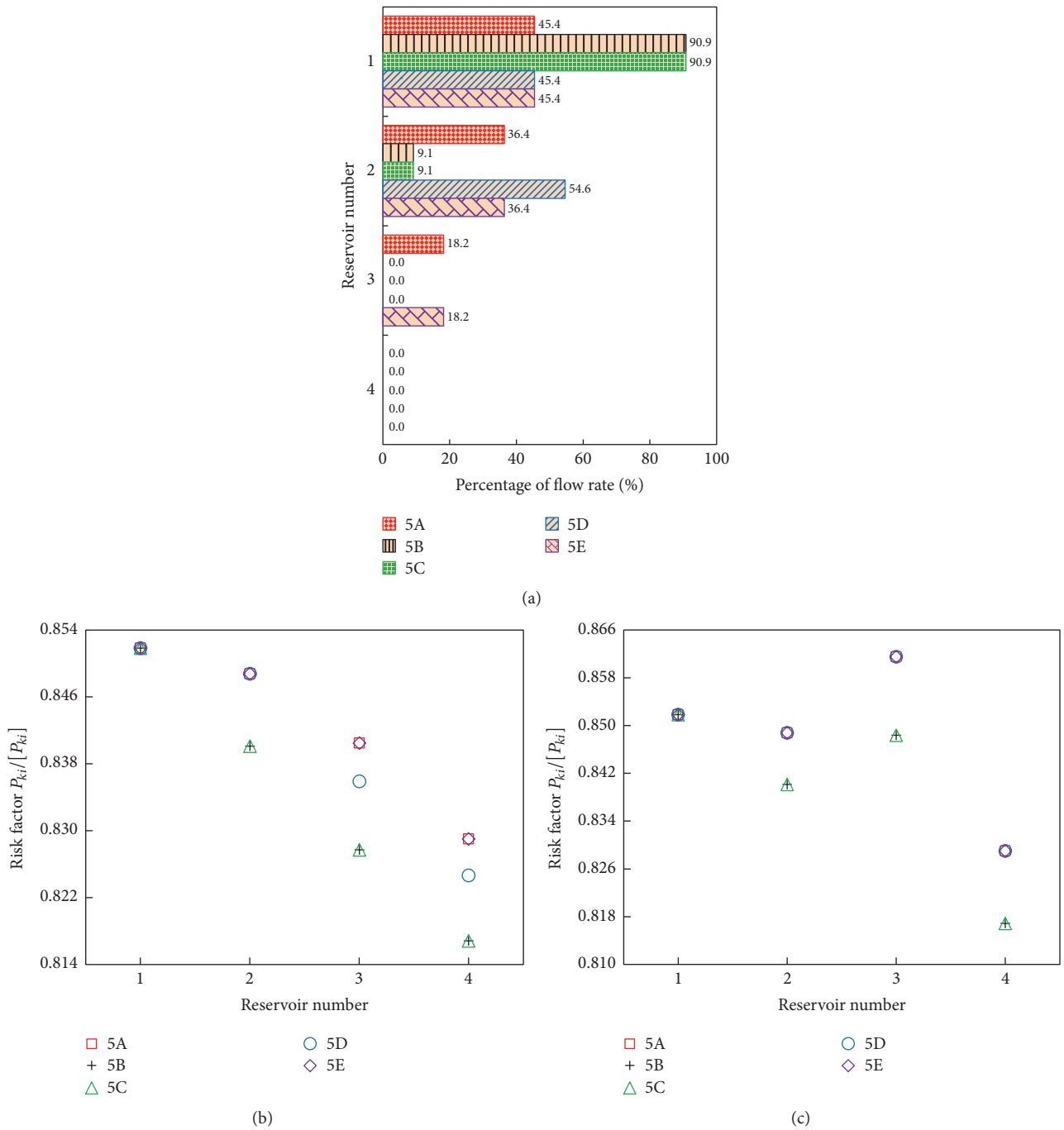

Figure 9: Proportions of the inflows (a) and risk factors of each reservoir for different reservoir permeabilities for the two scenarios of the conceptual engineering model. (b) and (c) are the risk-factor results for Scenarios S-1 and S-2, respectively.

injected fluid was mainly distributed in the upper reservoirs, and less CO_2 entered the lower reservoirs. This trend mainly occurred because deeper reservoirs have greater formation pressure; therefore, high formation pressures require higher injection pressures to maintain injectivity.

(2) The risk of the reservoir was mainly controlled by the injection pressure and the formation-fracturing pressure and was minimally related to the inflow of CO_2. Therefore, a reservoir could still be the CR even when the flow rate of CO_2 into that reservoir is close to zero.

(3) The injection parameters at the wellhead considerably affected the flow-rate distributions and risks of the reservoirs. More CO_2 entered the upper reservoirs than the lower reservoirs with increasing injection pressure (or decreasing injection rate). Moreover, the risks of all the reservoirs increased, and the risk-increasing trend of the upper reservoirs was

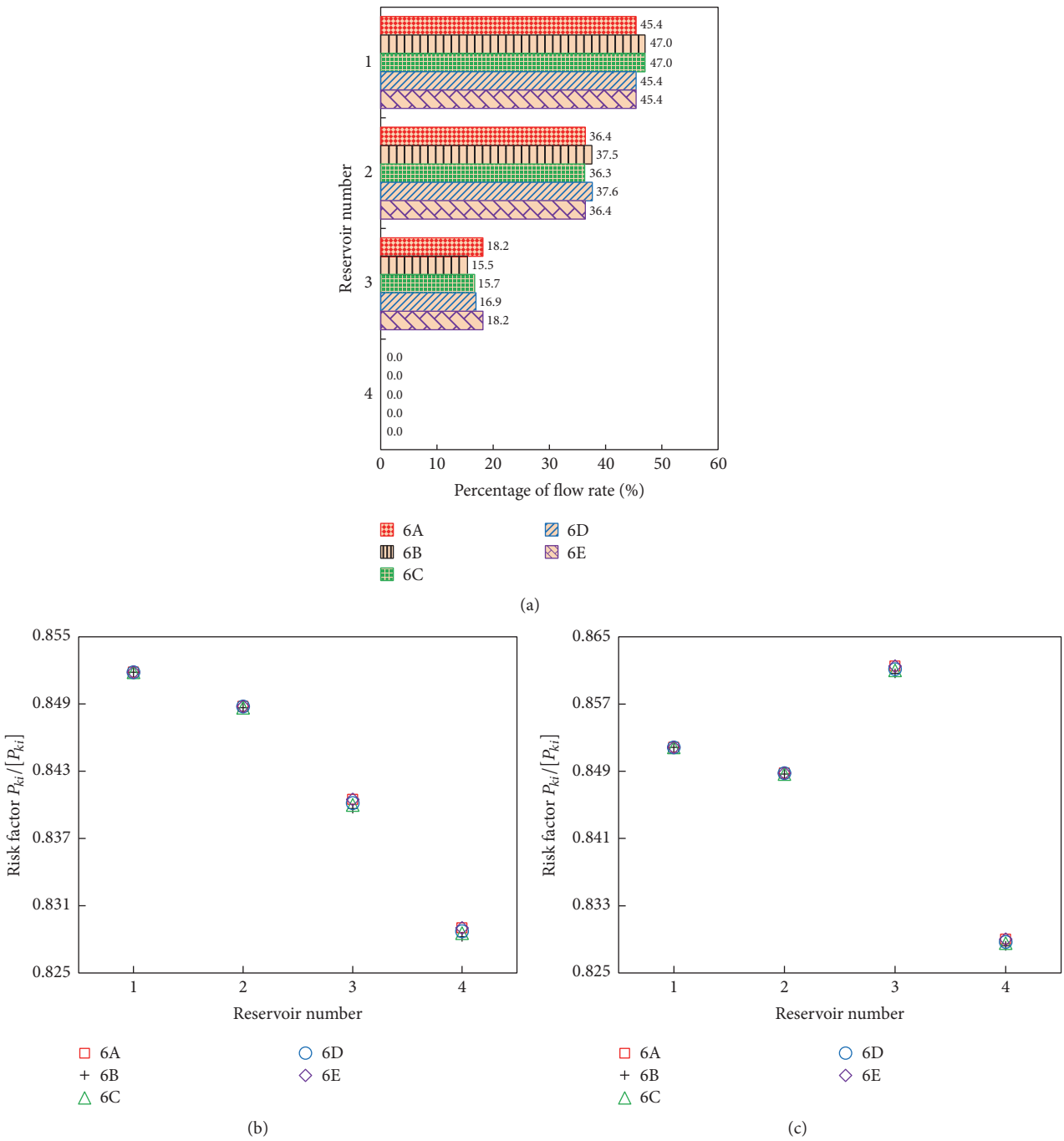

Figure 10: Proportions of the inflows (a) and risk factors of each reservoir for different reservoir porosities for the two scenarios of the conceptual engineering model. (b) and (c) are the risk-factor results for Scenarios S-1 and S-2, respectively.

notably greater than that of the lower reservoirs. Because the extent of the variation in each reservoir was different, the CR could shift. This result demonstrates that the injection pressure controls the overall risk level of the reservoir and the flow-rate distribution among the reservoirs can control the position of the CR. The CO_2 injection temperature had a similar effect as the injection flow rate, but the fluid injection temperature had no effect on the position of the CR.

(4) Although the formation-fracturing pressure does not affect the flow-rate distribution, it is one of the key factors for determining the reservoir risk and CR. Decreasing the formation-fracturing pressure increased the reservoir risk and cause the CR to shift. When the formation-fracturing pressures of all the reservoirs were decreased by the same factor, the risk of each reservoir increased equally without changing the CR. Under a constant flow rate, variations in

the reservoirs' porosities had a minimal effect on the flow-rate distribution and the reservoir risk. The thickness and permeability had similar effects on the flow-rate distributions and reservoir risks. For a specific reservoir, the flow rate increased with increasing thickness or permeability, and the flow rates of the lower reservoirs simultaneously decreased, whereas the flow rates of the upper reservoirs remained unchanged. Furthermore, only the risks of the lower reservoirs decreased with increases in these two parameters; therefore, the CR can shift to another reservoir. The initial formation pressure had the opposite effect as the reservoir thickness. Therefore, certain reservoirs can be selectively reformed according to their risks to decrease these risks and adjust the position of the CR, which can effectively improve the injection safety and utilization efficiency of the reservoirs.

(5) The injection flow rates notably influenced the flow-rate distribution. The position of the CR and injection flow rate may vary in actual CO_2 injection processes. The design of the maximum allowable wellhead injection pressure should consider multiple flow-rate scenarios to reduce uncertainties and to improve the reliability of the project.

(6) The results obtained from our investigations of the influence of the injection parameters on the flow-rate distributions and reservoir risks in the case study of the Shenhua CCS demonstration project can be used to guide subsequent injection operations. This research was based on a vertical wellbore that penetrated a number of reservoirs. Although the results for horizontal and inclined wells may be similar, further research on these topics is still required.

Conflicts of Interest

The authors declare that they have no conflicts of interest.

Acknowledgments

This work was sponsored by the International Science & Technology Cooperation Program of China (S2016G9005) under the cooperation framework of the US-China Clean Energy Research Center (CERC).

References

[1] S. Bachu, "CO_2 storage in geological media: role, means, status and barriers to deployment," *Progress in Energy and Combustion Science*, vol. 34, no. 2, pp. 254–273, 2008.

[2] S. Bachu, "Screening and ranking of sedimentary basins for sequestration of CO2 in geological media in response to climate change," *Environmental Geology*, vol. 44, no. 3, pp. 277–289, 2003.

[3] IPCC, *Climate Change 2014: Mitigation of Climate Change. Contribution of Working Group III to the Fifth Assessment Report of the Intergovernmental Panel on Climate Change*, Cambridge University Press, Cambridge, UK, 2014.

[4] IPCC., *IPCC special report on carbon dioxide capture and storage*, Cambridge University Press, Cambridge, UK, 2005.

[5] X. C. Li, Y. F. Liu, B. Bai, and Z. Fang, "Ranking and screening of CO_2 saline aquifer storage zones in China," *Chinese Journal of Rock Mechanics and Engineering*, vol. 25, no. 5, pp. 963–968, 2006 (Chinese).

[6] K. Michael, A. Golab, V. Shulakova et al., "Geological storage of CO_2 in saline aquifers—a review of the experience from existing storage operations," *International Journal of Greenhouse Gas Control*, vol. 4, no. 4, pp. 659–667, 2010.

[7] H. Kongsjorden, O. Karstad, and T. A. Torp, "Saline aquifer storage of carbon dioxide in the Sleipner project," *Waste Management*, vol. 17, no. 5-6, pp. 303–308, 1998.

[8] Z. Li, M. Dong, S. Li, and S. Huang, "CO_2 sequestration in depleted oil and gas reservoirs—caprock characterization and storage capacity," *Energy Conversion and Management*, vol. 47, no. 11-12, pp. 1372–1382, 2006.

[9] J. Underschultz, C. Boreham, T. Dance et al., "CO_2 storage in a depleted gas field: an overview of the CO2CRC Otway Project and initial results," *International Journal of Greenhouse Gas Control*, vol. 5, no. 4, pp. 922–932, 2011.

[10] X. Wu, "Shenhua group's carbon capture and storage (CCS) demonstration," *Mining Report*, vol. 150, no. 1-2, pp. 81–84, 2014.

[11] J. Rutqvist, J. Birkholzer, F. Cappa, and C.-F. Tsang, "Estimating maximum sustainable injection pressure during geological sequestration of CO_2 using coupled fluid flow and geomechanical fault-slip analysis," *Energy Conversion and Management*, vol. 48, no. 6, pp. 1798–1807, 2007.

[12] B. Bai, X. Li, H. Wu, Y. Wang, and M. Liu, "A methodology for designing maximum allowable wellhead pressure for CO2 injection: application to the Shenhua CCS demonstration project, China," *Greenhouse Gases: Science and Technology*, vol. 7, no. 1, pp. 158–181, 2017.

[13] J. E. Streit and R. R. Hillis, "Estimating fault stability and sustainable fluid pressures for underground storage of CO2 in porous rock," *Energy*, vol. 29, no. 9-10, pp. 1445–1456, 2004.

[14] B. Bai, X. Li, M. Liu, L. Shi, and Q. Li, "A fast explicit finite difference method for determination of wellhead injection pressure," *Journal of Central South University*, vol. 19, pp. 3266–3272, 2012.

[15] M. Liu, B. Bai, and X. Li, "A unified formula for determination of wellhead pressure and bottom-hole pressure," *Energy Procedia*, vol. 37, pp. 3291–3298, 2013.

[16] H. Wu, B. Bai, M. Liu, and X. Li, "The equivalent density method to estimate the wellbore pressure of CO2 well," *Special Oil and Gas Reservoirs*, vol. 22, pp. 114–117, 2015.

[17] J. M. Nordbotten, M. A. Celia, and S. Bachu, "Injection and storage of CO2 in deep saline aquifers: Analytical solution for CO2 plume evolution during injection," *Transport in Porous Media*, vol. 58, no. 3, pp. 339–360, 2005.

[18] H. J. Ramey, "Wellbore heat transmission," *Journal of Petroleum Technology*, vol. 140, no. 4, pp. 427–435, 1962.

[19] D. Y. Peng and D. B. Robinson, "A new two-constant equation of state," *Industrial and Engineering Chemistry Fundamentals*, vol. 15, no. 1, pp. 59–64, 1976.

[20] H. Wu, B. Bai, X. Li, S. Gao, M. Liu, and L. Wang, "An explicit integral solution for pressure build-up during CO2 injection into infinite saline aquifers," *Greenhouse Gases: Science and Technology*, vol. 6, no. 5, pp. 633–647, 2016.

[21] H. Wu, B. Bai, X. Li, M. Liu, and Y. He, "An explicit finite difference model for prediction of wellbore pressure and temperature distribution in CO2 geological sequestration," *Greenhouse Gases: Science and Technology*, vol. 7, no. 2, pp. 353–369, 2017.

Hindawi
Geofluids
Volume 2017, Article ID 8536724, 17 pages
https://doi.org/10.1155/2017/8536724

Research Article

Evaluating the Sealing Effectiveness of a Caprock-Fault System for CO_2-EOR Storage: A Case Study of the Shengli Oilfield

Bing Bai,[1] Qifang Hu,[1] Zhipeng Li,[2] Guangzhong Lü,[2] and Xiaochun Li[1]

[1] *State Key Laboratory of Geomechanics and Geotechnical Engineering, Institute of Rock and Soil Mechanics, Chinese Academy of Sciences, Wuhan 430071, China*
[2] *Shengli Oilfield Company, Sinopec, Dongying 257061, China*

Correspondence should be addressed to Bing Bai; bai_bing2@126.com

Received 6 March 2017; Revised 6 May 2017; Accepted 27 June 2017; Published 27 September 2017

Academic Editor: Tianfu Xu

An effective sealing system is crucial for CO_2-EOR storage, and these sealing systems are typically composed of the caprocks and faults that surround a reservoir. Therefore, the sealing effectiveness of a caprock-fault system must be evaluated at various stages of CO_2-EOR storage projects. This paper presents a new evaluation framework that considers specific site characteristics and a case study on the sealing effectiveness of the caprock-fault system in the Shengli Oilfield. The proposed method is a weighted ranking system where a set of 17 indicators has been developed for the assessment and ranking of the G89 block in terms of their sealing ability for CO_2 sequestration. Additional indicators are involved in the method, such as the newly proposed parameter, frontier displacement work which reflects the influence of formation pressure, displacement pressure resistance, and caprock thickness. The new approach considers the sealing mechanisms of caprocks and faults as well as the configuration relationships between them. The method was used to evaluate the sealing effectiveness of the G89 block that has a considerable number of faults and good sealing ability of caprock in the Shengli Oilfield.

1. Introduction

CO_2 geological storage (CGS) is widely recognized as an effective approach for reducing CO_2 levels in the atmosphere [1–3]. As a further CGS initiative, CO_2 geological utilization and storage (CGUS) [4], which fall under the wider scope of CCUS (Carbon Capture, Utilization, and Storage) technology, were proposed for the full utilization of CO_2 and the maximization of its additional value prior to underground storage. Of the identified CGUS options, CO_2-enhanced oil recovery (EOR) storage (CO_2-EOR storage), which is different from the CO_2-EOR operations traditionally used in Tertiary oil recovery, is a subject of increasing interest because of its overall advantages over other CGS options. CO_2-EOR storage is essentially a cooptimization process of CO_2 storage and EOR designed to improve oil production simultaneously sequestrating CO_2 [5, 6], which can achieve cost advantages and social and economic benefits [7, 8].

A number of CO_2-EOR projects have been conducted worldwide [9–11]. In China, several CO_2-EOR projects have been conducted by PetroChina, Yanchang Petroleum, and Sinopec in the Jilin Oilfield, Jingbian Oilfield, and Shengli Oilfield, respectively [8, 12–14]. The Shengli Oilfield (Figure 1) is the target site in this paper. The CO_2-EOR pilot operations designed to explore whether the gradual decreasing trend of oil production could be overcome began at this site early in 2007 [15]. The active enhancement effect observed at the site and a desire to improve CO_2 reductions inspired Sinopec to move forward with CO_2-EOR storage research in 2012 at the Shengli Oilfield with the support of the National Key Technology R&D Program of China. In this project, a method of screening suitable target blocks for CO_2-EOR storage was required and investigated. The effectiveness of a seal system is of overriding importance for realizing effective geological sequestration of CO_2 [16, 17]; therefore, such systems must be evaluated carefully.

Caprock is the principal seal system for CO_2 storage, and although the hydrodynamic sealing capacity of caprock has been frequently discussed for hydrocarbon migration [19], few studies have focused on the sealing capacity for

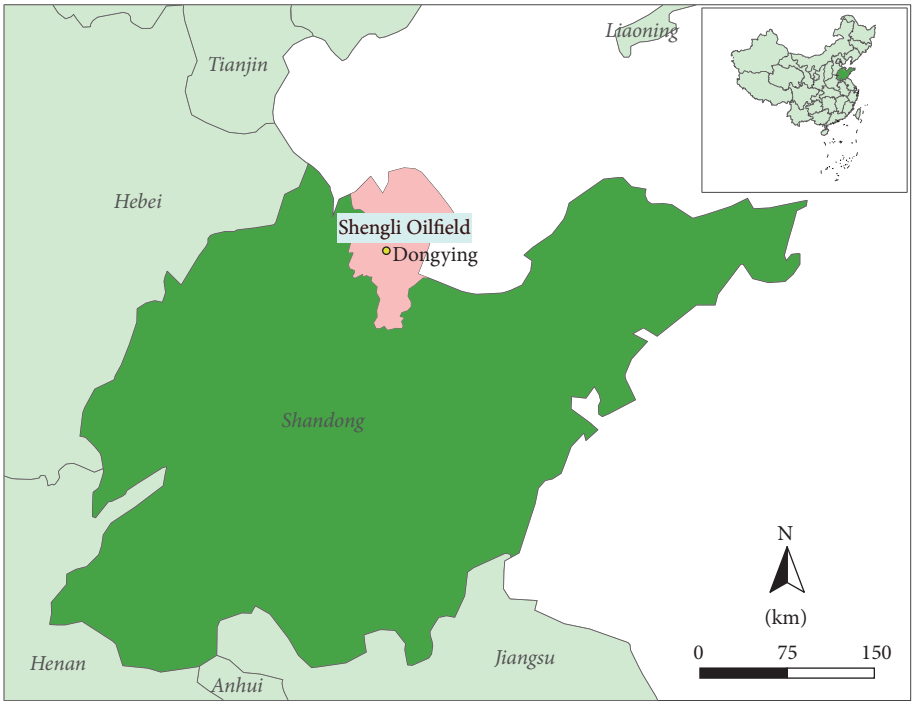

Figure 1: Location of the Sinopec Shengli Oilfield (after [18]).

CO_2 storage. In practice, most CO_2-EOR storage projects utilize the same evaluation methodologies and indicators [20]; however, the differences related to CO_2 storage are rarely discussed. Moreover, the structural or geometric characteristics of caprock, such as the thickness, have not been properly detailed [21].

Compared with many overseas projects, in the Shengli Oilfield reservoir, a considerable number of faults have been observed and the configuration relationships between caprock and faults are very complex. Therefore, the effectiveness of the fault sealing ability must be evaluated carefully when selecting appropriate sites. Current researches on the conditions that allow faults to seal or leak principally occur in the field of hydrocarbon exploration [19]. Although research on the structural control of fluid flow in hydrocarbon reservoirs is in nascent stages, various hydrocarbon leakage indicators have been identified for faults [22]. Integrity is a restraint on the fault sealing capacity, and it is currently a focal parameter in the literature; however, studies into the static sealing effectiveness of fault systems that consider CO_2 migration and the internal fault structure have made limited progress [23–25].

Here, we present a study detailing an approach to evaluating the baseline sealing effectiveness of the caprock-fault system of a CO_2-EOR storage project in the Shengli Oilfield based on a new evaluation framework. The baseline evaluation refers to an investigation of feasibility performed before the project begins. The new evaluation method is based on the evaluation criteria for CO_2-EOR storage and includes comprehensive key parameters related to caprocks, faults, and their matching relationships. Parametric normalization and ranking are employed to organize the indicator system. In the selection of evaluation indicators, we will pursue a balance among reliability, new CO_2 storage demands, and data availability.

2. Framework of the Evaluation Method

2.1. Identification of the Evaluation Objects. A potential reservoir block for CO_2-EOR storage is usually surrounded by different geological features, such as caprocks and faults. These features as a whole compose a network that determines the sealing ability of the seal system (Figure 2). A reservoir for CO_2 storage is usually deeper than 800 m underground, and more than one set of caprocks are positioned over the reservoir. The overlying caprock layer is usually specified as a leakage controlled layer, and it actually determines the scope of the sealing system that must be evaluated. The engineering target in this project requires a lack of direct CO_2 penetration into the caprock so that the injected CO_2 cannot leak through the caprock and to the upper reservoirs. Therefore, only the directly overlying caprock-fault system (composed of the caprock and the faults) associated with the reservoir for CO_2 storage will be evaluated in this paper (Figure 2).

CO_2-EOR risk assessments have tended to use risk scenarios, particularly scenarios related to wellbores, large faults, and an unspecified leaking caprock [26]. Figure 2 shows a conceptual model of a typical system that includes a reservoir, caprocks, and faults for CO_2-EOR storage. The sealing effectiveness of the system depends on the sealing ability of all components as shown in Figure 2(A)–(E). Therefore, the components must be assessed during the site evaluation

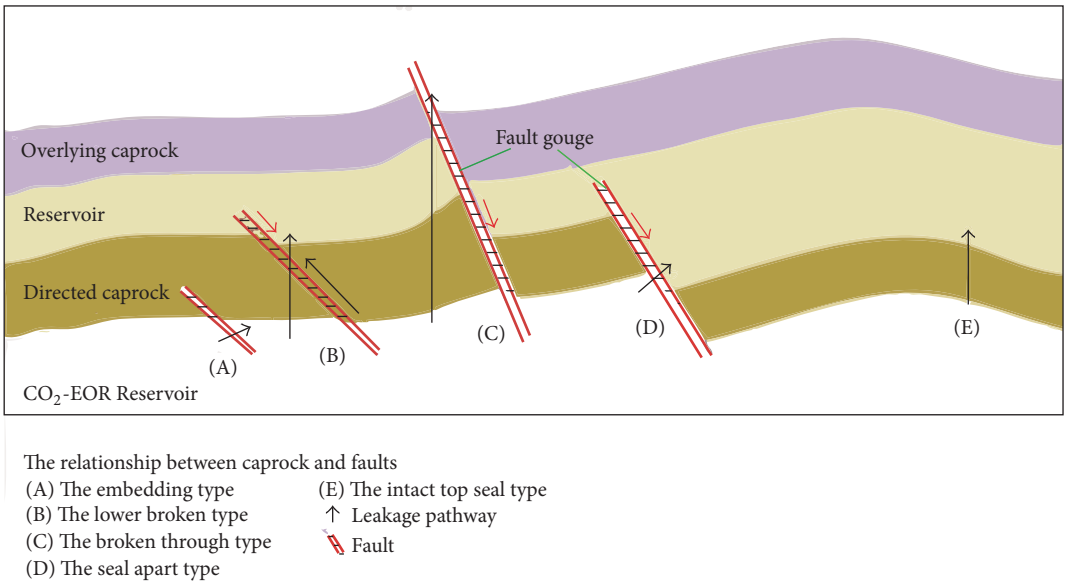

Figure 2: Conceptual model of caprock-fault system for CO_2-EOR storage.

stage. The caprocks are usually geologically cut by the faults and form several configurational relationships. Three types of configurational relationships have been identified: embedding type, lower broken type, and broken-through type [27, 28]. The embedding type refers to direct caprocks that are only partly penetrated by the fault (Figure 2(A)). The lower broken type refers to a direct caprock that has been cut through by a fault, although the overlying caprock has not been reached (Figure 2(B)). The broken-through type refers to a direct caprock and its overlying caprocks that have been cut through by a fault (Figure 2(C)).

The matching types between caprocks and faults can also be characterized by the relationship between the fault throw and the thickness of the direct caprock. The following three matching types have been defined: intact top seal type, seal connected type, and seal apart type [27]. The intact top seal type (Figure 2(E)) corresponds to an embedded type when the top of the direct caprock is not penetrated by faults. The seal connected type refers to a direct caprock that has been cut through by a fault but the throw is less than the thickness of the direct caprock. The seal apart type refers to a direct caprock that has been cut through by a fault but the throw is greater than the thickness of the direct caprock (Figure 2(D)).

2.2. Indicator System and Evaluation Criteria. The sealing effect of a caprock-fault system for CO_2-EOR storage depends mainly on the sealing ability of the caprocks and faults [29]. The sealing mechanisms for CO_2 storage are similar to that for hydrocarbons and include the capillary sealing mechanism, overpressure sealing mechanism, concentration sealing mechanism, and synergetic sealing mechanism composed of two or more sealing mechanisms [21]. Therefore, breakthrough pressure (or displacement pressure) and caprock overpressure are necessary indicators for evaluating the sealing effect of caprocks. In this paper, the two indicators will be merged as one indicator, that is, frontier displacement work described in Appendix. As a structural characteristic, the thickness of a caprock has no direct relationship with the breakthrough pressure, although it has been confirmed to have an outstanding sealing effect. The frontier displacement work can be calculated by the values of the thickness, breakthrough pressure, and overpressure of the caprock with the formula (A.3) in Appendix. In addition, permeability, shale content, and other caprock parameters are usually chosen as evaluation indicators. Liu [30] concluded a positive correction between permeability and porosity that was used to assess the sealing effect of caprocks. A fault can either be a seal or a leak depending on specific factors of the fault. In past decades, knowledge on fault sealing properties has been accumulated by the oil and gas industry, and these data could be directly applied when evaluating the sealing properties of CO_2-EOR storage. The following two types of fault seals have been recognized: juxtaposition seals and fault rock seals [31]. Juxtaposition seals originate from differences in the lithology and petrophysical properties (porosity, permeability, capillary pressure, etc.) of different rocks juxtaposed between the hanging wall and the footwall. Typical methods of evaluating the sealing properties of juxtaposition seals mainly include stratigraphic juxtaposition methods (e.g., the Allan map [32] and triangle juxtaposition diagram [33]) and clay smear indices. Compared with the stratigraphic juxtaposition methods, triangle juxtaposition diagram primarily focuses on the architecture of the fault juxtapositions, the stratigraphic units, and the fault geometry. The clay smear index methods emphasize the amount of clay that has been smeared along the fault planes. These methods include the Clay Smear Potential (CSP), Shale Smear Factor (SSF), and Shale Gouge Ratio (SGR). According to their definitions, these indicators are dependent on specific parameters, such as the shale bed thickness, distance from the source bed, the fault throw, and the shale layer thickness. The CSP and SSF estimate the fault sealing properties by considering the continuity of smearing

Table 1: Indicators and ranking system for a caprock-fault system for CO_2-EOR storage [27, 30, 37–40].

I	II	III Specific indicators	Very Good 5	Good 4	Normal 3	Poor 2	Very Poor 1
Fault caprock sealing system	Caprock	Displacement work (MPa·m)		>6300	2100~6300	350~2100	<350
		Porosity (%)		<5	5~10	10~15	>15
		Permeability (mD)		<0.1	0.1~1.87	1.87~10	>10
		Shale content (%)		>75	75~50	50~25	<25
		Well density (/10 km)	0	1~2	3~5	5~10	>10
	Fault	Fault activity time		Tranche	Syngenetic	Multiperiod	
		Configuration relationship between fault extension and caprock		Embedded type	Lower broken type	Broken-through type	
		Configuration relationship between fault throw and direct caprock thickness		Intact top seal type	Seal connected type	Seal apart type	
		Fault dip angle (°)		≤45	45~75	>75	
		Fault lateral displacement work (MPa·m)		>30	2.5~30		<2.5
		Fault vertical displacement work (MPa·m)		>6300	2100~6300	350~2100	<350
		Fault lateral permeability (mD)		<0.001	0.001~0.0187	0.0187~0.1	>0.1
		Fault vertical permeability (mD)		<0.001	0.001~0.0187	0.0187~0.1	>0.1
		Fault tightness coefficient	>1				<1
		Shale smear factor	<4		4~7		>7
		Clay smear potential	>35		15~35		<15
		Shale gouge ratio	>0.5		0.3~0.5		<0.3

of shale/mudstone beds, whereas the SGR calculates the average mixture of clays likely to be present at different points on a fault [31]. Compared with juxtaposition seals, where the fault is usually treated as a single plane, fault rock seals refer to faults as a fault zone composed of a series of fault planes and fault rocks. Therefore, the fault zone is similar to a thin caprock with high heterogeneity. Therefore, many caprock sealing indicators (permeability, capillary threshold pressure, etc.) could be used to evaluate the sealing properties of fault rock in the fault zones. The petrophysical properties of fault rocks are affected by many factors, the most important of which involve geostresses, subsurface temperatures, and their historical tendencies. Occasionally, these factors or their derived parameters have been selected as evaluation indicators of fault sealing properties, and they typically include differential displacement pressures between the caprock and the reservoir [34], the slip and offset of the formation lithology [29], and the fault tightness coefficient [35]. In many practical evaluations, the vertical and lateral sealing properties of faults might have different roles in specific projects and must be evaluated separately [36]. In addition, it is worth noting that although we strive to choose independent indicators, however, some of them in Table 1 might be intrinsically connected and actually not independent. Therefore, the indicators in Table 1 might be redundant. This is inevitable to some extent because, according to the current knowledge, we cannot get the exact quantitative relationship between these possible redundant indicators.

In the evaluations for specific engineering objectives, a comprehensive evaluation approach that uses multiple indicators, including redundant indicators, is widely adopted ([41, 42]) because a single indicator cannot characterize the sealing properties of a system with such a high degree of complexity and uncertainties. According to the objective of this study, we designed a system of multiple indicators considering the geometry, juxtaposition characteristics, and petrophysical properties of the caprock or faults (Table 1). Each of the indicators is classified into five grade levels, scoring, respectively, 1, 2, . . . , 5, which can be used to produce a comprehensive evaluation result in the next section.

2.3. Weighted Comprehensive Evaluation. To represent the sealing effectiveness of the caprock or the fault, the multiple indicators in Table 1 need to be synthetically integrated, which will be done with the idea similar to analytic hierarchy process (AHP). Hierarchical method was used to compute the weight of each indicator/criterion. AHP is applied with its extension to create weights for quantitative, expert opinion, and sensory panel data (listed in Table 2). The indicators/criteria adopted for evaluating the sealing ability of the caprock and faults are listed in Table 2, and the detailed evaluation method is similar to that described in Bachu [41]. To evaluate a specific part k, a monotonically decreasing numerical function $S_{i,j}$ (score)

Table 2: Scores and weights assigned to the various criteria and classes.

Class I	Class II	Criteria	Index i	Scores $j = 5$	$j = 4$	$j = 3$	$j = 2$	$j = 1$	Weight $\overline{\overline{w}}_i$
Caprock fault sealing system	Caprock	Displacement work	1		15	7	3	1	0.14
		Porosity	2		9	7	3	1	0.06
		Permeability	3		15	7	3	1	0.06
		Shale content	4		13	5	3	1	0.03
		Well density	5	15	9	7	3	1	0.02
		Fault active time	6		9	5	1		0.01
		Configuration relationship between fault extension and caprock	7		9	5	1		0.05
		Configuration relationship between fault throw and direct caprock thickness	8		9	5	1		0.05
	Fault	Fault dip angle	9		7	5	1		0.05
		Fault lateral displacement work	10		9	5		1	0.11
		Fault vertical displacement work	11		9	5		1	0.11
		Fault lateral permeability	12		9	7	5	1	0.03
		Fault vertical permeability	13		9	7	5	1	0.03
		Fault closed coefficient	14	15				1	0.11
		Shale smear factor	15	15		7		1	0.02
		Clay smear potential	16			7		1	0.02
		Shale gouge ratio	17	15		7		1	0.02

is assigned to indicator i according to its corresponding grade level j as determined in Table 1 (j from 5 to 1 indicates the best to the worst grade in terms of suitability for a particular criterion). The scores can be continuous or discrete, that is, they can be assigned to all five grades or only a portion of the grade levels of the corresponding criterion. Because the function S_i has different ranges of values for each criterion i, comparisons between different indicators of sealing effectiveness may be difficult. Therefore, a normalized value must be used for different indicators as in

$$P_i^k = \frac{S_{i,j} - S_{i,1}}{S_{i,n} - S_{i,1}}, \tag{1}$$

where $S_{i,j}$ is the specific score value for criterion i; $S_{i,1}$ is the function score value under the least favourable class conditions for criterion i; $S_{i,n}$ is the value under the most favourable class condition; the normalized value $P_i = 0$ represents the least favourable class; and the normalized value $P_i = 1$ represents the most favourable class.

The effect of parameterization and normalization pertains to the transformation of various site characteristics into dimensionless variables between 0 and 1. Considering the weight factor of each criterion, a synthetical score R^k can be obtained as follows:

$$R^k = \sum_1^i \overline{\overline{w}}_i P_i^k, \quad \sum_1^i \overline{\overline{w}}_i = 1, \tag{2}$$

where $\overline{\overline{w}}_i$ is the weight factor from Table 2, and it is used to estimate the impact degree of a corresponding criterion.

2.4. Application Steps of the Method. In practical evaluation work, a preliminary characterization of a candidate site is necessary and the fundamental geological and physical parameters are required to be prepared by lab tests or geophysical prospecting. Next, the target caprocks or faults of the candidate site are discretized into small pieces, and the evaluation parameters involved in Tables 1 and 2 could be obtained for each piece. In other words, the evaluation work is actually done for each piece and therefore the evaluation result will be a scoring or ranking distribution of the whole candidate site. The case study in the latter part of this paper will follow the evaluation process.

3. Target Site

3.1. Site Geology. The Shengli Oilfield branch company includes 65 oil fields and 2 gas fields, and it covers an aerial extent of approximately 2117 km^2 [43]. Almost 90% of the oil reserves lie at depths ranging from 950 m to 3200 m underground. The candidate target site is the Gao89-Fan142 district, which is located in the northern Zhenglizhuang Oilfield of the Dongying sag and the central Jinjia-Zhenglizhuang–Fanjia structure belt. The target site consists of the G899 block, G89-1 block, G891 block, F143 block, and F142 block as shown in Figure 3. The strata of the target site (from top to bottom) are the Pingyuan formation of the Quaternary system, the Minghuazhen formation and Guantao formation of the upper Tertiary system, the Dongying formation of the lower Tertiary system, and the 1st, 2nd, 3rd, and 4th

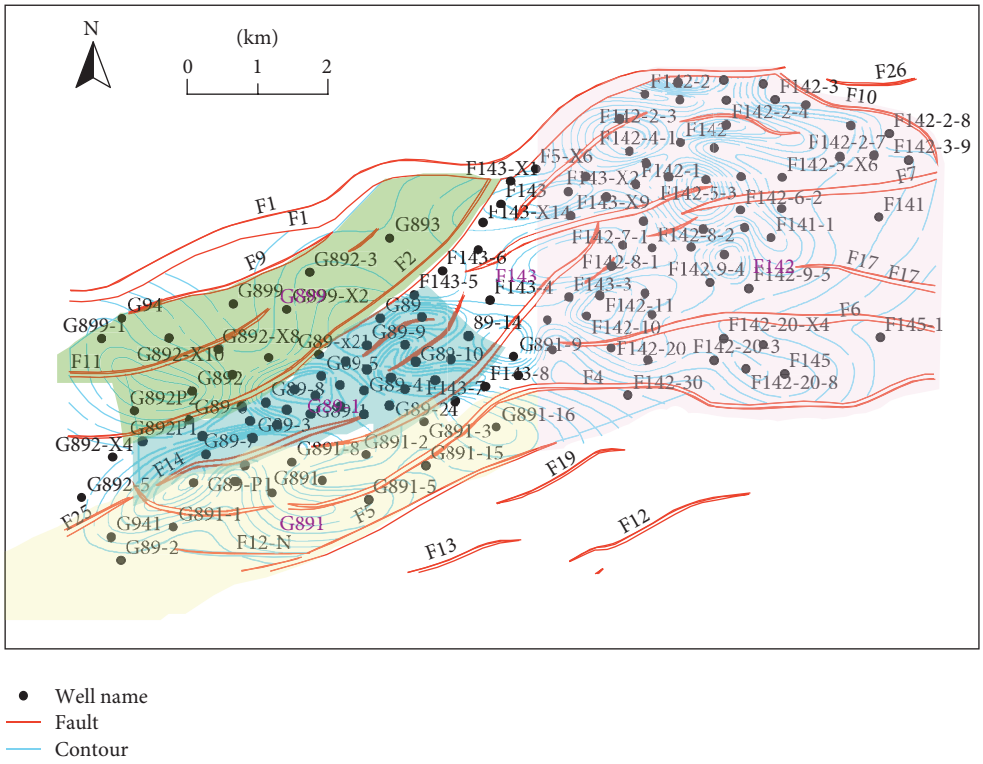

- Well name
- Fault
- Contour

Figure 3: The target area (G89-F142 area) for CO_2-EOR storage and the distribution of faults.

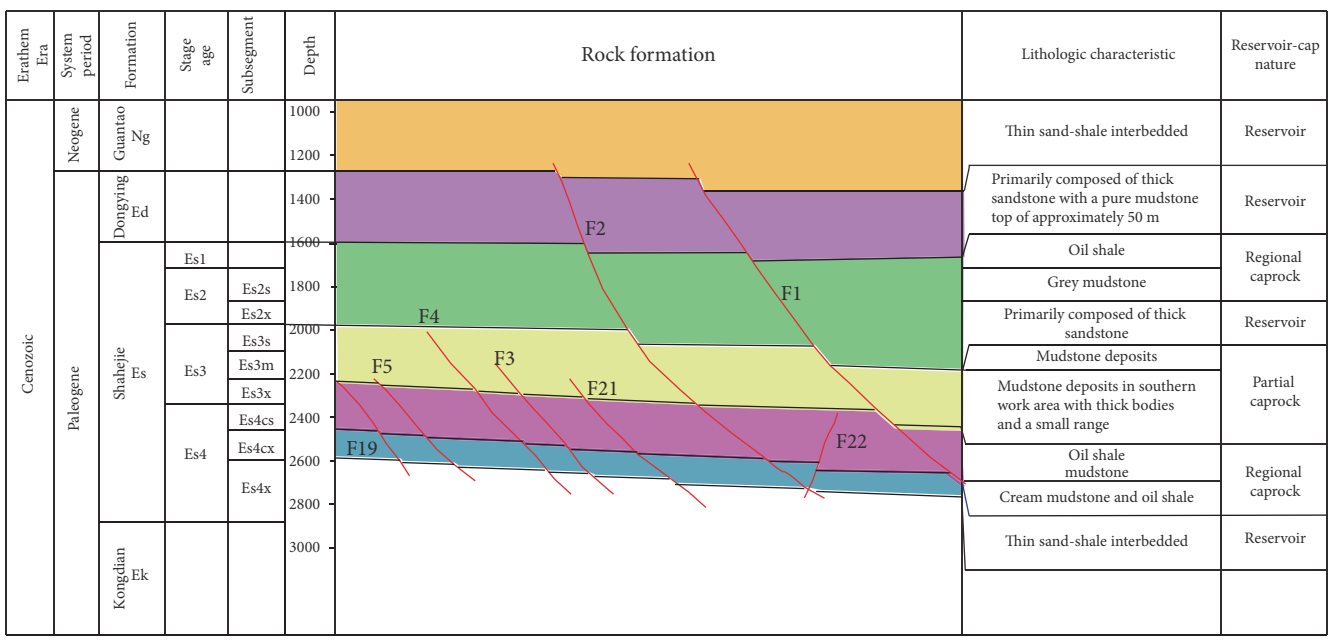

Figure 4: The strata of the target site.

members of the Shahejie formations and Kongdian formation in Cenozoic Erathem (Figure 4). In the blocks, five main sets of oil-bearing series have been found via exploration: Ed, ES1, ES2, ES3, and ES4. Among these series, the Shahejie ES4S formation, which is the main oil-bearing series, is buried at a depth of 2700–3200 m and the thickness of the strata is approximately 120–170 m. The lithology of the formation is mainly grey and light grey mudstone with thin sandstone. The Shahejie ES3 formation is a direct caprock of ES4S reservoir, and its lithology is mainly dark grey mudstone.

Table 3: Geostress data of the target area.

Well	Core depth (m)	Geostresses						Stress gradient (MPa/m)	
		Direction (°)			Size (MPa)				
		σ_H	σ_h	σ_v	σ_H	σ_h	σ_v	σ_H	σ_h
G892-3	3170	71.23	161.23	72.69	61.97	47.97	0.0229	0.0195	0.0151
G892-X8	3225	70	160	71.80	82.37	56.12	0.0223	0.0255	0.0174
G893	3281	118	208	73.95	88.67	57.67	0.0225	0.0271	0.0176

The target area is a southeast high, northwest low monoclinal structure with a strata dip angle of approximately 4~8°. The structure is divided into many terraces by a series of parallel faults running northwest and trending northeast. The largest structural gap can reach 500~700 m. According to strata comparisons and seismic interpretations, fault F1 extends upward to the Guantao formation; F2 extends upward to the ES1 formation; F3, F4, F6, and F7 mainly extend upward to the ES3M formation; F5 extends upward to the ES2 formation; and the other faults mainly extend to the ES3X formation. Approximately 26 faults intersect with the direct caprock as shown in Figure 3.

3.2. Current Geostresses. Geostresses and fault sealing properties are closely correlated, and geostress variations significantly affect the fault sealing effectiveness [44]. Therefore, the geostress data must be obtained to calculate the fault surface stress for the evaluation indexes. Current geostress characteristics of the target area have been obtained from a variety of sources, like the empirical formula of geostresses, measured geostress data, and so on.

The target area is located in the Bohai Bay basin, and the three principal stresses all increase with depth. When the depth is greater than a certain value, the three principal stresses will satisfy $\sigma_H > \sigma_v > \sigma_h$; thus, the vertical stress σ_v represents the intermediate principal stress. In the oil fields of the eastern region of China, the vertical stress σ_v is approximately equal to the lithostatic stress of the overlying rock formations. The Dongying sag is located in a district of medium tectonic stress controlled by plate tectonic movement. The hydraulic fracturing data of the Dongying sag show that the cracks caused by the oil well fracturing are mainly vertical cracks. Li [45] investigated the current geostress field of the 3rd Shahejie formation in the Dongying sag based on numerical modelling and found that the direction of the current maximum horizontal principal stress is approximately NE280° with the stress values ranging from 50 to 65 MPa, and the direction of the minimum principal stress is approximately NE10° with the stress values ranging from 35 to 50 MPa. The geostresses of the southern and eastern parts of Dongying sag are larger, and smaller stresses appear to occur along the north-western edges of the Boxing depression. Lower stresses occur in the fault zone belt. Moreover, because the 3rd Shahejie formation in the Dongying sag is under abnormally high formation pressure, the minimum horizontal principal stress in the sag is significantly higher than that of the surrounding formations.

Limited measured geostress data are available for the target area, and the latest measured data are listed in Table 3. To the authors' knowledge, no studies have focused on the geostress distribution in the target area; however, some measured data and research on the neighbouring regions could provide a partial supplement and reference for our research work. These data are listed in Table 4. In addition, the Geological Institute of the National Seismological Bureau recommended the following regression formula to estimate the geostress data for the Shengli Oilfield:

$$\begin{aligned} \sigma_H &= -22.58 + 0.034H, \\ \sigma_h &= -11.65 + 0.022H, \\ \sigma_v &= (0.021 \sim 0.022)\, H, \\ & \qquad H \in [1300, 3300]\ \text{m}. \end{aligned} \tag{3}$$

Wang [49] also studied the geostress of the L112 region in Chunliang and suggested the following approximate estimation formula:

$$\begin{aligned} \sigma_H &= 0.03731H - 21.6655, \\ \sigma_h &= 0.02955H - 23.8529, \\ \sigma_v &= 0.02335H + 1.36759, \end{aligned} \tag{4}$$

where H is the depth, m; σ_H is maximum principal stress, MPa; σ_h is minimum principal stress, MPa; and σ_v is the vertical principle stress, MPa.

4. Results and Analysis

4.1. Evaluation Parameter Values. Figures 5–9 show values of some key parameters of the caprock. The parameters of the faults will be detailed in a subsequent section. Figure 5 shows the contour map of the effective thickness of the target caprock, which has strong regularity. In the south, the caprock is thin, and, in the north, the caprock is thick. The caprock is especially thick near wells G899, G89-24, and F142-3, with an average thickness of approximately 540 m and a maximum thickness of up to 590 m. The region near wells F142-2-8 and F142-8-2 also presents considerable caprock thicknesses,. Starting at the positions of the two wells, the thickness of the caprock increases gradually, and the minimum value is approximately 450 m. Figure 6 shows the distribution of the mudstone displacement pressure ranging from 0 to 24 MPa in the ES3X region of the Shahejie formation. The

Table 4: Measured geostress data in the region near the target area.

Blocks	Well number	Well section /depth (m)	σ_H (MPa)	σ_v (MPa)	σ_h (MPa)	Maximum principal stress's direction N E (°)	Note
Fanjia	Fan8-511	2866~2874	—	66	43.6	89.3	[46]
	Fan10-513	2870~2894	60.6	66.3	46.1	82.7	
	Fan17-17	2867~2872	57.9	65.9	46.1	80	
	Fan15-8	3013~3076	71.6	70	52	123	
	Fan12-511	2866~2877	67.6	66.2	51.2	82	
	Fan19-720	3136.3~3156.1	76.4	72.4	56.4	138	
	Fan22-724	3144~3167	83.2	72.6	58.6	175	
	Fan24	2815~2825	66.2	64.9	49.6	100	
	Fan18-720	3142~3146	68.2	72.3	53.4	145	
	Fan23	3150~3155	73.5	72.5	58.1	143.3	
	Fan26	2980~3020	68	71.1	45	91.2	[45]
	Fan10	2914~2935	67	66.6	46	87.6	
	Fan162	2644.5~2652.0	59.5	63.5	46.5	107	
Bonan		3100	66	68	44	85	[47]
Fanjia		3000	66.7	68	45.8	100	
Ying11		3100	110–120	68	59–62	100	
Shanjiasi		2600	78	68	44	100	
Changwei		2400	66	54	45	80	
Niuzhuang		3250	91	68	66	105	
Binnan		2400	66	66	45	80	
Shengtuo		2100	58	—	44	90	
Gao89	G89-1		76.41		47.35	NE69.0	[48]
	G89-7		72.47		55.77	NE53.3	
Chun107	C97-6		—	—	49.64	—	
	C97-7		75.59		53.27	NE97.5	
L112	L112-32		78.03		50.79	NE128.6	[49]
	L112-8		83.00		55.8	NE103.0	
	L9-3		—	—	—	NE145.5	
	L112-12	2676.6~2701	81.64	64	54.26	102.6	
	L112-8	2717~2750	82.64	65	51.89	103.6	
	L112-61	2789.5~2818.6	79.07	66	52.39	151.0	
	L112-32	2722.4~2764.4	78.03		53.79	128.6	
	L112-43	2715.3~2759	80.38		52.43	132.9	
	L112-45	2729.5~2776.8	82.60		52.70	127.4	

displacement pressure gradually increases from the centre of wells G892-X4, G89-1, and F142-8-2 outwards. Figure 7 shows the distribution of the formation pressure in the range of 0 to 8 MPa. The formation pressure is large in the eastern part of well F143-8 and the northern part of wells F143-X9, F142-2-4, and F142-3-9, which present values that are all greater than 4 MPa, whereas in the remaining areas, the pressures are less than 4 MPa. Figure 8 shows the porosity distribution of the caprock, which gradually decreases from the centres of wells G891-10, G899-X2, and G89 outwards. The porosity gradually increases in a local area with a "人" shape at the eastern part of wells F142-1 and F142-11 and the west part of wells F142-11-2 and F142-16-2, and the maximum porosity is up to 24%. Figure 9 shows the frontier displacement work of the caprock calculated using the formulas (A.1)–(A.3). The distribution characteristics are similar to that of the displacement pressure of caprock in Figure 6.

The calculation results of the fault properties are shown in Table 5. Most of the fault activities ceased prior to the deposition of ES2. Faults F1 and F2 stopped growing at the late stage of the Guantao group, and the configuration relationship between F1, F2, and the caprock is the double break type. Therefore, faults F1 and F2 are active faults, and CO_2 might leak to the Guantao formation through the two faults.

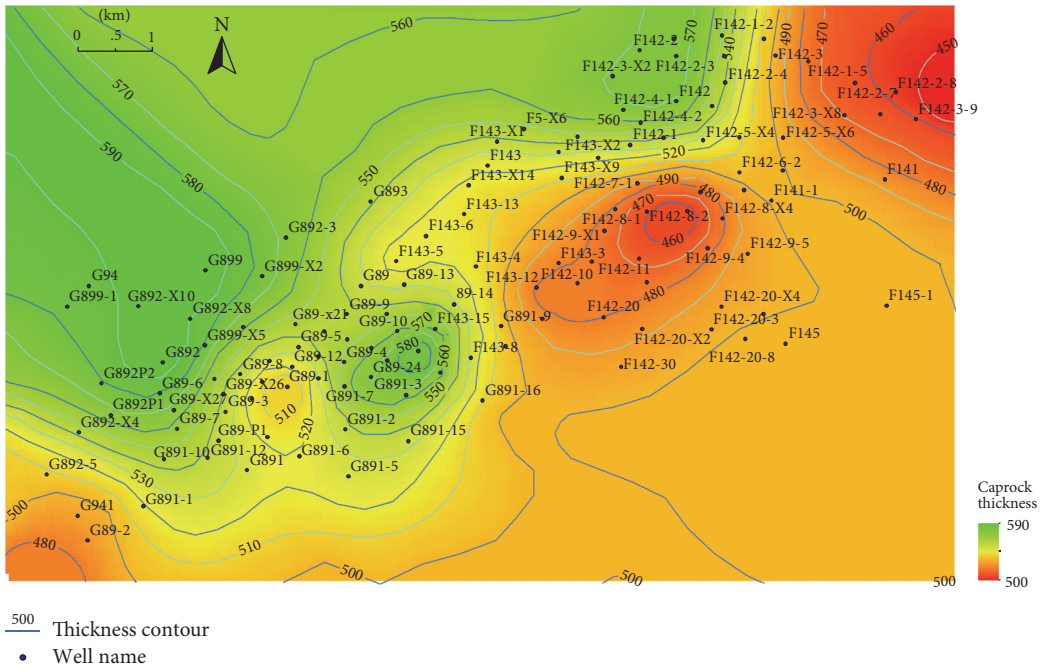

Figure 5: Thickness distribution of the caprock in the target area.

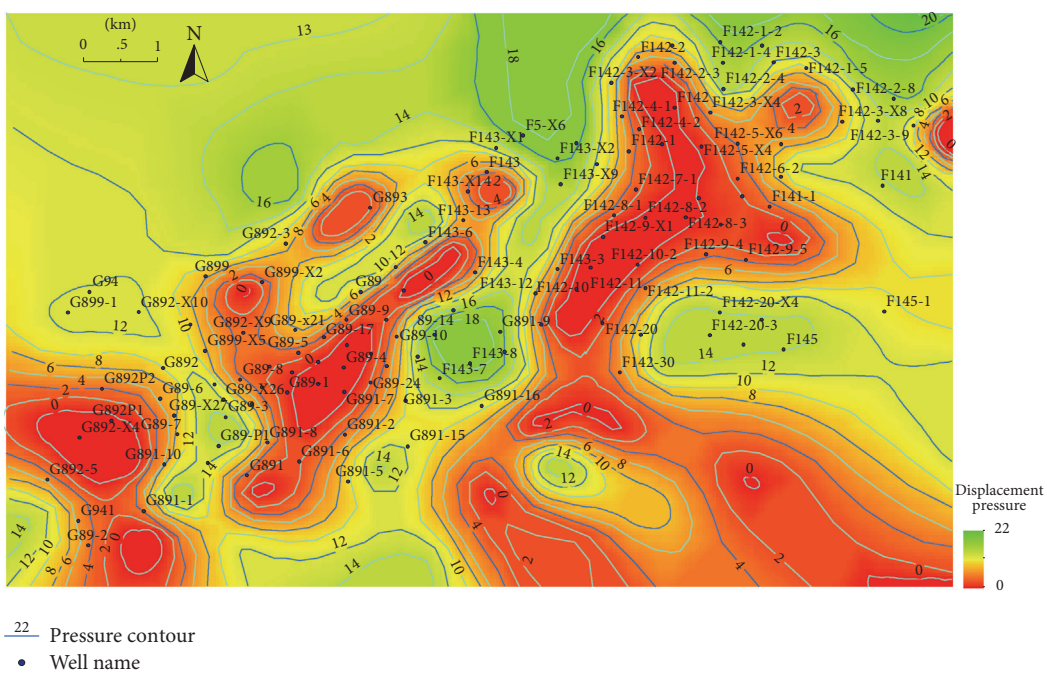

Figure 6: Displacement pressure distribution of the caprock in the target area.

The thicknesses of the fault rock are included in the evaluation methodology as shown in Table 5. However, scarce information is available on the thickness of the fault rock in the target area at the early stage of the project. In the literature, empirical formulas have been presented to estimate the thickness of fault rock [50, 51], and, therefore, a similar method is employed in this paper. The results show that the thicknesses of all the fault rocks are close to 1 m. An empirical formula [51] of permeability was used to estimate the permeability of the involved fault rocks. All the fault tightness coefficient values are greater than 1.0, as shown in Table 5.

4.2. Evaluation Results and Analysis. In Section 4.1, we determined all the primary parameter values as iso-values and spatial layers in the GIS tool for the target caprock-fault system

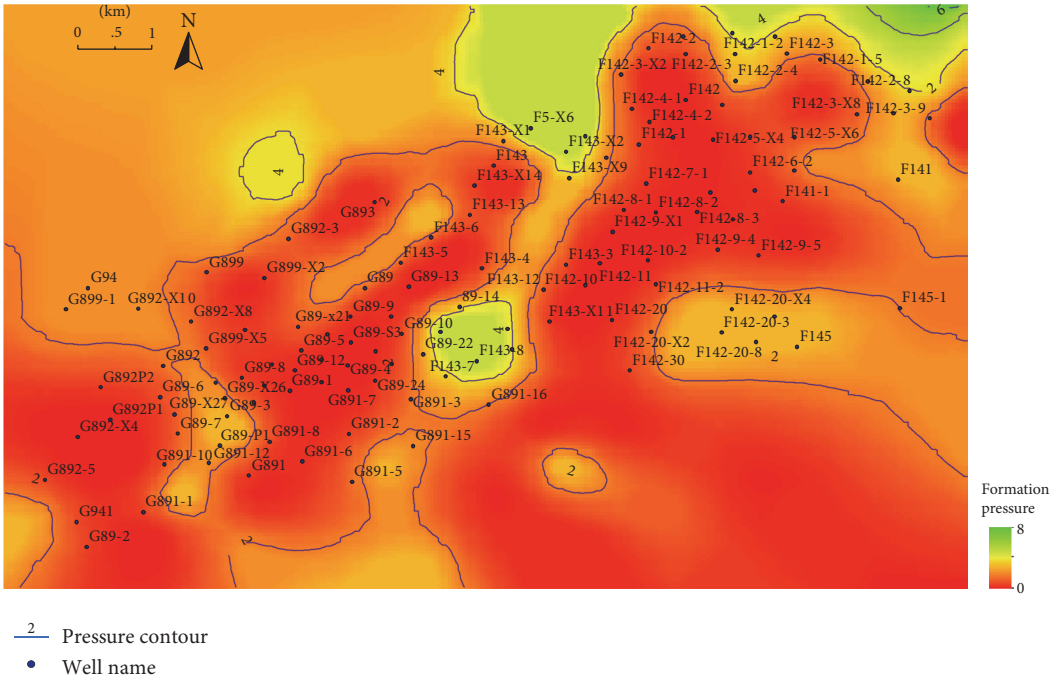

Figure 7: Formation pressure distribution in the target area.

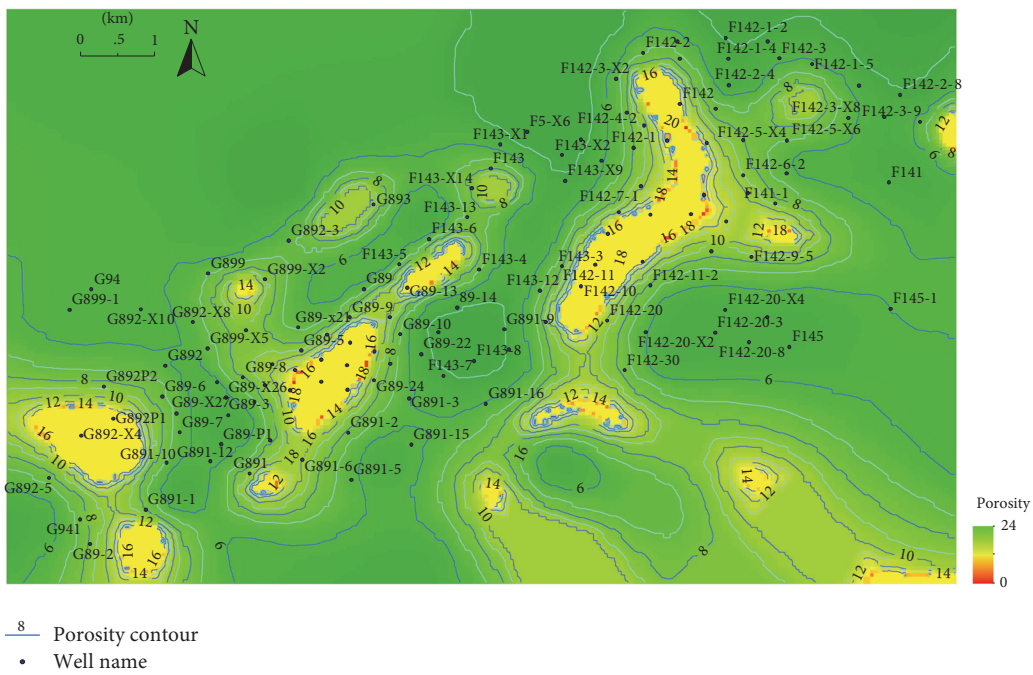

Figure 8: Caprock porosity distribution in the target area.

(Figures 5–9, Table 5). Spatial layers representing indicates were converted into 50 m × 50 m grid squares (or segments). Then using methodology presented in Section 2.3. and the spatial analysis functions of the GIS tool, we obtained the weighted comprehensive score for each grid square. Higher scores were correlated with a higher sealing effectiveness. Thus, the sealing effectiveness distributions for all segments of all the caprocks and faults were determined, and these distributions were used to define the sealing effectiveness of the whole caprock-fault system as shown in Figure 10. We classified the evaluation results into 5 grade levels, that is, Bad, Medium, Good, Better, and Best. Table 6 shows the area percentage assigned to each grade level. Figure 10 shows the evaluation results for the integral caprock and the faults.

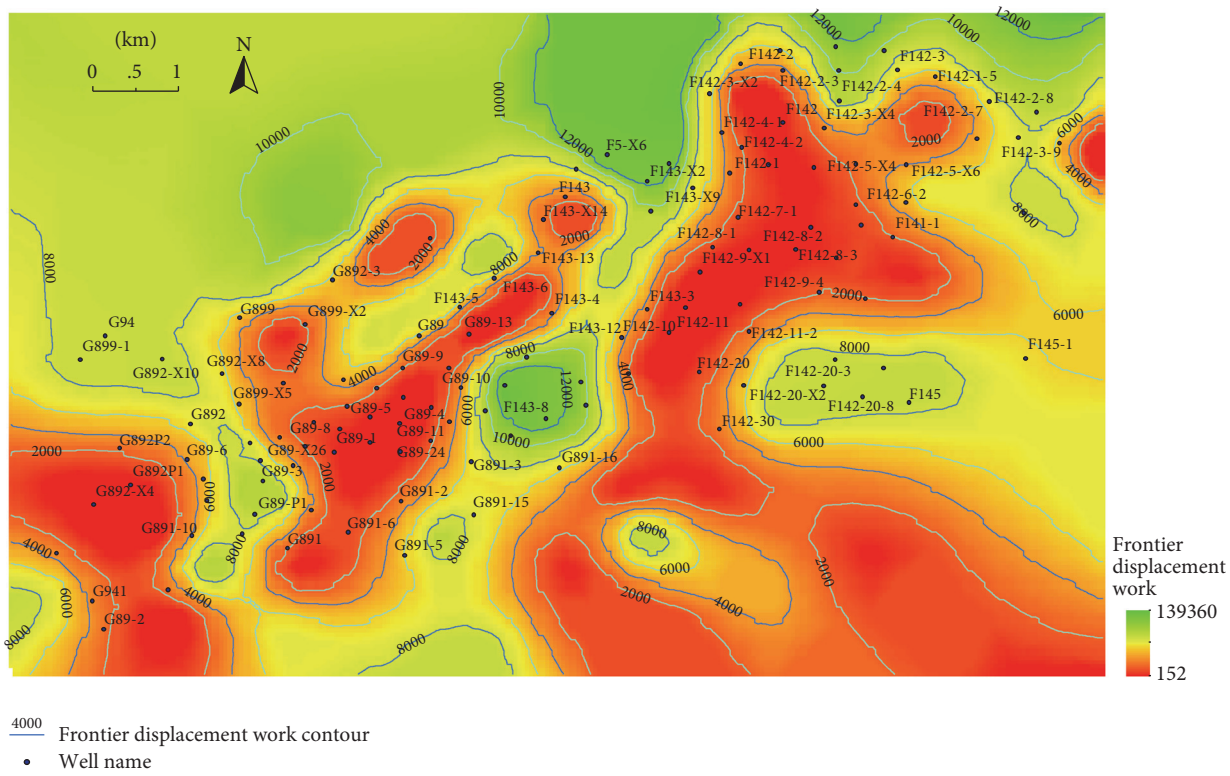

Figure 9: Frontier displacement work distribution of the caprock in the target area.

Figure 10: Evaluation results of the sealing effectiveness of the target formations and faults (middle and lower Shahejie formation, including three sections in G89-F142).

Table 5: Fault property sheet.

Fault name	Activity stopping time	Relationship between the fault lateral extension and caprock	Relationship between the fault throw and caprock thickness	Largest fault dip angle (°)	Vertical permeability (10^3 mD)	Fault rock thickness (m)	Minimum displacement pressure (MPa)	Minimum formation pressure (MPa)	Lateral displacement work	Lateral permeability (10^{-7} mD)	Closed coefficient	Upthrown SGR (%)	Upthrown SSF	Downthrow SGR (%)	Downthrow SSF
F1	The late Guantao	Broken through type	Seal connected type	62	1	1.02	19.61	31.600	25348.24	8.1	1.903	0	0.76	/	/
F2	The late Guantao	Broken through type	Seal connected type	49	1	1.04	18.302	29.797	10203.58	2.4	1.987	0	0.33	25–35	7
F3	ES3M	Embedded type	Seal connected type	52	1	1.03	17.724	29.059	7278.321	1.7	1.988	0	0.22	24–32	5.5
F4	Before the depositing of ES2	Embedded type	Seal connected type	41	1	1.03	16.872	27.896	10447.25	9.5	2.007	0	0.33	25–45	4
F5	Before the depositing of ES2	Embedded type	Seal connected type	48	1	1.03	16.42	27.304	15459.13	4.2	1.879	0	0.54	15–20	9
F6	Before the depositing of ES2	Embedded type	Seal connected type	49	1	1.03	18.632	30.250	15209.75	1.7	1.983	0	0.43	10–15	8
F7	Before the depositing of ES2	Embedded type	Seal connected type	52	1	1.02	19.729	31.827	8020.887	4.0	1.977	0	0.22	10–18	2.4
F8	Before the depositing of ES2	Embedded type	Seal connected type	46	1	1.03	18.757	30.609	6981.568	1.3	1.922	0	0.22	18–32	8.7
F9	Before the depositing of ES2	Embedded type	Seal connected type	47	1	1.03	20.025	32.342	7405.984	2.0	1.927	0	0.22	20–32	2

Table 5: Continued.

Fault name	Activity stopping time	Relationship between the fault lateral extension and caprock	Relationship between the fault throw and caprock thickness	Largest fault dip angle (°)	Vertical permeability (10^3 mD)	Fault rock thickness (m)	Minimum displacement pressure (MPa)	Minimum formation pressure (MPa)	Lateral displacement work	Lateral permeability (10^{-7} mD)	Closed coefficient	Upthrown SGR (%)	Upthrown SSF	Downthrow SGR (%)	Downthrow SSF
F10	Before the depositing of ES2	Embedded type	Seal connected type	52	1	1.01	19.44	30.723	10641.43	3.2	2.100	0	0.33	25–40	7.2
F11	Before the depositing of ES2	Embedded type	Seal connected type	55	1	1.02	19.331	31.241	8582.552	1.0	1.928	0	0.26	15–25	7.5
F12	Before the depositing of ES2	Embedded type	Seal connected type	45	1	1.03	16.15	26.665	3330.498	1.1	3.147	0	0.11	22	6.2
F13	Before the depositing of ES2	Embedded type	Seal connected type	44	1	1.02	15.627	26.259	2961.856	5.0	2.337	0	0.11	28–30	5.2
F14	Before the depositing of ES2	Embedded type	Seal connected type	45	1	1.03	17.167	28.283	5656.751	2.8	1.992	0	0.17	18–26	6.7
F25	The end of ES3X deposit	Embedded type	Seal connected type	41	1	1.03	16.962	28.040	3182.196	1.2	2.062	0	0.28	16–20	7.5
F15	The end of ES3X deposit	Embedded type	Intact top seal type	40	1	1.03	18.55	30.137	8951.203	2.0	1.763	25–35	0.75	32–44	0.75
F21	The end of ES3X deposit	Embedded type	Seal connected type	48	1	1.03	16.825	27.834	3157.941	1.5	2.165	32	2	32	2

Table 6: Comprehensive grading of the sealing effectiveness of the caprock-fault system.

Caprock-fault seal classification	Bad	Medium	Good	Better	Best
Score	<0.56	0.56~0.65	0.65~1.45	1.45~1.61	>1.61
Area percentage	1.59%	2.63%	14.89%	37.00%	43.55%

Figure 10 shows that the green areas representing the integral caprocks without disturbances in the northwest present integral caprocks that have almost the best sealing ability. In these areas, the porosity and the well density are very small, whereas the frontier displacement work is quite large. The distribution characteristics of the caprock sealing ability are consistent with that of the caprock porosity. In the region with the "人" shape lying between the wells F142-1 and F142-11 and the wells F142-11-2 and F142-16-2, the positions that have porosity ranging from 10% to 20% and 6% to 10% also present "Good" and "Better" sealing effectiveness, respectively.

The sealing ability of most faults in the target area is "Good." The sealing ability throughout F1, F9, F22, and F28 is "Good"; the sealing ability throughout F12 and F12-N is "Bad"; and the sealing ability of F2, F5, F19, F6, and F11 ranges from "Medium" to "Good." Thus, F2, F5, F19, F6, and F11 appear to have different sealing abilities, which might be caused by the properties of the caprock surrounding the faults. Li [27] considered that the vertical sealing ability of fault F1 is worse than that of F2 based on the fault properties and configuration relationship between the caprock and the faults. In this paper, the sealing ability of fault F1 is better than that of F2, although F1 and F2 have the same activity period and cut-through type. The sealing ability of the remaining faults is classified as "Better."

The area classified as "Good" accounts for approximately 70.55% of the total target area, whereas the area classified as "Bad" accounts for approximately 1.59% and is located near the fault crossings (i.e., throughout F12 and F12-N and local positions within F2, F5, F6, and F11). The area classified as "Medium" sealing capacity accounts for 2.63% of the total area and is affected by the caprock porosity, and these areas are mainly distributed in faults F25, F14, and F4, which present porosities of more than 10%. More attention should be paid to these positions of injection wells planned in this area. Larger frontier displacement work corresponds to a better sealing capacity. The sealing ability of a caprock-fault system is affected by the porosity of the caprock. Caprock-fault systems with good sealing ability often appear in the following areas: where the allocation relationships between the regional seals and the vertical fault extensions are the embedded type and lower broken type; where the allocation relationships between the fault throw and the direct seal thickness are the intact top seal type and the seal connected type (without the seal apart type); and where the fault dip is between 40° and 65°.

Figure 11 shows the sealing capacity of five blocks. The sealing capacity of the G89-1 and G891 blocks ranges from "Medium" to "Good," and they are suitable for CO_2-EOR storage. The sealing capacity of the F142 block is "Medium" to "Good" overall except at the western end of F6, which is "Bad" and not suitable for CO_2-EOR storage. The sealing ability of the head of the northeast extension direction of fault F11 in the G899 block is "Bad," but the remainder is suitable for CO_2-EOR storage. Fault F2 as the boundary line between F143 block and G899 block, and also the boundary line between the G899 block and G89-1 block, has the sealing ability level "Bad"; therefore, the adjacent area of fault F2 is not suitable for CO_2-EOR storage.

5. Conclusions

(1) A new framework for evaluating the sealing effectiveness of a caprock-fault system for CO_2-EOR storage was developed considering specific site characteristics. The method is a weighted ranking system with multiple indicators. In the method, caprocks and faults are considered as elements of the whole sealing system defined as "caprock-fault system."

(2) Additional indicators are involved in the method, such as the newly proposed parameter, frontier displacement work. The sealing mechanism of the caprock and faults as well as the configuration relationship between the caprock and faults were considered in the evaluation method.

(3) The method was used to evaluate the sealing effectiveness of the G89 block in the Shengli Oilfield, which presents many faults. A preliminary evaluation showed that higher scores corresponded with better sealing capacity of the caprock-fault system. Sealing systems classified as "Good" account for 70.55% of the total area, and they are mainly located in areas with large frontier displacement work, small porosity, and small well density. Sealing systems classified as "Bad" account for only 1.59% of the total area, and they are located at the tail and the head of the southwest extension direction of faults F12 and F2 and parts of F5, F19, F6, and F11. The sealing effectiveness of most regional caprock is classified as "Good."

(4) The sealing effectiveness of fault F1 is better than that of F2, although F1 and F2 have the same activity period and cut-through type. This result is inconsistent with the results presented in existing studies. Thus, more attention should be focused on these two faults.

(5) The sealing effectiveness of the G89-1 and G891 blocks is "Medium" and "Good," respectively, and the two blocks are suitable for CO_2-EOR storage. The overall sealing effectiveness of most parts of the F142 block is also "Medium" to "Good," although at the western end of F6, it is classified as "Bad." Therefore, this block is not suitable for CO_2-EOR storage. The sealing

Figure 11: Sealing capacity of five blocks in the target area.

effectiveness of the head along the northeast extension direction of F11 in the G899 block is classified as "Bad," although the remainder is suitable for CO_2-EOR storage. The sealing effectiveness of fault F2, which is the boundary line of the F143 block and G899 block (also the boundary line of the G899 block and G89-1 block), is classified as "Bad"; therefore, the regions near the F2 border are not suitable for CO_2-EOR storage.

(6) The evaluation parameters and methods in this research are essentially static because we do not consider the disturbances from CO_2-EOR storage production. Therefore, the evaluation method involved in this paper might be especially suitable for site selection prior to injection.

Appendix

Frontier Displacement Work

Frontier displacement work considers the formation pressure (pore pressure), caprock displacement pressure, and caprock thickness. The formation pressure and caprock displacement pressure represent the overpressure sealing and capillary sealing, respectively [21]. The top edge of the caprock is considered as the controlled leakage point and the critical state of the leading edge of the flow. We consider a conceptual model of CO_2 leaking through a caprock with a thickness H, as shown in Figure 12. The leakage process is actually a flooding

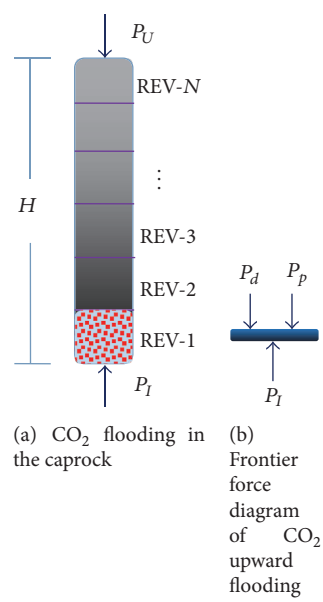

Figure 12: CO_2 flooding through caprock.

process of CO_2 displacing saline water in the caprock. The caprock in the model is uniform and divided hypothetically into N representative element volumes (REVs).

Assume the initial formation pressure of the caprock is P and the fluid gravity is not considered. We tested the sealing capacity of the caprock under the assumption that the fluid

injected slowly from the bottom of the caprock will overcome the formation pressure, capillary resistance, and drainage caprock pore water during the process of gradual upward migration. As shown in Figure 12(a), the injected fluid (i.e., CO_2 in this study) will overcome the displacement pressure of the REV-1 unit (red) and remain in a critical equilibrium state after the REV-1 unit becomes full of CO_2. The force diagram of the top edge of the REV-1 unit is shown in Figure 12(b).

To keep the fluid migrating slowly until it reaches the top of REV-2, we increase the injection pressure P_I until the leading edge of the fluid at the top of REV-N reached equilibrium. The process by which the fluid slowly advances and drains the caprock pore water on each REV is called quasi-static displacement. The fluid frontier has the following equation at each REV:

$$P_I = P_p + P_d. \tag{A.1}$$

In the quasi-static displacement process, the work done by the fluid pressure on a unit area is

$$W = \int_0^H P_I dl, \tag{A.2}$$

which is called specific displacement work (Pa·m) or simply referred to as displacement work through the paper.

Displacement work reflects the resistance of the formation pressure and displacement pressure as well as the influence of the flow path. Therefore, this value reflects the ease of draining fluid from the caprock and can be used as a measured index of the caprock sealing ability. If the pore pressure and displacement pressure of the formation are uniform in the process of CO_2 injection, the injection pressure P_I is constant. These indicators can be simplified directly as follows:

$$W = P_I H = \left(P_p + P_d\right) H, \tag{A.3}$$

where P_p is the caprock formation pressure (the pore pressure (MPa) is obtained by Wang's method [52]); and P_d is the caprock displacement pressure (MPa). The breakthrough pressure measured by Liu [30] is used to determine the relationship between the displacement pressure and acoustic time and the relationship between the displacement pressure and the depth to calculate the caprock displacement pressure; and the caprock thickness (m) is frequently obtained by combining the seismic and well information.

Conflicts of Interest

The authors declare that they have no conflicts of interest.

Acknowledgments

The authors gratefully acknowledge the support of this work by the National Natural Science Foundation of China (Grant no. 41672252).

References

[1] S. Bachu and J. J. Adams, "Sequestration of CO_2 in geological media in response to climate change: Capacity of deep saline aquifers to sequester CO_2 in solution," *Energy Conversion and Management*, vol. 44, no. 20, pp. 3151–3175, 2003.

[2] IPCC, *The IPCC Special Report on Carbon dioxide capture and storage*, Cambridge University Press, 2005.

[3] X. Li, Y. Liu, B. Bai, and Z. Fang, "Ranking and screening of CO_2 saline aquifer storage zones in China," *Chinese Journal of Rock Mechanics and Engineering*, vol. 25, pp. 963–968, 2006.

[4] H. Xie, X. Li, Z. Fang et al., "Carbon geological utilization and storage in China: Current status and perspectives," *Acta Geotechnica*, vol. 9, no. 1, pp. 7–27, 2014.

[5] H. R. Jahangiri and D. Zhang, "Ensemble based co-optimization of carbon dioxide sequestration and enhanced oil recovery," *International Journal of Greenhouse Gas Control*, vol. 8, pp. 22–33, 2012.

[6] M. A. Safarzadeh and S. M. Motahhari, "Co-optimization of carbon dioxide storage and enhanced oil recovery in oil reservoirs using a multi-objective genetic algorithm (NSGA-II)," *Petroleum Science*, vol. 11, no. 3, pp. 460–468, 2014.

[7] ACCA21, *An Assessment Report on CO_2 Utilization Technologies in China*, Science Press, 2014.

[8] G. Lv, Q. Li, S. Wang, and X. Li, "Key techniques of reservoir engineering and injection-production process for CO_2 flooding in China's SINOPEC Shengli Oilfield," *Journal of CO_2 Utilization*, vol. 11, pp. 31–40, 2015a.

[9] GCCSI, *Large Scale CCS Projects*, GCCSI, Ed., 2015.

[10] L. Koottungal, "Worldwide EOR Survey," *Oil & Gas Journal*, vol. 112, 2014.

[11] NETL, *NETL's Carbon Capture and Storage Database – Version 5*, NETL, Ed., 2015.

[12] J. F. Ma, X. Z. Wang, and R. Gao, "Monitoring the safety of CO_2 sequestration in Jingbian field, China," *Energy Procedia*, vol. 37, pp. 3469–3478, 2013.

[13] C. J. Vincent, N. E. Poulsen, Z. Rongshu, D. Shifeng, L. Mingyuan, and D. Guosheng, "Evaluation of carbon dioxide storage potential for the Bohai Basin, north-east China," *International Journal of Greenhouse Gas Control*, vol. 5, no. 3, pp. 598–603, 2011b.

[14] L. Zhang, H. Huang, Y. Wang et al., "CO_2 storage safety and leakage monitoring in the CCS demonstration project of Jilin oilfield, China," *Greenhouse Gases: Science and Technology*, vol. 4, no. 4, pp. 425–439, 2014.

[15] H. Shi, "Numerical simulation research on parameter optimization of CO_2 miscible flooding of Gao 89-1 Block in Zhenglizhuang Oilfield," *Offshore Oil*, pp. 68–73, 2008.

[16] R. Shukla, P. Ranjith, A. Haque, and X. Choi, "A review of studies on CO_2 sequestration and caprock integrity," *Fuel*, vol. 89, no. 10, pp. 2651–2664, 2010.

[17] J. Song and D. Zhang, "Comprehensive review of caprock-sealing mechanisms for geologic carbon sequestration," *Environmental Science and Technology*, vol. 47, no. 1, pp. 9–22, 2013.

[18] Q. Li, X. Liu, J. Zhang et al., "A novel shallow well monitoring system for CCUS: With application to shengli oilfield CO2-EOR project," in *Proceedings of the 12th International Conference on Greenhouse Gas Control Technologies, GHGT 2014*, pp. 3956–3962, October 2014.

[19] (IEAGHG), "I.G.G.R.D.P., 2011. Caprock systems for CO_2 geological storage".

[20] A. Hildenbrand, S. Schlömer, and B. M. Krooss, "Gas breakthrough experiments on fine-grained sedimentary rocks," *Geofluids*, vol. 2, no. 1, pp. 3–23, 2002.

[21] B. Bai, G. Lü, X. Li, Z. Li, Y. Wang, and Q. Hu, "Quantitative measures for characterizing the sealing ability of caprock with pore networks in CO_2 geological storage," in *Proceedings of the 12th International Conference on Greenhouse Gas Control Technologies, GHGT 2014*, pp. 5435–5442, October 2014.

[22] G. Jones and Q. J. F. R. J. Knipe, *Faulting, fault sealing and fluid flow in hydrocarbon reservoirs*, Geological Society Pub House, 1998.

[23] C. M. Aruffo, A. Rodriguez-herrera, E. Tenthorey, F. Krzikalla, J. Minton, and A. Henk, "Geomechanical modelling to assess fault integrity at the CO2CRC Otway Project, Australia," *Australian Journal of Earth Sciences*, vol. 61, no. 7, pp. 987–1001, 2014.

[24] A. Baroni, A. Estublier, O. Vincké, F. Delprat-Jannaud, and J. F. Nauroy, "Dynamic fluid flow and geomechanical coupling to assess the CO_2 storage integrity in faulted structures," *Oil and Gas Science and Technology*, vol. 70, no. 4, pp. 729–751, 2015.

[25] L. Chiaramonte, M. D. Zoback, J. Friedmann, and V. Stamp, "Seal integrity and feasibility of CO_2 sequestration in the Teapot Dome EOR pilot: Geomechanical site characterization," *Environmental Geology*, vol. 54, no. 8, pp. 1667–1675, 2008.

[26] J. Smith, S. Durucan, A. Korre, and J.-Q. Shi, "Carbon dioxide storage risk assessment: Analysis of caprock fracture network connectivity," *International Journal of Greenhouse Gas Control*, vol. 5, no. 2, pp. 226–240, 2011.

[27] Z. Li, "Evaluation on vertical safety of fault during carbon dioxide flooding and sequestration in the Gao89 area of Dongying sag," *Petroleum Geology and Recovery Efficiency*, vol. 22, pp. 41–46, 2015.

[28] G. Lv, Q. Li, S. Wang, and X. Li, "Key techniques of reservoir engineering and injection-production process for CO_2 flooding in China's SINOPEC Shengli Oilfield," *Journal of CO_2 Utilization*, vol. 11, pp. 31–40, 2015b.

[29] X. Fu, R. Jia, H. Wang, T. Wu, L. Meng, and Y. Sun, "Quantitative evaluation of fault-caprock sealing capacity: A case from Dabei-Kelasu structural belt in Kuqa Depression, Tarim Basin, NW China," *Petroleum Exploration and Development*, vol. 42, no. 3, pp. 329–338, 2015.

[30] S. Liu, *Research on preservaing conditions of gas in deep intelval of Jiyang basin*, China University of Petroleum, 2008.

[31] Y. Pei, D. A. Paton, R. J. Knipe, and K. Wu, "A review of fault sealing behaviour and its evaluation in siliciclastic rocks," *Earth-Science Reviews*, vol. 150, pp. 121–138, 2015.

[32] U. S. Allan, "Model for hydrocarbon migration and entrapment within faulted structures," *American Association of Petroleum Geologists Bulletin*, vol. 73, no. 7, pp. 803–811, 1989.

[33] R. J. Knipe, "Juxtaposition and seal diagrams to help analyze fault seals in hydrocarbon reservoirs," *AAPG Bulletin*, vol. 81, no. 2, pp. 187–195, 1997.

[34] Y. Lü, J. Huang, G. Fu, and X. Fu, "Quantitative study on fault sealing ability in sandstone and mudstone thin interbed," *Shiyou Xuebao/Acta Petrolei Sinica*, vol. 30, no. 6, pp. 824–829, 2009.

[35] H. Tong, "Quantitative analysis of fault opening and sealing," *oil & gas geology*, vol. 19, pp. 215–220, 1998.

[36] Y. Lv and S. Wang, "Quantitative evaluation of fault seal," *Journal of Daqing Petroleum Institute*, vol. 34, pp. 35–41, 2010.

[37] H. Liu, Z. Hou, X. Li, X. Tan, B. Bai, and P. Were, *Site selection criteria for combined geothermal production- CO_2 sequestration and its preliminary application in China*, 2015.

[38] X. Lu, "Evaluation on mudstone caprock of upper paleozoic group and its effect on oil accumulation in Chegu 20 buried hill," *Journal-Daqing Petroleum Institute*, vol. 27, pp. 1–3, 2003.

[39] Y. Lv, *Study on sealing of oil and gas*, Petroleum Industry Press, Beijing, 1996.

[40] Y. Lv, G. Fu, and F. xiaofei, *The Effect of Faults on Conductivity and Plugging of Oil And Gas*, Petroleum Industry Press, Beijing, 2013.

[41] S. Bachu, "Screening and ranking of sedimentary basins for sequestration of CO_2 in geological media in response to climate change," *Environmental Geology*, vol. 44, no. 3, pp. 277–289, 2003a.

[42] L. Zhang, X. Luo, G. Vasseur et al., "Evaluation of geological factors in characterizing fault connectivity during hydrocarbon migration: Application to the bohai bay basin," *Marine and Petroleum Geology*, vol. 28, no. 9, pp. 1634–1647, 2011.

[43] C. J. Vincent, N. E. Poulsen, Z. Rongshu, D. Shifeng, L. Mingyuan, and D. Guosheng, "Evaluation of carbon dioxide storage potential for the Bohai Basin, north-east China," *International Journal of Greenhouse Gas Control*, vol. 5, no. 3, pp. 598–603, 2011.

[44] K. Wang and J. Dai, "A quantitative relationship between the crustal stress and fault sealing ability," *Shiyou Xuebao/Acta Petrolei Sinica*, vol. 33, no. 1, pp. 74–81, 2012.

[45] G. Li, *Research on the Relation of the Stress Evolution and Hydrocarbon Migration-Accumulation in Dongying Depression China University of Petroleum*, 2010.

[46] S. Song, *Complex fault block group of four dimensional stress field model and reservoir prediction, Beijing*, 2003.

[47] Z. Liu, "In-situ stress technology application in oil field development," *Oil and Gas Recovery Technology*, vol. 1, pp. 48–56, 1994.

[48] F. Yang, "Characteristics of In-Situ stress of S4 in chun liang area," *Inner Mongolia Petrochemical*, pp. 230-231, 2008.

[49] Z. Wang, *Research on In-Situstress based on optimum technique and bearing law of casing pipe*, China University of Petroleum, 2009.

[50] J. Hull, "Thickness-displacement relationships for deformation zones," *Journal of Structural Geology*, vol. 10, no. 4, pp. 431–435, 1988.

[51] T. Manzocchi, J. J. Walsh, P. Nell, and G. Yielding, "Fault transmissibility multipliers for flow simulation models," *Petroleum Geoscience*, vol. 5, no. 1, pp. 53–63, 1999.

[52] G. Wang, *The Formation Pressure Characteristics and Its Hydrocarbon Accumulation Mechanism in the Upper Fourth Member of Shahejie Formation in the Boxing Area*, China University of Petroleum (East China), 2012.

Hindawi
Geofluids
Volume 2017, Article ID 6126505, 25 pages
https://doi.org/10.1155/2017/6126505

Review Article

Worldwide Status of CCUS Technologies and Their Development and Challenges in China

H. J. Liu,[1] P. Were,[2] Q. Li,[3] Y. Gou,[2,4] and Z. Hou[2,4,5]

[1] *INRS-ETE, Universite du Québec, Québec, QC, Canada*
[2] *Energie-Forschungszentrum Niedersachsen, Clausthal University of Technology, Goslar, Germany*
[3] *State Key Laboratory of Geomechanics and Geotechnical Engineering, Institute of Rock and Soil Mechanics, Chinese Academy of Sciences, Wuhan, China*
[4] *Sino-German Energy Research Center, Sichuan University, Chengdu, China*
[5] *Institute of Petroleum Engineering, Clausthal University of Technology, Clausthal-Zellerfeld, Germany*

Correspondence should be addressed to Y. Gou; yang.gou@efzn.de and Z. Hou; hou@tu-clausthal.de

Received 19 February 2017; Revised 12 May 2017; Accepted 20 June 2017; Published 28 August 2017

Academic Editor: Weon Shik Han

Carbon capture, utilization, and storage (CCUS) is a gas injection technology that enables the storage of CO_2 underground. The aims are twofold, on one hand to reduce the emissions of CO_2 into the atmosphere and on the other hand to increase oil/gas/heat recovery. Different types of CCUS technologies and related engineering projects have a long history of research and operation in the USA. However, in China they have a short development period ca. 10 years. Unlike CO_2 capture and CO_2-EOR technologies that are already operating on a commercial scale in China, research into other CCUS technologies is still in its infancy or at the pilot-scale. This paper first reviews the status and development of the different types of CCUS technologies and related engineering projects worldwide. Then it focuses on their developments in China in the last decade. The main research projects, international cooperation, and pilot-scale engineering projects in China are summarized and compared. Finally, the paper examines the challenges and prospects to be experienced through the industrialization of CCUS engineering projects in China. It can be concluded that the CCUS technologies have still large potential in China. It can only be unlocked by overcoming the technical and social challenges.

1. Introduction

Fossil fuels, especially coal that is rich in carbon, constitute the highest proportion of primary energy in China [1]. In recent years, the rapid urbanization and development of industries including power plants, cement factories, steel plants, biotransformation, and fossil fuel transformation plants, which are highly dependent on large consumption of fossil fuels, have been a great challenge to the Chinese environment [2, 3]. Since the winter of 2012/2013, most cities in China have been faced with serious atmospheric pollution from a haze formed from a combination of SO_2, NOx, and inhalable particles within the mist, containing fine particle concentrations of up to ca. 900 $\mu g/m^3$ [4]. Automobile exhausts, industrial emissions, waste incineration, and fugitive dust from construction sites are the main sources of the haze. Based on statistical data from Beijing, reported by China Central Television (CCTV) in 2014, haze particles from automobile exhausts contributed 22.2%, while the burning of coal, dust, and industrial emissions accounted for proportions of 16.7%, 16.3%, and 15.7%, respectively. Therefore, a reduction in the emissions from coal and industry has become the key to improving the quality of the environment.

The increase in the concentration of greenhouse gases has had a large impact on global climate change, since industrialization. Many countries have set targets for reducing the emissions of greenhouse gases in order to mitigate global warming. Among them, top on the list of CO_2 emissions in the world, China aims at reducing 40%–45% of its CO_2 emissions per unit GDP by 2020, based on the 2005 level [5–7]. This requires considerable changes not only in the framework of fossil fuel consumption, but also in the development of renewable energy from wind, solar, geothermal, and so on, together with an enlargement in the area covered by forests

and innovations in technologies that can enable permanent storage of the CO_2 underground.

CO_2 emissions in China come mainly from the combustion of fossil fuels (90%) and during the process of cement manufacturing (10%). For example, in 2012, 68% of the emitted CO_2 was sourced mainly from the combustion of coal, while 13% came from oil and 7% from natural gas [8]. According to the statistics, annual emissions of CO_2 from large stationary point sources, that is, >0.1 Mt/year, amount to 3.89 $GtCO_2$, which accounts for 67% of the total emissions. Among which, 72% is from power stations [9]. This demonstrates that a reduction of the CO_2 emissions from the large stationary point sources is the key to realizing China's target [10, 11].

China's main target for the transformation in its energy framework is to reduce the combustion of coal, while increasing the supply of natural gas and other clean energy, and controlling the emissions of CO_2, SO_2, NOx, and so on. CO_2 capture and sequestration (CCS) and utilization (CCUS) technologies can be applied to store CO_2 underground effectively, thus reducing its emission into the atmosphere. This technology is now highly developed and is likely to play a significant role in China, especially when the operation costs are reduced. This paper reviews the state of the art of CCS and CCUS technologies worldwide while paying more attention on its status and development in China. The mature technology will be examined in various engineering projects. Therefore, this paper considers the state of operation of CCS and CCUS projects in detail and concludes by presenting the likely challenges to be experienced through the industrialization of these projects in China. Due to space limitation, it has not been possible to include a review of the current research status on the conversion of CO_2 to produce some commercial products or its use in the food industry, for example, as an additive in beverages or as a preservative for fruits and vegetables. Henceforth, only its utilization for geologic and geoengineering purposes such as EOR, ECBM, ESG, and EGR has been considered in this paper.

2. Worldwide Development of CCS and CCUS

The CCS technology is a means to control emissions of CO_2 that are captured from different processes including precombustion, postcombustion, and oxy-fuel combustion. The stages of a CCS project can be divided into (1) CO_2 capture, (2) CO_2 transportation, (3) CO_2 injection, and (4) postinjection of CO_2 [12–19].

In the short term, depending on the purpose of the CCS project, CO_2 can be stored in different geological sites, including deep saline formations, depleted oil or gas reservoirs, deep unmineable coal seams, and shale formations, to reduce the CO_2 emissions [20, 21], Figure 1. In comparison with the pure CCS technology, CCUS technology pays more attention to utilization (U) of the captured CO_2 while sequestration (S) plays a secondary role. CCUS can reduce the cost of sequestration and bring benefits by enhancing the production of hydrocarbons or heat energy, thus becoming very popular in recent years. Based on the purpose of the CO_2 injection, a number of related technologies have been developed including (1) Enhanced Oil Recovery (EOR), (2) Enhanced Coalbed Methane Recovery (ECBM), (3) Enhanced Gas Recovery (EGR), (4) Enhanced Shale Gas Recovery (ESG), and (5) Enhanced Geothermal System (EGS).

The engineering projects for both CCS and CCUS technologies are systematically complicated, with their success depending on rigorous research in engineering and science disciplines including geology, geoengineering, geophysics, environmental engineering, mathematics, and computer sciences. In addition, key to success in site selection for any such a project demands strict considerations of safety, economy, environment, and public acceptance at all levels of operation, that is, countrywide, basin-wide, regional, or subbasin levels [22–26], Figure 2. Although CCS and CCUS technologies share similarities in site selection, each will induce a series of different physical and chemical responses in the underground porous or fractured rock formations, in terms of the existing local hydrological (H), thermal (T), mechanical (M), and chemical (C) fields [27–29], Figure 2. Coupling of the THMC processes during and after CO_2 injection related to CCS and CCUS technologies has become a research hotspot in recent years [26, 30–33]. The two technologies, however, have minor differences, in terms of purpose, storage duration, injection depth and rate, fluid and reservoir types, scheme of drilling, completion and monitoring, and so on.

2.1. CCS. CCS is a viable option for significantly reducing CO_2 emissions from large-scale emission sources. When its only purpose is for CO_2 sequestration, the storage sites may include deep saline formations, deep unmineable coal seam, depleted oil or gas reservoir, and rock salt caverns [35–38]. This technology is mature but still very expensive for widespread commercial application.

2.2. CCUS: CO_2-EOR. The first CO_2-EOR field test was held in 1964 in Mead Strawn Texas, in the USA. Since the 1970s, CO_2 has been used on a commercial scale for oil production projects [20, 21]. Up to the present time, there have been more than 100 CO_2-EOR projects in operation. Among them, the CO_2-EOR project in Weyburn, Canada, is the most successful example. It uses mixed gases separated from natural gas production, coal gasification, and coal power from the Great Plains Synfuels Plant near Beulah, North Dakota, USA [39]. The injection gas is mainly composed of CO_2 (96.8%), plus H_2S (1.1%) and a minor amount of hydrocarbons that are piped to the Weyburn Basin through a pipeline 339 km in length [7]. The purpose of the project is to inject 2 million tons of CO_2 into the depleting oil reservoir over a 20-year period, in order to increase oil recovery to 130 million barrels and to extend the production of oil in this oilfield to 25 years [40].

2.3. CCUS: CO_2-ECBM. The conventional method to produce coalbed methane is to decrease the pressure in the coalbed reservoir, making the methane desorb from the matrix. However, the recovery of coalbed methane production using this method is less than 50%. The alternative is to desorb more CH_4 from the coalbed matrix by injecting gases including CO_2 or N_2 [41–44]. Studies on enhancing

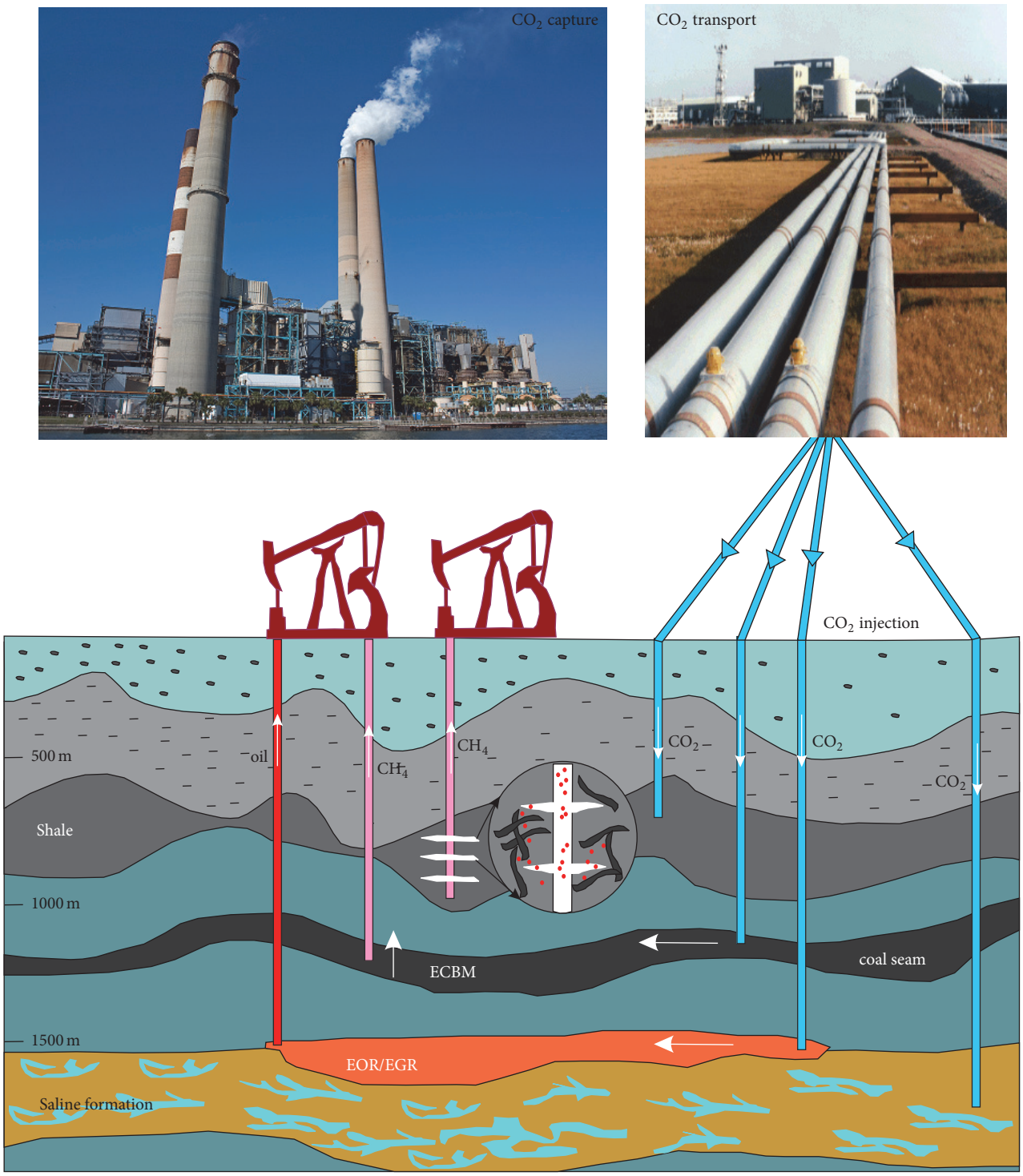

Figure 1: Schematic diagram of the CCUS technology in different geological reservoirs for both long and short-term sequestration of CO_2.

coalbed methane by CO_2 injection started in the 1990s [7, 45]. When CO_2 is injected in the coalbed layer, both the gaseous and adsorbed-state of CH_4 and CO_2 will exist in equilibrium [46]. Because the coalbed has a much stronger adsorption capacity for CO_2 than CH_4, the injection of CO_2 will make the adsorbed CH_4 desorb, thus enhancing the CH_4 recovery. A proportion of the injected CO_2 will be stored in the coalbed formation, making it difficult for it to leak to the surface. Therefore, this technology can bring both economic benefits and also guarantee the safe storage of CO_2 [47, 48].

The successful injection of CO_2 to enhance coalbed methane recovery has been proved by many experimental

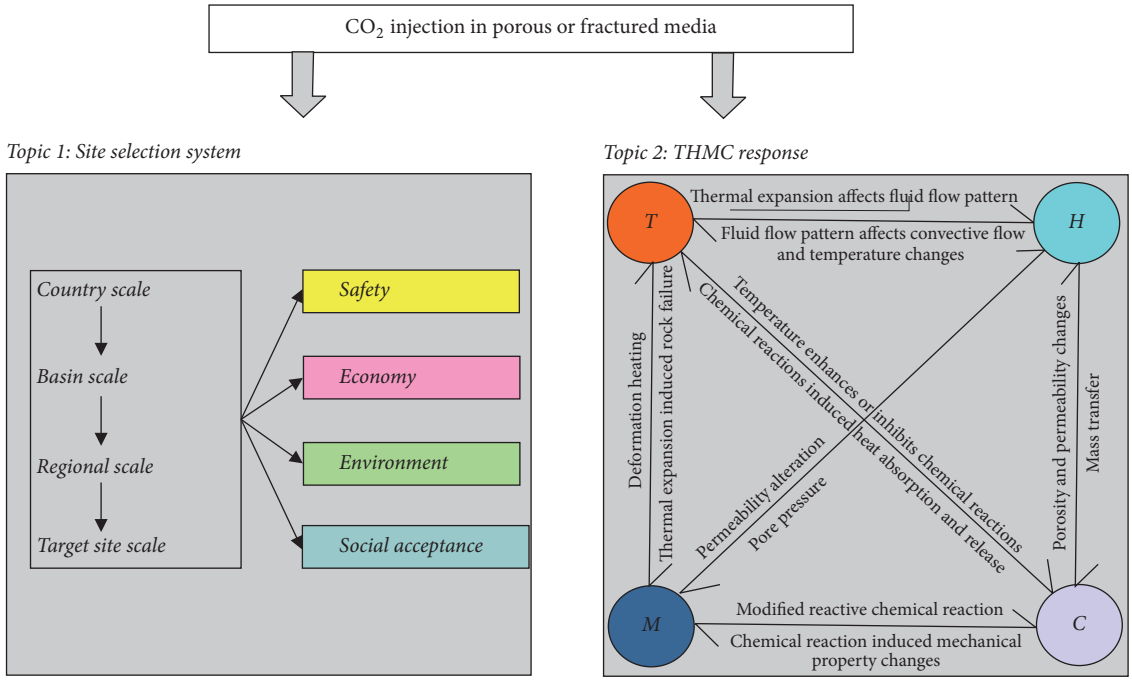

Figure 2: Schematics of the two main topics, that is, the site selection system (1) and the THMC responses (2) associated with CCS and CCUS technologies.

and numerical studies. However, the production efficiency is strongly site-dependent, in relation to the permeability of the coalbed matrix, production history, gas transportation process, maturation of coal, geological configuration, completion scheme, hydraulic pressure, and so on [42–44, 49–52]. Nevertheless, the maturity of its commercial application is still very low. Pilot-scale CO_2-ECBM projects so far include those in Alberta, Canada, which started in 1997, the Burlington project in the San Juan Basin of the USA, the RECOPOL project that started in 2001, the Yubari project in Japan, and the Qinshui basin project in China that started in 2002 [53].

2.4. CCUS: CO_2-EGR. Studies on injecting CO_2 into depleted gas reservoirs to enhance gas recovery started in the 1990s [54]. Unlike the CO_2-EOR technology, CO_2-EGR technology is still at the pilot-scale stage. Its efficiency is highly dependent on reservoir type, temperature and pressure conditions, heterogeneity, production strategy, and so on [55–60]. For some CO_2-EGR projects, the gas recovered can reach 10%, while other projects have seen less or no enhancement [61–63]. The rapid breakthrough of CO_2 in a production well, resulting in a high concentration of CO_2, restricts the production of pure natural gas [64]. Since 1999, the USA has carried out a pilot project of CO_2-EGR in Rio Vista. The Netherlands injected 60 kilotonnes of CO_2 into a depleted gas reservoir in the K12B project during 2004 and 2009 [7]. The CLEAN project in Germany started a CO_2-EGR project in the Altmark gas fields in 2009; however, public protests have prevented CO_2 injection on the site [65]. Many other countries including Australia and Norway are also positively developing this technology [64, 66–74].

2.5. CCUS: CO_2-ESG. The USA has been carrying out shale gas desorption since 1821. However, limited development of the technology made this process procedurally cumbersome and substantively difficult to apply before the 21st century. In 2000, shale gas contributed only 1% of the whole natural gas supply, while, by the end of 2011, this proportion had increased to 30% due to a breakthrough in horizontal drilling and horizontal multistaged fracturing technology. The revolution of shale gas in the USA is changing the energy structure of the world [75].

Encouraged by the successful application of CO_2 in oil and gas recovery, its application in aiding the production of shale gas began in recent years [76–81]. There has also been progress in replacing water by supercritical CO_2 as the injection fluid in the fracturing technology [82–86]. However, this process is still in the very early exploration stages.

2.6. CCUS: CO_2-EGS. The first study of EGS technology started in Fenton Hill, USA, in 1970 [87]. Since then, many other countries, including France, Germany, Austria, Italy, Japan, and Australia, have paid attention to the development of this technology. The conventional EGS technology uses water as the injection fluid and circulation media. Based on the research in [88], CO_2 is now regarded as a more favorable circulation fluid compared with water because of its large compressibility and expansibility. This idea has already been supported by many studies (e.g., [89–93]).

The application of CO_2 in a geothermal system is not restricted to the hot dry rock reservoirs but also includes the conventional hydrothermal reservoirs [38, 91, 94]. The injection of CO_2 can enhance the efficiency of reinjecting the hot wastewater by improving the porosity and permeability

through the activated water-rock geochemical reactions [95]. Besides being the main circulation fluid, CO_2 can also be regarded as a pressurized hydraulic fluid in the reservoir. Injection of CO_2 in a hydrothermal or hot dry rock reservoir can maintain the reservoir pressure, promoting the flow rate of the in situ water towards the production well, thus enhancing the heat recovery and even the recovery of the CH_4 dissolved in the aquifer water [96–99]. Reference [38] described this process as the CO_2-AGES (CO_2-aided geothermal extraction system) in which three stages are involved: (1) the production of hot water when CO_2 is used as the pressurized hydraulic fluid; (2) two-phase fluid flow in the production well after the CO_2 breakthrough; and (3) and as a circulation fluid, when CO_2 fills the production well, which is similar to CO_2-EGS.

3. CCS and CCUS Engineering Projects Worldwide

By the end of 2016, based on the statistics of Global Status 2016, there were 38 large-scale CCS + CCUS projects in operation or under construction and planning. Among them, 17 projects are located in North America (12 projects in the United States and 5 in Canada); 12 projects in Asia (8 in China, 2 in South Korea, 1 in Saudi Arabia, and 1 in United Arab Emirates), 5 in Europe (2 in Norway, 2 in United Kingdom, and 1 in the Netherlands), 3 in Australia, and 1 in Brazil. Among the 15 projects that are in operation, 12 projects are related to CO_2-EOR and the other 3 projects are pure CO_2 sequestration. There are 66 pilot-scale CCS + CCUS projects of which 22 are in operation, 5 under construction, 5 at the planning stage, and 34 have just been completed.

Among the 70 pilot-scale engineering CCUS projects worldwide, based on their distribution by regions or countries, 22 are located in North America, 1 in South America, 22 in Europe, 20 in Asia, 4 in Australia, and 1 in South Africa; see Figure 3 for more details.

There are still no concrete CO_2-ESG and CO_2-EGS projects anywhere in the world. Only a few countries, including the USA, Canada, China, and Argentina, can commercially produce shale gas. At the end of 2015, the daily shale gas output in the USA, Canada, China, and Argentina had reached 37, 4.1, 0.5, and 0.07 Bcf, respectively [100, 101]. Shale gas production in the USA abruptly increased after 2000, while Canada and China successfully produced shale gas for the first time in 2008 and 2012, respectively. There are now more than 100,000 shale gas drilling wells in the USA. In China, however, only about 600 wells have been drilled in the last few years [102]. The EGS technology is still at the research and development stage. Nevertheless, there are some experimental EGS plants and pilot projects, for example, at Fenton Hill, Coso, and Desert Peak in the USA, Bad Urach, Neustadt-Glewe, Bruchsal, Landau, and Unterhaching in Germany, and Soultz-sous-Forets and Bouillante in France [87]. Substantially higher research, development, and demonstration efforts are needed to ensure EGS technology becomes commercially viable in the near future.

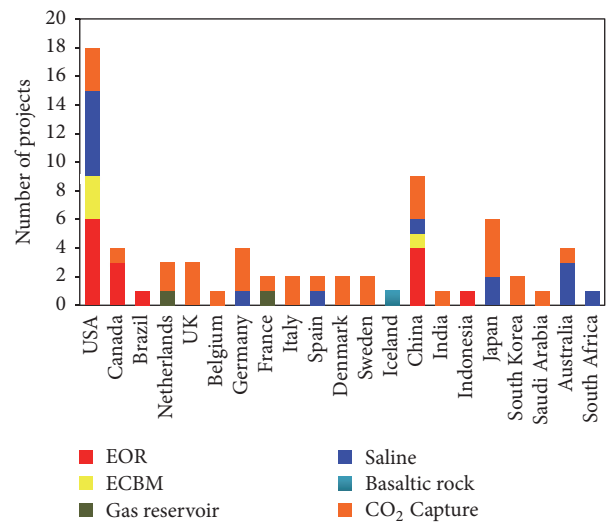

Figure 3: Global distribution of pilot-scale CCUS engineering projects based on project purpose and reservoir types, data sourced from http://www.globalccsinstitute.com/.

4. Current Status of CCS and CCUS Technologies in China

Since 2005, CCS has been listed as a frontier technology in China's mid-long term technical development program in order to realize the goal of zero emissions from fossil fuel energy [103]. Meanwhile, more attention has been paid to CCUS technology, especially CO_2-EOR and CO_2-ECBM [104–107]. Between 2006 and 2015, the Ministry of Science and Technology of China (MOST) funded eight National Basic Research Programs (also known as the 973 Program) and State High-Tech Development Plans (commonly known as the 863 Program). Three of these programs were related to CO_2-EOR and the others to the CO_2 capture technology, shale gas recovery, and the hot dry rock systems. The National Natural Science Foundation of China (NSFC) also generously funded basic research related to CCS and CCUS.

Based on the incomplete statistics of the research projects funded by MOST and NSFC during 2005–2016 (Figures 4 and 5 and Table 1), the distribution of funding for different aspects of CCS and CCUS is shown as follows: (1) CCS (32 projects), of which all the 7 projects funded by the MOST were related to CO_2 capture technology. The 23 projects funded by the NSFC and 1 project funded by the Ministry of Land and Resources were concerned with CO_2 storage; (2) CCUS: CO_2-EOR (18 projects), of which 6 projects were funded by the MOST and 10 by the NSFC; (3) CCUS: CO_2-ECBM (22 projects), of which 3 projects were funded by the MOST, and 17 by the NSFC; (4) CCUS: CO_2-EGR (4 projects); (5) CCUS: CO_2-ESG (4 projects); and (6) CCUS: CO_2-EGS (7 projects).

Several international cooperation research projects were also developed, including NZEC between China and Europe, CAGS between China and Australia, and CCERC between China and the USA; see Table 2 for further details.

Table 1: The research projects of CCUS funded by China Ministry of Science and Technology (MOST) and National Natural Science Foundation of China (NSFC) and so on during 2005–2016 (amount unit: 10,000 RMB or 1,450 US$).

Name of the research projects	Responsible institute	Funding sources	Amount
Type 1: CO_2-EOR			
Utilization of CO_2-EOR and geological storage of CO_2	Research Institute of Petroleum Exploration & Development (CNPC)	973 Program 2006–2010	3500
Key technologies of CO_2-EOR and sequestration		863 Program 2009–2011	—
Basic research on CO_2 geological sequestration, reduction in CO_2 emission and utilization		973 Program 2011–2015	—
Key technologies of CO_2-EOR and storage		Major Science & Technology 2011–2015	—
Microscopic mechanism of oil-water-rock multiple surface system of the porous media and their application	Tsinghua University	NSFC 2016 confirmed	20
CO_2 capture and storage technologies		2008–2010	—
Basic studies on the transportation of supercritical CO_2, water and oil in the low permeable porous media	Dalian University of Science and Technology	NSFC 2008–2011	180
Studies on microscopic flowing mechanism of supercritical CO_2, oil and water in the low permeable oil reservoir		NSFC 2013–2015	25
Studies on the CO_2 diffusion and mass transfer processes in oil and water bearing porous media		NSFC 2013 confirmed	25
Factors affect the CO_2 diffusion in the porous media and its mechanism studies	China University of Petroleum	NSFC 2009–2011	20
QSAR studies on the thermodynamics and transportation properties of CO_2-EOR system	Tianjin University	NSFC 2012–2014	—
CO_2-EOR and its damage mechanism to the reservoir	China University of Geosciences	NSFC 2012–2015	59
Studies on the surface properties using alkylol amine capture CO_2 and processes of CO_2-EOR	North China Electric Power University	NSFC 2012–2016	—
Microscopic mechanism, quantification and optimization of injection-production scheme of CO_2-EOR and CO_2 sequestration in the oilfield	Southwest Petroleum University etc.	NSFC 2014–2016	25
CO_2-EOR pilot project in Jilin oilfield	Jilin oilfield etc.	2007-	—
CO_2-EOR process and pilot project in Songliao basin		Major Science & Technology 2011–2015	—
CO_2 capture and CO_2-EOR pilot project in Shengli oilfield	Shengli oilfield etc.	2010-	—
Technical development of CO_2 capture from the flue gas of the large-scale coal-fired power station, EOR and storage and pilot projects		Major Science & Technology 2012–2016	—
CO_2 capture from coal gasification and EOR		Independent project	—
Type 2: CO_2-ECBM			
CO_2 storage and enhanced coalbed methane recovery	China United Coalbed Methane Corp., Ltd. etc.	International 2002–2007	—
CO_2 injection and storage in the deep coal seam and enhanced coalbed methane recovery		International 2011–2015	—
Test project of deep coalbed methane production technology of China United Coalbed Methane Corp. Ltd. (CUCMC)		Major Science & Technology 2011–2015	—
CO_2-ECBM potential in China and related basic scientific research issues	Institute of Rock and Soil Mechanics (CAS)	One hundred talent program 2005–2009	—
CO_2-ECBM potential in China and the suitability evaluation		GSC 2011	—
Mechanism of using mixtures of CO_2/N_2 displace coalbed methane in situ geological conditions and the best ratio of gas composition		NSFC 2012–2014	26
Impacts of coal matrix on the coal expansion and permeability changes of CO_2/CH_4 during the CO_2-ECBM process	Institute of Coal Chemistry (CAS)	NSFC 2007–2009	—
Solid-gas interaction during CO_2 sequestration in the deep coal seam and simulation of the sequestration experiment	Institute of Process Engineering (CAS)	NSFC 2007–2009	32

Table 1: Continued.

Name of the research projects	Responsible institute	Funding sources	Amount
Advanced models of CO_2-ECMB	China University of Mining and Engineering	NSFC 2007-2008	6
Adsorption and desorption mechanisms of multiple gases during CO_2-ECBM process		NSFC 2003–2005	
Experimental study of coal matrix on expansion effects during CO_2-ECBM process		NSFC 2008–2010	—
Two-phase gas and solid coupling effect and dual porosity effect during the CO_2 sequestration in the deep coal seam		NSFC 2011–2013	20
THM coupling mechanism of CO_2-ECBM		NSFC 2012–2014	25
Dynamic model of multiphase fluid CH_4-water flow in porous media of heterogeneous coal seam		NSFC 2012 confirmed	25
Fluid-solid coupling response and mechanism of supercritical CO_2 and minerals in the coal		NSFC 2013 confirmed	25
Theoretical study of CO2 sequestration in the deep coal seam and the efficiency of CH_4 recovery		NSFC 2014 confirmed	300
Interaction of supercritical CO_2 and organic matter in the coal and their responses to the coal structure		NSFC 2014 confirmed	25
The construction of 3D model of reservoir structure in the high grade coal and the geochemical response to the injection of CO_2		NSFC 2014 confirmed	23
CO_2 enhances CH_4 adsorbed by the coal, the permeability characteristics and mechanisms		NSFC 2015 confirmed	70
Multiphase gas-liquid-solid coupling mechanisms of CO_2 sequestration in the porous coal media		NSFC 2016 confirmed	62
Interaction of supercritical CO_2 and coal during CO_2 sequestration in the deep coal seam and its impact on the CO_2 storage	Shandong University of Science and Technology	NSFC 2012–2015	60
Transportation mechanisms of supercritical CO_2 injection into the stress partition residual coal pillar and its displacement of CH_4		NSFC 2015 confirmed	20
Basic research on the mechanism of CO_2-ECMB in the deep low permeable unmineable coal seam under THM coupling effect	Liaoning Technical University	NSFC 2009–2011	33
Microscopic mechanism of supercritical CO_2 on the recovery of CH_4 in the coal		NSFC 2014 confirmed	25
Type 3: CO_2-EGR			
Safety production of the CO_2 bearing gas reservoir and the utilization of CO_2	Research Institute of Petroleum Exploration & Development	Major Science & Technology 2008–2010	—
Pilot project of the production of the CO_2 bearing volcanic gas reservoir and utilization	Jilin oilfield etc.	CNPC 2008–2010	—
CO_2 sequestration mechanism in the depleted gas reservoir and the transportation rules	Southwest Petroleum University	NSFC 2013 confirmed	80
Phase behavior of supercritical CO_2 displacing CH_4 in the porous media and the seepage characteristics	Dalian University of Technology	NSFC 2015 confirmed	64
Type 4: CO_2-ESG			
Basic research of supercritical carbon dioxide enhanced shale gas development	Wuhan University	973 Program 2014–2018	—
Basic research of the supercritical CO_2 in the production of unconventional oil and gas reservoirs	China University of Petroleum	NSFC 2011–2014	258
CO_2 sequestration in the shale gas reservoir and mechanisms of CO_2-CH_4-shale interaction	Chongqing University	NSFC 2013–2015	25
Damage mechanism of using supercritical CO_2 as the hydraulic fluid in the shale reservoir		NSFC 2014 confirmed	25
Studies on the solid-fluid coupling mechanisms of CO_2 sequestration in the shale reservoir and its effect on the recovery of shale gas		NSFC 2014 confirmed	80
Brittle fracturing mechanism of supercritical CO_2 used as the hydraulic fluid in the shale reservoir and the transportation rule of the suspended sand	Qingdao University of Science & Technology	NSFC 2014–2016	80
The propagation evolution of the hydraulic fracture network induced by the supercritical CO_2 in the shale reservoir	Institute of Geology and Geophysics (CAS)	NSFC 2015–2017	85
Type 5: EGS/CO_2-EGS			
Simulation and prediction of CO_2-EGS	Jilin University etc.	Ph.D. program 2011–2013	—
Comprehensive utilization and production of hot dry rocks		863 Program 2012–2015	—

Table 1: Continued.

Name of the research projects	Responsible institute	Funding sources	Amount
The flowing characteristics of the man-made fractures in the hot dry rocks and the mechanisms of multifield coupling heat and mass transfer	Tianjin University	NSFC 2013 confirmed	76
Large scale CO_2 utilization and storage in the innovative EGS technology	Tsinghua University	International 2012–2014	—
Mechanisms of the production of geothermal energy in the high temperature depleted gas reservoir using CO_2 as the circulation fluid and the evaluation of potential	China University of Petroleum	NSFC 2016 confirmed	54
Heat transfer using supercritical CO2 enhances the geothermal recovery and the mechanisms of induced sliding of fractures	Institute of Rock and Soil Mechanics (CAS)	NSFC 2016 confirmed	54
Multiphase dynamic characteristics in the CO_2 plume type geothermal system and the optimization of the energy conversion	Jilin Jianzhu University	NSFC 2016 confirmed	20
Type 6: CO_2 capture technology			
R&D of the new type O_2/CO_2 circulated combustion equipment and the optimization of system	Huazhong University of Science and Technology	863 Program 2009–2011	—
Key technologies of CO_2 capture by using 35 MWth oxy-fuel combustion technology, R&D in equipment and pilot projects		National Sci-Tech support plan 2011–2014	—
R&D in key technologies of CO_2—oleaginous microalgae—biodiesel	Xin'ao Group etc.	863 Program 2009–2011	2070
IGCC-based CO_2 capture, utilization and sequestration technologies and pilot projects	Huaneng Group etc.	863 Program 2011–2013	5000
CO_2 capture and purification technology using high gravity method	Shengli oilfield etc.	National Sci-Tech support plan 2008–2010	—
Capture of high concentration of CO_2 in 0.3 million tons coal to oil industry, geological sequestration technology and pilot scale project	Shenhua Group etc.	National Sci-Tech support plan 2011–2014	—
Development of key technologies of reduction in CO_2 emission from the blast furnace iron making and their utilization	China Association of Metal	National Sci-Tech support plan 2011–2014	—
Research on key technologies related with large-scale CO_2 capture from the flue gases of the coal-fired power station	Tsinghua University	NSFC 2012 confirmed	230
Type 7: CO_2 storage in the saline formation (CCS technology)			
Potential assessment of CO_2 geological storage in China and pilot projects	China Geological Survey	Ministry of Land and Resources 2010–2014	—
Multiphase multicomponent reactive transportation mechanism of the sequestration of impure CO_2 and numerical simulation	Institute of Rock and Soil Mechanics (CAS)	NSFC 2016 confirmed	20
HMC coupling mechanism of CO_2 sequestration in the saline formations, stability of rock and the transportation rules of CO_2		NSFC 2011 confirmed	20
Geochemical studies on the supercritical CO_2-rock-saline water system	China University of Geosciences	NSFC 2011–2013	50
Mechanisms of the water-rock-gas interaction of the CO_2 sequestration in the saline aquifers in the pressurized sedimentary basin		NSFC 2012–2014	70
Experimental geochemical studies on the interaction of supercritical CO_2-water-basalt	Nanjing University	NSFC 2013–2015	85
Surface characteristics of supercritical CO_2-saline water in CO_2 geological sequestration	Dongnan University	NSFC 2012–2014	25
The diffusion mechanism of CO_2 in porous media and its quantitative relationship with the propagation rate of the CO_2 front	China University of Petroleum	NSFC 2013 confirmed	80
Factors affect the diffusion and mechanism of CO_2 in porous media		NSFC 2009 confirmed	20
Numerical simulation of the multiple field coupling processes in CO_2 geological sequestration using numerical manifold method	Beijing University of Technology	NSFC 2012 confirmed	62
Evolution of the damage in the near-field neighboring rocks of the CO_2 storage site in the rock salt and the integrity studies	Sichuan University	NSFC 2012 confirmed	25
Transportation rule and trapping mechanisms of CO_2 geological sequestration in the multiscale heterogeneous saline formations	Hehai University	NSFC 2012 confirmed	58
Impacts of reservoir heterogeneity on the capacity of CO_2 in the saline formations	Wuhan University	NSFC 2013 confirmed	25

Table 1: Continued.

Name of the research projects	Responsible institute	Funding sources	Amount
Flowing characteristics and mechanism of the supercritical CO_2 in the low permeable porous media	Qingdao University of Science & Technology	NSFC 2014 confirmed	80
Mechanism studies on the physical and dissolution trapping of the supercritical CO_2 in the microscopic porous aquifer	Tsinghua University	NSFC 2010 confirmed	20
Interaction of CO_2-saline water-caprocks in the CO_2 geological sequestration and the risk of CO_2 leakage		NSFC 2014 confirmed	84
Mechanisms of the difference in the distribution of the CO_2 saturation based on the high reliable saline formation model	GSC Hydrogeology & Environmental Geology	NSFC 2016 confirmed	18
Physical property measurements on the CO_2-saline water system in the CO_2 geological sequestration	Dalian University of Technology	NSFC 2011 confirmed	20
Impacts of the physical properties of the porous media on the two-phase (CO_2, saline water) fluid flow and the trapping mechanism of CO_2		NSFC 2014 confirmed	80
Two-phase CO_2-water fluid flow characteristics and trapping mechanism of CO_2 at the porous scale in the multiple porous media		NSFC 2015 confirmed	64
The convective mixing of CO_2 sequestration in the saline formations and its development characteristics		NSFC 2015 confirmed	21
Basic studies on the transportation of supercritical CO_2 in the geological sequestration in the saline formations		NSFC 2012 confirmed	25
Basic research on the wettability of CO_2-saline water-rock equilibrium system during the CO_2 sequestration in saline formations		NSFC 2013 confirmed	25
Viscous behavior and mechanism of the supercritical CO_2 on the rock surface in the geological sequestration condition		NSFC 2016 confirmed	60

Table 2: China's international collaboration on CCUS projects during 2005–2016.

Name of projects	Main responsible institutes in China	Funding sources	Funding
China-EU Cooperation on Near Zero Emissions Coal (NZEC)	The Administrative Center for China's Agenda 21 (ACCA21) etc.	MOST, EU, UK Environment, Food and Rural Affairs (DEFRA) 2007–2009	4.5 million US$
China-Australia Geological Storage of CO_2 (CAGS)		MOST, Australian Department of Resources, Energy and Tourism 2010–2018	>4.0 million US$
China-Italy CCS project		MOST, Italian Ministry of Environment 2010–2012	—
China-Netherlands CO_2-ECBM and CO_2 saline aquifer storage exchange center	Institute of Coal Chemistry (CAS) etc.	Ministry of Economic Affairs 2008-	—
China-U.S. low emission technology of IGCC	Institute of Engineering Thermophysics (CAS) etc.	MOST, U.S. DOE 2010–2012	—
China-U.S. Clean Energy Research Center (CCERC)	Huazhong University of Science and Technology	MOST, U.S. DOE 2010–2015	2 million US$/year
China-Germany CCUS project	Sichuan University etc.	NSFC, DFZ 2010–now	—

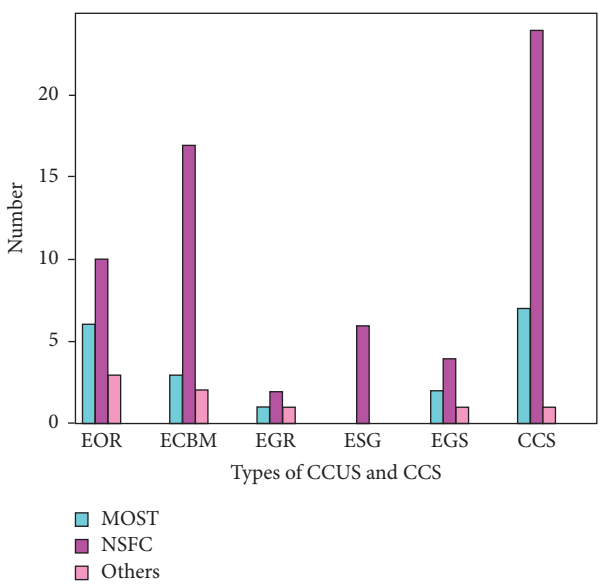

Figure 4: Research projects of CCS and CCUS in China during 2005–2016 based on Table 1.

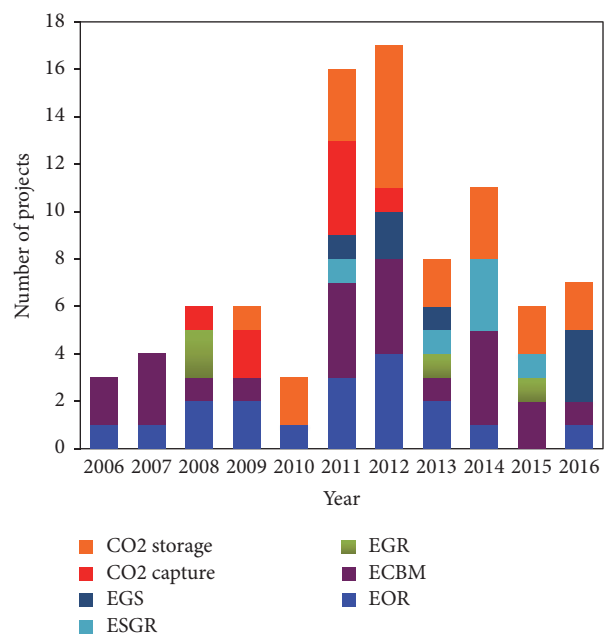

Figure 5: Different types of CCUS research projects in China during 2006–2016 based on Table 1.

4.1. CCS. China's Geological Survey compiled a series of atlases relating to the storage capacity and suitability evaluation of China and its main sedimentary basins [25, 108–112]. Combined with a selection indicator evaluation system for potential storage sites, the standardization of the CCS in China has a good foundation [20, 21, 113, 114]. A preliminary evaluation of the CO_2 storage potential in the saline formations at a depth of 1–3 km showed a capacity of 1.435×10^{11} tonnes, and most parts of the Huabei plain and Sichuan Basin can be regarded as favorable storage sites [115, 116]. Based on the studies on CO_2 sequestration in saline formations [117–124], the first full chain CCS project in China was successfully launched in the Ordos Basin with a storage target of 0.1 million tons of CO_2 injected in 2010 [125–130].

4.2. CCUS: CO_2-EOR in China. The theoretical CO_2 storage capacity of depleted onshore oil reservoirs is estimated to be 3.78 gigatons of CO_2 [131]. Conservative estimates reveal that

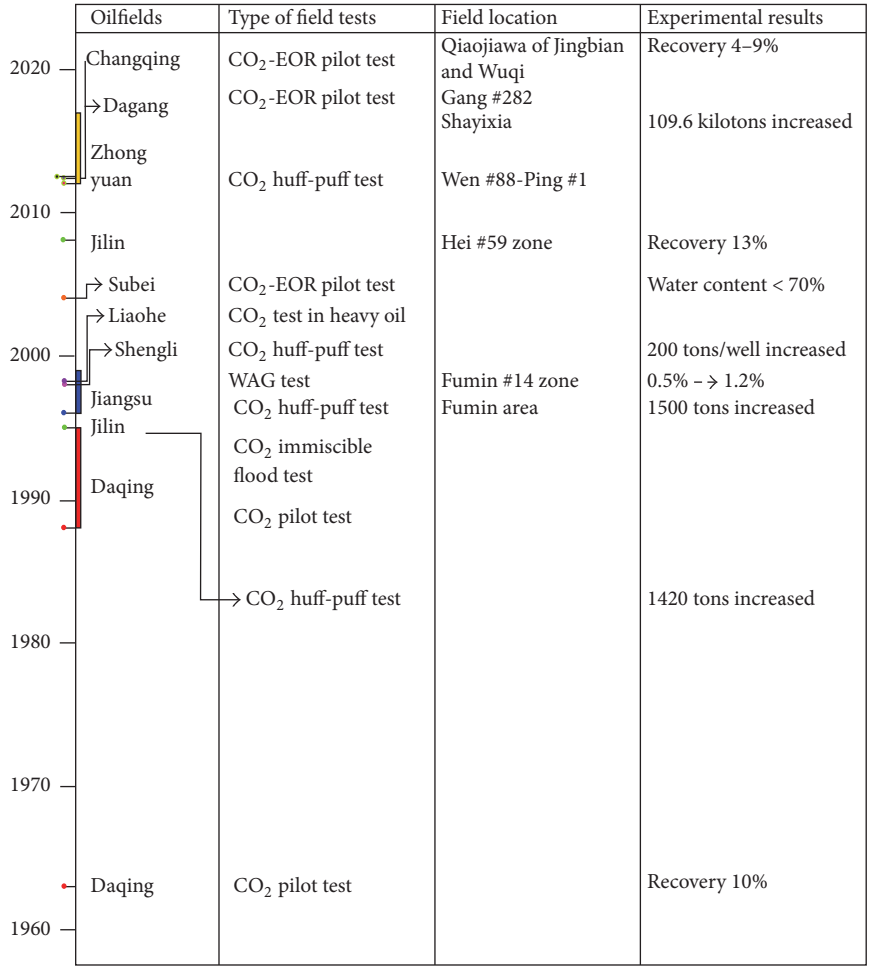

Figure 6: Development of CO_2-EOR pilot tests in several oilfields in China since the 1960s.

about 70% of the oil production comes from nine oilfields, that is, Changqing, Tarim, Daqing, Shengli, Yanchang, Bohai, Liaohe, Zhongyuan, and Jilin. However, most of them are facing or will soon be depleted after many years' production. Under these circumstances, CO_2-EOR technology may become an effective option to produce more oil from the depleting reservoir. In fact, China started the development of CO_2-EOR technology in the 1960s in several districts of the Daqing oilfield including Ta #112, Fang #48, and Shu #16 and #101 [132]. Several CO_2-EOR field tests have also been carried out in other fields including Jilin, Dagang, Shengli, and Liaohe (see Figure 6), with recovery increasing to about 10% [118, 121, 132–137]. Compared with the status of CO_2-EOR technology in the US, extensive application of CO_2-EOR in most oilfields of China may be difficult as the geologic structure of most reservoirs is characterized by many faults and low permeability [138]. Besides, a lack of policy and regulatory incentives, high commercial uncertainty, and technical challenges affect the rapid development of the CO_2-EOR technology in China.

4.3. CCUS: CO_2-ECBM in China. While studies on CO_2-ECBM technology first started in the 1990s, China began its basic research in this field (including adsorption, desorption and swelling mechanisms in the coal matrix, and the two-phase gas flow of CO_2 and CH_4 in different types of coal rocks) at the end of 20th century [139–145]. This research was further extended to include the CH_4 displacement mechanisms by using a mixture of CO_2 and N_2 [41, 146–151]. Based on the well test data for coalbed methane production in China, the recovery is in the range of 8.9%–74.5%, with an average value of 35%. By using CO_2-ECBM technology, the recovery can be increased to 59% [152]. Based on the preliminary evaluation of [153], the recoverable coalbed methane can increase to 1.632×10^{12} m^3 with CO_2 storage amount of about 120.78×10^8 tonnes for the coalbed at a depth ranging from 300 to 1500 m.

4.4. CCUS: CO_2-EGR in China. According to the results from the third oil and gas reserve investigation, if 75% of the porous volume derived from gas production is used for CO_2 sequestration, there will be a potential for a CO_2 storage capacity of 5.18 billion-tons [9, 154]. However, the gas industry in China started late and gas production is low, which means that there will not be many depleted gas reservoirs in the

short term, limiting the possibility of a commercial scale application of the CO_2-EGR technology. From the maturity point of view of this technology, very few research institutes in China are working on the improvement of CO_2-EGR at the present. Furthermore, the early breakthrough of CO_2 in gas production wells makes it difficult to attain good production efficiency from the application of CO_2-EGR technology [47]. A means of reducing the costs of separating the mixed gases, CO_2 and CH_4, is required to attain the widespread application of the CO_2-EGR technology in China.

4.5. CCUS: CO_2-ESG in China. Encouraged by the successful exploitation of shale gas in North America, China joined the exploration of shale gas in 2005 [155]. The published data from the Ministry of Land and Resources in 2002 confirms that China had a shale gas reserve of 25.1×10^{12} m^3. By the end of 2015, China had a technical shale gas reserve of about 1.3×10^{11} m^3 including the increased proved technical reserve of 1.09×10^{11} m^3.

In December 2010, China drilled its first shale gas exploration well, Wei201 in Weiyuan gas field [155]. In May 2012, the first shale gas horizontal well in China was drilled and operated by Yangchang oilfield, demonstrating a great breakthrough in the hydraulic fracturing technology for shale gas reservoirs. By the end of 2012, China's total shale gas production was 2.5×10^7 m^3, which increased to 2.0×10^8 m^3 in 2013, 1.3×10^9 m^3 in 2014, and 4.47×10^9 m^3 in 2015. The production of shale gas in China has increased greatly during the last few years, especially from the Peiling shale gas field in Chongqing with a proved reserve of more than 1.0×10^{11} m^3. It has produced shale gas of about 1.03×10^9 m^3, becoming the largest commercial shale gas field in China.

However, high production costs, a large amount of water consumption and a breakthrough in some key technologies related to shale gas production will restrict large-scale production in the near future [102]. In 2012, the National Energy Administration of China set a target for shale gas production of 6×10^{10}–1.0×10^{11} m^3 by 2020. But after a two years' practical experience during 2012-2013, it revised this target to 3.0×10^{10} m^3 by 2020. Using CO_2 to enhance the recovery of shale gas is now at an early exploration stage [156].

4.6. CCUS: CO_2-EGS in China. The 863 plan project that aims at investigating EGS was initiated by Jilin University in 2012 [157]. There are now several other projects in the country using CO_2 in geothermal production (see Table 1). This demonstrates that China is interested in developing EGS to exploit the deep geothermal resources from the hot dry rocks. Many Chinese researchers (e.g., [143, 158–162]) have already studied the operation mechanisms of the CO_2-EGS system and its optimization designs. A preliminary site selection system considering the role of CO_2 in the geothermal production was set up by [26]. Research in this technology is still at the very early stage and requires detailed work to attain pilot scheme status.

5. Status of CCUS Engineering Projects in China

The CO_2 emission sources are mainly located in the middle-eastern regions of China; see details in Figure 2.15, [34]. Therefore, pilot-scale CCUS (mostly CO_2-EOR) engineering projects in China are also located in these regions (Figure 7, Table 3). Based on published government and industrial reports and personal communications, the progress of pilot-scale CCUS engineering projects in China is as follows:

(1) A CO_2-EOR field test was executed for the first time in Daqing oilfield in 2003. In recent years, the industrial injection of CO_2 and the production of oil with the help of CO_2-EOR technology operated by the Daqing oilfield are mainly located in the Yushulin and Hailaer oilfields.

(2) A CO_2-EOR project with a CO_2 injection amount of 0.8–1 million tons/year in Jilin oilfield (still in operation) since 2005 for the exploitation of the CO_2-rich (21% CO_2 concentration) Changling gas field. A CO_2-EOR experiment has been carried out by Jilin oilfield in 2006 and oil recovery enhanced by 8%–10%. The Changling gas field was the first project to integrate natural gas production, CO_2 sequestration, and EOR technology [7]. As the conventional water injection method does not provide good production efficiency in low permeable oilfields, CO_2-EOR has played a large role in increasing production, such as in the Fuyang oilfield [137]. By March 2017, oil production increased to 100 kilotons by injecting 1.1 million tons of CO_2 underground.

(3) A full chain pilot-scale CO_2-EOR project has been injecting CO_2 at a rate of 40,000 tons/year in the Shengli oilfield (still in operation). The Sinopec Shengli oilfield cooperated with the Shengli power plant to install the largest equipment for capturing exhaust gases in a coal power plant [163]. Its purpose is to reduce CO_2 emission by 30 kilotons/year and enhance oil recovery by 20.5%. This project started in 2008 and about 251 kilotons of CO_2 had already been injected in the ultralow permeable oil reservoir through 11 injection wells by April 2015.

(4) A CO_2-EOR project operated by Zhongyuan oilfield (still in operation) injected CO_2 at a rate of 30,000 tons/year and managed to increase oil production by 3600 tons after injection of 2170 kilotons of CO_2 and 827 kilotons of water [7]. By February 2017, a total amount of about 553 kilotons of CO_2 was injected underground. As a result, oil recovery is proved to have enhanced by 10% in the Zhongyuan oilfield and by 60% in the Shayixia oilfield after the pilot-scale test.

(5) The CO_2-EOR project led by the Yangchang oilfield company was carried out in 2013 using captured CO_2 during the production of methanol and acetic acid. At present, the capture equipment designed for 360 kilotons/year of CO_2 is under construction. Pilot-scale CO_2-EOR field tests have been done in some

Table 3: Main engineering CCUS projects in China.

Projects	Location	Scale tons/yr	CO_2 capture method	Storage/utilization	Status
(1) CO_2-EOR project by Daqing oilfields	Yushulin, Hailaer	—	—	EOR	Operation
(2) CO_2-EOR project by Jilin oilfield	Songyuan	0.28 million	Liquefaction of FCC flue gas	EOR	Operation
(2-1) Second stage of EOR project in Jilin oilfield	Songyuan	Planned for 0.5 million	Precombustion from the separation of natural gas production	EOR	Operation
(3) CO_2-EOR project by Shengli oilfield	Dongying	40,000	Postcombustion	EOR	Operation
(4) EOR project by Zhongyuan oilfield	Puyang	100,000	Post-combustion	EOR	Operation
(5) EOR project by Yanchang oilfield	Yanchang	400,000	Coal liquefaction plant	EOR	Operation
(6) First stage of Huaneng greengen IGCC in Tianjin	Tianjin	—	Pre-combustion	Planed for EOR	Operation
(7) CO_2-ECBM by China United Coalbed Methane Ltd.	Jincheng	40/day	Purchase of CO_2	ECBM	Completed
(8) Full chain CCS project by Shenhua Group	Ordos	100,000	Coal liquefaction plant	Saline formation	Completed
(9) Pilot project of IGCC clean energy in Lianyungang	Lianyungang	1000,000	Pre-combustion	Planed in saline formation	Preparation
(10) 35 MWt oxy-fuel combustion in Zhongyan Yingcheng of Hubei	Yingcheng	100,000	Oxy-fuel combustion	Sequestration in the salt rock	Preparation
(11) CO_2 capture and storage pilot project by China Resources Power	Dongguan	1 million	Pre-/post-combustion from power station and oil refinery	Planed for EOR or saline formation	Prefeasibility study
(12) Coal-to-liquids project in Ningxia by Shenhua Group	Ningxia	2 million	Pre-combustion from the coal-to-liquids process	Undefined	Opportunity study
(13) Third stage of Huaneng greengen IGCC in Tianjin	Tianjin	2 million	Pre-combustion from the power station	Planed for EOR saline formation	Not start
(14) Second stage of coal-to-liquids project by Shenhua Group	Ordos	1 million	Pre-combustion from the coal-to-liquids process	Saline formation	Prefeasibility study
(15) CCS project by Sinopec Qilu Petrochemical	Dongying	0.5 million	Pre-combustion from oil refinery	EOR	Preliminary design
(16) CCS project of Shengli power station by Datang Group	Dongying	1 million	Post-combustion from the power station	EOR	Prefeasibility study
(17) CO2 capture and EOR in coal chemical industry by Yangchang Petroleum Co. Ltd.	Yanchang	5,0000	Pre-combustion from coal chemical industry	EOR	Operation
(17-1) Second stage of CO_2 capture and storage project by Yanchang Group	Yanchang	1 million	Pre-combustion from coal chemical industry	EOR	Not start
(18) CO_2 capture and storage pilot project in Daqing oilfield by Datang Group	Daqing	1 million	Oxy-fuel combustion from the power station	Planed for EOR + saline formation	Prefeasibility study
Coal-to-gas project by CNOOC Datong *	Datong	1 million	Pre-combustion from coal-to-gas process	Planed for EOR + saline formation	Prefeasibility study
Coal-to-gas project by CNOOC Ordos*	Ordos	1 million	Pre-combustion from coal-to-gas process	Planed for EOR + saline formation	Pre-feasibility study

Table 3: Continued.

Projects	Location	Scale tons/yr	CO_2 capture method	Storage/utilization	Status
Coal-to-olefin Ordos project by CPIC and TOTAL*	Ordos	1 million	Pre-combustion from coal-to-olefin process	Planed for EOR + saline formation	Prefeasibility study
CCUS project by Shanxi international energy group*	Shanxi	2 million	Oxy-fuel combustion from the power station	Undefined	Prefeasibility study
Industrial conversion of the captured CO_2, not for underground geological sequestration					
(19) Pilot project of CO_2 sequestration by microalgae of Xin'ao Group	Dalate qi	320,000	Flue gas of the coal chemistry factory	Microbe sequestration	Construction
(20) SNG project in Qinghua of Xinjiang	Yili in Xinjiang	—	Pre-combustion	Microbe sequestration	Operation
(21) Geothermal power station in Gaobeidian of Beijing by Huaneng	Beijing	3000	Post-combustion	Food and industry use	Operation
(22) Shidongkou project in Shanghai by Huaneng	Shanghai	120,000	Post-combustion	Food and industry use	Operation
(23) Shuanghuai power plant project	Chongqing	10,000	Post-combustion	N/A	Operation
(24) CO_2 project in Hainan	Dongfang	2100	Separation from natural gas	Biodegradable plastics	Operation
(25) CO_2 project in Jiangsu	Taixing	8000	Alcohol factory	Chemical material	Operation
(26) CO_2 pilot project in Tianjin	Tianjin	20,000	Post-combustion	Food	Preparation

Note. Projects marked with $*$ threaten cancellation in the near future for unknown reasons.

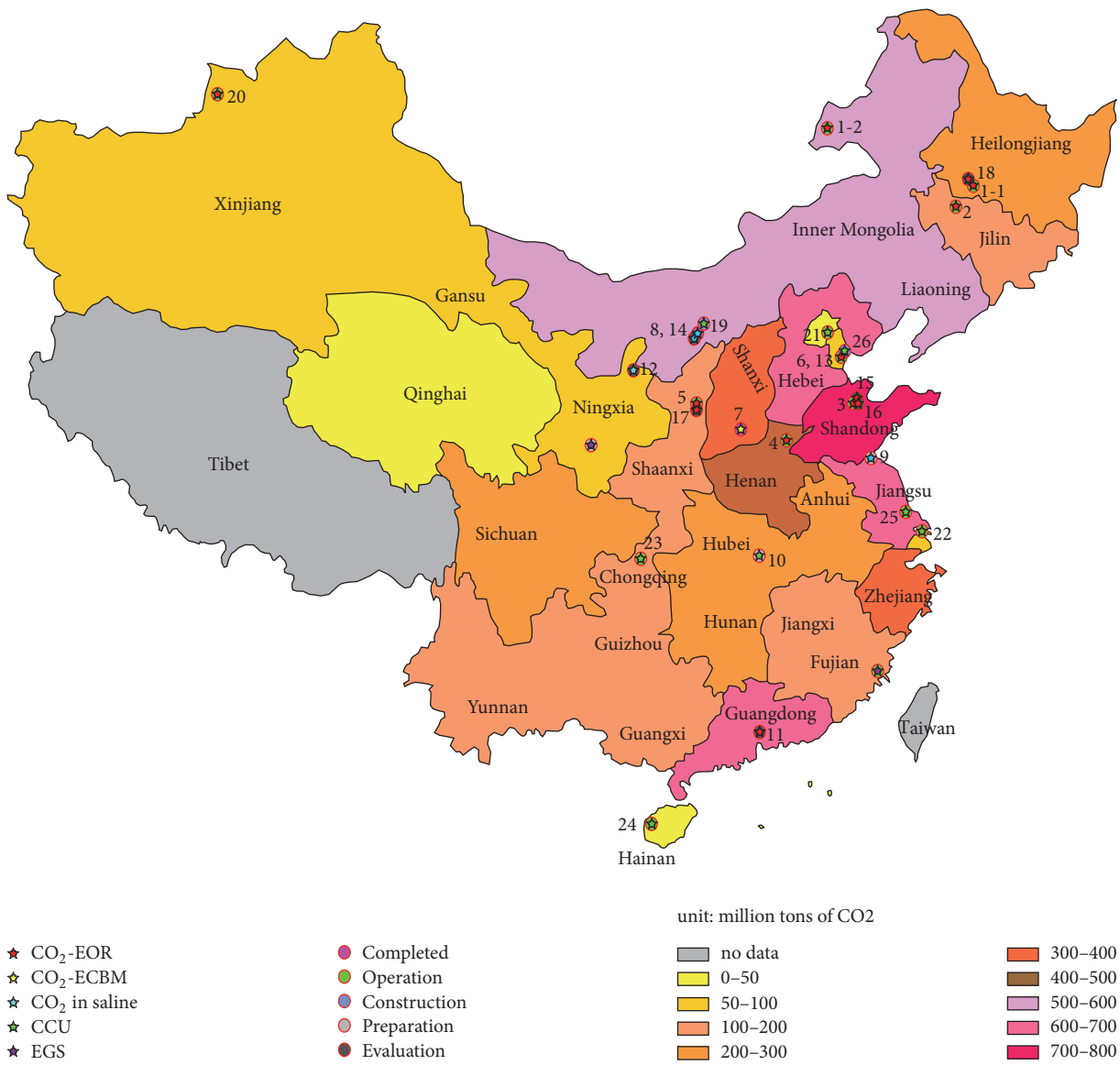

Figure 7: Distribution of CCUS engineering projects in China excluding the South China Sea Islands (numbers defined in Table 3) superimposed on the provincial CO_2 emission map for the year 2010 (from [34]).

districts of Jinbian and Wuqi, with a total of 90 kilotons CO_2 injected.

(6) As the first demonstration of IGCC power station in China, the first stage of the IGCC project at Tianjin combined with the CO_2 capture and EOR technology, with an installation capacity of 265 MW, has been in operation since November 2016.

(7) The CO_2-ECBM project located in the Qinshui basin of Shanxi Province operated by China United Coalbed Methane Corporation, Ltd (completed) [7, 164]. It is the only pilot-scale CO_2-ECBM field test in China and operates at an injection rate of 40 tonnes/day of CO_2. This is a cooperation project between the Zhonglian coalbed methane Ltd and Canada which aims at studying the feasibility of CO_2-ECBM in China [53].

(8) The full chain CCS project in the saline formations located in the Ordos of the Inner Mongolia (completed). This is the first full chain CCS project in China, with a capital investment of more than 28.6 million US$. The drilling of one injection (with a completion depth of 2826 m) and two monitoring wells (31 and 70 m away from the injection well) started in 2010. Since September 2011 until 2015, a total amount of 300,000 tons CO_2, produced by the coal liquefaction factory of the Shenhua Group, has been transported by oil tankers and injected in four saline formations and one carbonate formation [165]. The first stage of injection test started in 2011, with

the wellhead injection pressure ranging from 6.79 to 8.63 MPa. The second production test started in 2012 with varying injection rates of 6 m^3/h, 9 m^3/h, 12 m^3/h, and 15 m^3/h and constant wellhead injection pressure of 5.7 MPa and temperature of 5°C. Another large-scale CO_2 sequestration in the deep saline formations located in Lianyungang of Jiangsu Province is in preparation.

(9) A CO_2 storage project in the rock salt at Yingcheng in Hubei Province, where CO_2 will be captured by the oxy-fuel combustion technology, is in preparation [166].

(10) CO_2 sequestration by microbe algae has also been identified an effective means to reduce CO_2 concentration in the atmosphere. The two representative CO_2 sequestration projects using microbe algae are the Xin'ao and Qinghua groups both from China.

In the next few years, CO_2-EOR engineering projects will still be the most important CCUS technology in application. After the successful experience attained from the pilot-scale CCUS projects so far, China is now planning to run 13 large-scale CCUS projects. Based on the stages of the engineering projects, the project will be divided into the following study phases: opportunity → preliminary → prefeasibility → feasibility → construction drawing design → construction → operation → completed. All the stages before the construction drawing design phase, that is, preparation of the engineering projects, could be lumped together and called the "evaluation" stage. Due to the current low oil price and a lack of the motivation policy, the progress in developing most of these large-scale planning CCUS projects lags far behind the schedule. Most of these projects are still at prefeasibility or feasibility stages and some may even be cancelled.

Although capturing and industrial utilization of CO_2 in China are not the key aims of this paper, the related projects in operation include (1) Huaneng Beijing thermal power plant; (2) Huaneng Shanghai Shidongkou; (3) China Power Investment Corporation Chongqing Shuanghuai; (4) CO_2 project in Hainan operated by China National Offshore Oil Corporation (CNOOC); (5) CO_2 project in Jiangsu province operated by the Zhongke CO_2 Jinlong company. The CO_2 pilot-scale project in Tianjin organized by China Guodian Power is in preparation.

At present, China does not execute any CO_2-EGS field tests. However, a few engineering EGS projects exist at their early scientific field test stages. These include (1) the hot dry rock scientific drilling project in Zhangzhou Fujian province, in operation since May of 2015, with a drilling depth of 4000 m and a water temperature high enough for geothermal power generation and (2) a hot dry rock scientific drilling project in Qinghai Province, with a water temperature of 200°C at a depth of 3000 m [157]. Studies on power generation in traditional hydrothermal fields located in Yangyi, Xizang, and Tengchong in Yunnan Province are also undergoing. However, there are no active engineering projects related to CO_2-EGR and CO_2-ESG in China.

6. Challenges in the Widespread Application of CCUS in China

6.1. Tackling Problems in Key Technologies. The injection of CO_2 underground for the CCS and CCUS purposes involves multiple physical-chemical coupling interactions of multiple components in porous fractured media, especially the transmission and migration of fluids between porous media with a low/ultralow permeability and complex fractured network.

(a) There are mature commercial CO_2-EOR technologies in the USA and Canada. In China, however, because of the strong heterogeneity in oil reservoirs, the CO_2 channeling effect is serious [138]. Therefore, improving the sweep efficiency is the key to attaining widespread application of CO_2-EOR in China. Other efficient methods include the alternating injection of water and CO_2 (WAG) and the addition of foaming and gelling agent [132].

(b) There are currently no commercial scale CO_2-ECBM engineering projects being developed anywhere in the world. In China, studies on CO_2-ECBM technology are at a very early stage of exploration. More research is required to tackle key problems like the adsorption-desorption process between CH_4 and CO_2 in the coal seam [46, 146, 147], the mechanisms of the interaction between CO_2-CH_4-H_2O at molecular scale [150], the impact of the coal grade, water content and composition of coal, and so on on the diffusion and migration of mixed gases in the coal seam, the dynamic changes of phase behaviour during the process of CO_2 injection, and CH_4 production and so on.

(c) In the application of the CO_2-EGR technology, more effort is required to prevent the early breakthrough of CO_2 into the production well, thus enhancing the sweep efficiency of CO_2. Thus more studies are needed like the understanding of migration processes of the CO_2 after its injection into the depleted gas reservoir, phase behaviour, the mixing mechanism of CO_2 and CH_4, and so on [48, 60].

(d) Multistage hydraulic fracturing in the horizontal wells has been widely used in shale gas production in China. However, this technology is still not mature enough for the production of shale gas at depths >3500 m. The large amount of water consumed in the production of shale gas is a big challenge for its large-scale production, especially in southwestern China, where the existing water resources are very poor. Using CO_2 as the fracturing fluid has become a research hot spot in China [167]. Injection of CO_2 to extract brine or methane energy from the aquifers was also studied recently [168]. While the feasibility of using CO_2 to enhance shale gas recovery still requires more research and field tests.

(e) The direct use of geothermal energy in China has been the priority during the last few years, while its use for power generation largely lags behind that of

several countries, such as the USA, the Philippines, Japan, and Indonesia. Technologies including CO_2-AGES, EGS, and binary cycle power plants may have a positive effect on the development of China's geothermal power system. However, before obtaining mature engineering experiences, China needs to enlarge its investment in human, physical, and financial resources in these technologies.

6.2. Negative Impacts on the Environment and Resources. The risk of leakage of the injected CO_2 in the injection/production wells may have a serious environmental impact [169–173]. The groundwater quality may deteriorate if the CO_2 in the injection layer leaks into the freshwater aquifer through microfractures or faults [174, 175]. When hydraulic fracturing is applied to shale gas or geothermal energy production, it will induce microseismic events. In addition, the toxic chemical additives in the hydraulic fluid may have a serious negative impact on freshwater aquifers when they leak into the shallow layers because of possible geological hazard. Therefore, a long-term environmental monitoring activity should be carried in parallel with the CCUS engineering project to ensure its safety [104]. The dynamic migration process of CO_2, chemical interaction among CO_2 -reservoir fluid-rock, the deformation or eruption of injection/overlying caprocks, and temperature and pressure changes in the reservoir should be monitored for a long time after the injection [29, 176].

6.3. Storage Capacity Data Is Not Clear. The total amount of resources and the distribution of depleted oil and gas fields, deep unmineable coal seams, deep saline formations, shale gas, and rock salt reservoirs are not clearly known because of the inadequacy of the geological data. Thus to attain a widespread application of CCUS technologies, more accurate evaluation work should be done based on geological, geophysical, geochemical, rock mechanics data, and so on.

6.4. Policy Factor. The positive effect of China's involvement in CCUS technologies in recent years has been to focus on developing CO_2-EOR, the capture of CO_2, the shale gas and hot rock geothermal energy production, and especially shale gas production with a subsidy of 4 US¢/m^3 during 2016–2018 and 3 US¢/m^3 during 2019-2020. However, other fields of CCUS also need to be supported by the government.

6.5. High Investment Costs. The cost of a CCS or CCUS project mainly includes CO_2 capture, transportation, drilling, injection, and monitoring. Costs for the capture of CO_2 produced by the technologies of precombustion, postcombustion, or oxy-fuel combustion take the largest proportion in the investment of a specific CCS or CCUS project. Taking a coal-fired power station as an example, if 80% of the CO_2 emitted is captured and compressed to a certain pressure, its energy consumption will increase by 24%–40% [177]. In the US, the price of electricity generated from a coal-fired power station is 82–99 US$/MWh and 83–123 US$/MWh without and with the CO_2 capture technology, respectively, [178]. Depending on different situations and technologies in US, the capture cost is 42–87 US$/ton CO_2, transportation costs range from 4.3 to 7.2 US$/ton CO_2/250 km, while injection and storage costs are 1–12 US$/ton CO_2 based on the prices in 2013. In China, the cost of electricity generation by coal-fired power station increases by 30%–50% using CO_2 capture technology due to the extra consumption of electricity and steam. Taking the Huaneng Beijing coal-fired power station as an example, the capture price is about 24.3 US$/ton CO_2, with the CO_2 capture efficiency of 80%–85% [179]. On the other hand, simulation results of the IGCC coal-fired power station with the CCS technology in Tianjin show the capture price to range from 21.3 to 24.8 US$/ton CO_2, accounting for 80% of the price of a full-scale CCS project [180, 181]. However, the uncertainty in the CO_2 capture price is high depending on different capture technologies including precombustion, postcombustion, and oxy-fuel combustion at various stationary point sources including coal-fired power stations, cement factories, and coal chemical industries. From the aforementioned point of view, the uncertainty in the investment of a specific CCS or CCUS engineering project is determined by the cost of CO_2 capture. Therefore, a reduction in the cost of CO_2 capture is the key to the widespread application of CCS or CCUS technologies. Besides, drilling costs are large for all types of CCUS engineering projects and hydrocarbon/geothermal production, taking a shale gas well as an example, it costs 5.8 million US$ for a drilling length of 2500–3000 m, and 0.72 million US$ for a general gas well. The drilling cost of a geothermal production well in a hot dry rock will be much higher. The corrosion property of CO_2 requires a high quality of pipelines and ground equipment, increasing the production costs of oil, gas, and geothermal energy [182, 183].

6.6. Energy Price. The slump in the international oil price has greatly affected the investment in the oil/gas production and CCUS projects. Shale gas production in Peiling shale gas field in southwestern China with good geological conditions and large reserves is just above the breakeven point. If the oil/gas price remains low in the future, many industries will be unwilling to invest in these kinds of projects. With the exception of CO_2-EOR, it is difficult to profit from other CCUS projects. Due to completion from the increased installation capacity of wind and solar energy that have been much easier to make an economic return in recent years, the development in geothermal power generation will be continuously limited because of the difficulty in returning an economic benefit.

6.7. Social Acceptance. This is the biggest challenge for any CCS or CCUS project. It has a substantial impact on political decision makers and the implementation of energy projects such as nuclear power and wind energy programs [184]. It is the same for CCS and CCUS projects, and some CCS exploration activities in Schleswig-Holstein and Vattenfall Janschwalde in Germany, the Belchatow project in Poland, and so on were postponed or cancelled because of the lack of public acceptance over the exploration of storage sites [185, 186]. As the most unfamiliar technology to the general public in China, CCUS technology has been reluctantly accepted when compared with other low carbon technologies

including wind power, solar power, energy efficiency, or biomass for reasons of climate change mitigation [10, 187]. However, there is now a positive attitude towards CCUS policies in China. In order to stimulate public acceptance, the uncertainties regarding safety and environmental risks involved in CCUS will have to be reduced at the beginning of the development stage of any CCUS technology [188]. However, this will be largely dependent on the innovation of long-term monitoring techniques in both operating and planned pilot projects [189, 190].

7. Conclusions

(1) Many countries have participated in activities to tackle global climate changes during the last few years. The total CO_2 emissions for China in 2005 were 59.76×10^8 tonnes, accounting for 80.03% of the greenhouse gas emission of China in 2016. To perform its social responsibility, China plans to reduce its CO_2 emission per unit of GDP by 40%–45% in 2020 compared with the 2005 level. Therefore, on one hand, China needs to change its current energy framework by reducing the consumption of fossil fuels like coal energy, or applying a clean coal program, capturing the CO_2 produced by the combustion of coal. On the other hand, China needs to develop the renewable energy sector, including wind energy, solar energy, and geothermal energy.

(2) The serious air pollution problems in recent years are forcing the government of China to pay more attention to the development of green and clean energy aimed at saving energy and reducing the emissions of greenhouse gases. Some local governments have increased their investment in modern coal-fired power station coupled with the CCS technology. The CCUS engineering projects, especially those related to EOR, are also developing fast.

(3) Traditional CCS projects can store a large amount of CO_2, captured from large-scale point source emission sites, deep underground, thus effectively decreasing emissions in the atmosphere. CCUS is more attractive than the CCS technology in China because of the economic benefits accrued by using the CO_2. China has large reserves of low permeable oil and gas reservoirs. The conventional water injection methods cannot achieve good production efficiency in such reservoirs; therefore the CO_2-EOR and CO_2-EGR will have a great potential in enhancing the recovery of oil and natural gas in low and ultralow permeable reservoirs, as well as storing CO_2 in the underground space. The CCUS technology will play a considerable role in controlling the reduction of CO_2 emissions related to coal-fired power stations and the coal chemical industry. For a long period of time, coal will remain the main energy source in China; thus CCUS technology is very important for cleansing the coal-based industry. CO_2 has the potential to be used in the production of geothermal energy because of its favorable physical properties including large density and small viscosity. In addition, studies on replacing water by supercritical CO_2 as the fracturing fluid in the oil/gas/shale gas reservoirs are currently being carried out by many researchers. If this method is proved to be feasible, it will greatly decrease water consumption in the production of shale gas. This is particularly meaningful in the western regions of China where there is lack of groundwater resources.

Nomenclature

ACCA21:	Administrative Center for China's Agenda 21
ADB:	Asian Development Bank
CAS:	Chinese Academy of Sciences
CCERC:	China-U.S. Clean Energy Research Center
CCS:	Carbon capture, sequestration, or storage
CCTV:	China Central Television
CFHEG:	Center for Hydrogeology and Environmental Geology of Chinese Geological Survey
CCUS:	Carbon capture, sequestration, and utilization
CLEAN:	CO_2 Large-scale Enhanced Gas Recovery project in the Altmark Natural Gas Field
CNOOC:	China National Offshore Oil Corporation
CNPC:	China National Petroleum Corporation
CO_2-AGES:	CO_2 aided geothermal extraction system
CO_2-ECBM:	CO_2 enhanced coalbed methane recovery
CO_2-EGR:	CO_2 enhanced gas recovery
CO_2-EOR:	CO_2 enhanced oil recovery
CO_2-ESG:	CO_2 enhanced shale gas recovery
CRS:	Chromium Reducible Sulfur recovery technology
CSLF:	The Carbon Sequestration Leadership Forum
CUCMC:	China United Coalbed Methane Corporation, Ltd
DFZ:	Deutsche Friesenpferdezuchter
DEFRA:	UK Department for Environment, Food and Rural Affairs
FCC:	Fume from Catalytic Cracking
GCCSI:	Global Carbon Capture and Storage Institute
GDP:	Gross Domestic Product
IEO:	International Energy Outlook
IGCC:	Integrated Gasification Combined Cycle (IGCC)
IPCC:	Intergovernmental Panel on Climate Change
K12B:	K12B gas field located at the North Sea
MOST:	The Ministry of Science and Technology of China
NSFC:	The National Natural Science Foundation of China
NZEC:	China-EU Cooperation on Near Zero Emissions Coal project
RECOPOL:	Reduction of CO_2 emission by means of CO_2 storage in coal seams in the Silesian Coal Basin of Poland
SNG-EOR:	Synthetic Natural Gas-Enhanced Oil Recovery
USDOE:	United States Department of Energy.

Conflicts of Interest

The authors hereby declare that there are no conflicts of interest regarding the publication of this paper.

Acknowledgments

The authors would like to extend their gratitude to the National Natural Science Foundation of China (Grant no. NSFC51374147) and China CDM Fund "Update of China's CCUS Technical Roadmap" (Grant no. 2013085) for funding this work. Q. Li acknowledges financial support from the China-Australia Geological Storage of CO_2 (CAGS) Project funded by the Australian Government under the auspices of the Australia China Joint Coordination Group on Clean Coal Technology.

References

[1] D. Best and E. Levina, "Facing the development of coal in China in the future-prospects and challenges of CO_2 capture and sequestration technologies," *OECD/IEA2012*, 2012.

[2] H. Liu and K. S. Gallagher, "Driving Carbon Capture and Storage forward in China," in *Proceedings of the 9th International Conference on Greenhouse Gas Control Technologies, GHGT-9*, pp. 3877–3884, November 2008.

[3] Q. Li, Y.-N. Wei, and Y. Dong, "Coupling analysis of China's urbanization and carbon emissions: example from Hubei Province," *Natural Hazards*, vol. 81, no. 2, pp. 1333–1348, 2016.

[4] G. J. Zheng, F. K. Duan, H. Su et al., "Exploring the severe winter haze in Beijing: the impact of synoptic weather, regional transport and heterogeneous reactions," *Atmospheric Chemistry and Physics*, vol. 15, no. 6, pp. 2969–2983, 2015.

[5] B. Cai, W. Yang, D. Cao, L. Liu, Y. Zhou, and Z. Zhang, "Estimates of China's national and regional transport sector CO 2 emissions in 2007," *Energy Policy*, vol. 41, pp. 474–483, 2012.

[6] B. Cai and L. Zhang, "Urban CO2 emissions in China: Spatial boundary and performance comparison," *Energy Policy*, vol. 66, pp. 557–567, 2014.

[7] H. Xie, X. Li, Z. Fang et al., "Carbon geological utilization and storage in China: Current status and perspectives," *Acta Geotechnica*, vol. 9, no. 1, pp. 7–27, 2014.

[8] Z. Liu, "Chinas carbon emissions Report 2015," in *Proceedings of the Belfer Center for Science and International Affairs*, pp. 1–15, Harvard Kennedy School, 2015.

[9] X. Li, N. Wei, Y. Liu, Z. Fang, R. T. Dahowski, and C. L. Davidson, "CO2 point emission and geological storage capacity in China," in *Proceedings of the 9th International Conference on Greenhouse Gas Control Technologies, GHGT-9*, pp. 2793–2800, November 2008.

[10] Q. Li, J.-T. Zhang, L. Jia et al., "How to "capture the future by utilization of the past" in the coming revision of China CO2 technology roadmap?" in *Proceedings of the 12th International Conference on Greenhouse Gas Control Technologies, GHGT 2014*, pp. 6912–6916, October 2014.

[11] ACCA21-The Administrative Center for China's Agenda 21., *A report on CO_2 utilization technologies assessment in China*, Science Press, Beijing, China, 2015.

[12] IPCC., "IPCC special report on CO_2 capture and storage," pp. 1–431, Cambridge University Press, London, UK, 2005.

[13] S. Sun, "Geological issues related with CO_2 geological storage and its meaning on mitigating the climate change," *China Basic Science*, vol. 3, pp. 17–22, 2006 (Chinese).

[14] CSLF., "Estimation of CO_2 storage capacity in geological media," pp. 1–43, 2007.

[15] "Carbon sequestration Atlas of United States and Canada," pp. 1–88, USDOE (U.S. Department of Energy, Office of Fossil Energy), 2007.

[16] S. S. Xu and S. W. Gao, "CO_2 capture from the coal-fired power station and storage technology," *Shanghai Energy Conservation*, vol. 9, pp. 8–13, 2009 (Chinese).

[17] M. Bai, K. Song, Y. Li, J. Sun, and K. M. Reinicke, "Development of a novel method to evaluate well integrity during CO_2 underground storage," *SPE Journal*, vol. 20, pp. 628–641, 2014.

[18] M. Bai, J. Sun, K. Song, L. Li, and Z. Qiao, "Well completion and integrity evaluation for CO2 injection wells," *Renewable and Sustainable Energy Reviews*, vol. 45, pp. 556–564, 2015.

[19] M. Bai, J. Sun, K. Song, K. M. Reinicke, and C. Teodoriu, "Evaluation of mechanical well integrity during CO2 underground storage," *Environmental Earth Sciences*, vol. 73, no. 11, article no. 7, pp. 6815–6825, 2015.

[20] ACCA21-The Administrative Center for China's Agenda 21, Center for Hydrogeology and Environmental Geology (CFHEG), CGS, "*Guidance for site selection of CO_2 geological storage in China*" Geological Press, Beijing, China, 2012.

[21] ACCA21-Administrative Center for China's Agenda 21, Center for Hydrogeology and Environmental Geology, "*Research on the guideline for site selection of CO_2 geological storage in China*" Geological Publishing House, Beijing, China 2012.

[22] S. Bachu, "Screening and ranking of sedimentary basins for sequestration of CO2 in geological media in response to climate change," *Environmental Geology*, vol. 44, no. 3, pp. 277–289, 2003.

[23] CO2CRC., "site selection and characterization for CO_2 storage projects," Cooperative Research Centre for Greenhouse Gas Technologies RPT08–1001, Camberra, Australia, 2008.

[24] DOE., "Site screening, selection and initial characterization for storage of CO_2 in deep geologic formations," *Report*, pp. 1–3, 2013.

[25] S. Q. Zhang, J. Q. Guo, X. F. Li, J. J. Fan, and Y. J. Diao, *Geological conditions of CO_2 sequestration and geological assessment of site selection in China*, Geological Publishing House, Beijing, China, 2011.

[26] H. Liu, Z. Hou, X. Li, N. Wei, X. Tan, and P. Were, "A preliminary site selection system for a CO2-AGES project and its application in China," *Environmental Earth Sciences*, vol. 73, no. 11, article no. 10, pp. 6855–6870, 2015.

[27] Q. Li and K. Ito, "Numerical analysis and modeling of coupled thermo-hydro-mechanical (THM) phenomena in double porous media," in *Aquifers: Formation, Transport and Pollution*, R. H. Laughton, Ed., pp. 403–413, Nova Science Publishers, New York, NY, USA, 2010.

[28] K. Regenauer-Lieb, M. Veveakis, T. Poulet et al., "Multiscale coupling and multiphysics approaches in earth sciences: Theory," *Journal of Coupled Systems and Multiscale Dynamics*, vol. 1, pp. 49–73, 2013.

[29] H. Liu, Z. Hou, P. Were, Y. Gou, and X. Sun, "Numerical investigation of the formation displacement and caprock integrity in the Ordos Basin (China) during CO2 injection operation," *Journal of Petroleum Science and Engineering*, vol. 147, pp. 168–180, 2016.

[30] J. Rutqvist, Y.-S. Wu, C.-F. Tsang, and G. Bodvarsson, "A modeling approach for analysis of coupled multiphase fluid flow, heat transfer, and deformation in fractured porous rock," *International Journal of Rock Mechanics and Mining Sciences*, vol. 39, no. 4, pp. 429–442, 2002.

[31] O. Stephansson, J. A. Hudson, and L. Jing, "Coupled thermo-hydro-mechanical-chemical processes in geo-systems: fundamentals, modeling, experiments and applications," pp. 1–803, Elsevier, Inc., Oxford, UK, 2004.

[32] J. Taron, K.-B. Min, H. Yasuhara, K. Trakoolngam, and D. Elsworth, "Numerical simulation of coupled thermo-hydro-chemo-mechanical processes through the linking of hydrothermal and solid mechanics codes," in *Proceedings of the 41st US Symposiumon Rock Mechanics*, Colombia, South America, June 2006.

[33] R. Ganjdanesh, G. A. Pope, and K. Sepehrnoori, "Production of energy from saline aquifers: A method to offset the energy cost of carbon capture and storage," *International Journal of Greenhouse Gas Control*, vol. 34, pp. 97–105, 2015.

[34] Z. Liu, *Carbon emissions in China*, Springer Thesis, Springer-Verlag, Berlin, Germany, 2016.

[35] GCCSI., *The global status of CCS 2012*, Global CCUS Institute, Canberra, Australia, 2012.

[36] W. G. Liang and Y. S. Zhao, "Investigation on carbon dioxide geologic sequestration in salt caverns," *Chinese Journal of Underground Space and Engineering*, vol. 3, no. 8, pp. 1545–1550, 2007 (Chinese).

[37] L.-Z. Xie, H.-W. Zhou, and H.-P. Xie, "Research advance of CO_2 storage in rock salt caverns," *Rock and Soil Mechanics*, vol. 30, no. 11, pp. 3324–3330, 2009 (Chinese).

[38] H. Liu, Z. Hou, P. Were, X. Sun, and Y. Gou, "Numerical studies on CO_2 injection–brine extraction process in a low-medium temperature reservoir system," *Environmental Earth Sciences*, vol. 73, pp. 6839–6854, 2015.

[39] C. Preston, M. Monea, W. Jazrawi et al., "IEA GHG Weyburn CO_2 monitoring and storage project," *Fuel Processing Technology*, vol. 86, no. 14-15, pp. 1547–1568, 2005.

[40] "IEA GHG Weyburn CO_2 monitoring and storage project summary report 2000-2004," in *Proceedings of the 7th international conference on greenhouse gas control technologies*, M. Wilson and M. Monea, Eds., pp. 1–273, Vancouver, Canada, 2004.

[41] Z. Fang, X. C. Li, H. Li, and H. Q. Chen, "Feasibility study of gas mixture enhanced coalbed methane recovery technology," *Rock and Soil Mechanics*, vol. 31, no. 10, pp. 3223–3229, 2010 (Chinese).

[42] Z. Fang and X. Li, "Experimental study of gas adsorption-induced coal swelling and its influence on permeability," *Disaster Advances*, vol. 5, pp. 769–773, 2012.

[43] Z. Fang, X. Li, and L. Huang, "Laboratory measurement and modelling of coal permeability with different gases adsorption," *International Journal of Oil, Gas and Coal Technology*, vol. 6, no. 5, pp. 567–580, 2013.

[44] M. Godec, G. Koperna, and J. Gale, "CO_2-ECBM: a review of its status and global potential," in *Proceedings of the 12th International Conference on Greenhouse Gas Control Technologies, GHGT 2014*, pp. 5858–5869, October 2014.

[45] R. Puri and D. Yee, "Enhanced Coalbed Methane Recovery," in *Proceedings of the SPE Annual Technical Conference and Exhibition*, 26, 23 pages, Society of Petroleum Engineers, New Orleans, LA, USA, 1990.

[46] S. H. Tang, *Characteristics of coal reservoir in Jincheng area and properties of adsorption-desorption of multiple gases [Ph.D. thesis]*, China University of Mining & Technology, Beijing, China, 2001 (Chinese).

[47] X. L. Sun, F. G. Zeng, and H. J. Liu, "CO_2 geological storage and enhance natural gas recovery," *Bulletin of Science and Technology*, vol. 28, no. 10, pp. 11–16, 2012 (Chinese).

[48] X. Sun, F. Zeng, and H. Liu, "CO2-CH4 system mixing properties and enhanced natural gas recovery," *International Journal of Digital Content Technology and its Applications*, vol. 6, no. 21, pp. 532–541, 2012.

[49] C. W. Byrer and H. D. Guthrie, "Assessment of world coal resources for carbon dioxide (CO_2) storage potential—while enhancing potential for coalbed methane, US Department of Energy, Greenhouse Gas Mitigation, Technologies for Activities Implemented Jointly," in *Proceedings of Technologies for Activities Implemented Jointly*, pp. 573–576, Vancouver, Canada, 1997.

[50] C. W. Byrer and H. D. Guthrie, "Carbon dioxide potential in coalbeds: a near-term consideration for the fossil energy industry , US Department of Energy," in *Proceedings of the 23rd International Technical Conference on Coal Utilization and Fuel Systems*, pp. 593–600, Clearwater , FL, USA, 1998.

[51] S. H. Stevens and D. Spector, "Enhanced coalbed methane recovery: worldwide applications and CO_2 storage potential," Report prepared for IEA Greenhouse Gas R&D Programme, IEA/CON/97/27, 1998.

[52] S. H. Stevens, J. A. Kuuskraa, and D. Spector, "CO_2 storage in deep coal seams: pilot results and worldwide potential," in *Fourth International Conference on Greenhouse Gas Control Technologies*, Interlaken, Switzerland, 1998.

[53] J. Ye, S. Feng, Z. Fan et al., "Micro-pilot test for enhanced coalbed methane recovery by injecting carbon dioxide in south part of Qinshui Basin," *Acta Petrolei Sinica*, vol. 28, pp. 77–80, 2007.

[54] M. J. van der Burgt, J. Cantle, and V. K. Boutkan, "Carbon dioxide disposal from coal-based IGCC's in depleted gas fields," *Energy Conversion and Management*, vol. 33, no. 5-8, pp. 603–610, 1992.

[55] S. A. Jikich, D. H. Smith, W. N. Sams, and G. S. Bromhal, "Enhanced gas recovery (EGR) with carbon dioxide sequestration: a simulation study of effects of injection strategy and operational parameters," in *Proceedings of the SPE Eatern Meeting Conference and Exhibition*, Society of Petroleum Engineers, 2003.

[56] Z. Hou, Y. Gou, J. Taron, U. J. Gorke, and O. Kolditz, "Thermo-hydro-mechanical modeling of carbon dioxide injection for enhanced gas-recovery (CO 2-EGR): A benchmarking study for code comparison," *Environmental Earth Sciences*, vol. 67, no. 2, pp. 549–561, 2012.

[57] Y. Gou, Z. Hou, H. Liu, L. Zhou, and P. Were, "Numerical simulation of carbon dioxide injection for enhanced gas recovery (CO2-EGR) in Altmark natural gas field," *Acta Geotechnica*, vol. 9, no. 1, pp. 49–58, 2014.

[58] S. Kalra and X. Wu, "CO_2 injection for enhanced gas recovery," in *Proceedings of the SPE Western North American and Rocky Mountain Joint Meeting*, Society of Petroleum Engineers, 2014.

[59] M. Kühn, M. Streibel, N. Nakaten, and T. Kempka, "Integrated underground gas storage of CO_2 and CH_4 to decarbonise the "power-to-gas-to-gas-to-power" technology," *Energy Procedia*, vol. 59, pp. 9–15, 2014.

[60] Y. Gou, Z. Hou, M. Li, W. Feng, and H. Liu, "Coupled thermo–hydro–mechanical simulation of CO2 enhanced gas recovery

with an extended equation of state module for TOUGH2MP-FLAC3D," *Journal of Rock Mechanics and Geotechnical Engineering*, vol. 8, no. 6, pp. 904–920, 2016.

[61] T. Clemens, S. Secklehner, K. Mantatzis, and B. Jacobs, "Enhanced gas recovery—challenges shown at the example of three gas fields," in *Proceedings of the SPE EUROPEC/EAGE Annual Conference and Exhibition*, Society of Petroleum Engineers, 2010.

[62] C. M. Oldenburg, K. Pruess, and S. M. Benson, "Process modeling of CO_2 injection into natural gas reservoirs for carbon sequestration and enhanced gas recovery," *Energy & Fuels*, vol. 15, no. 2, pp. 726–730, 2001.

[63] C. M. Oldenburg and S. M. Benson, "CO_2 Injection for Enhanced Gas Production and Carbon Sequestration," in *Proceedings of the 2002 SPE International Petroleum Conference and Exhibition in Mexico*, 2002.

[64] S. Polak and A.-A. Grimstad, "Reservoir simulation study of CO2 storage and CO2 -EGR in the Atzbach-Schwanenstadt gas field in Austria," in *Proceedings of the 9th International Conference on Greenhouse Gas Control Technologies, GHGT-9*, pp. 2961–2968, November 2008.

[65] M. Kühn, M. Tesmer, P. Pilz et al., "CLEAN: Project overview on CO 2 large-scale enhanced gas recovery in the Altmark natural gas field (Germany)," *Environmental Earth Sciences*, vol. 67, no. 2, pp. 311–321, 2012.

[66] T. Maldal and I. M. Tappel, "CO2 underground storage for Snøhvit gas field development," *Energy*, vol. 29, no. 9-10, pp. 1403–1411, 2004.

[67] S. Solomon, M. Carpenter, and T. A. Flach, "Intermediate storage of carbon dioxide in geological formations: A technical perspective," *International Journal of Greenhouse Gas Control*, vol. 2, no. 4, pp. 502–510, 2008.

[68] D. S. Hughes, "Carbon storage in depleted gas fields: Key challenges," in *Proceedings of the 9th International Conference on Greenhouse Gas Control Technologies, GHGT-9*, pp. 3007–3014, November 2008.

[69] V. Becker, A. Myrttinen, P. Blum, R. Van Geldern, and J. A. C. Barth, "Predicting δ13CDIC dynamics in CCS: A scheme based on a review of inorganic carbon chemistry under elevated pressures and temperatures," *International Journal of Greenhouse Gas Control*, vol. 5, no. 5, pp. 1250–1258, 2011.

[70] J. Ennis-King, T. Dance, J. Xu et al., "The role of heterogeneity in CO2 storage in a depleted gas field: History matching of simulation models to field data for the CO2CRC Otway Project, Australia," in *Proceedings of the 10th International Conference on Greenhouse Gas Control Technologies*, pp. 3494–3501, September 2010.

[71] M. Kühn, A. Förster, J. Großmann et al., "CLEAN: Preparing for a CO2-based enhanced gas recovery in a depleted gas field in Germany," in *Proceedings of the 10th International Conference on Greenhouse Gas Control Technologies*, pp. 5520–5526, September 2010.

[72] V. Rouchon, C. Magnier, D. Miller, C. Bandeira, R. Gonçalves, and R. Dino, "The relationship between CO2 flux and gas composition in soils above an EOR-CO2 oil field (Brazil): A guideline for the surveillance of CO2 storage sites," in *Proceedings of the 10th International Conference on Greenhouse Gas Control Technologies*, pp. 3354–3362, September 2010.

[73] J. Underschultz, C. Boreham, T. Dance et al., "CO_2 storage in a depleted gas field: an overview of the CO2CRC Otway Project and initial results," *International Journal of Greenhouse Gas Control*, vol. 5, no. 4, pp. 922–932, 2011.

[74] R. J. Arts, V. P. Vandeweijer, C. Hofstee et al., "The feasibility of CO_2 storage in the depleted P18-4 gas field offshore the Netherlands (the ROAD project)," *International Journal of Greenhouse Gas Control*, vol. 11S, pp. S10–S20, 2012.

[75] F. Bilgili, E. Koçak, Ü. Bulut, and M. N. Sualp, "How did the US economy react to shale gas production revolution? An advanced time series approach," *Energy*, vol. 116, pp. 963–977, 2016.

[76] "Special Report on Carbon Dioxide Capture and Storage," in *IPCC (Intergovernmental Panel on Climate Change)*, B. Metz, O. Davidson, de. Coninck, M. Loos, L. A. Meyer, and H. C. de Coninck, Eds., Cambridge University Press, Cambridge, UK, 2005.

[77] K. C. Schepers, B. Nuttall, A. Y. Oudinot, and R. Gonzalez, *Reservoir Modeling And Simulation of The Devonian Gas Shale of Eastern Kentucky for Enhanced Gas Recovery and CO_2 Storage*, 2009.

[78] C. Ou and Y. Zeng, "Research prospect of CO_2 sealing up for safekeeping and CO_2 enhanced CH4 recovery in adsorption reservoir bed," *Chemical Industry and Engineering Progress*, vol. 30, pp. 258-63, 2011.

[79] H. Wang, Z. Shen, and G. Li, "Feasibility analysis on shale gas exploitation with supercritical CO_2," *Petroleum Drilling Techniques*, vol. 39, pp. 30–35, 2011.

[80] F. Liu, P. Lu, C. Griffith et al., "CO 2-brine-caprock interaction: Reactivity experiments on Eau Claire shale and a review of relevant literature," *International Journal of Greenhouse Gas Control*, vol. 7, pp. 153–167, 2012.

[81] P. Pei, K. Ling, J. He, and Z. Liu, "Shale gas reservoir treatment by a CO2-based technology," *Journal of Natural Gas Science and Engineering*, vol. 26, pp. 1595–1606, 2015.

[82] P. C. Harris, R. J. Haynes, and J. P. Egger, "Use of CO_2-based fracturing fluids in the red fork formation in the anadarko basin," *Society of Petroleum Engineers of AIME*, pp. 1003–1008, 1984.

[83] R. Mazza, "Liquid-free stimulations - CO_2\sand dry-frac," in *Proceedings of the Conference of Emerging Technologies for Natural Gas Industry*, 1997, http://www.netl.doe.gov/KMD/cds/Disk28/NG10-5.PDF.

[84] D. Gupta, "Nonconventional fracturing fluids," in *Proceedings of the SPE Hydraulic Fracturing Technology Conference*, The Woodlands, TX, USA, 2009.

[85] T. Ishida, K. Aoyagi, T. Niwa et al., "Acoustic emission monitoring of hydraulic fracturing laboratory experiment with supercritical and liquid CO_2," *Geophysical Research Letters*, vol. 39, no. 16, Article ID L16309, 2012.

[86] H. Wang, G. Li, and Z. Shen, "A feasibility analysis on shale gas exploitation with supercritical carbon dioxide," *Energy Sources, Part A: Recovery, Utilization and Environmental Effects*, vol. 34, no. 15, pp. 1426–1435, 2012.

[87] K. Breede, K. Dzebisashvili, X. Liu, and G. Falcone, "A systematic review of enhanced (or engineered) geothermal systems: past, present and future," *Geothermal Energy*, vol. 1, no. 1, article no. 4, 2013.

[88] D. W. Brown, "A hot dry rock geothermal energy concept using supercritical CO_2 instead of water," in *Proceedings of the 25th Workshop on Geothermal Reservoir Engineering*, pp. 233–238, 2000.

[89] K. Pruess, "Enhanced geothermal systems (EGS) using CO_2 as working fluid—a novel approach for generating renewable energy with simultaneous sequestration of carbon," *Geothermics*, vol. 35, no. 4, pp. 351–367, 2006.

[90] K. Pruess, Enhanced geothermal systems (EGS) comparing water with CO_2 as heat transmission fluids , Paper LBNL 63627, 2007.

[91] J. B. Randolph and M. O. Saar, "Impact of reservoir permeability on the choice of subsurface geothermal heat exchange fluid: CO_2 versus water and native brine," in *Proceedings of the geothermal resources council 35th annual meeting*, San Diego, CA, USA, 2011.

[92] T. A. Buscheck, M. Chen, Y. Sun, Y. Hao, and T. R. Elliot, "Two-Stage, Integrated, Geothermal-CO_2 Storage Reservoirs: An Approach for Sustainable Energy Production, CO_2-Sequestration Security, and Reduced Environmental Risk," Tech. Rep. LLNL-TR-526952, 2012.

[93] C. Xu, P. Dowd, and Q. Li, "Carbon sequestration potential of the Habanero reservoir when carbon dioxide is used as the heat exchange fluid," *Journal of Rock Mechanics and Geotechnical Engineering*, vol. 8, no. 1, pp. 50–59, 2016.

[94] J. B. Randolph and M. O. Saar, "Combining geothermal energy capture with geologic carbon dioxide sequestration," *Geophysical Research Letters*, vol. 38, 2011.

[95] Z. H. Pang, F. T. Yang, and Z. F. Duan, "Status and prospect of CO_2 geological storage technology," in *Proceedings of the in proceedings of the 2nd waste underground storage workshop*, Dunhuang, China, 2008.

[96] S. A. Hosseini and J.-P. Nicot, "Scoping analysis of brine extraction/ re-injection for enhanced CO 2 storage," *Greenhouse Gases: Science and Technology*, vol. 2, no. 3, pp. 172–184, 2012.

[97] H. Salimi and K.-H. Wolf, "Integration of heat-energy recovery and carbon sequestration," *International Journal of Greenhouse Gas Control*, vol. 6, pp. 56–68, 2012.

[98] L. Zhang, J. Ezekiel, D. Li, J. Pei, and S. Ren, "Potential assessment of CO_2 injection for heat mining and geological storage in geothermal reservoirs of China," *Applied Energy*, vol. 122, pp. 237–246, 2014.

[99] R. Ganjdanesh, S. L. Bryant, R. L. Orbach, G. A. Pope, and K. Sepehrnoori, "Coupled carbon dioxide sequestration and energy production from geopressured/geothermal aquifers," *SPE Journal*, vol. 19, no. 2, pp. 239–248, 2014.

[100] U.S. Energy Information Administration (EIA), "*International Energy Outlook 2016*", DOE/EIA-0484, 2016.

[101] U.S. Energy Information Administration (EIA), "*Annual Energy Outlook 2016 with projections to 2040*", DOE/EIA-0383, 2016.

[102] D. Sandro, J. C. Wu, Q. Yang, A. D. Hou, and J. D. Lin, *Suggestions on realization the targets of shale gas production in China*, 2014.

[103] X. Wu, Ed., *Carbon Dioxide Capture and Geological Storage: The First Massive Exploration in China*, Science Press, Beijing, China, 2013.

[104] Q. Li, X. Liu, L. Du et al., "Economics of acid gas injection with comparison to sulfur recovery in China," in *Proceedings of the 11th International Conference on Greenhouse Gas Control Technologies, GHGT 2012*, pp. 2505–2510, November 2012.

[105] L.-C. Liu, Q. Li, J.-T. Zhang, and D. Cao, "Toward a framework of environmental risk management for CO2 geological storage in china: gaps and suggestions for future regulations," *Mitigation and Adaptation Strategies for Global Change*, vol. 21, no. 2, pp. 191–207, 2016.

[106] Y. Wu, J. C. Carroll, and Q. Li, Eds., *Gas Injection for Disposal and Enhanced Recovery , Hardcover*, Wiley-Scrivener, New York, NY, USA, 2014.

[107] N. Wei, X. Li, Z. Fang et al., "Regional resource distribution of onshore carbon geological utilization in China," *Journal of CO2 Utilization*, vol. 11, pp. 20–30, 2014.

[108] S. Q. Zhang, J. Q. Guo, Y. J. Diao et al., "Technical method for selection of CO_2 geological storage project sites in deep saline aquifers," *Geology in China*, vol. 38, no. 6, pp. 1640–1651, 2011 (Chinese).

[109] S. Q. Zhang, J. Q. Guo, and X. F. Li, *Basics of CO_2 Geological Sequestration in China And Site Selection Geological Evaluation*, Geological Press, Beijing, China, 2011.

[110] J. Q. Guo, S. Q. Zhang, Y. J. Diao et al., "Site selection method of CO_2 geological storage in deep saline aquifers," *Journal of Jilin University (Earth Science Edition)*, vol. 41, no. 4, pp. 1084–1091, 2011 (Chinese).

[111] J. Q, D. G. Guo, S. Q. Zhang et al., "Potential evaluation of CO_2 geological storage and pilot-scale projects," *Geological Survey of China*, vol. 2, no. 4, pp. 36–46, 2015 (Croatian).

[112] X. F. Jia, Y. Zhang, H. Zhang et al., "Method of target area selection of CO_2 geological storage in China," *Journal of Jilin University (Earth Science Edition)*, vol. 4, pp. 255–267, 2014 (Chinese).

[113] X. C. Li and Z. M. Fang, "Status quo of connection technologies of CO_2 geological storage in China," *Rock and Soil Mechanics*, vol. 28, no. 10, pp. 2229–2233, 2007 (Chinese).

[114] Q. Li, X. Li, N. Wei, and Z. Fang, "Possibilities and potentials of geological co-storage CO2 and SO2 in China," in *Proceedings of the 10th International Conference on Greenhouse Gas Control Technologies*, pp. 6015–6020, September 2010.

[115] X. C. Li, Y. F. Liu, B. Bai, and Z. M. Fang, "Ranking and screening of CO_2 saline aquifer storage zones in China," *Chinese Journal of Rock Mechanics and Engineering*, vol. 25, no. 5, pp. 744–748, 2006 (Chinese).

[116] Y. F. Liu, X. C. Li, and B. Bai, "Preliminary estimation of CO_2 storage capacity of the deep saline formations in China," *Earth Science- Journal of China University of Geosciences*, vol. 25, no. 5, pp. 126–131, 2006 (Chinese).

[117] H. T. Zhang, D. G. Wen, and Y. L. Li, "Analysis of the CO_2 geological storage conditions in China and some suggestions," *Geological Bulletin of China*, vol. 24, no. 12, pp. 1101–1110, 2005 (Chinese).

[118] H. Y. Jiang, P. P. Sheng, X. F. Li et al., "Study into technologies for estimating theoretical volume of CO_2 stored underground worldwide," *Sino-Global Energy*, vol. 13, no. 2, pp. 93–99, 2008 (Chinese).

[119] W. Zhang, Y. L. Li, Y. Zheng, L. Jiang, and G. B. Qiu, "CO_2 storage capacity estimation in geological sequestration: issues and research progress," *Advances in Earth Science*, vol. 23, no. 10, pp. 1061–1069, 2008 (Chinese).

[120] Z. G. Xu, D. Z. Chen, and R. S. Zeng, "Principles of CO_2 geological storage and conditions," *Journal of Southwest Petroleum University (Science & Technology Edition)*, vol. 31, no. 1, pp. 91–97, 2009 (Chinese).

[121] Z. Xu, D. Chen, R. Zeng et al., "Geological storage framework of CO_2 subsurface burial trial area of daqingzijing block in the jilin oilfield," *Acta Geologica Sinica*, vol. 83, no. 6, pp. 875–884, 2009 (Chinese).

[122] Y. Z. Yang, P. P. Sheng, X. M. Song, S. Y. Yang, and Y. L. Hu, "Greenhouse gas geo-sequestration mechanism and capacity evaluation in aquifer," *Journal of Jilin University (Earth Science Edition)*, vol. 39, no. 4, pp. 744–748, 2009 (Chinese).

[123] W. Xu, X. S. Su, S. H. Du et al., "Capacity assessment and uncertainty analysis of CO_2 storage in deep saline aquifer in the central depression of Songliao Basin," *Quaternary Sciences*, vol. 31, no. 3, pp. 483–490, 2011 (Chinese).

[124] C. Guo, L. Pan, K. Zhang, C. M. Oldenburg, C. Li, and Y. Li, "Comparison of compressed air energy storage process in aquifers and caverns based on the Huntorf CAES plant," *Applied Energy*, vol. 181, pp. 342–356, 2016.

[125] X. K. Ren, Y. J. Cui, X. P. Bu, Y. J. Tang, and J. Q. Zhang, "Analysis on CO_2 storage potentiality in Ordos Basin," *Energy of China*, vol. 32, no. 1, pp. 29–32, 2010 (Chinese).

[126] J. Xie, K. N. Zhang, and L. T. Hu, "Numerical investigation of geological CO_2 storage with multiple injection wells for the Shenhua Ordos CCS project," *Journal of Beijing Normal University (Natural Science)*, vol. 51, no. 6, pp. 90–96, 2015 (Chinese).

[127] J. Xie, K. N. Zhang, Y. S. Wang, L. Q. Tan, and C. B. Guo, "Performance assessment of CO_2 geological storage in deep saline aquifers in Ordos Basin, China," *Rock and Soil Mechanics*, vol. 37, no. 1, pp. 166–174, 2016 (Chinese).

[128] B. He, T. F. Xu, Y. L. Yuan et al., "An analysis of the influence factors on CO_2 injection capacity in a deep saline formation: a case study of Shiqianfeng Group in the Erdos Basin," *Hydrogeology & Engineering Geology*, vol. 43, no. 1, pp. 136–142, 2016.

[129] X. Li, Q. Li, B. Bai, N. Wei, and W. Yuan, "The geomechanics of Shenhua carbon dioxide capture and storage (CCS) demonstration project in Ordos Basin, China," *Journal of Rock Mechanics and Geotechnical Engineering*, vol. 8, no. 6, pp. 948–966, 2016.

[130] C. Luo, A. L. Jia, T. J. Wei et al., "CO_2 storage conditions in the saline formation of the Shanxi Group 2 section in the Zizhou area of the Ordos basin and its capacity estimation," *Journal of Northeast Petroleum University*, vol. 40, no. 1, pp. 26–36, 2016 (Chinese).

[131] ADB, "Promoting carbon capture utilization and storage through carbon dioxide-enhanced oil recovery in the Peoples Republic of China," p. 16, 2015.

[132] M. Hao and Y. C. Song, "Research status of CO_2-EOR technology," *Drilling & Production Technology*, vol. 33, pp. 59–63, 2010 (Chinese).

[133] X. G. Dong, P. H. Han et al., *Pilot-scale field test of the CO_2-EOR in Daqing oilfield*, Petroleum Industry Press, Beijing, China, 1999.

[134] P. Guo, S. Y. Zhang, Y. Wu et al., "The minimum miscible pressure of CO_2 flooding in Dagang oilfield," *Journal of Southwest Petroleum University (Science & Technology Edition)*, vol. 21, no. 3, pp. 19–21, 1999 (Chinese).

[135] H. Y. Jiang, P. P. Shen, and T. X. Zhong, "The relationship between CO_2 geological storage and enhanced oil recovery," *Petroleum Geology and Recovery Efficiency*, vol. 15, no. 6, pp. 52–55, 2008 (Chinese).

[136] P. P. Shen and X. W. Liao, *CO_2 geological storage and enhance oil recovery*, Petroleum Industry Press, Beijing, China, 2009.

[137] H. J. Yu, G. J. Zhu, and J. Tian, "EOR by CO_2 injection into offshore heavy oil-cap reservoir with strong edge and bottom waters," *Petroleum Geology & Oilfield Development in Daqing*, vol. 32, no. 5, pp. 137–142, 2013 (Chinese).

[138] X. A. Yue, R. B. Zhao, and F. L. Zhao, *Technological Challenges for CO_2 EOR in China*, Science paper online, 2007.

[139] B. W. Guo, "Characteristics of tectonic coal and analysis on the location of CO_2," *Coal Geology & Exploration*, vol. 29, no. 1, pp. 28–30, 2001 (Chinese).

[140] L. Zhou, Q. Y. Feng, and X. D. Li, "Mechanism and application potential of geological sequestration of carbon dioxide in deep coal seams," *Earth and Environment*, vol. 35, no. 1, pp. 9–14, 2007 (Chinese).

[141] Q. Li, W. Fei, X. Liu, X. Wei, M. Jing, and X. Li, "Challenging combination of CO2 geological storage and coal mining in the Ordos basin, China," *Greenhouse Gases: Science and Technology*, vol. 4, no. 4, pp. 452–467, 2014.

[142] J. Yang, "Studies on the injection of CO_2 into coalbed reservoir," *Petrochemical Industry Application*, vol. 12, pp. 26–28, 2015 (Chinese).

[143] L. Hou, J. J. Tian, and Y. X. Zhang, "Numerical simulation on geological sequestration of CO_2 and coalbed methane displacement," *Shanxi Coal*, vol. 1, pp. 78–81, 2016 (Chinese).

[144] K. Jiang, Z. P. Li, H. E. Dou, Z. Y. Cao, and G. Hong, "Potential evaluation model of CO_2 geological storage in Qinshui basin," *Special Oil and Gas Reservoirs*, vol. 23, no. 2, pp. 116–118, 2016 (Chinese).

[145] J. Shen, Y. Qin, C.-J. Zhang, Q.-J. Hu, and W. Chen, "Feasibility of enhanced coalbed methane recovery by CO_2 sequestration into deep coalbed of Qinshui Basin," *Journal of China Coal Society*, vol. 41, no. 1, pp. 156–161, 2016 (Chinese).

[146] S.-H. Tang, D.-Z. Tang, and Q. Yang, "Variation regularity of gas component concentration in binary-component gas adsorption-desorption isotherm experiments," *Journal of China University of Mining & Technology*, vol. 33, no. 4, pp. 448–452, 2004 (Chinese).

[147] S. H. Tang, D. Z. Tang, and Q. Yang, "Binary-component gas adsorption isotherm experiments and their significance to exploitation of coalbed methane," *Earth Science- Journal of China University of Geosciences*, vol. 29, no. 2, pp. 219-22, 2004.

[148] H. G. Yu, *Study of characteristics and prediction of CH_4, CO_2, N_2 and binary GAS adsorption on coals and CO_2/CH_4 replacement*, Shandong University of Science and Technology, Qingdao, China, 2005.

[149] W. P. Jiang, Y. J. Cui, Q. Zhang, and Y. H. Li, "The quantum chemical study on the coal surface interacting with CH_4 and CO_2," *Journal of China Coal Society*, vol. 31, no. 2, pp. 237–242, 2006 (Chinese).

[150] W. Z. Wu, *Characteristics of the inert group structure of the coal in Shendong and the molecular simulation of its reaction with CH_4 [M. S., thesis]*, Taiyuan University of Technology, 2010 (Chinese).

[151] W. B. Fei, Q. Li, X. C. Wei, R. R. Song, M. Jing, and X. C. Li, "Interaction analysis for CO_2 geological storage and underground coal mining in Ordos Basin, China," *Engineering Geology*, vol. 196, pp. 194–209, 2015.

[152] J. P. Ye, Y. Qin, and D. Y. Lin, *Coalbed methane resources in China*, China University of Mining & Technology Press, Xuzhou, China, 1998.

[153] Y. F. Liu, X. C. Li, and B. Bai, "Preliminary estimation of CO_2 storage capacity of coalbeds in China," *Chinese Journal of Rock Mechanics and Engineering*, vol. 24, no. 16, pp. 2947–2952, 2005 (Chinese).

[154] Y. F. Liu, X. C. Li, Z. M. Fang, and B. Bai, "Preliminary estimation of CO_2 storage capacity of gas reservoirs in China," *Rock and Soil Mechanics*, vol. 27, no. 12, pp. 2277–2281, 2006.

[155] D. Z. Dong, C. N. Zou, H. Yang et al., "Progress and prospects of shale gas exploration and development in China," *Acta Petrolei Sinica*, vol. 33, supplement 1, pp. 107–114, 2012 (Chinese).

[156] Y. S. Zhu, X. X. Song, Y. T. Guo et al., "High-pressure adsorption characteristics and controlling factors of CH_4 and CO_2 on shales from Longmaxi formation, Chongqing, Sichuan Basin," *Natural Gas Geoscience*, vol. 27, pp. 1942–1952, 2016 (Chinese).

[157] T. F. Xu and W. Zhang, "Enhanced geothermal systems: international developments and Chinas prospects," *Petroleum Science Bulletin*, vol. 1, no. 1, pp. 38–44, 2016 (Chinese).

[158] F. G. Wang, *Effect of CO_2-EGS-water-rock on the characteristics of formation porosity and permeability , Master thesis at [M, S. thesis]*, Jilin University, 2013 (Chinese).

[159] F. G. Wang, J. Na, and X. X. Geng, "The impacts of different CO_2 injection temperature on heat extraction rate in CO_2 enhanced geothermal system: based on the CCS demonstration project in Erdos," *Science & Technology Review*, vol. 31, no. 8, pp. 34–39, 2013 (Chinese).

[160] Y. Shi, *The operating mechanism and optimization research on carbon dioxide plume geothermal system in Quantou formation of Songliao Basin [Ph.D. thesis]*, Jilin University, 2014 (Chinese).

[161] Z. Y. Hou, T. F. Xu, B. He, B. Feng, and J. Na, "Laboratory experimental study of dissolution using supercritical CO_2 as a stimulation agent for enhanced geothermal system (EGS) in SongLiao basin," in *Renewable Energy Resources*, vol. 1, pp. 122–128, 2016.

[162] M. Z. Liu, B. Bai, X. C. Li, and rtal, "Experimental study of fracturing characteristics of sandstone under CO_2-water two-phase condition and effective stress model," *Chinese Journal of Rock Mechanics and Engineering*, vol. 35, no. 2, pp. 38–47, 2016 (Chinese).

[163] G. Z. Lv, Q. Li, S. Wang, and X. Li, "Key techniques of reservoir engineering and injection-production process for CO_2 flooding in China's SINOPEC Shengli oilfield," *Journal of CO_2 Utilization*, vol. 11, pp. 31–40, 2015.

[164] "China United Coalbed Methane Corporation (CUCMC), Ltd," Alberta Research Council, "*The pilot-scale field test of CO_2-ECBM technology in China*" Geological Press, Beijing, China, 2008.

[165] C. H. Qu, "Discussion on developing the technology of CO_2 capture and storage," *China Science and Technology Periodical Database Industry*, vol. 8, pp. 1–3, 2015.

[166] Department of Social Development (DSD), "CO_2 capture, utilization and storage technologies in China," *The Administrative Center for China's Agenda 21 ACCA21*, p. 22, 2010 (Chinese).

[167] Y. K. Du, *Study on the mechanism of supercritical carbon dioxide efflux in the rock breaking mechanism [Ph.D. thesis]*, China University of Petroleum, Huadong, China, 2009 (Chinese).

[168] Q. Fang, *CO_2 Geological Storage Combined with Brine Production in High-salinity and Low-permeability Aquifers [Ph.D. thesis]*, China University of Geosciences, Wuhan, China, 2014 (Chinese).

[169] X. H. Zhang, X. B. Lu, and Q. J. Liu, "The effect of the characteristics of Cap on the escaping velocity of CO_2," *Soil Engineering and Foundation*, vol. 23, no. 3, pp. 67–70, 2009 (Chinese).

[170] S. Q. Zhang, Y. J. Diao, X. X. Cheng et al., "geological storage leakage routes and environment monitoring," *Journal of Glaciology and Geocryology*, vol. 32, no. 6, pp. 1251–1261, 2010 (Chinese).

[171] Q. Li, "The potential environmental impacts and risk studies during CO_2 geological storage-safety evaluation," in *Workshop on Greenhouse Gas Control and Environmental Impacts Evaluation, Chinese Academy for Environmental Planning, Shamen*, p. 20, 2011.

[172] L. H. Peng, J. J. Wang, W. J. You, and L. S. Xu, "Environmental issues and advances of carbon dioxide geological storage," *Hydrogeology & Engineering Geology*, vol. 40, no. 5, pp. 104–110, 2013 (Chinese).

[173] H. Shi, L. C. Liu, and Q. Li, "A comparative study of geo-environmental impacts of CO_2 geological storage and high level nuclear waste geo-disposal , China Population," *Resources and Environment*, vol. 25, pp. 203–207, 2015.

[174] X. Y. Zhang, J. M. Cheng, and J. Liu, "Advances on the research of CO_2 sequestration," *Hydrogeology & Engineering Geology*, vol. 4, pp. 58–88, 2006 (Chinese).

[175] Z. G. Xu, D. Z. Chen, and R. S. Zeng, "The leakage risk assessment and remediation options of CO_2 geological storage," *Geological Review*, vol. 54, no. 2, pp. 373–385, 2008.

[176] The Climate Group, *CCUS in China: 18 hot-spot problems*, 2011.

[177] Greengen Corporation Limited, *Challenging the global climate changes-CO_2 capture and storage*, China Water & Power Press, Beijing, China, 2008.

[178] E. S. Rubin, J. E. Davison, and H. J. Herzog, "The cost of CO2 capture and storage," *International Journal of Greenhouse Gas Control*, vol. 40, pp. 378–400, 2015.

[179] B. Huang, S. Xu, S. Gao et al., "Industrial test and techno-economic analysis of CO2 capture in Huaneng Beijing coal-fired power station," *Applied Energy*, vol. 87, no. 11, pp. 3347–3354, 2010.

[180] W. Y. Chen, Z. X. Wu, and W. Z. Wang, "The strategy of CO_2 capture and storage and its potential effect on the long term reduction in CO_2 emission in China," *Environmental Science*, vol. 28, no. 6, pp. 1178-1179, 2007 (Chinese).

[181] J. Chen, C. Zheng, W. Chen, and W. Y. Fei, "The emergency in reducing the CO_2 emission and the development of capture technology," in *Proceedings of the in Proceedings of the 10th Annual Meeting of China Association for Science and Technology: reduction in CO₂ emission and its clean utilization and development workshop*, pp. 10–13, 2008.

[182] X. Y. Zhang, C. Di, and L. C. Lei, *CO_2 corrosion and treatment*, Chemistry Industry Press, Beijing, China, 2000.

[183] M. J. Wu, "Studies on the corrosion of the ground system in tertiary oil recovery with CO_2 flooding and treatment," *Oil-Gasfield Surface Engineering*, vol. 23, no. 1, pp. 16–18, 2004 (Chinese).

[184] K. van Alphen, Q. van Voorst tot Voorst, M. P. Hekkert, and R. E. H. M. Smits, "Societal acceptance of carbon capture and storage technologies," *Energy Policy*, vol. 35, no. 8, pp. 4368–4380, 2007.

[185] J. K. Haug and P. Stigson, "Local acceptance and communication as crucial elements for realizing CCS in the Nordic region," in *Proceedings of the 8th Trondheim Conference on CO2 Capture, Transport and Storage, TCCS 2015*, pp. 315–323, June 2015.

[186] Z. Kapetaki, J. Simjanović, and J. Hetland, "European carbon capture and storage project network: Overview of the status and developments," in *Proceedings of the 8th Trondheim Conference on CO2 Capture, Transport and Storage, TCCS 2015*, pp. 12–21, June 2015.

[187] Z.-A. Chen, Q. Li, L.-C. Liu et al., "A large national survey of public perceptions of CCS technology in China," *Applied Energy*, vol. 158, pp. 366–377, 2015.

[188] Q. Li and G. Liu, "Risk assessment of the geological storage of CO_2: a review," in *Geologic Carbon Sequestration: Understanding Reservoir Behavior*, V. Vishal and T. N. Singh, Eds., pp. 249–284, Springer, New York, NY, USA, 2016.

[189] Q. Li, Z. A. Chen, J.-T. Zhang, L.-C. Liu, X. C. Li, and L. Jia, "Positioning and revision of CCUS technology development in China," *International Journal of Greenhouse Gas Control*, vol. 46, pp. 282–293, 2016.

[190] Q. Li, R. Song, X. Liu, G. Liu, and Y. Sun, "Monitoring of carbon dioxide geological utilization and storage in China: a review," in *Acid Gas Extraction for Disposal and Related Topics*, Y. Wu, J. J. Carroll, and W. Zhu, Eds., pp. 331–358, Wiley-Scrivener, New York, NY, USA, 2016.

Hindawi
Geofluids
Volume 2017, Article ID 2041072, 17 pages
https://doi.org/10.1155/2017/2041072

Research Article

An Approximate Solution for Predicting the Heat Extraction and Preventing Heat Loss from a Closed-Loop Geothermal Reservoir

Bisheng Wu,[1] Tianshou Ma,[2,3] Guanhong Feng,[4] Zuorong Chen,[1] and Xi Zhang[1]

[1] *CSIRO Energy, 71 Normanby Road, Clayton, VIC 3168, Australia*
[2] *State Key Laboratory of Oil & Gas Reservoir Geology and Exploitation, Southwest Petroleum University, Chengdu, Sichuan 610500, China*
[3] *State Key Laboratory of Geomechanics and Geotechnical Engineering, Institute of Rock and Soil Mechanics, Chinese Academy of Sciences (CAS), Wuhan, Hubei 430071, China*
[4] *Key Laboratory of Groundwater Resources and Environment, Jilin University, Changchun 130021, China*

Correspondence should be addressed to Bisheng Wu; bisheng.wu@csiro.au and Tianshou Ma; matianshou@126.com

Received 1 April 2017; Revised 5 June 2017; Accepted 19 June 2017; Published 16 August 2017

Academic Editor: Weon Shik Han

Approximate solutions are found for a mathematical model developed to predict the heat extraction from a closed-loop geothermal system which consists of two vertical wells (one for injection and the other for production) and one horizontal well which connects the two vertical wells. Based on the feature of slow heat conduction in rock formation, the fluid flow in the well is divided into three stages, that is, in the injection, horizontal, and production wells. The output temperature of each stage is regarded as the input of the next stage. The results from the present model are compared with those obtained from numerical simulator TOUGH2 and show first-order agreement with a temperature difference less than 4°C for the case where the fluid circulated for 2.74 years. In the end, a parametric study shows that (1) the injection rate plays dominant role in affecting the output performance, (2) higher injection temperature produces larger output temperature but decreases the total heat extracted given a specific time, (3) the output performance of geothermal reservoir is insensitive to fluid viscosity, and (4) there exists a critical point that indicates if the fluid releases heat into or absorbs heat from the surrounding formation.

1. Introduction

With the rapid increasing demand for clean and renewable energy, geothermal energy has become one of the most promising alternatives for energy supplies due to its many advantages. First, geothermal energy is inexhaustible and renewable due to radioactive decay from below the earth [1] and there is a wide range of geothermal resources in the world including in the USA, Mexico, Germany, Italy, Finland, Norway, Iceland, Sweden, New Zealand, Australia, Indonesia, and China [1, 2]. Second, geothermal energy is much cleaner and environmentally friendly compared to the conventional fossil fuels. It has been reported that the geothermal energy based plants produce 1/12 carbon dioxide of the coal based plant [3]; Third, up to date, as only small amount of geothermal resource has been utilized for heating or power generation compared to its large reserve, there is a large potential for extraction.

Closed-loop geothermal system represents an important mean to extract heat from below the earth and study on maximizing its output performance is very important [4, 5]. The basic principle of a closed-loop system is simple: a cold fluid (CO_2 or water) is injected into the well, absorbs heat from hotter surrounding rocks when flowing in a channel such as wellbore or fracture, and then is pumped out from the production well. In the present paper, the connecting channel is chosen to be a wellbore. In addition to extracting heat from the reservoir by fluid circulation, the closed-loop system can prevent contaminants in fluids from leaking into the reservoir. As the output performance, including temperature

and thermal power, of a geothermal reservoir is affected by many factors such as number and location of wells and fractures, flow rates, and velocity and direction of areal flow [6, 7], an efficient mathematical model is required for studying the relationship between reservoir performance and these parameters depending on specific system configuration.

Fluid flow and heat transfer in a wellbore/pipe have received a great deal of attention during the last several decades due to their importance in oil and gas industry. For example, the thermoelastic stress change is significant near the wellbore; it may change the fracture initiation and path during hydraulic fracturing [10–12]. The mathematical models can be mainly classified into two types, that is, analytical and numerical. Many studies belong to the first type. For example, Bullard [13] and Moss and White [14] used a line/source model to study the time for a wellbore to attain temperature equilibrium and the temperature evolution in a water-injection well, respectively. Recently, the infinite, cylindrical, and finite line source theories [15] have been widely used for geothermal simulation. For example, Eskilson [16], Zeng et al. [17], Sutton et al. [18], Bandos et al. [19], Michopoulos and Kyriakis [20], Molina-Giraldo et al. [21], Hecht-Méndez et al. [4], Rivera et al. [22], and Zhou et al. [23] used line source models to predict the temperature evolution in the ground source heat pumps. In addition, Ramey [24] presented approximate solutions for the wellbore/reservoir (W/R) system involved in injection of hot or cold fluid. Dowdle and Cobb [25] applied the Horner temperature plot method, which is similar to conventional pressure build-up, to predict the static wellbore temperature from well logs. Edwardson et al. [26] and Tragesser et al. [27] studied the wellbore temperature during mud circulation by using an exact method which is based on the solution of differential equation of heat conduction. Because the above models do not consider the heat exchange between the fluid inside and that outside the drill pipe, they cannot be used as a general tool for predicting the thermal behaviour in a wellbore/reservoir systems.

As for fluid circulation in a wellbore/reservoir system, the work by Raymond has to be mentioned [28]. In addition to providing systematic derivation of the governing equations characterizing the transient fluid flow and heat transfer, Raymond [28] obtained the analytical solutions for the case with steady state heat transfer in the wellbore by using Laplace transformation and also numerically solved the problem with transient heat transfer in both wellbore and formation by using the finite difference method (FDM). Most of the models studied later on fluid circulation in a wellbore/reservoir system more or less borrow some concepts from Raymond's work [28]. For example, Holmes and Swift [29] solved approximately similar governing equations under assumption of steady state heat transfer between the annular fluid and the formation. Keller et al. [30] considered the effects of heat generated by fluid friction, sliding casing strings, and other energy sources in the system. García et al. [31], Espinosa-Paredes et al. [32], Fomin et al. [33], and Izgec et al. [34] presented a fully transient FDM model by considering the transient heat behaviour during fluid circulation in a W/R system. Wu et al. [35] solved analytically the transient heat transfer both in the wellbore and formation during drilling with fluid circulation in the wellbore.

In addition to the above-mentioned approaches, recently a large number of numerical open sources or commercial software are available for geothermal simulation. For example, HYDROTHERM by US Geological Survey [36] and TOUGH2 by Lawrence Berkeley National Laboratory [37] based on FDM, OpenGeoSys by Helmholtz Centre of Environmental Research, Germany [38], ROCKFLOW by Kolditz et al. [39], FEFLOW by Diersch et al. [40, 41], FEHM by Los Alamos National Laboratory [42] and COMSOL [43] based on finite element method (FEM), ECLIPSE by Schlumberger [44], and Fluent by ANSYS [45] based on finite volume method (FVM) have been applied successfully to model the heat extraction from geothermal reservoirs with complicated geometries. In addition, the boundary element method (BEM) was also used for modelling similar problems. For example, Ding [46], Ghassemi et al. [47], Kumar and Gutierrez [48], and McClure and Horne [49] used the BEM or displacement discontinuity element method (DDM) to simulate the heat and mass transfer in geothermal reservoir with single fracture or fracture networks.

Although the above numerical methods can be used to solve complex problems, they sometimes are computationally costly. The analytical methods cannot be directly used to solve the present closed-loop geothermal model because of the complex model geometry. This is the main motivation for carrying out the present work.

The objective of the present work is to provide an approximate approach to predict the heat extraction and thermal power from a closed-loop geothermal reservoir. This paper is organized as follows: in Section 2, the problem description and formulation, including governing equations and boundary and initial conditions, are presented; Section 3 provides the dimensionless formulation, followed by solution method in Section 4. The model validation and numerical results are given in Section 5 and conclusions are presented in Section 6.

2. Problem Formulation

2.1. Problem Description and Assumptions. The model geometry studied is shown in Figure 1. It contains one simplified well containing two vertical parts and one horizontal part. The initial temperature of the system is a function of depth; that is, $T_0 = A_0 z + B_0$, where A_0 is the geothermal gradient and B_0 is the surface ground temperature. At time $t > 0$, a fluid (water) with a constant temperature T_{in} is injected into the system at a constant volumetric rate Q_1. The geometrical sizes of the wellbore shown in Figure 1 are defined as follows: the lengths of the injection, horizontal, and production well sections are L_1, L_2, and L_3 ($L_3 = L_1$), respectively; the radius of the wellbore is r_{hi} ($i = 1, 2, 3$), possibly including all layers such as steel casing and cementation if they exist as shown in Figure 1. The origin of the general coordinate system (GCS), denoted by the coordinates (x, y, z), is located at the injection point of the vertical well and coincides with the origin of the local cylindrical coordinate system (LCCS), denoted by the coordinate (r_1, z), for the injection well. The

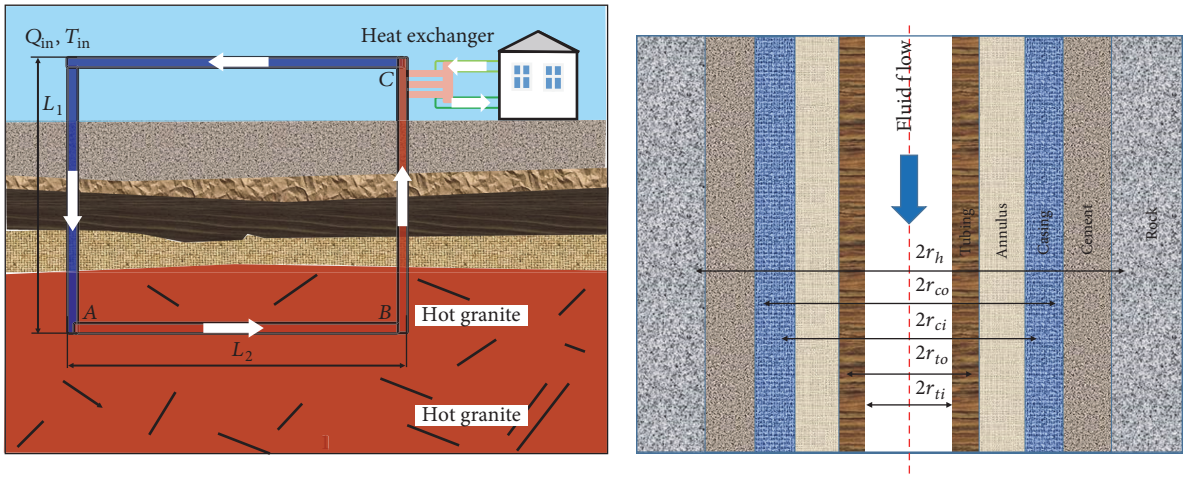

(a) (b)

Figure 1: Model geometry. (a) Injection well system and (b) cross section of the well system.

origin of the LCCS, denoted by the coordinate (r_2, x), for the horizontal well is at the bottom of the injection well, that is, intersection A. In a similar way, the origin of the local cylindrical coordinate system (LCCS), denoted by the coordinate (r_3, z_1), for the production well is located at the bottom of the production well, that is, $(L_2, 0, L_1)$ in the GCS.

In order to make the problem tractable, some assumptions are made:

(a) The fluid is single phase, incompressible, and Newtonian, and the rock is impermeable.

(b) The material properties of the fluid and the rock are constants, independent of temperature.

(c) When there are multiple layers around the wellbore, the heat transfer through the layers is characterized by one overall heat transfer coefficient.

(d) The heat diffusion around the wellbore can be regarded to be axis-symmetric.

Assumption (d) is the most important one based on which the present model is simplified. According to JiJi [50, page 242–246], for a semi-infinite domain with a homogenous initial temperature and one time-dependent surface heat flux imposed at the boundary at time $t > 0$, the penetration depth of the thermal layer is in the order of $(6\kappa_r t)^{1/2}$, where $\kappa_r = \lambda_r/(\rho_r c_r)$ is the thermal diffusivity with λ_r, ρ_r, and c_r being the thermal conductivity, mass density, and specific heat capacity, respectively, of the media. Take shale, for example, when $\lambda_r = 1.42\,\mathrm{W/(m{\cdot}K)}$, $\rho_r = 2057\,\mathrm{Kg/m^3}$, and $c_r = 2151\,\mathrm{J/(Kg{\cdot}K)}$ (pp 106, [8]), the thermal diffusivity $\kappa_r = 3.209 \times 10^{-7}\,\mathrm{m^2/s}$. This means that, after 60 days and 30 years, the thermal layer is about 3.16 m and 42.68 m, respectively, illustrating the slow movement of the thermal front in rock. Because the reservoir size is large enough (say in the order of 1 km), the interaction of heat transfer in the horizontal and vertical directions around the bottom of the vertical wells can be neglected.

Based on the above assumptions, the current model can be simplified greatly without causing large errors in predicting the temperature profiles.

2.2. Governing Equations. The governing equations can be written in the corresponding local cylindrical coordinate system (LCCS) for the vertical and horizontal parts of the well. Besides, temperature continuity is enforced at the intersection point at the heel of the horizontal well.

2.2.1. Heat Exchange along the Wellbore. As the heat flow is uniform along the well, the transient energy equations for the fluid flow are written as follows, according to their LCCSs [28]:

$$\begin{aligned}
&\rho_f c_f A_1 v_1 \frac{\partial T_{f1}}{\partial z} + 2\pi r_{t1} U_1 \left(T_{f1} - T_{b1}\right) \\
&\quad = -\rho_f c_f A_1 \frac{\partial T_{f1}}{\partial t}, \quad \text{(injection)}, \\
&\rho_l c_l A_3 v_3 \frac{\partial T_{f3}}{\partial z_1} + 2\pi r_{t3} U_3 \left(T_{b3} - T_{f3}\right) = \rho_f c_f A_3 \frac{\partial T_{f3}}{\partial t}, \\
&\qquad\qquad \text{(production)},
\end{aligned} \tag{1}$$

for the vertical wells, and

$$\begin{aligned}
&\rho_f c_f A_2 v_2 \frac{\partial T_{f2}}{\partial x} + 2\pi r_{t2} U_2 \left(T_{f2} - T_{b2}\right) \\
&\quad = -\rho_f c_f A_2 \frac{\partial T_{f2}}{\partial t},
\end{aligned} \tag{2}$$

for the horizontal well, where ρ_f and c_f are the mass density and specific heat capacity, respectively, of the fluid and $r_{t\ell}$, A_ℓ, U_ℓ, v_ℓ, $T_{f\ell}$, and $T_{b\ell}$ ($\ell = 1$ for injection, $\ell = 2$ for horizontal, and $\ell = 3$ for production) denote the radius of fluid flow

channel, the areas of the wellbore cross section, overall heat transfer coefficients (OHTCs), fluid velocity in the wellbore, fluid temperature, and the temperature at the wellbore wall, respectively. The value of the radius of fluid flow channel will be determined based on the condition as follows. If fluid flows in a pipe, it is equal to the pipe radius; if the fluid contacts directly with the rock formation, it is equal to the wellbore radius; that is, $r_{t\ell} = r_{h\ell}$.

The OHTCs U_ℓ can be calculated based on Willhite's equation [51] which considers a multilayered wellbore structure

$$\frac{1}{U_\ell} = \frac{r_{to}}{r_{t\ell}h_\ell} + \frac{r_{to}\ln(r_{to}/r_{t\ell})}{k_{\text{tub.}}} + \frac{r_{to}\ln(r_{\text{ins.}}/r_{to})}{k_{\text{ins}}} + \frac{r_{to}}{r_{\text{ins.}}(h'_c + h'_r)} + \frac{r_{to}\ln(r_{co}/r_{ci})}{k_{\text{cas.}}} + \frac{r_{to}\ln(r_h/r_{co})}{k_{\text{cem.}}}, \tag{3}$$

where $\ell = 1$ or 2, for two well parts. The cross-section geometry can be found in Figure 1(b) and the subscripts provide the layers. k denote the thermal conductivities for different layers. h'_c is the natural convection and conduction HTC through the annulus, and h'_r is the radiation HTC through the annulus; h_ℓ is the HTC between the fluid and tubing. If the effects of the annulus, casing, and cements are not taken into account, the first two terms on the right side of (3) are used to calculate U_ℓ. If the fluid contacts directly with the rock formation, $r_{to} = r_{t\ell}$ and $U_\ell = h_\ell$. From (3) we also know that the OHTC is mainly determined by the minimum value of the denominators of the terms on the right side. This indicates that if the thermal conductivity of some layer is very small, this layer will work as a thermal insulator.

When fluid flows in a tubing, the HTC between the fluid and tubing, that is, h_ℓ, is obtained by using the relationship $\text{Nu}_\ell = h_\ell D/k_f$, where N_u denotes the Nusselt number, k_f is the thermal conductivity of the fluid, and D is the hydraulic diameter of the tubing. For fully developed laminar flow in a pipe with circular cross section, the Nusselt number $N_u = 3.66$, while, for transitional and turbulent flows, the Nusselt number is obtained by using the well-known Gnielinski correlation [52]

$$\text{Nu} = \frac{(\xi/8)(\text{Re} - 1000)\,\text{Pr}_f}{1 + 12.7\sqrt{\xi/8}\left(\text{Pr}_f^{2/3} - 1\right)}\left(\frac{\text{Pr}_f}{\text{Pr}_r}\right)^{0.11}, \qquad \xi = [0.79\ln(\text{Re}) - 1.64]^{-2}, \tag{4}$$

when $0.5 < \text{Pr}_f < 2000$ and $3000 < \text{Re} < 5 \times 10^6$. In the present model, the Reynolds and Prandtl numbers related to fluid flowing in the tubing or wellbore and the rock formation are expressed as

$$\text{Re}_\ell = \frac{\rho_f v_\ell 2r_{t\ell}}{\mu}, \quad \text{Pr}_f = \frac{\mu c_f}{k_f}, \quad \text{Pr}_{r\ell} = \frac{\mu c_{r\ell}}{k_{r\ell}}, \tag{5}$$

where ρ_f and c_f denote the mass density and heat capacity, respectively, of the fluid and $k_{r\ell}$ and $c_{r\ell}$ denote the thermal conductivity and heat capacity, respectively, of the rock formation.

2.2.2. Heat Conduction in the Rock Formation Surrounding the Wellbore. As the radial heat conduction dominates the thermal diffusion process around the wellbore, the equations are written as follows in their corresponding LCCS:

$$\frac{\partial T_{r\ell}}{\partial t} = \kappa_{r\ell}\frac{1}{r_\ell}\frac{\partial}{\partial r_\ell}\left[r_\ell\frac{\partial T_{r\ell}}{\partial r_\ell}\right], \quad (\ell = 1, 2, 3), \tag{6}$$

where T_{r1}, T_{r2}, and T_{r3} denote the temperature of the formation around the injection, horizontal, and production wells, respectively. The thermal diffusivities of the rock formation are denoted by $\kappa_{r\ell} = k_{r\ell}/(\rho_{r\ell}c_{r\ell})$, with $\rho_{r\ell}$ being the mass density of the rock formation. It should be noted that the radial spatial variables for the injection, horizontal, and production wells are r_1, r_2, and r_3, respectively.

The heat transfer conditions between the rock and the whole well system are given as

$$2\pi r_{t\ell}U_\ell\left(T_{b\ell} - T_{f\ell}\right) = 2\pi r_{h\ell}\lambda_{r\ell}\frac{\partial T_{r\ell}}{\partial r_\ell}, \quad \text{at } r_\ell = r_{h\ell}. \tag{7}$$

Based on the above equation, if the OHTC $U_\ell = 0$, $\partial T_{r\ell}/\partial_{r\ell} = 0$, indicating no heat flowing into or out of the rock formation. From the point of view of heat extraction, a thermal insulation layer along the production well can enhance the heat production by preventing the heat loss along the well during fluid flowing upwards.

2.3. Boundary and Initial Conditions. The injection rate Q_1 is prescribed and the injection temperature is

$$T_{f1} = T_{\text{in}}, \quad \text{at } (0, 0, 0) \text{ in GCS}. \tag{8}$$

The bottomhole temperature (BHT) of the vertical well is used as the input conditions for the horizontal well and the output temperature of the horizontal well is used as the input conditions for the production well, that is, at the intersections A and B

$$T_{f1} = T_{f2}, \quad \text{at } (0, 0, H) \text{ in GCS}, \qquad T_{f2} = T_{f3}, \quad \text{at } (L, 0, H) \text{ in GCS}. \tag{9}$$

The ground temperature at the surface is a constant

$$T_{r1} = B_0, \quad \text{on } z = 0, \tag{10}$$

and the initial temperature of the whole system is a function of depth

$$T_0 = A_0 z + B_0. \tag{11}$$

The heat extraction rate or thermal power output by the fluid with output temperature T_{out} is expressed as

$$W = Q_3 \rho_w c_w T_{\text{out}} - Q_1 \rho_w c_w T_{\text{in}}, \tag{12}$$

where $Q_1 = Q_3 = Q_{\text{in}}$ and from which the total heat extracted is

$$\Phi = \int_0^t W(t)\, dt = \int_0^t Q_{\text{in}} \rho_w c_w \left(T_{\text{out}} - T_{\text{in}}\right) dt. \tag{13}$$

3. Dimensionless Formulation

The governing equations, boundary and initial conditions, are simplified with the following transformation:

$$\begin{aligned}
Z &= \frac{z}{L_z}, \\
X &= \frac{x}{L_x}, \\
R_\ell &= \frac{r_\ell}{r_{h\ell}}, \\
\tau &= \frac{\kappa_{r1} t}{r_{h1}^2}, \\
\Theta_{f\ell} &= \frac{T_{f\ell}}{T^*}, \\
\Theta_{b\ell} &= \frac{T_{b\ell}}{T^*}, \\
\Theta_{f\ell} &= \frac{T_{f\ell}}{T^*}, \\
\varepsilon_\ell &= \frac{\kappa_{r\ell} r_{h1}^2}{\kappa_{r1} r_{h\ell}^2}, \\
\text{Bi}_\ell &= \frac{r_{t\ell} U_\ell}{\lambda_{r\ell}}, \\
\chi_\ell &= \frac{L_\ell \kappa_{r\ell}}{r_h^2 \nu_\ell}, \\
\alpha_\ell &= \frac{2\pi L_\ell r_{t\ell} U_\ell}{\rho_f c_f Q_\ell}, \\
\gamma_1 &= \frac{A_0 H}{T^*}, \\
\Theta_{r1}^0 &= \Theta_{f1}^0 = \gamma_1 (Z - 1) + 1, \\
T^* &= A_0 H + B_0, \\
L_z &= L_1, \\
L_x &= L_2,
\end{aligned} \tag{14}$$

where $\Theta_{f\ell}$, $\Theta_{b\ell}$, and $\Theta_{r\ell}$ ($\ell = 1$ for injection, $\ell = 2$ for horizontal, and $\ell = 3$ for production) denote dimensionless temperature in the fluid, at the wall and in the formation, respectively.

By using the above variables, the simplified formulation for the three subproblems of the original model is listed as follows.

(a) Injection Well. The governing and heat balance equations for the injection well are

$$\begin{aligned}
\frac{\partial \Theta_{r1}}{\partial \tau} &= \frac{1}{R_1} \frac{\partial}{\partial R_1} \left[R_1 \frac{\partial \Theta_{r1}}{\partial R_1} \right], \\
\text{Bi}_1 \left(\Theta_{b1} - \Theta_{f1}\right) &= \frac{\partial \Theta_{r1}}{\partial R_1} \qquad \text{at } R_1 = 1, \\
\chi_1 \frac{\partial \Theta_{f1}}{\partial \tau} + \frac{\partial \Theta_{f1}}{\partial Z} &= \alpha_1 \left(\Theta_{b1} - \Theta_{f1}\right),
\end{aligned} \tag{15}$$

with the initial and boundary conditions

$$\begin{aligned}
\Theta_{r1} = \Theta_{f1} &= \gamma_1 (Z - 1) + 1, \quad \text{on } \tau = 0, \\
\Theta_{f1} &= \Theta_{\text{in}}, \quad \text{at } (1, 0) \text{ in LCCS.}
\end{aligned} \tag{16}$$

(b) Horizontal Well. The governing and heat balance equations for the horizontal well are

$$\begin{aligned}
\frac{\partial \Theta_{r2}}{\partial \tau} &= \frac{\varepsilon_2}{R_2} \frac{\partial}{\partial R_2} \left[R_2 \frac{\partial \Theta_{r2}}{\partial R_2} \right], \\
\text{Bi}_2 \left(\Theta_{b2} - \Theta_{f2}\right) &= \frac{\partial \Theta_{r2}}{\partial R_2} \qquad \text{at } R_2 = 1, \\
\chi_2 \frac{\partial \Theta_{f2}}{\partial \tau} + \frac{\partial \Theta_{f2}}{\partial X} &= \alpha_2 \left(\Theta_{b2} - \Theta_{f2}\right),
\end{aligned} \tag{17}$$

with the initial and boundary conditions becoming

$$\Theta_{f2} = \Theta_{f1}, \quad \text{at } (1,0) \text{ in LCCS},$$
$$\Theta_{r2} = \Theta_{f2} = 1, \quad \text{on } \tau = 0. \tag{18}$$

(c) Production Well. The governing and heat balance equations for the production well are

$$\frac{\partial \Theta_{r3}}{\partial \tau} = \frac{\varepsilon_3}{R_3}\frac{\partial}{\partial R_3}\left[R_3 \frac{\partial \Theta_{r3}}{\partial R_3}\right],$$
$$\mathrm{Bi}_3\left(\Theta_{b3} - \Theta_{f3}\right) = \frac{\partial \Theta_{r3}}{\partial R_3} \quad \text{at } R_3 = 1, \tag{19}$$
$$\chi_3 \frac{\partial \Theta_{f3}}{\partial \tau} + \frac{\partial \Theta_{f3}}{\partial Z} = \alpha_3\left(\Theta_{b3} - \Theta_{f3}\right),$$

with the initial and boundary conditions

$$\Theta_{r3} = \Theta_{f3} = \gamma_3 \overline{Z} + 1, \quad \text{on } \tau = 0,$$
$$\Theta_{f3} = \Theta_{f2}, \quad \text{at } (0,0) \text{ in LCCS}, \tag{20}$$

where $\overline{Z} = 1 - Z$ denotes the distance of the point from the bottom of production well, $\gamma_3 = -\gamma_1$. The subproblem for production well is similar to that for injection well as it can be regarded as a model with the origin of the CS at the bottom of production well and with a negative geothermal gradient $\gamma_3 = -\gamma_1$.

4. Solution Method

By using the Laplace transformation, the analytical solutions for the three stages are obtained. In the following equations, the symbol $\wedge$ denotes the variables which are Laplace transformed and s is a complex number as the Laplace symbol. For example, $\hat{f}(s)$ denotes the Laplace transform of the function $f(t)$.

4.1. Injection Well. From the Laplace transform of the governing equation, that is, the first of (15), for the heat diffusion in the rock around the injection well, we obtain the rock temperature

$$\widehat{\Theta}_{r1} = F_1(Z,s) K_0\left(\sqrt{s}R_1\right) + F_2(Z,s) I_0\left(\sqrt{s}R_1\right) + \frac{\gamma_1(Z-1)+1}{s}, \tag{21}$$

where $\widehat{\Theta}_{r1}$ is the Laplace transform of the dimensionless temperature Θ_{r1}; I_n and K_n are the modified Bessel functions of the first and second kind of order n, respectively; and $F_1(s)$ and $F_2(s)$ are unknowns to be determined by the boundary conditions. As Θ_{r1} is finite when $R_1 \to +\infty$, it is easy to know that $F_2(Z) = 0$. Therefore, the temperature at the wellbore wall is obtained

$$\widehat{\Theta}_{b1} = \widehat{\Theta}_{r1}\big|_{R_1=1} = F_1(Z,s) K_0\left(\sqrt{s}\right) + \frac{\gamma(Z-1)+1}{s}. \tag{22}$$

By substituting (21) and (22) into the second of (15) we have

$$\widehat{\Theta}_{f1} = F_1(Z,s)\Delta + \frac{\gamma(Z-1)+1}{s},$$
$$\Delta = \frac{\sqrt{s}K_1\left(\sqrt{s}\right)}{\mathrm{Bi}_1} + K_0\left(\sqrt{s}\right), \tag{23}$$

which, after being used in the third of (15), produces an ordinary differential equation with respect to the unknown $F_1(Z,s)$; that is,

$$\frac{\mathrm{d}F_1}{\mathrm{d}z} + \frac{\beta_1}{\Delta_1}F_1 + \frac{\gamma_1}{s\Delta_1} = 0,$$
$$\text{where } \beta_1 = \chi_1 s\Delta_1 + \alpha_1\left(\Delta_1 - K_0\left(\sqrt{s}\right)\right). \tag{24}$$

The solution of the above equation is found to be

$$F_1(Z,s) = -\frac{\gamma_1}{s\beta} + e^{-\beta Z/\Delta}C_1(s), \tag{25}$$

where the unknown function $C_1(s)$ can be determined by using (23), (25), and the injection boundary condition (16)

$$C_1 = \frac{\widehat{\Theta}_{\mathrm{in}}s\beta + \beta\gamma_1 - \beta + \Delta\gamma_1}{s\beta\Delta} = \frac{\widehat{\Theta}_{\mathrm{in}}s + \gamma_1 - 1}{s\Delta} + \frac{\gamma_1}{s\beta}. \tag{26}$$

Therefore, the solutions for the temperatures of the rock, $\widehat{\Theta}_{r1}$, and fluid, $\widehat{\Theta}_{f1}$, are obtained and rewritten as

$$\widehat{\Theta}_{r1} = \left[\frac{\widehat{\Theta}_{\mathrm{in}}s + \gamma_1 - 1}{s}A_1 + \frac{\gamma_1}{s}A_2\right]e^{-Z/A_3} - \frac{\gamma_1}{s}A_2 + \frac{\gamma_1(Z-1)+1}{s},$$
$$\widehat{\Theta}_{f1} = \left[\frac{\widehat{\Theta}_{\mathrm{in}}s + \gamma_1 - 1}{s} + \frac{\gamma_1}{s}A_3\right]e^{-Z/A_3} - \frac{\gamma_1}{s}A_3 + \frac{\gamma_1(Z-1)+1}{s}, \tag{27}$$

where the functions A_1, A_2, and A_3 are defined as

$$A_1 = \frac{\mathrm{Bi}_1 K_0\left(\sqrt{s}R_1\right)/K_1\left(\sqrt{s}\right)}{\sqrt{s} + \mathrm{Bi}_1 K_0\left(\sqrt{s}\right)/K_1\left(\sqrt{s}\right)},$$
$$A_2 = \frac{\mathrm{Bi}_1 K_0\left(\sqrt{s}R_1\right)/K_1\left(\sqrt{s}\right)}{\chi_1 s\left[\sqrt{s} + \mathrm{Bi}_1 K_0\left(\sqrt{s}\right)/K_1\left(\sqrt{s}\right)\right] + \alpha_1\sqrt{s}}, \tag{28}$$
$$A_3 = \frac{\sqrt{s} + \mathrm{Bi}_1 K_0\left(\sqrt{s}\right)/K_1\left(\sqrt{s}\right)}{\chi_1 s\left[\sqrt{s} + \mathrm{Bi}_1 K_0\left(\sqrt{s}\right)/K_1\left(\sqrt{s}\right)\right] + \alpha_1\sqrt{s}},$$

where $\widehat{\Theta}_{\mathrm{in}}$ is the Laplace transform of the injection temperature.

The Laplace transformation of the bottomhole temperature (BHT) of the injection well is

$$\begin{aligned}\mathrm{BHT}_1 &= G(s)\\ &= \left[\frac{\widehat{\Theta}_{\mathrm{in}}s+\gamma_1-1}{s}+\frac{\gamma_1}{s}A_3\right]e^{-1/A_3}-\frac{\gamma_1}{s}A_3\\ &\quad+\frac{1}{s},\end{aligned} \tag{29}$$

which will be used as the input condition for the horizontal well.

4.2. Horizontal Well. Initially, the temperature along horizontal well is identical due to the same depth. Based on the above calculations, the thermal front only penetrates less than 50 meters into the rock within 30 years. In the region between the upper and lower thermal front, the largest temperature is less than 4°C. Therefore, it is reasonable to assume a constant temperature in the rock formation around the horizontal well.

In a similar way, the solutions for the horizontal well are obtained

$$\begin{aligned}\widehat{\Theta}_{r2} &= \frac{sG(s)-1}{s}e^{-X/B_3}B_1+\frac{1}{s},\\ \widehat{\Theta}_{f2} &= \frac{sG(s)-1}{s}e^{-X/B_3}+\frac{1}{s},\end{aligned} \tag{30}$$

where the functions B_1 and B_3 are defined as

$$\begin{aligned}B_1 &= \frac{\mathrm{Bi}_2K_0\left(\sqrt{s/\varepsilon_2}R_2\right)/K_1\left(\sqrt{s/\varepsilon_2}\right)}{\mathrm{Bi}_2K_0\left(\sqrt{s/\varepsilon_2}\right)/K_1\left(\sqrt{s/\varepsilon_2}\right)+\sqrt{s/\varepsilon_2}},\\ B_3 &= \frac{\sqrt{s/\varepsilon_2}+\mathrm{Bi}_2K_0\left(\sqrt{s/\varepsilon_2}\right)/K_1\left(\sqrt{s/\varepsilon_2}\right)}{\chi_2 s\left[\sqrt{s/\varepsilon_2}+\mathrm{Bi}_2K_0\left(\sqrt{s/\varepsilon_2}\right)/K_1\left(\sqrt{s/\varepsilon_2}\right)\right]+\alpha_2\sqrt{s/\varepsilon_2}}.\end{aligned} \tag{31}$$

The Laplace transformation of the temperature at the end of the horizontal well, also BHT of the production well, is obtained by using $X = 1$; that is,

$$\mathrm{BHT}_2 = H(s) = \frac{sG(s)-1}{s}e^{-1/B_3}+\frac{1}{s}, \tag{32}$$

which will be used as the input condition for the production well.

4.3. Production Well. The temperatures for the fluid in the production well and neighboring rock formation can be obtained in the same way as those for injection and horizontal well and the calculation details are omitted here

$$\begin{aligned}\widehat{\Theta}_{r3} &= \left[\frac{H(s)s-1}{s}C_1+\frac{\gamma_3}{s}C_2\right]e^{-\overline{Z}/C_3}-\frac{\gamma_3}{s}C_2\\ &\quad+\frac{\gamma_3\overline{Z}+1}{s},\\ \widehat{\Theta}_{f3} &= \left[\frac{H(s)s-1}{s}+\frac{\gamma_3}{s}C_3\right]e^{-\overline{Z}/C_3}-\frac{\gamma_3}{s}C_3\\ &\quad+\frac{\gamma_3\overline{Z}+1}{s},\end{aligned} \tag{33}$$

where the functions C_1, C_2, and C_3 are defined as

$$\begin{aligned}C_1 &= \frac{\mathrm{Bi}_3K_0\left(\sqrt{s/\varepsilon_3}R_1\right)/K_1\left(\sqrt{s/\varepsilon_3}\right)}{\mathrm{Bi}_3K_0\left(\sqrt{s/\varepsilon_3}\right)/K_1\left(\sqrt{s/\varepsilon_3}\right)+\sqrt{s/\varepsilon_3}},\\ C_2 &= \frac{\mathrm{Bi}_3K_0\left(\sqrt{s/\varepsilon_3}R_1\right)/K_1\left(\sqrt{s/\varepsilon_3}\right)}{\chi_3 s\left[\mathrm{Bi}_3K_0\left(\sqrt{s/\varepsilon_3}\right)/K_1\left(\sqrt{s/\varepsilon_3}\right)+\sqrt{s/\varepsilon_3}\right]+\alpha_3\sqrt{s/\varepsilon_3}},\\ C_3 &= \frac{\sqrt{s/\varepsilon_3}+\mathrm{Bi}_3K_0\left(\sqrt{s/\varepsilon_3}\right)/K_1\left(\sqrt{s/\varepsilon_3}\right)}{\chi_3 s\left[\sqrt{s/\varepsilon_3}+\mathrm{Bi}_3K_0\left(\sqrt{s/\varepsilon_3}\right)/K_1\left(\sqrt{s/\varepsilon_3}\right)\right]+\alpha_3\sqrt{s/\varepsilon_3}}.\end{aligned} \tag{34}$$

The Laplace transformation of the temperature at the end of the horizontal well, also BHT of the production well, is obtained by using $X = 1$; that is,

$$\mathrm{BHT}_2 = H(s) = \frac{sG(s)-1}{s}e^{-1/B_3}+\frac{1}{s}, \tag{35}$$

which will be used as the input condition for the production well.

5. Validation and Numerical Results

5.1. Method Validation. In the present model, in order to obtain analytical solutions for temperature prediction in a closed-loop geothermal reservoir, the wellbore for fluid flow and heat transfer is divided into three parts with the output of one well part as the input conditions of the next well part. In order to show that these assumptions are reasonable and to show the error resulting from decoupling of the whole process, the results from the present model are compared with those from numerical simulator TOUGH 2. An automatic Laplace inversion technique developed by D'Amore et al. [53] based on Fourier series is used in the present model to obtain the values in the time space.

Figure 2 shows spatial discretization of the rock formation for the numerical calculation by using TOUGH2. As the temperature of the fluid in the radial direction in the pipe is assumed to be the same, it is denoted by blue node. The node for the rock is located in the middle of the each element. Figure 3 compares the temperature variations at points A,

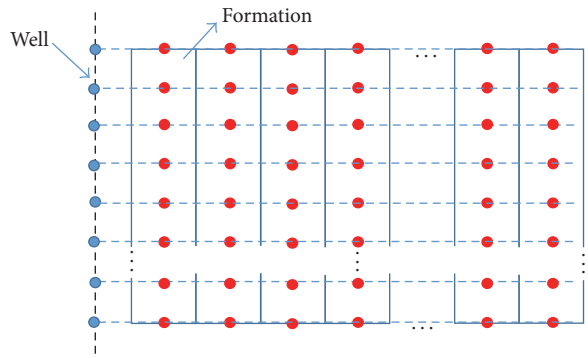

Figure 2: Grid for numerical calculation by using TOUGH2. The blue node is for the fluid and red node for the rock formation.

B, and C, which corresponds to the output points of the injection, horizontal, and production well parts, respectively, between TOUGH2 [37] and the present model. The solid curves denote results from TOUGH2 and the dashed ones are results from the present model. Figures 3(a) and 3(b) are for temperatures at short (20 days) and long (2.74 years) times of circulation, respectively, for the case $Q = 0.05\,\mathrm{m}^3/\mathrm{s}$, while Figures 3(c) and 3(d) are for small $Q = 0.01\,\mathrm{m}^3/\mathrm{s}$ and large $Q = 0.20\,\mathrm{m}^3/\mathrm{s}$, respectively. Other parameters used here are $L_1 = 2000\,\mathrm{m}$, $L_2 = 3000\,\mathrm{m}$, $B_0 = 20^\circ\mathrm{C}$, and $T_{\mathrm{in}} = 30^\circ\mathrm{C}$.

It can be seen that the temperature results at points A, B, and C predicted from both methods do not match at short time period, say 10 days, as shown in Figure 3(a) for the case when $Q = 0.05\,\mathrm{m}^3/\mathrm{s}$. The temperature difference is mainly caused by the neglect of thermal interaction at the heel of the injection and production wells (i.e., around points A and B) in the present model. However, for large time of circulation, the difference in the temperature results from both methods is very small, generally less than 4°C, as shown in Figure 3(b). The temperature differences after 365 days and 1000 days between the present model and TOUGH2 are −3.87°C and −3.65°C, respectively. In order to further show the accuracy of the present model, the temperatures at these three points in another two cases, that is, $Q = 0.01\,\mathrm{m}^3/\mathrm{s}$ and $Q = 0.20\,\mathrm{m}^3/\mathrm{s}$, are also compared with those obtained from TOUGH2 and show good agreement. This means that the present model can be used to predict approximately the output temperature of the closed-loop system without causing large errors.

5.2. Numerical Results. In this section, the case with fluid fully contacted (without any tubing, casing, and cement) with the wellbore is first investigated. Under this condition, the radius of the tubing for fluid flow, r_{ti}, is equal to the wellbore radius, r_{hi}. By doing so, two objectives are achieved. First, the important factors affecting the fluid and heat flow behaviour are identified; second, the critical location determining whether the heat is flowing into or out of the rock formation is identified for thermal isolation design, especially for production well. Water is chosen for the fluid; sandstone and shale are chosen for the rock around the vertical and horizontal wells, respectively, for the following calculations. The parameters used for the examples are listed in Table 1 unless otherwise specified.

Table 1: Physical parameters for the present calculation (the parameter values for thermal properties of shale are from Eppelbaum et al. [8] and the value of geothermal gradient is from Quick et al. [9]).

Parameter	Value
Wellbore radius, r_h (m)	0.1
Length of vertical well, H (m)	2000
Length of horizontal well (m)	3000
Geothermal gradient, A_0 (K/m)	0.047
Surface temperature, B_0 (°C)	20
Fluid density (Kg/(m^3))	900
Injection rate, Q (m^3/s)	0.05
Injection temperature (°C)	30.0
Fluid specific heat (J/(Kg·K))	4200
Fluid thermal conductivity (W/(m·K))	0.68
Fluid viscosity (Pa·s)	0.0004
Shale thermal conduct (W/(m·K))	1.42
Shale specific heat (J/(Kg·K))	2151
Shale density (Kg/(m^3))	2057

5.2.1. Temperature along the Vertical Wells. Figure 4 displays the dimensionless temperature changes, which are defined by physical temperature changes with respect to the initial state divided by $(A_0H + B_0)$, along the injection and production wells, respectively. The red curves refer to the initial state. For the injection well, we can see from Figure 4(a) that (1) before the cold fluid reaches the bottom of the wellbore, the temperature change of the fluid on the upper part of the wellbore decreases linearly with depth, while that on the lower part of the wellbore is almost a constant; (2) the temperature along the injection well decreases very quickly, with a temperature of 46.3°C at the bottom after 3 hours of circulation; and (3) as the injection temperature is lower than the initial ground temperature for most of the well length, most of the fluid flowing downwards absorbs heat from the surrounding rock except a small portion of fluid on the upper part of the wellbore.

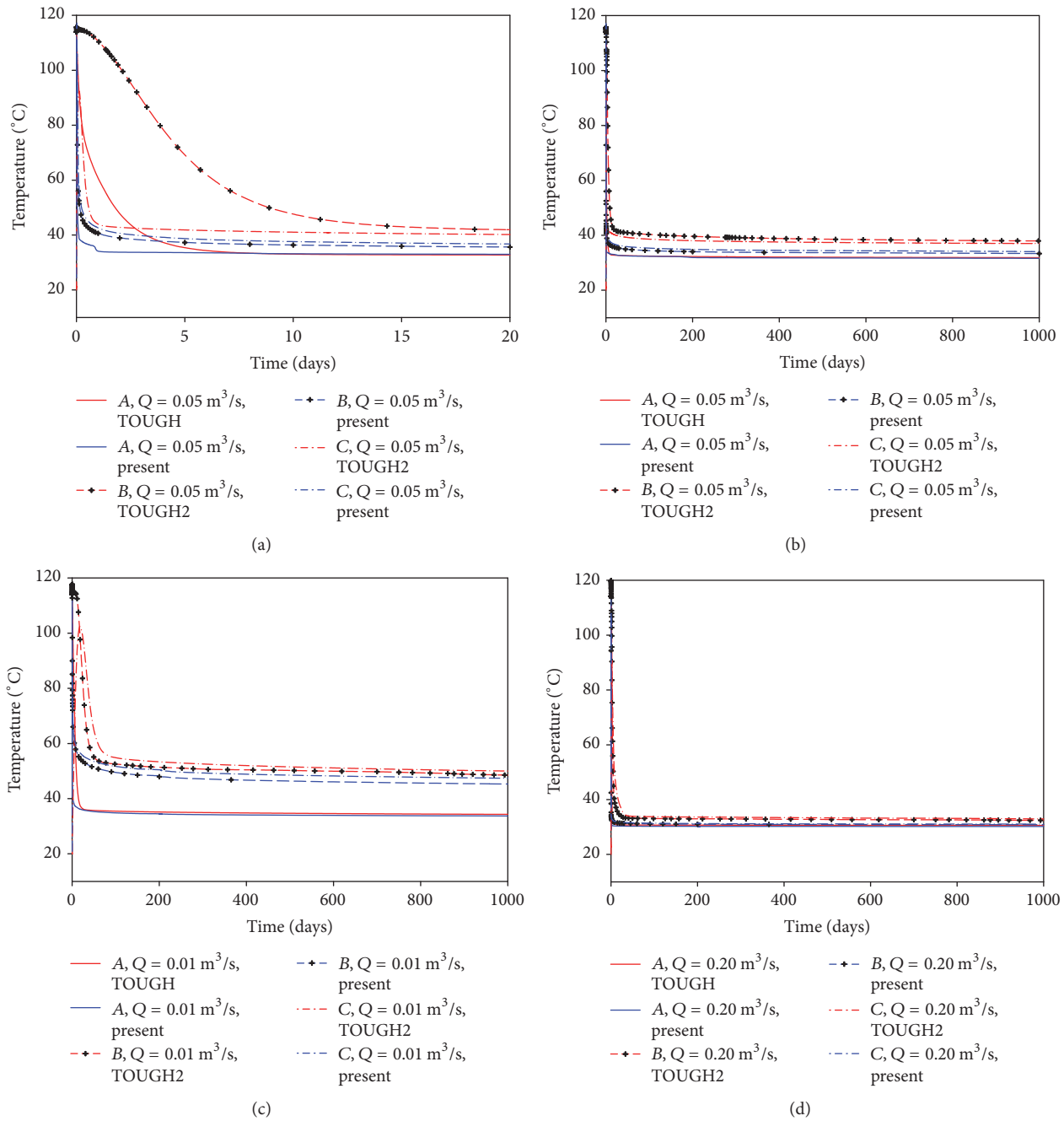

Figure 3: Comparison of the temperatures at points A, B, and C. (a) For small time and (b) for large time when $Q = 0.05\,\mathrm{m}^3/\mathrm{s}$; (c) for small $Q = 0.01\,\mathrm{m}^3/\mathrm{s}$ and (d) for large $Q = 0.2\,\mathrm{m}^3/\mathrm{s}$.

Before the cold fluid reaches the production well, the temperature along the whole production well increases because of hot fluid flowing upwards, as shown by solid and dashed curves in Figure 4(b). The production temperature increases from 57°C to 152°C when the time varies from 10 mins to 1.0 hours and then decreases to 126°C after 3 hours. The small difference in temperature change between times $t = 10$ days and $t = 30$ years means that the heat transfer in the fluid approaches pseudo-steady state after 10 days. Moreover, the critical position which indicates if the fluid absorbs heat from or releases heat to the rock formation is around $Z_c = 0.2$ or $z_c = 700$ m.

5.2.2. Effect of Flow Rates on Output Performance. Figure 5 presents the output temperature for different injection rates ranging from $Q = 0.01\,\mathrm{m}^3/\mathrm{s}$ to $0.14\,\mathrm{m}^3/\mathrm{s}$. It can be seen that the injection rate plays a major influence on the output temperature. First, for each injection rate, the output temperature increases quickly to a maximum value, as shown

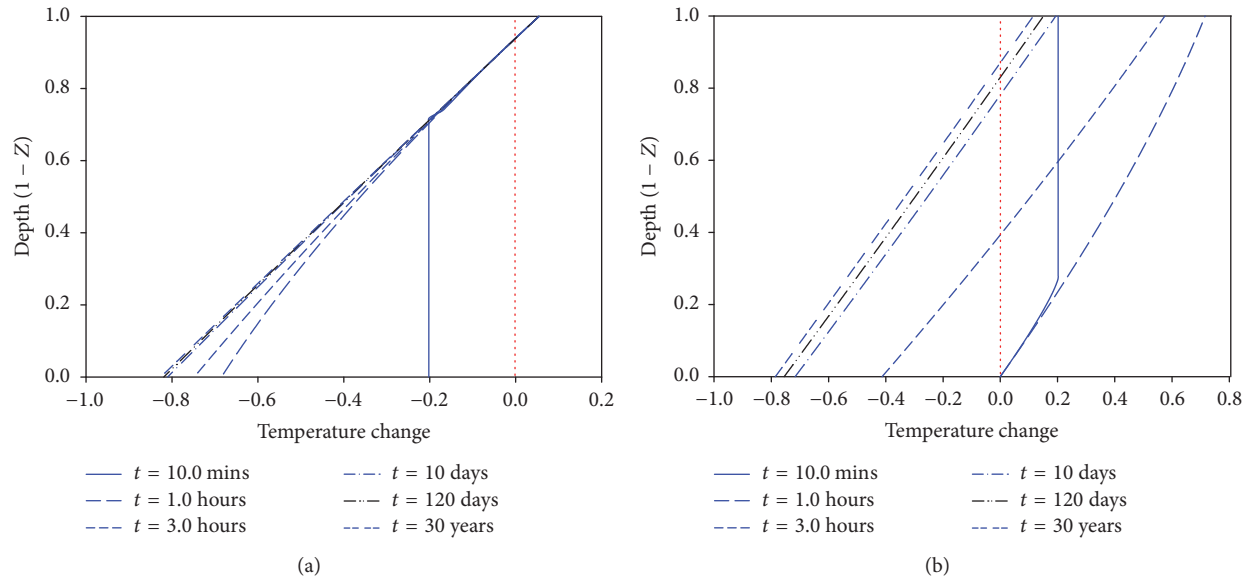

Figure 4: Temperature change profiles along the (a) injection and (b) production wells when $Q = 0.05\ m^3/s$, $L_1 = 3500$ m, and $L_2 = 6000$ m.

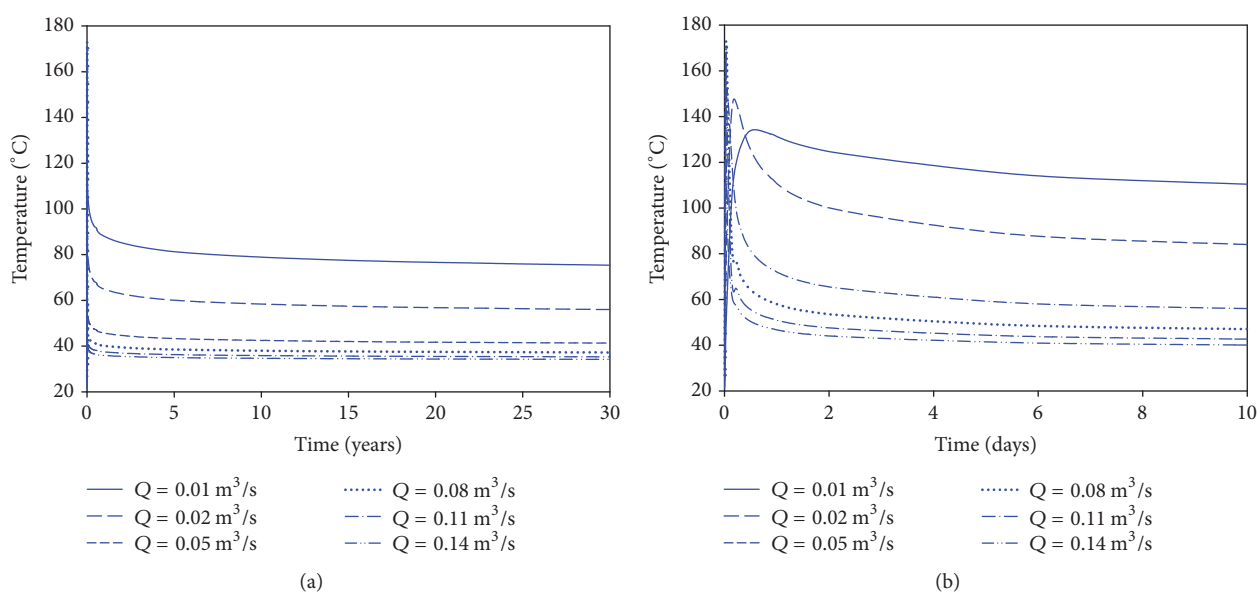

Figure 5: Variation with time of output temperature of the production well under different injection rates when $L_1 = 3500$ m and $L_2 = 6000$ m: (a) for general view and (b) for local view.

in Figure 5(b), and then decreases steadily to a constant value, as shown in Figure 5(a). Second, with increasing the injection rate, the production temperature is decreased. This is due to shortened time as a result of larger fluid speed for heat exchange between fluid and the surrounding rock. In addition, the temperature difference after 30 years between the cases $Q = 0.01\ m^3/s$ and $Q = 0.14\ m^3/s$ is around 40°C. However, when the injection rate is increased to some value ($0.05\ m^3/s$ for the present case), there is no large difference in the final production temperature, as shown in Figure 5(a).

The thermal power and total heat extracted for the above cases are plotted in Figure 6. According to the definition of thermal power in (12), thermal power is linearly proportional to the injection rate and temperature. However, as lower production temperature is obtained when the injection rate is increased, the curves for thermal power shown in Figure 6(b) do not exhibit similar trends to the production temperature in Figure 5(b). It has to be mentioned that the long-time thermal power ranges from 1.71 MWs to 2.21 MWs when Q is changed from $0.01\ m^3/s$ to $0.14\ m^3/s$.

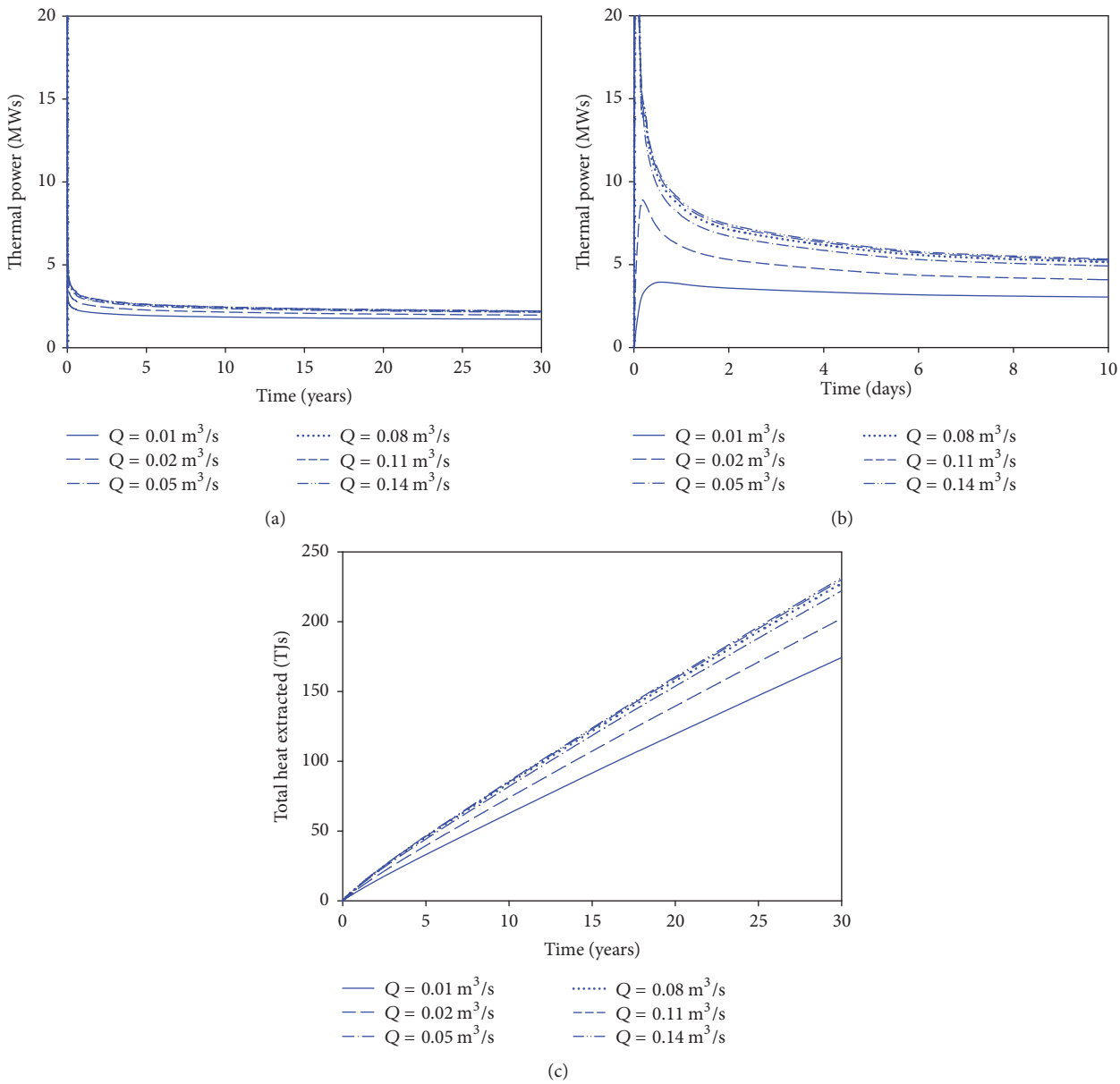

Figure 6: Thermal power and total heat extracted for different injection rates: thermal power (a) for large time and (b) for short time and (c) total heat extracted.

Figure 6(c) displays the total heat extracted from the reservoir up to 30 years under different injection rates. The total heat extracted is expected to increase when the injection rate is increased. However, the total heat extracted after 30 years when $Q = 0.14\,\mathrm{m}^3/\mathrm{s}$ is only 32.75% larger than that when $Q = 0.01\,\mathrm{m}^3/\mathrm{s}$. This means that the cost related to higher pressure required for larger flow rates has to be balanced with the total energy extracted.

5.2.3. Effect of Injection Temperatures on Output Performance. The effect of injection temperatures on output performance is displayed in Figures 7 and 8. As for output temperature, it increases evenly with increasing the injection temperature, as shown in Figure 7(a), and the maximum value of output temperature is not sensitive to the injection temperature, as shown in Figure 7(b).

Figure 8 presents the thermal power and total heat extracted up to 30 years. As the thermal power is linearly proportional to the temperature and the injection rate is kept constant, the thermal power exhibits a similar trend to the output temperature, as shown in Figures 8 and 7. In addition, it is interesting to find that although higher output temperature is obtained under larger injection temperature, the total heat extracted from the reservoir is reduced, as shown in Figure 8(c).

5.2.4. Effect of Fluid Viscosity on Output Performance. Figures 9 and 10 display the final output performance for different

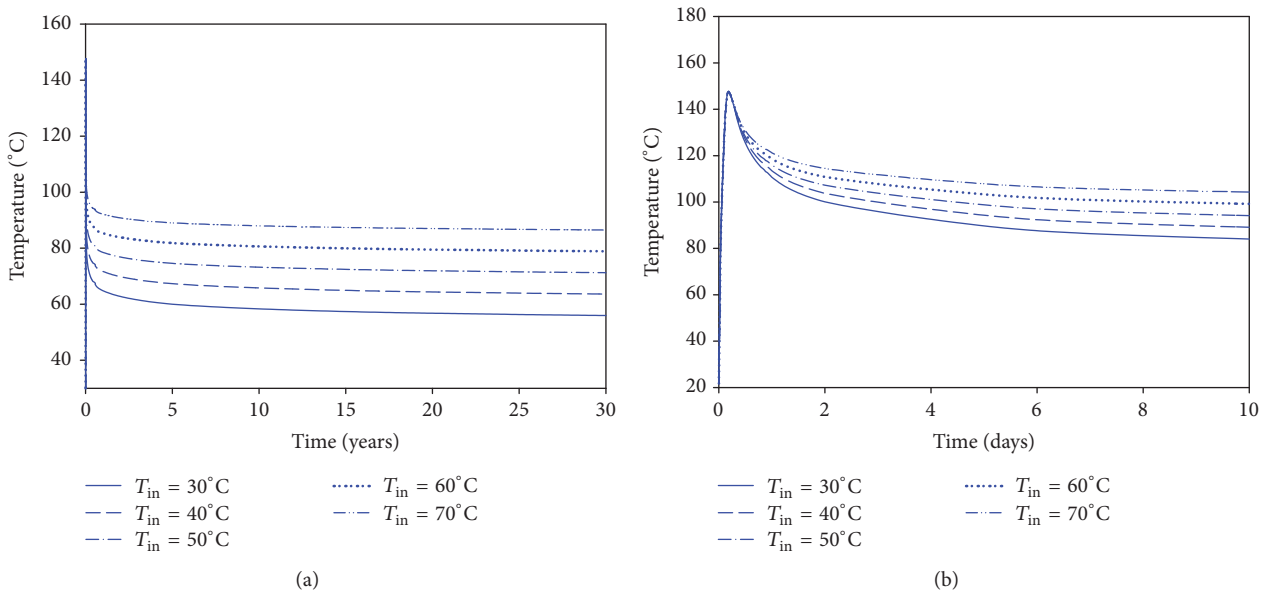

Figure 7: Variation with time of output temperature of the production well under different injection temperatures: (a) for large time period and (b) for short time period.

fluid viscosities. The water viscosity ranges from about 2.8 $\times 10^{-4}$ Pa·s to 1.3 $\times 10^{-3}$ Pa·s when the temperature changes from 100°C to 10°C, which can be found in the website link (https://en.wikipedia.org/wiki/viscosity). Here $\mu = 10^{-4}$, 5 $\times 10^{-4}$, 2.5 $\times 10^{-3}$, and 1.2 $\times 10^{-2}$ Pa·s are chosen to show the effect of the viscosity on the output temperature. From Figure 9 the output temperature follows almost the same curve under these four cases and the decreasing trend for rapid temperature drop in less than 5 hrs is insensitive to the fluid viscosity.

5.2.5. Effect of Geothermal Gradient on the Output Performance. The output temperatures under different gradient geothermal gradients, A_0, are displayed in Figure 11 when other parameters are kept the same. It can be found that (1) as the depth of the vertical well is the same, larger geothermal gradient produces larger maximum output temperature (MOT), which is increased by around 42.2°C if A_0 has an increase of 1.5°C. For example, the MOTs for the cases with A_0 = 0.020, 0.035, 0.050, 0.065, 0.080, and 0.095 K/m are 76.2, 118.4, 160.5, 202.7, 244.9, and 287.0°C, respectively. However, the output temperature after a long time (say 30 years) is found to be increased by around 4°C when A_0 has an increase of 1.5°C, as shown in Figure 11(b), where the output temperature is 34.2, 38.2, 42.1, 46.0, 49.9, and 53.8°C, respectively, for the above six cases. This means that, compared to the injection conditions, the geothermal gradient plays much less important role in the output performance.

5.2.6. Fully Insulated Case. Figure 12 compares the production temperatures under fully contacted and fully insulated conditions. The parameters used for the fully insulated case are the same as those in Figure 4 except that the overall heat transfer coefficient along the production well is set to zero.

It is found from Figure 12 that there is no large difference in production temperature between these two cases and the production temperature predicted from fully insulated case is a little smaller than that predicted from fully contacted case. From the curves for t = 10 days and t = 30 years in Figure 4(b) without any casing and cementing, it can be found that (1) the final output temperature decreases very quickly and approaches some pseudo-steady value which is dominated by the inject conditions and (2) the fluid along a larger part (around 80 percent) of wellbore length absorbs heat from the surrounding rock formation and the fluid along the rest of the wellbore releases heat into the formation. Compared with this openhole case, if an insulated layer is put along the whole wellbore, the final output temperature will become smaller although the heat loss into the formation, which occurs along a small part of wellbore length in the openhole case, is prevented in the insulated case, as confirmed in Figure 12.

6. Conclusion

This paper deals with the heat extraction from a closed-loop geothermal system. Through reasonable assumptions and the temperature continuity conditions at the intersection, the whole well is divided into three portions, two vertical wellbores and one horizontal wellbore, which can be solved independently based on the input conditions. Conclusions

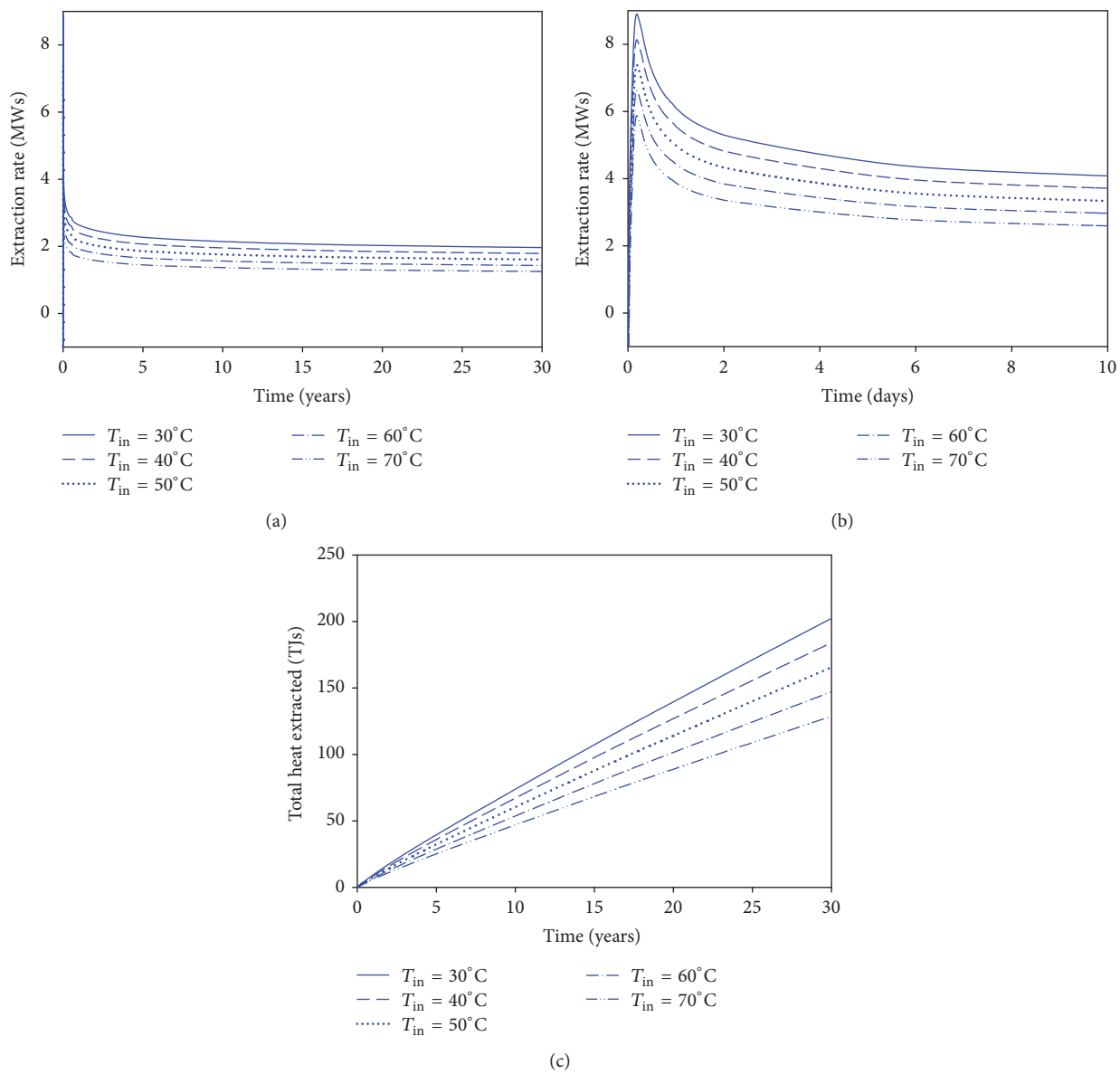

Figure 8: Thermal power and total heat extracted for different injection temperatures: thermal power (a) for large time and (b) for short time and (c) total heat extracted.

that can be made based on our numerical results are as follows:

(1) The difference in the output temperature predicted from the proposed model and TOUGH2 is very small, less than 4°C in the present numerical study, and thus can be used to approximately predict the heat extraction from the closed-loop geothermal system.

(2) The injection rate plays the dominant role in affecting the output performance; although it can increase the thermal power, the reduced temperature as a result of high flow rate compromises its production performance.

(3) Higher injection temperature produces larger output temperature but decreases the total heat extracted given a specific time.

(4) The output performance of geothermal reservoir is insensitive to fluid viscosity.

(5) There exists a critical point that indicates if the fluid above and below this point releases heat into or absorbs heat from surrounding formation.

(6) This approximation model proposed in this work runs in terms of seconds on a personal notebook computer and thus provides an efficient tool for reservoir optimization.

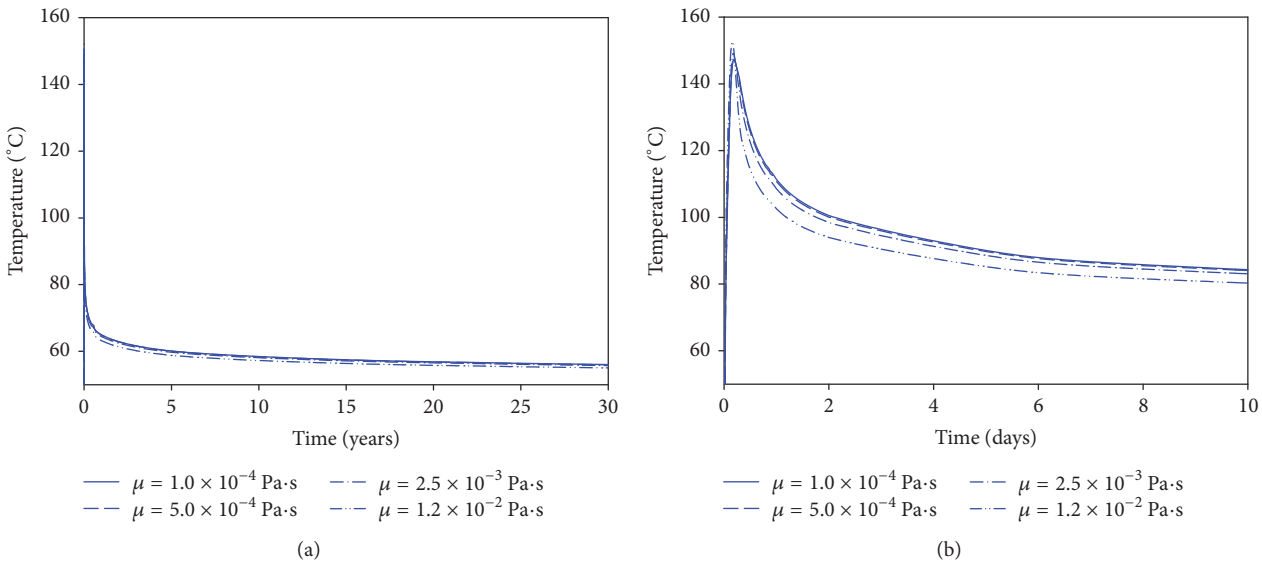

Figure 9: Variation with time of output temperature of the production well under different viscosities μ: (a) for large time period and (b) for short time period.

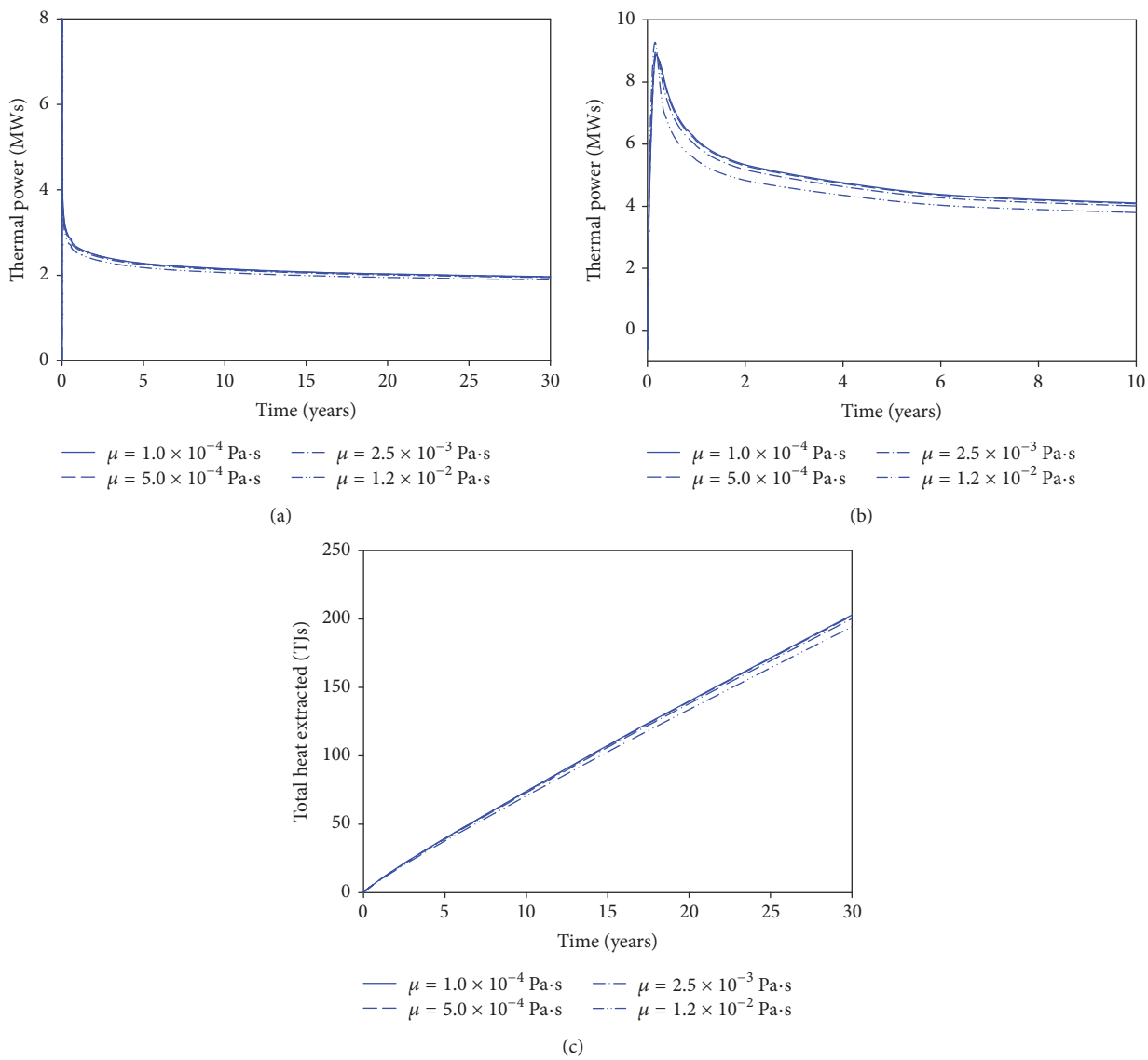

Figure 10: Thermal power and total heat extracted for different fluid viscosities: thermal power (a) for large time and (b) for short time and (c) total heat extracted.

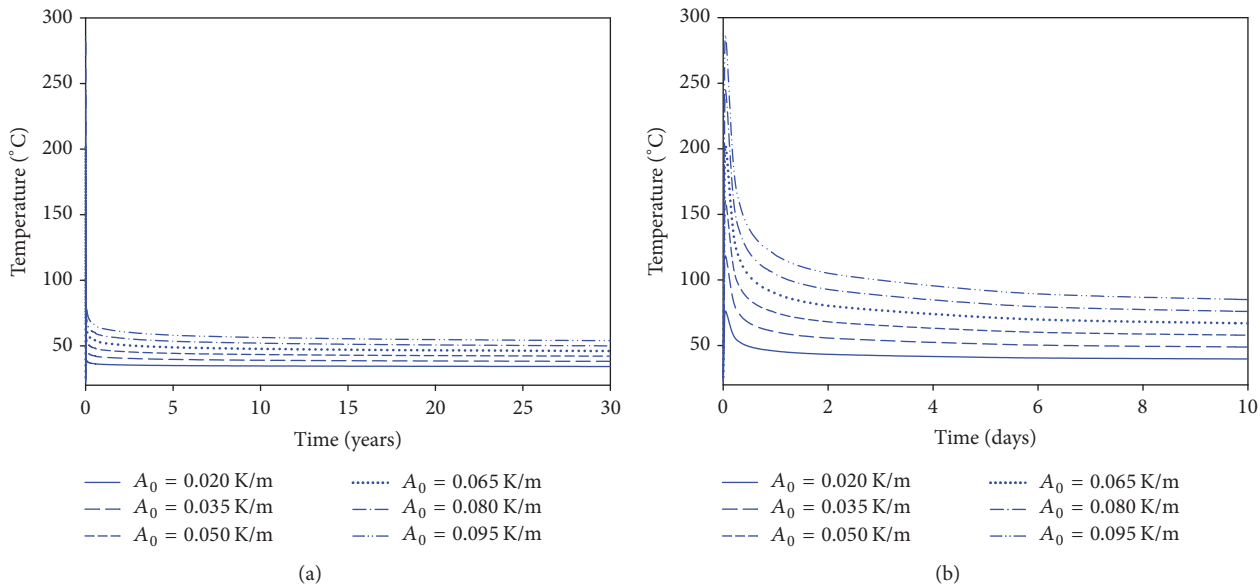

Figure 11: Variation with time of output temperature of the production well under different geothermal gradient A_0: (a) for large time period and (b) for short time period.

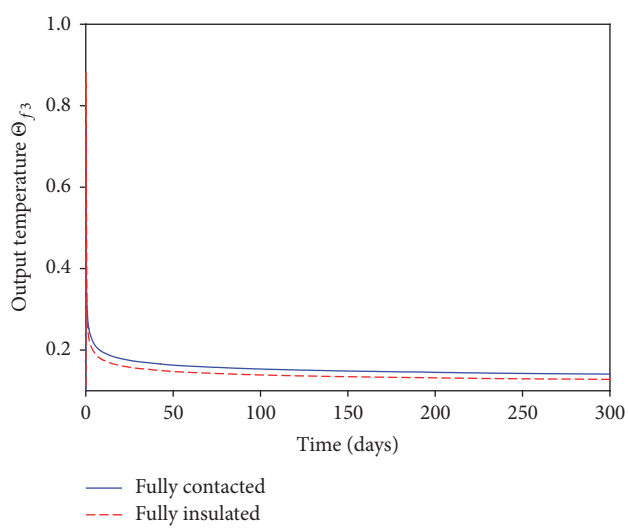

Figure 12: Production temperature under fully contacted and fully insulated conditions along the production well when $Q = 0.05\,\mathrm{m}^3/\mathrm{s}$, $L_1 = 3500\,\mathrm{m}$, and $L_2 = 6000\,\mathrm{m}$.

Conflicts of Interest

The authors declare that there are no conflicts of interest regarding the publication of this paper.

Acknowledgments

The authors thank CSIRO for permission to publish the research outcomes. This work was supported by the Scientific Research Foundation of International Cooperation and Exchanges of Sichuan Province (Grant no. 2017HH0061), the National Natural Science Foundation of China (Grant no. 51604230), the China Postdoctoral Science Foundation (Grant nos. 2016M600626 and 2017T100592), and the Fund of the State Key Laboratory of Oil and Gas Reservoir Geology and Exploitation of Southwest Petroleum University (Grant nos. G201604 and PLN201611).

References

[1] J. W. Lund and T. L. Boyd, "Direct utilization of geothermal energy 2015 worldwide review," *Geothermics*, vol. 60, pp. 66–93, 2016.

[2] A. Bahadori, S. Zendehboudi, and G. Zahedi, "RETRACTED: A review of geothermal energy resources in Australia: Current status and prospects," *Renewable and Sustainable Energy Reviews*, vol. 21, pp. 29–34, 2013.

[3] J. M. Sharp Jr., "Energy and momentum transport model of the Ouachita Basin and its possible impact on formation of economic mineral deposits," *Economic Geology*, vol. 73, no. 6, pp. 1057–1068, 1978.

[4] J. Hecht-Méndez, M. De Paly, M. Beck, and P. Bayer, "Optimization of energy extraction for vertical closed-loop geothermal systems considering groundwater flow," *Energy Conversion and Management*, vol. 66, pp. 1–10, 2013.

[5] A. Casasso and R. Sethi, "Efficiency of closed loop geothermal heat pumps: A sensitivity analysis," *Renewable Energy*, vol. 62, pp. 737–746, 2014.

[6] B. Wu, X. Zhang, A. P. Bunger, and R. G. Jeffrey, "An efficient and accurate approach for studying the heat extraction from multiple recharge and discharge wells," in *Effective and Sustainable Hydraulic Fracturing*, A. Bunger, J. McLennan, and R. Jeffrey, Eds., p. 16, InTech, 2013.

[7] B. Wu, G. Zhang, X. Zhang, R. G. Jeffrey, J. Kear, and T. Zhao, "Semi-analytical model for a geothermal system considering the effect of areal flow between dipole wells on heat extraction," *Energy*, vol. 138, pp. 290–305, 2017.

[8] L. Eppelbaum, I. Kutasov, and A. Pilchin, *Applied Geothermics*, Lecture Notes in Earth System Sciences, Springer-Verlag, Berlin, Germany, 2014.

[9] H. Quick, J. Michael, U. Arslan, and H. Huber, "Geothermal application in low-enthalpy regions," *Renewable Energy*, vol. 49, pp. 133–136, 2013.

[10] B. Wu, X. Zhang, R. G. Jeffrey, and B. Wu, "A semi-analytic solution of a wellbore in a non-isothermal low-permeability porous medium under non-hydrostatic stresses," *International Journal of Solids and Structures*, vol. 49, no. 13, pp. 1472–1484, 2012.

[11] T. Ma, Q. Zhang, P. Chen, C. Yang, and J. Zhao, "Fracture pressure model for inclined wells in layered formations with anisotropic rock strengths," *Journal of Petroleum Science and Engineering*, vol. 149, pp. 393–408, 2017.

[12] T. Ma, B. Wu, J. Fu, Q. Zhang, and P. Chen, "Fracture pressure prediction for layered formations with anisotropic rock strengths," *Journal of Natural Gas Science and Engineering*, vol. 38, pp. 485–503, 2017.

[13] E. C. Bullard, "The time necessary for a bore hole to attain temperature equilibrium," *Geophysical Journal International*, vol. 5, pp. 127–130, 1947.

[14] J. T. Moss and P. D. White, "How to calculate temperature profiles in a water injection well," *The Oil and Gas Journal*, vol. 57, pp. 174–177, 1959.

[15] H. S. Carslaw and J. C. Jaeger, *Conduction of Heat in Solids*, The Clarendon Press, Oxford, UK, 1st edition, 1946.

[16] P. Eskilson, *Thermal analysis of heat extraction boreholes [Ph.D. thesis]*, University of Lund, Lund, Sweden, 1987.

[17] H. Y. Zeng, N. R. Diao, and Z. H. Fang, "A finite line-source model for boreholes in geothermal heat exchangers," *Heat Transfer—Asian Research*, vol. 31, no. 7, pp. 558–567, 2002.

[18] M. G. Sutton, D. W. Nutter, and R. J. Couvillion, "A ground resistance for vertical bore heat exchangers with groundwater flow," *Journal of Energy Resources Technology, Transactions of the ASME*, vol. 125, no. 3, pp. 183–189, 2003.

[19] T. V. Bandos, Á. Montero, E. Fernández et al., "Finite line-source model for borehole heat exchangers: effect of vertical temperature variations," *Geothermics*, vol. 38, no. 2, pp. 263–270, 2009.

[20] A. Michopoulos and N. Kyriakis, "Predicting the fluid temperature at the exit of the vertical ground heat exchangers," *Applied Energy*, vol. 86, no. 10, pp. 2065–2070, 2009.

[21] N. Molina-Giraldo, P. Blum, K. Zhu, P. Bayer, and Z. Fang, "A moving finite line source model to simulate borehole heat exchangers with groundwater advection," *International Journal of Thermal Sciences*, vol. 50, no. 12, pp. 2506–2513, 2011.

[22] J. A. Rivera, P. Blum, and P. Bayer, "Influence of spatially variable ground heat flux on closed-loop geothermal systems: Line source model with nonhomogeneous Cauchy-type top boundary conditions," *Applied Energy*, vol. 180, pp. 572–585, 2016.

[23] G. Zhou, Y. Zhou, and D. Zhang, "Analytical solutions for two pile foundation heat exchanger models in a double-layered ground," *Energy*, vol. 112, pp. 655–668, 2016.

[24] H. Ramey, "Wellbore heat transmission," *Journal of Petroleum Technology*, vol. 14, no. 04, pp. 427–435, 2013.

[25] W. L. Dowdle and W. M. Cobb, "Static formation temperature from well logs - an empirical method," *JPT, Journal of Petroleum Technology*, vol. 27, pp. 1326–1330, 1975.

[26] M. Edwardson, H. Girner, H. Parkison, C. Williams, and C. Matthews, "Calculation of formation temperature disturbances caused by mud circulation," *Journal of Petroleum Technology*, vol. 14, no. 04, pp. 416–426, 2013.

[27] A. Tragesser, P. B. Crawford, and H. R. Crawford, "A method for calculating circulating temperatures," *Journal of Petroleum Technology*, vol. 19, no. 11, pp. 1507–1512, 2013.

[28] L. Raymond, "Temperature distribution in a circulating drilling fluid," *Journal of Petroleum Technology*, vol. 21, no. 03, pp. 333–341, 2013.

[29] C. S. Holmes and S. C. Swift, "Calculation of circulating mud temperatures," *Journal of Petroleum Technology*, vol. 22, no. 6, pp. 670–674, 1970.

[30] H. Keller, E. Couch, and P. Berry, "Temperature distribution in circulating mud columns," *Society of Petroleum Engineers Journal*, vol. 13, no. 1, pp. 23–30, 2013.

[31] A. García, E. Santoyo, G. Espinosa, I. Hernández, and H. Gutiérrez, "Estimation of temperatures in geothermal wells during circulation and shut-in in the presence of lost circulation," *Transport in Porous Media*, vol. 33, no. 1-2, pp. 103–127, 1998.

[32] G. Espinosa-Paredes, A. Garcia, E. Santoyo, and I. Hernandez, "TEMLOPI/V.2: A computer program for estimation of fully transient temperatures in geothermal wells during circulation and shut-in," *Computers and Geosciences*, vol. 27, no. 3, pp. 327–344, 2001.

[33] S. Fomin, T. Hashida, V. Chugunov, and A. V. Kuznetsov, "A borehole temperature during drilling in a fractured rock formation," *International Journal of Heat and Mass Transfer*, vol. 48, no. 2, pp. 385–394, 2005.

[34] B. Izgec, C. S. Kabir, D. Zhu, and A. R. Hasan, "Transient fluid and heat flow modeling in coupled wellbore/reservoir systems," *SPE Reservoir Evaluation and Engineering*, vol. 10, no. 3, pp. 294–301, 2007.

[35] B. Wu, X. Zhang, and R. G. Jeffrey, "A model for downhole fluid and rock temperature prediction during circulation," *Geothermics*, vol. 50, pp. 202–212, 2014.

[36] K. L. Kipp, P. A. Hsieh, and S. R. Charlton, "Transport Simulator: HYDROTHERM — Version 3," U.S. Geological Survey, 2008.

[37] K. Pruess, C. Oldenburg, and G. Moridis, "TOUGH2 User's Guide Version 2," Tech. Rep. LBNL-43134, Lawrence Berkeley National Laboratory, Berkeley, Calif, USA, 1999.

[38] N. Böttcher, N. Watanabe, U. J. Görke, and O. Kolditz, *Modeling I: Geothermal Processes in Fractured Porous Media*, Springer, 2017.

[39] O. Kolditz, A. Habbar, R. Kaiser et al., *ROCKFLOW users manual release 3.5. Institute of fluid mechanics and computer applications in civil engineering*, University of Hannover, 2001.

[40] H.-J. G. Diersch, D. Bauer, W. Heidemann, W. Rühaak, and P. Schätzl, "Finite element modeling of borehole heat exchanger systems. Part 2. Numerical simulation," *Computers and Geosciences*, vol. 37, no. 8, pp. 1136–1147, 2011.

[41] H.-J. G. Diersch, *FEFLOW: Finite Element Modeling of Flow, Mass and Heat Transport in Porous and Fractured Media*, Springer, Berlin, Germany, 2014.

[42] N. Tenma, K. Yasukawa, and G. Zyvoloski, "Model study of the thermal storage system by FEHM code," *Geothermics*, vol. 32, no. 4, pp. 603–607, 2003.

[43] K. J. Bakhsh, M. Nakagawa, M. Arshad, and L. Dunnington, "Modeling thermal breakthrough in sedimentary geothermal system," in *Proceedings of the 41st Workshop on Geothermal Reservoir Engineering Stanford University*, pp. 22–24, Stanford, Calif, USA, 2016.

[44] Schlumberger, "Eclipse, reference manual 2008," Tech. Rep., Schlumberger Information Solutions, Business Development Central and Eastern Europe, Hannover, Germany, 2008.

[45] V. Hamm and B. Bazargan Sabet, "Modelling of fluid flow and heat transfer to assess the geothermal potential of a flooded coal mine in Lorraine, France," *Geothermics*, vol. 39, no. 2, pp. 177–186, 2010.

[46] Y. Ding, "Using boundary integral methods to couple a semi-analytical reservoir flow model and a wellbore flow model," in *Proceedings of the 15th Symposium on Reservoir Simulation*, pp. 195–205, February 1999.

[47] A. Ghassemi, S. Tarasovs, and A. H.-D. Cheng, "An integral equation solution for three-dimensional heat extraction from planar fracture in hot dry rock," *International Journal for Numerical and Analytical Methods in Geomechanics*, vol. 27, no. 12, pp. 989–1004, 2003.

[48] D. Kumar and M. Gutierrez, "Three-dimensional heat flow model for enhanced geothermal systems using boundary element method," in *Proceedings of the 38th Workshop on Geothermal Reservoir Engineering Stanford University*, Stanford, California, February 2013.

[49] M. W. McClure and R. N. Horne, "An investigation of stimulation mechanisms in Enhanced Geothermal Systems," *International Journal of Rock Mechanics and Mining Sciences*, vol. 72, pp. 242–260, 2014.

[50] L. M. Jiji, *Heat Conduction*, Springer, Berlin, Germany, 3rd edition, 2009.

[51] G. Willhite, "Over-all heat transfer coefficients in steam and hot water injection wells," *Journal of Petroleum Technology*, vol. 19, no. 05, pp. 607–615, 2013.

[52] V. Gnielinski, "New equations for heat and mass transfer in turbulent pipe and channel flow," in *Proceedings of the International Chemical Engineering 16*, vol. 16, pp. 359–368, 1976.

[53] L. D'Amore, G. Laccetti, and A. Murli, "An implementation of a Fourier series method for the numerical inversion of the Laplace transform," *ACM Transactions on Mathematical Software*, vol. 25, no. 3, pp. 279–305, 1999.

Hindawi
Geofluids
Volume 2017, Article ID 4278621, 17 pages
https://doi.org/10.1155/2017/4278621

Research Article

Numerical Investigation into the Impact of CO_2-Water-Rock Interactions on CO_2 Injectivity at the Shenhua CCS Demonstration Project, China

Guodong Yang,[1] Yilian Li,[1] Aleks Atrens,[2] Ying Yu,[1] and Yongsheng Wang[3]

[1] *School of Environmental Studies, China University of Geosciences, Wuhan 430074, China*
[2] *The Queensland Geothermal Energy Centre of Excellence, School of Mechanical and Mining Engineering, The University of Queensland, St Lucia, QLD 4072, Australia*
[3] *China Shenhua Coal Liquefaction Co., Ltd., Ordos 017209, China*

Correspondence should be addressed to Yilian Li; yl.li@cug.edu.cn

Received 25 February 2017; Revised 17 May 2017; Accepted 28 June 2017; Published 3 August 2017

Academic Editor: Tianfu Xu

A 100,000 t/year demonstration project for carbon dioxide (CO_2) capture and storage in the deep saline formations of the Ordos Basin, China, has been successfully completed. Field observations suggested that the injectivity increased nearly tenfold after CO_2 injection commenced without substantial pressure build-up. In order to evaluate whether this unique phenomenon could be attributed to geochemical changes, reactive transport modeling was conducted to investigate CO_2-water-rock interactions and changes in porosity and permeability induced by CO_2 injection. The results indicated that using porosity-permeability relationships that include tortuosity, grain size, and percolation porosity, other than typical Kozeny-Carman porosity-permeability relationship, it is possible to explain the considerable injectivity increase as a consequence of mineral dissolution. These models might be justified in terms of selective dissolution along flow paths and by dissolution or migration of plugging fines. In terms of geochemical changes, dolomite dissolution is the largest source of porosity increase. Formation physical properties such as temperature, pressure, and brine salinity were found to have modest effects on mineral dissolution and precipitation. Results from this study could have practical implications for a successful CO_2 injection and enhanced oil/gas/geothermal production in low-permeability formations, potentially providing a new basis for screening of storage sites and reservoirs.

1. Introduction

Geological storage of carbon dioxide (CO_2) in deep saline formations is widely considered as a significant method for reducing CO_2 emissions in the atmosphere [1, 2]. Currently, a number of CO_2 storage operations and demonstration projects (e.g., Sleipner, Norway, 1996; Weyburn, Canada, 2000; Ketzin, Germany, 2006; Cranfield, USA, 2008; Otway, Australia, 2008) have been conducted around the world [3–7]. The first pilot project of CO_2 capture and storage (CCS) in China, the Shenhua CCS demonstration project, successfully completed its goal of injecting CO_2 at a rate of 100,000 tons/year into the onshore saline aquifer in the Ordos Basin [8]. The site of the Shenhua CCS project is in the Chenjiacun village of Wulam Len town, Ejinhoro county, about 45 km southeast of the Ordos City, Inner Mongolia. The Ordos Basin covers an area of $25 \times 10^4\,km^2$, is the second largest sedimentary basin in China, and has low porosity and permeability typical of continental basins in China. Deep saline aquifers are widely distributed in the basin, with large potential for CO_2 storage [9]. The Shenhua CCS project used a single vertical well to inject CO_2 into five reservoir-caprock assemblages deeper than 1576 m: the Liujiagou, Shiqianfeng, Shihezi, Shanxi, and Majiagou formations. More than 80% of the total CO_2 injected entered the first three formations [8].

During CO_2 injection at the Shenhua CCS demonstration, a unique phenomenon was observed: the injection index increased nearly tenfold from $4.056\,m^3/h/MPa$ in 2011 to $40.018\,m^3/h/MPa$ in 2013 for the main injection layer, without strong pressure build-up [10]. This indicates that CO_2

injectivity increases after injection started, which is different from earlier predictions [8].

For large-scale injection of CO_2 into saline formations, CO_2 injectivity is a key technical and economic issue of concern. Previous studies and applications show that CO_2 injectivity can be affected by the following mechanisms: (1) pressure build-up due to massive and continuous CO_2 injection; (2) dry-out of the near-well zone due to evaporation of H_2O into unsaturated CO_2; (3) CO_2-water-rock interactions induced by the injection of CO_2 (Bacci et al. 2011) [11–13]. Among these processes, CO_2-water-rock interactions could alter the rock matrix and potentially lead to porosity and permeability changes in the near-well zone [14–17], which is of particular importance for CO_2 injectivity.

Laboratory experiments related to CO_2 injection into sandstone and carbonate rocks have been reported in the previous studies [15, 18–22]. These experiments indicate that CO_2-water-rock interactions can have a substantial effect on porosity and permeability, depending on fluid composition, rock mineralogy, and subsurface thermodynamic conditions. They found that carbonate dissolution processes seem to be the main cause of permeability increases and promote a rapid spreading of the reaction front in short time scales.

Reactive transport modeling has been previously used to investigate geochemical reactions and their effects on permeability and porosity evolution [14, 15, 23–26]. André et al. [14] simulated CO_2 storage in the carbonate-rich Dogger aquifer in the Paris Basin (France) using the reactive transport simulator TOUGHREACT. They found that the porosity in the near-well zone increased significantly due to mineral dissolution. This was in accordance with the reactive flow-through experimental study by Luquot and Gouze [15] for the same basin. Some studies [25, 26] also reported that geochemical reactions dissolved the host rock increasing porosity and permeability thereby affecting fluid flow through reactive transport modeling. On the other hand, Izgec et al. [23] found that CO_2 injection into carbonate aquifers simulated using CMG's STARS could result in permeability reduction as well as improvement depending on the balance between mineral dissolution and precipitation. Furthermore, Sbai and Azaroual [24] found that CO_2 injection could in some circumstances cause particulates to clog reservoir pores leading to a permeability reduction and injectivity decline near the injection well.

Laboratory experiments, imaging characterization, and numerical modeling have previously been combined to describe mineral alteration and associated reactive transport processes and mechanisms in porous media induced by CO_2 injection (Bacci et al. 2011) [16, 27, 28]. Those studies focused on pore- or continuum-scale transport and reaction processes and indicated that CO_2 injectivity increases from dissolution of both carbonate and silicate minerals (especially feldspars). They also confirmed the rapid reaction kinetics of carbonate minerals compared to silicate minerals. Among these research approaches, numerical modeling is an excellent technique in which CO_2 injection and geochemical performance can be modeled at different temporal and spatial scales.

In general, previous studies reveal that CO_2-water-rock interactions induce mineral dissolution and precipitation which can consequently change the porosity and permeability of the subsurface matrix and thus affect the CO_2 injectivity and overall storage capacity. The trend and magnitude of change in porosity and permeability are highly reservoir specific and depend on reservoir properties, which are related to particle sizes, brine composition, and as well the thermodynamic conditions.

Analyses of geohydrological, mechanical, thermal, and geochemical processes involved in Shenhua CCS project have been reported [29–33]. However, few of these have focused on the considerable CO_2 injectivity increase during CO_2 injection period. Liu et al. [33] examined this unique phenomenon through numerical simulation and concluded that it could be explained through heterogeneities in reservoir permeability. However their approach did not consider the possible role of CO_2-water-rock interactions on CO_2 injectivity.

In this study, we applied a 2D radial injection model using the reactive transport code TOUGHREACT to investigate the effect of CO_2-water-rock geochemical reactions on CO_2 injectivity through the evolution of the formation porosity and permeability at the Shenhua CCS site. We focus on Liujiagou, Shiqianfeng, and Shihezi formations, which are the three main formations that sequestrate more than 90% of total CO_2 injected. The goal is to determine the key mechanisms controlling the CO_2-water-rock interactions during CO_2 injection, particularly focusing on investigation of the reasons for CO_2 injectivity improvement in the Shenhua CCS project. Moreover, we examined the impact of various parameters on mineral dissolution/precipitation as well as relevant porosity and permeability changes and compared the simulation results with available experimental data. Understanding of these mechanisms could have important practical implications for a successful CO_2 injection and storage operation in low-permeability formations, providing a new basis for screening of the storage sites and reservoirs and assessing CO_2 injectivity from a geochemical point of view.

2. Modeling Approach

2.1. Numerical Tool. The simulations presented in this study were carried out using the reactive transport code TOUGHREACT [34, 35], which introduces reactive geochemistry into the multiphase fluid and heat flow code TOUGH2 V2 [36]. A fluid property module ECO2N [37] was used to describe isothermal or nonisothermal multiphase flow in H_2O-NaCl-CO_2 system under conditions typically encountered in saline aquifers of interest for CO_2 sequestration ($31^\circ C \leq T \leq 110^\circ C$; $7.38\,MPa < P \leq 60\,MPa$). TOUGHREACT is a thermal-physical-chemical code applicable to one-, two-, or three-dimensional geologic systems with physical and chemical heterogeneity. The numerical method for fluid flow and chemical transport simulation is based on the integral finite difference (IFD) method for space discretization. The system of chemical reaction equations is solved on a grid-block basis by Newton-Raphson iteration. Thermodynamic data used in the simulations were

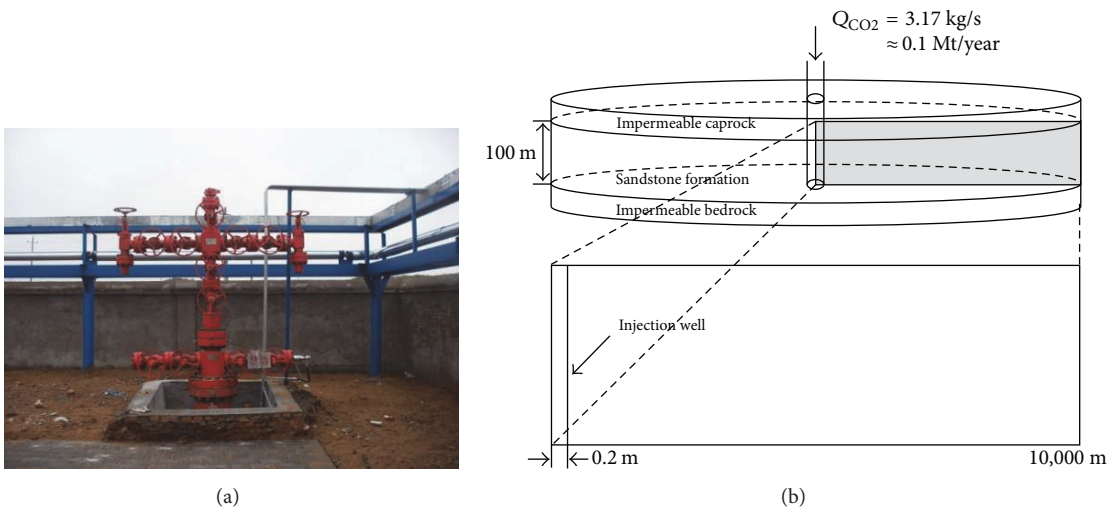

Figure 1: (a) Injection well (Zhongshenzhu 1) at the Shenhua CCS site and (b) schematic diagram of the 2D model.

taken from the EQ3/6 database [38], which derived using SUPCRT92. Local equilibrium constants and kinetic rates used in TOUGHREACT refer to Xu et al. [35].

Porosity changes in the matrix are directly tied to the volume changes as a result of mineral dissolution and precipitation. The porosity of the reservoir in the TOUGHREACT code is calculated by

$$\phi = 1 - \sum_{b=1}^{ab} \mathrm{fr}_b - \mathrm{fr}_u, \tag{1}$$

where ab is the number of minerals; fr_b is the volume fraction of mineral b in the rock ($V_{\mathrm{mineral}}/V_{\mathrm{medium}}$, including porosity); and fr_u is the volume fraction of nonreactive rock.

Reservoir permeability changes are calculated from changes in porosity using ratios of permeabilities as per the Kozeny-Carman grain model [35], as follows:

$$k = k_i \frac{(1-\phi_i)^2}{(1-\phi)^2} \left(\frac{\phi}{\phi_i}\right)^3, \tag{2}$$

where k_i is the initial permeability; ϕ and ϕ_i are current and initial porosity, respectively.

Full details on numerical methods are given in [34, 35].

2.2. Model Description. A two-dimensional (2D) radial model is employed as a conceptual framework to study the CO_2-water-rock interactions on CO_2 injectivity in the three main formations (Liujiagou, Shiqianfeng, and Shihezi) at the Shenhua CCS demonstration project site (Figure 1). The 2D homogeneous model represents a 100 m thick sandstone reservoir with a radial extent of 10 km, sufficiently large to ensure that boundary pressure conditions are maintained constant at initial values, that is, equivalent to an infinitely acting system. Other authors have used similar approximations in previous studies (Bacci et al. 2011) [35, 39]. The grid is composed of 4010 cocentered cell elements. The radius of the first cell containing the injection well is 0.2 m. Away from the injection well, 200 grid cells are considered between 0.2 and 1,000 m, 100 grid cells between 1,000 m and 3,000 m, and 100 grid cells between 3,000 m and 10 km. In each interval, the radius of the cells follows a logarithmic progression. The vertical discretization is achieved by a division of the reservoir into 10 layers with a constant spacing of 10 m. The bedrock and caprock are assumed to be impermeable no-flow boundaries.

CO_2 is injected into the reservoir at a constant flow rate of 3.17 kg/s (corresponding to 0.1 Mt/year) at the bottom 4 layers of the injection well uniformly for 30 years. The physical properties used to model the three formations (which have depth ranges from 1576 m to 2232 m) at the Shenhua CCS site are from previous works [8, 40] and are summarized in Table 1. The initial pressure is in hydrostatic equilibrium determined using the model, and the temperature of the three formations is fixed at 55°C, 62°C, and 67°C, respectively. The porosity and permeability of the three formations are obtained from well log data, and permeabilities are assumed to be isotropic. Pore compressibility of the formations is set to be 4.5×10^{-10}. The capillary pressure and liquid relative permeability are computed by van Genuchten [41], and gas relative permeability is calculated after Corey [42]. Different scenarios have been simulated to determine the different mechanisms of CO_2-water-rock interactions.

2.3. Mineral Composition. The initial rock mineral composition was derived from the laboratory analysis as described in [8, 43–45]. The Liujiagou formation is characterized as feldspar sandstone and lithic arkose. It consists mainly of quartz, alkali feldspar, plagioclase, the multilayer of chlorite and smectite, illite, and kaolinite. The Shiqianfeng formation consists mainly of feldspar rich sandstone and lithic arkose, which is mainly composed of quartz, feldspars, calcite, and small amount of clay minerals (illite and smectite). Feldspathic quartz sandstone and feldspathic lithic sandstone are the main rock type of the Shihezi formation. It consists mainly of quartz with some clay minerals (illite and smectite),

Table 1: Hydrogeological parameters of the formations used in this study.

Parameter	Liujiagou formation	Shiqianfeng formation	Shihezi formation
Permeability (m^2)	2.81×10^{-15}	6.58×10^{-15}	5.99×10^{-15}
Porosity	0.10	0.129	0.126
Pore compressibility (Pa^{-1})	4.5×10^{-10}	4.5×10^{-10}	4.5×10^{-10}
Rock grain density (kg/m^3)	2600	2600	2600
Formation heat conductivity (W/m °C)	2.51	2.51	2.51
Rock grain specific heat (J/kg °C)	920	920	920
Temperature (°C)	55	62	67
Pressure (MPa)	16	18.9	21
Salinity (wt.%)	6	3	0.9
Relative permeability model			
Liquid [41]			
$k_{rl} = \sqrt{S^*}\left\{1 - \left(1 - [S^*]^{1/\lambda}\right)^{\lambda}\right\}^2$		$S^* = \frac{(S_l - S_{lr})}{(1 - S_{lr})}$	
Residual liquid saturation		$S_{lr} = 0.30$	
Exponent		$\lambda = 0.457$	
Gas [42]			
$k_{rg} = \left(1 - \hat{S}\right)^2\left(1 - \hat{S}^2\right)$		$\hat{S} = \frac{(S_l - S_{lr})}{\left(1 - S_{lr} - S_{gr}\right)}$	
Residual gas saturation		$S_{gr} = 0.05$	
Exponent *capillary pressure model [41]*		$\lambda = 0.457$	
$P_{\text{cap}} = -P_0\left([S^*]^{-1/\lambda} - 1\right)^{1-\lambda}$		$S^* = \frac{(S_l - S_{lr})}{(1 - S_{lr})}$	
Residual liquid saturation		$S_{lr} = 0.00$	
Exponent		$\lambda = 0.457$	
Strength coefficient		$P_0 = 19.61$ kPa	

carbonates (calcite and dolomite), and plagioclase. It should be noted that alkali feldspar is represented as K-feldspar, plagioclase is represented as an ideal solid solution of oligoclase, and smectite is divided into Na-smectite and Ca-smectite equally by volume fraction referring to previous studies [46–48]. The detailed mineral composition is given in Table 2.

Simulation results can be influenced profoundly by the choice of secondary mineral assemblage. Almost all possible secondary minerals are considered in the simulations according to previous studies [35, 49].

2.4. Water Geochemistry. The main ions contained in pore water within the three formations are Na^+, Ca^{2+}, and Cl^-; however, the total dissolved solids (TDS) content varies substantially. The Liujiagou formation water is high salinity, with a TDS content of about 56,000 mg/L. The TDS content of Shiqianfeng formation water is 31,200 mg/L, and the TDS content of Shihezi formation water is 9,390 mg/L [44, 45, 50]. Prior to simulating reactive transport, batch geochemical modeling of water-rock interaction was performed to equilibrate the initial formation water composition with the primary formation minerals (Table 2) at the reservoir temperature and CO_2 partial pressure. The background CO_2 partial pressure is chosen to match the measured pH according to Xu et al. [51]. The resulting water chemistry of the three formations (Table 3) is used as the initial conditions for the reactive transport simulation of CO_2 injection.

3. Results and Discussion

3.1. Influence of Porosity and Permeability Changes on CO_2 Injectivity. Injectivity, J, is the flow rate of CO_2 achieved for a particular pressure difference between the injection well and the reservoir. It is linearly proportional to reservoir permeability as given by

$$J = \frac{q}{\Delta P} \propto \frac{2\pi kh}{\mu \ln\left(r_r/r_w\right)}, \tag{3}$$

where q is the volumetric flow rate of injected CO_2, ΔP is a pressure differential between injection pressure and reservoir pressure, h is the vertical thickness of the reservoir, μ is the fluid viscosity, and r is the radial distance with subscripts denoting the well-reservoir interface and boundary of the reservoir. Permeability changes close to the injection well have a comparatively larger effect than permeability changes in distant regions of the reservoir due to the logarithm of radial distance in the denominator. The precise effect of localized changes in permeability can be estimated using an average weighted by the logarithm of the radial distance as defined by

$$\frac{J}{J_i} = \frac{k}{\sum_i^n k_i \ln\left(r_i/r_{i-1}\right)}. \tag{4}$$

For a preliminary analysis of the potential effect of permeability changes, it is not necessary to solve (4) precisely;

Table 2: Mineralogical compositions of the three formations, initial mineral volume fractions introduced in the model, and possible secondary mineral phases used in the simulations.

Mineral	Chemical composition	Volume fraction (%)		
		Liujiagou	Shiqianfeng	Shihezi
Primary				
Quartz	SiO_2	27	65	66
K-feldspar	$KAlSi_3O_8$	14	9	—
Oligoclase	$Ca_{0.2}Na_{0.8}Al_{1.2}Si_{2.8}O_8$	24	16	6
Calcite	$CaCO_3$	—	3	3
Dolomite	$CaMg(CO_3)_2$	—	—	3
Illite	$K_{0.6}Mg_{0.25}Al_{1.8}(Al_{0.5}Si_{3.5}O_{10})(OH)_2$	17	4.5	18.5
Kaolinite	$Al_2Si_2O_5(OH)_4$	6	—	—
Chlorite	$Mg_{2.5}Fe_{2.5}Al_2Si_3O_{10}(OH)_8$	8.5	—	—
Na-smectite	$Na_{0.290}Mg_{0.26}Al_{1.77}Si_{3.97}O_{10}(OH)_2$	1.75	1.25	1.75
Ca-smectite	$Ca_{0.145}Mg_{0.26}Al_{1.77}Si_{3.97}O_{10}(OH)_2$	1.75	1.25	1.75
Total		100	100	100
Secondary:				
Magnesite	$MgCO_3$			
Albite~low	$NaAlSi_3O_8$			
Siderite	$FeCO_3$			
Ankerite	$CaMg_{0.3}Fe_{0.7}(CO_3)_2$			
Dawsonite	$NaAlCO_3(OH)_2$			
Hematite	Fe_2O_3			
Halite	$NaCl$			
Anhydrite	$CaSO_4$			

Table 3: Initial component concentrations of the formation water in the three formations.

Component	Concentration (mol/kg H_2O)		
	Liujiagou	Shiqianfeng	Shihezi
Na^+	1.09	4.19×10^{-1}	1.97×10^{-1}
Ca^{2+}	1.32×10^{-2}	5.66×10^{-2}	2.70×10^{-5}
Mg^{2+}	7.09×10^{-7}	5.59×10^{-13}	2.25×10^{-5}
K^+	6.84×10^{-5}	1.82×10^{-3}	2.87×10^{-5}
Fe^{2+}	1.02×10^{-4}	1.25×10^{-5}	9.52×10^{-11}
Cl^-	1.12	5.06×10^{-1}	1.50×10^{-1}
SO_4^{2-}	3.93×10^{-4}	1.85×10^{-2}	2.26×10^{-7}
HCO_3^-	1.77×10^{-3}	6.50×10^{-4}	4.57×10^{-2}
AlO_2^-	1.32×10^{-8}	2.77×10^{-8}	7.59×10^{-8}
SiO_2 (aq)	5.15×10^{-4}	5.89×10^{-4}	6.63×10^{-4}
pH	7.03	6.68	7.92
Temperature	55°C	62°C	67°C

the order of magnitude of the effect on injectivity can be assessed by assuming a uniform change in permeability. On that basis, injectivity increases linearly with permeability with a gradient of unity. The maximum permeability increases of 0.32%, 0.40%, and 1.39% for the three reservoirs would cause an identical increase in CO_2 injectivity. Consequently the permeability change estimated using (2) and (3) is insufficient to explain the obvious increase in injectivity observed during the Shenhua CCS project.

However, this result relies on the use of the Kozeny-Carman grain model (2) as an estimate of permeability changes in response to porosity change from mineral precipitation/dissolution. Implicit in this model are the assumptions that tortuosity and mineral grain size remain constant as porosity changes, which may not be the case. Furthermore, the Kozeny-Carman model excludes the possibility of a percolation limit to permeability, that is, a minimum porosity below which permeability is zero due to a lack of hydraulic connectivity between pores. Alternative forms of the Kozeny-Carman model have been proposed which account for these factors [52], such as

$$k = k_i \frac{d^2}{d_i^2} \frac{\tau_i^2}{\tau^2} \frac{\left(1 - \phi_i + \phi_p\right)^2}{\left(1 - \phi + \phi_p\right)^2} \frac{\left(\phi - \phi_p\right)^3}{\left(\phi_i - \phi_p\right)^3}, \quad (5)$$

where d represents mineral grain size, τ is tortuosity, and ϕ_p is the percolation porosity for the reservoir rock. From (5), if the CO_2-water-rock interaction-induced mineral dissolution causes grain size increase or tortuosity reduction, it could result in larger permeability increase than calculated from (2).

Grain size does not anticipate increase substantially. Percolation porosity is estimated to typically be 1–3% [52], which is insufficient to explain increases in injectivity: a percolation porosity of 3% would lead to maximum permeability increases of 0.45%, 0.50%, and 1.87% for the three reservoirs. However, tortuosity has been reported to vary widely at fixed porosity for similar rock or other porous medium samples [53]. A large decrease in tortuosity would

cause a very substantial difference in permeability (e.g., a halving of tortuosity would increase permeability by a factor of four). A large decrease in tortuosity can be explained, at least in theory, by mineral precipitation-dissolution that selectively occurs in relation to major fluid flow paths. That is, if dissolution predominates along larger and more direct flow paths, and precipitation mainly occurs in pores that are not part of flow pathways, small changes in total porosity may lead to substantial increase in tortuosity and consequently permeability. Furthermore, it is possible that tortuosity can be decreased by the removal of fine particulates that plug, bridge, or impinge existing or potential fluid flow paths. Only small amounts of dissolution may be necessary to dislodge fines and allow them to settle out of fluid flow.

These possible explanations provide a conceptual framework which could explain injectivity increases in terms of CO_2-water-rock-interaction-induced mineral dissolution and precipitation. Further research would be needed to evaluate whether they are appropriate to apply to this reservoir system. In particular, flow models incorporating fines migration and the effect of mechanical forces on precipitation and dissolution reactions, as well as empirical studies using reservoir core samples, may provide insights into possible geological mechanisms for CO_2 injectivity increase. This further work may assist in differentiating between geochemical changes and permeability heterogeneity as competing explanations for the observed CO_2 injectivity increase.

3.2. Analysis of Mineral Dissolution/Precipitation on Porosity Changes. The amount of dissolution and precipitation of minerals induced by CO_2-water-rock interactions determines porosity change. In order to investigate this process, clarify the key minerals leading to porosity changes, and analyze the differences between different mineral assemblages of the Liujiagou, Shiqianfeng, and Shihezi formations, we investigate the distribution of changes in mineral volume fraction and concentrations of major aqueous species for these three formations along the horizontal direction at the depth of −75 m after 30 years of CO_2 injection.

The change in mineral composition and major aqueous species as a function of CO_2-water-rock interaction-induced dissolution and precipitation for different formations can be seen in Figure 2. Figure 2(a) shows the horizontal distribution of changes in main mineral volume fraction and porosity for Liujiagou formation after 30 years of CO_2 injection. It can be seen that porosity changes throughout the simulation are distinctly tied to the mineral dissolution and precipitation. The spatial distribution of mineral alteration varies in different regions. Mineral dissolution and precipitation are most substantial in zone II because there is sufficient aqueous CO_2 to decrease pH to values as low as 5.0 perturbing the equilibrium state of the system. This is consistent with changes in concentrations of major aqueous species (Figure 2(b)). The main dissolved minerals are oligoclase, chlorite, K-feldspar, and kaolinite, with the oligoclase dissolution providing the main source of volume fraction reduction, in agreement with minerals behavior in laboratory experiments [45]. The main precipitated minerals are Na-smectite, Ca-smectite, illite, and siderite, consuming Ca^{2+} and Mg^{2+} provided by the dissolution of oligoclase and chlorite. The net volume fraction change of minerals is a reduction, resulting in porosity increase.

The resulting porosity changes of the Shiqianfeng formation are explored in Figure 2(c), where the volume fraction changes of minerals versus radial distance are shown after 30 years of CO_2 injection. The injection of CO_2 displaces the liquid flow away from the injection well, but some liquid flow reverses due to capillary-drive, providing water for CO_2-water-rock interactions. The porosity increases slightly in zone I, which can be explained by the large amount of calcite dissolution relative to the anhydrite precipitation. This is consistent with the increase of Ca^{2+} concentration (Figure 2(d)). However, this effect is reduced in the region approximately 30 m away from the well due to many minerals precipitating. In zone II, oligoclase, illite, and calcite volumes decreased relative to initial conditions, while kaolinite, quartz, dawsonite, K-feldspar, Na-smectite, and Ca-smectite volumes increased. Overall, the most important contributor to net volume change caused by precipitation and dissolution was oligoclase dissolution. There was no noticeable change in porosity in zone III because CO_2 has not reached that region of the reservoir.

As shown in Figure 2(e), there is a distinct difference in the mineral alterations between the Shihezi formation and the other two formations, particularly in terms of variation in dolomite and calcite. In the Shihezi formation as the volume fraction of dolomite decreases (6), the volume fraction of calcite increases. This is also demonstrated by the experimental study [44]. The effect of dolomite dissolution and calcite precipitation is substantial in zone I and determines the change in porosity. The changes in this zone can be explained by liquid flow reversal into zone I due to capillary-drive combined with the high reactivity of dolomite resulting in fast CO_2-water-rock interactions. It can be inferred that the dissolution of dolomite provides Ca^{2+} for calcite precipitation ((6)-(7)), with Ca^{2+} making no significant changes (Figure 2(f)). In zone II, the dolomite dissolution and calcite precipitation are also substantial, although the porosity change is also altered by oligoclase dissolution and Na-smectite and Ca-smectite precipitation. The overall effect is a reduction in net mineral volume fraction that leads to porosity increase. Oligoclase dissolution also occurs in zone III, mainly due to precipitation of Na-smectite and Ca-smectite ((8)-(9)), consuming Ca^{2+} and Na^{+} and consequently promoting the dissolution of oligoclase (10):

$$\mathrm{CaMg(CO_3)_2\,(dolomite) + 2H^+ \longrightarrow Ca^{2+} + Mg^{2+} + 2HCO_3^-} \tag{6}$$

$$\mathrm{Ca^{2+} + HCO_3^- \longleftrightarrow CaCO_3\,(calcite) + H^+} \tag{7}$$

$$\begin{aligned}&\mathrm{0.26Mg^{2+} + 0.29Na^+ + 1.77Al(OH)_3 + 3.97H_4SiO_4}\\&\quad\mathrm{\longrightarrow Na_{0.290}Mg_{0.26}Al_{1.77}Si_{3.97}O_{10}(OH)_2}\\&\quad\mathrm{\cdot (Na-smectite) + 0.81H^+ + 9.19H_2O}\end{aligned} \tag{8}$$

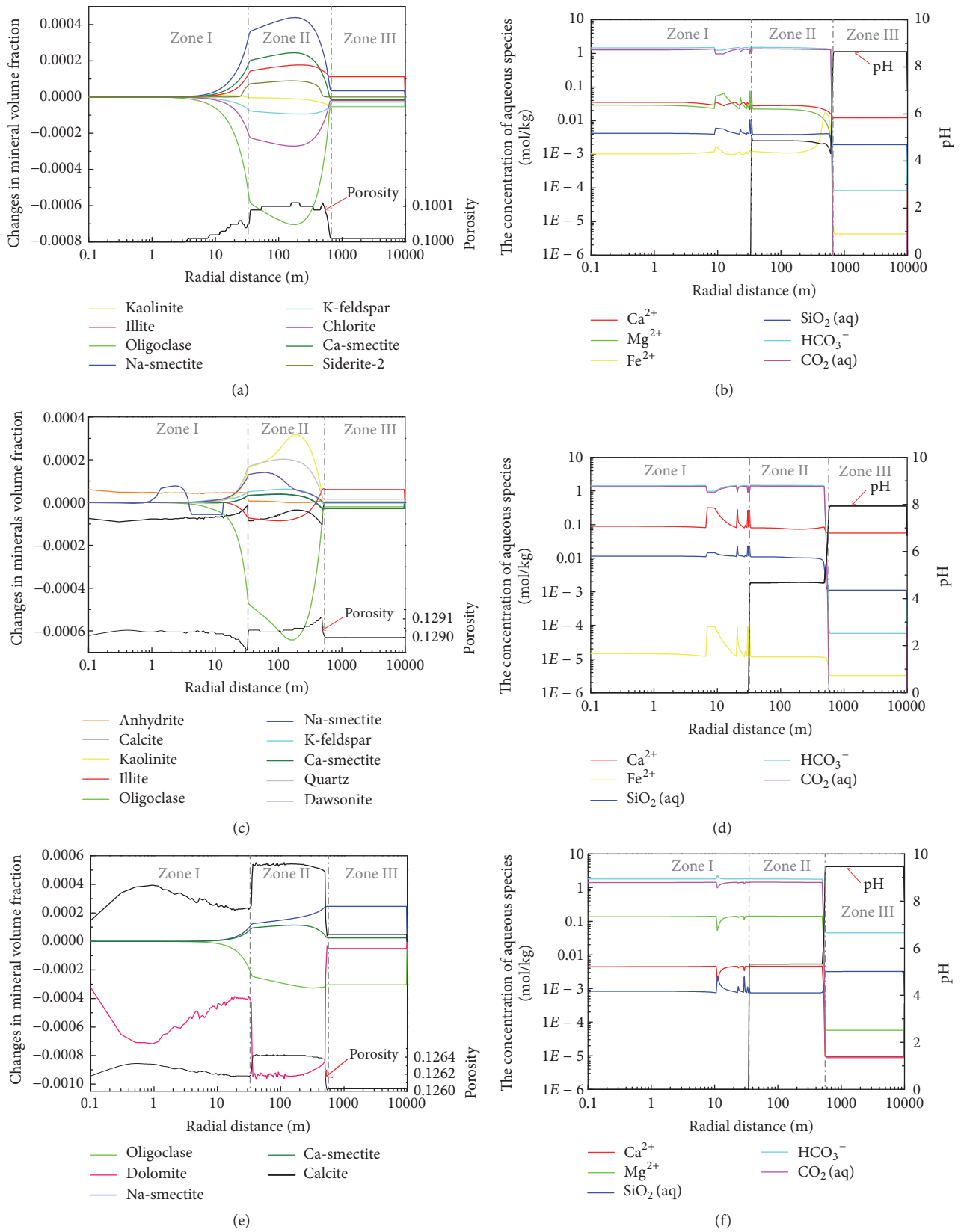

FIGURE 2: The horizontal distribution of changes in main mineral volume fraction, porosity, and concentrations of major aqueous species and pH for Liujiagou formation (a, b), Shiqianfeng formation (c, d), and Shihezi formation (e, f) along the horizontal direction at the depth of −75 m after 30 years of CO_2 injection.

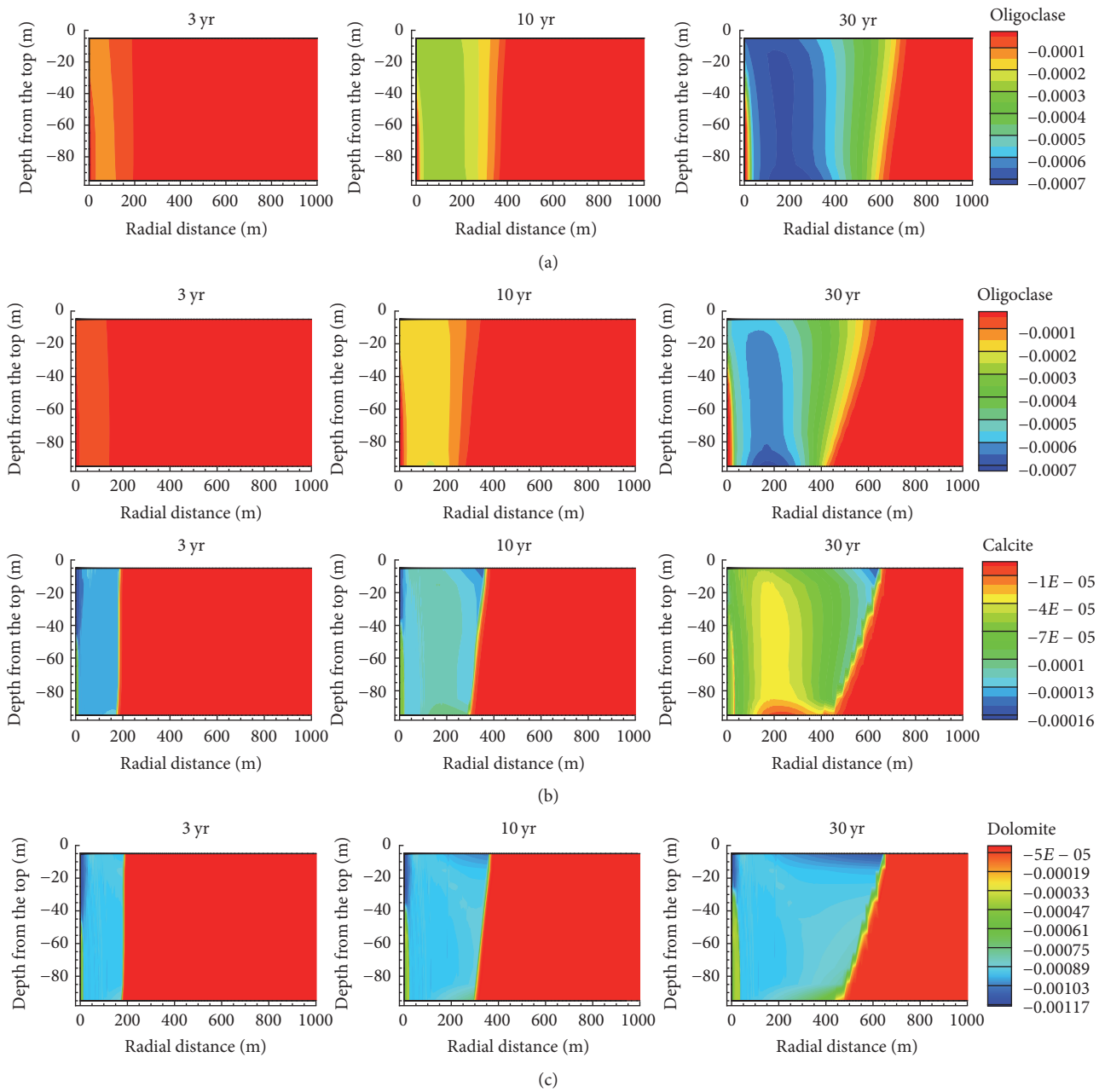

FIGURE 3: Temporal and spatial evolution of the key minerals volume fraction in the three formations ((a) Liujiagou formation; (b) Shiqianfeng formation; (c) Shihezi formation).

$$0.26Mg^{2+} + 0.145Ca^{2+} + 1.77Al(OH)_3 + 3.97H_4SiO_4 \longrightarrow Ca_{0.145}Mg_{0.26}Al_{1.77}Si_{3.97}O_{10}(OH)_2 \cdot (Ca-\text{smectite}) + 0.81H^+ + 9.19H_2O \quad (9)$$

$$CaNa_4Al_6Si_{14}O_{40}\,(\text{Oligoclase}) + 6H^+ + 34H_2O \longrightarrow Ca^{2+} + 4Na^+ + 6Al(OH)_3 + 14H_4SiO_4 \quad (10)$$

The temporal and spatial evolution of the volume fraction of key minerals within the three formations is shown in Figure 3. By analyzing the porosity changes and mineral alteration in Figures 2 and 3, it can be seen that the key minerals affecting porosity in the near-well region (zone I) are calcite and dolomite. In zone II, the dissolution of oligoclase and dolomite plays the key role in porosity increases, which is consistent with the phenomenon observed by Hao et al. [16] through the study of CO_2-induced dissolution processes of low-permeability carbonate reservoirs. It can be concluded that oligoclase, dolomite, and calcite are the key minerals that

Table 4: Summary of the simulation cases.

Simulation scenarios	Variable changed	Alternative value
Case 1	Dolomite volume fraction (%)	0
Case 2		15
Case 3	Calcite volume fraction (%)	0
Case 4		15
Case 5	Oligoclase volume fraction (%)	0
Case 6		15
Case 7	Temperature (°C)	50
Case 8		80
Case 9	Pressure (MPa)	10
Case 10		30
Case 11	Salinity (wt.%)	0.09
Case 12		9
Case 13		15

affect porosity increases in the Shenhua CCS demonstration project during CO_2 injection.

These results indicate the importance of localized mineral dissolution during CO_2-water-rock interactions, which can lead to a large increase in the volume of void space thereby increasing the porosity and permeability of the reservoir, and potentially CO_2 injectivity via mechanisms previously discussed.

3.3. Analysis of Factors Affecting Porosity Change. Mineral composition, temperature, pressure, and salinity may each influence CO_2-water-rock interactions (mineral dissolution/precipitation) thereby affecting porosity and permeability changes. In order to investigate the influence of these factors, an additional 13 simulation cases were analyzed, each varying one factor relative to a base case for the Shihezi formation (Table 4). It should be noted that the mineral composition (especially dolomite, calcite, and oligoclase) and formation physical properties (e.g., temperature, pressure, and brine salinity) are the key difference between the different formations. Therefore, a series of analyses are conducted to assess how the porosity and permeability changes and mineral alteration are affected by these parameters.

3.3.1. Impacts of Key Minerals. Dolomite is one of the key primary minerals in the system. Figures 4(a) and 4(b) show the difference in the porosity change and mineral alteration if the reservoir contains larger or smaller amounts of dolomite. It can be seen that the maximum porosity is above 12.61% in the CO_2 plume when there is no dolomite in the system. The maximum porosity increases to 12.645% when the initial volume fraction of dolomite is 3%. However, when the initial volume fraction of dolomite is 15%, porosity is not markedly increased, and in fact porosity changes in zone II coincide with results for a dolomite volume fraction of 3%. As dolomite content increases in the near-well region (zone I), it has less effect on porosity change; this is because reactivity is limited by lack of water (due to evaporation of water into the free CO_2 phase) and excessive initial mineral (i.e., dolomite supersaturation). This was also observed in a flow-through experiment performed by Tutolo et al. [22].

The complex effect of dolomite on the porosity results from the different behavior of minerals alteration induced variation in dolomite content. As shown in Figures 4(b) and 4(c), when there is no dolomite in the system, the minerals and major aqueous species show very different behavior compared with the base case. Under those circumstances, calcite is dissolved rather than precipitated in zone I and zone II, and oligoclase mainly dissolves in zone II, while there is no Mg^{2+} provided by dolomite. Some kaolinite and quartz precipitated, which is also very different from the base case.

The overall effect of increased dolomite volume fraction is a reduction in net mineral volume fraction, leading to a minor porosity increase. When dolomite is present (and consequently Ca^{2+} and Mg^{2+}), dedolomitization occurs: dolomite transforms into calcite. This result agrees well with Yan and Zhang's study [54]. It occurs because the change in Gibbs free energy (ΔG) for dolomite dissolution is smaller than that for calcite dissolution; that is, the required energy for dolomite dissolution is less than that for calcite [27, 55]. Consequently the dissolution of dolomite occurs more readily than that of calcite. Furthermore, the presence of dolomite can promote the precipitation of Na-smectite and Ca-smectite and the dissolution of oligoclase outside the CO_2 plume.

Compared with dolomite, calcite has minimal effects on the mineral alteration, porosity, and major aqueous species changes in the system, as shown in Figures 4(d)–4(f). It should be noted that the black line representing 3% volume fraction calcite coincides with the blue line representing 15% calcite. When calcite is absent in the primary minerals, calcite is still precipitated in the system, due to the increase in Ca^{2+} supplied by dolomite dissolution (dedolomitization) mentioned above. Only when dolomite is absent can calcite dissolve to make a contribution to the porosity increase (Figures 2(c) and 4(b)).

Figures 4(g)–4(i) show the changes in major aqueous species, porosity, and relevant mineral alteration with respect to radial distance for different initial oligoclase content. These results indicate that oligoclase also plays an important role in porosity and permeability changes (Figure 4(g)). It can be seen that the greater the oligoclase content, the smaller the porosity increases and the concentration of Mg^{2+} supplied by dolomite, which is mainly because oligoclase can inhibit the dissolution of dolomite (Figure 4(h)). This further suggests that dolomite is an important mineral for formation porosity increases and CO_2 injectivity improvement.

3.3.2. Impacts of Physical Parameters. In order to investigate the impact of physical parameters, temperature, pressure, and salinity, we have used the Shihezi formation as the base case to vary one factor to obtain the temperature, pressure, and salinity targeted allowing more comparable, consistent, and making sense results. The initial temperature and pressure of the Shihezi formation are 67°C and 21 MPa, and the variation of temperature is 50°C (Case 7) and 80°C (Case 8), and the pressure is 10 MPa (Case 9) and 30 MPa (Case 10). The initial

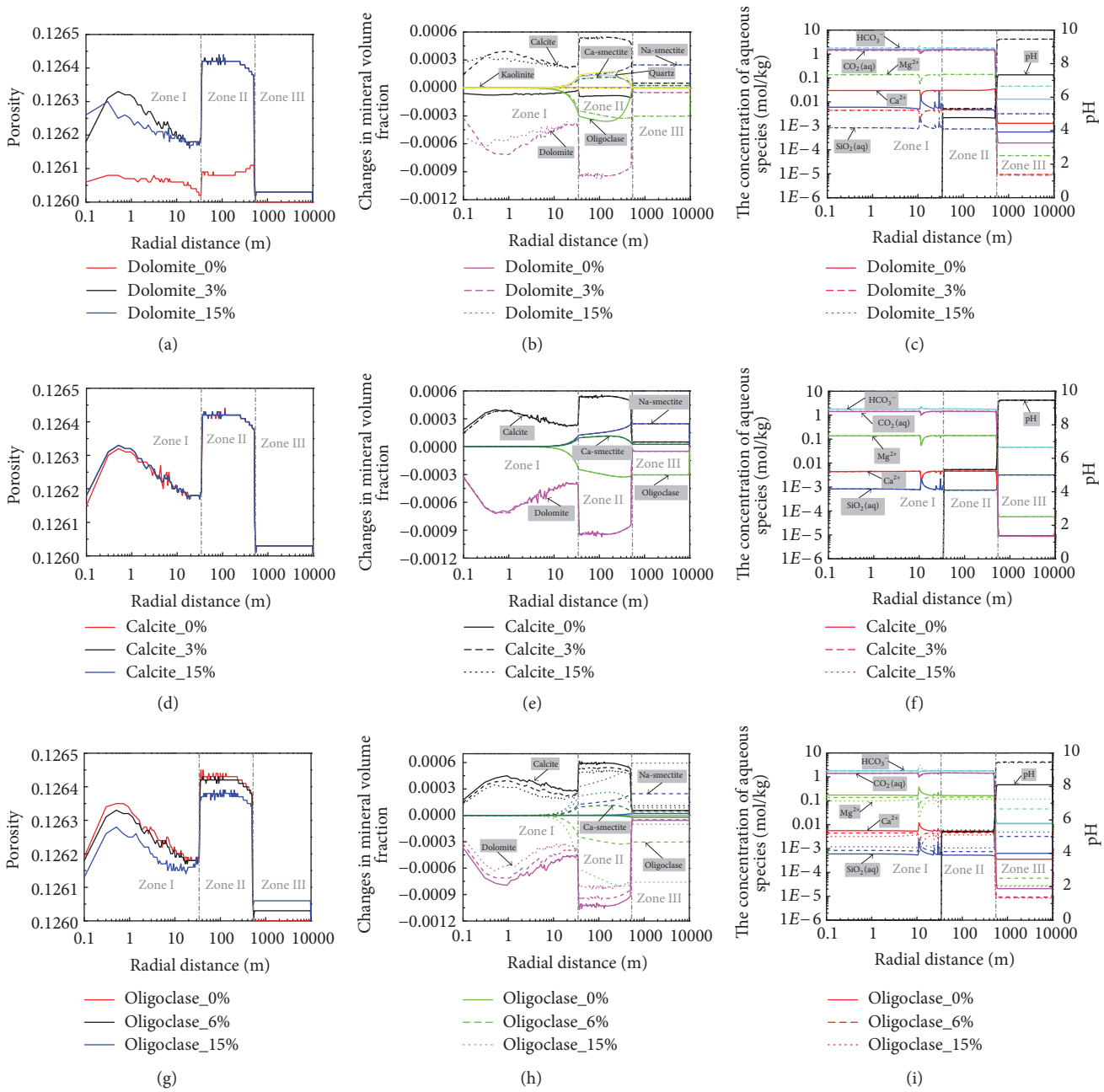

Figure 4: The horizontal distribution of changes in porosity, mineral volume fraction, and concentrations of major aqueous species and pH for different amounts of dolomite (a, b, and c), calcite (d, e, and f), and oligoclase (g, h, and i) at the depth of −75 m after 30 years of CO_2 injection.

water salinity of the Shihezi formation is 0.9 wt.% dissolved NaCl, and it is evaporated to 9 (Case 12) and 15 (Case 13) wt.% dissolved NaCl and diluted to 0.09 wt.% dissolved NaCl (Case 11) to evaluate the salinity effect, as can be seen in Table 4.

Temperature. Figure 5(a) shows that the porosity change at the reservoir temperature of 67°C is larger than at the temperature of 50°C and 80°C, indicating that the changes in porosity increase first and then decrease with increasing reservoir temperature in zone I and zone II, with the maximum value occurring between 50°C and 80°C. This is attributed to the changes in mineral volume fraction that the dissolution of dolomite increases first and then decreases with increasing temperature in zone I and zone II (Figure 5(b)), which is consistent with the study conducted by Yan et al. [56]. Although the dissolution of oligoclase increases with increasing temperature, the precipitation of Na-smectite and Ca-smectite increases correspondingly in zone II, such that there is nearly no net contribution to porosity increases. Porosity increases with larger temperatures in zone III without CO_2, resulting

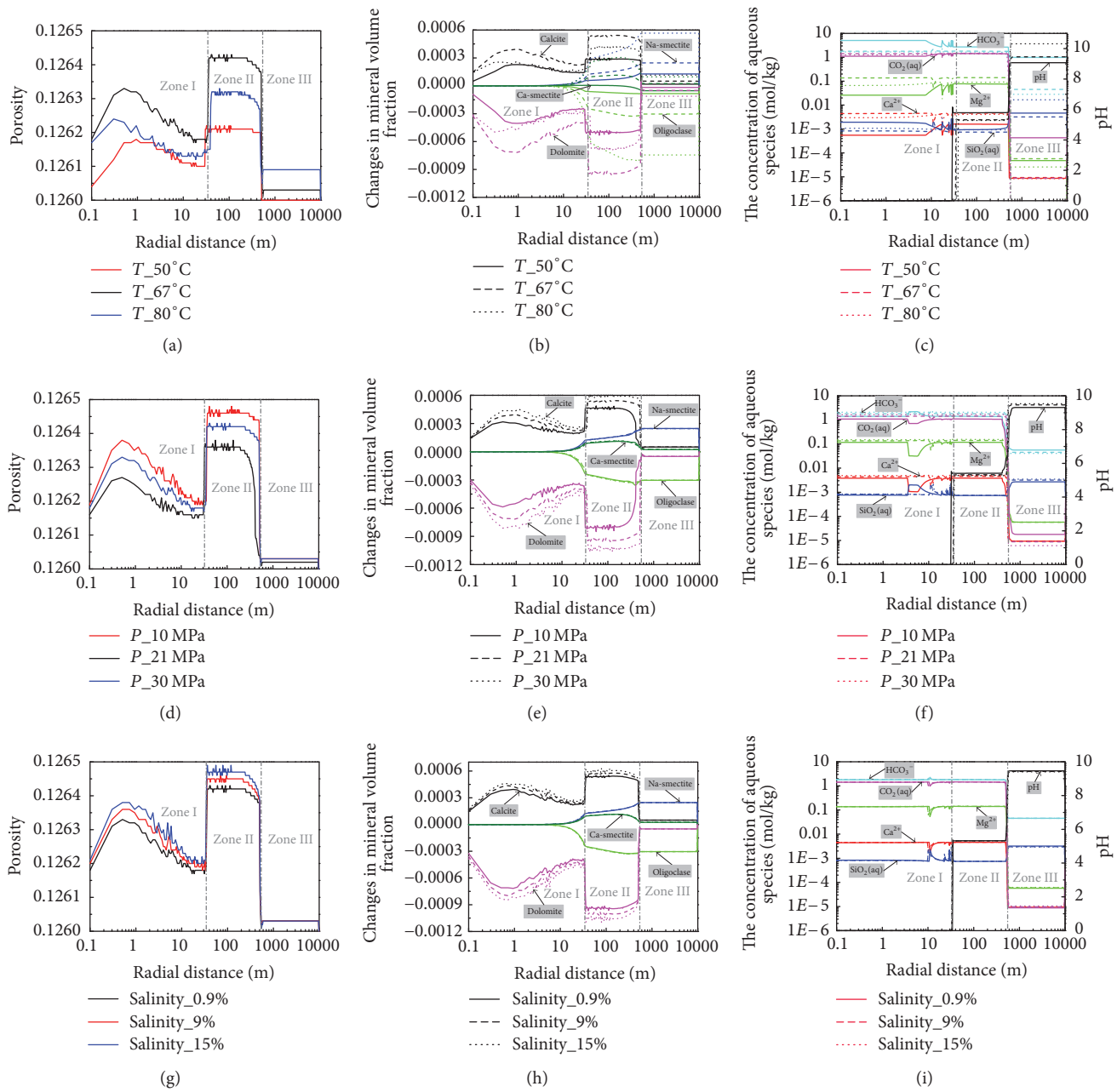

Figure 5: The horizontal distribution of changes in porosity, mineral volume fraction, and concentrations of major aqueous species and pH for different temperature (a, b, and c), pressure (d, e, and f), and salinity (g, h, and i).

from the dissolution of oligoclase. The effect of temperature on the horizontal distribution of changes in major aqueous species is shown in Figure 5(c), which agrees well with the mineral alteration. It can be concluded that temperature has a large effect on mineral dissolution and precipitation as well as consequent porosity and permeability changes.

Pressure. The impact of pressure on the horizontal distribution of changes in porosity, mineral volume fraction, and major aqueous species is shown in Figures 5(d)–5(f). It can be seen that the change in porosity increases with increasing pressure from 10 MPa to 30 MPa (Figure 5(d)). However, the impact of pressure on the precipitation and dissolution of different minerals varies. This also leads to the complex behavior of major aqueous species (Figure 5(f)). The dissolution of dolomite increases with pressure resulting in corresponding calcite precipitation, while no effect of pressure on oligoclase dissolution is observed within the pressure range investigated. This also supports the idea that the porosity increases resulted from the key carbonate mineral-dolomite dissolution.

Salinity. The effect of salinity on porosity was evaluated by evaporating the initial water of the Shihezi formation

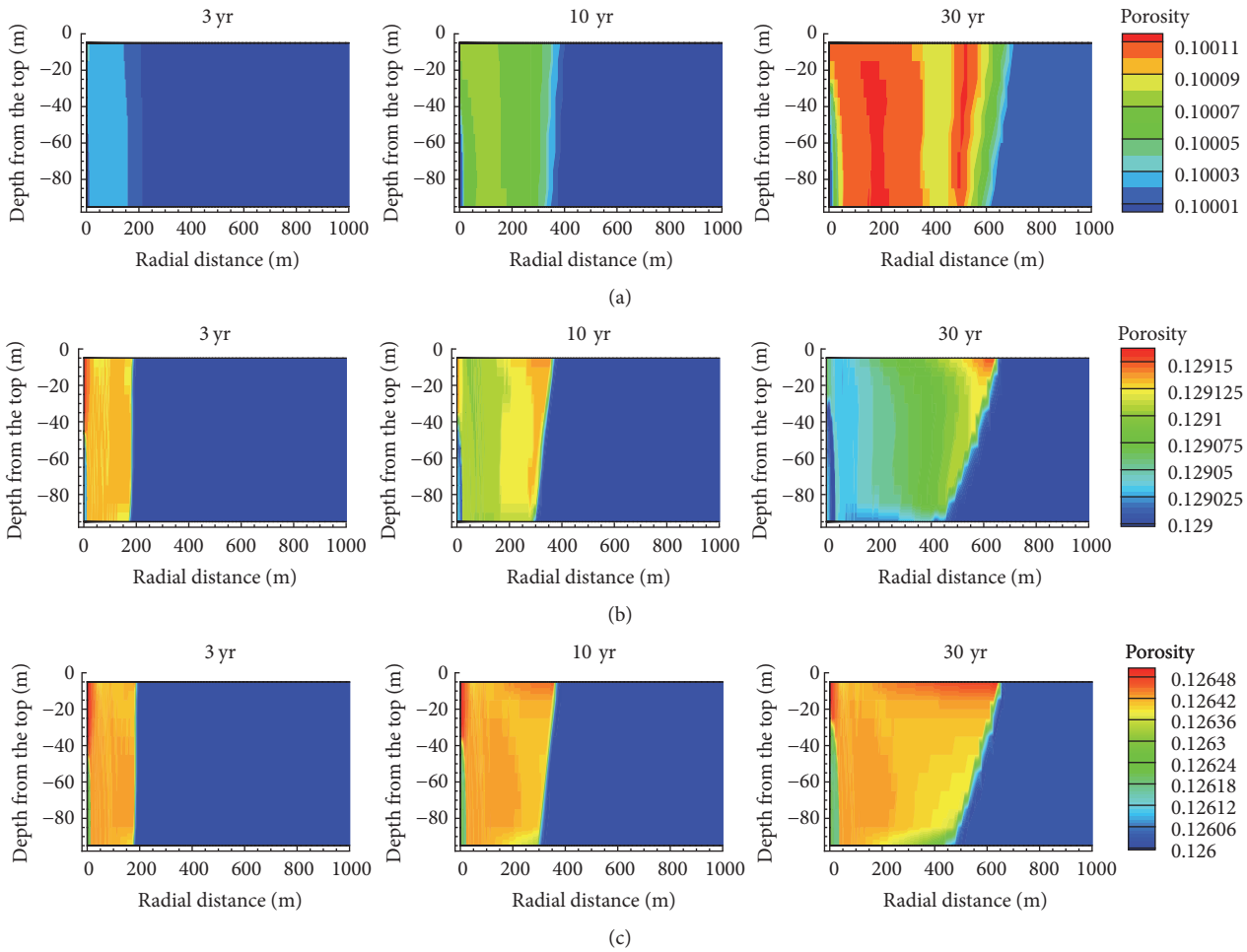

Figure 6: The evolution of porosity in the three formations ((a): Liujiagou formation; (b): Shiqianfeng formation; (c): Shihezi formation).

(0.9 wt.% dissolved NaCl) to increase salinity to 9 and 15 wt.% dissolved NaCl and diluting the initial water to decrease the salinity to 0.09 wt.% dissolved NaCl. As shown in Figure 5(g), the changes in porosity increase with salinity between 0.9 and 15 wt.% dissolved NaCl. It can be inferred that the overall effect of salinity is a reduction in net mineral volume fraction. Figures 5(h) and 5(i) show the horizontal distribution of changes in mineral volume fraction and major aqueous species, which demonstrate this. It can be seen that the dissolution of dolomite increases with increasing salinity, while the dissolution-precipitation of other minerals and major aqueous species does not change except for minor calcite precipitation. This is in accordance with previous studies [22, 54] and can be explained by the ionic strength of the solution increasing with salinity and reducing the activity of aqueous species, thereby promoting dolomite dissolution. There was no obvious difference in the porosity changes between salinities of 0.09% (not shown) and 0.9 wt.% dissolved NaCl. This is probably because both those salinities are so low that there is no significant effect on mineral alteration and consequent porosity changes.

3.4. Temporal and Spatial Evolution of Porosity and Permeability. The injection of CO_2 into the deep saline aquifers results in a sequence of CO_2-water-rock interactions, inducing mineral dissolution and precipitation, which can have a substantial impact on the porosity and permeability of the reservoir. Figure 6 shows the evolution of porosities in the Liujiagou, Shiqianfeng, and Shihezi formations. Porosity within each formation increases gradually with time, and the variation range of porosity is consistent with the migration scope of CO_2; this is consistent with the field observations [8]. However, the distribution of porosities is nonuniform in the range of CO_2 plume. This might be due to different geochemical reactions in different regions. The three reservoirs experienced increases in porosity of up to 0.10%, 0.12%, and 0.42%, respectively, depending on the primary mineral compositions and reservoir conditions.

Figure 7 shows the temporal and spatial evolution of permeability in the Liujiagou, Shiqianfeng, and Shihezi formations. The three formations experienced increases in permeability of up to 0.32%, 0.40%, and 1.39%. The variations in permeability agree with those of porosity (Figure 6),

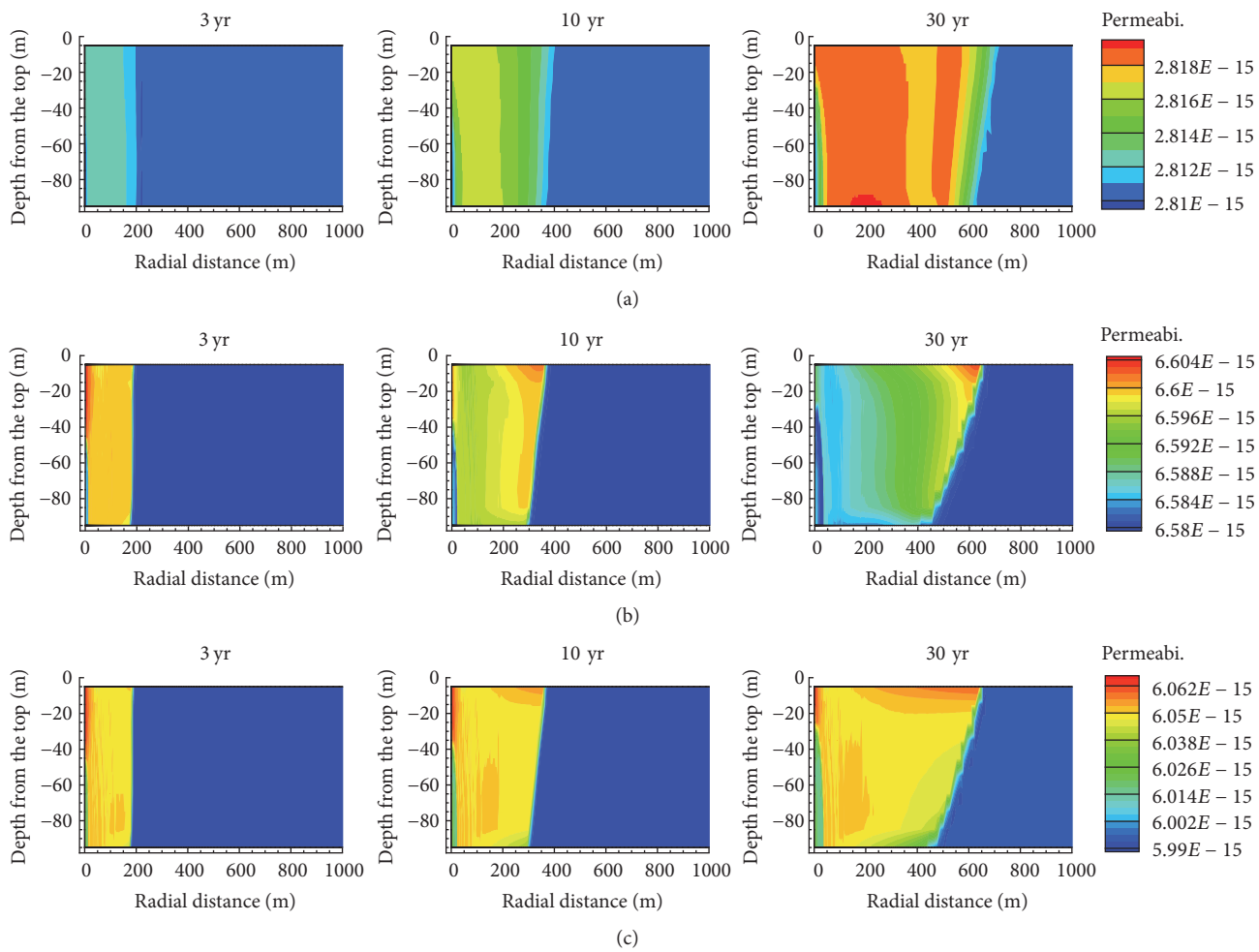

Figure 7: The evolution of permeability in the three formations ((a): Liujiagou formation; (b): Shiqianfeng formation; (c): Shihezi formation).

because that permeability is calculated from porosity using (2).

The supercritical CO_2 saturation and nonuniform distribution of porosity change along the horizontal direction at the depth of −75 m after 30 years of CO_2 injection are shown in Figure 8. It can be seen that the distribution of reservoir porosity is closely related to the change of supercritical CO_2 saturation. The reservoir system could be divided into three regions according to supercritical CO_2 saturation, which are (1) zone I: supercritical CO_2 region, where all the water has been displaced or has evaporated and Sg is close to one, (2) zone II: CO_2 and saline water region, where the pH decreases due to CO_2 dissolution in the water phase and stabilizes at a pseudoequilibrium value of approximately 5.0, and (3) zone III: saline water region, consisting of formation waters undisturbed by injected CO_2. The distribution of porosity change corresponds to these three distinct regions of supercritical CO_2 saturation (Figure 8). Porosity changes are different between the three formations due to their different physical and chemical properties and the corresponding balance of mineral dissolution and precipitation induced by CO_2-water-rock interactions.

The porosity change in the Liujiagou formation is the most limited: it increases slightly within zone I at distances of more than 3 m from the injection well, and there is a moderate uniform increase in porosity in zone II. In zone III, the porosity does not change because the system maintains its initial equilibrium state without CO_2 disturbance. The changes in porosity of the Shiqianfeng formation are slightly larger than Liujiagou formation, and the variation trend is different in each region, especially in zone I. Among the three formations, the changes in porosity of the Shihezi formation are largest, with the maximum changes located in zone II.

The CO_2-water-rock interactions after CO_2 injection lead to changes in porosity and permeability. These changes are directly tied to mineral dissolution and precipitation, calculated by (1)-(2) [35]. If the volume of minerals dissolved is larger than the volume of those precipitated, a porosity increase results. This will lead to an increase in permeability, which consequently enhances the injectivity of CO_2 into the formation. The differences in porosity changes between the three formations indicate that different CO_2-water-rock interactions occur in the Liujiagou, Shiqianfeng, and Shihezi formations. It can be concluded that porosity changes of zone

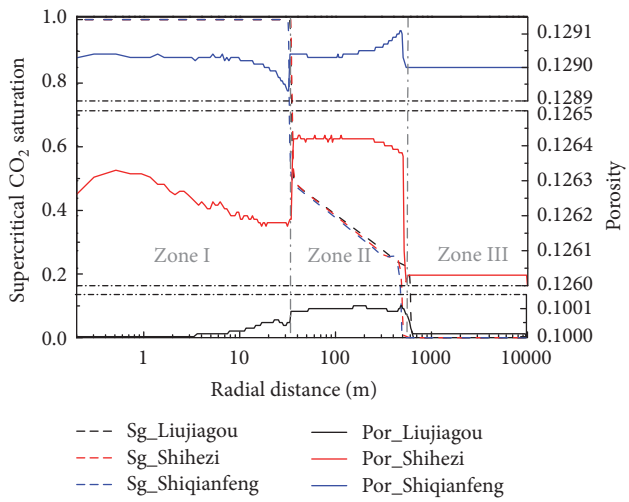

Figure 8: The distribution of porosity and supercritical CO_2 saturation in the horizontal plane at the depth of −75 m after 30 years of CO_2 injection in the three formations.

II are larger than those in zone I. This is mainly because no condensed water is present in zone I and consequently mineral reactions are limited, while zone II is a two-phase region with sufficient saline water and CO_2 for CO_2-water-rock reactions to proceed rapidly.

3.5. Comparison with Laboratory Experiments and Previous Other Modeling Work. With regard to Shenhua CCS demonstration project, the CO_2-water-rock interactions and associated mineral dissolution/precipitation after CO_2 injection have been tested in laboratory experiments [43–45] and we find good qualitative agreement with our results. Tao [45] conducted batch reaction experiments with sandstone using a mixture of CO_2 and brine fluids at temperatures of 60°C, 80°C, and 100°C and a pressure of 16 MPa for 1 to 25 days. The sandstone samples were sourced from the Liujiagou group at the Shenhua CCS demonstration project site. After the dissolution of CO_2, SEM and EDS analyses showed significant dissolution of primary minerals such as K-feldspar, albite, and chlorite and precipitation of secondary minerals such as siderite and some clay minerals. It should be noted that albite here is corresponding to oligoclase in our studies. These mineral alteration patterns are well consistent with our simulations.

Batch reactions were also conducted by Wang [43] and Yang [44] using sandstone samples from the Shiqianfeng formation and Shihezi formation, Ordos Basin, China. The experiments were conducted for 24 days at temperatures of 55°C, 70°C, 85°C, and 100°C and the same pressures of 18 MPa. SEM and EDS analyses showed albite and carbonates such as calcite and dolomite dissolved following the decrease of pH after CO_2 injection. During the experiment, the dissolution of carbonates buffered the fluid pH between 5 and 7.3. The concentration of K^+, Na^+, and Ca^{2+} increased due to the dissolution of initial dolomite and albite. Their findings on the amount of minerals alteration are in general agreement with our simulations, in which the dissolution of minerals is larger than the precipitation, and mineral dissolution amount increased with increasing temperature in a certain temperature range. This can explain field observations well that the injectivity increased after CO_2 injection.

The experiments discussed showed there were only intermediate states of carbonate minerals and some unknown aluminosilicate minerals precipitated, and the precipitation of clay minerals was rarely observed. This is in contrast to our simulation results where precipitation of carbonates such as dawsonite and calcite and clay minerals such as smectite and kaolinite precipitation associated with oligoclase dissolution were predicted. The differences are explained by factors such as kinetic and nucleation effects that likely prevent the formation of these minerals over the short time scales (only 24 days) of the laboratory experiments [44, 57].

In addition to batch experiments discussed above, we have also compared our results with previous reactive transport modeling results [39, 57, 58]. These simulations suggested that mineral dissolution and precipitation induced by CO_2 injection have a major impact on the porosity and permeability changes. Liu et al. [58] performed coupled reactive flow and transport modeling of CO_2 injection in the Mt. Simon sandstone formation, Midwest USA. They found dissolution of K-feldspar, oligoclase, and dolomite originating in the matrix caused increase in porosity, from the original 15% to 15.7% in the near-well zone during the injection period, which is in line with our simulation. In another recent paper [57], the initial mineral composition used in this work was similar with Shiqianfeng formation in our studies, but the minerals contents and in situ conditions (e.g., temperature and pressure) are different. Despite these differences, their results are well consistent with our studies that the increase in porosity is caused by the acidic brine that triggered the dissolution of minerals such as calcite and albite (corresponding to oligoclase in our studies). Also, the formation of dawsonite was observed in both models.

4. Conclusions

This study investigated CO_2-water-rock geochemical reactions during CO_2 injection at the Shenhua CCS demonstration site using two-dimensional (2D) reactive transport model. The potential role of mineral dissolution and precipitation (and resulting porosity change) in explaining the nearly tenfold increase in injectivity observed at that site was explored using conventional and alternative porosity-permeability models. The effect on mineral dissolution/precipitation of key mineral composition (e.g., dolomite, calcite, and oligoclase) and formation physical properties (e.g., temperature, pressure, and brine salinity) was also examined. The conclusions are as follows.

The CO_2-water-rock interactions induced by CO_2 injection into the deep saline aquifers affect the porosity evolution of the reservoir due to mineral dissolution and precipitation. The porosities of the three formations increase gradually over time during CO_2 injection, and the spatial distribution of porosity change is consistent with the migration scope of CO_2. The porosities of the Liujiagou, Shiqianfeng, and Shihezi reservoirs experienced maximum increases of 0.10%,

0.12%, and 0.42%, respectively. The differences in porosity changes between these three formations are a consequence of the different CO_2-water-rock interactions occurring due to their different primary mineral compositions and reservoir conditions.

The reservoir permeability will increase as a consequence of the porosity increase. Using a typical Kozeny-Carman porosity-permeability relationship, the nearly tenfold injectivity increase observed cannot be attributed to CO_2-water-rock interaction-induced mineral dissolution. However, using porosity-permeability relationships that include tortuosity, grain size, and percolation porosity, it is possible to explain the injectivity increase as a consequence of mineral dissolution. These models might be justified in terms of selective dissolution along flow paths and by dissolution or migration of plugging fines. Empirical studies using core samples would be necessary to evaluate the suitability of applying these alternative models to the Shenhua CCS site. Further research could also explore the near-wellbore porosity-permeability changes at the early stage of CO_2 injection and also as to whether more extreme variations in reservoir properties could explain permeability changes under a Kozeny-Carman porosity-permeability relationship.

Variation of key mineral composition and physical reservoir parameters illustrates that dolomite is the key mineral that affects porosity increase during CO_2 injection, and the dissolution of dolomite can inhibit the dissolution of calcite. The dissolution of oligoclase can also lead to porosity increase, although oligoclase can also inhibit the dissolution of dolomite, which is not conducive to porosity increase. Formation physical properties such as temperature, pressure, and brine salinity are all important factors that affect mineral dissolution and precipitation as well as relevant porosity and permeability changes.

The simulation results are compared with available experimental data and found to show reasonably good agreement. These results indicate the importance of localized mineral dissolution during CO_2-water-rock interactions, which can lead to a large increase in the volume of void space thereby increasing the porosity and permeability of the reservoir. This study helps deepen our understanding of how geochemical changes may affect CO_2 injectivity. Results from this study could have important practical implications for a successful CO_2 injection and enhanced oil/gas/geothermal production in low-permeability formations, providing a new basis for screening of the most effective storage sites and reservoirs and assessing CO_2 injectivity by considering specific mineralogy and in situ conditions.

Conflicts of Interest

The authors declare that there are no conflicts of interest regarding the publication of this paper.

Acknowledgments

This work was supported by the National Natural Science Foundation of China (NSFC, Grant nos. 41602272 and 41572233), a bilateral project China Australia Geological Storage of CO2 Project Phase 2 (CAGS2), and the project funded by China Postdoctoral Science Foundation (Grant no. 2016M592405).

References

[1] S. Bachu, "Sequestration of CO_2 in geological media in response to climate change: Road map for site selection using the transform of the geological space into the CO_2 phase space," *Energy Conversion and Management*, vol. 43, no. 1, pp. 87–102, 2002.

[2] IPCC, "IPCC Special Report on carbon dioxide capture and storage," in *Prepared by Working Group III of the Intergovernmental Panel on Climate Change*, p. 442, Cambridge University Press, Cambridge, UK, 2005.

[3] P. J. Cook, "Demonstration and Deployment of Carbon Dioxide Capture and Storage in Australia," in *Proceedings of the 9th International Conference on Greenhouse Gas Control Technologies, GHGT-9*, pp. 3859–3866, November 2008.

[4] C. Hermanrud, T. Andresen, O. Eiken et al., "Storage of CO_2 in saline aquifers-Lessons learned from 10 years of injection into the Utsira Formation in the Sleipner area," *Energy Procedia*, vol. 1, pp. 1997–2004.

[5] S. Whittaker, B. Rostron, C. Hawkes et al., "A decade of CO_2 injection into depleting oil fields: monitoring and research activities of the IEA GHG Weyburn-Midale CO_2 Monitoring and Storage Project," *Energy Procedia*, vol. 4, pp. 6069–6076, 2011.

[6] J. Lu, Y. K. Kharaka, J. J. Thordsen et al., "CO_2—rock—brine interactions in Lower Tuscaloosa Formation at Cranfield CO_2 sequestration site, Mississippi, U.S.A," *Chemical Geology*, vol. 291, pp. 269–277, 2012.

[7] T. Kempka and M. Kühn, "Numerical simulations of CO_2 arrival times and reservoir pressure coincide with observations from the Ketzin pilot site, Germany," *Environmental Earth Sciences*, vol. 70, pp. 3675–3685, 2013.

[8] X. Wu, *Carbon Dioxide Capture and Geological Storage: The First Massive Exploration in China*, Beijing, Science Press, Beijing, China, 2013.

[9] Q. Li, G. Liu, X. Liu, and X. Li, "Application of a health, safety, and environmental screening and ranking framework to the Shenhua CCS project," *International Journal of Greenhouse Gas Control*, vol. 17, pp. 504–514, 2013.

[10] China Shenhua Coal to Liquid and Chemical Engineering Company, *The operation report of the Shenhua 0.1 Mt CCS Demonstration Project*, 2014.

[11] T. A. Buscheck, Y. Sun, M. Chen et al., "Active CO_2 reservoir management for carbon storage: Analysis of operational strategies to relieve pressure buildup and improve injectivity," *International Journal of Greenhouse Gas Control*, vol. 6, pp. 230–245, 2012.

[12] L. André, Y. Peysson, and M. Azaroual, "Well injectivity during CO_2 storage operations in deep saline aquifers - Part 2: Numerical simulations of drying, salt deposit mechanisms and role of capillary forces," *International Journal of Greenhouse Gas Control*, vol. 22, pp. 301–312, 2014.

[13] Q. Li, Y.-N. Wei, G. Liu, and Q. Lin, "Combination of CO_2 geological storage with deep saline water recovery in western China: Insights from numerical analyses," *Applied Energy*, vol. 116, pp. 101–110, 2014.

[14] L. André, P. Audigane, M. Azaroual, and A. Menjoz, "Numerical modeling of fluid-rock chemical interactions at the supercritical CO_2-liquid interface during CO_2 injection into a carbonate reservoir, the Dogger aquifer (Paris Basin, France)," *Energy Conversion and Management*, vol. 48, pp. 1782–1797, 2007.

[15] L. Luquot and P. Gouze, "Experimental determination of porosity and permeability changes induced by injection of CO_2 into carbonate rocks," *Chemical Geology*, vol. 265, pp. 148–159, 2009.

[16] Y. Hao, M. Smith, Y. Sholokhova, and S. Carroll, "CO_2-induced dissolution of low permeability carbonates. Part II: Numerical modeling of experiments," *Advances in Water Resources*, vol. 62, pp. 388–408, 2013.

[17] G. P. D. De Silva, P. G. Ranjith, and M. S. A. Perera, "Geochemical aspects of CO_2 sequestration in deep saline aquifers: A review," *Fuel*, vol. 155, pp. 128–143, 2015.

[18] C. F. J. Colón, E. H. Oelkers, and J. Schott, "Experimental investigation of the effect of dissolution on sandstone permeability, porosity, and reactive surface area," *Geochimica et Cosmochimica Acta*, vol. 68, pp. 805–817, 2004.

[19] O. Izgec, B. Demiral, H. Bertin, and S. Akin, "CO_2 injection into saline carbonate aquifer formations I: Laboratory investigation," *Transport in Porous Media*, vol. 72, pp. 1–24, 2008.

[20] M. M. Smith, Y. Sholokhova, Y. Hao, and S. A. Carroll, "CO_2-induced dissolution of low permeability carbonates. Part I: Characterization and experiments," *Advances in Water Resources*, vol. 62, pp. 370–387, 2013.

[21] A. J. Luhmann, X.-Z. Kong, B. M. Tutolo et al., "Experimental dissolution of dolomite by CO_2-charged brine at 100∘C and 150 bar: Evolution of porosity, permeability, and reactive surface area," *Chemical Geology*, vol. 380, pp. 145–160, 2014.

[22] B. M. Tutolo, A. J. Luhmann, X. Kong, M. O. Saar, and W. E. Seyfried, "Experimental Observation of Permeability Changes In Dolomite at CO_2 Sequestration Conditions," in *Environmental Science & Technology*, vol. 48, pp. 2445–2452, 2014.

[23] O. Izgec, B. Demiral, H. Bertin, and S. Akin, "CO_2 injection into saline carbonate aquifer formations II: Comparison of numerical simulations to experiments," *Transport in Porous Media*, vol. 73, pp. 57–74, 2008.

[24] M. A. Sbai and M. Azaroual, "Numerical modeling of formation damage by two-phase particulate transport processes during CO_2 injection in deep heterogeneous porous media," *Advances in Water Resources*, vol. 34, pp. 62–82, 2011.

[25] S. Sadhukhan, P. Gouze, and T. Dutta, "Porosity and permeability changes in sedimentary rocks induced by injection of reactive fluid: A simulation model," *Journal of Hydrology*, vol. 450-451, pp. 134–139, 2012.

[26] J. P. Nogues, J. P. Fitts, M. A. Celia, and C. A. Peters, "Permeability evolution due to dissolution and precipitation of carbonates using reactive transport modeling in pore networks," *Water Resources Research*, vol. 49, pp. 6006–6021, 2013.

[27] S. Molins, D. Trebotich, L. Yang et al., "Pore-scale controls on calcite dissolution rates from flow-through laboratory and numerical experiments," *Environmental Science & Technology*, vol. 48, pp. 7453–7460, 2014.

[28] B. M. Tutolo, A. J. Luhmann, X.-Z. Kong, M. O. Saar, and W. E. Seyfried, "CO_2 sequestration in feldspar-rich sandstone: Coupled evolution of fluid chemistry, mineral reaction rates, and hydrogeochemical properties," *Geochimica et Cosmochimica Acta*, vol. 160, pp. 132–154, 2015.

[29] N. Wei, M. Gill, D. Crandall et al., "CO_2 flooding properties of Liujiagou sandstone: Influence of sub-core scale structure heterogeneity," *Greenhouse Gases: Science and Technology*, vol. 4, pp. 400–418, 2014.

[30] W. B. Fei, Q. Li, X. C. Wei et al., "Interaction analysis for CO_2 geological storage and underground coal mining in Ordos Basin, China," *Engineering Geology*, vol. 196, pp. 194–209, 2015.

[31] Q. Zhu, D. Zuo, S. Zhang et al., "Simulation of geomechanical responses of reservoirs induced by CO_2 multilayer injection in the Shenhua CCS project, China," *International Journal of Greenhouse Gas Control*, vol. 42, pp. 405–414, 2015.

[32] Q. Li, H. Shi, D. Yang, and X. Wei, "Modeling the key factors that could influence the diffusion of CO_2 from a wellbore blowout in the Ordos Basin, China," *Environmental Science and Pollution Research*, vol. 24, pp. 3727–3738, 2017.

[33] D. Liu, Y. Li, S. Song, and R. Agarwal, "Simulation and analysis of lithology heterogeneity on CO_2 geological sequestration in deep saline aquifer: a case study of the Ordos Basin," *Environmental Earth Sciences*, vol. 75, pp. 1–13, 2016.

[34] T. Xu, E. Sonnenthal, N. Spycher, and K. Pruess, "TOUGHREACT—A simulation program for non-isothermal multiphase reactive geochemical transport in variably saturated geologic media: Applications to geothermal injectivity and CO_2 geological sequestration," *Computers & Geosciences*, vol. 32, pp. 145–165, 2006.

[35] T. Xu, N. Spycher, E. Sonnenthal, L. Zheng, and K. Pruess, "TOUGHREACT user's guide: a simulation program for non-isothermal multiphase reactive transport in variably saturated geologic media, Version 2.0," Earth Sciences Division, Lawrence Berkeley National Laboratory University of California, Berkeley, CA, USA, 2012.

[36] K. Pruess, C. Oldenburg, and G. Moridis, "TOUGH2 user's guide, Version 2.0," Lawrence Berkeley Laboratory Report LBL-43134, Berkeley, CA, USA, 1999.

[37] N. Spycher and K. Pruess, "CO_2-H_2O mixtures in the geological sequestration of CO_2. II. Partitioning in chloride brines at 12–100∘C and up to 600 bar," *Geochimica et Cosmochimica Acta*, vol. 69, pp. 3309–3320, 2005.

[38] T. J. Wolery, "Software package for geochemical modeling of aqueous system: Package overview and installation guide (version 8.0)," Lawrence Livermore National Laboratory Report UCRL-MA-110662 PT I, Livermore, California, USA, 1992.

[39] L. André, M. Azaroual, and A. Menjoz, "Numerical simulations of the thermal impact of supercritical CO_2 injection on chemical reactivity in a carbonate saline reservoir," *Transport in Porous Media*, vol. 82, pp. 247–274, 2010.

[40] Y. Wang, *The Research Report of the Shenhua 0.1 Mt CCS Demonstration Project*, The Appraisal Meeting of the Shenhua 0.1 Mt CCS Demonstration Project, Ordos, China, 2014.

[41] M. T. van Genuchten, "A closed-form equation for predicting the hydraulic conductivity of unsaturated soils," *Soil Science Society of America Journal*, vol. 44, no. 5, pp. 892–898, 1980.

[42] A. T. Corey, *The Interrelation between Gas and Oil Relative Permeabilities*, 1954.

[43] H. Wang, "Study on the interaction of CO_2 fluid with sandstone in Shiqianfeng," *Jilin University*, 2012.

[44] X. Yang, *Experimental study of CO_2 fluid on the geological transformation of reservoir sandstone. In*, Jilin University, 2012.

[45] Y. Tao, *Experimental study on the interaction of CO_2/CO_2-H_2S fluid with sandstone in Liujiagou*, Jilin University, 2013.

[46] T. Xu, J. A. Apps, and K. Pruess, "Numerical simulation of CO_2 disposal by mineral trapping in deep aquifers," *Applied Geochemistry*, vol. 19, pp. 917–936, 2004.

[47] T. Xu, J. A. Apps, and K. Pruess, "Mineral sequestration of carbon dioxide in a sandstone-shale system," *Chemical Geology*, vol. 217, pp. 295–318, 2005.

[48] W. Zhang, Y. Li, T. Xu et al., "Long-term variations of CO_2 trapped in different mechanisms in deep saline formations: A case study of the Songliao Basin, China," *International Journal of Greenhouse Gas Control*, vol. 3, no. 2, pp. 161–180, 2009.

[49] G. Yang, Y. Li, X. Ma, and J. Dong, "Effect of chlorite on CO_2-water-rock interaction," *Earth Science—Journal of China University of Geosciences*, vol. 39, pp. 462–472, 2014.

[50] Y. Wan, *Migration and transformation of CO_2 in CO_2geological sequestration process of Shiqianfeng saline aquifers in Ordos Basin*, Jilin University, 2012.

[51] T. Xu, Y. K. Kharaka, C. Doughty, B. M. Freifeld, and T. M. Daley, "Reactive transport modeling to study changes in water chemistry induced by CO_2 injection at the Frio-I Brine Pilot," *Chemical Geology*, vol. 271, pp. 153–164, 2010.

[52] C. T. Gomez, J. Dvorkin, and T. Vanorio, "Laboratory measurements of porosity, permeability, resistivity, and velocity on Fontainebleau sandstones," *Geophysics*, vol. 75, pp. 191–204, 2010.

[53] A. S. Ziarani and R. Aguilera, "Pore-throat radius and tortuosity estimation from formation resistivity data for tight-gas sandstone reservoirs," *Journal of Applied Geophysics*, vol. 83, pp. 65–73, 2012.

[54] Z. Yan and Z. Zhang, "The effect of chloride on the solubility of calcite and dolomite," *Hydrogeology & Engineering Geology*, vol. 36, pp. 113–118, 2009.

[55] L. Xiao and S. Huang, "Model of thermodynamics for dissolution of carbonate and its geological significances," *Journal of Mineralogy & Petrology*, vol. 23, pp. 113–116, 2003.

[56] Z. Yan, H. Liu, and Z. Zhang, "Influences of temperature and P_{CO_2} on the solubility of calcite and dolomite," *Carsologica Sinica*, vol. 28, pp. 7–10, 2009.

[57] S. M. Amin, D. J. Weiss, and M. J. Blunt, "Reactive transport modelling of geologic CO_2 sequestration in saline aquifers: The influence of pure CO_2 and of mixtures of CO_2 with CH_4 on the sealing capacity of cap rock at 37 degrees C and 100 bar," *Chemical Geology*, vol. 367, pp. 39–50, 2014.

[58] F. Liu, P. Lu, C. Zhu, and Y. Xiao, "Coupled reactive flow and transport modeling of CO_2 sequestration in the Mt. Simon sandstone formation, Midwest U.S.A," *International Journal of Greenhouse Gas Control*, vol. 5, pp. 294–307, 2011.

Hindawi
Geofluids
Volume 2017, Article ID 2759267, 14 pages
https://doi.org/10.1155/2017/2759267

Research Article

On Heat and Mass Transfer within Thermally Shocked Region of Enhanced Geothermal System

Kamran Jahan Bakhsh, Masami Nakagawa, Mahmood Arshad, and Lucila Dunnington

Department of Mining Engineering, Colorado School of Mines, Golden, CO, USA

Correspondence should be addressed to Kamran Jahan Bakhsh; kjahanba@mines.edu

Received 13 January 2017; Revised 14 April 2017; Accepted 26 April 2017; Published 27 July 2017

Academic Editor: Weon Shik Han

An Enhanced Geothermal System (EGS) is an artificially created geothermal reservoir formed by hydrofracturing hot dry rock. Thermal shock occurs when the cold water contacts the hot rock near the injection borehole, creating a network of small, disorganized, closely spaced micro cracks. As the cold-water injection continues, the hot rock cools down and the micro cracks coalesce, becoming a better-defined network of thermal fractures. Thermal fractures in an EGS reservoir are believed to improve reservoir performance by increasing the surface area for heat exchange and lowering flow impedance; however, it is difficult to precisely predict how they grow and affect the permeability of the reservoir. The goal of this paper is to provide an insight into the transport mechanisms within the thin, permeable, thermally shocked region of an EGS reservoir. COMSOL Multiphysics® is used to set up an indealized porous region with identical geometrical features at different domain scales to show the scale dependence of heat and mass transport in the initial microscale crack network and in the later coalesced thermal fractures. This research shows the importance of EGS maturity in determining how heat and mass are transferred and how to select appropriate analytical tools for different stages of development.

1. Introduction

Global demand for electricity generation from alternative energy sources is increasing. More countries are evaluating the potential of geothermal energy as their alternative energy source for electricity generation [1]. An Enhanced Geothermal System (EGS) has the potential to take geothermal energy production to a new level of utility-scale energy production. For the last several decades, starting with the Fenton Hill project, several EGS projects have been developed with the hope of understanding the complex nature of man-made geothermal reservoirs. This type of man-made geothermal reservoir requires a cold-water injection to a hot but dry granitic rock at several kilometers deep to create an artificial reservoir and recover the injected water as hot steam through production wells. Hot dry granitic rocks are easier to find at that depth. One of the main engineering problems has been the inability to connect the injection well with production well that are several hundred meters apart. This is partially due to the lack of our understanding of how the state of stresses from the weight of the overlaying strata and locked-in stresses of the tectonic origin combine to interact with the induced thermal changes. The authors assume that the initial development of thermal fractures caused by the cold-water injection controls the patterns of fracture propagation, as this pattern development will initially define the connecting paths between injection and production wells. Thus, it is important to investigate how heat and mass are transferred in the thermally shocked region and how they will influence the development of reservoir permeability.

Thermal fractures are believed to improve reservoir performance [2–4]. In an EGS reservoir, as the cooling process continues, thermal fractures are widened and penetrate deeper into the hot rock. This stimulation increases the reservoir's ability to transport heat and mass by lowering the flow impedance and by increasing the heat exchange surface areas. Thus far, thermal fractures have not been extensively studied or incorporated into reservoir simulations

because they add another layer of complexity to the modeling; however, their inclusion is vital to understanding the thermal and hydrologic effects of cold-water injection.

Several authors have studied how thermal stresses are developed in brittle materials due to cold-water injection. Chen and Marovelli [5] conducted an experiment to analyze thermal stresses in a rock disk subjected to an external thermal shock. Perkins and Gonzalez [6] as well as Kocabas [7] proposed analytical models to investigate the state of stresses induced by cold fluid injection. Ghassemi et al. [8] developed an integral equation to calculate thermally induced stresses associated with the cooling of a planar fracture in a hot rock. The findings from these studies are relevant to the induced tensile stresses present in the cooled region of the EGS reservoir that stimulate thermal fractures. Another key finding from these studies is the direct correlation between the difference in the applied temperature and the crack density.

A series of studies have also been conducted to understand the mechanical and thermal behavior of thermally induced fractures and their interactions in brittle-elastic materials [9–12]. Nemat-Nasser et al. [13] investigated stability of growing thermal fractures. Barr [14] investigated the branching of thermal fractures by examining the potential of crack propagation away from the surface of the primary fracture in a hot dry rock (HDR) system. Bažant and Ohtsubo [15] as well as Murphy [3] and Barr [14] show that, during the heat extraction process, a network of closely spaced thermal fractures, which resembles a "waffle" grid of grooves [2], is formed adjacent to the primary fractures. One of the common observations of these studies is that the growth patterns of thermal fractures are complex, particularly under the large thermal strain close to the surfaces of primary fractures.

Although these studies present a comprehensive view of the impact of thermal fracturing, thermal fractures have not clearly been integrated into EGS reservoir modeling. In fact, a common practice of reservoir modeling neglects the positive effects of thermal fractures by excluding them from the core structure of simulation, and this exclusion hinders progress towards a better understanding of the contribution of thermal fractures in reservoir performance.

Only a small number of studies have been conducted to investigate the effect of thermal fractures on reservoir performance. Harlow and Pracht [16] were probably the first to integrate thermal fractures into a reservoir model as an additional porosity. Stephenes and Voight [17] show that the presence of thermal stresses lowers the pressure requirement to initiate hydraulic fractures in the reservoir. Tran [18] also indicates that the presence of thermal fractures in a reservoir could change both the shape and aperture of the primary hydraulic fractures, and as a consequence, reservoir performance is affected. Huang et al. [12] developed a quasi-static discrete element model to simulate fracture propagation induced by thermal stresses. Huang et al.'s model of thermal fractures has a significant influence on heat conduction within the rock matrix. These studies highlight the importance of thermal fractures in an EGS reservoir model; however, the heat and mass transport mechanisms within the thermally shocked region of an EGS reservoir have not yet been clearly investigated.

Motivated by these observations, this paper investigates the transport mechanisms within a thermally shocked region to provide a better understanding of the overall heat and mass transport in an EGS reservoir. In response to the cold-water injection, a thin thermally shocked region is formed adjacent to the hydraulically induced fracture. The thermally shocked region initially acts as a transition zone between the hydraulically induced fracture and thermal fractures. The structure of the thermally shocked region and its transport properties can affect overall reservoir performance in two ways: first by controlling the growth behavior of the thermal fractures and second by altering heat transfer from the rock mass to the working fluid. In this study, a porous medium consisting of a solid skeleton and fluid pathways is considered as a conceptual model of the thermally shocked region. The pore-scale approach is adopted, and mathematical formulation and numerical examples are developed to investigate the transport mechanisms within the region of interest.

2. Conceptual Model

Figure 1(a) shows a conceptual model of an EGS reservoir comprising a series of parallel hydraulically induced fractures connected to define a doublet system of an injection and a production well embedded in hot dry crystalline rock. This system is commonly used to characterize an idealized EGS reservoir [2, 20, 21], although the geometrical configuration of the model does not fully portray a realistic EGS reservoir.

As mentioned earlier, the occurrence of the thermal fractures in an EGS reservoir has been proven theoretically and experimentally [3, 5, 13–15]. Their presence has also been acknowledged in induced seismicity studies in several operating geothermal sites [22]. However, thermal fractures are excluded from the geometrical representation of the conceptual model of an EGS reservoir. A representation of the thermally shocked region adopted from earlier studies [3, 10] is shown in Figure 1(b).

This paper focuses on the transport behavior of a thin thermally shocked region adjacent to a hydraulically induced lenticular fracture. The goal of simulation of the thermally shocked region is to generate randomized flow paths at different length scales to gain a better insight into how heat and mass are transported. The thermally shocked region with micro cracks is idealized as a granular porous medium. Following this assumption, MATLAB® was used to generate a random 2D porous region composed of randomly placed, nonoverlapping circles. To this end, the authors are less concerned with the specific shape of particles, as long as the nonoverlapping packing of circular particles can create similar tortuous paths that are created by a collection of small fractures. Various arrangements of clustered and differently sized circles approximate irregular shaped matrix elements. The resulting clusters of randomly sized particles create preferential flow paths that can be used to effectively measure the scale effect on mass transport and temperature distribution.

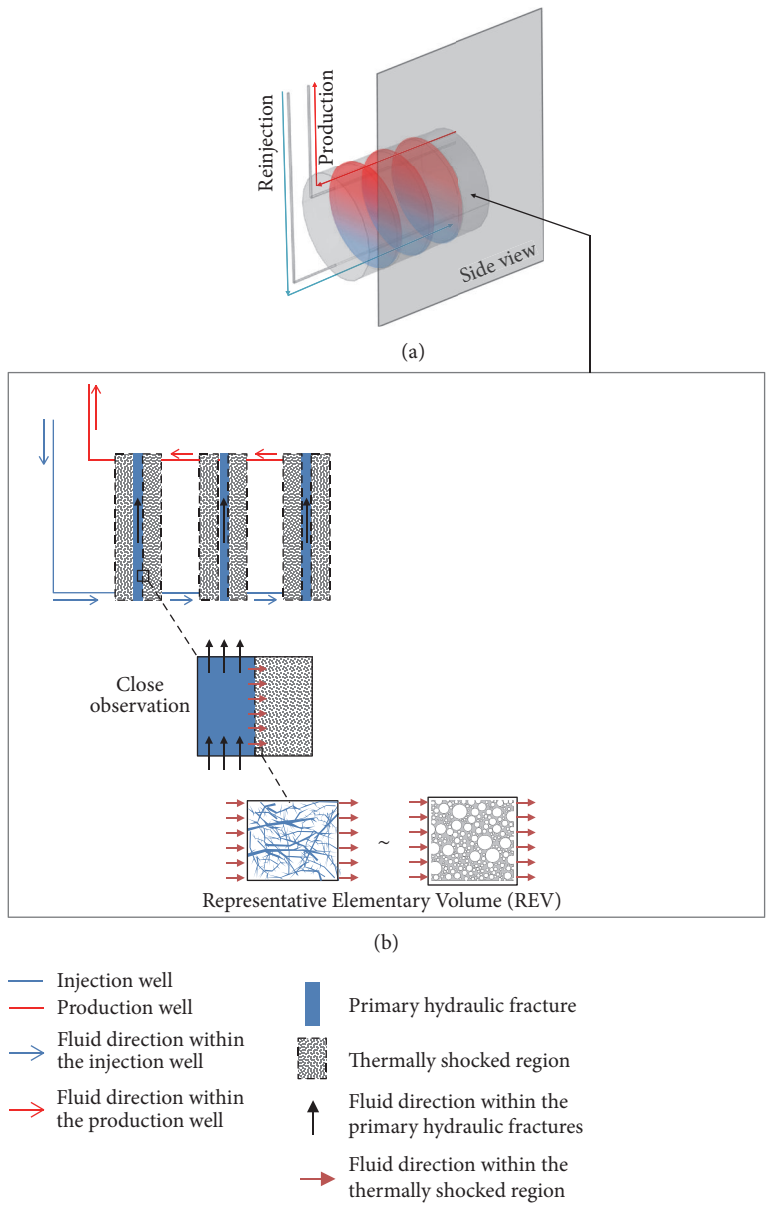

Figure 1: Conceptual model of EGS reservoir (a); side view of the model (b). The width of the hydraulic fractures and thermally shocked regions is exaggerated for clarity.

The degree of fragmentation due to thermal shock depends on several factors, such as the severity of the temperature gradient, the depth of reservoir, the temperature mismatch between the rock and the water at the fracture surfaces, the thermal expansion coefficient, Young's modulus of the rock, and the rate of water circulation [2]. Since we cannot determine the exact density of the fractures within the thermally shocked region, defining a Representative Elementary Volume (REV) with different length scales can be a practical option to characterize the density of the thermal fractures within this region. In this work, we utilize REVs with different side lengths, from 1 mm to 500 mm. The REV with the side length of 1 mm can yield a value representative of the thermally shocked region with the highest density of fractures. Therefore, the REV with the length scale of 1 mm is considered a severely thermally shocked region. Proportionally, a model with the length scale of 100 mm can be considered a moderately thermally shocked region.

The 1 mm scale model represents the initial stage of the thermally shocked region, and the 100 mm represents the latter stage once the cracks have coalesced or the initial region that can be developed when the thermal shock was not severe enough so that fragmentation was coarse. Porous media with length scales lower than 1 mm and larger than 500 mm are beyond the scope of this paper. The former length range may cause nanoscale pore spaces, and the latter may cause an unwanted turbulent flow regime.

3. Contributing Physics

In order to describe the transport mechanisms within the thermally shocked porous region of an EGS reservoir, a set of equations that describe the fluid flow, heat, and mass transport are required. Furthermore, these equations must be coupled to capture the multiphysics nature of the described transport phenomena. In this work, a sequential coupling approach is taken. Initially, fluid flow and mass transport are considered to be the only contributing transport processes without heat transfer. Thus, the connected pore network alone is responsible for fluid and mass transport and they are coupled in an isothermal manner. Later, the solid rock matrix is added in conjunction with the pore network, and the equation of heat transfer is added to the mass transport model to build the sequential coupling for heat and mass transport. This sequentially but fully coupled system is capable of analyzing the nonisothermal transport behavior of a thermally shocked region. The physics of fluid flow, heat, and mass transport in porous media exhibit complex phenomena that stem from different length scales. The transport phenomena in the severely thermally shocked region with many small fractures can be best described by coupling the Navier-Stokes and advection-diffusion equations together with conjugate heat transport. In order to investigate the distinct transport phenomena of different scales, we create computational domains that are geometrically identical but different in scale. In each scale, the small identical Reynolds number assures that the flow is laminar.

4. Pore-Scale Modeling

In this section, we will describe our sequential coupling method to analyze heat and mass transport at the pore-scale.

4.1. Mass Transport (Isothermal Coupling). Following the sequential coupling approach, the physics of fluid flow and mass transport are first coupled. There is no thermal interaction between the fluid in the pore and the solid rock matrix. The flow is assumed to be isothermal single-phase laminar flow, and the Navier-Stokes equation governs the fluid flow. Figure 2 shows the computational domain. Relative Concentrations of mass and temperature arrivals are monitored at discrete locations (A, B, C, and D) of this simulation domain.

$$\rho_f \frac{\partial \mathbf{u}}{\partial t} + \rho_f \mathbf{u} \cdot \nabla \mathbf{u} = -\nabla p + \nabla \cdot \left[\mu \left(\nabla \mathbf{u} + (\nabla \mathbf{u})^T \right) - \frac{2}{3} \mu (\nabla \cdot \mathbf{u}) \mathbf{I} \right] + \mathbf{F}, \quad (1)$$

where ρ_f denotes the density of the fluid (kg/m^3), $\mathbf{u}$ the fluid velocity (m/s), p the pressure (Pa), $\mathbf{F}$ a body force term (N/m^3), and $\mathbf{I}$ the identity matrix. The low-pressure gradient of $\nabla p = (p_i - p_o) = 0.1$ Pascals is applied on the boundaries

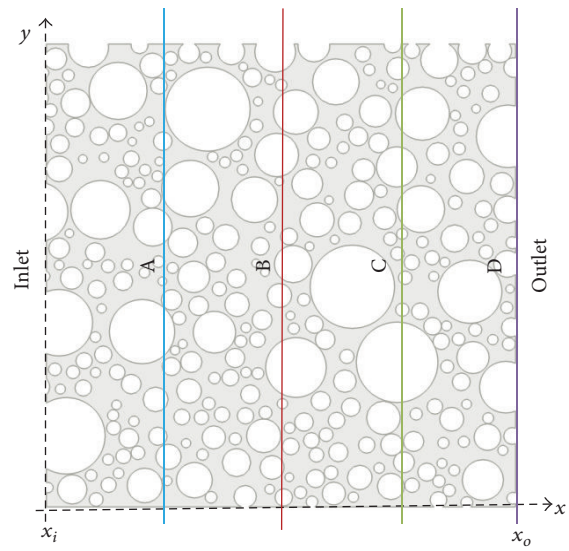

Figure 2: Computational domains adopted for the pore-scale modeling. Reference lines A, B, C, and D divide the computational domain into four equal subdomains.

to keep the flow regime laminar. The initial and boundary conditions can be expressed as

$$\begin{aligned} &\mathbf{u}(x, y, 0) = 0 \quad x, y \in \text{ pore space}, \\ &p(x_i, y, t) = p_i, \\ &p(x_o, y, t) = p_o. \end{aligned} \quad (2)$$

A no-slip boundary condition is applied at the interior walls (solid skeleton surfaces), as well as on the upper and the lower walls. The transient advection-diffusion equation governs transport of nonreactive species of mass in a laminar flow regime.

$$\frac{\partial C}{\partial t} + \nabla \cdot (-D \nabla C) + \mathbf{u} \cdot \nabla C = R, \quad (3)$$

where C denotes mass concentration (mol/m^3), D the diffusion coefficient (m^2/s), $\mathbf{u}$ the velocity (m/s), and R the source or sink term (mol/m^{3}s).

The complex geometry of the pore network in conjunction with the coupling of the contributing physics makes the simulation computationally expensive. To maintain numerical accuracy with a manageable simulation time, a Gaussian profile is given to express the initial condition of the mass transport. For the initial condition, the concentration of the mass within the domain is defined as follows:

$$C(x, y, 0) = C_0 \quad x, y \in \text{ pore space}, \quad (4)$$

$$C_0 = C_{\max} \times \exp\left[1000 \times \left(-\left(\frac{x}{0.5} \right)^2 \right) \right]. \quad (5)$$

According to (5), within the pore-network domain very close to the left boundary (adjacent to the inlet, $x \to 0$), the mass concentration is equal to $C_{\max}$. However, within the rest of the

pore-network domain the mass concentration is almost zero (see Figure 13).

For the boundary conditions, a constant concentration of $C_{\max}$ is applied to the inlet boundary, and the species are transported out of the domain by fluid motion to the right side of the model.

$$C(x_i, y, t) = C_{\max},$$
$$\mathbf{n} \cdot (-D\nabla C) = 0 \quad \text{at outlet, } x_o, \tag{6}$$

where $\mathbf{n}$ is the normal vector, used to identify the component of the mass flux perpendicular to the boundary. All other boundaries, including solid skeleton surfaces and the upper and lower boundaries, are assumed to be insulating boundaries where no mass flows in or out.

$$-D_i \nabla C_i + \mathbf{u} C_i = \mathbf{N}_i,$$
$$\mathbf{n} \cdot \mathbf{N}_i = 0. \tag{7}$$

For a complex flow field geometry such as the one considered here, the Stokes equations do not have simple analytical solutions; however, the transport of species in one dimension has been analytically solved [23–27] and it can be expressed as

$$\frac{C}{C_0} = 0.5\left[\operatorname{erfc}\left(\frac{d - \mathbf{v}\cdot t}{\sqrt{D\cdot t}}\right) + \exp\left(\frac{\mathbf{v}\cdot d}{D}\right)\operatorname{erfc}\left(\frac{d + \mathbf{v}\cdot t}{\sqrt{D\cdot t}}\right)\right], \tag{8}$$

where C/C_0 is the Relative Concentration (RC) defined as the ratio of the species concentration to its initial value at a distance d from the inlet (m), erfc is the complementary error function, $\mathbf{v}$ is the flow speed (m/s), D is the diffusion coefficient (m^2/s), and t is the time (s).

Using (8), the Mass Breakthrough Time (MBT) is calculated against velocity for a given RC value. This RC specific MBT is calculated at the outlet D, that is, the time to travel 1 mm in distance. Two major trends can be observed in Figure 3. First, when the velocity becomes small enough, that is, less than $10E{-}6$ m/s, then MBT for each RC value becomes constant. This is an indication that mass is transported by diffusion, and the MBT depends only on the concentration gradient. On the other hand, when the velocity becomes large enough, MBT values for each RC value merge to a single value that can be calculated as the time that takes the fluid velocity to travel 1 mm in distance. This is the indication that the mass is now transported along the movement of fluid. More specifically, for example, for RC of 0.1, the MBT due to pure diffusion can be found by reading off the value for the point where the plotted red line intersects with the smallest velocity value. On the other hand, the MBT due to pure advection can be found as the point where the red line intersects with the largest velocity value. Any MBT between these two extremes are due to the combined effect of diffusion and advection. The precise contribution of each effect is unknown. However, it is clear from Figure 3 that, for slower velocities, the MBT is influenced more by the diffusional mass transfer. Here,

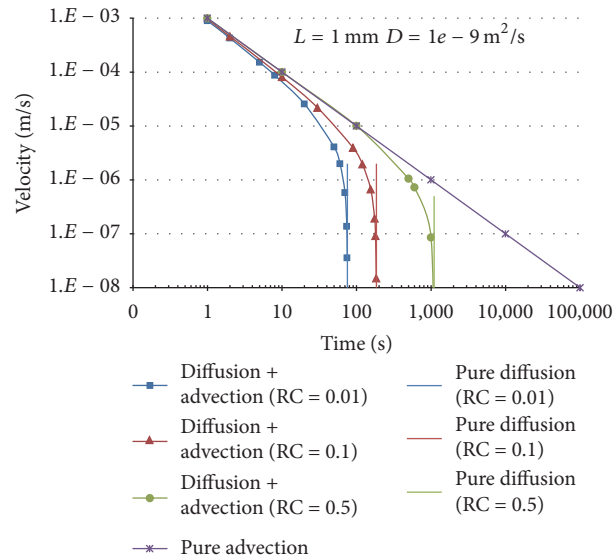

Figure 3: Mass Breakthrough Time (MBT) as a function of velocity for pure diffusion, diffusion with advection, and pure advection (analytical solution for the case with scale length of 1 mm, modified from [19]).

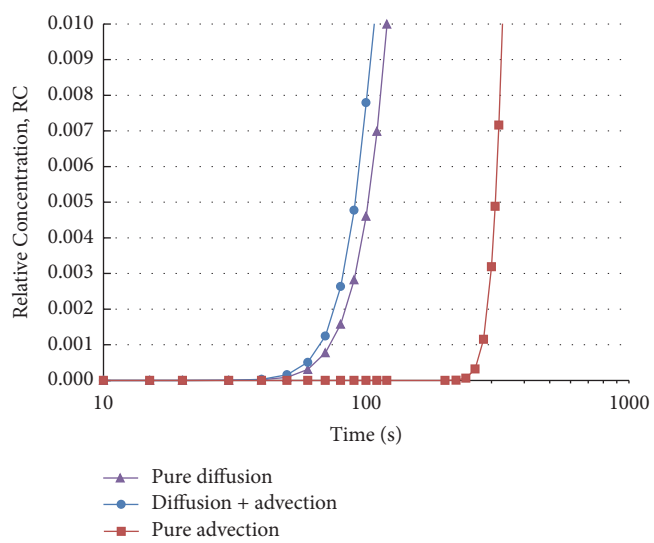

Figure 4: Relative Concentration (RC) over time at the outlet for pure diffusion, diffusion with advection, and pure advection (numerical solution for the case with length scale of 1 mm).

only the case with the length scale of 1 mm is considered for validation. It is noted that the coefficient of diffusion is assumed to be equal to that of self-diffusion (or tracer-diffusion) of water, $1E - 9$ m^2/s.

In Figure 3, based on our theoretical analysis, we show which transport mechanisms are at work for a given velocity and Relative Concentration. Now, the model is validated by measuring the RC values as the flow passes through the outlet D (see Figure 2). Figure 4 shows that, for a given RC value, the MBT is the shortest when both diffusion and advection participate in transfer mechanisms and the longest when pure

advection controls the dispersion. It is also noted that, for the advection dominated flow, the mass passes the outlet D with a large concentration gradient.

4.2. Heat and Mass Coupled Transport (Nonisothermal). A fully coupled nonisothermal, transient model is needed to capture the transport phenomena within the thermally shocked porous region of the EGS. Unlike the isothermal coupling model where only the fluid phase in the pore network was responsible for mass transport, for the nonisothermal coupled case, both the pore fluid network and solid rock matrix participate in heat and mass transfer. The conjugate heat transport concept [28] is used to couple the physics of heat transfer in both domains.

It is assumed that heat is transferred within the solid matrix only due to conduction; therefore, Fourier's law can define the temperature field in this domain.

$$\rho_r C_{P_r} \frac{\partial T}{\partial t} = \nabla \cdot (k_r \nabla T) + Q, \tag{9}$$

where $\rho_r C_{P_r}$ is the effective volumetric heat capacity of the solid phase at constant pressure (J/m$^{3\circ}$C) and k_r is the thermal conductivity of the solid (J/ms$^\circ$C). In the pore fluid network, the energy equation is modified to reflect the influence due to viscous effect and the temperature-dependent pressure work. Accordingly, the following equations are used to govern the energy transport in the system:

$$\rho_f C_{P_f} \frac{\partial T}{\partial t} + \rho_f C_{P_f} \mathbf{u} \cdot \nabla T + \nabla \cdot \mathbf{q} = Q, \tag{10}$$

$$\mathbf{q} = -k_f \nabla T, \tag{11}$$

where $\rho_f C_{P_f}$ indicates the effective volumetric heat capacity of the fluid at constant pressure (J/m$^{3\circ}$C), k_f the thermal conductivity of fluid (J/ms$^\circ$C), and $\mathbf{u}$ the fluid velocity. Initial and boundary conditions are applied as follows:

$$\begin{aligned} &T_s(x, y, 0) = T_f(x, y, 0) = T_0 \\ &\qquad\qquad x, y \in \text{both domains}, \\ &T_0 = (T_{\max} - T_{\text{in}}) \\ &\quad \times \left[1 - \exp\left[1000 \times \left(-\left(\frac{x}{0.5}\right)^2\right)\right]\right] \\ &\quad + T_{\text{in}}. \end{aligned} \tag{12}$$

A constant temperature of T_{in} is prescribed at the inlet. It is also assumed that there is no heat flux across the upper and lower boundaries.

$$\begin{aligned} &T_f(x_i, y, t) = T_{\text{in}} \quad x, y \in \text{pore network}, \\ &-\mathbf{n} \cdot \mathbf{q} = 0. \end{aligned} \tag{13}$$

By accommodating these coupled equations in the numerical model, COMSOL Multiphysics was used to numerically study coupled heat and mass transport phenomena in a complex fractured rock. COMSOL Multiphysics is a Finite Element (FE) simulation software, well suited for simulating mechanical-thermal-hydrological coupled problems. The computational domain of interest is discretized explicitly for both pore-network and solid rock domains. Time is also discretized by utilizing the Backward Differentiation Formula (BDF) time stepping method. The BDF is a family of implicit, linear multistep methods used to numerically integrate ordinary differential equations, and its transient solver is both stable and versatile and provides extra robustness required for transport applications. Parameters used in the simulation are listed in Table 1. For more details on the numerical model and the initial and boundary conditions see Appendix.

Table 1: Parameters used in the simulation.

Parameter	Symbol	Value/unit
Solid phase		
Thermal conductivity	k_r	2.9 W/(m K)
Heat capacity	C_{P_r}	850 J/(kg K)
Density	ρ_r	2600 kg/m^3
Porosity	ε	0.431
Fluid (water)		
Thermal conductivity	k_f	0.6 W/(m K)
Heat capacity	C_{P_f}	Function of temperature (see Appendix)
Density	ρ_f	
Dynamic viscosity	μ	
Inflow temperature	T_{in}	15°C
Initial temperature	T_0	85°C

5. Results and Discussion

Fully coupled models were simulated at the domain length scales of 1 and 100 mm. A small pressure difference of 0.1 Pa between the inlet and outlet quickly led to a steady-state condition. Due to the Venturi effect, fluid velocity locally increases as the fluid passes through constrictions and evolves to an uneven flow field. The fluid velocity in the preferential paths is higher and rapidly drops to almost zero as the fluid diverts from the preferred paths to locally stagnant regions. The flow patterns of the preferred flow paths for both length scales are identical. Although the flow patterns are identical to both domain length scales because the local velocity gradients define flow paths, the values are different by two orders of magnitude proportional to the scale of the domain, as can be seen in Figure 5. In the following discussion of the results, the mass that is dispersed is interpreted as a tracer.

Figure 6 shows the transport of a tracer (as an example of mass transport) within the pore network for both domain length scales. The RC value of 0.5 measured at the center line B is used as a criterion to define this specific MBT for both length scales. For the model with the domain length scale of 1 mm, it takes about 300 seconds for the tracer to reach the RC of 0.5 at B, whereas, for the model with the length scale of 100 mm, it takes about 500 seconds. It is important to note

Table 2: The average velocity, Reynolds number, and Péclet number of different length scales.

Length scale l (mm)	Average velocity $\bar{\mathbf{u}}$ (m/s)	Reynolds number Re	Péclet number (Pe)	
			For mass	For heat
1	$7.53E-07$	$1.36E-03$	0.75275	$4.87E-03$
2	$1.51E-06$	$5.44E-03$	3.0108	$1.95E-02$
3	$2.26E-06$	$1.22E-02$	6.7737	$4.39E-02$
5	$3.76E-06$	$3.40E-02$	18.82	$1.22E-01$
10	$7.53E-06$	$1.36E-01$	75.324	$4.88E-01$
20	$1.50E-05$	$5.43E-01$	300.4	$1.94E+00$
30	$2.33E-05$	$1.27E+00$	700.44	$4.54E+00$
50	$3.84E-05$	$3.47E+00$	1922.25	$1.24E+01$
100	$7.72E-05$	$1.40E+01$	7720.9	$5.00E+01$
500	$3.99E-04$	$3.60E+02$	199455	$1.29E+03$

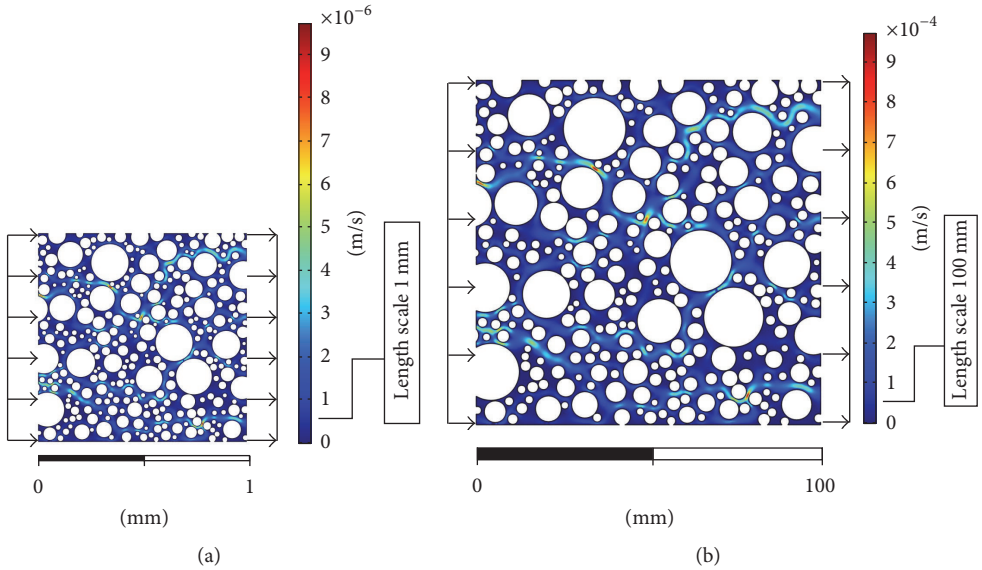

Figure 5: Velocity field in thermally shocked regions. 1 mm and 100 mm domain length scale models are shown on (a) and (b), respectively. There are two orders of magnitude difference in the velocity.

that there is a significant difference in the way the tracer is spatially dispersed. For the 1 mm domain length scale, the tracer transport is distributed uniformly across the domain with a flat propagating concentration front, while, for the 100 mm scale model, unevenly propagating tracer front with preferential paths can clearly be observed. This difference clearly shows that, at the smaller domain scale, the tracer is dispersed by diffusion due to the concentration gradient, and at the larger scale, mass is dispersed by advection. It is reminded that similar flow patterns do not assume similar mass transport. As shown in Table 2, the Reynolds numbers for flows at 1 and 100 mm scales are $1.36E-3$ and 1.40 m/s, respectively. In both scales, the flow is extremely slow and laminar.

Figure 7 shows how temperature is transported at both domain scales. While the fluid with lower temperature sweeps the rock domain with a higher initial temperature, thermal energy is transported through conduction in the rock matrix and through both conduction and convection in the pore network. The Relative Temperature (RT) is defined as the ratio of the current temperature to its initial value, and the RT value of 0.5 at B is used to define the Temperature Breakthrough Time. Results in Figure 7 indicate that, for the model with the length scale of 1 mm, the average temperature at B achieves the criterion in less than 1 (0.26 sec) second of the cold fluid injection. However, for the model with domain length scales of 100 mm, it takes 471 seconds for the RT to reach the value of 0.5 at B. It is noted that, for the smaller geometry, heat is transported uniformly across the model with a straight temperature propagation front, while, for the larger geometry, an uneven heat front can clearly be observed. This difference can also be explained based on (10). In the

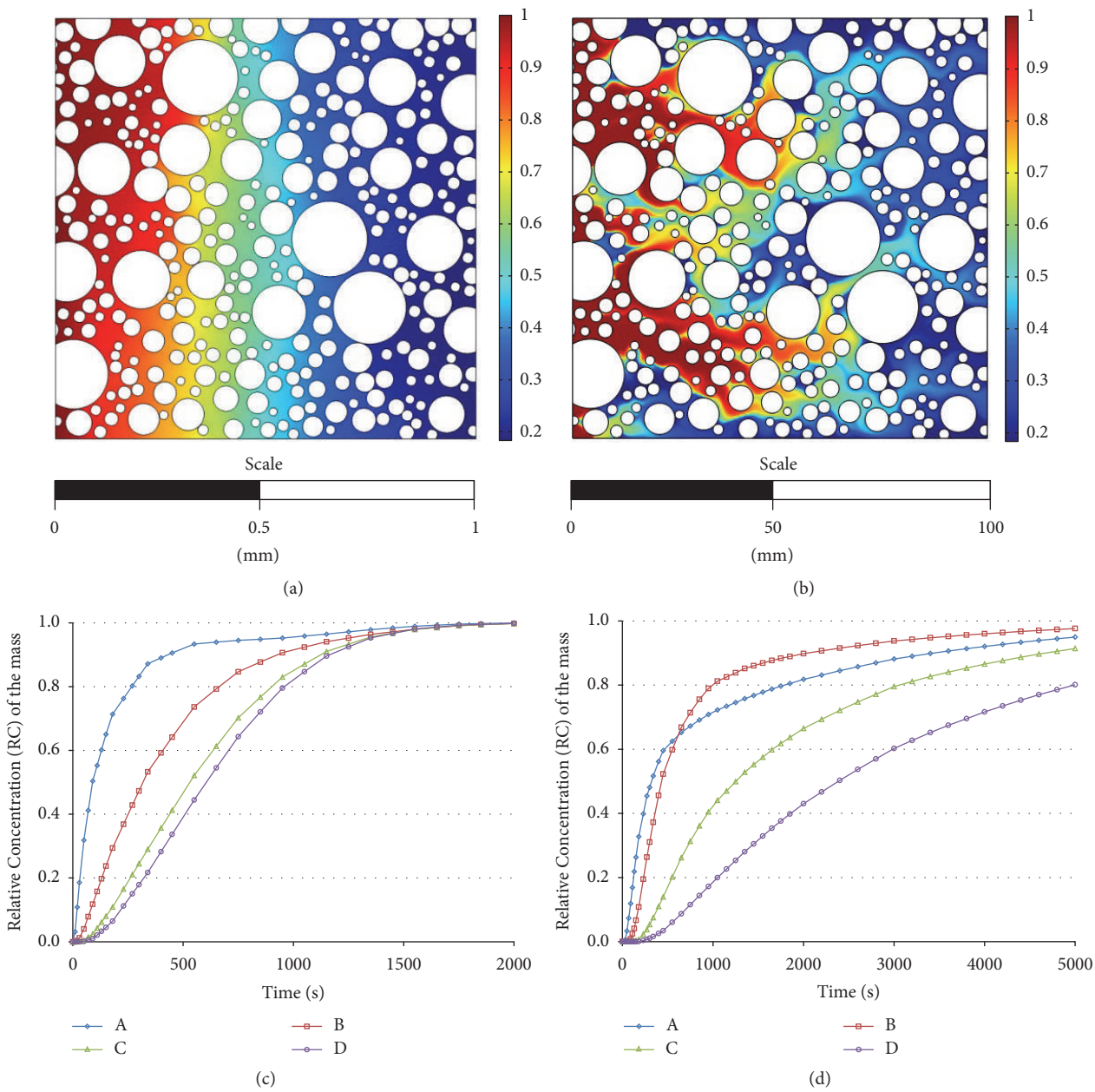

Figure 6: Relative Concentration (RC) of the tracer within each scale domain. For the model with the length scale of 1 mm (a), it takes 306 seconds for the tracer to reach the Relative Concentration of 0.5 at the center line B, whereas, for the model with the length scales of 100 mm (b), it takes 500 seconds. Evolution of the Relative Concentration (RC) over time at reference lines for models with the length scale of 1 mm (c) and 100 mm (d).

case with the length scale of 100 mm, the energy transported by the fluid motion is dominant, whereas, in the case with 1 mm scale length, the dominant heat transport mechanism is conduction.

Table 2 summarizes which mechanisms are dominant for heat and mass transport at each domain scale. It is noted that the small Reynolds numbers indicate that the flow remains laminar at all scales, and furthermore for the domain length scale up to a few millimeters, the given pore structure produces a Stokes flow with creeping motion. The Reynolds number defines the relative influence between inertial and viscous resistance on flow behavior. The Péclet number (Pe) was also calculated to define the ratio of the rate of advection to the rate of diffusion of the same physical quantity driven by an appropriate gradient. In the context of mass transfer, the Péclet number is calculated as the product of the Reynolds number and the Schmidt number. In the context of heat transfer, the Péclet number is equivalent to the product of the Reynolds number and the Prandtl number. As can be seen in Figure 8, mass transfer is dominated by diffusion for the length scale of 1 mm but as the length scale increases, mass transfer due to advection quickly becomes more dominant.

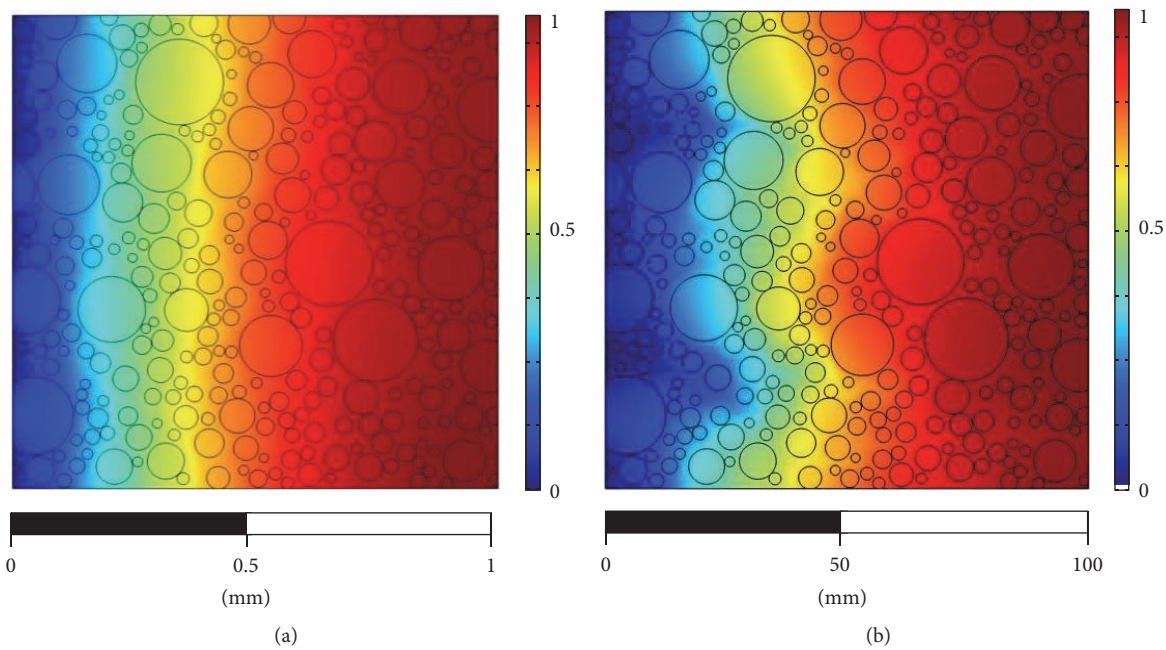

Figure 7: Relative Temperature (RT) within the computational domain. For the model with the length scale of 1 mm (a) it takes 0.26 seconds for the heat to reach the Relative Temperature of 0.5 at the center of the domain, whereas for the model with the length scale of 100 mm (b) it takes 471 seconds.

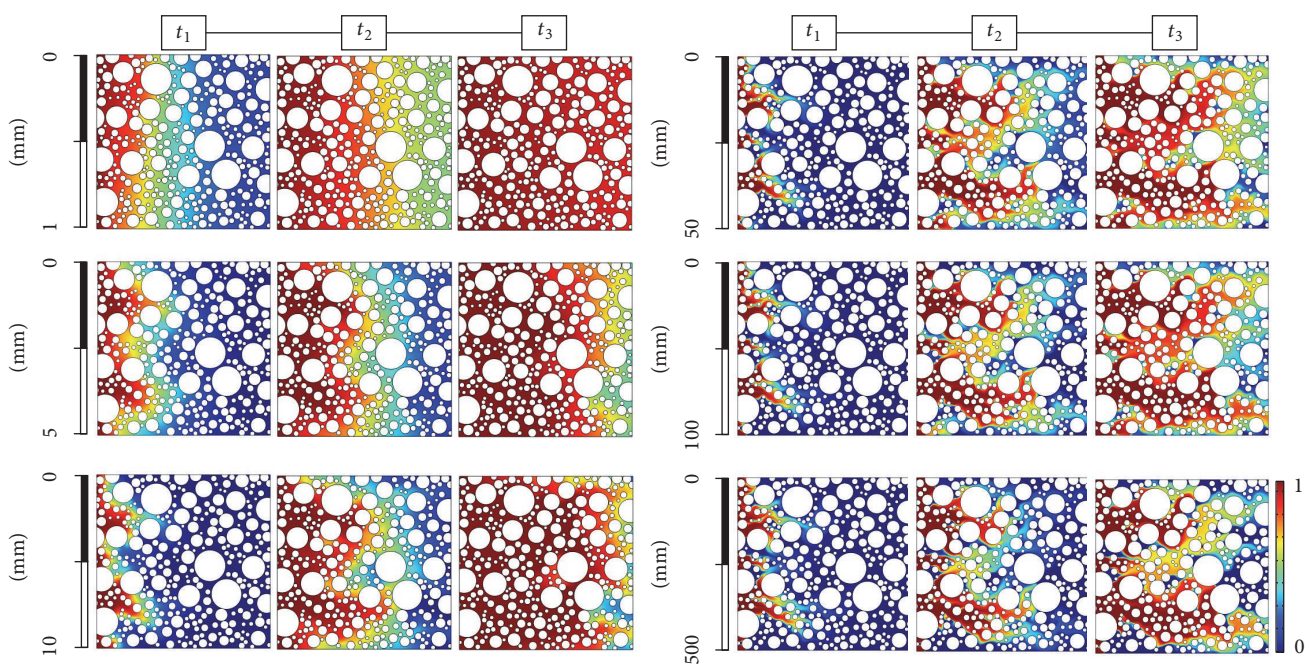

Figure 8: Relative Concentration (RC) of the mass (tracer) for the model with the length scale of 1, 5, 10, 50, 100, and 500 mm.

On the other hand, heat transfer remains diffusion dominated up to the scale of 10 mm, whereas advection and diffusion are equally important for the length scales between 10 and 30 mm, and beyond the length scale of 50 mm, heat transfer will be dominated by advection (Figure 9). In summary, for the flow considered here at different domain length scales, advection has a greater influence on how mass is transported for length scales for a few millimeters or greater. However, the way heat is transported goes through three different combinations of mechanisms, and they are diffusion up to around 10 mm, advection-diffusion between 10 and 30 mm, and advection greater than 50 mm of domain length scales.

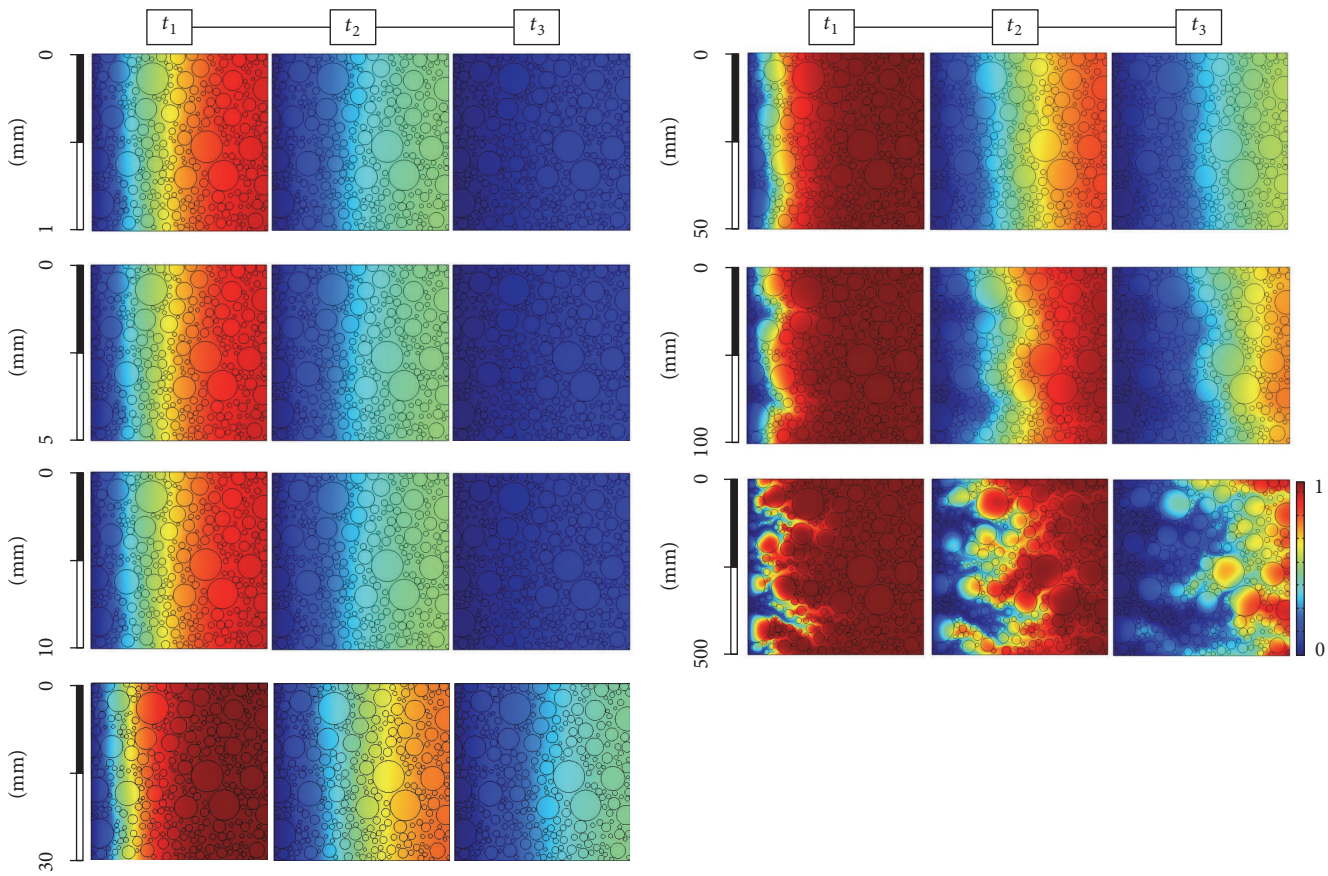

Figure 9: Relative Temperature (RT) for the model with the length scale of 1, 5, 10, 30, 50, 100, and 500 mm.

5.1. Thermal versus Mass Breakthrough Time. Quantitative criteria to assess EGS reservoir performance are divided into two groups. The criteria are used to judge the hydraulic performance and those that evaluate the thermal performance of the EGS reservoir. Mass Breakthrough Time (MBT) and Thermal Breakthrough Time (TBT) are usually used to identify the distribution of fluid residence times within the reservoir and temperature decline in the recovery as a function of time. The MBT and TBT have been used in the previous sections of this paper to evaluate the thermal and transport properties in the different scale studies.

The scale of the thermally shocked region and its transport properties can affect overall reservoir performance. Comparing MBT and TBT at different length scales can give a better understanding of the transport mechanism within a specific region and its effect on overall EGS performance.

Figure 10 shows the mass and heat breakthrough times at the outlet for the length scales of 1 and 100 mm. Results show that, for the case with the length scale of 1 mm (Figure 10(a)), heat transport is much faster than mass transport. For example, it takes 193 seconds for the mass to reach RC of 0.1 at the outlet; however, for the heat, it takes less than one second to reach a RT of 0.9 at the outlet. For both cases, the time for 10% of the original concentration of mass (tracer) or temperature to reach at the outlet was measured. Three orders of magnitude difference in breakthrough times of heat and mass indicate the critical role of diffusion at the model with the length scale of 1 mm. For the case with the length scale of 100 mm, the mass transport is faster than the heat; however, unlike the smaller scale, heat and mass transport operate on the same order of magnitude (Figure 10(b)). For example, it takes 529 seconds for mass to reach the RC of 0.1 at the outlet of the model. The time for the RT of 0.9 at the outlet is about 844 seconds. Unlike the smaller case, the role of advection is pronounced in the model with the length scale of 100 mm.

6. Conclusion and Recommendation

The mechanisms of the heat and mass transport within a thermally shocked region of an EGS reservoir were studied. In this numerical study, the thermally shocked region adjacent to the primary hydraulic fractures was assumed to be a porous medium. A pore-scale simulation approach was considered to study its applicability and limitations in capturing coupled transport physics of heat and mass. For the pore-scale modeling, mass and heat transfer at two domain length scales of 1 and 100 mm were considered to represent a thermally shocked region with two different degrees of fragmentation or fracture coalescence. Using the COMSOL platform, contributing physical laws were sequentially coupled to capture

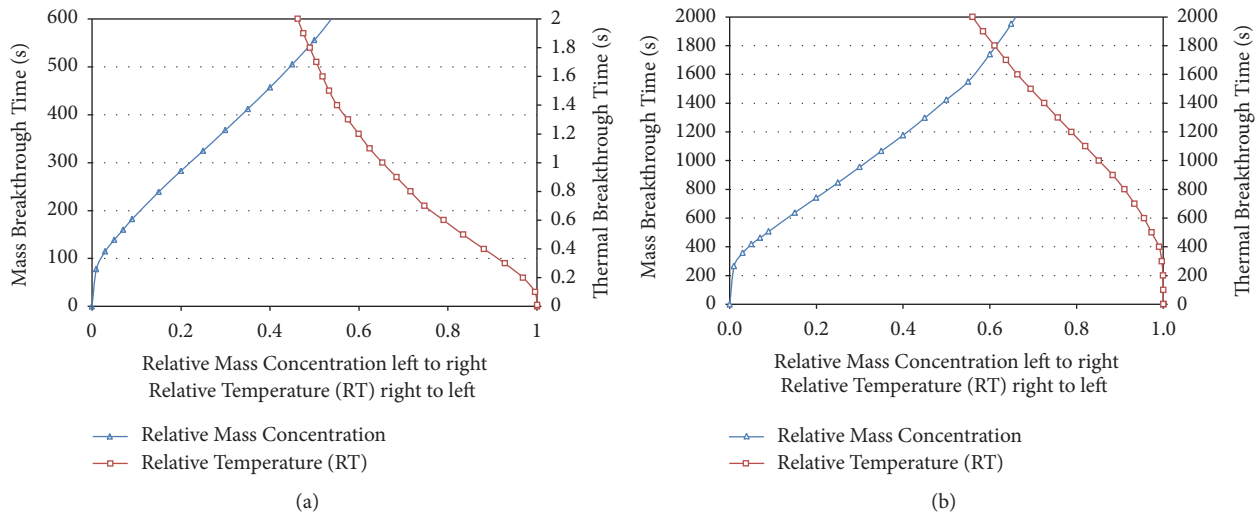

Figure 10: Relative Concentration (RC) of the mass and Relative Temperature (RT) of the fluid at the outlet as a function of time: model with the length scale of 1 mm (a) and model with the length scale of 100 mm (b).

multiphysics features of the problems investigated. The results showed that, for the severely thermally shocked region represented by the domain length scale of 1 mm, diffusion is responsible for both heat and mass transfer. The TBT was found to be three orders of magnitude faster than the MBT. In other words, the ratio of thermal diffusivity to molecular diffusivity was also found to be 10^3 for this model. This ratio can determine the relationship between heat and mass transfer in a diffusion-dominated small system where the flow speed is insignificant. The pore-scale simulation results also indicate that, for a moderately thermally shocked region represented by the domain length scale of 100 mm, mass transfer is mainly accomplished by advection, but heat is transferred via both fluid motion and conduction. Thermal and Mass Breakthrough Times were found to be in the same orders of magnitude.

Although a simple model has been presented in this paper, the results of pore-scale analyses confirm that the transport behavior of the thermally shocked region of an EGS strongly depends on the degree of fragmentation. In actual field cases, one can identify the following appropriate regions of an EGS reservoir where the presented pore-scale analysis may be beneficial:

(i) Near the injection point of water: this is where intense cooling on the surface of the primary hydraulic fracture produces a thin thermally shocked region with a high degree of fragmentation (i.e., higher fracture density).

(ii) Near the production point of hot water: this is where the cooling effect becomes less intense, and the adjacent thermally shocked region is less fragmented.

(iii) Early stage of EGS fluid circulation: this is when the thermal front advances very rapidly along the primary hydraulic fracture and isotherms in the rock matrix are parallel to the main hydraulic fracture.

(iv) Later stage of EGS fluid circulation: this is when the cold front penetrates more into the rock matrix and isotherms in the rock matrix become perpendicular to the main hydraulic fracture.

Differences in the transport behavior of the thermally shocked region due to the variation in its fragmentation may cause temporally and spatially sensitive behavior in the reservoir as speculated above. The exact fragment geometry of the inside of an EGS reservoir will never be known, but incorporating representative elements into a reservoir simulation may help more accurately depict and predict the heat and mass transport processes in the EGS circulation system.

Appendix

Numerical Model Description

The computational domain in COMSOL Multiphysics was created in 2D space dimension. In the direct pore-scale approach, the geometry is discretized explicitly for both pore network and solid phases. As shown in Figure 11 the domain is discretized spatially with triangular elements for both pore network and solid skeleton subdomains. Table 3 shows the statistics of the elements. Time is also discretized by utilizing the Backward Differentiation Formula (BDF) time stepping method. The initial time step size is set to 0.001 and as the simulation approaches the convergence, the time steps are increased incrementally to the value of 0.1 s and step size of 0.1 seconds is kept to the end of simulation.

The pore network was assumed to be fully saturated with water and the granite with predefined properties was designated as the solid domain. The properties of the assigned fluid, such as heat capacity, density, and thermal conductivity, were assumed to be temperature dependent (Figure 12) while the properties of the solid phases were considered constant.

Table 3: Statistics of the elements.

Elements	Statistics	Element quality histogram
Type of elements	Triangle	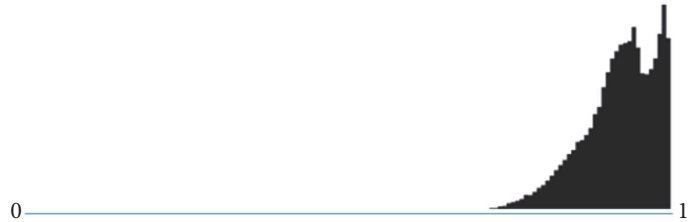
Number of elements	102956	
Minimum element quality	0.003662	
Average element quality	0.9204	
Element ratio area	$6.66E-5$	
Maximum growth rate	3.412	
Average growth rate	1.395	

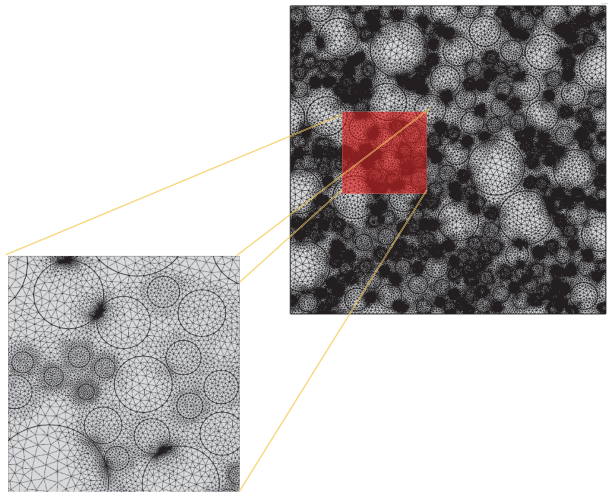

Figure 11: The mesh scheme of model domain utilized in the numerical simulation.

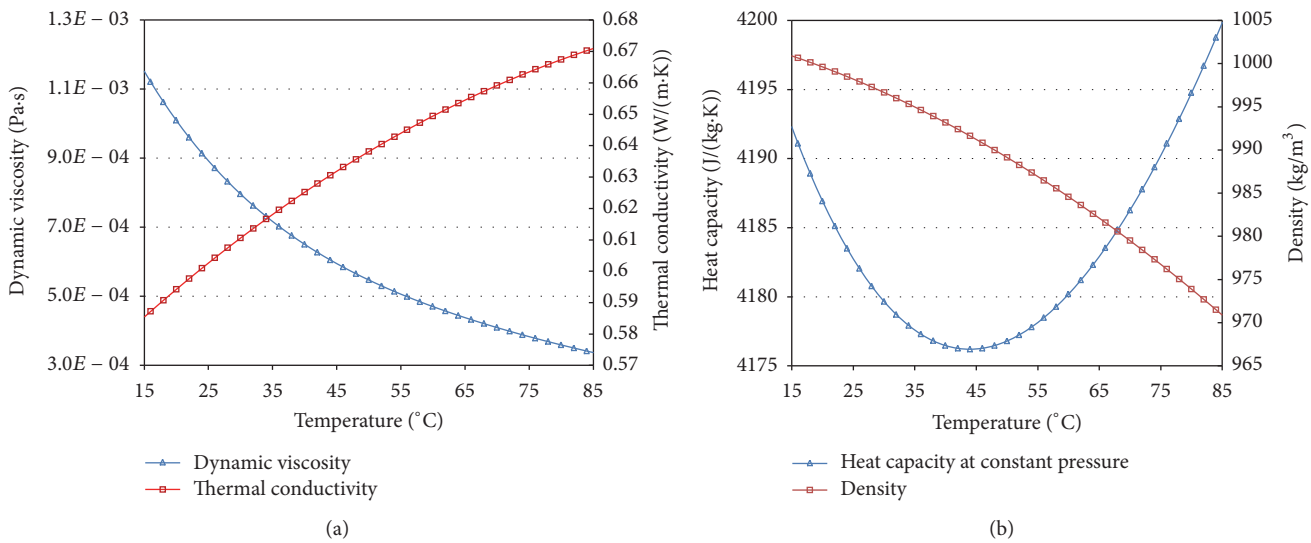

Figure 12: Properties of the fluid as a function of temperature. (a) Dynamic viscosity (blue curve) and thermal conductivity (red curve). (b) Heat capacity at constant pressure (blue curve) and density (red curve).

The values of the basic properties of the solid phases are $\rho_r = 2600\,\mathrm{kg/m^3}$, $C_{p_r} = 850\,\mathrm{J/(kg\,^\circ C)}$, and $k_r = 2.9\,\mathrm{W/(m\,^\circ C)}$. An unstructured triangular mesh was created for both solid and pore-network domains. The mesh is adequately sized and is refined at the region adjacent to the inlet where both the species and temperature gradients are higher. The element size of the pore network and solids is calibrated according to the contributing physics, and the average element quality of

Table 4: The initial and boundary conditions for the fluid flow, mass, and heat transport.

Physics	Initial conditions	Boundary condition	
Fluid flow	$\mathbf{u}(x, y, t = 0) = 0$	$p(x_i, y, t) = p_i$	At boundary (1)
	$x, y \in$ pore space	$p(x_o, y, t) = p_o$	At boundary (2)
		$\mathbf{u} = 0$	No-slip boundaries (3) and (4)
		$\mathbf{u} = 0$	No-slip boundary (5)
Mass transport	$C(x, y, t = 0) = C_0$	$C(x_i, y, t) = C_{\max}$	At boundary (1)
	$x, y \in$ pore space	$\mathbf{n} \cdot (-D\nabla C) = 0$	At boundary (2)
	$C_0 = C_{\max} \times \exp\left[1000 \times \left(-\left(\frac{x}{0.5}\right)^2\right)\right]$	$-D_i \nabla C_i + \mathbf{u} C_i = \mathbf{N}_i$	No flow at boundaries (3), (4), and (5)
		$\mathbf{n} \cdot \mathbf{N}_i = 0$	
Heat transport	$T_s(x, y, 0) = T_f(x, y, 0) = T_0$	$T_f(x_i, y, t) = T_{\text{in}}$	At boundary (1)
	$x, y \in$ both domains	$-\mathbf{n} \cdot (-k\nabla T) = 0$	At boundary (2)
	$T_0 = (T_{\max} - T_{\text{in}}) \times \left[1 - \exp\left[1000 \times \left(-\left(\frac{x}{0.5}\right)^2\right)\right]\right] + T_{\text{in}}$	$-\mathbf{n} \cdot \mathbf{q} = 0$	No heat flux at boundaries (3) and (4)
Boundary conditions at locations (1) Inlet (2) Outlet (3) Lower wall (4) Upper wall (5) Interior wall (solid skeleton surfaces)			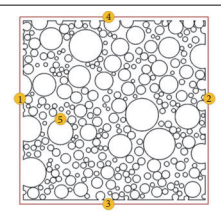

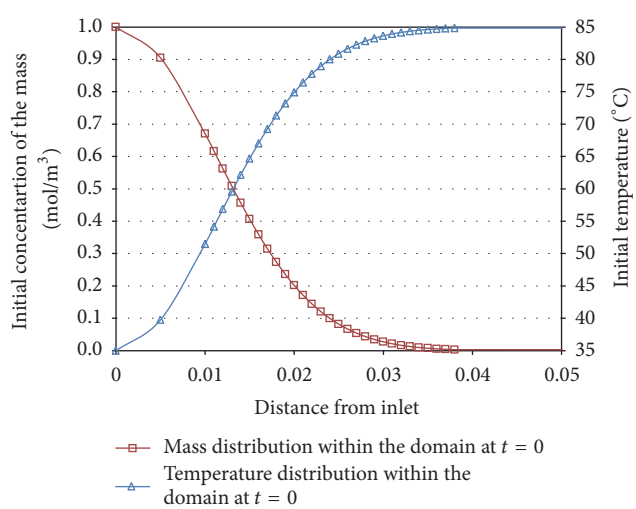

Figure 13: The initial condition for both physics of mass and heat transport.

the mesh for both 1 and 100 mm models is computed higher than 0.94. The porosity of the generated domain is calculated through dividing the integration of the pore-network region by the length and width of the structure:

$$\varepsilon_p = \frac{1}{L_1 L_2} \int_0^{L_1} \int_0^{L_2} 1 \, dx \, dy, \tag{A.1}$$

where L_1 and L_2 denote dimensions of the computational domain in x and y directions. The porosity results in a value of 0.431.

As mentioned, to avoid high numerical dispersion, a gradual profile was given to express the initial condition for both the physics of heat and mass transport (Figure 13). The initial mass concentration everywhere in the domain is zero except in the vicinity of the inlet where the concentration is equal to the inlet concentration. The initial temperature was also assumed to be 85°C everywhere, except adjacent to the inlet where the temperature is assigned to be the same as the inlet temperature. Table 4 describes the initial and boundary conditions for the fluid flow, mass, and heat transport.

Conflicts of Interest

The authors declare that there are no conflicts of interest regarding the publication of this paper.

References

[1] E. Huenges, *Geothermal Energy Systems—Exploration, Development, and Utilization*, Wiley-VCH Verlag GmbH & Co. KGaA, Weinheim, Germany, 2010.

[2] H. Armstead and J. Tester, *Heat Mining*, E. & F. N. Spon Ltd, New Fetter Lane, London, UK, 1987.

[3] H. Murphy, "Thermal stress cracking and the enhancement of heat extraction from fractured geothermal reservoirs," in *Proceedings of the Geothermal Resources Council Meeting*, Hilo, Hawaii, USA, 1978.

[4] S. Tarasovs and A. Ghassemi, *Propagation of a System of Cracks under Thermal Stress*, American Rock Mechanics Association, San Francisco, Calif, USA, 2011.

[5] T. S. Chen and R. L. Marovelli, *Analysis of Stresses in a Rock Disk Subjected to Peipheral Thermal Shock*, U.S. Dept. of The Interior, Bureau of Mine, Washington, DC, USA, 1966.

[6] T. Perkins and J. Gonzalez, "The effect of thermoelastic stresses on injection well fracturing," *Society of Petroleum Engineers Journal*, vol. 25, no. 01, pp. 78–88, 2013.

[7] I. Kocabas, "An analytical model of temperature and stress fields during cold-water injection into an oil reservoir," *SPE Production and Operations*, vol. 21, no. 2, pp. 282–292, 2006.

[8] A. Ghassemi, S. Tarasovs, and A. H.-D. Cheng, "Integral equation solution of heat extraction-induced thermal stress in enhanced geothermal reservoirs," *International Journal for Numerical and Analytical Methods in Geomechanics*, vol. 29, no. 8, pp. 829–844, 2005.

[9] J. F. Geyer and S. Nemat-Nasser, "Experimental investigation of thermally induced interacting cracks in brittle solids," *International Journal of Solids and Structures*, vol. 18, no. 4, pp. 349–356, 1982.

[10] H.-A. Bahr, G. Fischer, and H.-J. Weiss, "Thermal-shock crack patterns explained by single and multiple crack propagation," *Journal of Materials Science*, vol. 21, no. 8, pp. 2716–2720, 1986.

[11] H.-A. Bahr, H.-J. Weiss, U. Bahr et al., "Scaling behavior of thermal shock crack patterns and tunneling cracks driven by cooling or drying," *Journal of the Mechanics and Physics of Solids*, vol. 58, no. 9, pp. 1411–1421, 2010.

[12] H. Huang, M. Plummer, and R. Podgorney, "Simulated evolution of fractures and fracture networks subject to thermal cooling: a coupled discrete element and heat conduction model," in *Proceedings of the Thirty-Eighth Workshop on Geothermal Reservoir Engineering*, Standford, Calif, USA, February 2013.

[13] S. Nemat-Nasser, L. M. Keer, and K. S. Parihar, "Unstable growth of thermally induced interacting cracks in brittle solids," *International Journal of Solids and Structures*, vol. 14, no. 6, pp. 409–430, 1978.

[14] D. Barr, *Thermal Cracking in Nonporous Geothermal Reservoirs [M.S. thesis]*, Massachusetts Institute of Technology, Cambridge, Mass, USA, 1980.

[15] Z. P. Bažant and H. Ohtsubo, "Geothermal heat extraction by water circulation through a large crack in dry hot rock mass," *International Journal for Numerical and Analytical Methods in Geomechanics*, vol. 2, no. 4, pp. 317–327, 1978.

[16] F. H. Harlow and W. E. Pracht, "A theoretical study of geothermal energy extraction," *Journal of Geophysical Research*, vol. 77, no. 35, pp. 7038–7048, 1972.

[17] G. Stephenes and B. Voight, "Hydraulic fracturing theory for conditions of thermal stress," *International Journal of Rock Mechanics and Mining Sciences & Geomechanics Abstracts*, vol. 19, pp. 279–284, 1982.

[18] D. D. Tran, *Effects of Thermally-Induced Secondary Cracks on Hydraulic Fractures, [Ph.D. thesis]*, University of Calgary, 2013.

[19] M. Manassero and C. D. Shackelford, "The role of diffusion in contaminant migration through soil barriers," *Rivista Italiana di Geotecnica*, vol. 1, p. 94, 1994.

[20] D. B. Fox, D. Sutter, K. F. Beckers et al., "Sustainable heat farming: modeling extraction and recovery in discretely fractured geothermal reservoirs," *Geothermics*, vol. 46, pp. 42–54, 2013.

[21] M. Li and N. Lior, "Analysis of hydraulic fracturing and reservoir performance in enhanced geothermal systems," *Journal of Energy Resources Technology, Transactions of the ASME*, vol. 137, no. 4, Article ID 042904, 2015.

[22] A. Zang, E. Majer, and D. Bruhn, "Preface to special issue: induced seismicity in geothermal operations," *Geothermics*, vol. 52, pp. 1–5, 2014.

[23] A. Ogata and R. Banks, "A solution of the differential equation of longitudinal dispersion," U.S. Geological Survey Professional Paper 411-A, 1961.

[24] J. Bear, *Dynamics of Fluids in Porous Media*, American Elsevier Publishing, New York, NY, USA, 1972.

[25] J. Bear, *Hydraulics of Groundwater*, McGraw-Hill, 1979.

[26] R. Freeze and J. Cherry, *Ground Water*, Prentice-Hall, Englewood Cliffs, NJ, USA, 1979.

[27] M. T. van Genuchten and W. J. Alves, "Analytical solutions of the one-dimensional convective-dispersive solute transport equation," USDA Technical Bulletin 1661, 1982.

[28] D. Lee, H. Kim, J. Lee, Y. Park, and G. Kim, "Numerical investigations of enhancement of a convective fin efficiency by convection-radiation gonjugate heat transfer," *Journal of the Korean Society of Marine Engineering*, pp. 146–154, 2001.

Hindawi
Geofluids
Volume 2017, Article ID 1958463, 10 pages
https://doi.org/10.1155/2017/1958463

Research Article

Effect of Flow Direction on Relative Permeability Curves in Water/Gas Reservoir System: Implications in Geological CO_2 Sequestration

Abdulrauf Rasheed Adebayo,[1] Assad A. Barri,[2] and Muhammad Shahzad Kamal[1]

[1] *Center for Integrative Petroleum Research, King Fahd University of Petroleum & Minerals, Dhahran 31261, Saudi Arabia*
[2] *Petroleum Engineering Department, King Fahd University of Petroleum & Minerals, Dhahran 31261, Saudi Arabia*

Correspondence should be addressed to Abdulrauf Rasheed Adebayo; abdulrauf@kfupm.edu.sa

Received 29 March 2017; Revised 24 May 2017; Accepted 12 June 2017; Published 26 July 2017

Academic Editor: Weon Shik Han

The effect of gravity on vertical flow and fluids saturation, especially when flow is against gravity, is not often a subject of interest to researchers. This is because of the notion that flow in subsurface formations is usually in horizontal direction and that vertical flow is impossible or marginal because of the impermeable shales or silts overlying them. The density difference between two fluids (usually oil and water) flowing in the porous media is also normally negligible; hence gravity influence is neglected. Capillarity is also often avoided in relative permeability measurements in order to satisfy some flow equations. These notions have guided most laboratory core flooding experiments to be conducted in horizontal flow orientation, and the data obtained are as good as what the experiments tend to mimic. However, gravity effect plays a major role in gas liquid systems such as CO_2 sequestration and some types of enhanced oil recovery techniques, particularly those involving gases, where large density difference exists between the fluid pair. In such cases, laboratory experiments conducted to derive relative permeability curves should take into consideration gravity effects and capillarity. Previous studies attribute directional dependence of relative permeability and residual saturations to rock anisotropy. It is shown in this study that rock permeability, residual saturation, and relative permeability depend on the interplay between gravity, capillarity, and viscous forces and also the direction of fluid flow even when the rock is isotropic. Rock samples representing different lithology and wide range of permeabilities were investigated through unsteady-state experiments covering drainage and imbibition in both vertical and horizontal flow directions. The experiments were performed at very low flow rates to capture capillarity. The results obtained showed that, for each homogeneous rock and for the same flow path along the core length, the relative permeability and residual saturation are dependent on flow direction. The results were reproducible in all experiments conducted on the samples. This directional dependence, when accounted for in numerical simulation, can significantly improve simulation accuracy in the flow processes described.

1. Introduction

Reservoir rocks are often made of horizontal layers called sand beds that are usually interbedded with impermeable shales or silts that prevent cross flow between rock layers. As a result, flows in underground reservoirs are often considered to be principally in horizontal directions. In order to mimic reservoir flow conditions, laboratory flow experiments are often conducted with rock samples in horizontal orientation. However, there are field case scenarios where flows occur in vertical direction such as during water or gas flooding from horizontal well sections, gas upward/vertical migration due to buoyancy in thick rock beds during gas sequestration or gas-enhanced oil recovery (EOR), and cross flow between reservoir beds with good vertical permeabilities. In such cases, modelling upward migration of CO_2 plume or cross flow between reservoir beds using laboratory relative permeability data obtained from horizontal core flooding experiments will not be adequately representative and accurate. Furthermore, most commonly used relative permeability calculation methods are based on the assumption that two fluids flowing in the same direction are under pressure gradients that are

relatively larger than the buoyant force of gravity as well as capillary forces. Hence, both gravity and capillarity are often neglected. Laboratory measurements conducted to obtain relative permeability and end saturations are thus required to obey such assumptions by conducting core flooding experiments at high flow rates such that viscous forces dominate and capillary forces are negligible. These assumptions also become invalid and greatly erroneous when studying a liquid-gas system, where significant buoyancy exists because of the high variation in fluids densities. According to Corey [1], the assumption of neglecting both gravitational and capillary effects in the fractional flow equations is not accurate. He argued that capillary effect is not entirely eliminated and still exists during displacement process. He also pointed out that a large density difference occurs between water and oil in a soil-water system, which makes it impractical to ignore the gravitational terms. In addition, fluids' flow in actual reservoirs is mainly in capillary dominated regions with capillary number of $\leq 10^{-6}$. It is therefore essential to make laboratory measurements at conditions closely representative of reservoir conditions. This involves combining viscous, capillary, and gravity forces [2].

Bennion and Bachu [3, 4] did an extensive work on the role of lithology, permeability, and viscosity ratio on relative permeability in a horizontal core flooding of CO_2/brine system under different reservoir pressure and fluid conditions. Akbarabadi and Piri [5] conducted a CO_2/brine experiment with the rock samples in vertical position and flow in upward vertical direction under a capillary dominated flow regime. However, there was no comparative analysis of the effect of vertical flow on relative permeability and residual saturation as compared to the case when the flow is in horizontal direction. Niu et al. [6] investigated the effect of variation in pressure, temperature, and brine salinity on residual trapping of CO_2 in a horizontal core flooding of Berea sandstones. Reynolds et al. [7] studied the effect of viscosity ratio and interfacial tension (IFT) under a capillary dominated flow regime of CO_2/brine system in a single Bentheimer sandstone sample flooded in a horizontal direction. Many other authors [8–11] investigated, through either simulation or laboratory experiment, the effect of flow rate/capillarity on multiphase flow of CO_2/brine in a horizontal core-flood. Many other published relative permeability curves considered only the effect of the viscous forces and neglected the contribution of capillary and gravitational forces. Few studies [12–14] have observed through experimental studies that relative permeability and end saturations are dependent on flow directions. However, the directional dependence of these parameters was thought to have been influenced by rock heterogeneity such as permeability anisotropy and presence of lamination. This study takes a step further to investigate whether the directional dependency of residual saturation and relative permeability are actually due to only the rock heterogeneity or also due to the flow direction and the dominating forces during the interplay between capillarity, viscous, and gravitational forces.

The objective of this study is to highlight the directional dependence of relative permeability and end saturations even for a homogeneous and isotropic system. This dependence, when accounted for in numerical simulation, can significantly improve simulation accuracy in flow processes involving vertical flow. Finally, it should be noted that directional flow as meant in this study may not necessarily be only due to directional permeability caused by heterogeneous features like anisotropy or laminations, as these have been sufficiently discussed in the literature [12–15]. In the context described here, the variations in relative permeability and residual saturation exist due to flow direction even if the rock is very homogeneous and has an isotropic permeability.

Table 1: Sample properties.

Sample #	Lithology	Length (cm)	Diameter (cm)	Porosity (%)	k_{brine} (mD)
Sample 1	Sandstone	30.3	3.8	19.49	158
Sample 2	Limestone	25.4	3.8	13.88	269
Sample 3	Limestone	25.4	3.8	11.83	79

*Brine permeability was measured in horizontal orientation.

Table 2: Fluid properties at 45 degree Celsius and atmospheric pressure.

	Density (g/cc)	Viscosity (cp)	Viscosity ratio, μ_g/μ_w	Density ratio, ρ_g/ρ_w	IFT, σ_{gw} (dynes/cm)
Brine	1.0204	0.5653	0.0329	0.1019	62
Nitrogen	0.104	0.0186			

μ_g and μ_w denote the viscosity of gas and water, while ρ_g and ρ_w denote the density of gas and water. IFT denotes interfacial tension between gas and water and is denoted by σ_{gw}.

2. Experimental Procedures

Experiments were conducted using three samples, which include sandstone and limestone obtained from Berea sandstones and Indiana limestone, respectively. The porosities of the samples range from 11.8% to 19.5%, while the liquid permeabilities range from 79 mD to 270 mD as seen in Table 1. Soxhlet reflux extraction method was used to clean samples at elevated temperature of 80°C and then dried in a vacuum oven at 60°C. Table 1 summarizes the samples' dimensions and physical properties. Synthetic aquifer brine was prepared with TDS of 58 g/l and a density of 1.03 g/cc and high purity (99.9%) Nitrogen was used as the gas phase. Nitrogen gas was used instead of CO_2 to avoid complexities in saturation estimation because of mass transfer and active rock fluid interaction. However, the results obtained using gas can be applicable to other gases such as CO_2. The fluids properties were measured at 45°C and at atmospheric pressure as given in Table 2.

2.1. Description of Experiments. A series of unsteady-state and low flow rates core flooding experiments were performed to represent actual flow conditions during CO_2 injection in saline aquifer, using the set-up shown in Figure 1. The

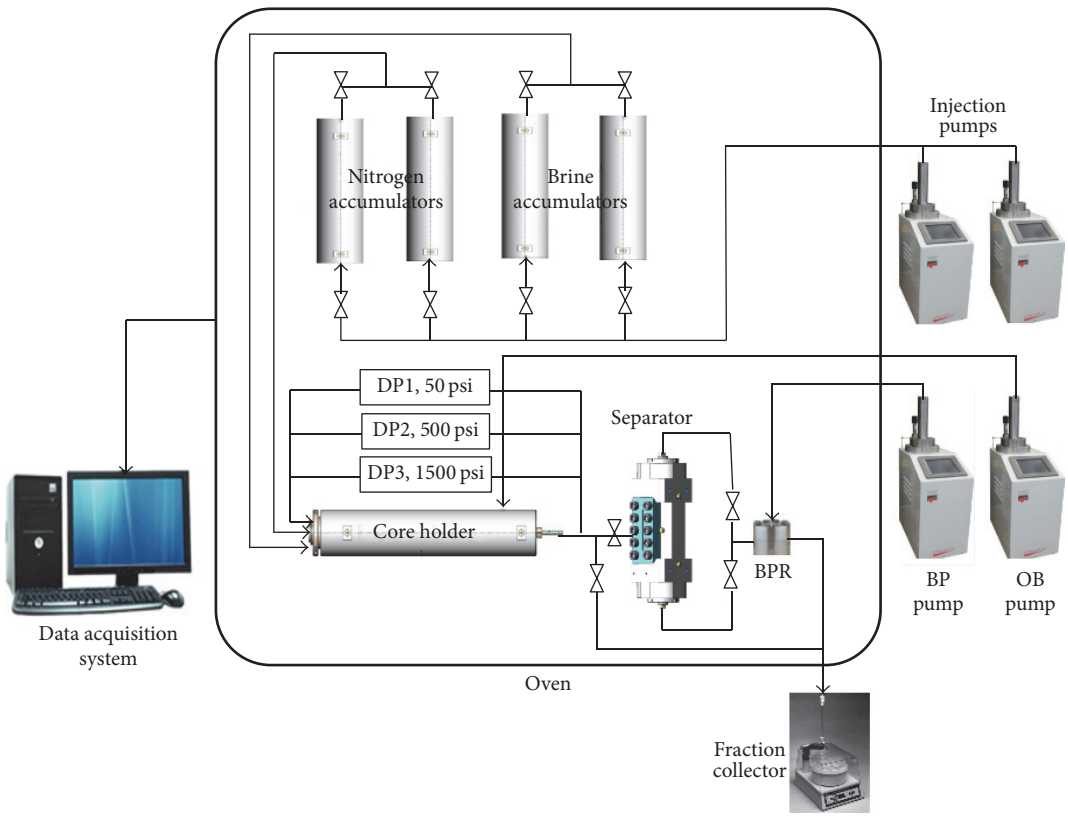

Figure 1: Experimental setup. BPR is backpressure regulator, BP means backpressure, and OB is overburden pressure.

core holder is a hydrostatic core holder, which holds the cylindrical rock sample, and is capable of applying a confining pressure on the sample. It can be rotated such that core flooding is conducted in either horizontal or vertical orientation. The core holder is also capable of holding samples of varying lengths as long as 30.48 cm with diameter of 3.8 cm. Reservoir fluids (brine and nitrogen) were stored in floating piston accumulators made of Hastelloy and stainless steel. A dual injection pump is connected to the accumulators through stainless steel tubing. The pump was used to drive fluid from the floating piston accumulators into the core sample through another set of stainless tubing connecting the accumulators to the core holder. The injection pump is capable of continuous fluid injection at a specified constant rate (0.01–50 cc/min) and injection pressure as high as 10,000 psi. Another automated syringe pump was used to supply a constant confining pressure of 2,000 psi (or net confining pressure of 450 psi) on the sample, while a third pump was used to provide a constant backpressure of 1,450 psi. A video separator is placed between the backpressure regulator and the core outlet to record the amount of fluid produced from the sample. High-resolution differential pressure transducers (±50 psi, ±500 psi, and ±1,500 psi with resolutions of ±0.1% of full scale) were used to measure the pressure drop across the samples. An industrial oven encloses and applies constant temperature of 45°C on all the accumulators, core holders, separator, and tubing. Fluid flow into the sample was controlled and alternated with air actuated automated pneumatic valves. All core flooding data such as rates, pressure gradient, oven temperature, backpressure, overburden pressure, and fluid production were continuously recorded at a stipulated time interval of 5 seconds on a computer station.

The samples were presaturated with the formulated brine using vacuum saturation method. Each sample was subsequently placed in the core holder and circulated with about 2PV of brine at a constant injection rate of 0.5 cc/min. This was to ensure that all trapped gases are removed and the sample comes to thermodynamic equilibrium with the brine. Absolute permeability of brine was measured on each sample in both horizontal and vertical flow orientations. The procedure involved measurement of pressure drop across the sample at different flow rates. Darcy's equation was then used to compute the absolute permeability from a linear plot of pressure gradient versus flow rates. At the end of permeability measurement, the flow rate was reduced back gradually to 0.5 cc/min and allowed to stabilize. Afterwards, unsteady-state drainage and imbibition experiments were conducted on each rock sample at a constant injection rate of 0.5 cc/min and at other experimental conditions mentioned above. Drainage involved injecting gas to displace the brine from the sample until a stabilized flow and irreducible water saturation were attained. Imbibition then followed by injecting brine to displace the gas until residual gas saturation was attained. Stabilized flow at irreducible/residual fluid saturation is indicated by stabilized pressure drop and production curve. Core flooding experiments were repeated multiple times with the

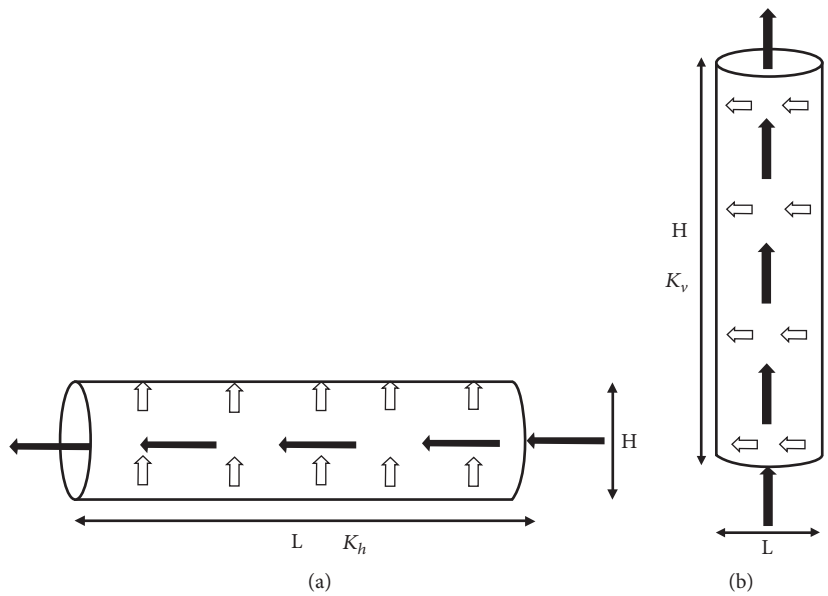

Figure 2: Illustration of flow directions during (a) horizontal flow and (b) vertical upward flow for the same sample.

same fluids and the same experimental conditions but with different flow directions in order to isolate the effect of heterogeneity and permeability anisotropy. In this way, comparison can be fairly made between horizontal and vertical flows without the influence of rock heterogeneity and anisotropy.

2.2. Dimensionless Number. Dimensionless numbers were used to characterize the flow behavior in both horizontal and vertical flows. Different dimensionless numbers exist such as those derived by Fulcher et al. [16], Zhou et al. [17], Chia-Wei and Sally [18], and Reynolds and Krevor [19]. In this paper, we use capillary number as given by Fulcher et al. [16] in (1) and gravity number given by Zhou et al. [17] in (2). The gravity number in (2) was used because it can be used to compare the ratio of the forces acting in transverse and longitudinal direction in horizontal flow as in Figure 2(a) with that where the principal flow direction is vertically upward as in Figure 2(b). In case (a), gravity and capillary effect are associated with the vertical direction (H), while viscous effect is associated with the horizontal direction (L) (i.e., direction of pressure drop). Hence, (2) was used to compute the gravity number. In Figure 2(b), both viscous and gravity forces are associated with H, while capillary force can drive flow in L direction. Hence, the ratio of fluid flow in the vertical direction (H) due to gravity and viscous force to that in horizontal direction (L) due to capillary forces is thus given in (3).

$$N_{\text{ca}} = \frac{\mu_g V_t}{\sigma_{gw}}, \tag{1}$$

$$N_{gv\ (\text{hori})} = \frac{LgK_h \Delta\rho_{gw}}{H\mu_g V_t}, \tag{2}$$

$$N_{gv\ (\text{vert})} = \frac{K_v g \Delta\rho_{gw}}{\mu_g V_t}, \tag{3}$$

where H is height or vertical distance through which fluid flows, L is the distance the fluid flows in horizontal direction, K is absolute permeability in the transverse flow direction (K_h in case (a) and K_v in case (b) in Figure 2) in mD, V_t is total flow velocity in the principal flow direction in m/s, $\mu_g$is gas viscosity in cp, g is acceleration due to gravity in m/s^2, σ is interfacial tension in N/m, and $\Delta\rho_{gw}$ is density difference between gas and brine in Kg/m^3.

2.3. Relative Permeability Models. Since the experimental conditions under which the experimental data presented above were obtained violate the assumption of Weldge, Johnson-Bossler-Naumann (JBN) method, and other explicit relative permeability methods, empirical correlations are used to generate the relative permeability curves for the different flow processes. The two most commonly used empirical correlations are Corey's [20] two-phase relations (theoretical approach) for drainage in a consolidated rock and Naar and Henderson's [21] two-phase model for imbibition. Corey's [20] model is given as follows:

$$\begin{aligned} S_w^* &= \frac{S_w - S_{iw}}{1 - S_{iw}}, \\ k_{rw} &= \left(S_w^*\right)^{((2+3\lambda)/\lambda)}, \\ k_{rn} &= \left(1 - S_w^*\right)^2 \left(1 - \left(S_w^*\right)^{((2+\lambda)/\lambda)}\right), \end{aligned} \tag{4}$$

where k_{rn} and k_{rw} are the nonwetting and wetting phase relative permeabilities, respectively, S_w^* is the normalized wetting phase saturation, λ is the pore size distribution index, S_w is the water saturation, S_{iw} is the irreducible water saturation, and S_{rnw} is the residual nonwetting phase saturation. The pore size distribution index, λ, was obtained

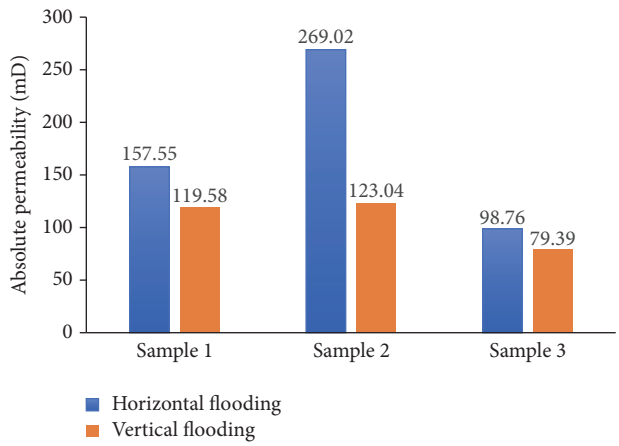

Figure 3: Absolute permeability to brine for horizontal and vertical core orientation.

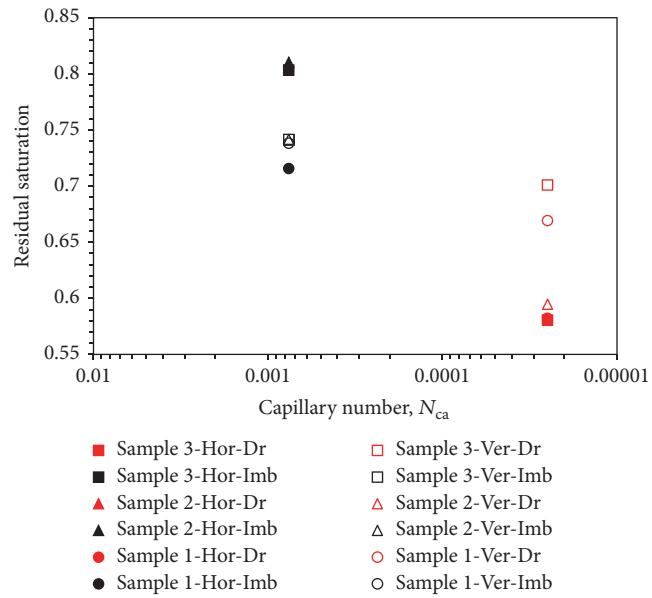

Figure 4: Residual saturation versus capillary number for horizontal and vertical flow. "Hor" means horizontal, "Ver" means vertical, "Dr" means drainage, and "Imb" means imbibition.

empirically from capillary pressure data using Brooks and Corey [22], which relates capillary pressure to normalized wetting phase saturation.

$$\log P_c = \log P_e - \frac{1}{\lambda} \log S_w^*, \tag{5}$$

where P_c is the capillary pressure, P_e is the minimum threshold pressure, and S_w^* is the normalized water saturation. Naar and Henderson's [21] two-phase model for imbibition is given as follows:

$$k_{rw} = \left(S_w^*\right)^{((2+3\lambda)/\lambda)}, \tag{6}$$

$$k_{rn} = \left(1 - 2S_w^*\right)^{3/2} \left[2 - \left(1 - 2S_w^*\right)^{1/2}\right]. \tag{7}$$

In this study, a λ value of 2 was used for all the samples assuming that they fall within Wyllie's equation for cemented sandstones and oolitic and small vug limestone. This value is sufficient for approximation purpose, since the intent is to show how flow direction influences relative permeability for the same rock sample. The value used does not affect the comparison between vertical and horizontal flows, since the same rock samples were used for both flow directions.

3. Results and Discussions

The absolute permeability values of brine for the three samples are shown in Figure 3. The absolute permeabilities of brine in horizontal and vertical core flooding, respectively, are compared. It can be seen that K_V was lower than K_H. This is due to the gravity term and higher pressure gradient required to overcome gravity force during K measurements. Dimensionless numbers (see (1), (2), and (3)) were then used to characterize the different flow experiments in the three samples, namely, horizontal drainage, horizontal imbibition, vertical drainage, and vertical imbibition.

3.1. Residual Saturation. As discussed earlier, the cross plot of residual saturation versus capillary number is a very useful tool in understanding the interplay between viscous and capillary forces. It explains how these forces affect residual saturation during immiscible displacements in rock samples. The capillary number for all the flow experiments conducted in this study was computed using (1) to get a capillary number of 0.8×10^{-5} for both vertical imbibition and horizontal imbibition and 2.5×10^{-5} for both vertical drainage and horizontal drainage as seen in Figure 4. The capillary numbers were the same because the same values of injection rates, fluid pairs, and experiment conditions were used in both flow directions. In addition, the range of capillary number for both drainage and imbibition is within the capillary dominated flow range in actual reservoir flow. According to Willhite [23], capillary dominated flow processes have capillary number in the range of $\sim 10^{-6}$. Gravity number, on the other hand, can be seen in Figure 5 to vary from sample to sample and from vertical flow to horizontal flow because of the effect of gravity and permeability variation from sample to sample and from vertical flow to horizontal flow. The gravity number relates the effect of gravity force to viscous force according to (2). As seen in Figure 5, increasing gravity number resulted in lower residual/irreducible saturations in all the samples and flow experiments. The higher gravity numbers are for the horizontal flows, while the lower ones are for the vertical flow experiments. A Lower gravity number means that gravity was not in favor of flow and hence the observed higher residual saturations. Similarly, a high gravity number means that gravity dominates and was in favor of flow. The work of Kuo and Benson [10] also showed that a higher gravity number resulted in a lower residual saturation and vice versa.

The cumulative fluid productions during drainage are also shown in Figures 6–8 for both vertical and horizontal core flooding. For drainage process, it can be seen that

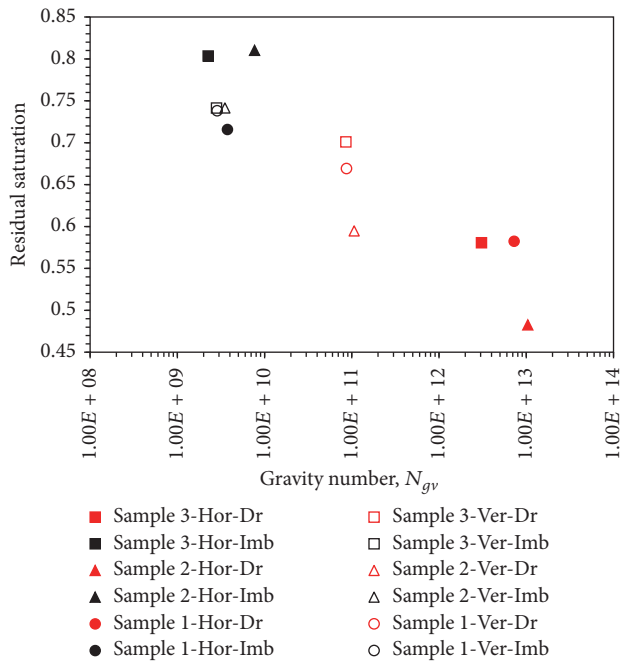

Figure 5: Residual saturation versus gravity number for horizontal and vertical flow. "Hor" means horizontal, "Ver" means vertical, "Dr" means drainage, and "Imb" means imbibition.

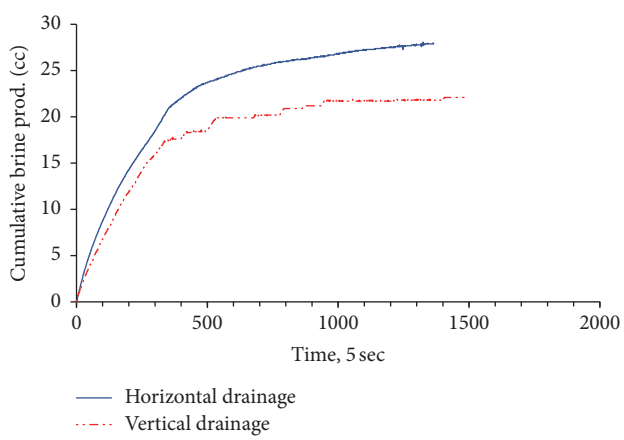

Figure 6: Comparison of cumulative brine production during gas injection in horizontal and vertical core flooding in sample 1.

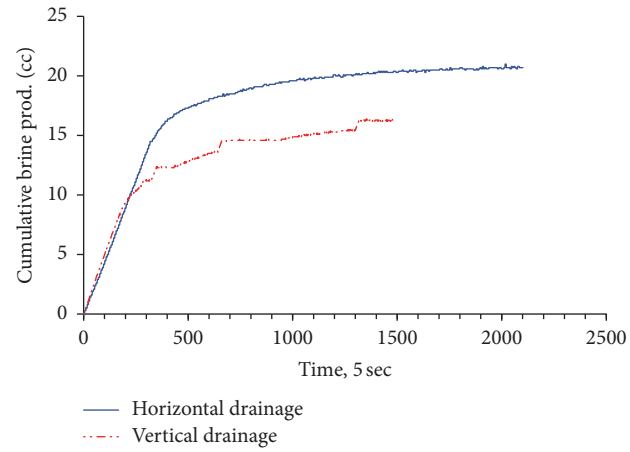

Figure 7: Comparison of cumulative brine production during gas injection in horizontal and vertical core flooding in sample 2.

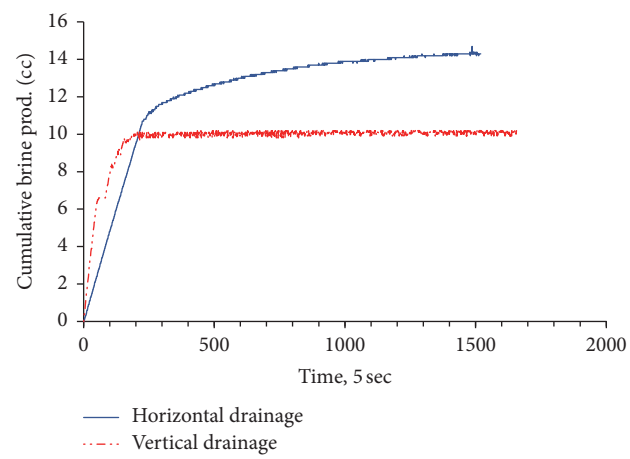

Figure 8: Comparison of cumulative brine production during gas injection in horizontal and vertical core flooding in sample 3.

horizontal core flooding yielded more brine production (i.e., lower residual water saturation) than when the same core sample was flooded from bottom to top in a vertical core orientation. The gravity number in horizontal flow is higher than that in vertical flow. Moortgat et al. [24] observed a similar gravitational effect during their study in which oil recovery was compared between core flooding in horizontal, vertical up, and vertical down CO_2 flooding. In their study, CO_2 density was higher than the oil density used; hence, gravitational frontal instability was observed during vertical CO_2 injection from top to bottom. In our study, gravitational instability was observed during nitrogen injection from bottom to top because nitrogen density is much lower than brine density. Gravitational fingering will be significantly higher during vertical multiphase flow of two fluids of wide density difference than during horizontal multiphase flow of the same fluid pair in the same sample and at the same experimental conditions. Because of the wide difference in fluids' density and the very low injection rates, gravitational fingering caused by gravity segregation dominated the flow process in comparison to viscous and capillary forces. Since the injection rate is quite low, the viscous force is weak and is unable to overcome the gravity effects; hence, some of the residual brine in the rock sample gradually replaces the injected gas at the bottom (causing a downward flow). Since the core sample is quite long and the injection rate is low, fluid segregation and replacement have sufficient time and space to take place. Furthermore, the rate of fluid segregation and replacement may be higher than the rate of brine production, a possible phenomenon that may explain the lower recovery from vertical upward

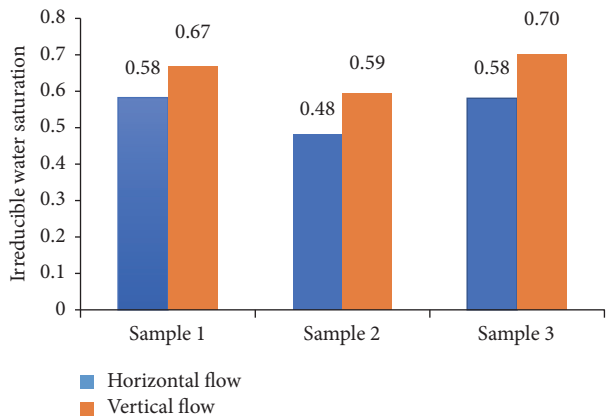

Figure 9: Comparison of irreducible water saturation during horizontal drainage and vertical drainage.

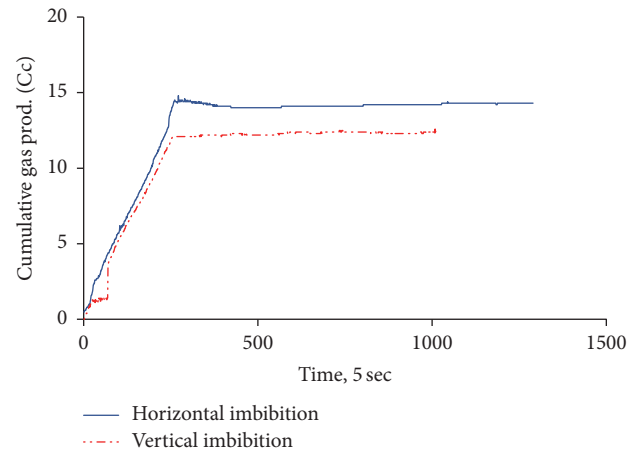

Figure 10: Comparison of cumulative gas production during secondary brine injection in horizontal and vertical core flooding in sample 1.

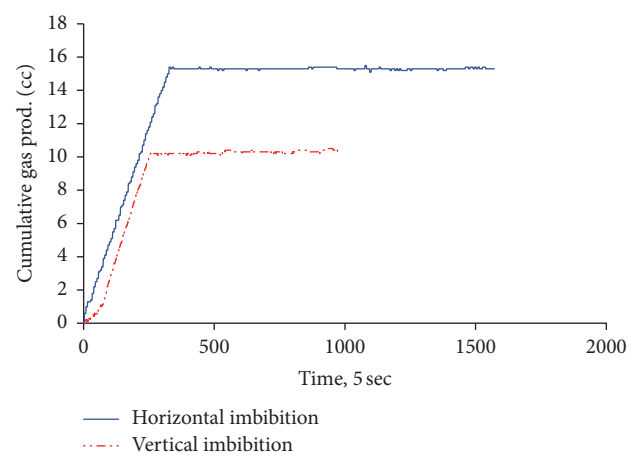

Figure 11: Comparison of cumulative gas production during secondary brine injection in horizontal and vertical core flooding in sample 2.

flow and the production rate not being equal to the injection rate as can be observed in the production curves in Figures 6–8. The irreducible water saturations after vertical drainage and horizontal drainage are also compared in Figure 9. It can be seen in the figure that the irreducible water saturation in vertical flow is higher than that in the horizontal flow. The reason is obviously due to the gravity fingering of gas during gas injection from the bottom to the top of the sample, which resulted in an unstable displacement. As discussed above, the very low injection rate allowed gravity segregation to dominate both viscous and capillary forces, causing the water in the sample to settle down to replace the injected gas instead of being produced at the outlet; hence, not much water is produced from the top.

For gas-EOR methods in horizontal wells, gravity fingering effect can be dampened by injecting the gas at an optimum high injection rate. High injection rates can be achieved only at the near wellbore area, while the far field area will continue to be in the low flow rate regime. Another method of dampening gravity fingering is by designing the well completion such that the injection well is placed at the top and production well at the bottom so that injected gas sweeps the oil from top to bottom. In the case of gas sequestration such as CO_2 sequestration, a low injection rate in a vertical upward flow will be most desirous, since the optimum goal is to increase the amount of gas trapped permanently. Gravity fingering will thus facilitate capillary trapping of the injected gas. The optimum injection rate that will cause the maximum residual gas saturation will be sought through a dimensionless-saturation correlation. A study to derive these correlations is ongoing.

Figures 10–12 show the cumulative gas recovery during secondary imbibition. Similar to drainage experiments, recovery during horizontal flooding is also consistently higher than recovery during vertical flooding. The higher gas recovery observed in the horizontal core flooding during secondary imbibition can be explained by the initial-residual (IR) gas theory. That is, the higher the initial gas saturation, the higher the recovered gas. The gas injected in the horizontal core flooding was higher than that injected during vertical flooding because a lower irreducible water saturation was attained during horizontal injection. Figure 13 compares the residual gas saturation in horizontal and vertical flow directions. One would expect that, under the same initial gas saturation, vertical upward water injection would give higher gas recovery than the horizontal flow because of the expected more stable displacement front. However, because the initial gas saturation during horizontal drainage is quite higher than the initial gas saturation during vertical drainage for a given sample, the horizontal imbibition experiment will produce more gas than the vertical secondary imbibition experiments on the same sample. This then explains the higher recovered gas (Figures 10–12) or higher trapped gas saturation (Figure 13) during horizontal flow. Another important feature of the imbibition process is the piston-like displacement of the gas as manifested in the production curves. The production curves sharply progressed from a linear increase to no production (a flat and stable line).

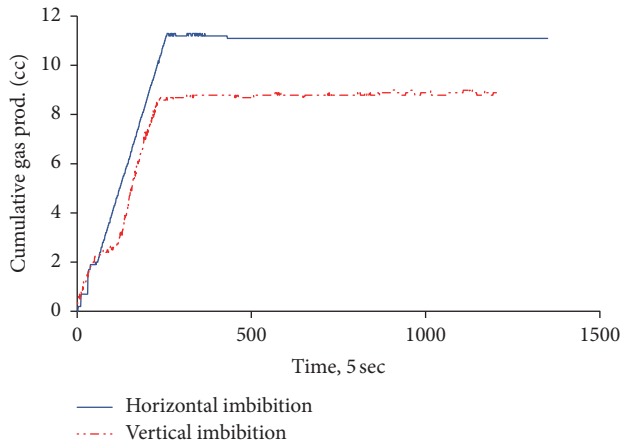

FIGURE 12: Comparison of cumulative gas production during secondary brine injection in horizontal and vertical core flooding in sample 3.

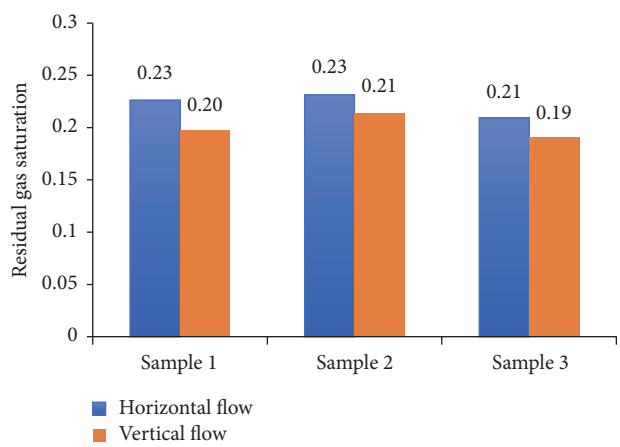

FIGURE 13: Comparison of residual gas saturation during horizontal and vertical secondary imbibition.

3.2. Relative Permeability Curves. The relative permeability curves are generated for each sample, using (4) to (7). As can be seen from these equations, relative permeability is strongly dependent on the end saturation values. Since end saturation in vertical flow differs from that in horizontal flow for the same sample, the relative permeability curves will also differ accordingly as shown in Figures 14–16. The relative permeability of all the samples tested showed strong dependence on flow direction. Such difference in relative permeability and end saturation can have significant bearing on the numerical simulation carried out in forecasting CO_2 distribution (in the case of CO_2 sequestration) or recovery (in the case of EOR). For example, the predicted CO_2 saturation distribution and CO_2 travel time may be either significantly underestimated or overestimated. It is therefore crucial that the right relative permeability curves are selected which are representative of the actual flow direction in a reservoir.

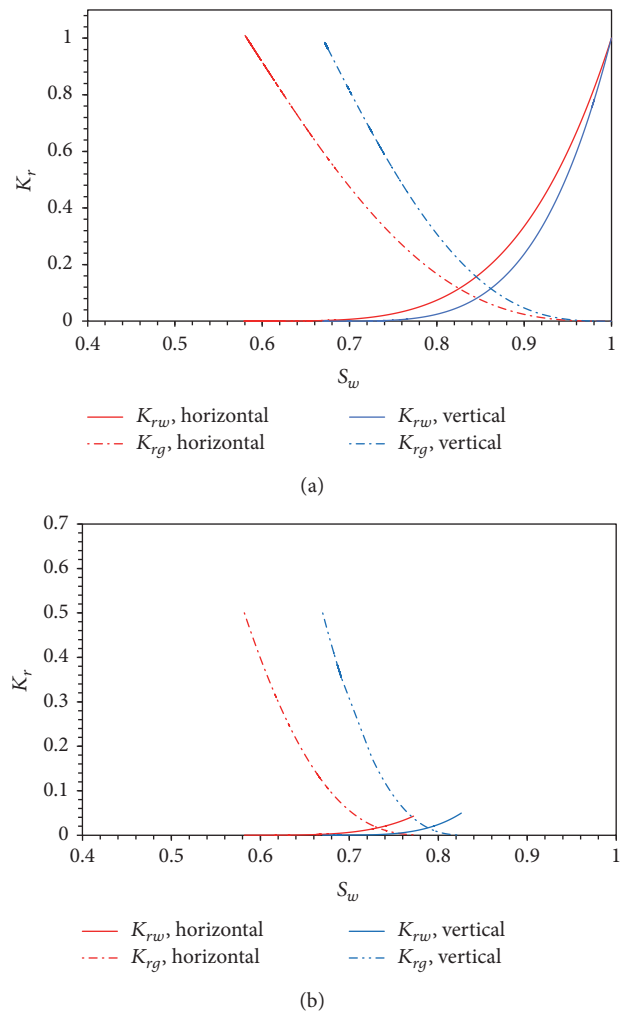

FIGURE 14: Comparison of relative permeability curves: (a) drainage and (b) imbibition for sample 1.

4. Conclusions

In this study, a reservoir condition core flooding experiments were conducted in two flow directions, namely, horizontal and vertical flows. The flow conditions capture unsteady-state flow, gravity, and capillarity that are common in actual field scenario but are often neglected in many laboratory estimations of relative permeability of gas-liquid systems. The following conclusions are drawn from this study:

(1) Directional dependence of relative permeability and end saturations is not only due to heterogeneity (caused by permeability anisotropy and heterogeneity) but also due to the flow direction itself as observed in homogeneous and isotropic rocks tested.

(2) Residual fluid saturation is higher when flow is in vertical direction as compared to horizontal flow direction even in an isotropic rock.

(3) The interplay between viscous and gravity forces during flow in horizontal and vertical directions as

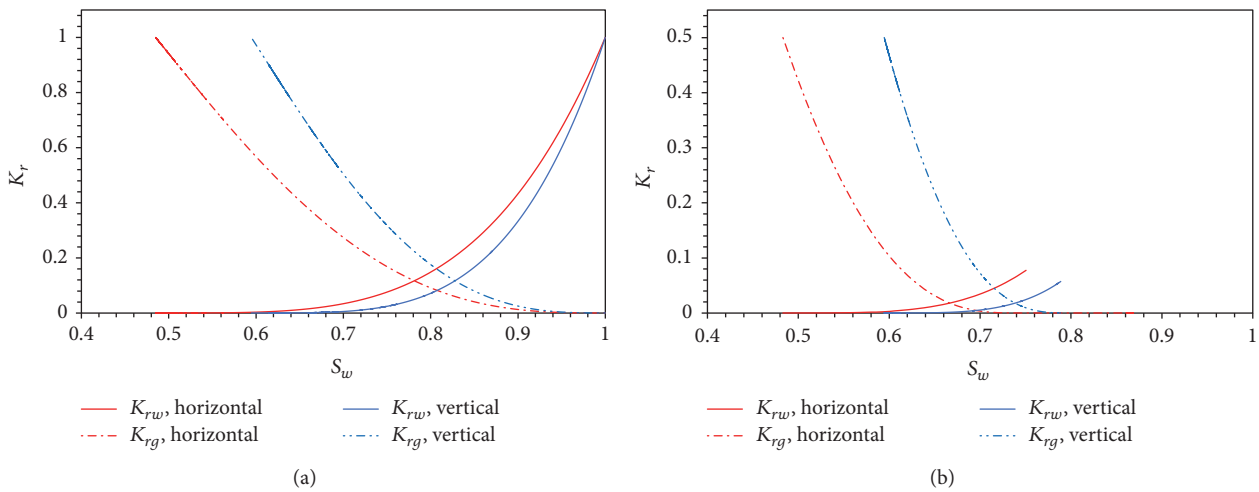

Figure 15: Comparison of relative permeability curves: (a) drainage and (b) imbibition for sample 2.

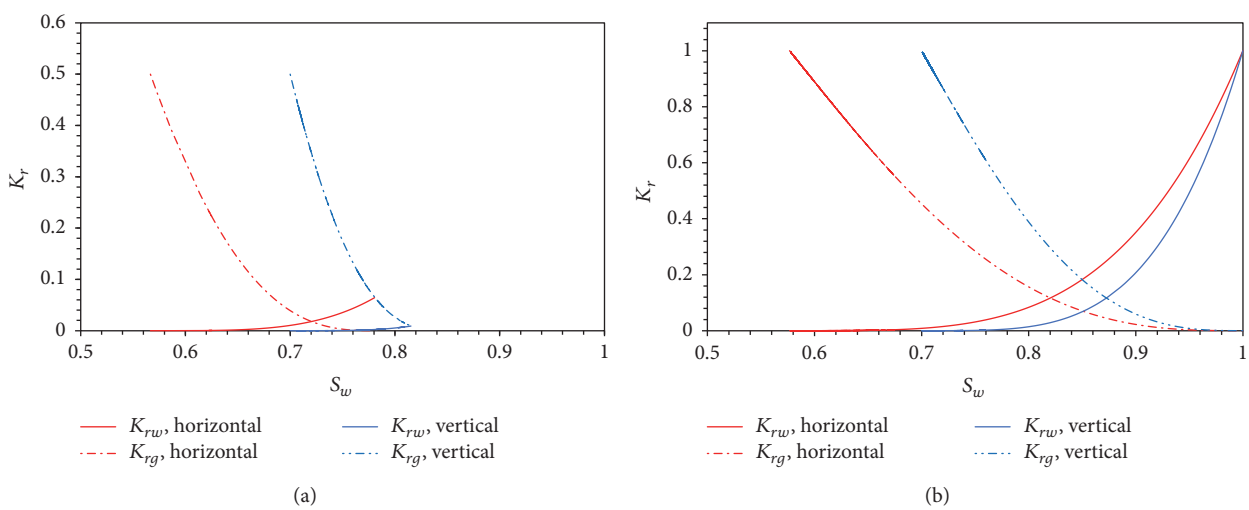

Figure 16: Comparison of relative permeability curves: (a) drainage and (b) imbibition for sample 3.

indicated by the gravity numbers shows that the gravity number is lower in vertical flow than in horizontal flow because of the effect of gravitational fingering and flow against gravity. The gravity number versus residual saturation plot also showed that residual saturation decreases as gravity number increases

(4) Core holder orientation and flow direction in laboratory flow studies are important, since flow direction affects rock and fluid properties such as permeability, residual fluid saturation, and relative permeability. Core orientation should therefore be determined to represent actual reservoir flow.

(5) The higher residual saturation resulting from vertical flow could be taken as an advantage in CO_2 sequestration, where higher residual (trapped) gas saturation is desired

(6) Finally, this study underpins the importance of measuring residual saturations, permeability, and relative permeabilities of plug samples in the same direction fluid flows in them during 2D or 3D flow in actual reservoir flow scenarios. Plugs extracted horizontal to the bedding plane should be measured horizontally, while plugs extracted perpendicular to the bedding plane should be measured vertically and the flow in this case should be from bottom to top if the end use of the data is to simulate CO_2 migration in the formation. It is thus strongly recommended that reservoir simulation experts understand details of the core flooding experiments used to generate relative permeability curves. They must ensure that the lab-generated relative permeability curves represent the actual flow directions in the reservoir under study.

Conflicts of Interest

The authors declare that there are no conflicts of interest regarding the publication of this paper.

Acknowledgments

The authors acknowledge the Center for Integrative Petroleum Research and College of Petroleum Engineering and Geosciences at King Fahd University of Petroleum & Minerals for the research support.

References

[1] A. T. Corey, *Mechanics of Heterogeneous Fluids in Porous Media*, Water Resources Publications, Fort Collins, Colo, USA, 1977.

[2] M. Honarpour and S. M. Mahmood, "Relative permeability measurements: an overview," *Journal of Petroleum technology*, vol. 40, no. 8, pp. 963–966, 1988.

[3] B. Bennion and S. Bachu, "Relative permeability characteristics for supercritical CO_2 displacing water in a variety of potential sequestration zones in the western canada sedimentary basin," in *Proceedings of the SPE Annual Technical Conference and Exhibition*, October 2005.

[4] B. Bennion and S. Bachu, "Drainage and imbibition relative permeability relationships for supercritical CO_2/brine and H_2S/brine systems in intergranular sandstone, carbonate, shale, and anhydrite rocks," in *Paper SPE 99326-MS presented Society of Petroleum Engineers*, 2008.

[5] M. Akbarabadi and M. Piri, "Relative permeability hysteresis and capillary trapping characteristics of supercritical CO_2/brine systems: an experimental study at reservoir conditions," *Advances in Water Resources*, vol. 52, pp. 190–206, 2013.

[6] B. Niu, A. Al-Menhali, and S. Krevor, "A study of residual carbon dioxide trapping in sandstone," in *Proceedings of the 12th International Conference on Greenhouse Gas Control Technologies, GHGT 2014*, pp. 5522–5529, October 2014.

[7] C. Reynolds, M. Blunt, and S. Krevor, "Impact of reservoir conditions on CO_2-brine relative permeability in sandstones," in *Proceedings of the 12th International Conference on Greenhouse Gas Control Technologies, GHGT 2014*, pp. 5577–5585, October 2014.

[8] J.-C. Perrin, M. Krause, C.-W. Kuo, L. Miljkovic, E. Charoba, and S. M. Benson, "Core-scale experimental study of relative permeability properties of CO2 and brine in reservoir rocks," in *Proceedings of the 9th International Conference on Greenhouse Gas Control Technologies, GHGT-9*, pp. 3515–3522, November 2008.

[9] C.-W. Kuo, J.-C. Perrin, and S. M. Benson, "Simulation studies of effect of flow rate and small scale heterogeneity on multiphase flow of CO_2 and brine," in *Proceedings of the 10th International Conference on Greenhouse Gas Control Technologies*, pp. 4516–4523, September 2010.

[10] C.-W. Kuo and S. M. Benson, "Numerical and analytical study of effects of small scale heterogeneity on CO2/brine multiphase flow system in horizontal corefloods," *Advances in Water Resources*, vol. 79, pp. 1–17, 2015.

[11] T. Suekane, T. Nobuso, S. Hirai, and M. Kiyota, "Geological storage of carbon dioxide by residual gas and solubility trapping," *International Journal of Greenhouse Gas Control*, vol. 2, no. 1, pp. 58–64, 2008.

[12] A. T. Corey and C. H. Rathjens, "Effect of stratification on relative permeability," *Society of Petroleum Engineers*, vol. 8, no. 12, 1956.

[13] M. M. Honarpour and N. Saad, "Influence of small-scale rock laminations on core plug oil/water relative permeability and capillary pressure , society of petroleum engineers," *Society of Petroleum Engineers*, 1994.

[14] M. M. Honarpour, A. S. Cullick, N. Saad, and N. V. Humphreys, "Effect of Rock Heterogeneity on Relative Permeability: Implications for Scale-up , Society of Petroleum Engineers," Tech. Rep. 10., Society of Petroleum Engineers. doi, 10.2118/29311-PA, 1995.

[15] M. A. Crotti and J. A. Rosbaco, "Relative permeability curves: the influence of flow direction and heterogeneities," *Society of Petroleum Engineers*, 1998.

[16] R. A. Fulcher, T. Ertekin, and C. D. Stahl, "Effect of capillary number and its constituents on two-phase relative permeability curves," *Society of Petroleum Engineers*, vol. 37, no. 2, 1985.

[17] D. Zhou, F. J. Fayers, and F. M. Orr, "Scaling of multiphase flow in simple heterogeneous porous media," *Society of Petroleum Engineers*, vol. 12, no. 3, 1997.

[18] K. Chia-Wei and M. Sally, "Analytical study of effects of flow rate, capillarity, and gravity on CO_2/brine multiphase-flow system in horizontal corefloods," *SPE Journal*, vol. 92, no. IR2, pp. 61–88, 2013.

[19] C. A. Reynolds and S. Krevor, "Characterizing flow behavior for gas injection: relative permeability of CO_2-brine and N_2-water in heterogeneous rocks," *Water Resources Research*, vol. 51, no. 12, pp. 9464–9489, 2015.

[20] A. T. Corey, "The Interrelation between gas and oil relative permeabilities," *Producers Monthly*, vol. 19, p. 38, 1954.

[21] J. Naar and J. H. Henderson, "An imbibition model—its application to flow behavior and the prediction of oil recovery: society of petroleum engineers," *Society of Petroleum Engineers*, vol. 1, no. 2, 1961.

[22] R. H. Brooks and A. T. Corey, "Properties of porous media affecting fluid flow," *Journal of the Irrigation and Drainage Division*, vol. 92, no. IR2, pp. 61–88, 1966.

[23] G. P. Willhite, *Waterflooding*, Society of Petroleum Engineers, Richardson, TX, USA, 1986.

[24] J. B. Moortgat, A. Firoozabadi, Z. Li, R. O. Esp, and R. O. Espósito, "CO_2 Injection in Vertical and Horizontal Cores: Measurements and Numerical Simulation," *Society of Petroleum Engineers*, vol. 18, no. 2, Article ID 135563, 2013.

Hindawi
Geofluids
Volume 2017, Article ID 9692517, 12 pages
https://doi.org/10.1155/2017/9692517

Research Article

On Fluid and Thermal Dynamics in a Heterogeneous CO_2 Plume Geothermal Reservoir

Tianfu Xu, Huixing Zhu, Guanhong Feng, Yilong Yuan, and Hailong Tian

Key Laboratory of Groundwater Resources and Environment, Ministry of Education, Jilin University, Changchun 130021, China

Correspondence should be addressed to Hailong Tian; myname1978@163.com

Received 23 March 2017; Accepted 25 May 2017; Published 3 July 2017

Academic Editor: Stefano Lo Russo

CO_2 is now considered as a novel heat transmission fluid to extract geothermal energy. It can achieve both the energy exploitation and CO_2 geological sequestration. The migration pathway and the process of fluid flow within the reservoirs affect significantly a CO_2 plume geothermal (CPG) system. In this study, we built three-dimensional wellbore-reservoir coupled models using geological and geothermal conditions of Qingshankou Formation in Songliao Basin, China. The performance of the CPG system is evaluated in terms of the temperature, CO_2 plume distribution, flow rate of production fluid, heat extraction rate, and storage of CO_2. For obtaining a deeper understanding of CO_2-geothermal system under realistic conditions, heterogeneity of reservoir's hydrological properties (in terms of permeability and porosity) is taken into account. Due to the fortissimo mobility of CO_2, as long as a highly permeable zone exists between the two wells, it is more likely to flow through the highly permeable zone to reach the production well, even though the flow path is longer. The preferential flow shortens circulation time and reduces heat-exchange area, probably leading to early thermal breakthrough, which makes the production fluid temperature decrease rapidly. The analyses of flow dynamics of CO_2-water fluid and heat may be useful for future design of a CO_2-based geothermal development system.

1. Introduction

The enhanced geothermal system (EGS) is defined as an engineered reservoir that has been created to extract economical amounts of heat from geothermal resources of low permeability and/or porosity [1]. As part of an effort to reduce atmospheric emissions of carbon dioxide (CO_2), a novel concept of operating the EGS using CO_2 instead of water as the working fluid (CO_2-EGS) and achieving simultaneous geologic sequestration of CO_2 has been proposed and evaluated [2, 3].

In recent years, a similar concept, the so-called CO_2 plume geothermal (CPG) system, has been proposed [4]. The CPG system utilizes existing, naturally porous, high permeability geologic formations (reservoirs) for geothermal energy recovery. The major benefit of the CPG system over the EGS is that the CPG system does not require hydrofracturing, which helps increase fracture permeability but may induce seismicity. The EGS has encountered considerable unfavorable conditions and sociopolitical issues (resistances). Consequently, the CPG system that can use the CO_2 sequestration site to recover geothermal energy may be practical.

The advantages of carbon dioxide as a working fluid compared to water in geothermal energy recovery include (1) large expansivity and compressibility, which result in great density difference between the injector and the producer and reduce the power consumption for circulation on account of buoyancy force, (2) low viscosity coefficient, which leads to the larger flow rate under fixed differential pressure, (3) low salt solubility, and (4) low chemical reactivity; CO_2 does not mostly tend to react with rocks. Pruess [3] has built a homogeneous five-spot "fully developed" fractures reservoir model and indicated that, for a given pressure difference between injection and production wells, CO_2 would generate 50% larger net heat extraction rate and four times larger mass flow rate compared to water. Atrens et al. [5] drew a conclusion without consideration of frictional pressure that CO_2 thermosiphon could produce similar amount of electric power with the same quantity of heat extraction compared to water but with simpler surface equipment. Xu et al. [6] performed wellbore-reservoir coupled five-spot model and pointed out that the specific enthalpy change of CO_2 in the wellbore is so small relative to its intrinsic specific

enthalpy that the wellbore flow can be regarded as isenthalpic process, and the temperature of the fluids in production well will decrease rapidly with pressure. Compared to water, the advantage of CO_2 as a working fluid is more noticeable in low permeability and low temperature reservoirs.

Actually, the investigations mentioned above were carried out under an assumption that the target reservoirs are homogeneous. However, the permeability and porosity heterogeneity of a reservoir significantly affect the CO_2 migration and production. Garapati et al. [7] analyzed the effects of multilayered reservoirs on a CPG system; they found that the produced CO_2 mass fraction is dominated by high permeability layers and their position within reservoirs. In addition, the heat extraction rate comes down as the permeability of the bottom reservoirs decreases. Yang et al. [8] considered the effects of permeability and porosity heterogeneity on the liquid invasion in tight gas reservoir and drew a conclusion that both the liquid invasion depth and invasion rate increased as the heterogeneity coefficient of permeability decreased. Tian et al. [9] established a two-dimensional model with the consideration of heterogeneity in hydrological parameters of a caprock and indicated that the hydrological heterogeneity significantly affects the containment of intruded CO_2 within a caprock. Bu et al. [10] constructed a 2D numerical model to study the influence of high-porosity and high permeability faults within a reservoir and found that the high-porosity and high permeability faults influence CO_2 migration and spatial distribution and then increase the CO_2 storage capacity of reservoir.

In this paper, we built a three-dimensional geological model with spatially varying permeability and porosity, based on Qingshankou Formation in Songliao Basin, China, to evaluate the effects of hydrological heterogeneity in terms of permeability and porosity on the performance of a CPG system. The temperature change, temporal and spatial distribution of CO_2, rate of production flow, heat extraction rate of system, and storage capacity of CO_2 were chosen as the metrics to evaluate the performance.

2. Problem Setup

A great deal of detailed information is required to assess the feasibility of injected CO_2 as a heat transmission fluid at any specific site and to develop engineering designs for CO_2-based geothermal systems. Before moving into site-specific investigations, general features and issues should be explored. This can be done by investigating deep brine systems that abstract site-specific features and thereby attempt to represent characteristics that are common to many such systems. Here, geological characteristics and thermophysical conditions are mainly extracted from the central depression of Songliao Basin, Northeastern China. The basin has a pretty high geothermal gradient and heat flow among sedimentary basins in China and can meet the temperature requirement for geothermal development.

2.1. Conceptual Model and Boundary Condition Settings. To investigate processes of fluid migration and heat exchange within both wellbores and geologic formation, a three-dimensional conceptual model with a size of 10000 m × 10000 m × 100 m, including two wellbores and a reservoir formation (Figure 1), to represent a 100 m thick sandstone layer extending 10 km horizontally in Qingshankou Formation in Songliao Basin, was used. The distance between the injection and production wellbores is 600 m, and both wellbores vertically perforate the whole thickness of reservoir. The length of the model set to be 10000 m laterally is aimed at avoiding the influence of lateral boundaries. Moreover, for the lateral boundaries, Dirichlet-type condition (here, constant pressure and temperature) was imposed. As for the top and bottom boundaries, no-flow conditions were assigned (see the following section for more details). The wellbores with the surrounding formation are also set to be no-flow conditions but the heat exchange is allowed. The mesh of the modeling domain is generated using TOUGHVISUAL [11], which is able to create regular and irregular grids for TOUGH family codes [12]. During simulation, the accuracy and computational demand should be considered. Therefore, the mesh for the area around wellbores is refined, as shown in Figure 1.

2.2. Geological and Thermophysical Parameters. The top of Qingshankou Formation in Songliao Basin is at 2510 m depth and the thickness of this formation is about 250~550 m, including about 100 m thick sandstone layer with porosity of 10%~30% and permeability of 3 to 300 millidarcys which is the main oil and gas reservoir in this formation and with overlying and underlying mudstone as the caprock and bedrock [13]. The average geothermal gradient of the basin is 38.7°C/km [14]. In our model, the depth of the sandstone reservoir is 3000 m with the thickness of 100 m. The initial temperature of the reservoir was set to be 120°C according to the average geothermal gradient and the local mean annual surface temperature (about 4°C). The initial pressure of the model was obtained by hydrostatic equilibrium, and the reservoir was initially saturated with resident water (i.e., CO_2 saturation Sg = 0). The details of reservoir geological and thermophysical conditions used in our model are listed in Table 1, and the specification of physical parameters of the wellbores is summarized in Table 2.

2.3. Heterogeneity Implementation. From a realistic view, natural aquifer is intrinsically heterogeneous. The fluids are more likely to flow through the highly permeable zone, especially for CO_2, because of its strong mobility. It may lead to an early breakthrough. Among the properties of reservoir, permeability and porosity have the largest influence on flow field and heat extraction. Therefore, we just take them as the main variables to study heterogeneity effects.

As shown in Figure 1, the reservoir extends 10 km laterally, including a one square kilometer subdomain in the center. Here we assume that the subdomain is a geothermal reservoir with heterogeneities in permeability (k) and porosity (φ). Neuzil [15] observed that there exists a log-linear relationship between permeability and porosity in argillaceous sediments.

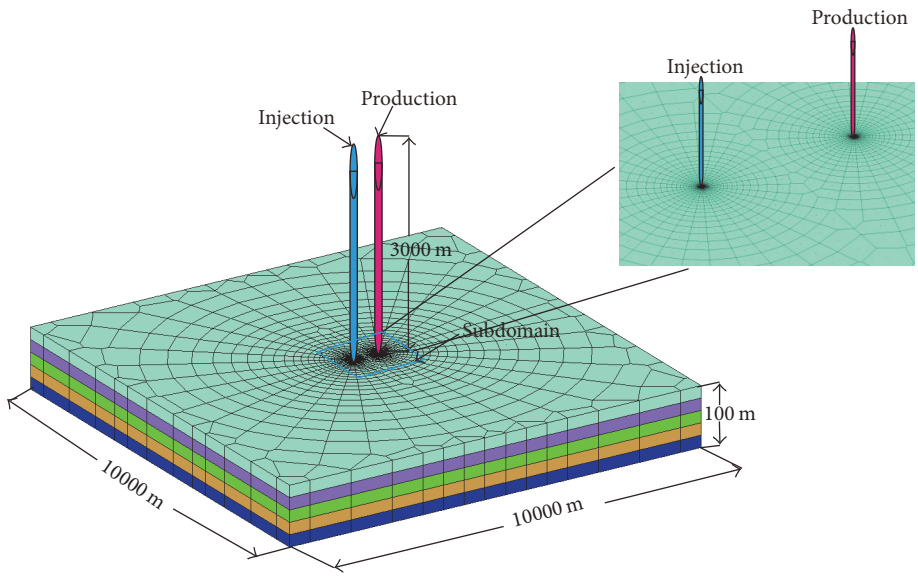

Figure 1: Two-spot reservoir-wellbore concept model with grid dissection.

Table 1: Geological and thermophysical conditions of the reservoir.

Reservoir parameter	Value
Depth (m)	3000
Thickness (m)	100
Temperature (°C)	120
Thermal conductivity ($W \cdot m^{-1} \cdot {}^{\circ}C^{-1}$)	2.51
Rock grain specific heat ($J \cdot kg^{-1} \cdot {}^{\circ}C^{-1}$)	920
Permeability (10^{-15} m^2)	3~300
Porosity	0.1~0.3
Rock grain density ($kg \cdot m^{-3}$)	2600
Average pressure (MPa)	29.4
Initial CO_2 saturation/Sg	0

Table 2: Specification for wellbores.

Parameter	Value
Roughness (mm)	0.046
Diameter (m)	0.2
The distance between two wells (m)	600
Thermal conductivity ($W \cdot m^{-1} \cdot {}^{\circ}C^{-1}$)	2.51

Tian et al. [9] drew a similar conclusion by regression analysis. In addition, Nelson [16] suggested a linear relationship between $\log(k)$ and φ in quartz sandstone. In this study, we assumed that the above discussed relationship between permeability and porosity is suitable for the Qingshankou Formation, and the relationship can be expressed as

$$\log_{10}(k) = a \times \varphi + b, \tag{1}$$

where a and b are data-fitted parameters, k is the permeability in m^2, and φ is the porosity. Based on the data in Table 1, we figured out the value of a and b in our model as 10 and −15.52, respectively.

We assumed that the permeability of reservoir is subject to a lognormal distribution, and thereby the porosity obeys a normal distribution inferred from (1). More realistically, the permeability obeys spatial random distribution in the reservoir rather than simply random distribution in probability and statistics. So we introduced the variation function, a concept derived from geostatistics, to depict the spatial distributions of permeability and porosity in the reservoir. In this study, a variance of 0.3 and correlation length of 300 m were chosen [9]. The simulator T2well provides a flexible function inherited from TOUGH2 V2 for permeability modification for each individual grid expressed as

$$k_n' = k_n \times \zeta_n, \tag{2}$$

where k_n is the absolute permeability of grid n, as specified in data block ROCKS and ζ_n is the permeability modification coefficient which can be defined internally or externally and may be provided as part of the geometry data in block ELEME and then employed to multiply the absolute permeability k_n for each grid in the subdomain. When the permeability modification is accomplished, the porosity is yielded according to (1) and stored in block INCON. More details about permeability modification coefficient generation and heterogeneity realization can be found in previous research [9]. The permeability and porosity range is shown in Table 3.

Infinite types of heterogeneous permeability and porosity fields can be generated randomly. As shown in Figure 2, six cases with heterogeneity in permeability and porosity were selected to represent the conditions: (i) high permeability belt connecting two wellbores (hh1, hh2); (ii) highly permeable zones expanding away from the production wellbore (hp1, hp2); and (iii) low permeability zone between the two wellbores (hl1, hl2). They are not expected to match with any existing geologic formation; we aim to make some theoretical analysis and quantitatively evaluation of the effects of

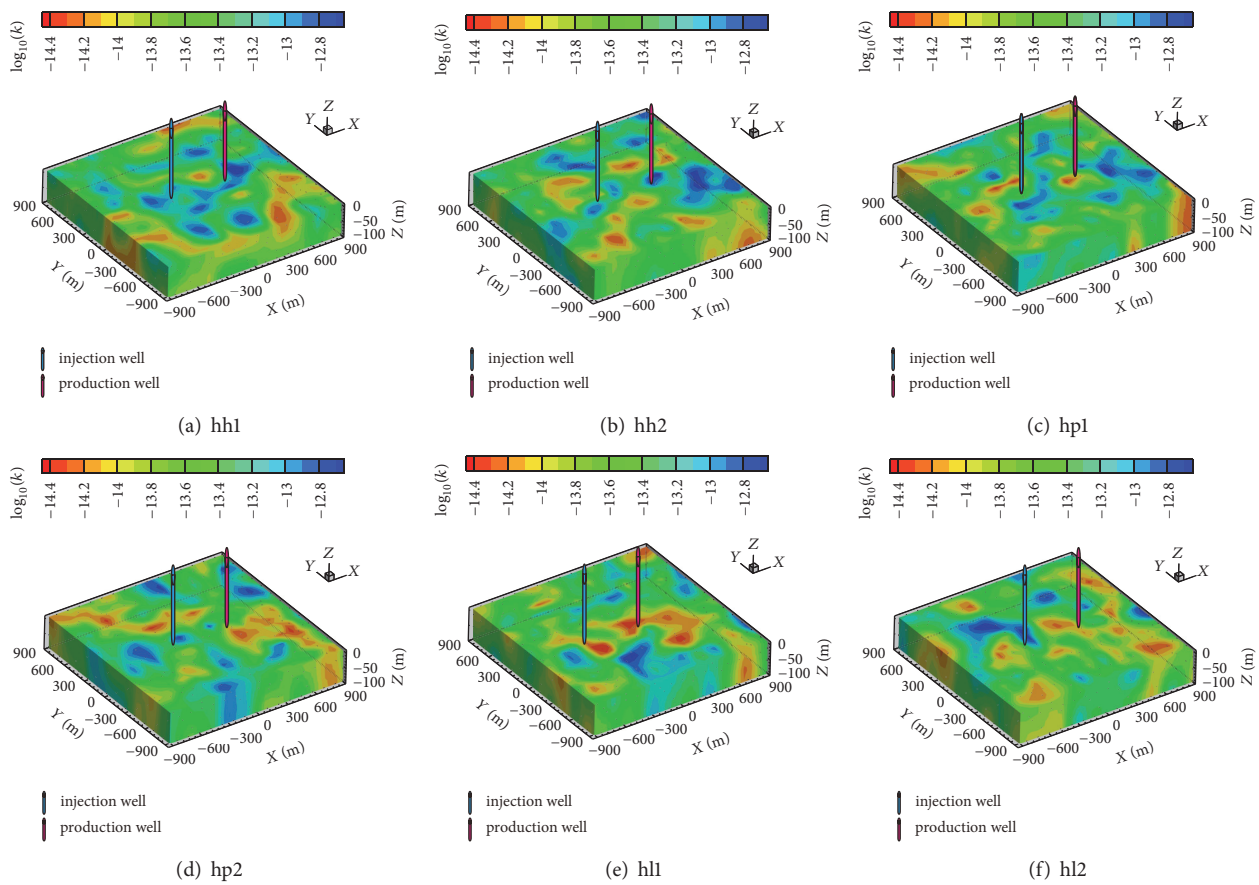

Figure 2: Permeability distribution of six heterogeneous cases.

Table 3: Parameter setting of different modeling scheme.

Modeling scheme	Permeability (10^{-15} m^2)	Porosity
Homogeneity (homo)	30	0.2
Heterogeneity		
Subdomain	3~300	0.1~0.3
Remaining parts	30	0.2

heterogeneities on a CPG system and elucidate the affecting mechanism.

2.4. Modeling Scenario. The CO_2 migrates simultaneously as the CO_2 is injected into the reservoir through injection wellbore, which pushes the existing resident water to move. Therefore, the production fluid is expected to be water at the early age. So the injection and production pressures at the wellhead are set to be 12 MPa and 0.1 MPa (atmospheric condition) to make CO_2 get breakthrough as soon as possible. After a period of propagation, CO_2 passes through the reservoir and can be observed from the production wellhead, and then the saturation of CO_2 (Sg) in production fluids increases rapidly, and the temperature of carbon dioxide decreases sharply with the pressure decline in the production wellbore, which is called the Joule-Thomson effect. To get a higher production fluid temperature and control the flow rate for a stable operation of the binary system, a constant pressure of 8.0 MPa is imposed both on the wellhead of production and injection after the production well is occupied by CO_2 (about 3 years). CO_2 is injected into the reservoir at a constant temperature of 15°C for 20 years.

3. Simulation Approach

3.1. Governing Equations. The process of fluid flow in subsurface can be divided into two parts, flow in the wellbores and flow in the reservoir formation. Therefore, we employed the wellbore-reservoir coupled simulator T2well [17–19]. It is an extension of the general multiphase, multicomponent, non-isothermal simulator TOUGH2 V2 [12]. The program assigns the wellbore and reservoir as two subdomains, in which flows are controlled by appropriate laws, respectively. In the reservoir, the flow is described as Darcy's law and in wellbore, it is momentum conservation. To consider a comprehensive description of the thermophysical properties of H_2O-CO_2 mixtures, the ECO2N V2.0 module was introduced, which reproduces fluid properties including density, viscosity, and specific enthalpy, largely within experimental errors under the temperature and pressure conditions of $10^\circ C < T < 300^\circ C$, $P < 600$ bar [20]. These fundamental flow equations, used in the T2Well code [18], are summarized in Table 4.

Table 4: The governing equations for numerical simulation.

Description	Equation
Mass and energy conservation	$\frac{d}{dt}\int M^{\kappa} dV_n = \int F^{\kappa}\cdot n d\Gamma_n + \int q^{\kappa} dV_n$
For mass	$M^{\kappa} = \phi\sum_{\beta}\rho_{\beta}S_{\beta}X_{\beta}^{\kappa}$ $F^{\kappa} = \sum_{\beta}\rho_{\beta}u_{\beta}X_{\beta}^{\kappa}$
For energy	$M^{\kappa} = \sum_{\beta}\rho_{\beta}S_{\beta}\left(h_{\beta} + \frac{u_{\beta}^2}{2} + gz\cos\theta\right)$ $F^{\kappa} = -\lambda\frac{dT}{dz} + \sum_{\beta}h_{\beta}\rho_{\beta}u_{\beta} + \frac{d}{dz}\sum_{\beta}\left(\frac{u_{\beta}^2}{2} + gz\cos\theta\right)$
Momentum equation	$\frac{\partial}{\partial t}\left(\sum_{\beta}\rho_{\beta}S_{\beta}u_{\beta}\right) + \frac{\partial}{\partial z}\left(\sum_{\beta}\rho_{\beta}S_{\beta}u_{\beta}^2\right) = -\frac{\partial P}{\partial z} - \frac{\Gamma\tau_w}{A} - \sum_{\beta}\rho_{\beta}S_{\beta}g\cos\theta$

In Table 4, M means the accumulation term, and F represents the flux term of mass or energy. β represents phase and κ is the index for fluid species. For mass conservation, $\rho_{\beta}, S_{\beta}, u_{\beta}$ are density, volumetric fraction, and velocity of phase-β, respectively. X_{β}^{κ} is the mass fraction of component κ in phase-β. For energy conservation, λ, h, and θ are heat conductivity, specific enthalpy of fluid, and inclination angle of wellbore, respectively. For momentum equation, Γ is perimeter of wellbore, and τ_w is the wall shear stress.

3.2. Drift-Flux Model. Drift-Flux Model [21, 22] is introduced to calculate the two-phase velocities of CO_2-water mixtures in wellbores by the following equations.

First, the velocity of gas phase can be described by the constitutive relation as below:

$$u_G = C_0 j + u_d, \tag{3}$$

where the profile parameter C_0 is used to account for the effect of local gas saturation and velocity profiles over the pipe (wellbore) cross-section [23]; j is the volumetric flux of total mixture, which is defined as

$$j = S_G u_G + (1 - S_G) u_L. \tag{4}$$

Thus, the velocity of liquid could be determined as

$$u_L = \frac{1 - S_G C_0}{1 - S_G} j - \frac{S_G}{1 - S_G} u_d. \tag{5}$$

Then the mixture velocity can be calculated in light of

$$u_m = \frac{S_G \rho_G u_G + (1 - S_G)\rho_L u_L}{\rho_m}. \tag{6}$$

By inserting (3) and (5) into (6), the volumetric flux j could be described as a function of mixture velocity u_m and the drift velocity u_d, as (7) shows:

$$j = \frac{\rho_m}{\rho_m^{\#}} u_m + \frac{S_G(\rho_L - \rho_G)}{\rho_m^{\#}} u_d, \tag{7}$$

where $\rho_m^{\#} = S_G C_0 \rho_G + (1 - S_G C_0)\rho_L$, and it is the profile-adjusted average density. The major task is now to calculate the mixture velocity and the drift velocity.

4. Results and Discussion

4.1. Migration of CO_2 in the Reservoir. The distribution of CO_2 saturation in the reservoir after 3 years of injection is shown in Figure 3. By comparing Figure 3(a) through 3(f) (6 heterogeneous cases) with the homogeneous cases of Figure 3(g), it can be found that the migration of CO_2 is significantly affected by the media (permeability and porosity) heterogeneity. In the homogenous reservoir, the CO_2 saturation distributes circularly around the injection well. However, in the heterogeneous cases, the CO_2 tends to flow through the highly permeable zone and leads to a preferential flow. It bypasses the low permeability zone to reach the production well, even if the flow path is longer (shown in Figures 3(e) and 3(f)). The positions holding high CO_2 saturation match well with highly permeable zone. For the cases that the highly permeable zones locate far away from the production well (Figures 3(c) and 3(d)), there would be more injected CO_2 stay in reservoir instead of being extracted from the production well.

4.2. CO_2 Saturation in Production Fluids. Being injected through the injection wellbore, CO_2 displaced the original water in the reservoir formation, and then water was first produced from the production well. At early stage, the production fluid was pure water, and CO_2 plume expanded within reservoir over time. When it reached the production well, the output fluids became into a mixture of water and CO_2. As can be seen in Figure 4(b), the time of CO_2 breakthrough was quite different in different cases. In homogeneous case, it takes about 1.3 years for CO_2 to reach the production well, while the breakthrough time of most heterogeneous cases is earlier; for example, it only takes 0.8 years for CO_2 to get through the reservoir and reach the production well in hh2 case, within which there is a highly

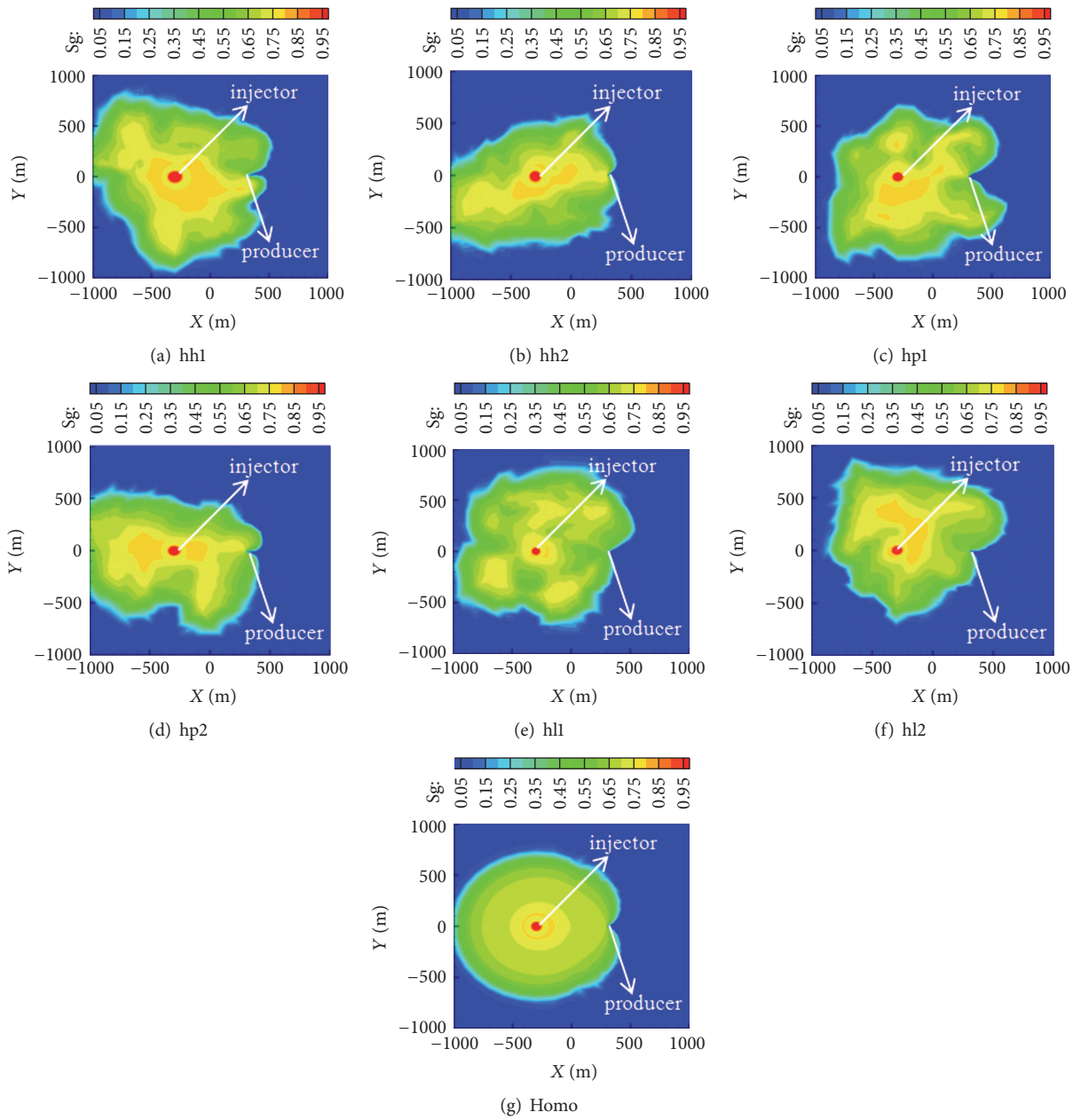

Figure 3: Carbon dioxide saturation distribution in the cross-section of subdomain in the depth of 3050 m for different cases after 3 years.

permeability zone between two wells. Correspondingly, in hl1 and hl2 cases, the breakthrough time is 1.4 years and 1.5 years, respectively, due to the low permeable belt between the injection and production wells. After CO_2 reached the production well, the saturation of CO_2 in the output fluids increased rapidly to over 0.9 (Figure 4(a)). The dive of curves in the figures is caused by the increasing of production pressure (from 0.1 MPa to 8 MPa as mentioned before). After that, the saturation of CO_2 recovered smoothly and stayed at about 0.92 during the rest operation time.

4.3. Injection and Production Rate of Fluids. The evolution of injection rate of CO_2 of different cases is presented in Figure 5. As shown in the figure, the injection rate of CO_2 rises rapidly after it reaches the production well. When injection and production wellhead pressures are imposed to be 8 MPa, the cyclic pressure difference ($P_{inj} - P_{pro}$) reduces to zero from 11.9 MPa, the injection rate of CO_2 instantly fell and stayed relatively constant during the rest time of simulation. The injection rate of CO_2 in hh1 and hh2 is relatively higher compared to other cases due to its high permeability and porosity zone between the two wellbores.

Figure 6(b) shows the evolution of production rate of water. It can be seen that the rate increases dramatically like an eruption, when CO_2 appears from the production wellhead. This phenomenon is caused by the CO_2 accumulation

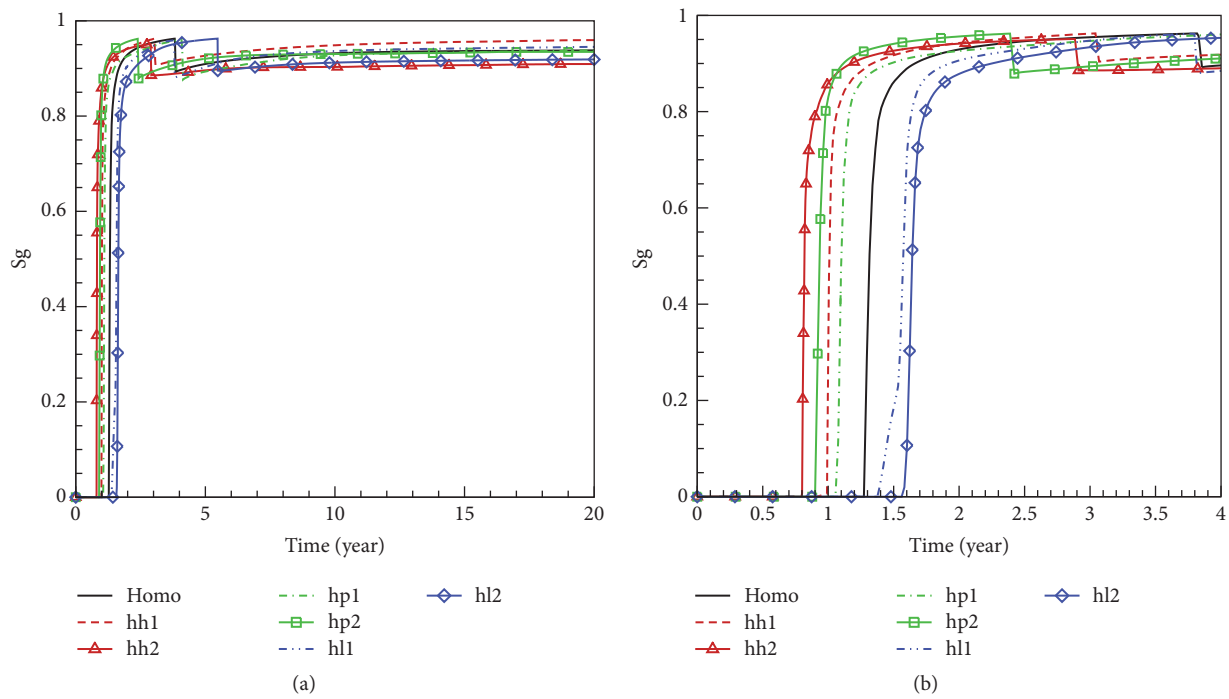

Figure 4: Variation of CO_2 saturation in output fluids versus time at the wellhead.

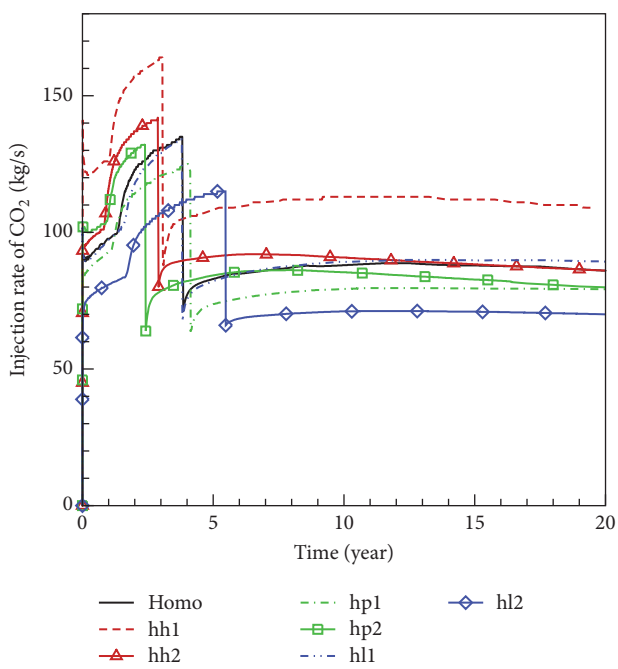

Figure 5: Variation of injection rate of CO_2 versus time for different cases.

in production; when it exceeds a certain quantity, an eruption event would take place. This phenomenon can likely account for some cold geysers eruptions [24, 25]. After the eruption, the content of water in the mixture fluids goes down. At the instant of raising the production pressure and reducing the injection pressure to 8 MPa, both the production rate of water and CO_2 fall off. Note that the production rate of water declines continually but that of CO_2 rises gradually. Even though the heat transmission fluid is CO_2, water still takes a large proportion of the production fluids because of the huge density difference in production well. Simulation results show that low permeability zone between the wellbores (hl1 and hl2) does not correspond to the lowest production rate of fluids as we expected. On the contrary, water production rate is relatively larger compared to other cases. This is because the resident water saturation at production well bottom in hl1 and hl2 is higher than that of other cases. On the other hand, the highly permeable belts connecting two wells may cause the high production rate of CO_2 and low production rate of water (hh1 and hh2). As can be seen in the graph, the fluids production rates of hp1 and hp2 are really low during the simulation time, which could affect the economic feasibility of the CPG system.

4.4. Temperature of Production Fluids. The temperature of production fluids is affected by the flow path and heat exchange within the reservoir. As shown in Figure 7, the temperature of production water distributes between 100 and 115°C before CO_2 reaches the production wellhead, which is somewhat less than the reservoir initial temperature (120°C). This temperature drop in the production well is due to the heat exchange (loss) with the surrounding rock around the wellbore. Consequently, when CO_2 begins to produce in the wellhead, the temperature of mixture output fluids drops rapidly. It is caused by the Joule-Thomson expansion in the wellbore with the pressure decrease from the downhole to the wellhead. It can be seen that the temperature drop of output fluids from the downhole to wellhead is approximate 40°C.

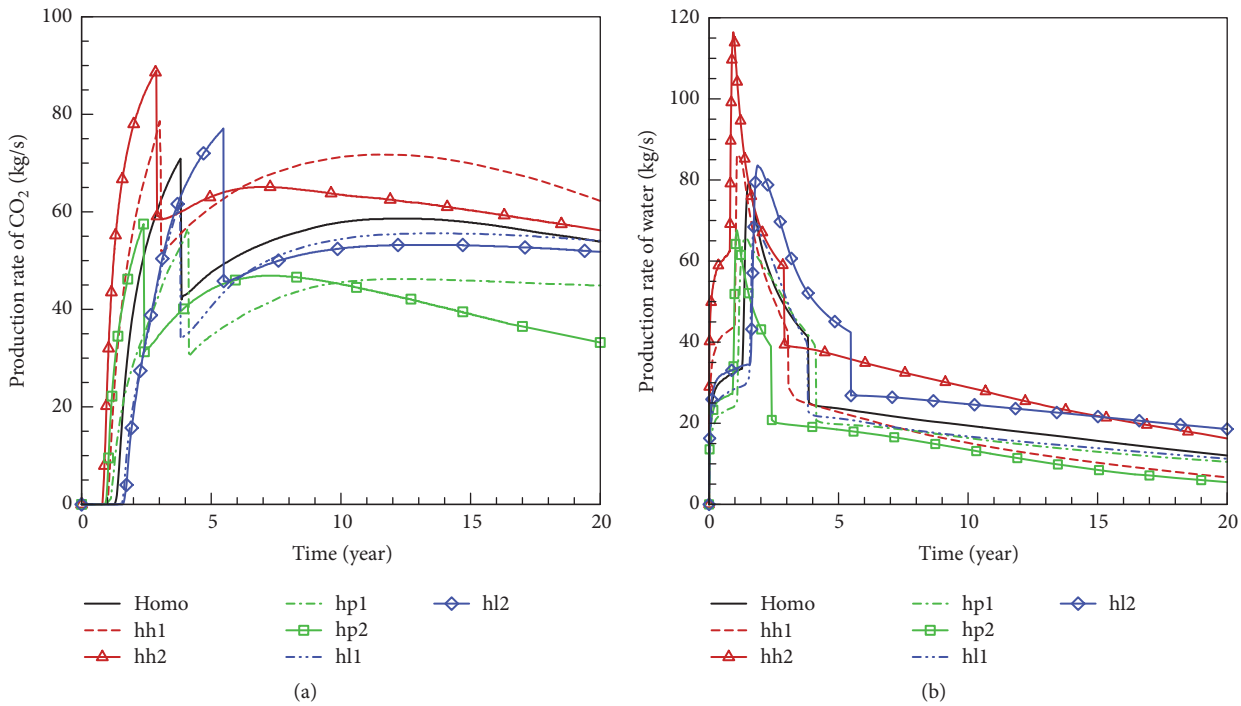

Figure 6: Variation of production rate of CO_2 (a) and water (b) versus time for different cases.

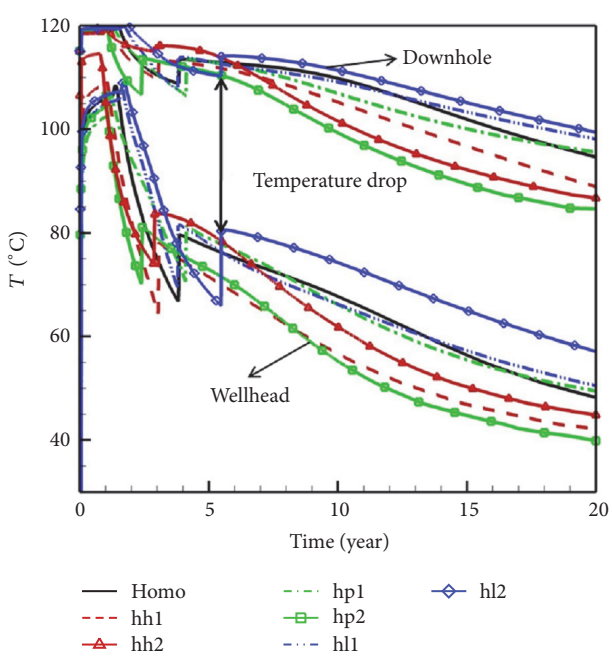

Figure 7: Temperature variation of output liquids.

Enhancing the production pressure increases the temperature of output fluids by 10 to 14°C.

Comparing the temperature of production fluids between different cases, it can be found that, to a certain extent, the temperature of output mixture fluids is proportional to the water output rate. It can be explained from two aspects. Firstly, water can counteract the Joule-Thompson effect and help keep the temperature. Secondly, higher water output rate implicates that more space of reservoir is occupied by CO_2, and more energy is extracted by the output fluid. That is just the reason why the cases with low permeability zone between the two wells correspond to a higher output fluids temperature (hl1 and hl2).

4.5. CO_2 Storage. To investigate the CO_2 storage capacity in the reservoir, we define the storage rate of CO_2 as the injection rate minus production rate of CO_2 ($CO_{2inj} - CO_{2pro}$). The storage rate of CO_2 of different cases is shown in Figure 8(a). More CO_2 is stored in the cases with highly permeable zone located away from production well. The storage amount of CO_2, that is, the storage rate of CO_2 integral of time, is shown in Figure 8(b). Similarly, the storage amount of CO_2 of cases hp1 and hp2 (with highly permeable zone deviating from production well) is relatively higher compared to other cases. However, the storage amount of CO_2 is also affected by cumulative injection of CO_2. So the storage ratio of CO_2 is calculated by storage amount of CO_2 divided by cumulative injection of CO_2 and is shown in Figure 9. In cases hh1 and hh2, CO_2 tends to migrate to production wellbore through high permeability zone between the two wellbores and the storage ratio of CO_2 in the reservoir is less than homogeneous case. On the contrary, in cases hp1 and hp2 (with high permeability belt deviating from producer) a portion of CO_2 will transport away from production wellbore and trapped in the reservoir. The storage ratio of cases hp1 and hp2 is 52.7% and 55.3%, respectively, which is relatively higher compared to homogeneous case (45%).

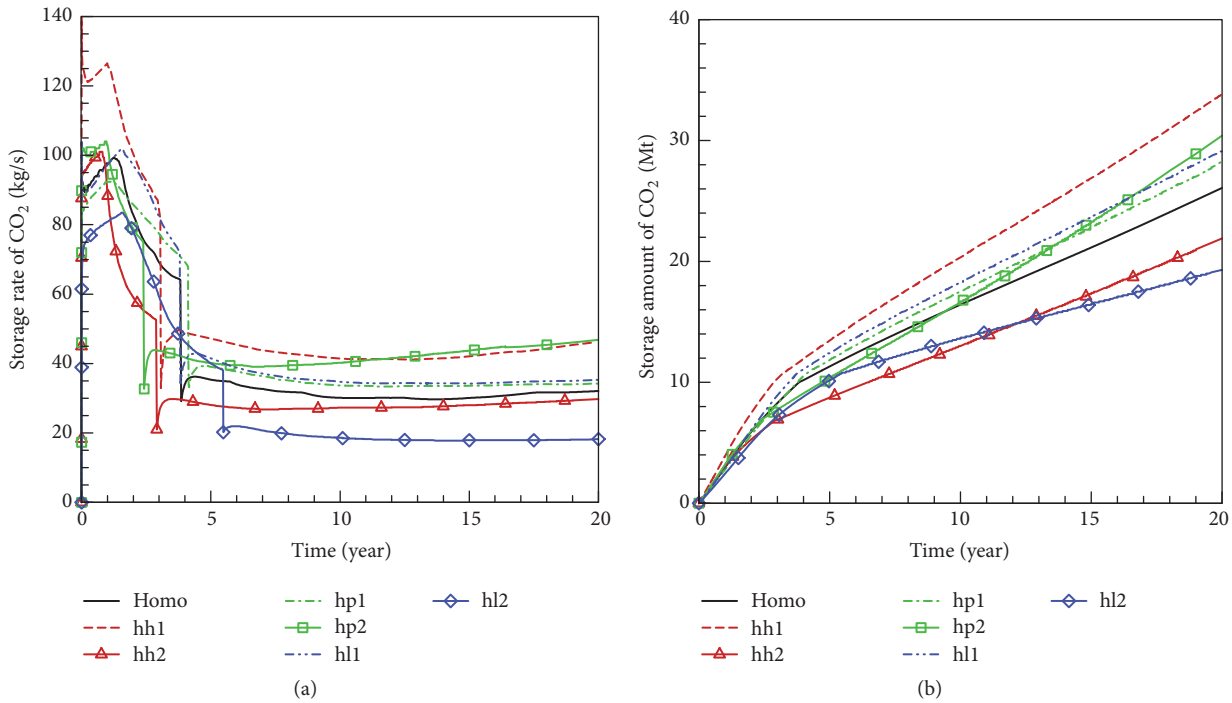

FIGURE 8: Storage rate (a) and storage amount (b) of CO_2 within reservoir versus time.

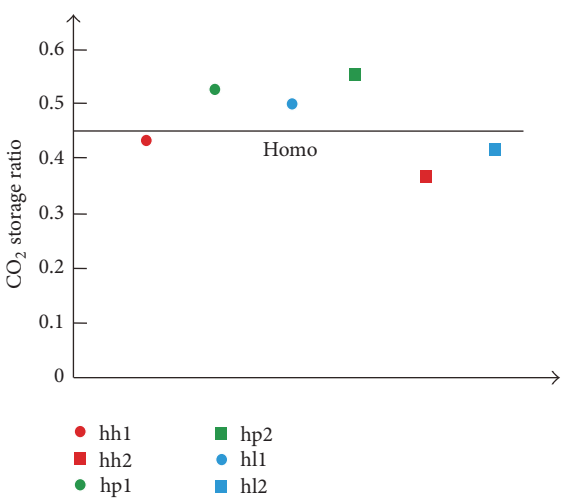

FIGURE 9: Storage ratio of CO_2 in reservoir after 20 years for different cases.

4.6. Temperature Distribution of Reservoir. The temperature drop in reservoir is caused by heat transfer between rock and fluids. After 20 years of production, the temperature of the rock matrix between the injector and producer is significantly reduced. It is highly affected by the hydrological heterogeneity. In cases hl1 and hl2 (Figures 10(e) and 10(f)), the temperature drop around the production wellbore is less than other cases due to the low permeability and porosity zone between the two wellbores.

4.7. The System Heat Extraction Rate. The net heat extraction rate is calculated by the following [26]:

$$G = F\left(h_{\text{pro}} - h_{\text{inj}}\right), \tag{8}$$

where G is the net heat extraction rate, F is the production flow rate, h_{inj} is the specific enthalpy of injection fluids, and h_{pro} is the specific enthalpy of production fluids.

The simulated heat extraction results (Figure 11) indicate that media heterogeneity affects the heat extraction rate greatly. In cases with low permeability zone between production and injection wells (hl1 and hl2), the heat extraction rates are similar with the homogeneity case and stay relatively constant in the middle and later periods. Cases hp1 and hp2, with high permeability zones extending far away from production well, have low heat extraction rates during the entire simulation time. The other heterogeneous cases with high permeability zone between two wells (hh1 and hh2) obtain the maximum extraction rates at early time (2 to 3 years) and decrease quickly in the later periods.

5. Concluding Remarks

We have built a three-dimensional wellbore-reservoir coupled model with consideration of permeability and porosity heterogeneity based on the geological and thermal-physical conditions of Songliao Basin, China. A total of 7 case simulations were performed. The following conclusions can be drawn.

Heterogeneity of reservoir's hydrological properties (in terms of permeability and porosity) affects the migration of

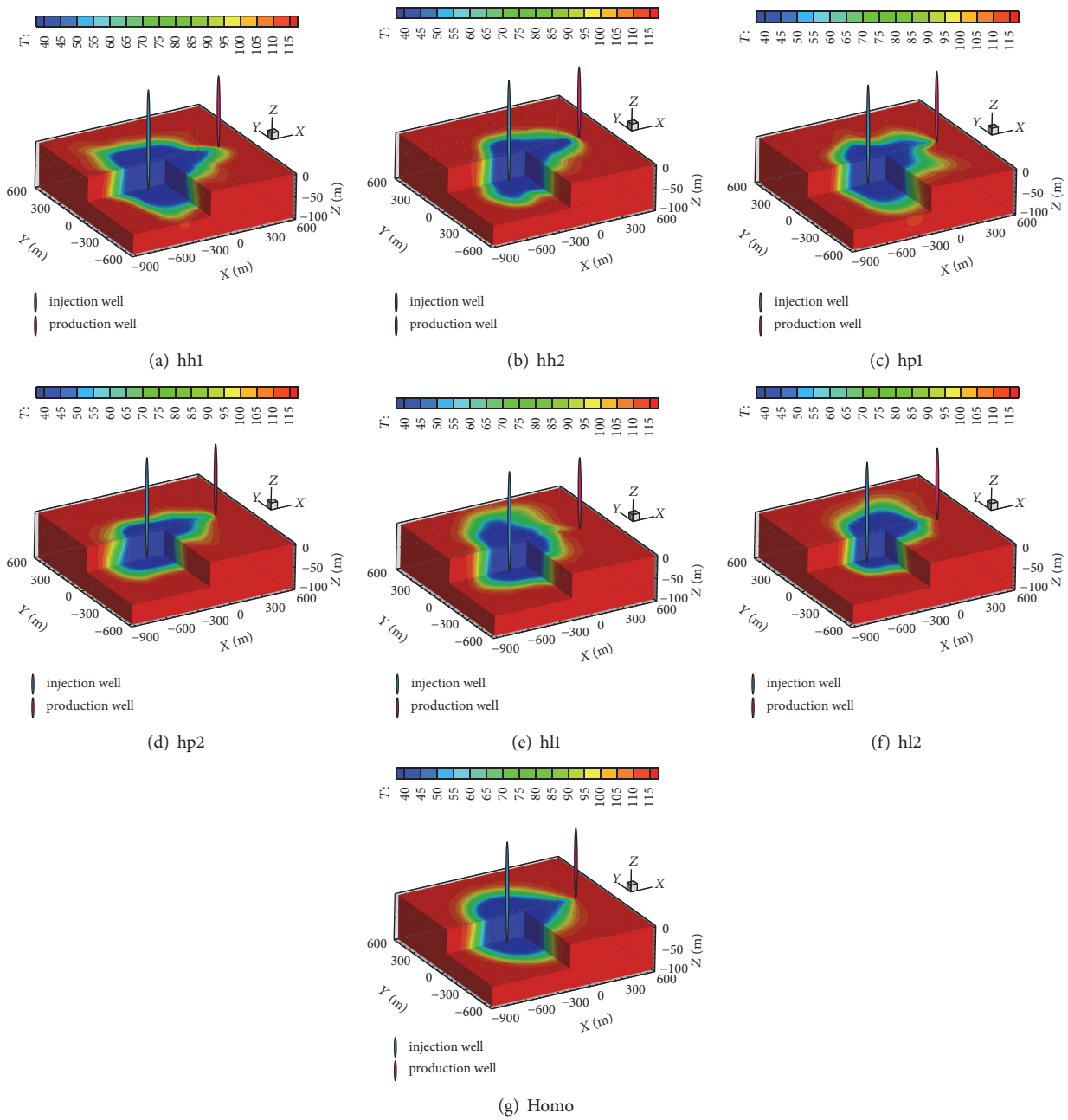

Figure 10: Temperature distribution of reservoir after 20 years.

CO_2 in the reservoir significantly. Due to the strong mobility of CO_2, as long as a highly permeable zone exists between the two wells, it is more likely to flow through the highly permeable zone to reach the production well, even though the flow path is longer. The preferential flow shortens circulation time and reduces heat-exchange area, probably leading to early thermal breakthrough, which makes the production fluid temperature decrease rapidly. The highly permeable zone located away from production wellbore is more in favor of the storage of CO_2 in the reservoir; however, it leads to quick decline in temperature of production fluids and heat extraction rate, which could affect the economic feasibility of the CPG system. Both of cases mentioned above should be paid more attention in the future design of an actual CPG demonstration project.

The range of problems concerning the process in CO_2-based geothermal systems is very broad. The present simulation results are specific to the conditions and parameters considered. The "numerical experiments" give a detailed understanding of the dynamic evolution and provide useful insight into fluid flow and thermal dynamic processes along the wellbores and reservoir.

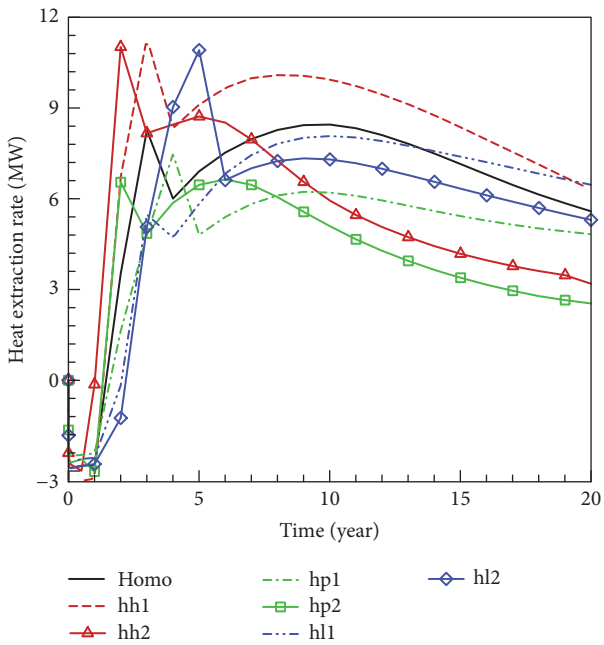

Figure 11: Variation of heat extraction rate over time for different cases.

Conflicts of Interest

The authors declare that they have no conflicts of interest.

Acknowledgments

This work was jointly supported by National Program on Key Research and Development Project (no. 2016YFB0600804), by the National Natural Science Foundation of China (Grant no. 41572215), by the 111 project (no. B16020), and by the project of CO_2 geological storage in China Junggar basin of China Geological Survey (Grant no. 121201012000150010).

References

[1] J. W. Tester, B. J. Anderson, A. S. Batchelor et al., The Future of Geothermal Energy, 2006.

[2] D. W. Brown, "A hot dry rock geothermal energy concept utilizing supercritical CO_2 instead of water," *Stanford University*, pp. 233–238, 2000.

[3] K. Pruess, "Enhanced geothermal systems (EGS) using CO_2 as working fluid—a novel approach for generating renewable energy with simultaneous sequestration of carbon," *Geothermics*, vol. 35, no. 4, pp. 351–367, 2006.

[4] J. B. Randolph and M. O. Saar, "Coupling carbon dioxide sequestration with geothermal energy capture in naturally permeable, porous geologic formations: Implications for CO_2 sequestration," *Energy Procedia*, pp. 2206–2213, 2011.

[5] A. D. Atrens, H. Gurgenci, and V. Rudolph, "CO_2 Thermosiphon for competitive geothermal power generation," *Energy and Fuels*, vol. 23, no. 1, pp. 553–557, 2009.

[6] T. Xu, G. Feng, Z. Hou, H. Tian, Y. Shi, and H. Lei, "Wellbore–reservoir coupled simulation to study thermal and fluid processes in a CO_2-based geothermal system: identifying favorable and unfavorable conditions in comparison with water," *Environmental Earth Sciences*, vol. 73, no. 11, article 6, pp. 6797–6813, 2015.

[7] N. Garapati, J. B. Randolph, J. L. Valencia, and M. O. Saar, "CO_2-Plume geothermal (CPG) heat extraction in multi-layered geologic reservoirs," in *Proceedings of the 12th International Conference on Greenhouse Gas Control Technologies, Ghgt-12*, vol. 63, pp. 7631–7643, 2014.

[8] X. Yang, Y. Meng, X. Shi, and G. Li, "Influence of porosity and permeability heterogeneity on liquid invasion in tight gas reservoirs," *Journal of Natural Gas Science Engineering*, vol. 37, pp. 169–177, 2016.

[9] H. L. Tian, F. Pan, T. Xu, B. J. McPherson, G. Yue, and P. Mandalaparty, "Impacts of hydrological heterogeneities on caprock mineral alteration and containment of CO_2 in geological storage sites," *International Journal of Greenhouse Gas Control*, vol. 24, pp. 30–42, 2014.

[10] F. Bu, T. Xu, F. Wang, Z. Yang, and H. Tian, "Influence of highly permeable faults within a low-porosity and low-permeability reservoir on migration and storage of injected CO_2," *Geofluids*, vol. 16, no. 4, pp. 769–781, 2016.

[11] Y. Yang, T. Xu, F. Bu et al., "TOUGHVISUAL a friendly graphical user interface for building TOUGHREACT models under complex 3D geological environments," in *Proceedings of the International Conference on Software Engineering and Computer Science*, 2013.

[12] K. Pruess, C. Oldenburg, and G. Moridis, "TOUGH2 User's Guide Version 2.0," Tech. Rep. LBNL-43134, 1999.

[13] S. Zhang, F. U. Xiu-Li, and C. C. Zhang, "The sedimentary evolution and response to hydrocarbon accumulation of quantou and qingshankou formation in songliao basin," *Journal of Oil & Gas Technology*, vol. 33, pp. 6–10, 2011.

[14] Q. L. Wu, "The geothermal field of songliao basin," *Journal of seismological research*, vol. 14, pp. 31–40, 1991.

[15] C. E. Neuzil, "How permeable are clays and shales?" *Water Resources Research*, vol. 30, no. 2, pp. 145–150, 1994.

[16] P. H. Nelson, "Permeability-Porosity Relationships in Sedimentary Rocks," *Log Analyst*, vol. 35, no. 3, pp. 38–62, 1994.

[17] L. Pan, C. M. Oldenburg, Y. S. Wu, and K. Pruess, "Wellbore flow model for carbon dioxide and brine," *Office of Scientific & Technical Information Technical Reports*, pp. 71–78, 2009.

[18] L. Pan and C. M. Oldenburg, "T2Well-An integrated wellbore-reservoir simulator," *Computers and Geosciences*, vol. 65, pp. 46–55, 2014.

[19] L. Pan, B. Freifeld, C. Doughty, S. Zakem et al., "Fully coupled wellbore-reservoir modeling of geothermal heat extraction using CO_2 as the working fluid," *Geothermics*, vol. 53, pp. 100–113, 2015.

[20] L. Pan, N. Spycher, C. Doughty, and K. Pruess, "ECO2N V2.0: a tough2 fluid property module for mixtures of water, NaCl, and CO_2," Tech. Rep. LBNL-6930E, 2015.

[21] N. Zuber, "Average Volumetric Concentration in Two-Phase Flow Systems," *Journal of Heat Transfer*, vol. 87, no. 4, pp. 453–468, 1965.

[22] G. B. Wallis, "Critical two-phase flow," *International Journal of Multiphase Flow*, vol. 6, no. 1-2, pp. 97–112, 1969.

[23] L. Pan, S. W. Webb, and C. M. Oldenburg, "Analytical solution for two-phase flow in a wellbore using the drift-flux model," *Advances in Water Resources*, vol. 34, no. 12, pp. 1656–1665, 2011.

[24] W. S. Han, M. Lu, B. J. Mcpherson et al., "Characteristics of CO_2-driven cold-water geyser, Crystal Geyser in Utah: Experimental observation and mechanism analyses," *Geofluids*, vol. 13, no. 3, pp. 283–297, 2013.

[25] Z. T. Watson, W. S. Han, E. H. Keating, N. H. Jung, and M. Lu, "Eruption dynamics of CO_2-driven cold-water geysers: crystal, tenmile geysers in utah and chimayó geyser in new Mexico," *Earth and Planetary Science Letters*, vol. 408, pp. 272–284, 2014.

[26] K. Pruess, "On production behavior of enhanced geothermal systems with CO_2 as working fluid," *Energy Conversion and Management*, vol. 49, no. 6, pp. 1446–1454, 2008.

Hindawi
Geofluids
Volume 2017, Article ID 9587872, 17 pages
https://doi.org/10.1155/2017/9587872

Research Article

Mesoscale Assessment of CO_2 Storage Potential and Geological Suitability for Target Area Selection in the Sichuan Basin

Yujie Diao,[1,2] Guowei Zhu,[1] Hong Cao,[2] Chao Zhang,[2] Xufeng Li,[2] and Xiaolin Jin[2]

[1] *State Key Laboratory of Coal Resource and Mine Safety, China University of Mining & Technology, Beijing 100083, China*
[2] *Key Laboratory of Carbon Dioxide Geological Storage, Center for Hydrogeology and Environmental Geology Survey, China Geological Survey, Baoding City, Hebei Province 071051, China*

Correspondence should be addressed to Yujie Diao; diaoyujie1983@163.com

Received 11 January 2017; Revised 14 March 2017; Accepted 26 April 2017; Published 2 July 2017

Academic Editor: Meng Lu

In China, south of the Yangtze River, there are a large number of carbon sources, while the Sichuan Basin is the largest sedimentary basin; it makes sense to select the targets for CO_2 geological storage (CGUS) early demonstration. For CO_2 enhanced oil and gas, coal bed methane recovery (CO_2-EOR, EGR, and ECBM), or storage in these depleted fields, the existing oil, gas fields, or coal seams could be the target areas in the mesoscale. This paper proposed a methodology of GIS superimposed multisource information assessment of geological suitability for CO_2 enhanced water recovery (CO_2-EWR) or only storage in deep saline aquifers. The potential per unit area of deep saline aquifers CO_2 storage in Central Sichuan is generally greater than 50×10^4 t/km^2 at $P50$ probability level, with Xujiahe group being the main reservoir. CO_2 storage potential of depleted gas fields is 53.73×10^8 t, while it is 33.85×10^8 t by using CO_2-EGR technology. This paper recommended that early implementation of CGUS could be carried out in the deep saline aquifers and depleted gas fields in the Sichuan Basin, especially that of the latter because of excellent traps, rich geological data, and well-run infrastructures.

1. Introduction

The Intergovernmental Panel on Climate Change (IPCC) noted in its fifth assessment report that climate change is more serious than the original understanding, and perhaps more than 95% of it is caused by human behavior [1]. In China, south of the Yangtze River, there are a large number of carbon sources; among that about 104.58 Mt CO_2 are discharged in Sichuan Province and Chongqing City mainly from cement and thermal power plants [2]. Therefore, as the largest sedimentary basins in Southern China, the Sichuan Basin covers about 20×10^4 km^2, with its craton basic structure, thick marine carbonate, and clastic sedimentary strata, and has great significance in analyzing mesoscale potential and geological suitability for CO_2 geological utilization and storage technologies (CGUS), including CO_2 enhanced oil, gas, coal bed methane, shale gas and water recovery (CO_2-EOR, EGR, ECBM, ESGR, and EWR), CO_2 enhanced geothermal systems, and uranium leaching (CO_2-EGS and EUL). Furthermore, CO_2 geological storage technologies include depleted oil or gas fields, unmineable coal seams, and deep saline aquifers CO_2 storage [3].

Evaluation of CO_2 storage potential is required to assess the contribution towards the reduction of CO_2 emissions. The Carbon Sequestration Leadership Forum (CSLF) and US Department of Energy (USDOE) both proposed the standards and methodologies for CO_2 storage capacity estimation and site selection and also the atlas [4–9], which provided the basic methodologies. Some researchers developed the methodologies or key parameters to evaluate the CO_2 storage potential or site selection [10, 11], and Goodman et al. [12] provided a detailed description of the USDOE's methodology for CO_2 storage potential evaluation. In China, Zhang et al. [13] first carried out a preliminary assessment of the national scale potential of CO_2 geological storage

in depleted oil and gas fields, unmineable coal seams, and deep saline aquifers. Subsequently, Liu et al. [14] and Li et al. [15] carried out evaluation of the potential of CO_2 geological storage in depleted natural gas fields and deep saline aquifers, respectively. Guo et al. [16] evaluated the national scale potential of CO_2 geological storage in depleted oil and gas fields, unmineable coal seams, and deep saline aquifers in 417 onshore and offshore sedimentary basins supported by China Geological Survey (CGS) and evaluated the suitability for prospective selection in the macroscale. As the CGUS methodologies are paid more and more attention, Li et al. [17] preliminary evaluated CO_2 geological storage potential of CO_2-EOR, EGR, and ECBM. ACCA21 [3] first evaluated the national scale potential of CGUS, and Wei et al. [18] developed the methodology of potential assessment of CO_2 geological utilization and storage in the macroscale in China.

From the view of spatial scale and time scale, the mesoscale corresponds to target between basin and site which needs more geological survey for CCUS demonstration or industrialization in the short term, generally before 2030 according to carbon reduction target of China. Therefore, because of the large area and complicated geology different from abroad, the methodologies and parameters of potential evaluation of CGUS should be more suitable for geology in the Sichuan Basin.

2. Methodology

In the mesoscale, oil and gas fields and CBM fields under production could be the target areas for CO_2 geological utilization or storage. However, for deep saline aquifer CO_2 geological storage or CO_2-EWR, the assessment of potential and geological suitability for target area selection should follow the order of candidate prospective area to target area, because of fast changing lithology and strong heterogeneity in terrestrial sedimentary formations and also the different distribution of aquifers in lateral and vertical direction. Based on the detailed studies of reservoirs and caprocks in sedimentary basins and the basic requirements for geological safety, the candidate prospective areas in the Sichuan Basin should be selected first, and then potential and geological suitability assessment could be carried out for target area selection next.

2.1. Method of Assessment of CO_2 Geological Utilization and Storage Potential

2.1.1. Depleted Oil Fields CO_2 Storage and CO_2-EOR

(1) Depleted Oil Fields CO_2 Storage. The method of assessment of CO_2 storage potential of CO_2-EOR is as follows [12]:

$$G_{CO_2} = \frac{\text{OOIP}}{\rho_{\text{oil}}} \cdot B \cdot \rho_{CO_2} \cdot E_{\text{oil}}, \tag{1}$$

where G_{CO_2} is CO_2 geological storage potential; OOIP is the proven original oil reserves in place of existed oil and gas fields presented by Ministry of Land and Resources of China (MLR), in accordance with the research scale in this paper; ρ_{oil} is oil density at standard atmospheric pressure; B is oil volume factor; ρ_{CO_2} is CO_2 density at reservoir temperature and pressure conditions (according to Berndt Wischnewski formula); E_{oil} is storage efficiency (or effective coefficient), recommend as 75% by Li et al. [17] based on the largest oil production rate of most depleted oil fields in China and the possible amount of CO_2 could be injected.

Table 1: The value of EXTRA with different API gravity.

EXTRA (%)	API
5.3	<31
1.3 (API—31) + 5.3	31 ≤ API ≤ 41
18.3	>41

Table 2: Four EOR cases with different depth/pressure and API gravity.

Depth	API	P_{LCO_2} (%)	P_{HCO_2} (%)
<2000	>35	100	0
	≤35	66	33
>2000	>35	33	66
	≤35	0	100

(2) CO_2-EOR. The method of CO_2 geological storage potential assessment of CO_2-EOR is as follows [19]:

$$G_{CO_2\text{-EOR}} = \frac{\text{OOIP}}{\rho_{\text{oil}}} \cdot B \cdot E_{\text{oil}} \cdot \text{EXTRA} \cdot \left(P_{LCO_2} \cdot R_{LCO_2} + P_{HCO_2} \cdot R_{HCO_2}\right), \tag{2}$$

$$\text{API} = \left(\frac{141.5}{S_g}\right) - 131.5, \tag{3}$$

where $G_{CO_2\text{-EOR}}$ is storage potential of CO_2 by using CO_2-EOR technology; EXTRA is the proportion of extra recovery to OOIP (Table 1); P_{LCO_2} is the lowest probability of oil recovery (Table 2); P_{HCO_2} is the highest probability of oil recovery (Table 2); $R_{LCO_2} = 2.113\ \text{t/m}^3$; $R_{HCO_2} = 3.522\ \text{t/m}^3$; S_g is specific gravity; other parameters are the same as formula (1).

2.1.2. Depleted Gas Fields CO_2 Storage and CO_2-EGR

(1) Depleted Gas Fields CO_2 Storage. USDOE [12] and CSLF [5] have the same assumptions for assessments of both CO_2-EGR storage potential and CO_2-EOR storage potential. Therefore, the calculation formulas are basically the same:

$$G_{CO_2} = \frac{\text{OGIP}}{\rho_{\text{gasstd}}} \cdot B \cdot \rho_{CO_2} \cdot E_{\text{gas}}, \tag{4}$$

Table 3: The values of R_{CO_2/CH_4} and C of different types of coal (USDOE, 2003).

Types of coal	R_{CO_2/CH_4}	C
Lignite	10	1.00
Noncaking coal	10	0.67
Weakly caking coal	10	1.00
Long flame coal	6	1.00
Gas coal	3	0.61
Fat coal	1	0.55
Coking coal	1	0.50
Lean coal	1	0.50
Meager coal	1	0.50
Anthracite	1	0.50

Table 4: Storage efficiency of unmineable coal seams [12].

P_{10}	P_{50}	P_{90}
21%	37%	48%

where OGIP is the proven original natural gas reserves in place, similar to OOIP; ρ_{gasstd} is gas density under standard atmospheric pressure; B is natural gas volume factor; E_{gas} is storage efficiency (effective coefficient), 75% [17]; other parameters are the same as formula (1).

(2) CO_2-EGR. Whether the feasibility of CO_2-EGR technique is possible or not, we could evaluate the storage potential of CO_2 using the following formula:

$$G_{CO_2\text{-EGR}} = \frac{\text{OGIP}}{\rho_{gasstd}} \cdot B \cdot \rho_{CO_2} \cdot E_{gas} \cdot C, \quad (5)$$

where $G_{CO_2\text{-EGR}}$ is CO_2 geological storage potential by using CO_2-EGR technology; C is reduction coefficient, compared with depleted gas storage, Li et al. recommend it as 63% [17]; other parameters are the same as formula (4).

2.1.3. Unmineable Coal Seams CO_2 Storage and CO_2-ECBM

(1) Unmineable Coal Seams CO_2 Storage. The formula to calculate the storage potential is as follows:

$$G_{CO_2} = G_{CBM} \cdot R_{CO_2/CH_4} \cdot \rho_{CO_2 std} \cdot E_{coal}, \quad (6)$$

where G_{CBM} is coal bed methane reserves (there is only prospective reserves proposed by MLR, less credible than the oil and gas reserves); R_{CO_2/CH_4} is the absorption capacity ratio of CO_2 and CH_4 in coal seams; E_{coal} is storage efficiency (effective coefficient); other parameters are the same as formula (4).

The values of R_{CO_2/CH_4} and E_{coal} were proposed by USDOE (2003) and Goodman et al. [12] as shown in Tables 3 and 4.

Table 5: CO_2 storage efficiency coefficients E_{saline} at regional scales [12].

Lithology	P_{10}	P_{50}	P_{90}
Clastics	1.2%	2.4%	4.1%
Dolomite	2.0%	2.7%	3.6%
Limestone	1.3%	2.0%	2.8%

(2) CO_2-ECBM. The formula to calculate the storage potential of CO_2-ECBM is as follows:

$$G_{CO_2\text{-ECBM}} = G_{CBM} \cdot R_{CO_2/CH_4} \cdot \rho_{CO_2 std} \cdot E_{coal} \cdot C, \quad (7)$$

where $G_{CO_2\text{-ECBM}}$ is CO_2 geological storage potential by using CO_2-ECBM technology; C is recovery coefficient of different types of coal; other parameters are the same as formula (6).

2.1.4. Deep Saline Aquifers CO_2 Storage and CO_2-EWR. The calculation formulas of CO_2-EWR and the only geological storage in saline aquifers technology are the same as follows:

$$G_{CO_2} = A \cdot h \cdot \varphi_e \cdot \rho_{CO_2} \cdot E_{saline}, \quad (8)$$

where A is reservoir distribution area; h is reservoir thickness; φ_e is saline aquifer average effective porosity; E_{saline} is storage efficiency (effective coefficient), shown in Table 5; other parameters are defined above.

2.2. Method of Suitability Assessment for Saline Aquifers Storage Target Selection

2.2.1. Mathematical Model

(1) GIS Superimposed Multisource Information Assessment Technology. Superimposed multisource information assessment technology is an integrated method of processing multisource geological data. Based on the two-dimensional space determined by geographical coordinates, the unity of the geographical coordinates within the same region but with different information, that is, the so-called spatial registration, is achieved, which is performed by using geographic information software (ArcGIS or MapGIS).

(2) Mathematical Model. The selected candidate prospective areas undergo the GIS spatial analysis into grids of 1000 m × 1000 m. The thematic information map prepared for each factor is screened by key veto factors. Thus, the single factor unfit to carry out CO_2 geological storage is identified to abandon the unsuitable grid for deep saline aquifer CO_2 storage.

Table 6: Index system for geological suitability assessment to select suitable targets for deep saline aquifer CO_2 storage.

Level one index	Weight	Level two index	Weight	Level three index	Weight	Good	General	Poor	Key veto factor
Reservoir conditions and storage potential	0.50	Characteristic of the best reservoir	0.60	Lithology	0.07	Clastic	Mix of clastic and carbonate	Carbonate	
				Single layer thickness h/m	0.11	≥ 80	$30 \leq h < 80$	$10 \leq h < 30$	<10
				Sedimentary facies	0.36	River, delta	Turbidity, alluvial fan	Beach bar, reef	
				Average porosity φ/%	0.20	≥ 15	$10 \leq \varphi < 15$	$5 \leq \varphi < 10$	<5
				Average permeability k/mD	0.27	≥ 50	$10 \leq k < 50$	$1 \leq k < 10$	<1
		Storage potential	0.40	Storage potential per unit area G (10^4 t/km^2)	1.00	≥ 100	$10 \leq G < 100$	<10	
Geological safety	0.50	Characteristic of the main caprock	0.62	Lithology	0.30	Evaporites	Argillite	Shale and dense limestone	
				Thickness h/m	0.53	≥ 100	$50 \leq h < 100$	$10 \leq h < 50$	<10
				Depth D/m	0.11	$1000 \leq D \leq 2700$	<1000	>2700	
				Buffer caprock above the main caprock	0.06	Multiple sets	Single set	None	
		Hydrodynamic conditions	0.24	Hydrodynamic conditions	1.00	Groundwater high-containment area	Groundwater containment area	Groundwater semicontainment area	Groundwater open area
		Seismic activity	0.14	Peak ground acceleration	0.50	<0.05 g	0.05 g, 0.10 g	0.15 g, 0.20 g, 0.30 g	≥ 0.40 g
				Development degree of fractures	0.50	Simple	Moderate	Complex	Within 25 km of active faults

Then, GIS spatial analysis and evaluation are carried out using formula (9).

$$P = \sum_{i=1}^{n} P_i A_i \quad (i = 1, 2, 3, \ldots, n). \tag{9}$$

Here, P is suitability scores of unit for CO_2 geological storage; n is the total number of evaluation factors; P_i is given point of the factor i; A_i is index weight of the factor i.

Single metric suitability rating is as follows: "good": 9 points, "general": 5 points, and "poor": 1 point. The evaluation result suitability rating is as follows: "highly suitable": value range $7 \leq P \leq 9$, "suitable": $5 \leq P < 7$, "less suitable": $3 \leq P < 5$, and "unsuitable": $1 \leq P < 3$.

2.2.2. Index System for Geological Suitability Assessment. As shown in Table 6, the index system for geological suitability has three hierarchies. The index weights at all levels are determined using the Analytic Hierarchy Process (AHP) [20, 21].

The assessment indexes are described detailed in the following.

(1) Characteristic of the Best Reservoir

Depth. Only if the theoretical storage depth is more than 800 meters can CO_2 enter the supercritical state, normally low than 3500 meters.

Lithology. According to the existing commercial-scale CO_2 geological storage projects (e.g., [22–24]), reservoir characteristics of oil and gas fields in China [25], and the engineering verification by the Shenhua CCS demonstration project in the Ordos Basin in China [26], clastic reservoirs are generally better than carbonate reservoirs.

Single Layer Thickness. Because of terrestrial sedimentary facies in most formations in onshore basins of China, it is difficult to find the large thick aquifers for CO_2 storage similar as Sleipner project in Norway. The minimum single layer thickness of reservoirs recommended in this paper is 10 m.

Sedimentary Facies. Most Cenozoic sedimentary basins in China are terrestrial sedimentary formations. The main part of the reservoir is the deltaic sand body, followed by the turbidite sand and alluvial fan glutinite body and finally the sand beach dams and a small amount of reef.

Porosity and Permeability. Low porosity and permeability is a special feature in terrestrial sedimentary oil and gas reservoirs and saline aquifers in China. Generally, for both the clastic and carbonate rock reservoirs, the porosity should be greater than or equal to 5% and permeability should be greater than or equal to 1 mD (e.g., [27–30]).

(2) Characteristic of the Main Caprock

Lithology. The most common caprocks of oil and gas fields in China are argillite (mudstone and shale) and evaporites (gypsum and rock salt), followed by carbonate rocks (marl, argillaceous dolomite, compact limestone, and dense dolomite) and frozen genesis caps. Sometimes there are local chert layers, seams, dense volcanic rocks, and intrusive rock caps.

Thickness. There are certain relationships between cap thickness and the size and height of the reservoir. With the combination of existing cap thickness grading standards [30] and considerations of the differences between CO_2 and oil and gas, the reference criteria for grading the classification of CO_2 geological storage cap thickness can be specified. The minimum thickness of CO_2 geological storage caprocks recommended in this paper is 10 m.

Burial Depth. The cap type is argillaceous rocks. The diagenesis has different effects on the performance of the caprock at different stage [31]. When the burial depth of argillaceous rocks is less than 1000 m, the diagenetic degree is poor and the sealing mainly relies on the capillary pressure. The porosity and permeability are good but with poor plasticity. At the burial depth of 1000–2700 m, the diagenesis is enhanced; mineral particles inside the argillaceous rock become more compacted; the porosity and permeability deteriorate; the plasticity increases; the capillary flow capacity declines; sealing ability improves; and there is abnormal sealing pressure. When the burial depth is greater than 2700 m, it is equivalent to the tightly compacted stage of the Argillite. The diagenesis is boosted further; the plasticity decreases and fragility increases; with the increase in the abnormal pressure, microcracks appear on the argillaceous rocks; and capillary sealing ability deteriorates.

The "Buffer Cap" above the Main Caprock. When the CO_2 breaks through the main cap, the "buffer cap" above the main cap has to provide a certain sealing capability to reduce or prevent the escape of CO_2.

(3) Geological Safety

Hydrodynamic Conditions. Ye et al. [32] divided the effect of hydrogeological conditions controlling coalbed methane into three categories: hydraulic transport dissipation effect, hydraulic seal effect, and hydraulic block effect. The more closed the hydrogeological conditions are, the more favorable they are for CO_2 geological storage. Basin lots with complex geological structure and powerful water alternating are not suitable CO_2 geological storage candidate prospective areas due to the high degree of hydrogeology and strong groundwater activities.

Peak Ground Acceleration. The GB 18306-2001 "The Peak Ground Acceleration Zoning in China" shows the Chinese seismic zonation map, its technical elements, and user provisions. It also applies to the CO_2 geological storage construction project. The greater the peak ground acceleration is, the more unfavorable it is for CO_2 geological storage. In general, the peak ground acceleration should be less than 0.40 g. Besides, active faults are not only CO_2 leakage pathways but also cause damage to the strata continuity, resulting in CO_2

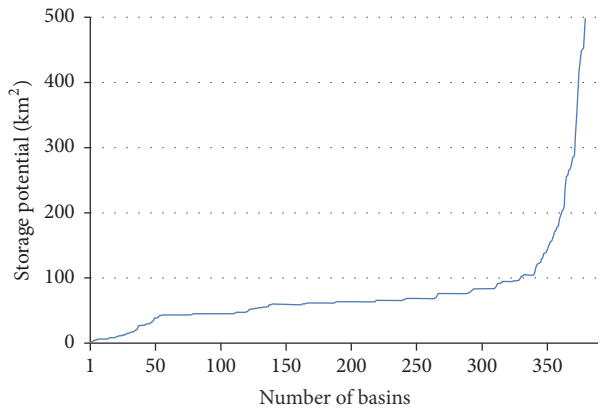

Figure 1: The statistical profile of CO_2 geological storage potential per square kilometer of 390 onshore basins in China.

leakage through the caprock. According to the GB 17741-2005 "Project site seismic safety evaluation" [33], the identification of the capable fault has to be made within a 5 km range of the first class venues and epitaxy. For seismic safety evaluation, the near-field region should be extended to a radius of 25 km range. Therefore, areas within 25 km of the active faults are inappropriate as the candidate prospective areas.

Development Degree of Fractures. CO_2 could leak by tectonic pathways including faults, fractures, and ground fissures (e.g., [28, 34–36]). Due to the complexity of geological structure and faults development in the Sichuan Basin, the qualitative assessment is based on the faults development and the existing seismic data. The more complex the fault system is, the more unfavorable it is for CO_2 geological storage. In addition, there have been more frequent seismic activities in the Sichuan Basin in recent years.

(4) Storage Potential per Unit Area. Guo (2014) evaluated the national scale potential of CO_2 geological storage in deep saline aquifers of 390 onshore basins in China supported by China Geological Survey. As shown in Figure 1, the potential of CO_2 geological storage in deep saline aquifers in most of the sedimentary basins is 50×10^4–100×10^4 t generally, and a small part of the basins are less than 10×10^4 t or more than 100×10^4 t.

3. Candidate Prospective Areas for CO_2 Geological Utilization and Storage

The fine forming conditions of the reservoir mediums for oil, gas, and CBM make them possible that the existing oil and gas fields under production are the mesoscale candidate prospective areas or target areas in the short future. Because of no official basin-scale data available, the CO_2 storage potential of other CO_2 geological utilization technologies is not discussed further in this paper.

3.1. Geology

3.1.1. Geostructure. As shown in Figure 2 [37], the current geostructure of the Sichuan Basin consists of the Southeast Sichuan fold belt, Central Sichuan low uplift, and Northwest Sichuan depression.

Table 7: Proven OGIP of 27 natural gas fields in the Sichuan Basin.

Gas fields	OGIP/10^8 m^3
Puguang	4050.79
Guang'an	1355.58
Hecuan	1187.06
Datianchi	1067.55
Xinchang	843.02
Luojiazhai	797.36
Moxi	702.31
Wolonghe	408.86
Weiyuan	408.61
Tieshanpo	373.97
Dukouhe	359
Bajiaochang	351.07
Luodai	323.83
Qiongxi	323.25
Qilibei	282.21
Baimamiao	268.72
Dachigan	258.71
Gaofengchang	227.26
Qilixia	225.48
Hebaochang	222.12
Tieshan	187.82
Zhongba	186.3
Majing	175.58
Xindu	175.32
Chongxi	136.35
Fuchengzhai	103.3
Jiannan	100.25

3.1.2. Stratigraphy. The Sichuan Basin sedimentary strata are complete, with a total thickness of 6000–12000 m. Only the Permian and the younger strata are considered in this paper, as follows from old to new:

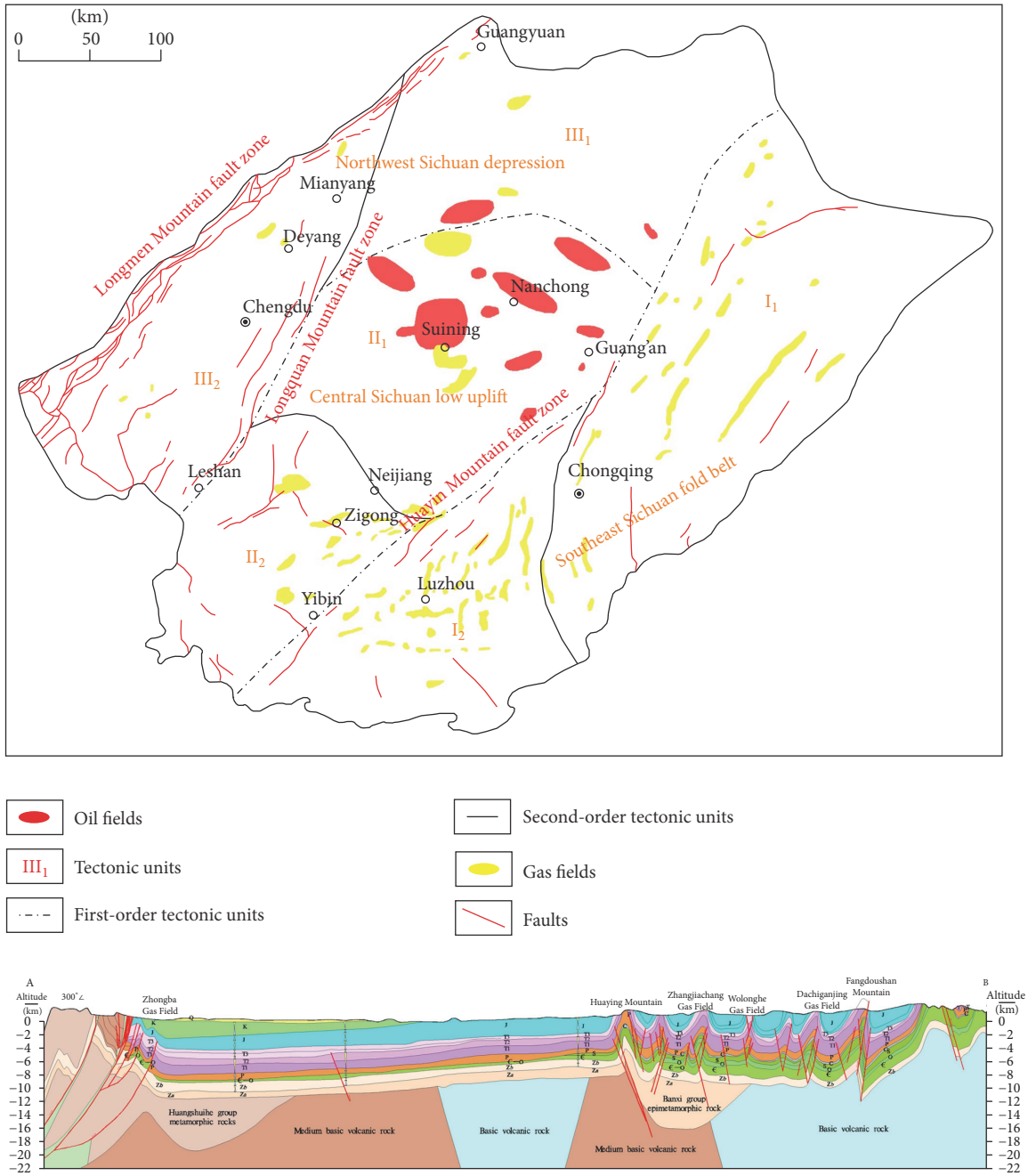

Figure 2: Sichuan Basin geological structure unit zoning map. There are three first-order tectonic units in the Sichuan Basin, that is, the Southeast Sichuan fold belt, the Central Sichuan low uplift, and the Northwest Sichuan depression. The Southeast Sichuan fold belt consists of the high steep fold belt in Eastern Sichuan (I1) and the low steep bottom fold belt in Southern Sichuan (I2); the Central Sichuan low uplift is composed of the flat fold belt in Central Sichuan (II1) and the low steep fold belt in Southwestern Sichuan (II2); the Northwest Sichuan depression consists of the low-lying fold belt in Northern Sichuan (III1) and the low steep fold belt in Western Sichuan (III2).

(1) The Permian: Liangshan group (P_1l), Qixia group (P_2q), Maokou group (P_2m), Longtan group (P_3l), and Changxing group (P_3c).

(2) The Triassic: Feixianguan group (T_1f), Jialing Group (T_1j), Leikoupo group (T_2l), Tianjingshan group (T_2t), Ma'antang group (T_3m), Xiaotangzi group (T_3t), and Xujiahe group.

(3) The Jurassic: Ziliujing group (J_1z), Qianfoya group (J_2q), Shaximiao group (J_2s), Suining group (J_3s), and Penglaizhen group (J_3p).

(4) The Cretaceous (K) and the Quaternary (Q).

3.1.3. Hydrodynamic Condition. The Sichuan Basin is essentially an artesian basin dominated by Permian and Triassic

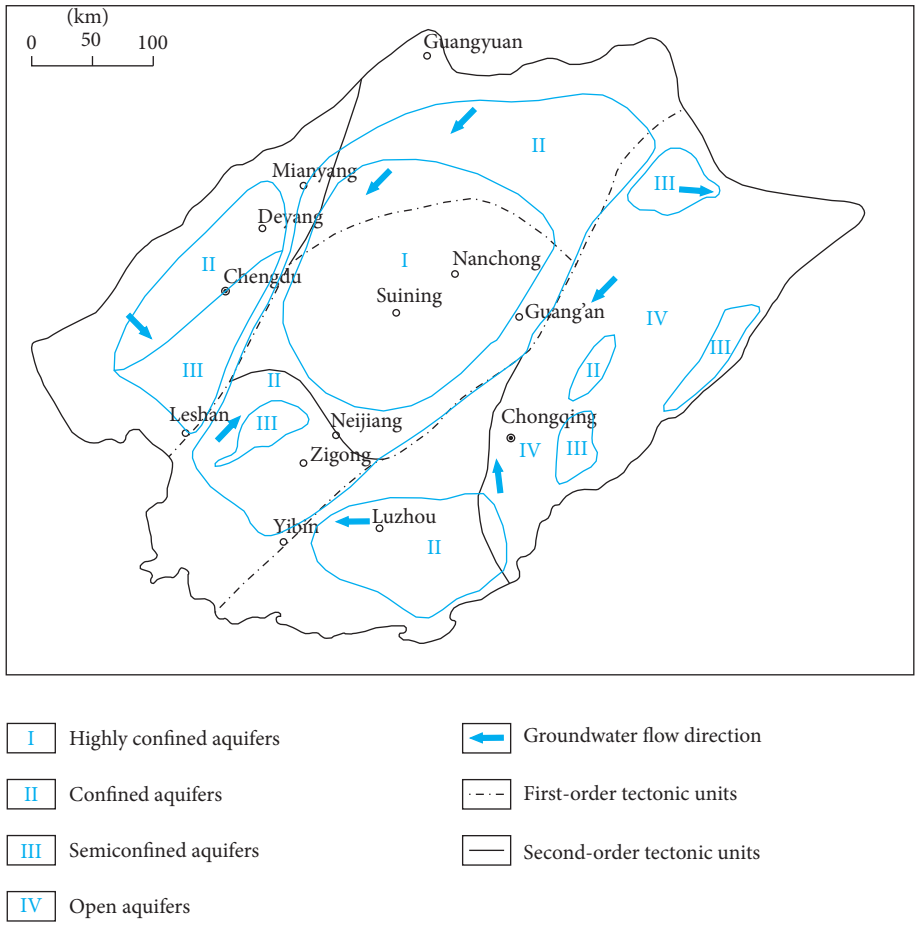

Figure 3: Hydrodynamic conditions in the Sichuan Basin. The groundwater activities are very strong in the peripheral target exposure area. In contrast, the groundwater activities inside the basin are relatively weak, with better hydrogeological confinement. On the edge of the mountain around the Sichuan Basin and the eastern fold belt experiencing infiltration of fresh water due to the complex structure and strong water alternating.

strata. The upper Jurassic and Cretaceous formations are mostly a large set of terrestrial clastic sedimentary rocks with red sandstones and mudstones throughout the basin. They are extremely thick with poor permeability, generally low in moisture, but exceedingly uneven, which could be good caprocks for the reservoirs below them. The lower upper Triassic Xujiahe consists of sandstones and shale, and the sandstone may be good aquifers for CO_2 geological storage due to its huge thickness. The lower and middle Triassic and Permian carbonate rocks are the main saline aquifers, in which Triassic carbonate rocks often form alternate layers with evaporites. Therefore, an aqueous rock series based on many stacked white aquifers is formed in the Sichuan Basin (Figure 3).

3.1.4. Geological Safety. There are many late Quaternary active faults on the boundary of the Sichuan Basin; for example, the Longmenshan fault zone in Northwestern Sichuan has experienced more intense activity in recent years. It is the induced fracture of the "5.12" Wenchuan 8.0 earthquake. The Lushan 7.0 earthquake on April 20, 2013, is another devastating earthquake that followed the Wenchuan 8.0 earthquake nearly five years later. It is also closely linked with the Longmenshan fault belt.

However, the crust in the Central and Eastern Sichuan Basin is more stable. Historical earthquakes with magnitude above 6 mainly took place in Western Sichuan and Southwestern Sichuan Basin. And the peak ground acceleration zoning according to the GB 18306-2001 "The Peak Ground Acceleration Zoning in China" is shown in Figure 4.

3.2. Oil and Gas Fields. The Sichuan Basin has abundant natural gas resources, mainly in Eastern Sichuan, but a relatively small amount of oil resources. The petroleum geological reserves in the Sichuan Basin amount to 4.38×10^8 t, and only 0.75×10^8 t of proven OOIP in Central and Northern Sichuan flat structure area [38].

By the end of 2008, the Ministry of Land and Resources of China (MLR) announced 125 gas fields in the Sichuan Basin (Figure 1), and the total amount of proven OGIP is 17225.02 $\times 10^8$ m^3. Among them, there are 27 medium to large-sized confirmed gas fields with OGIP exceeding 100×10^8 m^3, of

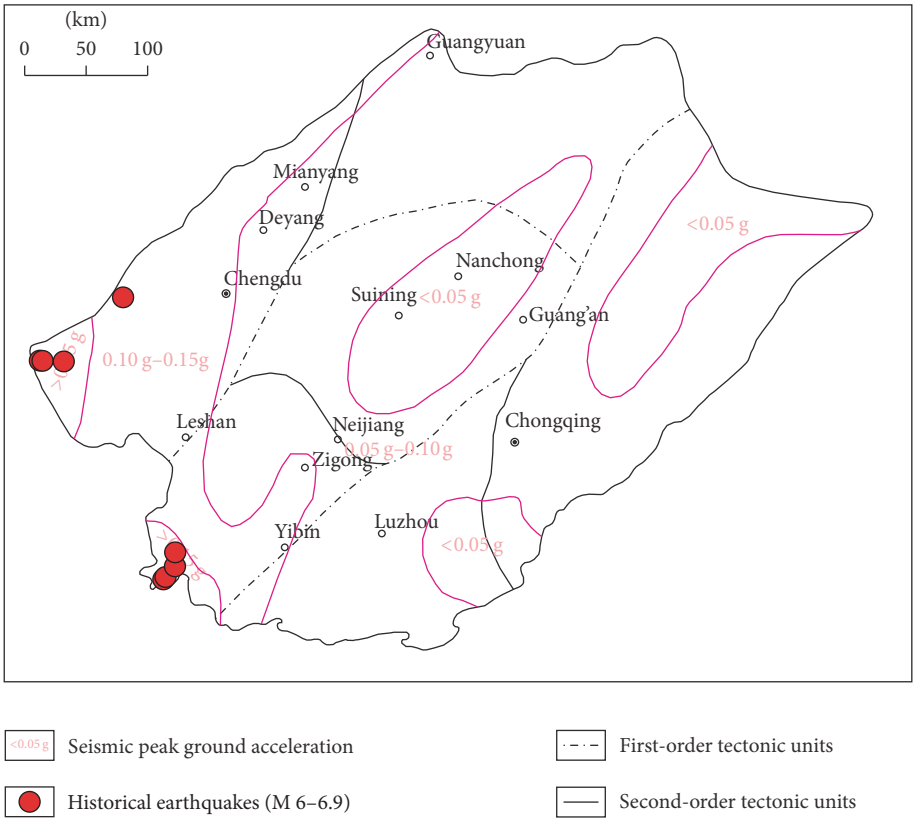

Figure 4: Seismic peak ground acceleration and large historical earthquakes in the Sichuan Basin. The peak ground acceleration is less than 0.10 g in most parts of the Sichuan Basin. Only in the western margin of the Sichuan Basin, the peak ground acceleration is larger than 0.15 g.

which the total natural gas reserves are 15092.68×10^8 m^3, accounting for 87.6% of the total proven OGIP in the basin (Table 7).

3.3. Unmineable Coal Seams. The CBM geological reserves in the Sichuan Basin amount to 3471.40×10^8 m^3 in Sichuan province and Chongqing city, 5084.57×10^8 m^3 in Southern Sichuan province and Northern Guizhou province, respectively, from 1000 to 2000 meters depth [39]. Among these, the coalfields in Southern Sichuan province are the most abundant, accounting for 82% of the province's total resources.

3.4. Deep Saline Aquifers. Compared with oil fields, gas fields, and unmineable coal seams, the analysis of geological conditions for saline aquifers CO_2 geological storage is much more complex. The CO_2 geological storage candidate prospective area for deep saline aquifers CO_2 storage was selected from the map projection on the ground of all potential underground CO_2 reservoirs. In addition, the hydrodynamic and geological safety conditions must be studied to delineate the candidate prospective areas.

3.4.1. Candidate Prospective Area Delineation Standards. As mentioned above, this report presents the delineation standards of the CO_2 geological storage candidate prospective areas shown in Table 8. Further potential and suitability assessments can be carried out for target area selection.

Table 8: Veto over key factors of CO_2 geological storage candidate prospective areas delineation.

Key factors	Veto
Reservoir conditions	
Layer thickness	<10 m
Porosity	<5%
Permeability	<1 mD
Hydrogeological conditions	
Formation water salinity	<3 g/L
Groundwater hydrodynamic condition	Groundwater zone
Geological safety conditions	
Active faults	<25 km
Peak ground acceleration	≥0.40 g

3.4.2. Vertical Reservoir Cap Combination and Candidate Prospective Areas Distribution. The reservoirs for deep saline aquifer CO_2 storage consist of the Permian, the lower Triassic carbonates, and upper Triassic and Jurassic clastic reservoirs (Figure 5). The reservoir space includes carbonate karst pores and cracks and clastic pores and cracks. Overall, all reservoirs

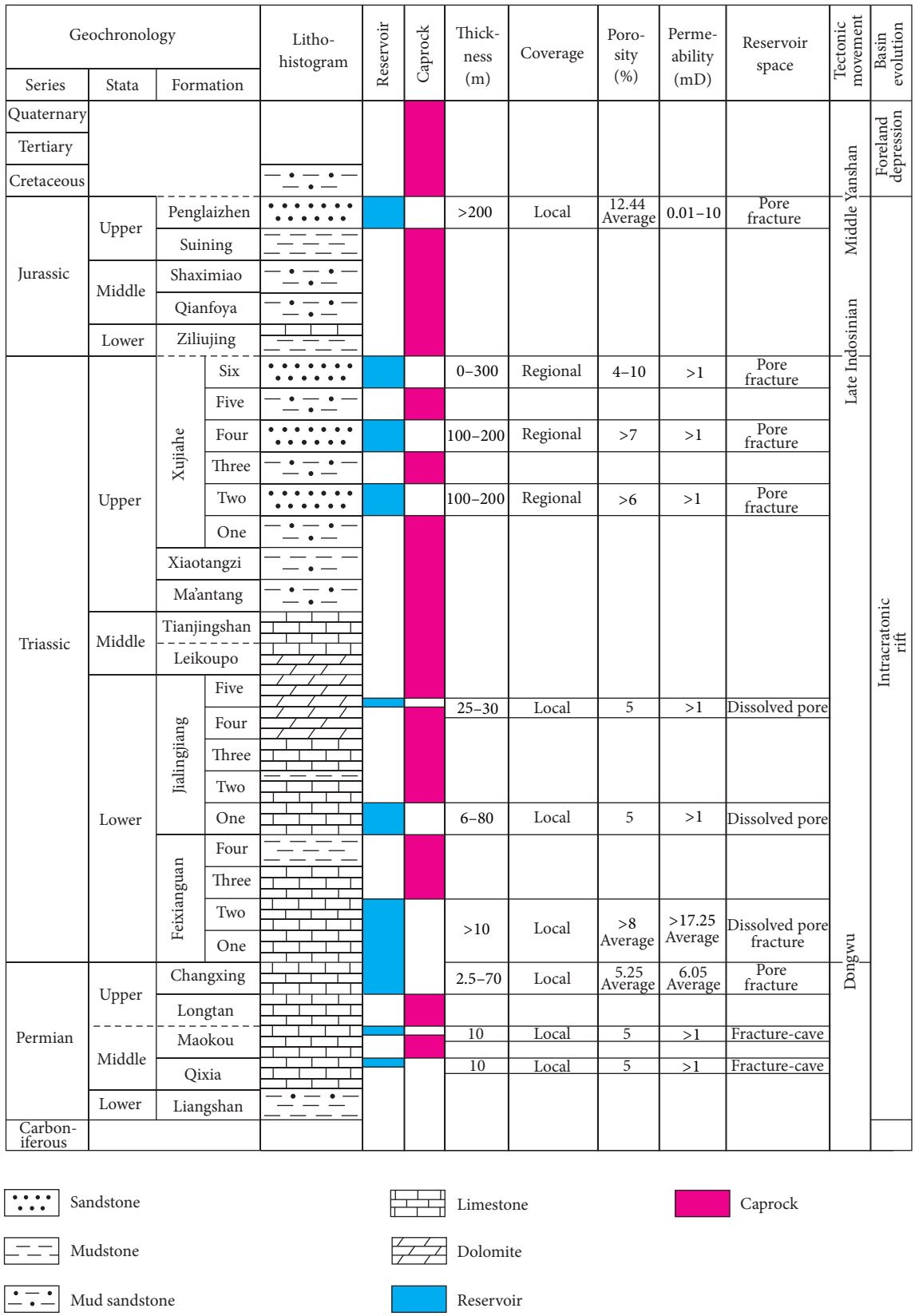

FIGURE 5: CO_2 geological storage vertical reservoir cap combination in the Sichuan Basin. There are nine sets of reservoirs in the Sichuan Basin, and the section four of Xujiahe group is the primary reservoir with large thickness and area, which almost cover the whole basin.

Table 9: Storage potential of CO_2 geological storage in depleted oil fields.

Tectonic unit	OOIP/10^8 t	Oil density (kg/m^3)	B (—)	Reservoir pressure/Mpa	Oil temperature/°C	ρ_{CO_2} (kg/m^3)	E_{oil}	$G_{CO_2}/10^8$ t
Central Sichuan flat structure area	0.58	850	1.18	21.26	64.42	712.63	0.75	0.57
Northern Sichuan flat structure area	0.17	850	1.18	21.26	64.42	712.63	0.75	0.17

Table 10: CO_2-EOR geological storage potential in the Sichuan Basin.

Tectonic unit	API	EXTRA (%)	P_{LCO_2} (%)	P_{HCO_2} (%)	E_{oil}	$G_{CO_2\text{-EOR}}/10^8$ t
Central Sichuan flat structure area	34.97	10.46	33	66	0.75	0.16
Northern Sichuan flat structure area	34.97	10.46	33	66	0.75	0.05

in the Sichuan Basin have poor physical properties, with ultra-low porosity and low permeability. Comparing with the natural gas fields in the Sichuan Basin, these reservoirs for CO_2 storage have better caprock conditions too. For example, the extensive deposits of gypsum rocks in the Leikoupo phase and the widely developed dark mudstone in the Lower Jurassic can provide good sealing conditions for the underlying reservoirs.

(1) The Permian. The reef flat facies on the top of Qixia group form a good reservoir through dolomitization, with favorable reservoir conditions (P_2q) [40]. Part of them form the natural gas reservoirs, with a thickness of approximately 10 m. Similar to the Qixia group, the Maokou group (P_2m) is a fracture-cave type of reservoir. Changxing group (P_3c) reservoirs are pore type and fracture-pore type. The porosity is generally 2.03%–15.85%, with an average value of 5.25%; the permeability is less than 1000 mD, with an average value of 6.05 mD. The reservoir thickness is large, with a monolayer thickness of 0.5–5 m and a single well cumulative thickness of 2.5–70 m [41].

(2) The Triassic. The Feixianguan group (T_1f) is similar to the Changxing group. The quality and distribution of the reef beach reservoir are mainly controlled by sedimentary facies and diagenesis. The evaporative platform oolitic dolomite reservoir is mainly distributed in Northeast Sichuan, with a monolayer thickness of 1.5–15 m and total thickness of 20–50 m. The porosity ranges from 2% to 26.8%, on the average of 8.29%; and the permeability is less than 1160 mD, with an average value of 59.73 mD. The porosity of the open platform edge oolitic dolomite reservoir is 2.05%–22.62%, on the average of 8.42%, and the permeability is less than 410 mD with an average value of 17.25 mD. The reservoir monolayer thickness is generally 0.5–6 m, and the total thickness is 10–45 m typically.

The favorable Jialingjiang reservoir facies are the platform interior shoal and the platform margin shoal facies. For example, section five of Jialingjiang reservoirs consists of limestone and dolomite, with a thickness of 25–30 m, of which approximately 60% is the porosity layer, and the average of the porosity is 5%, with the highest value reaching 18%.

The sandstone aquifers in section two, section four, and section six of Xujiahe formation could be reservoirs for CO_2 geological storage, composed of residual intergranular pore, intergranular dissolved pore, and fracture. The sand ratio of the sandstones is greater than 70% in 80% generally. In addition, the porosity of section four is higher than section two and section six, usually between 5%–10%, while the porosity of sandstones in section two and section is less than 7% generally.

Figure 6 shows the candidate prospective areas in the Sichuan Basin in the Sichuan Basin for deep saline aquifer CO_2 storage based on geology study.

4. Results

4.1. Potential

4.1.1. Depleted Oil Fields CO_2 Storage and CO_2-EOR. The primary CO_2-EOR prospective areas in the Sichuan Basin are located in the flat tectonic area in Central and Northern Sichuan Basin. As shown in Tables 9 and 10, the CO_2 geological storage potential of storage in depleted oil fields is only 0.74×10^8 t, while the storage potential is about 0.21×10^8 t by using CO_2-EOR technology.

4.1.2. Depleted Gas Fields CO_2 Storage and CO_2-EGR. The CO_2 geological storage potential of depleted gas fields is 53.73×10^8 t. By using CO_2-EGR technology, the Sichuan Basin gas fields could achieve CO_2 geological storage of 33.85×10^8 t. Among that 27 large and medium gas fields have the greatest potential, with the possibility of achieving a CO_2 geological storage capacity of 42.39×10^8 t in depleted gas fields, while the storage potential is about 26.70×10^8 t by using CO_2-EGR technology.

4.1.3. Unmineable Coal Seams CO_2 Storage and CO_2-ECBM. The Sichuan Basin has abundant coal bed methane resources. As shown in Table 11, the total CO_2 geological storage

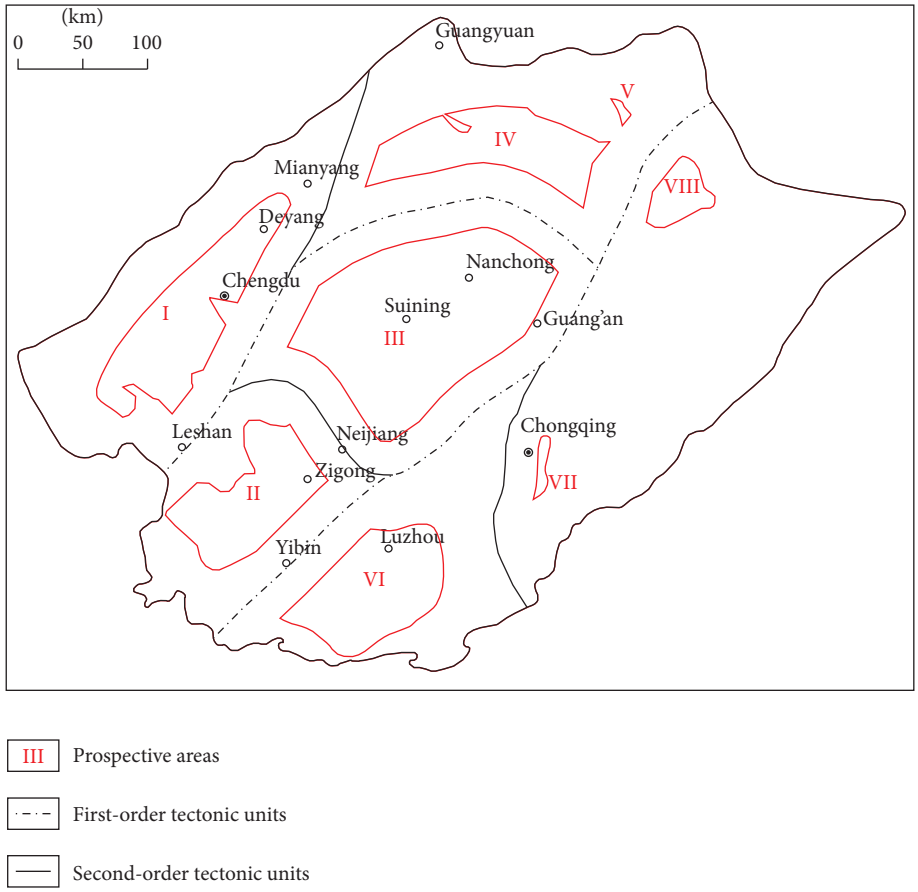

Figure 6: Candidate prospective areas in the Sichuan Basin. There are eight candidate prospective areas in the Sichuan Basin for deep saline aquifer CO_2 storage which cover more than 5×10^4 km^2 and mainly locate in Central Sichuan Basin (districts II–V). Only district I is in Northwestern Sichuan. The candidate prospective areas (districts VI–VIII) in Eastern Sichuan are relatively small due to the effects of formation depth, geological safety, and hydrogeological conditions.

Table 11: Storage potential of CO_2 in unmineable coal seams and CO_2-ECBM in the Sichuan Basin.

Area	$G_{CBM}/10^8$ m^3	Types of coal	R_{CO_2/CH_4}	C	$\rho_{CO_2 std}$ (kg/m^3)	$G_{CO_2}/10^8$ t	$G_{CO_2\text{-ECBM}}/10^8$ t
Southern Sichuan and Northern Guizhou	5084.57	Mainly anthracite	1	0.50	1.977	3.72	1.86
Sichuan and Chongqing	3471.40	Mainly coking coal and lean coal	1	0.50	1.977	2.54	1.27

potential of unmineable coal seams can vary in the range from 3.55×10^8 t to 8.12×10^8 t (6.26×10^8 t on the average), while the storage potential of CO_2-ECBM technology is half of the unmineable coal seams CO_2 geological storage.

However, the coal bed methane in the Sichuan Basin proposed by Ministry of Land and Resources (MLR) is just the theoretical geological reserves in place but not proven reserves, so the reliability of potential of unmineable coal seams and CO_2-ECBM is much lower than depleted oil and gas fields CO_2 storage and CO_2-EOR and CO_2-EGR.

4.1.4. Deep Saline Aquifers CO_2 Storage or CO_2-EWR. The total CO_2 geological storage potential in deep saline aquifers varies in the range of 77.81×10^8 t to 262.08×10^8 t (154.20×10^8 t on the average). However, the main CO_2 geological reservoirs are sections two, four, and six of Xujiahe formation, with the storage potential of 71.98×10^8 t to 245.95×10^8 t (143.98×10^8 t on the average), that is, approximately 93.37% of the total storage potential.

According to the statistics of the structural position, the total expected storage potential in Central Sichuan is the largest, reaching 89.26×10^8 t on the average. The total expected storage potentials in Western Sichuan and Eastern Sichuan are 45.68×10^8 t and 19.27×10^8 t on the average, respectively. The potential per unit area is shown in Figure 7.

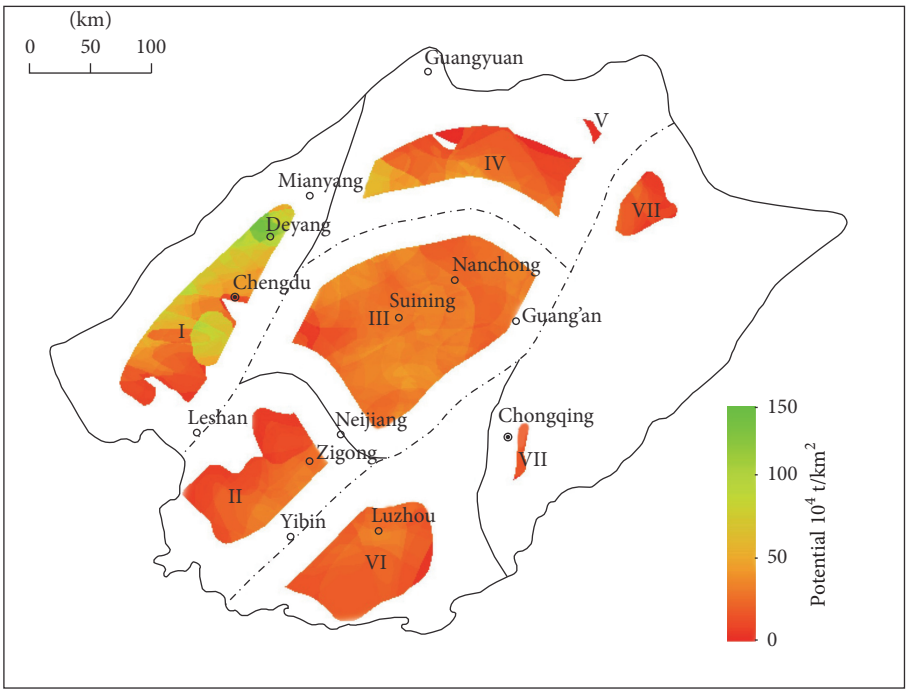

Figure 7: Storage potential per unit area for each prospective area. Due to the large stratigraphic thickness and many reservoir layers, the storage potential per unit area in most depressions in Northwestern Sichuan is quite large, with the largest up to 140×10^4 t/km^2, at $P50$ probability level. The storage potential per unit area in Central Sichuan is generally greater than 50×10^4 t/km^2, at $P50$ probability level.

Table 12: Geological suitability assessment information of the main reservoir distribution area (within section four of Xujiahe formation).

Level one index	Level two index	Level three index	Distribution information of the main reservoir in Xujiahe section 4	Geological information outside of Xujiahe section 4 distribution
Reservoir conditions and storage potential	Reservoir geological characteristics	Lithology	Clastic	Mix of clastic and carbonate
		Thickness/m	≥80	<30
		Sedimentary facies	River, delta	Beach bar, reef
		Average porosity/%	GIS partition processing	<10
		Average permeability/mD	<10	<10
	Storage potential	Storage potential per unit area (10^4 t/km^2)	GIS partition processing	GIS partition processing
Geological safety	Cap geological characteristics	Lithology	Argillite	Argillite
		Thickness/m	≥100	≥100
		Main cap depth	1000–2700	1000–2700
		Buffer cap above main cap	Multiple sets	Multiple sets
	Hydrodynamic conditions	Hydrodynamic conditions	GIS partition processing	GIS partition processing
	Seismic activity	Peak ground acceleration	GIS partition processing	GIS partition processing
		Fracture development	GIS partition processing	GIS partition processing

The main reservoir is the section four of Xujiahe formation, and the main cap is the lower Jurassic strata. The GIS partition processing must be carried out separately for the prospective areas within and outside of section four of Xujiahe formation. The geological information outside of section four of Xujiahe formation is from the best value of other eight reservoirs.

Table 13: Storage potential results in this paper compared with studies before.

CCUS	Study scales	Authors	Results before (10^8 t)	Basic data
CO_2 geological utilization				
CO_2-EOR	National	ACCA 21, 2014		MLR, 2010
	National	Wei, 2015		
	Target	*This paper*	*0.21*	
CO_2-EGR	National	ACCA 21, 2014		MLR, 2010
	National	Wei, 2015		
	Target	*This paper*	*26.70*	
CO_2-ECBM	National	ACCA 21, 2014		MLR, 2009
	National	Wei, 2015		
	Target	*This paper*	*3.13*	
CO_2 geological storage				
Depleted oil fields	National	Zhang, 2005		
	Basin	Li, 2009	0.20	Li, 2002
	National	ACCA 21, 2014		MLR, 2010
	Basin	Guo, 2014	Unpublished	
	National	Wei, 2015		
	Target	*This paper*	*0.74*	
Depleted gas fields	National	Zhang, 2005		
	National	Liu, 2006	10.14	900~3500 m Recoverable reserves [25]
	Basin	Li, 2009	10.50	
	National	ACCA 21, 2014		MLR, 2010
	Basin	Guo, 2014	Unpublished	
	National	Wei, 2015		
	Target	*This paper*	*42.39*	
Unmineable coal seams	National	Zhang, 2005		
	National	ACCA 21, 2014		MLR, 2009
	Basin	Guo, 2014	Unpublished	
	National	Wei, 2015		
	Target	*This paper*	*6.26*	
Deep saline aquifers	National	Zhang, 2005		
	National	Li, 2006	64.07	
	National	Li, 2009		
	National	ACCA 21, 2014		
	Basin	Guo, 2014	Unpublished	
	National	Wei, 2015		
	Target	*This paper*	*154.20*	*Further geological study*

4.2. Target Areas for Deep Saline Aquifers CO_2 Storage

4.2.1. Data. On the basis of systematic analysis of the deep saline aquifer CO_2 geological storage cap, through the geological suitability evaluation index system, the superimposed multisource information evaluation was successively carried out using ArcGIS software. The basic information is shown in Table 12. As mentioned in Section 3.4.2, the main reservoir in the Sichuan Basin is the section four of Xujiahe formation.

4.2.2. Target Areas. As shown in Figure 8, most prospective areas are suitable for CO_2 geological storage. The suitable areas could be used as the target areas for CO_2 geological storage. By further ground suitability evaluation and social economic surveys, some project sites can be identified from those target areas for large-scale saline aquifers CO_2 geological storage.

5. Discussion and Conclusions

5.1. Discussion. The purpose of this paper is not only to evaluate the mesoscale potential of different CCUS technologies but also select the suitable target areas for early demonstration in the Sichuan Basin. On the basis of geology study, the CO_2 storage potential of CO_2-EOR, CO_2-EGR, CO_2-ECBM, and saline aquifer CO_2 storage technologies was first evaluated comprehensively. Compared with the

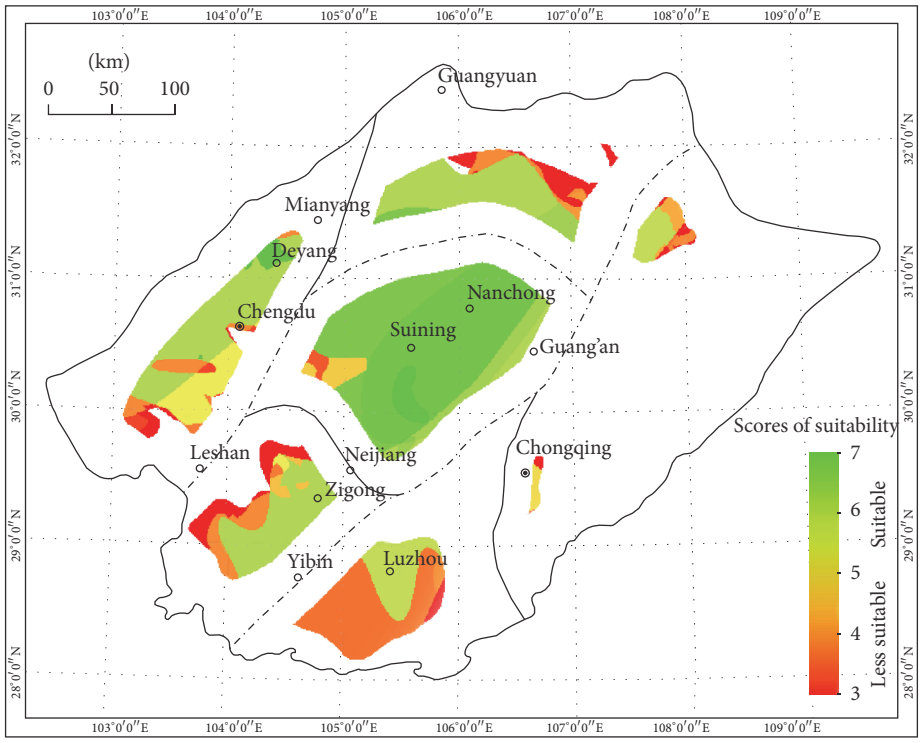

Figure 8: Assessment results of CO_2 geological storage suitability (suitable area is the "target area"). Most prospective areas in the Sichuan Basin are suitable for CO_2 geological storage, which could be the "target areas" for CO_2 geological storage. The main reservoirs in the Central Sichuan Basin are sections two, four, and six of Xujiahe formation with large thickness and good physical properties. They are far from the basin boundary faults, with weak hydrodynamic and good geological safety conditions.

similar studies before, the study scale in this paper is more detailed especially for CO_2 storage in deep saline aquifers, which is based on further geological study of reservoirs, seals, hydrogeology, and geological safety. The basic data for potential assessment are from MLR, PetroChina, and other authorities; thus the potential results are more credible, and more in accordance with geology. Table 13 shows the storage potential results in this paper compared with studies before.

5.2. Conclusions. Taking the low technical application levels of CO_2-EWR and CO_2-EGR into account, it is recommended that deep saline aquifers and depleted gas fields CO_2 geological storage in the Sichuan Basin could be early demonstrated, especially that of the latter because of excellent traps, rich geological data, and well-run infrastructures.

5.2.1. Deep Saline Aquifers CO_2 Geological Storage. For deep saline aquifers CO_2 geological storage, based on the consideration of deep saline aquifer CO_2 geological storage mechanism and geology of the Sichuan Basin, this paper proposes the study order of "prospective areas" to "target areas" and a new GIS superimposed multisource information evaluation method of geological suitability for target selection. The index system of geological suitability assessment for target selection is appropriate for multiple tectonics, facies, and reservoirs, to evaluate the suitability of prospective areas to select suitable target areas. The GIS superimposed multisource information evaluation results show that most areas are suitable for CO_2 geological storage, and only some local peripheral areas are not suitable for CO_2 geological storage. The areas selected through geological suitability assessment can be used as target areas for CO_2 geological storage.

The geology in Central Sichuan provides the best conditions, and the storage potential per unit area in Central Sichuan is generally greater than 50×10^4 t/km^2, at $P50$ probability level, with Xujiahe group is the main reservoir. However, deep saline aquifers CO_2 geological storage could only be used in the future due to its lack of other economic benefits, high investment, and multiple barriers in the short term.

5.2.2. Depleted Gas Fields CO_2 Geological Storage. In the mesoscale, gas fields under exploration or exploitation can be used as target areas for depleted gas fields CO_2 geological storage. The MLR has announced that there are 125 gas fields in the Sichuan Basin and 27 medium to large-sized confirmed gas fields among them. There are many gas reservoirs or traps becomes depleted, which provide a great chance for early demonstration first for the CO_2 resources located in the Sichuan Basin. Even in the long run, the depleted gas fields could be the main reservoirs for CO_2 geological storage in the Sichuan Basin.

Conflicts of Interest

The authors declare that they have no conflicts of interest.

Acknowledgments

The authors gratefully acknowledge the financial support of the project of China National Natural Science Foundation, "Mechanism of the Different CO_2 Distribution Saturation in Saline Aquifers Based on High Reliable Modeling (Grant no. 41602270)"; the China Clean Development Mechanism Fund project of National Development and Reform Commission, *"Research on the Guidelines for the Management of Underground Space Development for CO_2 Geological Storage (Grant no. 2014088)";* the geological survey project of China Geological Survey, *"Comprehensive Geological Survey of CO_2 Geological Storage in the Junggar and Other Basins (Grant no. 121201012000150010)"*; the UK-China Strategic Prosperity Fund (CPF) project of British Embassy Beijing, *"Identifying CO_2 Storage Opportunities in Depleted Gas Reservoirs: Joint UK-China Studies in Sichuan Basin"* and *"Research on Assessment of CO_2 Geological Utilization, Storage Potential and Early Demonstration Opportunity in the Sichuan Basin"*; the China-Australia Geological Storage of CO_2 project of Geoscience Australia and the Administrative Center for China's Agenda 21. The authors also gratefully acknowledge the support of Institute of Rock and Soil Mechanics, Chinese Academy of Sciences, and Chongqing University.

References

[1] IPCC, "IPCC Fifth Assessment Report: Working Group I Report "Climate Change 2013: The Physical Science Basis," Tech. Rep., 2013, http://www.ipcc.ch/report/ar5/wg1/.

[2] B. Bai, X. Li, Y. Liu, and Y. Zhang, "Preliminary study on CO_2 industrial point sources and their distribution in China," *Chinese Journal of Rock Mechanics and Engineering*, vol. 25, no. 1, pp. 2918–2923, 2006.

[3] ACCA21 (The Administrative Centre for China's Agenda 21), "The 3rd Report on National Assessment of Climate Change - Special Report on CO_2 Utilization Technologies," Tech. Rep., Science Press Ltd., Beijing, China, 2014.

[4] CSLF, "Phase I Final Report from the Task Force for Review and Identification of Standards for CO_2 Storage Capacity Measurement, Prepared by the task force on CO_2 storage capacity estimation for the technical group of the Carbon Sequestration Leadership Form August," Tech. Rep., 2005, ed, p. 22, 2005.

[5] CSLF, "Estimation of CO_2storage capacity in geological media (Phase), Prepared by the task force on CO_2 storage capacity estimation for the technical group of the Carbon Sequestration Leadership Form 15 June," Tech. Rep., 2007, ed, p. 24, 2007.

[6] CSLF (Carbon Sequestration Leadership Forum), *Task Force for Review and Identification of Standards for CO2 Storage Capacity Estimation*, 2010, http://www.cslforum.org/.

[7] DOE-NETL, *Carbon Sequestration Atlas of the United States and Canada*, 2006, http://www.netl.doe.gov/technologies/carbonseq/refshelf/atlas/.

[8] DOE-NETL, *Carbon Sequestration Atlas of the United States and Canada*, 2nd edition, 2008, http://www.netl.doe.gov/technologies/carbon seq/refshelf/atlas/.

[9] DOE-NETL, *Carbon Sequestration Atlas of the United State and Canada*, 3rd edition, 2010, http://www.netl.doe.gov/technologies/carbonseq/refshelf/atlas/.

[10] S. Bachu, D. Bonijoly, J. Bradshaw et al., "CO_2 storage capacity estimation: methodology and gaps," *International Journal of Greenhouse Gas Control*, vol. 1, no. 4, pp. 430–443, 2007.

[11] S. Bachu, "Review of CO_2 storage efficiency in deep saline aquifers," *International Journal of Greenhouse Gas Control*, vol. 40, pp. 188–202, 2015.

[12] A. Goodman, A. Hakala, G. Bromhal et al., "U.S. DOE methodology for the development of geologic storage potential for carbon dioxide at the national and regional scale," *International Journal of Greenhouse Gas Control*, vol. 5, no. 4, pp. 952–965, 2011.

[13] H. Zhang, D. Wen, Y. Li, J. Zhang, and J. Lu, "Conditions for CO_2 Geological Sequestration in China and some suggestions," *Geological Bulletin of China*, vol. 24, no. 12, pp. 1107–1110, 2005.

[14] Y. Liu, X. Li, Z. Fang, and B. Bai, "Preliminary estimation of CO_2 storage capacity in gas fields in China," *Rock and Soil Mechanics*, vol. 27, no. 12, pp. 2277–2281, 2006 (Chinese).

[15] X. C. Li, Y. F. Liu, B. Bai, and Z. Fang, "Ranking and screening of CO_2 saline aquifer storage zones in China," *Chinese Journal of Rock Mechanics and Engineering*, vol. 25, no. 5, pp. 963–968, 2006 (Chinese).

[16] J. Guo, D. Wen, S. Zhang et al., "Potential and suitability evaluation of CO_2 geological storage in major sedimentary basins of China," *Acta Geological Sinica (English Edition)*, vol. 89, no. 4, pp. 1319–1332, 2015.

[17] X. Li, N. Wei, Y. Liu, Z. Fang, R. T. Dahowski, and C. L. Davidson, "CO_2 point emission and geological storage capacity in China," in *Proceedings of 9th International Conference on Greenhouse Gas Control Technologies, GHGT-9*, pp. 2793–2800, November 2008.

[18] N. Wei, X. Li, Z. Fang et al., "Regional resource distribution of onshore carbon geological utilization in China," *Journal of CO_2 Utilization*, vol. 11, pp. 20–30, 2014.

[19] R. T. Dahowski, J. J. Dooley, C. L. Davidson, S. Bachu, and N. Gupta, "Building the Cost Curves for CO_2 Storage: North America," Technical Report 2005/3. IEA Greenhouse Gas R&D Programme, 2005.

[20] T. Saaty, *The Analytic Hierarchy Process*, McGraw-Hill Book Company, New York, NY, USA, 1980.

[21] T. Saaty and K. Kearns, *Analytical Planning: The Organization of Systems*, vol. 7, Pergamon Press, Oxford, Uk, 1985.

[22] R. Haddadji, "The In-Salah CCS experience Sonatrach, Algeria," in *Proceedings of the First International Conference on the Clean Development Mechanism*, Riyadh, Saudi Arabia, September 2006.

[23] I. Wright, "The In Salah Gas CO_2 Storage Project," in *Proceedings of The International Petroleum Technology Conference*, paper 11326, Dubai, U.A.E, December 2007.

[24] O. Skalmeraas, "The Sleipner CCS experience," in *Proceedings of the United Nations Framework Convention on Climate Change*, Bonn, Germany, October 2014.

[25] G. Li and M. Lü, *Atlas of China's Petroliferous Basins [M]*, Petroleum Industry Press, Beijing, China, 2nd edition, 2002.

[26] X. Wu, *Carbon dioxide capture and geological storage-The First Massive Exploration in China*, Science Press, 2013.

[27] S. Bachu and J. J. Adams, "Sequestration of CO_2 in geological media in response to climate change: Capacity of deep saline aquifers to sequester CO_2 in solution," *Energy Conversion and Management*, vol. 44, no. 20, pp. 3151–3175, 2003.

[28] IPCC., *Special Report on Carbon Dioxide Capture and Storage*, Cambridge University Press, Cambridge, UK/New York, NY, USA, 2005.

[29] C. M. Oldenburg, "Screening and ranking framework for geologic CO_2 storage site selection on the basis of health, safety, and environmental risk," *Environmental Geology*, vol. 54, no. 8, pp. 1687–1694, 2008.

[30] Y. Diao, S. Zhang, J. Guo, X. Li, J. Fan, and X. Jia, "Reservoir and caprock evaluation of CO_2 geological storage site selection in deep saline aquifers," *Rock and Soil Mechanics*, vol. 33, no. 8, pp. 2422–2428, 2012.

[31] S. Liu, M. Zha, J. Qu, and Z. Chen, "Characteristics and sealing ability of mid-deep layer caprock in Dongying depression," *Journal of Oil and Gas Technology*, vol. 30, no. 2, pp. 390–393, 2008.

[32] J. Ye, Q. Wu, and Z. Wang, "Controlled characteristics of hydrogeological conditions on the coalbed methane migration and accumulation," *Journal of China Coal Society*, vol. 26, no. 5, pp. 459–462, 2001.

[33] General Administration of Quality Supervision, Inspection and Quarantine of China, Standardization Administration of China, 2005. GB 17741-2005 Project site seismic safety evaluation.

[34] K. Pruess, "On CO_2 fluid flow and heat transfer behavior in the subsurface, following leakage from a geologic storage reservoir," *Environmental Geology*, vol. 54, no. 8, pp. 1677–1686, 2008.

[35] J.-M. Lemieux, "Review: the potential impact of underground geological storage of carbon dioxide in deep saline aquifers on shallow groundwater resources," *Hydrogeology Journal*, vol. 19, no. 4, pp. 757–778, 2011.

[36] Y. Diao, S. Zhang, Y. Wang, X. Li, and H. Cao, "Short-term safety risk assessment of CO_2 geological storage projects in deep saline aquifers using the Shenhua CCS Demonstration Project as a case study," *Environmental Earth Sciences*, vol. 73, no. 11, article 65, pp. 7571–7586, 2014.

[37] J. Fan, J. Guo, S. Zhang, and X. Ji, "CO_2 geological storage suitability assessment of sichuan basin," *Journal of Applied Mathematics and Physics*, vol. 02, no. 11, pp. 1009–1021, 2014.

[38] MLR (Ministry of Land and Resources of the People's Republic of China), *The National Oil and Gas Resources Evaluation*, China Land Press, Beijing, China, 2010.

[39] MLR (Ministry of Land and Resources of the People's Republic of China), *The National Coalbed Methane Resources Evaluation*, China Land Press, Beijing, China, 2009.

[40] Z. Zhao, H. Zhou, X. Chen et al., "Sequence lithofacies paleogeography and favorable exploration zones of the permian in sichuan basin and adjacent areas, China," *Acta Petrolei Sinica*, vol. 33, no. 2, pp. 35–51, 2012.

[41] J. Du, *Natural Gas Exploration of Permian—Triassic Reef & Oolite in Sichuan Basin*, Petroleum Industry Press, Beijing, China, 2010.

Hindawi
Geofluids
Volume 2017, Article ID 4653278, 15 pages
https://doi.org/10.1155/2017/4653278

Research Article

On the Role of Thermal Stresses during Hydraulic Stimulation of Geothermal Reservoirs

Gunnar Jansen and Stephen A. Miller

Center for Hydrogeology and Geothermics (CHYN), Laboratory of Geothermics and Geodynamics, University of Neuchâtel, Neuchâtel, Switzerland

Correspondence should be addressed to Gunnar Jansen; gunnar.jansen@unine.ch

Received 30 March 2017; Accepted 18 May 2017; Published 28 June 2017

Academic Editor: Weon Shik Han

Massive quantities of fluid are injected into the subsurface during the creation of an engineered geothermal system (EGS) to induce shear fracture for enhanced reservoir permeability. In this numerical thermoelasticity study, we analyze the effect of cold fluid injection on the reservoir and the resulting thermal stress change on potential shear failure in the reservoir. We developed an efficient methodology for the coupled simulation of fluid flow, heat transport, and thermoelastic stress changes in a fractured reservoir. We performed a series of numerical experiments to investigate the effects of fracture and matrix permeability and fracture orientation on thermal stress changes and failure potential. Finally, we analyzed thermal stress propagation in a hypothetical reservoir for the spatial and temporal evolution of possible thermohydraulic induced shear failure. We observe a strong influence of the hydraulic reservoir properties on thermal stress propagation. Further, we find that thermal stress change can lead to induced shear failure on nonoptimally oriented fractures. Our results suggest that thermal stress changes should be taken into account in all models for long-term fluid injections in fractured reservoirs.

1. Introduction

One of the primary driving mechanisms for permeability creation in engineered geothermal systems (also known as enhanced geothermal systems), or EGS, involves shear failure induced by fluid injection at high pressures. In environments with low differential stress, tensile fractures may develop if the injection pressure exceeds the minimal principal stress (e.g., fracking). The injection of cold water into a reservoir at substantially higher temperature also induces thermal stress changes that contribute to the overall evolution of the local stress and failure potential. This rapid cooling of the reservoir can lead to thermal cracking and thus further enhance permeability [1–4], but thermal fracturing, fracture propagation, or fracture reactivation may also contribute to premature cold water breakthrough into producing wells.

The basis for EGS is usually geothermal plays of the "hot dry rock" type where the available water in the porous medium is considered negligible. These conditions are found primarily in metamorphic or igneous terrains with low permeability and porosity containing fractures and faults that provide the major pathways for fluid flow. In geothermal energy systems, the fracture's surfaces serve as the main heat exchanger. Clearly, preexisting, critically stressed, and optimally oriented fractures provide the most favorable conditions for enhancing permeability of EGS [5, 6].

In this paper, we focus on the role of thermal stresses during cold fluid injection and stimulation of an EGS site. Of special interest, here is the interplay of hydraulic and thermally induced stresses. The processes involved in permeability creation during hydraulic stimulation act on different timescales. While the poromechanical coupling is active throughout the injection, its dominance over thermomechanical effects depends on the state of the injection. Thermomechanical coupling plays a particularly important role during prolonged periods of injection (weeks to years) because the variation of injectivity with injection water temperatures can be attributed to thermal stress [7].

A major concern in EGS is induced seismicity at levels above that tolerated by the local population, in either

frequency or magnitude. Usually induced seismic events are attributed to the change in effective stress due to the change in fluid pressure [8–10]. However, thermal stress also significantly contributes to induced seismicity in petroleum and geothermal fields [7, 11, 12]. Stark [12] found that, in the Geysers geothermal field in northern California, USA, half of the measured earthquakes appear associated with cold water injection.

In this paper, we present the theoretical basis for thermal stresses, evaluate the temperature distribution during injection in a borehole, and determine a modeling framework for evaluating the influences of thermal stress generation and propagation in a hypothetical reservoir. We describe the numerical method and present results of numerical experiments focusing on the influence of thermal stress on permeability, fracture orientation, and failure potential. We discuss the results in terms of thermal influence on induced seismicity and reservoir characteristics.

2. Theory

Here we present the mathematical basis for the formulation of thermal stresses. In addition, the temperature profile in an injection well is considered because this has a significant impact on the initial conditions of the numerical simulations.

2.1. Mathematical Description of Thermal Stress. A body will change its shape and/or volume when exposed to a temperature change ΔT. This change is called *thermal strain* and can be expressed as

$$\epsilon_T = \alpha \Delta T, \tag{1}$$

where α is the coefficient of linear thermal expansion in 1/K. In most materials, α is positive and on the order of 10^{-6} 1/K. In isotropic materials, the thermal strain acts only on the normal strains with the same magnitude. If the body's deformation is restricted, as it would be the case for a small volume inside a rock mass, the strain results in thermal stress.

$$\sigma_T = C \cdot \epsilon_T, \tag{2}$$

where C is the elastic stiffness tensor of the material. If we restrict ourselves to isotropic conditions, the thermal strain has only normal components with equal magnitude in which case we can simplify the previous expression to

$$\sigma_{T_{ij}} = \frac{E}{1-2\nu} \cdot \alpha \Delta T \delta_{ij}, \tag{3}$$

where E is Young's modulus (Pa) and ν Poisson's ratio (—). It is important to note that (3) is only nonzero for the three normal stresses $\sigma_{T_{xx}}, \sigma_{T_{yy}}, \sigma_{T_{zz}}$. It is immediately obvious that larger temperature differences will result in higher thermal stress changes. Additionally, the thermal stress is positive (relative compression) if the temperature difference is positive ($\Delta T > 0$), and if the temperature difference is negative, the thermal stress is negative (relative tension). The magnitude of thermal stress can change widely depending on the material. Assuming a constant thermal expansion coefficient $\alpha = 10^{-6}$ 1/K and fixed temperature difference of $\Delta T = -10^{\circ}$C, the resulting thermal stress for an elastic sandstone ($E = \sim 20$ GPa) is 60% smaller than the resulting thermal stress in a typical granite ($E = \sim 50$ GPa). The granite would undergo a stress change of 1 MPa in this case compared to a 0.4 MPa stress change in the sandstone.

Thermal expansion coefficients are well-constrained by experiments and show only minor influences of temperature and pressure on the thermal expansion coefficients [13, 14]. Cooper and Simmons [15] attributed some of the change in the thermal expansion coefficient to the formation of microcracks by differential expansion of mineral grains. Considering the small magnitude in the change of the thermal expansion coefficient compared with the order of magnitude expected in temperature and pressure change, it is a valid assumption that the thermal expansion coefficient is constant.

In the following, we assume that the thermal stress is independent of the fluid pressure and the in situ stress state of the rock. Thus, the resulting stress can be obtained by superposition of the effective stress ($\sigma_{\text{eff}} = \sigma_{\text{tot}} - p$) and the thermal stress. Changes in the in situ stress of the rock are negligible on the timescales of interest for hydraulic stimulation. Considering only stress changes resulting from pore pressure and thermal expansion, we can formulate the total stress change as

$$\Delta\sigma = \Delta p + \Delta\sigma_T \tag{4}$$

Clearly, other stress contributions as slip-induced stresses and stresses induced by chemical reaction have to be considered in a general case. However, for reasons of simplicity, we restrict ourselves to only pore pressure and thermally induced stress changes.

2.2. Induced Shear Failure Potential. Induced shear failure potential is estimated by a Mohr-Coulomb failure condition. We restrict ourselves to a cohesion-less material with a friction coefficient of $\mu = 0.6$. A fracture segment is able to slip and is thus categorized as "potential slip" if the following condition is met:

$$\tau - \mu\overline{\sigma_n} > 0 \tag{5}$$

The effective normal stress $\overline{\sigma_n}$ is defined as

$$\overline{\sigma_n} = \sigma_{\text{eff}} + \sigma_T = \sigma_n - p_f + \sigma_T, \tag{6}$$

where σ_n is the normal stress, p_f is the fluid pressure, and σ_T the thermal stress as introduced in the previous section. The effective normal stress $\overline{\sigma_n}$ and shear stress τ acting on a fracture segment are

$$\begin{aligned} \overline{\sigma_n} &= \frac{\sigma_1 + \sigma_3 - 2p_f + 2\sigma_T}{2} \cos 2\theta \\ \tau &= \frac{\sigma_1 + \sigma_3}{2} \sin 2\theta, \end{aligned} \tag{7}$$

where σ_1 and σ_3 are the maximum and minimum principal stresses acting in the far field and θ is the angle between σ_1

and the fracture segment measured from the normal to the σ_1 plane.

The poroelastic deformation of the fractured reservoir during the injection as well as the deformation due to fracture slip is not included in the present model. Consequently, this simple model does not predict magnitudes or estimation of the amount of slip but rather identifies when a frictional failure condition is met, similar to other approaches in modeling EGS [9, 10].

2.3. Heat Distribution in a Geothermal Well. The temperature inside an injection well is not constant with depth. The injected water is heated by the rock mass surrounding the borehole while moving downwards through the borehole. Although the heat distribution in geothermal boreholes can be measured, in many cases it is still useful to describe it mathematically. Such calculations can be used in numerical simulations and aid the drilling crews during their operation. In most cases, description of well bore heat transmission is based on a well bore heat balance equation. Most of the literature is based on the initial work of Ramey [16] in which they derived the temperature distribution in a well used for hot fluid injection. The work was later enhanced by the rate of heat loss from the well to the formation by Ramey [17]. Recent work from Hagoort [18] reevaluated Ramey's classical work and found that it is an excellent approximation.

Following Satman and Tureyen [19], the temperature in an injection well into which a single-phase fluid is injected is given by

$$T(z) = T_{\text{surf}} + \alpha \cdot z + \left(T_{\text{inj}} + T_{\text{surf}} + \alpha A\right) \cdot e^{(-z/A)}. \quad (8)$$

Here, z is the distance downwards from surface in meters, α is the geothermal gradient in °C/m, T_{surf} is the surface temperature in °C, and T_{inj} is the temperature in °C of the injected fluid. A is a variable defined as

$$A = \frac{Qc_{pf} f(t)}{2\pi\lambda}, \quad (9)$$

where Q is the mass flow rate in ks/s, c_{pf} the heat capacity of the fluid (assumed constant), and λ the thermal conductivity of the formation (also assumed constant with depth). The dimensionless function $f(t)$ describes the transient heat transfer to the formation. There are a number of different formulations for function $f(t)$ available. Kutun et al. [20] provide a simple formulation:

$$f(t) = \ln\left(1 + 1.7\sqrt{t_D}\right) \quad (10)$$

which is based on a best curve fit of the data provided by Ramey [16] and Ramey [17, 21]. According to Satman and Tureyen [19], it is accurate within 1% for the relevant timescales. In (10), t_D is a dimensionless time defined by

$$t_D = \frac{\kappa \cdot t}{r_w^2}, \quad (11)$$

where κ is the mean thermal diffusivity of the formation in m^2/s and r_w the well radius in meters.

Table 1: Properties used in estimation of well temperature profiles.

Surface temperature	20°C
Injection temperature	40°C
Geothermal gradient	0.04°C/m
Well depths	5000 m
Well radius	0.11 m
Injection rate	20/40 kg/s
Rock density	2650 kg/m^3
Mean thermal conductivity (formation)	2.92 J/ms°C
Mean thermal diffusivity (formation)	$1.102 \cdot 10^{-6}$ m^2/s
Specific heat capacity (fluid)	3160 J/kg°C

A detailed review on the methods to describe well bore heat distributions, prevalent assumptions, and different formulations for the transient heat transfer function $f(t)$ can be found in Satman and Tureyen [19].

2.4. Heat Distribution in a Geothermal Well. Based on (8) to (11), the general characteristics of fluid injection in the well are presented and examined in detail. The model parameters are given in Table 1. Figure 1 shows the temperature distribution with depth of well bore temperature during prolonged fluid injection. The profiles are plotted for different injection times: 1 d, 10 d, 30 d, and 365 d. The geothermal gradient shown as a dashed line represents also the static (long term) temperature distribution in the well bore. It is clearly visible that it is not a static profile but contains a dynamic evolution with time. During the first days of injection, the temperature profile changes most rapidly. After about 10 days of continuous injection, the rates of the temperature profile change decrease. After 365 days of continuous injection, the bottom hole temperature has decreased from 70°C after 1 day of injection to 52°C in the case of an injection rate of 40 kg/s. When the injection rate is lower at 20 kg/s, the temperature decreases from initially 93°C after 1 day of injection to 63°C after one year. This demonstrates the highly dynamic temperature distribution during injection with respect to time and injection rates.

The dynamic behavior is driven by advective heat transfer during injection of the fluid at the well head and conductive heat exchange with the formation. Initially heat transfer from the formation to the fluid is high, leading to a rapid increase in the fluid temperature. During the course of injection, the formation is cooled by the injected fluid leading to reduced conductive heat transfer from the formation to the fluid. This subsequently lowers the overall temperature distribution in the well bore.

Figure 1 shows that the assumption of a constant temperature boundary in numerical modeling of fluid injection is not valid either in space or in time. Especially for very low injection rates (not shown here), the thermal gradient in the borehole is comparable to the static geothermal gradient. In long duration high injection rate scenarios, a constant temperature at the borehole becomes more acceptable as the formation is cooled quickly and the well bore temperature approaches

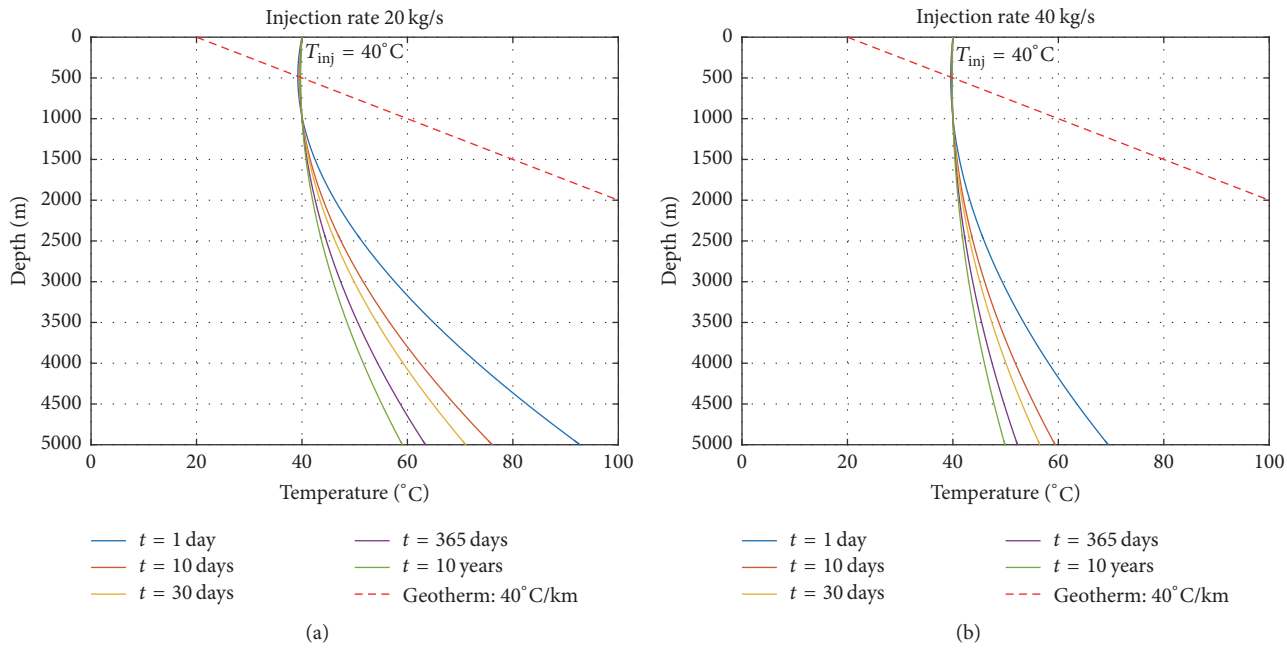

Figure 1: Temperature profiles in a 5 km deep injection well for an injection temperature of 40°C and an injection rate of 20 kg/s (a) and 40 kg/s (b).

the injection temperature. From the findings of this section we can conclude that the temperature change in the well bore is significant and must be taken into account when thermal stresses are to be evaluated accurately.

3. Methods

We developed an embedded discrete fracture model (EDFM) using the phenomenology described in other studies [22–24]. The conceptual idea of the EDFM is the distinct separation of a fractured reservoir into a fracture and a damaged matrix domain. We introduce a transfer function to account for coupling effects between the two domains (Figure 2), so the fracture and matrix domains are computationally independent except for the transfer function. As the fractures are generally very thin and highly permeable compared to the surrounding matrix rock, the gradient of fracture pressure normal to the fracture is negligible. This allows for a lower dimensional representation of fractures (i.e., 1D objects within a 2D reservoir).

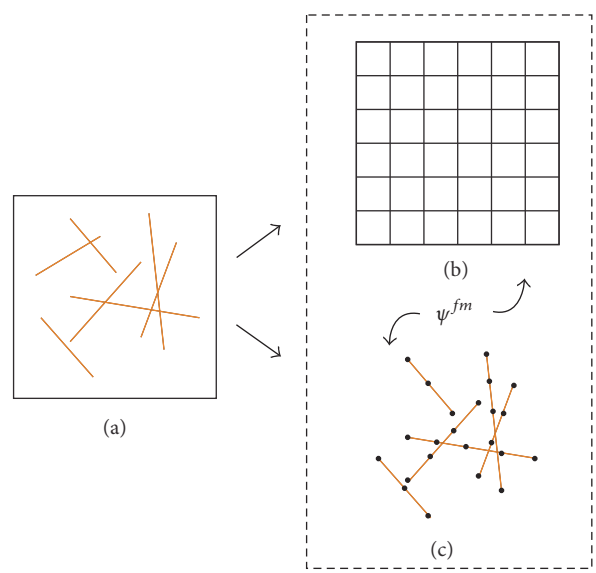

Figure 2: A fractured domain (a) is separated in a uniform grid (b) and a fracture grid (c). The two resulting domains are coupled using the transfer function Ψ^{fm}.

3.1. Governing Equations. The flow in naturally fractured reservoirs is often described by the equations for nearly incompressible single-phase flow. We include gravity effects in the formulation because gravity can play an important role in the flow field evolution of a reservoir fluid with variable densities. We note that the following equations are assumed valid in both the damaged matrix and the fractures. From mass balance and single-phase fluid flow, the pressure equation is

$$\phi\left(\beta_f + \beta_r\right)\frac{\partial p}{\partial t} = \nabla \cdot \left[\frac{\mathbf{k}}{\mu}\nabla\left(p - \rho_f g\right)\right] + Q, \qquad (12)$$

where ϕ [—] is the porosity, ρ [kg/m^3] is the fluid density, and p [Pa] is the fluid pressure. Compressibilities β [Pa^{-1}] are denoted with subscripts f for fluid and r for rock, respectively. Moreover $\mathbf{k}$ [m^2] is the permeability and μ [1/s] the fluid viscosity. In general, the permeability $\mathbf{k}$ is an anisotropic 2nd-order tensor. However, only an isotropic permeability k is used hereafter and in the implementation.

From the fluid pressure p, the fluid velocity is calculated using Darcy's law; that is,

$$\mathbf{v} = -\frac{k}{\mu}\nabla p. \tag{13}$$

The total mass balance equation derived above is separated into the matrix and the fracture domains, that is,

$$\begin{aligned} \phi^m\left(\beta_f+\beta_r\right)\frac{\partial p^m}{\partial t} &= \nabla\cdot\left[\frac{k^m}{\mu^m}\nabla\left(p^m-\rho_f g\right)\right]+\Psi^{mf} \\ &\quad + Q^m, \\ \phi^f\left(\beta_f+\beta_r\right)\frac{\partial p^f}{\partial t} &= \nabla\cdot\left[\frac{k^f}{\mu^f}\nabla\left(p^f-\rho_f g\right)\right]+\Psi^{fm} \\ &\quad + Q^f, \end{aligned} \tag{14}$$

where Ψ^{mf} and Ψ^{fm} are the flux transfer functions between the damaged matrix and the fractures. Superscripts m and f denote matrix and fracture quantities, respectively.

The velocities can subsequently be used in the heat transport equation. The heat transport equation is derived similarly to the continuity equation by the balancing the heat transport mechanisms and described as

$$\overline{c_p}\rho\frac{\partial T}{\partial t} + c_p^f\mathbf{v}\nabla T - \overline{\lambda}\nabla^2 T = 0, \tag{15}$$

if local thermal equilibrium is assumed. Overlined properties denote volume averaged mean values for the porous medium (i.e., $\overline{c_p} = \phi c_{pf} + (1-\phi)c_{pr}$). The heat transport equation is separated into matrix and fracture parts according to the same procedure as for the fluid pressure.

3.2. Fracture-Matrix Coupling. We apply a transfer function governing the mass and heat exchange between the two domains since flow in the damaged matrix is treated separately from flow in the fractures. The transfer function is treated as a source/sink term in the pressure and heat transport equations for damaged matrix and fracture, respectively, similar to classical well models (Peaceman [25]), that is,

$$\Psi_{fm} = \mathrm{CI}\cdot\Lambda\left(p_f - p_m\right), \tag{16}$$

with Λ being the mean total mobility of the fluid, defined as the fraction of permeability and viscosity. CI is the connectivity index between matrix and fracture that is grid dependent and defined based on the linear pressure distribution assumed within a grid cell intersected by a fracture [22]. The connectivity index is defined as the length fraction $A_{ij,k}$ of fracture segment k inside matrix cell ij divided by the average distance $\langle d\rangle_{ij,k}$ between matrix cell ij and fracture segment k:

$$\mathrm{CI}_{ij,k} = \frac{A_{ij,k}}{\langle d\rangle_{ij,k}}. \tag{17}$$

The average distance $\langle d\rangle_{ij,k}$ can be calculated as

$$\langle d\rangle_{ij,k} = \frac{\int x_k\left(x'\right)dx'}{V_{ij}}, \tag{18}$$

where x_k is the distance from the fracture within the matrix cell and V_{ij} the volume of the matrix cell. This allows properly accounting for the reduced influence of a fracture segment on a matrix cell if the fracture segment does not cross the matrix cell through its center. In many cases, (18) has to be evaluated by numerical integration. For rectangular grids, however, there exists an analytical solution [22] for fracture intersections horizontally, vertically, or on the diagonal to a grid cell. For enhanced efficiency, the analytical expressions are used in the present implementation. From the separated mass balance equations, it becomes immediately clear that the total flux between matrix and fracture has to be conserved:

$$\int \Psi^{mf}dV = -\int \Psi^{fm}dA. \tag{19}$$

Obviously, Ψ^{fm} is only nonzero in matrix cells that are actually intersected by at least one fracture segment.

3.3. Fracture Intersections. Fractures often intersect other fractures in naturally fractured reservoirs, which potentially significantly impact flow dynamics in the reservoir. Therefore we must also consider fracture-fracture coupling in the model. The additional transmissivity at a fracture intersection can be obtained similarly to the approach used in electrical engineering known as the star-delta transformation in circuits (Karimi-Fard et al. [26]). The additional fracture-fracture transmissivity can be calculated as

$$T_{i,j} = \frac{\alpha_i\cdot\alpha_j}{\alpha_i+\alpha_j} \quad \text{with } \alpha_i = \frac{A_i^f\Lambda_i}{0.5\cdot dx_f}, \tag{20}$$

where A_i^f denotes the fracture aperture, Λ_i the total mobility, and dx_f the numerical discretization spacing in the fracture. This approach can be generalized to more than two fractures intersecting in a single point on a fracture segment but is omitted here due to its rare occurrence.

3.4. Discretized EDFM Equations. The EDFM equations in two dimensions are discretized by the Finite Volume Method (FVM). Both the pressure equation and the heat transport equation are discretized by a two-point flux approximation scheme. The time derivatives in (12) and (15) are treated by an implicit time discretization. The advection term in the heat transport equation is treated by the QUICK scheme [27]. Although an explicit coupling also exists between the pressure and transport equations themselves, the current implementation uses a serial scheme to solve the coupled problem. Instead of assembling and solving one very large system for pressure and transport, the problem is divided into two parts. In a first step, the pressure system is assembled and solved. Using Darcy's law, the fluid velocities can be calculated in an intermediate step. Once the fluid velocities are found, the transport system can be assembled and subsequently solved. In strongly coupled flow and transport problems, an iterative scheme must be used to capture any arising nonlinearities. In most cases, the flow and transport exhibit rather loose coupling in which only few iterations are needed to converge to the solution. It is restated that both equations are discretized

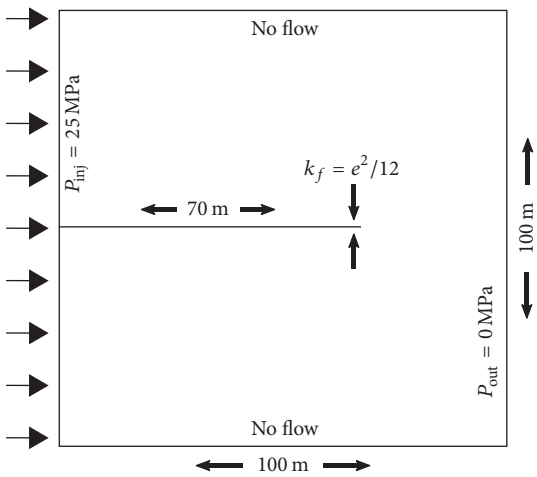

Figure 3: Numerical setup to evaluate the influence of fracture permeability on thermal stress. A constant injection pressure is applied to the left side of the domain. The right side serves as a zero pressure outflow well.

by an unconditionally stable implicit time-discretization scheme. In case the problem shows nonlinear behavior, issues with nonconvergence might appear and place an indirect restriction for the time step. Nonetheless, much larger time steps are allowed in the implemented approach when compared to explicit schemes.

4. Results and Discussion

We present the results of three numerical experiments that provide insight into the effects of thermal stress on the stimulation of a geothermal reservoir. First we evaluate the influence of contrasts in the fracture permeability and the fracture-matrix permeability. We then investigate the influence of the fracture orientation on potential slip in combination with thermal stress. In a final numerical experiment, we simulate fluid injection into a complex fracture network over a prolonged period of time to evaluate the temporal evolution of thermal stress and failure potential. In all experiments, the pressure and/or temperature dependence of the fluid density and viscosity is taken into account. The underlying equation of state is given by Sun et al. [28] for density and Al-Shemmeri [29] for the viscosity of water. In this section, we combine results and their discussion to emphasize each experiment's outcome. A more general discussion of the results as well as a conclusion is provided in Section 5.

4.1. Influence of Fracture and Matrix Permeability on Thermal Stress. Fracture permeability is one of the most important variables to be determined in EGS reservoirs to accurately predict flow in the reservoir. Here we evaluate to what degree the fracture permeability has an impact on thermal stress. To this end, we model the fluid injection in a well that is intersected by a single fracture as depicted in Figure 3.

Table 2 lists the physical parameters for the matrix and fracture used in this study. In this experiment, we investigate the results after a continuous injection of 30 days. In contrast to the previously presented temperature distribution in the well, we assume a homogeneous temperature distribution in the open hole section throughout the injection as the open hole section is short (100 m) compared to the length of the borehole. The injection temperature is variable with time and obtained by a least-squares fit of the data presented in Figure 1 for a depth of 5 km. The initial temperature is set at $T_0 = 200^\circ$C. The injection pressure is constant at 25 MPa. Gravity is neglected in this experiment. We vary the fracture permeability in five steps over a range within $8.33 \cdot 10^{-8}$–$1 \cdot 10^{-12}$ m^2. Further we evaluate two matrix permeabilities 10^{-16} m^2 and 10^{-18} m^2.

Figure 4 shows the temperature distribution and resulting thermal stress after 30 days of fluid injection for a matrix permeability of 10^{-16} m^2. The temperature profiles along the fracture show significant differences based on fracture permeability. For the two lowest fracture permeabilities ($k_{fr} = 10^{-12}/10^{-11}$ m^2), the profiles are very similar and show temperature variations only within the first 10 meters of the fracture. At the injection point, the temperature dropped down to approximately 140°C. The resulting thermal stress is approximately −70 MPa. An intermediate fracture permeability of $k_{fr} = 10^{-10}$ m^2 shows a further propagation of the thermal front within the 30 days. We observe temperature change on almost 60 m of the fracture resulting thermal stress perturbations along the same length. At an approximate distance of 30 m from the injection point, the thermal stress reaches −9 MPa. The two highest tested permeabilities ($k_{fr} = 8.33 \cdot 10^{-8}/8.33 \cdot 10^{-10}$ m^2) show distinctively different profiles compared to the lower permeability values. Here the temperature propagates the full length of the fracture with an almost linear profile. The temperature at the injection point however is greater than for the other permeabilities with approximately 150°C. Due to the temperature profiles, the thermal stress is significantly larger along the whole length of the fracture for these very permeable fractures.

We further evaluated the mean velocity in the fracture throughout the 30 days of injection. The result is shown in Figure 5. Overall the mean velocity varies over four orders of magnitude due to the wide range of fracture permeabilities. For all fracture permeabilities, an initial decline in the fracture velocity is visible. This is more pronounced for high fracture permeabilities ($k_{fr} = 8.33 \cdot 10^{-8}/8.33 \cdot 10^{-10}$ m^2) with a "stabilization time" of only a couple of days. Lower fracture permeabilities show less variability in the mean fracture velocity.

Figure 6 shows the temperature distribution and resulting thermal stress after 30 days of fluid injection for a matrix permeability of 10^{-18} m^2. The temperature profiles along the fracture show significantly less differences compared to higher matrix permeability. The three highest permeabilities show nearly identical behavior. The temperature front advanced as far as 25 m which is the maximum for a matrix permeability of $k_m = 10^{-18}$ m^2. The two lower fracture permeabilities ($k_{fr} = 10^{-12}/10^{-11}$ m^2) show less temperature change after 30 days compared to the other permeabilities as

Table 2: Properties used in the fluid injection simulation. Subscripts: *fr*, fracture; *m*, matrix; *f*, fluid; *r*, rock.

Permeability	$k_{fr} = 8.33 \cdot 10^{-8}$–$1 \cdot 10^{-12}\,\mathrm{m}^2$	$k_m = 10^{-16}$–$10^{-18}\,\mathrm{m}^2$
Porosity	$\phi_{fr} = 1.0$	$\phi_m = 0.1$
Compressibility	$\beta_f = 5 \cdot 10^{-10}\,\mathrm{Pa}^{-1}$	$\beta_r = 1 \cdot 10^{-10}\,\mathrm{Pa}^{-1}$
Specific heat	$c_{p_f} = 4000\,\mathrm{J/(kg \cdot K)}$	$c_{p_r} = 1000\,\mathrm{J/(kg \cdot K)}$
Heat conductivity	$\lambda_f = 2.92\,\mathrm{W/(m \cdot K)}$	$\lambda_r = 0.5\,\mathrm{W/(m \cdot K)}$
Thermal expansion coeff.	$\alpha = 7.9 \cdot 10^{-6}\,\mathrm{K}^{-1}$	
Shear modulus	$G = 29.0\,\mathrm{GPa}$	
Poisson's ratio	$\nu = 0.25$	

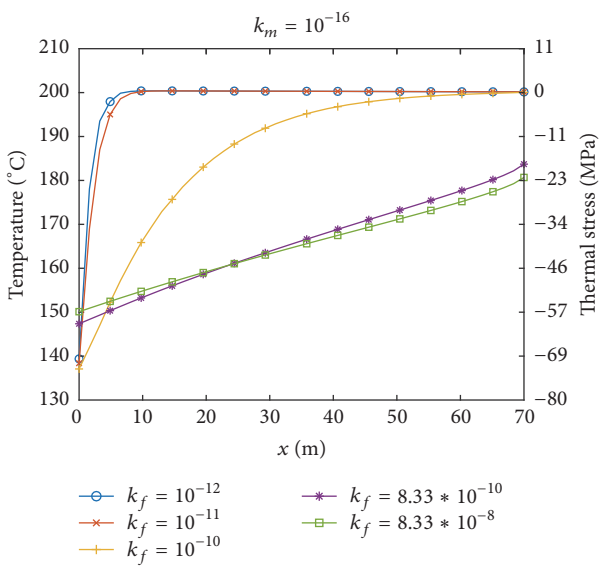

Figure 4: Temperature and thermal stress distributions after 30 days of injection for a matrix permeability of $k_m = 10^{-16}\,\mathrm{m}^2$.

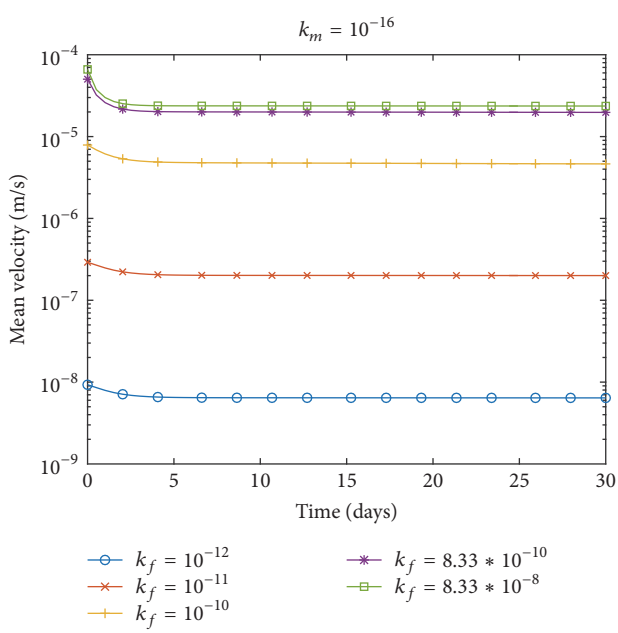

Figure 5: Mean fracture velocity during the simulated 30 days of injection.

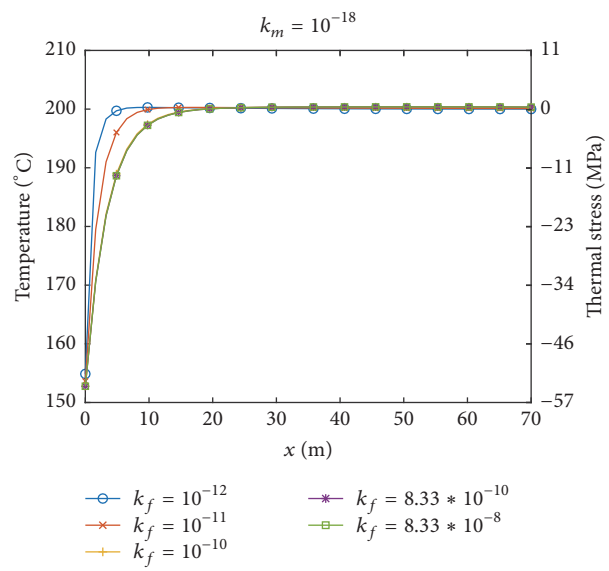

Figure 6: Temperature and thermal stress distributions after 30 days of injection for a matrix permeability of $k_m = 10^{-18}\,\mathrm{m}^2$.

well as the higher matrix permeability. All profiles exhibit a temperature at the injection point of 150–155°C.

A comparison of thermal stress distribution for the fracture permeability $k_{\mathrm{fr}} = 10^{-10}\,\mathrm{m}^2$ with both matrix permeabilities is shown in Figure 7. As already discussed earlier, the different propagation depths of the temperature and thus thermal stress are visible. Additionally the matrix effect is also shown. For the higher matrix permeability, the thermal stress front propagates as far as 6 m into the reservoir, and we observe a wedge-shaped thermal stress disturbance close to the fracture. In the case of the lower matrix permeability, the thermal stress front barely penetrates the matrix. The 1 MPa isoline is already at a distance of approximately 2 meters from the injection well. Close to the fracture a more pronounced thermal stress, alteration zone is visible. In contrast to higher matrix permeability this zone is relatively small.

Figure 8 shows that the pressure diffusion for the higher matrix permeability is much more homogeneous than for a lower matrix permeability, leading to a significant pressure gradient in the fracture. If the matrix permeability is very low, a high pressure zone develops around the fracture causing a

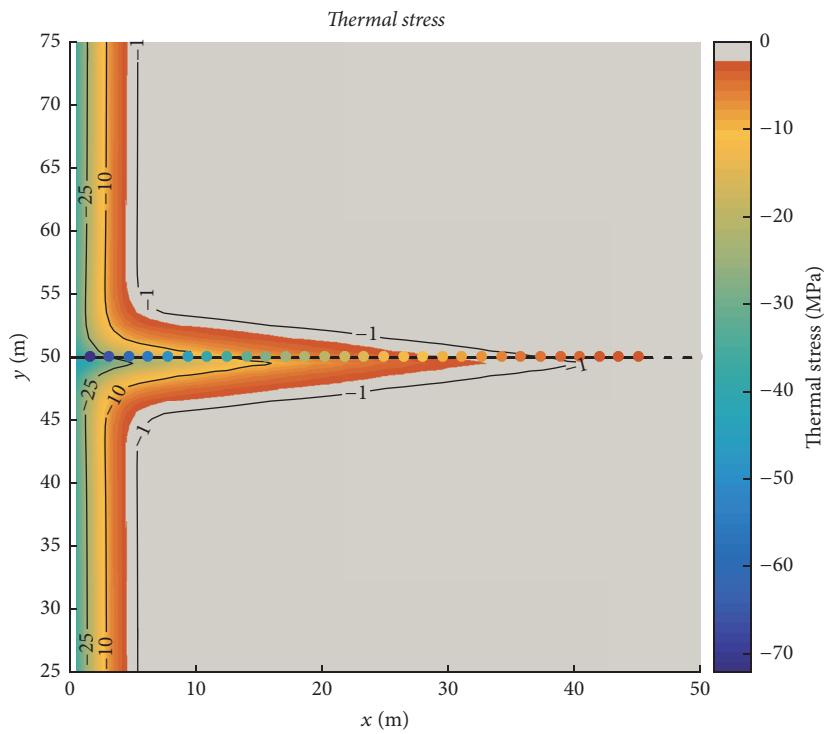

(a)

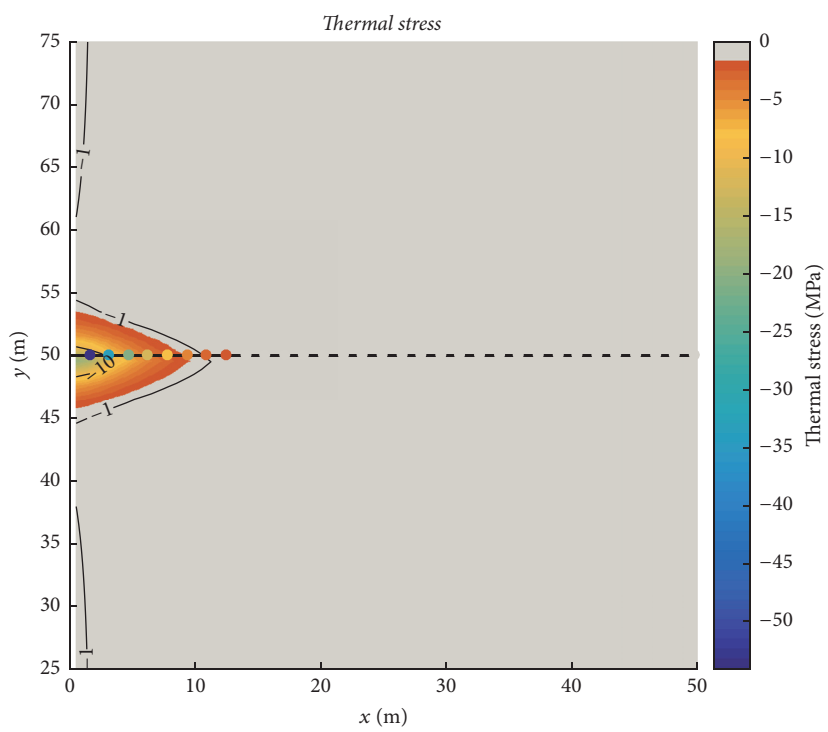

(b)

Figure 7: Thermal stress distribution after 30 days of injection. Fracture permeability $k_{\mathrm{fr}} = 10^{-10}\,\mathrm{m}^2$: (a): higher matrix permeability $k_m = 10^{-16}\,\mathrm{m}^2$; (b): lower matrix permeability $k_m = 10^{-18}\,\mathrm{m}^2$.

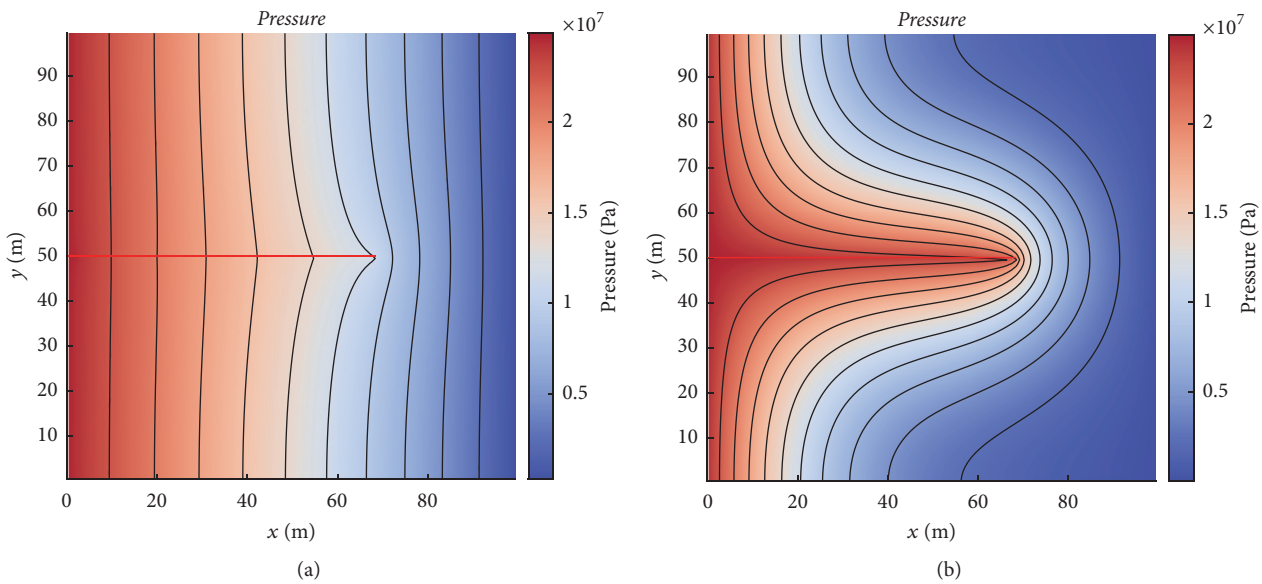

Figure 8: Pressure distribution after 30 days of injection. Fracture permeability $k_{fr} = 10^{-10}$ m^2: (a): higher matrix permeability $k_m = 10^{-16}$ m^2; (b): lower matrix permeability $k_m = 10^{-18}$ m^2.

smaller pressure gradient in the fracture. This is also observable in the mean fracture velocities. For high fracture permeabilities, the difference in fracture velocity increases one order magnitude with increasing matrix permeability. For low fracture permeabilities, there is no significant change in observed mean fracture velocity with respect to matrix permeability. The observed "stabilization time" in the fracture velocities is caused by the initial pore pressure diffusion through the matrix and fracture.

The differences in the pressure field and the fracture velocities can, however, not fully explain the observed thermal stress distributions. In order to explain these differences, we examine the heat transport in more detail. It is clear that the matrix-fracture interaction plays an important role in the thermal stress propagation. With increasing matrix and fracture permeabilities, also the interface permeability between matrix and fracture is increased allowing heat transfer by advection between matrix and fracture. Only by advection has the fluid in the fracture a chance to cool down the surrounding matrix. Once the surrounding matrix is cooled to a certain extent, the temperature front can also advance within the fracture. In case of a low matrix permeability, the main heat transfer mechanism between matrix and fracture is heat diffusion. Here heat diffusion from the matrix into the fracture dominates, leading to a heating of the fracture and thus significantly slowing down the thermal stress propagation. The second scenario is favorable in terms of sustainability of an geothermal reservoir. Here the heat is efficiently extracted from the matrix rather than prematurely cooling down the matrix surrounding the fractures.

4.2. Influence of Thermal Stress on Shear Failure Potential. In this section, we investigate the thermal stress influence on shear failure potential. As mentioned in the introduction and methods, shear failure in the reservoir occurs mainly on optimally oriented fractures. Here we investigate whether thermal stress leads to earlier onset of slip and how this is influenced by fracture orientation and model the fluid injection into a single fracture (Figure 9).

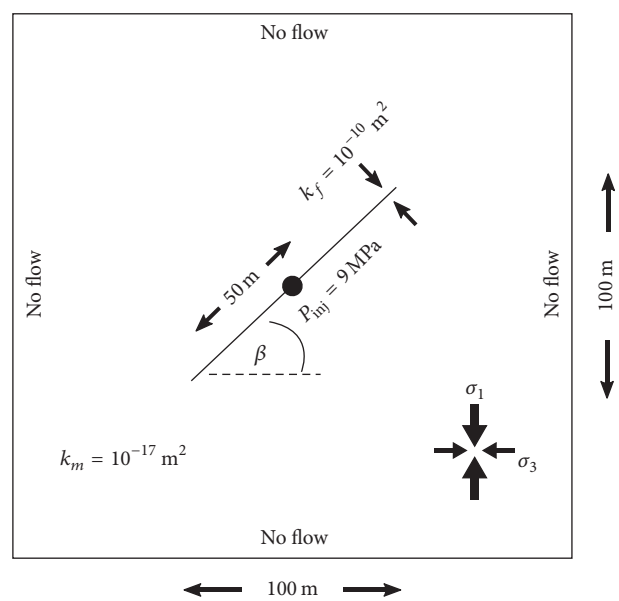

Figure 9: Numerical setup to evaluate the influence of fracture orientation and thermal stress on shear failure potential. A constant injection pressure is applied to the middle of the fracture. On the outer boundaries, a no-flow boundary condition is applied.

All parameters except for the matrix and fracture permeabilities are identical to the previous experiment and shown in Table 2. We apply a fracture permeability of $k_{fr} = 10^{-10}$ m^2

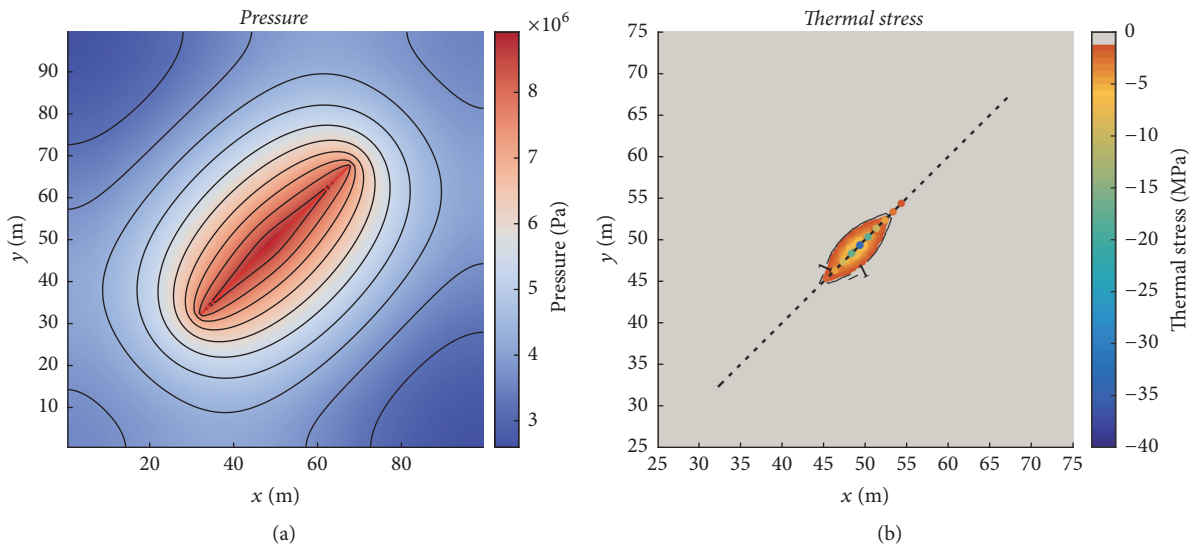

Figure 10: Results after 10 days of injection into the fracture. Fracture permeability $k_{\mathrm{fr}} = 10^{-10}\,\mathrm{m}^2$. Matrix permeability $k_m = 10^{-17}\,\mathrm{m}^2$. (a) Pressure distribution. (b) Thermal stress distribution.

with a matrix permeability of $k_m = 10^{-17}\,\mathrm{m}^2$. The injection pressure is constant at 9 MPa. The minimum and maximum principal stresses are 45 MPa and 20 MPa, respectively. Stresses are oriented in alignment to the coordinate axis as shown in Figure 9. We vary the fracture orientation (measured in degree from the normal to the maximum principal stress) from 35° to 85° in steps of 2.5°. The injection pressure was chosen so that only very close to optimally oriented fractures at 60° are eligible for slip. In this experiment, we investigate the results after a continuous injection of 10 days. The injection temperature is variable with time and obtained as presented in the previous experiment. The initial temperature is set again at $T_0 = 200^\circ\mathrm{C}$ and we neglect gravity.

Figure 10 shows the result for a rotation of 45° after 10 days of injection. It shows a pressure ellipse with its principal axis aligned with the fracture. The initial point source is not recognizable in the matrix pressure after 10 days of continuous injection. This can be explained by the fast pressure diffusion in the fracture and consequential pressure diffusion from the fracture to the matrix. The thermal stress is distributed symmetrically around the injection point in the fracture. The temperature front propagates roughly 10 m in each direction. The maximum cooldown and consequently maximum thermal stress are found at the injection point. Thermal stress in the matrix is propagated again from the fracture. The propagation direction is normal to the fracture leading to an elliptic thermal stress alteration zone surrounding the injection point. The rotation of the fracture barely influences the pressure and thermal stress distributions. Minor differences were observed but can be attributed to numerical effects.

We use the Mohr-Coulomb diagram to evaluate the failure potential due to thermal stress with respect to fracture orientation. Figure 11 shows the failure potential for each fracture orientation, where each point in the diagram is the mean normal and shear stress calculated over the whole fracture length. We show the effective stress modified solely by the fluid pressure as well as modified by thermal stress and fluid pressure combined. Figure 11 shows that, accounting only for fluid pressure in the effective normal stress, only fractures oriented at 55°–65° are able to slip. All other orientations do not meet the failure condition. If we further consider the effects of thermal stress, we observe a wide range of fracture orientations that fulfill the failure condition and are able to slip. The results after 10 days of injection show that fractures oriented up to 17.5° from the optimum (42.5°–77.5°) are critically stressed. As Figure 11 only considers the average stress state in the fracture, we evaluate the failure potential in greater detail with a histogram. Figure 12 shows the percentage of fracture segments for each orientation that could demonstrate slip. Considering only fluid pressure effects, we find that the injection pressure of 9 MPa propagated as far as necessary to induce slip over the whole length of the optimally oriented fracture. Fractures oriented at 5° from the optimum already show significantly less segments with failure potential (−(25–50)%). Adding the thermal stress effect, we observe a broad spectrum of potential slip in up to 35% of the fracture segments (at ±7.5°). However, also fractures with an orientation further from the optimum show a significant ability to slip with ~20% at ±15° and ~5–10% for fracture oriented at ±25° from the optimum.

The observed asymmetry in the failure potential is of numerical origin because as the fracture is rotated, the number of matrix grid cells intersected by the fracture is changing. Consequently, this leads to small differences in the solution that propagate to the failure potential.

This experiment shows that thermal stress can greatly enhance the range of fracture orientations eligible for slip. This has a potentially large impact for the stimulation of geothermal reservoirs with a complex tectonic history and multiple fracture sets. If one or more fracture sets are nonoptimally oriented and unsuitable for hydraulic stimulation, they might still be suitable for thermal stimulation. However, due to

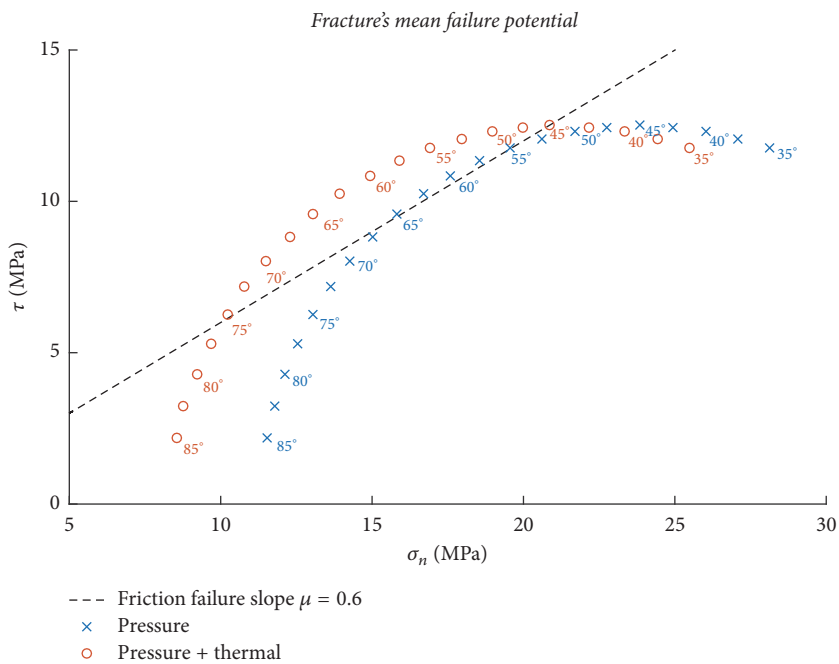

Figure 11: Failure potential for rotated fractures due to thermal stress. The failure potential is depicted in the classical Mohr-Coulomb diagram. A fracture is eligible for slip if its corresponding point in the diagram touches/crosses the failure line (black dashed). Failure occurs only in a narrow range of orientations with the selected injection pressure. After 10 days of injection, thermal stress leads to possible slip in a wide range of orientations.

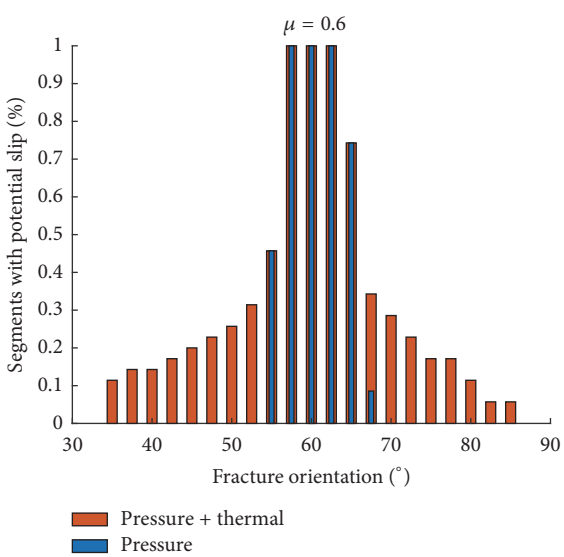

Figure 12: Failure potential for rotated fractures due to thermal stress in a bar diagram. It shows the percentage of fracture segments eligible for slip. Again, failure occurs only in a narrow range of orientations with the selected injection pressure. After 10 days of injection, thermal stress leads to possible slip in a wide range of orientations.

different propagation speeds of the fluid pressure and thermal front, thermal stimulation might be challenging for short stimulation scenarios. The significantly slower propagation of the thermal front suggests that enhanced slip on close to optimally oriented fractures is unlikely. Nevertheless, thermal stresses can be expected to add to slip in the reservoir on nonoptimally oriented fractures and on fractures with highly heterogeneous frictional properties in the long run. The role of the different timescales of fluid pressure and thermal stress will be examined in more detail, the third numerical experiment.

4.3. Cold Water Fluid Injection into a Complex Fracture Network. In the third numerical experiment, we investigate the spatial and temporal evolution of potential failure due to fluid pressure and thermal stress. We model the fluid injection into a complex fracture network with a range of fracture orientations. The initial setup is shown in Figure 13. The domain represents a fractured reservoir at a depth of 5 km. We used the fracture network generator *FracSim3D* [30] to create the fracture network used in this study. It consists of a total of 310 large-scale fractures within a damaged rock matrix. The borehole is located in the middle of the domain with an open hole length of 50 m (cf. Figure 13).

All parameters except for the matrix and fracture permeabilities are identical to the previous experiments (cf. Table 2). We apply a fracture permeability of $k_{\mathrm{fr}} = 10^{-11}\,\mathrm{m}^2$ with a matrix permeability of $k_m = 10^{-18}\,\mathrm{m}^2$. The injection pressure is constant at 35.1 MPa. The minimum and maximum principal stresses are 113 MPa and 175 MPa, respectively. The in situ pore pressure is assumed to be hydrostatic at 50 MPa. We neglect the hydrostatic gradient within the reservoir due to the relatively small vertical extent of the model. Stresses are oriented with 2° rotation to the coordinate axis as shown in

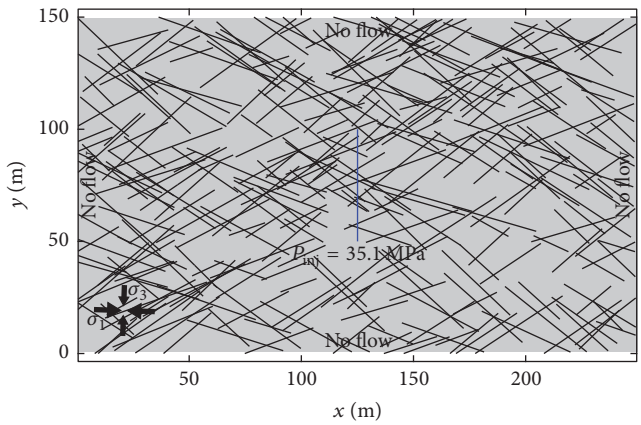

Figure 13: Numerical setup to evaluate the spatial and temporal evolution of potential slip due to fluid pressure and thermal stress. A constant injection pressure is applied to the borehole in the middle of the domain (blue). On the outer boundaries, a no-flow boundary condition is applied.

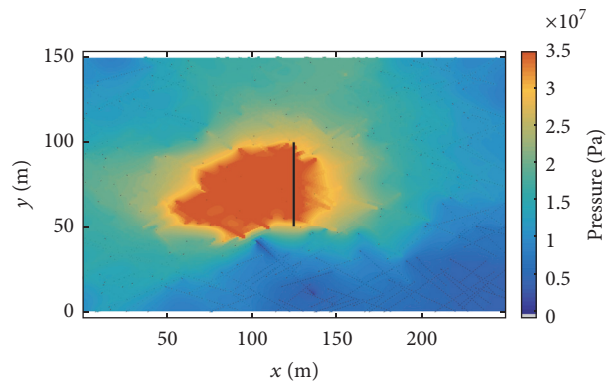

Figure 14: Pressure distribution after 30 days of injection into the fracture network. The heterogeneous fracture distribution influences the pressure field and leads to preferential flow directions in the reservoir. Fracture permeability $k_{fr} = 10^{-11}\,m^2$. Matrix permeability $k_m = 10^{-18}\,m^2$.

Figure 13. In this experiment, we investigate the results during a continuous injection of 30 days. The injection temperature is variable with time and obtained as discussed previously. The initial temperature is set to $T_0 = 200^\circ C$, and we include gravity effects.

An important addition to this experiment is a stepwise change in fracture permeability when a fracture segment reaches the failure condition [31]. That is, when the failure condition is reached, then the permeability adopts $k_{fr} = x \cdot k_{fr}$, where x is a multiplication factor. For the simulations presented here, the enhancement factor x is set to 100. The geological basis for stepwise change in permeability [31] rests with the strong aperture dependence of permeability (e.g., Nemčok et al. [32]), where small changes in aperture result in very large changes in permeability. The proposed model has been used to successfully describe the distribution of the induced seismicity in the Basel EGS site and for modeling fluid-driven aftershock sequences [10, 33].

Figure 14 shows the pressure distribution after 30 days of injection. Due to the heterogeneity of the fracture network, the pressure distribution is complex. As is also visible in Figure 13, the fracture density on the left side of the injection well is much higher than on the right side. This leads to more flow towards the left side of the reservoir as clearly indicated by the pressure field. The pressure distribution is dominated by the fracture network. After 30 days of injection, a pressure change of at least 1 MPa is measured in the whole domain. The maximum extent of the area with at least 30 MPa is approximately 30 m on the right side of the injection and up to 75 m on the left side of the well. A distinct anisotropy is visible between the horizontal and vertical extents of the high pressure zone. Vertically the pressure propagates slower compared to the horizontal direction and is caused by the main direction of the fracture set.

Figure 15 shows the thermal stress caused by the fluid injection into the reservoir. As predicted by the results of the previous experiments, the thermal stress alteration is concentrated to a region close to the injection well. Thermal stress evolves around the fractures intersecting the well as most of the fluid enters the reservoir here. The color scale in the figure starts at 0.65 MPa with the darkest blue. Everything below is neglected in the graphical representation and shown in the background color. This low cutoff shows the extent of the thermal stress alterations in the domain. The propagation of thermal stress in the matrix is rather homogeneous and mainly driven by heat diffusion. Additional thermal stress of 0.65 MPa occurs in a distance of 6–10 m from the borehole. Close to the borehole, thermal stress in the matrix reaches up to 20 MPa. The thermal stress in the fractures differs from the thermal stress in the matrix. Maximal thermal stress perturbation is measured at the fracture intersections at the borehole with up to 40 MPa additional stress. Due to the complex flow pattern, the thermal stress propagation in the fractures is equally strong. Some fractures show stress perturbations up to 10 m from the borehole, while, for others alterations, they do not reach 5 m into the reservoir. This shows that heat in the fractures is transported also by advection. A distinctive separation of the heat transfer mechanisms as previously performed for a single fracture is not possible here due to the interplay of the various effects.

We further evaluate failure potential in the reservoir due to the fluid injection. Figure 16 shows the distribution of potentially slipping failure segments in the reservoir at the end of the injection period. Each fracture segment is tested for potential failure based on (5). If the failure criterion is met, a star is shown in the figure to indicate potential slip on this segment. The color indicates the failure mechanism. Symbols in red indicate potential shear failure solely due to the fluid pressure. Blue symbols, on the other hand, signal failure due to the combined effects of increased fluid pressure and thermal stress. Pressure induced shear failure (or hydraulic failure) occurs mainly on the left side of the injection well and up to 65 m away from the well. Note that not all fractures are hydraulically stimulated as their orientation is not suitable for slip, although the fluid pressure inside the fractures is comparable (cf. Figure 14). Close to the well thermohydraulic failure is visible. The extent corresponds to the size of the thermal

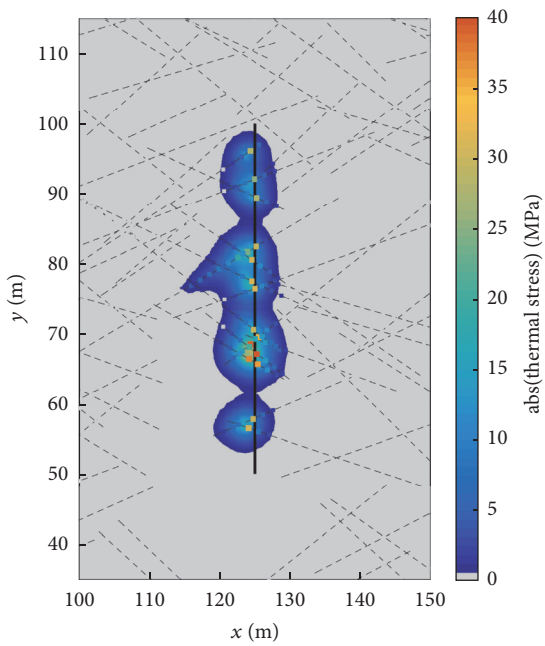

Figure 15: Thermal stress after 30 days of injection into the fracture network. The thermal stress is concentrated close to the injection well. Note that the absolute value of the thermal stress is shown and all thermal stress here is tensional.

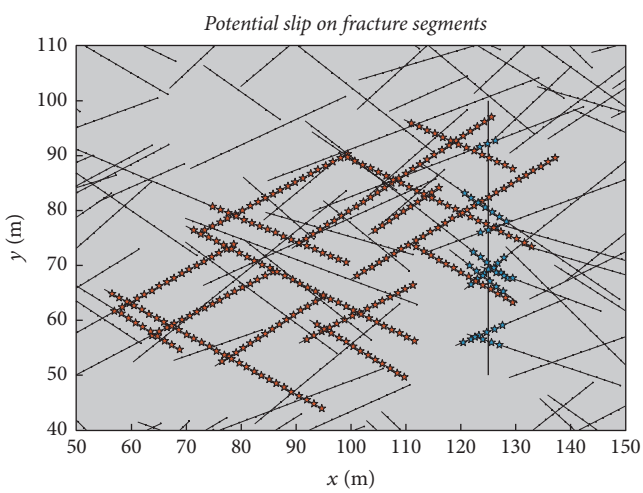

Figure 16: Potentially slipping fracture segments after 30 days of injection into the fracture network. The two colors indicate the mechanism of failure. Red: fracture segments failing due to fluid pressure alone. Blue: failure due to the combined effects of fluid pressure and thermal stress.

stress alteration zone. These fractures are not aligned optimally for slip and thus do not show potential failure with hydraulic stimulation alone. Once thermohydraulic stimulation is taken into account, the reduction in effective normal stress on these fractures is high enough to make them eligible for slip as indicated by the blue symbols in Figure 16.

The temporal evolution of the failure potential has been neglected so far. In Figure 17, we evaluate the simulated seismic events to gain more insight into the mechanisms at play

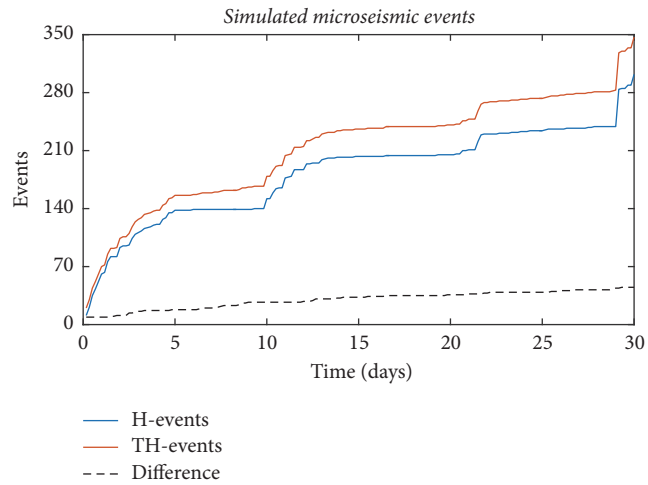

Figure 17: Temporal evolution of the simulated seismic events during the injection period. An event is counted if the corresponding fracture segment is eligible for slip. The two colors indicate the mechanism of failure. Blue: fracture segments failing due to fluid pressure alone (H). Red: failure due to the combined effects of fluid pressure and thermal stress (TH).

and their evolution. An event is counted if the corresponding fracture segment is eligible for slip. So-called H-events indicate failure only due to fluid pressure. The TH-events are all events including both hydraulic failure and thermohydraulic failure. Initially, during the first days of injection, both event curves are close to each other. Later in the injection cycle, the difference between the curves grows larger, indicating the increased significance of the thermohydraulic failure events. Throughout the 30 days of fluid injection, the difference between H- and TH-events is about 15%. With continued injection, this difference is expected to increase as the fluid pressure propagation slows down the higher the radial distance from the well and thermal stress propagation continues. Note that both curves share many of the sharp gradients and subsequent plateaus. This indicates that hydraulic failure dominates the shape of the measured event curves. Steep gradients indicate abrupt failure in many connected fracture segments possibly leading to microseismicity. Overall, the microseismicity is likely to increase due to combined thermohydraulic failure. However, large felt microseismic events are not a necessary consequence as there are no sharp gradients in the difference between the two curves (black dashed line in Figure 17) during the 30 days of injection into the reservoir.

This third numerical experiment shows that thermal stress can play and important role in shear stimulation of a fractured reservoir. Figure 16 showed that two distinct stress domination regimes can be defined. In one region, only hydraulic failure is observed, while, in the other region (more or less confined close to the well), thermohydraulic failure occurs. We showed that these regions act on different timescales. Fractures that are not optimally oriented for failure and are not prone to slip early in the injection cycle might be triggered due to the combined thermohydraulic stress changes later during the injection. This could help to explain

the sometimes nonintuitive temporal evolution of microseismicity observed during fluid injection.

We can compare our results to typical changes in the static Coulomb stress transfer model that is widely used. Typical changes in Coulomb stress during fluid injection are observed in the range of −2 MPa to 1 MPa [34, 35]. In our experiments, we showed that thermally induced stress changes can easily exceed these changes in close proximity to the fractures and the injection point. This further emphasizes the importance of thermal stress during reservoir stimulation.

5. Conclusion

We developed and implemented a fast and efficient methodology for investigating the role of thermal stress in a geothermal reservoir. The numerical experiments presented in this study give insight into the role of thermal stress during hydraulic stimulation over short and long periods. We showed that thermal stresses can facilitate slip on nonoptimally oriented fractures and that thermal stress propagation is largely influenced by the hydraulic properties of both fracture and matrix. We found that thermal stress change is spatially more concentrated and generally propagates much slower than fluid pressure. Nevertheless thermal stress changes can exceed fluid pressure especially close to the well.

Some of our simulations showed that the combination of pore pressure and thermal stress can exceed the minimum principal stress, which would thermally induce tensile cracks. However, these tensile cracks are not self-propping, so hydraulic pressurization would be needed to facilitate flow. This is not considered in our current model but could be introduced as shown, for example, in Ghassemi [36]. Figure 6 uses a damage methodology for the matrix blocks surrounding the fracture. Including these effects would lead to an enhanced heat exchange between matrix and fracture in addition to that discussed previously. We also identified two different failure regimes that act on different timescales. The hydraulic failure regime acts on the timescale of days to weeks, whereas the thermohydraulic regimes acts on the scale of weeks to years. Future studies should aim to determine whether this can be observed in microseismic data from real-world fluid injection experiments.

Finally, we showed that thermal stress changes can be significantly larger than the injected fluid pressure as well as the slip-induced Coulomb stress change in some situations. This is especially important in long-term injection scenarios where the thermal stress changes become more significant with time and during the production phase of high flow rate geothermal systems.

Although we assumed water as the working fluid, it would be interesting to observe how the model behaves by implementing an equation of state for CO_2 as the working fluid. Since CO_2 is typically at supercritical conditions in a similar reservoir, we would expect similar hydraulic outcomes. However, specific heat capacity, density, and viscosity of supercritical CO_2 differ significantly from those of water, which could affect the spatial evolution and heat flow, consequently influencing thermal stress propagation within the reservoir.

Our model using simplified mechanics provided important insight into the dominant thermoelastic effects and helped to identify some challenges and opportunities for future studies. More advanced models currently under development will consider both preexisting fractures as in the present work but also the generation of new fractures in response to the evolving stress state from both thermo- and hydraulic perturbations. Future models might also include fracture roughness and morphology and solving the full equilibrium equations to estimate aperture changes that influence permeability. Finally, including a method to estimate magnitude from computed slip [37], not currently modeled, is essential for a mechanistic assessment of seismic hazard associated with injection. Induced seismicity cannot be quantified in terms of magnitude as fracture slip in the fractures is not computed. These are all areas that we are currently pursuing.

We conclude that thermal stress changes in the reservoir should be incorporated in models that seek to fully understand the processes at play during fluid injection (covering initial stimulation as well as the production phase) in fractured reservoirs over long periods.

Conflicts of Interest

The authors declare that they have no conflicts of interest.

Acknowledgments

The authors appreciate the helpful discussions with B. Galvan and R. Sohrabi. This work was supported by the Swiss National Fond (SNF), for the financial support through Grant "NFP70: Energy Turnaround" under Project no. 153971.

References

[1] H. F. Wang, B. P. Bonner, B. J. Carlson Kowallis, and H. C. Heard, "Thermal stress cracking in granite," *Journal of Geophysical Research: Solid Earth*, vol. 940, no. B2, pp. 1745–1758, 1989.

[2] F. H. Harlow and W. E. Pracht, "A theoretical study of geothermal energy extraction," *Journal of Geophysical Research*, vol. 770, no. 35, pp. 7038–7048, 1972.

[3] A. C. Gringarten, "Man-made geothermal reservoirs," *Geophysical Aspects of the Energy Problem*, vol. 1:0, pp. 134–158, 1980.

[4] C. F. Pearson, M. C. Fehler, and J. N. Albright, "Changes in compressional and shear wave velocities and dynamic moduli during operation of a hot dry rock geothermal system," *Journal of Geophysical Research: Solid Earth*, vol. 880, no. B4, pp. 3468–3475, 1983.

[5] A. Ghassemi and G. Suresh Kumar, "Changes in fracture aperture and fluid pressure due to thermal stress and silica dissolution/precipitation induced by heat extraction from subsurface rocks," *Geothermics*, vol. 360, no. 2, pp. 115–140, 2007.

[6] J. Combs, S. K. Garg, and J. W. Pritchett, "Geothermal well stimulation technology: A preliminary review," in *Proceedings of the Geothermal Energy: The Reliable Renewable - Geothermal Resources Council 2004 Annual Meeting, GRC*, pp. 207–212, usa, September 2004.

[7] A. Ghassemi, S. Tarasovs, and A. H.-D. Cheng, "Integral equation solution of heat extraction-induced thermal stress in enhanced geothermal reservoirs," *International Journal for*

Numerical and Analytical Methods in Geomechanics, vol. 290, no. 8, pp. 829–844, 2005.

[8] S. A. Shapiro and C. Dinske, "Fluid-induced seismicity: Pressure diffusion and hydraulic fracturing," *Geophysical Prospecting*, vol. 570, no. 2, pp. 301–310, 2009.

[9] B. P. Goertz-Allmann and S. Wiemer, "Geomechanical modeling of induced seismicity source parameters and implications for seismic hazard assessment," *Geophysics*, vol. 780, no. 1, pp. KS25–KS39, 2012.

[10] S. A. Miller, "Modeling enhanced geothermal systems and the essential nature of large-scale changes in permeability at the onset of slip," *Geofluids*, vol. 150, no. 1-2, pp. 338–349, 2015.

[11] S. Sherburn, "Seismic monitoring during a cold water injection experiment, wairakei geothermal field: preliminary results," in *Proceedings of the 6th New Zealand Geothermal Workshop*, vol. 6, pp. 129–133, 1984.

[12] M. Stark, "Imaging injected water in The Geysers reservoir using microearthquake data," in *Proceedings of the Geothermal Resources Council Trans*, pp. 1697–1704, August 1990.

[13] D. Richter and G. Simmons, "Thermal expansion behavior of igneous rocks," in *International Journal of Rock Mechanics and Mining Sciences & Geomechanics Abstracts*, vol. 11, pp. 403–411, Elsevier, 1974.

[14] T.-F. Wong and W. F. Brace, "Thermal expansion of rocks: some measurements at high pressure," *Tectonophysics*, vol. 570, no. 2, pp. 95–117, 1979.

[15] H. W. Cooper and G. Simmons, "The effect of cracks on the thermal expansion of rocks," *Earth and Planetary Science Letters*, vol. 360, no. 3, pp. 404–412, 1977.

[16] H. J. Ramey, "Wellbore Heat Transmission," *Journal of Petroleum Technology*, vol. 140, no. 04, pp. 427–435, 1962.

[17] H. J. Ramey, "How to calculate heat transmission in hot fluid injection," *Pet. Eng*, vol. 36, p. 110, 1964.

[18] J. Hagoort, "Ramey's Wellbore heat transmission revisited," *SPE Journal*, vol. 90, no. 4, pp. 465–474, 2004.

[19] A. Satman and O. I. Tureyen, "Geothermal wellbore heat transmission: Stabilization times for "static" and "transient" wellbore temperature profiles," *Geothermics*, vol. 64, pp. 482–489, 2016.

[20] K. Kutun, O. I. Tureyen, and A. Satman, Analysis of wellhead production temperature derivatives. 1981.

[21] HJ. Ramey, *Reservoir engineering assessment of geothermal systems*, Department of Petroleum Engineering, Stanford university, 1981.

[22] H. Hajibeygi, D. Karvounis, and P. Jenny, "A hierarchical fracture model for the iterative multiscale finite volume method," *Journal of Computational Physics*, vol. 2300, no. 24, pp. 8729–8743, 2011.

[23] D. C. Karvounis, *Simulations of enhanced geothermal systems with an adaptive hierarchical fracture representation [Ph.D. thesis]*, 2013, Diss., Eidgenössische Technische Hochschule ETH Zürich, Nr. 21222.

[24] S. B. Pluimers, *Hierarchical fracture modeling approach [Ph.D. thesis]*, TU Delft, Delft University of Technology, 2015.

[25] D. W. Peaceman, "Interpretation of well-block pressures in numerical reservoir simulation (includes associated paper 6988)," *Society of Petroleum Engineers Journal*, vol. 18, no. 03, pp. 183–194, 1978.

[26] M. Karimi-Fard, L. J. Durlofsky, and K. Aziz, "An efficient discrete-fracture model applicable for general-purpose reservoir simulators," in *SPE Reservoir Simulation Symposium*, Society of Petroleum Engineers, 2003.

[27] B. P. Leonard, "A stable and accurate convective modelling procedure based on quadratic upstream interpolation," *Computer Methods in Applied Mechanics and Engineering*, vol. 190, no. 1, pp. 59–98, 1979.

[28] H. Sun, R. Feistel, M. Koch, and A. Markoe, "New equations for density, entropy, heat capacity, and potential temperature of a saline thermal fluid," *Deep-Sea Research I: Oceanographic Research Papers*, vol. 550, no. 10, pp. 1304–1310, 2008.

[29] T. Al-Shemmeri, *Engineering Fluid Mechanics*, Bookboon, 2012.

[30] C. Xu and P. Dowd, "A new computer code for discrete fracture network modelling," *Computers and Geosciences*, vol. 360, no. 3, pp. 292–301, 2010.

[31] S. A. Miller and A. Nur, "Permeability as a toggle switch in fluid-controlled crustal processes," *Earth and Planetary Science Letters*, vol. 1830, no. 1, pp. 133–146, 2000.

[32] M. Nemčok, A. Henk, R. A. Gayer, S. Vandycke, and T. M. Hathaway, "Strike-slip fault bridge fluid pumping mechanism: Insights from field-based palaeostress analysis and numerical modelling," *Journal of Structural Geology*, vol. 240, no. 12, pp. 1885–1901, 2002.

[33] S. A. Miller, C. Collettini, L. Chiaraluce, M. Cocco, M. Barchi, and B. J. P. Kaus, "Aftershocks driven by a high-pressure CO_2 source at depth," *Nature*, vol. 4270, no. 6976, pp. 724–727, 2004.

[34] M. Schoenball, C. Baujard, T. Kohl, and L. Dorbath, "The role of triggering by static stress transfer during geothermal reservoir stimulation," *Journal of Geophysical Research: Solid Earth*, vol. 1170, no. B9, Article ID B09307, 2012.

[35] F. Catalli, M.-A. Meier, and S. Wiemer, "The role of Coulomb stress changes for injection-induced seismicity: The Basel enhanced geothermal system," *Geophysical Research Letters*, vol. 400, no. 1, pp. 72–77, 2013.

[36] A. Ghassemi, "A review of some rock mechanics issues in geothermal reservoir development," *Geotechnical and Geological Engineering*, vol. 300, no. 3, pp. 647–664, 2012.

[37] T. Heinze, B. Galvan, and S. A. Miller, "A new method to estimate location and slip of simulated rock failure events," *Tectonophysics*, vol. 651, pp. 35–43, 2015.